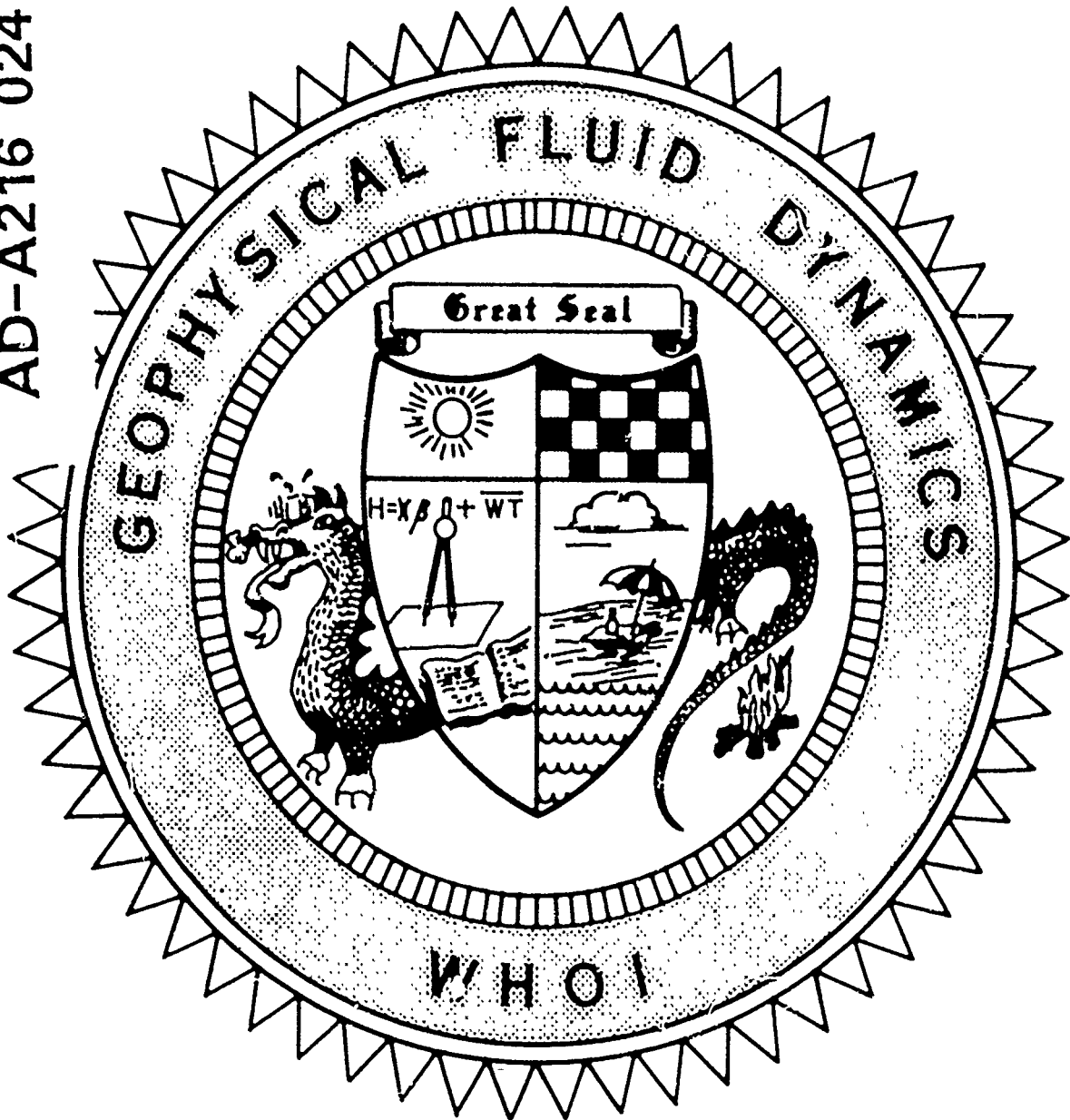


DTIC
ELECTE
DEC 12 1989
S D D

WHOI-89-26
1988

2

AD-A216 024



DISTRIBUTION STATEMENT A
Approved for public release
Distribution Unlimited

Course Lectures
Abstracts of Participants
Fellows Project Reports

89 12 11 008

WHOI-89-26

1988 Summer Study Program
in
Geophysical Fluid Dynamics

The Influence of Convection on Large-Scale Circulations

by

Glenn R. Flierl

Edited by
Pamela J. Goulart

Woods Hole Oceanographic Institution
Woods Hole, Massachusetts 02543

July 1989

Technical Report

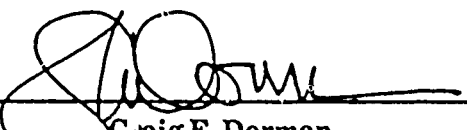
Accession For	
NTIS CRASH	<input checked="" type="checkbox"/>
DTIC TAB	<input type="checkbox"/>
Unannounced	<input type="checkbox"/>
Justification	
By	
Distribution	
Availability Codes	
Dist	Avail. Codes
A-1	Special

Funding was provided by the Office of Naval Research under contract Number N00014-82-G-0079, and the National Science Foundation through grant Number DMS-85-04166.

Reproduction in whole or in part is permitted for any purpose of the United States Government. This report should be cited as:
Woods Hole Oceanog. Inst. Tech. Rept., WHOI-89-26.

Approved for publication; distribution unlimited.

Approved for Distribution:


Craig E. Dorman
Acting Dean of Graduate Studies

GEOPHYSICAL FLUID DYNAMICS PROGRAM
Summer 1988
Staff and Visitors

NAME	AFFILIATION
Anderson, James	Stevens Institute of Technology
Berger, Mel	University of Massachusetts
Betts, Alan	Middlebury, Vermont
Brotherton, Chris	University of Washington
Dewar, William	Florida State University
Elphick, Christian	Columbia University
Emanuel, Kerry	Massachusetts Inst. of Technology
Flierl, Glenn	Massachusetts Inst. of Technology
Garrett, Christopher	Dalhousie University
Ierley, Glenn	Michigan Tech. University
Killworth, Peter	Hooke Institute - ENGLAND
Lindzen, Richard	Massachusetts Inst. of Technology
Malkus, Willem V.R.	Massachusetts Inst. of Technology
Nof, Doron	Florida State University-Tallahassee
Olson, Donald	University of Miami-Rosenstiel School of Marine & Atmospheric Science
Raymond, David	New Mexico Institute of Mining and Technology
Rooth, Claes	University of Miami-Rosenstiel School of Marine & Atmospheric Science
Roman, Richard	NCAR
Salmon, Rick	University of California-Scripps Institute of Oceanography
Spiegel, Edward	Columbia University
Stern, Melvin	Florida State University
Veronis, George	Yale University
Young, William	University of California-Scripps Institute of Oceanography
Zabusky, Norman	University of Pittsburgh

FELLOWS

Countryman, James	Yale University
Douady, Stephane	Ecole Normale Supérieure De Lyon
Dowling, Tim	California Institute of Technology
Maltrud, Mathew	Scripps Institute of Oceanography
Siems, Steven	University of Washington
Thuburn, John	Brasenose College-Oxford, ENGLAND
Waleffe, Fabian	Massachusetts Institute of Tech.
Woods, Andrew	University of Cambridge-Cambridge ENGLAND

PREFACE

The topic for the 30th Geophysical Fluid Dynamics Summer Program was "The Influence of Convection on Large-Scale Motions." The principal lecturer, Kerry Emanuel, presented the essential elements of dry convection, the thermodynamics of moist air, and moist convection (both precipitating and not). Building upon this excellent summary of the fundamentals of atmospheric convection, he then discussed its role in the dynamics of squall lines, tropical cyclones, and the 40-day tropical wave. Moist convection has not been discussed in recent GFD seminars, and Kerry's lectures provided a superb introduction to the topic for both Fellows and Staff. Other meteorologists discussed recent theoretical and observational research on atmospheric convecting systems.

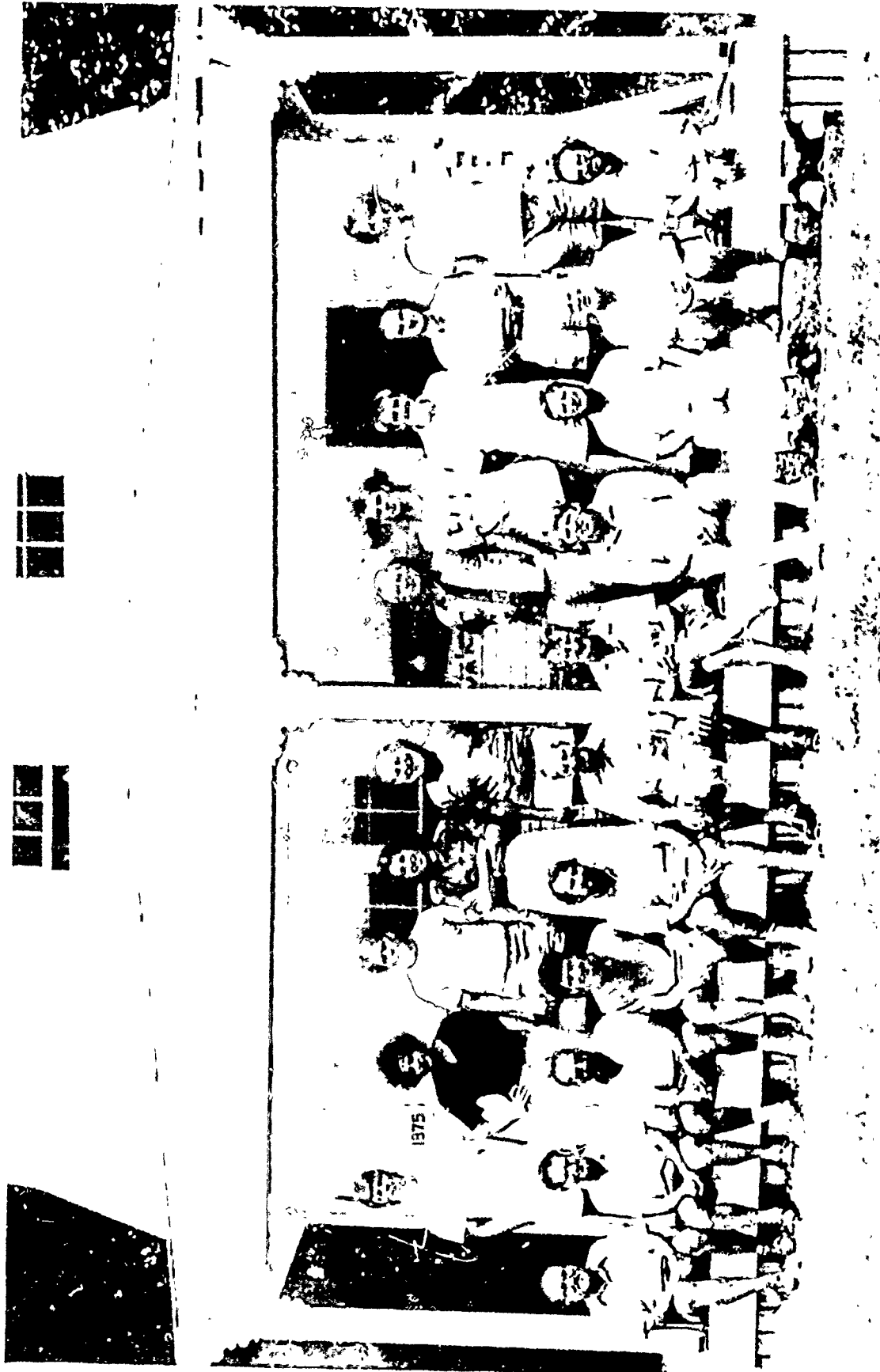
Convectively-driven flows in the ocean were described by Peter Killworth; Ed Spiegel and Christian Elphick reviewed the theory of nonlinear convection. These views of convection in other systems lent valuable perspectives on the atmospheric problem.

As always, lectures on many other topics enriched our summer program and suggested new research approaches to both Staff and Fellows. The reports from the Summer Fellows completed the program; many explored aspects of atmospheric convection or convectively influenced flows. Their reports are to be treated as unpublished manuscripts; some of this work will be developed into publications in the future.

Our summer was also enriched by other notable events. The softball team beat the PO team. The Education Office hosted a 30th Anniversary picnic and brought three of our alumni, Chris Garrett, Ruby Krishnamurti, and Frank Richter, to give anniversary lectures. Our thanks to Jack Whitehead and Education for a very pleasant event. Finally we were extremely pleased by the award of the Presidential Medal of Science to Joe Keller.

We thank the Office of Naval Research and the National Science Foundation for their support. Elizabeth Shadid provided secretarial assistance for the selection of Fellows, while Pamela Goulart provided essential support for our efforts during the summer and in preparing this final report. Finally we thank A.L. Peirson for his administrative efforts in making this program possible.

Glenn Flierl
Director



Seated Left to Right - Melvin Stern, Norman Zabusky, Richard Rotunno, Fabian Waleffe, Kerry Emanuel,
George Veronis, Bill Young, Timothy Dowling, Alan Betts, Claes Rooth, Glenn Flierl

Standing Left to Right - Nathew Maltrud, Stephane Douady, Steven Siems, Paola Cessi, Joe Keller,
Willem Malkus, John Thuburn, Rick Salmon, Lorenzo Polvani, Jim Countryman

C O N T E N T S

CONTENTS	PAGE
1. Review of Dry Convection	8
2. Other Buoyant Plumes And Thermals.	16
3. Global Convection.	22
4. Moist Thermodynamics	30
5. Non Precipitating Cloud.	35
6. Taxonomy Of Precipitating Clouds	45
7. The Dynamics Of Precipitating Convection	55
8. Tropical Cyclones: Observations And Energetics, .	67
9. Dynamics Of Tropical Cyclones,	89
10. Oscillations In Convectively-Adjusted Flows. . . .	97

ABSTRACTS OF PARTICIPANTS

Interaction Of The Oceanic Convective Boundary Layer And Tropical Climate

Alan Betts 110

Convective Parameterization In Large Scale Models

Alan Betts 111

Gravity Waves, Compensating Subsidence And Moist Convective Adjustment

Chris Bretherton - Title Only

Energy Extremization By Pseudo-Advection

George Carnevale & Geoff Vallis 111
William Young

A Nonlinear, Time Dependent Thermocline Theory

Bill Dewar 113

Large-Scale Dynamics And Topology Near The Onset Of Convection

Christian Elphick & E. A. Spiegel 116

Generation Of Baroclinic Motions From Barotropic Eddies

Glenn Flierl 131

Some Strait Talk

Chris Garrett 133

Nonlinear Waves, Solitons, And Wave Transport In Buoyant Conducts

Karl Helfrich & Jack Whitehead 134

Exact Non-Reflecting Boundary Conditions	
Joseph Keller & Dan Givoli	135
Deep Convection In The World Ocean	
Peter Killworth	138
Flows Produced By Discrete Sources Of Buoyancy	
Peter Killworth	139
Large Scale Flow In Turbulent Rayleigh-Benard Convection	
Ruby Krishnamurti	139
Upper Bounds On Functions Of The Dissipation Rate In Turbulent Shear Flow	
Willem Malkus and L. Smith	140
Eddy-Wall Interactions	
Doron Nof	141
Mesoscale Convection In The Ocean	
Don Olson	142
Entrainment And Detrainment In Cumulus Clouds	
David Raymond	143
Dynamical Models For Melt Segregation	
Frank Richter	154
Effects Of Geothermal Heat Flux And Topography On The Convective Ventilation Of Confined Basins	
Claes Rooth	154

A Theory For A Strong, Long-Lived Squall Line	
Richard Rotunno	156
A Geometric View Of Dynamical Approximations	
Rick Salmon	157
Separation Of A Barotropic Jet From A Coast: Theory And Experiment	
Melvin Stern	159
Vertex Dynamics Of Stratified Flows	
Gretar Tryggvason	159
Diffusion Coefficients And Velocities From Tracers	
George Veronis	160
Arrested Shear Dispersion And Other Models Of Anomalous Diffusion	
William Young	164
Recent Results On Vortex Reconnection In 3D Flows	
Norman Zabusky	165

ABSTRACTS OF FELLOWS

Faraday Instability

Stephane Douady

114

Jupiter's Great Red Spot As A Shallow
Water System

Timothy Dowling

114

The Fluid Dynamics And Thermodynamics
Of Eruption Columns

Andrew Woods

161

FELLOWS PROJECT REPORTS

Baroclinic Models And Hurricane Motion

Jim Countryman 166

**Capillary-Gravity Surface Wave Modes In A
Closed Vessel With Edge Constraint: Eigen-
Frequency And Dissipation**

Stephane Douady 198

**Rotating Rayleigh-Benard Convection
With Fixed Flux Boundaries**

Tim Dowling 230

**Low Frequency Oscillations In A
Linear Coupled Atmosphere-Ocean Model**

Mat Maltrud 248

One-Dimensional Model For Microbursts

Steve Siems 268

**The 30-60 Day Oscillation In The Tropics-Wind
Evaporation Feedback And Up-Down Asymmetry**

John Thuburn 284

3D Instability Of Bounded Elliptical Flow

Fabian Waleffe 302

A Model Of Squall Line Propagation

Andrew Woods 316

1988 Summer Study Program

in

Geophysical Fluid Dynamics

THE INFLUENCE OF CONVECTION

ON LARGE-SCALE CIRCULATION

LECTURES

Kerry Emanuel

Massachusetts Institute of Technology

INTRODUCTION

The topic of this Woods Hole GFD summer course, "The effect of convection on large scale circulations," is applicable to atmosphere, ocean, and mantle motions. The lectures will focus on atmospheric convection. Here, the phase changes of water introduce crucial and irreversible physics not present in dry convection.

The necessity of considering moist convection poses the following challenge: Traditionally, the style of GFD research, especially at Woods Hole, has been to make clear the dominant physics by combining mathematical rigor in investigating simple models with complementary controlled lab experiments. In this way, GFD theory has expanded to encompass numerous "simple" model motions that by limiting the number of physical processes makes clear dominant interactions. This is invaluable in interpreting *in situ* data where a myriad of physical processes act together. Unfortunately, no laboratory analog exists that includes the micro-physics of water phase changes (and associated condensate fallout) coupled with convective dynamics. One way to bridge the gap between theoretical models and observational data is numerical simulations. With simulation, though, care needs be especially taken with parameterizations, since careless choice of parameterization can produce expected, but wrong, results.

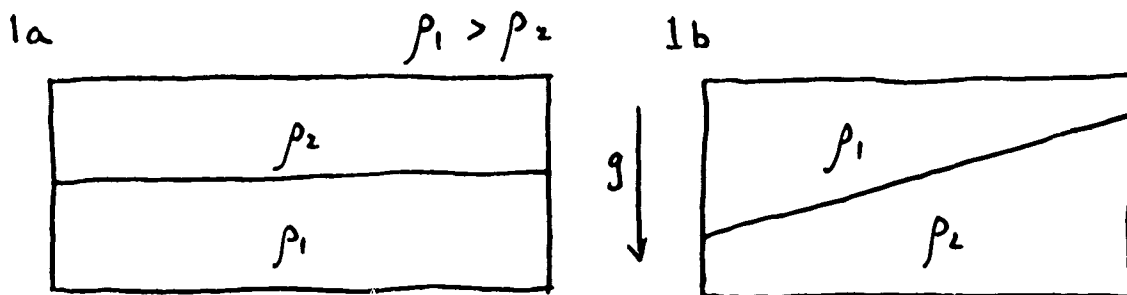
Outline of Course:

First, an overview of dry convection will be given, including theory and laboratory experiments. Then, after developing relevant thermodynamics, moist convection is addressed. The new sets of phenomenon introduced by moisture are significant: cumulus clouds are very unlike dry plumes. Finally, large scale dynamical systems in convectively adjusted atmospheres are discussed.

1. REVIEW OF DRY CONVECTION

What is Convection?

An encyclopedia definition of convection is "Any motion resulting from action of a temporally uniform body force acting on density fluctuations." The configurations shown in both figures below would then result in convection. By making the definition that follows, only configuration 1a results in convection: "Motion due to an unstable density distribution along the vector of the body force."



In the first lecture we define the buoyancy force, develop a simplified system of equations using the anelastic and Boussinesq approximations, and begin our consideration of dry convection by studying a plume above a point source of heat.

Buoyancy

For this summer the only body force considered is gravity. We now develop the associated buoyancy term which expresses the acceleration of the fluid due to gravity acting on density variations.

The vertical momentum equation for a fluid in a constant vertical gravity field is:

$$\frac{dw}{dt} = -\alpha \frac{\partial p}{\partial z} - g \quad (1.1)$$

where

$\alpha \equiv$ specific volume

$p \equiv$ pressure

$w \equiv$ vertical velocity

The specific volume and pressure are defined as the sum of mean and perturbation components:

$$\alpha(x, y, z, t) = \bar{\alpha}(z) + \alpha'(x, y, z, t) \quad (1.2)$$

$$p(x, y, z, t) = \bar{p}(z) + p'(x, y, z, t) \quad (1.3)$$

The mean state is assumed to be in hydrostatic equilibrium:

$$\bar{\alpha} \frac{\partial \bar{p}}{\partial z} = -g \quad (1.4)$$

Expanding the vertical momentum equation:

$$\frac{dw}{dt} = -\bar{\alpha} \frac{\partial \bar{p}}{\partial z} - \alpha' \frac{\partial \bar{p}}{\partial z} - \alpha \frac{\partial p'}{\partial z} - g$$

The first and last terms on the right hand side cancel by (1.4) and making the substitution $-\partial \bar{p} / \partial z = g / \bar{\alpha}$ we obtain:

$$\frac{dw}{dt} = B(x, y, z, t) - \alpha \frac{\partial p'}{\partial z} \quad (1.5)$$

where B is buoyancy defined as:

$$B \equiv \frac{g \alpha'}{\bar{\alpha}} \quad (1.6)$$

The buoyancy is the component of vertical acceleration due to density perturbations. The second component of vertical acceleration, $-\alpha(\partial p' / \partial z)$, is commonly called the non-hydrostatic pressure gradient acceleration and usually arises from dynamical effects of forced momentum changes.

For a general fluid, specific volume is a function of pressure, volume, and other possible parameters (ie. salinity, suspended water content) which we heuristically group together in one variable, S . By the chain rule:

$$\frac{d\alpha}{\alpha} = \frac{1}{\alpha} \left(\frac{\partial \alpha}{\partial T} \right)_{p,S} dT + \frac{1}{\alpha} \left(\frac{\partial \alpha}{\partial p} \right)_{T,S} dp + \frac{1}{\alpha} \left(\frac{\partial \alpha}{\partial S} \right)_{p,T} dS \quad (1.7)$$

The coefficient of thermal expansion is defined:

$$\beta \equiv \frac{1}{\alpha} \left(\frac{\partial \alpha}{\partial T} \right)_{p,S} \quad (1.8)$$

We define temperature and S as mean plus perturbation (primed) components,

$$T = \bar{T} + T'$$

$$S = \bar{S} + S'$$

For small T' , p' , and S' , by (7), buoyancy can be approximated as:

$$B = g \left[\beta T' + \frac{1}{\alpha} \left(\frac{\partial \alpha}{\partial p} \right)_{T,S} p' + \frac{1}{\alpha} \left(\frac{\partial \alpha}{\partial S} \right)_{p,T} S' \right] \quad (1.9)$$

For an ideal gas,

$$p\alpha = RT \quad (1.10)$$

Consequently, $\beta = 1/T$ and $\frac{1}{\alpha} \left(\frac{\partial \alpha}{\partial p} \right)_T = -1/p$. Note that, by the ideal gas law (1.10), $\frac{1}{\alpha} \left(\frac{\partial \alpha}{\partial S} \right)_{p,T} = 0$. Substituting in (1.9) gives

$$B = g \left[\frac{T'}{T} - \frac{p'}{p} \right] \quad (1.11)$$

We now demonstrate that the contribution to buoyancy in an ideal gas due to pressure variations can be neglected when the fluid velocities are substantially subsonic. Integrating the horizontal momentum equation:

$$\frac{Du}{Dt} = -\alpha \frac{\partial p'}{\partial x} \quad (1.12)$$

with respect to x , and assuming the Lagrangian horizontal velocity derivative scales as $U_0(\partial U_0/\partial x)$ we obtain:

$$p'\alpha \sim U_0^2/2 \quad (1.13)$$

Rearranging and using the gas law:

$$\frac{p'}{p} \sim \frac{U_0^2}{RT} = \frac{\gamma U_0^2}{c^2} \quad (1.14)$$

where $c \equiv (\gamma RT)^{1/2}$ is the speed of sound and $\gamma \equiv c_p/c_v$

So, if $U_0^2/c^2 \ll T'/T$ the contribution to density due to pressure variations is negligible and the buoyancy becomes simply:

$$B = g\left(\frac{T'}{T}\right) \quad (1.15)$$

Anelastic and Boussinesq Approximations

In this section we obtain two approximations by scaling the momentum and mass continuity equations. In full form the mass continuity equation is prognostic, containing the time derivative $\partial\rho/\partial t$. When the flow is considerably subsonic, $U_0 \ll c$, dropping negligible terms results in a diagnostic continuity equation relating velocity divergence to vertical advection of mass. This, the anelastic approximation, eliminates sound waves.

The Boussinesq approximation neglects small terms that arise from the condition that the vertical extent of the motion is much less than the scale height, H . The scale height is defined as the vertical scale over which density changes are $O(1)$. With both approximations, the mass continuity eqn. becomes simply the statement of zero 3-D velocity divergence. Furthermore, the specific volume (or density) is replaced by a constant mean value in the momentum equations except when coupled with gravity. It is worth noting that the conditions for the Boussinesq approximation, $D \ll H$, are typically not as well met as the anelastic condition, $U_0 \ll c$. However, qualitatively, the Boussinesq approximation seldom eliminates phenomenon and usually results only in quantitative changes.

We begin by rewriting the mass continuity equation using the ideal gas law and the first law of thermodynamics. From the ideal gas law

$$\frac{1}{\rho} \frac{d\rho}{dt} = \frac{1}{p} \frac{dp}{dt} - \frac{1}{T} \frac{dT}{dt} \quad (1.16)$$

and from the adiabatic form of the first law of thermodynamics:

$$\frac{1}{p} \frac{dp}{dt} = \frac{c_p}{RT} \frac{dT}{dt} \quad (1.17)$$

Finally, using $c_v + R = c_p$, we now write the continuity equation:

$$-\left(\frac{\partial u}{\partial x} + \frac{\partial v}{\partial y} + \frac{\partial w}{\partial z}\right) = \frac{c_v}{c_p} \frac{1}{p} \frac{dp}{dt} = \frac{c_v}{c_p} \left[\frac{\partial}{\partial t} + u \frac{\partial}{\partial x} + v \frac{\partial}{\partial y} + w \frac{\partial}{\partial z} \right] \log(p) \quad (1.18)$$

We use the following scaling (primed variables are $O(1)$ and dimensionless):

$$\begin{aligned} (u, v) &= U_0(u', v') \\ (x, y) &= L(x', y') \\ w &= W_0(w') \\ z &= D(z') \end{aligned}$$

Assuming the various terms of the velocity divergence have similar magnitude allows:

$$\frac{U_0}{L} \sim \frac{W_0}{D}$$

Now we scale the pressure terms. On the basis of the vertical momentum equation we take:

$$\frac{\partial \log p}{\partial z} \sim \frac{-g}{RT} \equiv \frac{1}{H}$$

where H is the scale height of the atmosphere.

We then scale both the local time derivative and the horizontal pressure gradient by equating their magnitudes to the inertial terms of the horizontal momentum equation:

$$\frac{\partial \log p}{\partial t} \sim U_0 \frac{\partial \log p}{\partial x} \sim \frac{U_0^2}{RT} \frac{\partial U_0}{\partial x} \sim \frac{U_0^3}{RTL}$$

The separate scaling for the various pressure derivatives are then

$$\frac{\partial \log p}{\partial z} = \frac{1}{H} \left(\frac{\partial \log p}{\partial z} \right)'$$

$$\frac{\partial \log p}{\partial t} = \frac{U_0^3}{RTL} \left(\frac{\partial \log p}{\partial t} \right)'$$

$$\frac{\partial \log p}{\partial x} = \frac{U_0^2}{RTL} \left(\frac{\partial \log p}{\partial x} \right)'$$

With this scaling, equation (1.18) becomes:

$$-\left(\frac{\partial u'}{\partial x'} + \frac{\partial v'}{\partial y'} + \frac{\partial w'}{\partial z'} \right) = \frac{U_0^2}{c^2} \left[\frac{\partial}{\partial t'} + u' \frac{\partial}{\partial x'} + v' \frac{\partial}{\partial y'} \right] \log p' + \frac{c_v}{c_p} \frac{D}{H} w' \frac{\partial}{\partial z'} \log p' \quad (1.19)$$

where $c = [(c_p/c_v)RT]^{1/2}$ is the speed of sound in an ideal gas.

For atmospheric and oceanic motions, $U_0 \ll c$. We make the anelastic approximation to the mass continuity equation, dropping $O(U_0/c)$ terms and obtain:

$$-\left(\frac{\partial u'}{\partial x'} + \frac{\partial v'}{\partial y'} + \frac{\partial w'}{\partial z'} \right) = \frac{c_v}{c_p} \frac{D}{H} w' \frac{\partial}{\partial z'} \log p' \quad (1.20)$$

The Boussinesq approximation assumes $D/H \ll 1$. The continuity equation then simplifies to:

$$-\left(\frac{\partial u'}{\partial x'} + \frac{\partial v'}{\partial y'} + \frac{\partial w'}{\partial z'} \right) = 0 \quad (1.21)$$

For energetic consistency, it can be shown that the perturbation densities, when they multiply inertial terms in the momentum equations, need to be dropped. Therefore, the Boussinesq approximation neglects density variations except where they are coupled with

gravity. Noting that we have neglected all forms of diffusion we now write our complete system in dimensional variables:

$$\frac{du}{dt} = -\bar{\alpha} \frac{\partial p'}{\partial x} \quad (1.22)$$

$$\frac{dv}{dt} = -\bar{\alpha} \frac{\partial p'}{\partial y} \quad (1.23)$$

$$\frac{dw}{dt} = -\bar{\alpha} \frac{\partial p'}{\partial z} + B \quad (1.24)$$

$$\frac{\partial u}{\partial x} + \frac{\partial v}{\partial y} + \frac{\partial w}{\partial z} = 0 \quad (1.25)$$

$$\frac{dB}{dt} = 0 \quad (1.26)$$

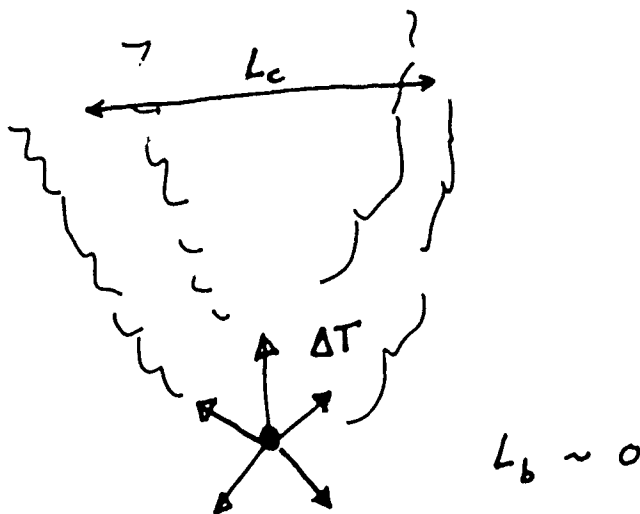
where we have divided the pressure and specific volume into mean and perturbation parts with the mean field in hydrostatic balance. The buoyancy, B , was previously defined, $B \equiv g(\alpha'/\bar{\alpha})$. Note that we have switched notations again, and primed variables p' and α' now refer to dimensional perturbation variables.

1A. LOCAL AND GLOBAL CONVECTION

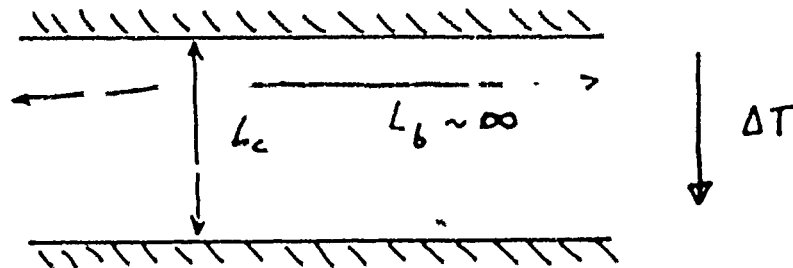
Definition:

We have to compare the length scale of the source of buoyancy L_b and the convective length scale L_c :

- 1) the convection is said to be local if $L_b \ll L_c$ for instance in case of a point source of heat:



- 2) the convection is said to be global if $L_b \gg L_c$ for instance in case of convection between two plates:

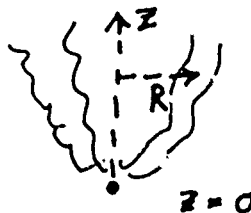


LOCAL CONVECTION

Point Source of Heat

We consider a plume (a continuous buoyant jet) above a point which provides a constant heat flux. We assume the plume to be fully turbulent, with a very high Reynolds number $Re = UL/\nu$, where U and L are respectively the typical velocity and length scale, and ν is the viscosity. We also assume that the ambient fluid is infinite and homogeneous.

Experimentally, it has been observed that if Re is sufficiently high, the flow becomes independent of its value. So we assume $Re = \infty$ and that the effect of turbulent mixing is dominant compared to molecular diffusion. We thus neglect the viscosity and the thermal diffusion.



External Parameter

In this approximation, the external quantities are:

- the gravity g
- the temperature flux F_T
- the thermal expansion coefficient β

These lead physically to only one relevant external parameter, the buoyancy flux:

$$F_0 = g\beta F_T \quad [L^4 t^{-3}]$$

Dimensional Analysis

As we neglect the viscosity, and the thermal diffusion, the only length scale at a high z is z itself. So we can only use F_0 and z in order to build the other quantities. As the plume is turbulent, we look only at the time average of the different quantities. The only way to obtain a velocity is to use the quantity

$$F_0^{\frac{1}{2}} z^{-\frac{1}{2}} \quad [L t^{-1}]$$

Thus the time average velocity is:

$$\bar{w} = F_0^{\frac{1}{2}} z^{-\frac{1}{2}} \cdot \text{Function}(r/R)$$

where r is the radial
As is usual in

the radius of the plume.
, we thus take the typical velocity as:

$$\bar{w} \propto F_0^{\frac{1}{2}} z^{-\frac{1}{2}}$$

with a coefficient of order 1.

In the same way, we write the buoyancy as:

$$\bar{B} \propto F_0^{\frac{1}{2}} z^{-\frac{1}{2}} \quad [L t^{-2}]$$

and the radius of the plume:

$$\bar{R} \propto z$$

Of course, all these arguments work only because we assume a infinite fluid without viscosity and molecular diffusion, i.e. without any other length scale than z .

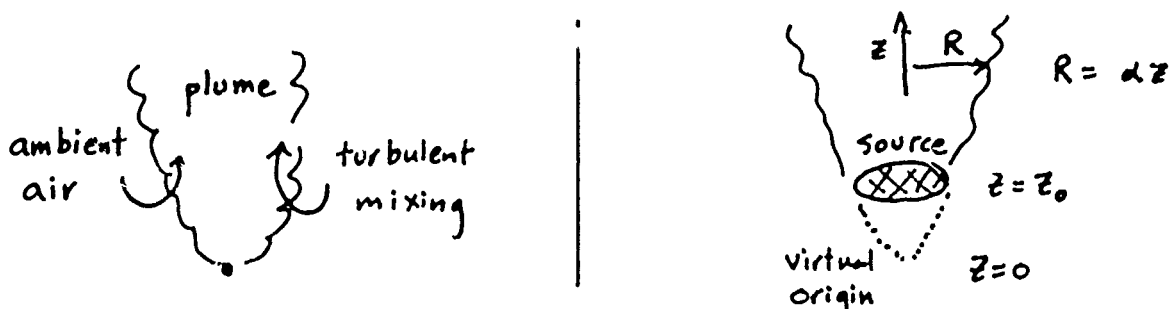
But experimentally, these arguments work even in a closed room, as Yih measured in 1951:

$$\bar{w} = 4.7 F_0^{\frac{1}{2}} z^{-\frac{1}{2}} \exp(-96 r^2 / z^2)$$

One can remark that the mass flux increases with height as

$$\overline{w R^2} \propto z^{\frac{3}{2}}$$

This result is characteristic of turbulent convection can be explained by the entrainment of the ambient air by the turbulent motion.



Dimensional analysis gives \bar{w} and \bar{B} becoming infinite when z goes to zero, but this just comes from the assumption of a point source of heat. In a laboratory experiment, the source has a finite dimension; the theory can be corrected by definition of a virtual origin.

Notes by Jim Countryman and Stephane Douady

2. OTHER BUOYANT PLUMES AND THERMALS

First, recall the results from the previous lecture for a dry convecting plume. Scale analysis led to the following relationships: $R \sim z$, $B \sim z^{-5/3} F_0^{2/3}$, $w \sim (F_0/z)^{1/3}$. From these relationships we can calculate that the mass flux must be $MF \sim wR^2 \sim z^{5/3}$. This increase in mass flux is interpreted as entrainment by the plume of the ambient fluid, which then acquires finite buoyancy by mixing with the plume fluid. Rouse, Yih, and Humphreys (1952) performed plume experiments to confirm these similarity solutions, and succeeded in finding mean plume properties that fit the following expressions:

$$\bar{w} = 4.7(F/z)^{1/3} \exp(-96r^2/z^2)$$

$$B = g(\overline{T - T_0})/T_0 = 11.0 F_0^{2/3} z^{-5/3} \exp(-71r^2/z^2)$$

which are in agreement with the dimensional analysis.

Now consider a line source of buoyancy, with flux per unit length, F_0 . In analogy with a point source, F_0 is the relevant dimensional parameter. The dimensions of F_0 are $L^3 t^{-3}$, which implies $t \sim z f_0^{-1/3}$. Thus in this case dimensional analysis yields

$$\begin{aligned} w &\sim F_0^{1/3} \quad (\text{independent of } z) \\ B &\sim F_0^{2/3} z^{-1} \\ R &\sim z \end{aligned} \tag{2.1}$$

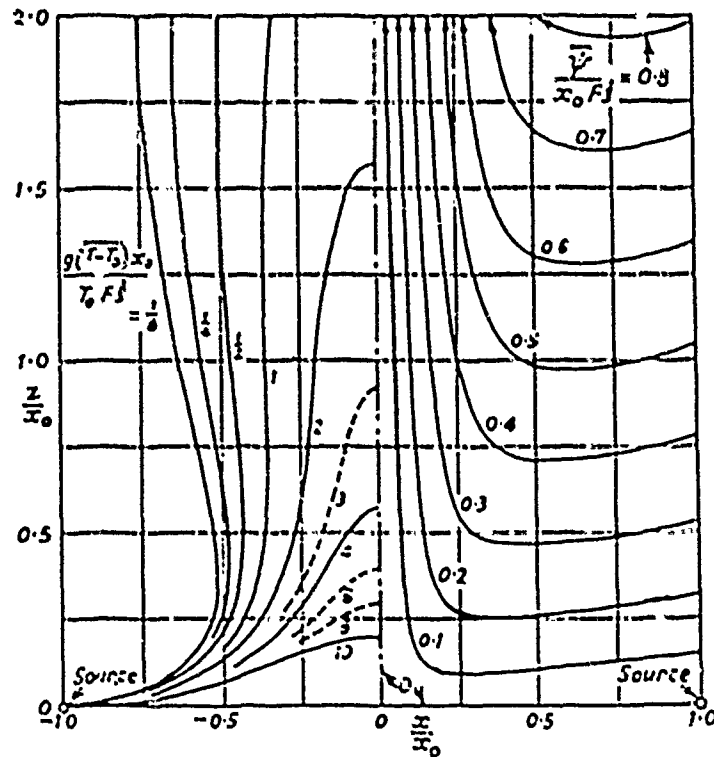
Notice that w and B do not fall off with height as quickly as in the point source case, due to the loss of one dimension.

Consider the case of two parallel line sources, each of strength F_0 . For large z we expect that the two lines will be indistinguishable from a single line of double strength $2F_0$. (See figure.) Experimentally, the two plumes entrain each other at surprisingly small z , giving the appearance of a single plume.

Now we will reexamine a point source of buoyancy, but this time it will also be a point source in time (i.e., a flash or explosion). The resulting buoyant cloud is called a thermal. In this case, the relevant dimensional parameter is the volume-integrated buoyancy, which we denote by Q . The dimensions of Q are L^4/t^2 , which implies $t \sim z^2 Q^{-1/2}$. Dimensional analysis yields

$$\begin{aligned} w &\sim Q^{1/2} z^{-1} \\ B &\sim Q z^{-3} \\ R &\sim z \end{aligned} \tag{2.2}$$

The thermal experiences a greater fall off with height of w and B than does the steady plume, due to the gain of one dimension (time). Notice that the mass flux $wR^2 \sim z$ again increases with height, implying entrainment. In this case both the drag due to entrainment and the loss of buoyancy with height ($B \sim z^{-3}$) act to slow down the rate of ascent of the thermal.



Mean isotherms and streamlines for turbulent convection due to two parallel line sources located at the left and right boundaries (after Rouse, Baines, and Humphreys, 1953)

We now leap into a new regime. What happens if we have a local source of heat in a stratified fluid? We introduce a stratification parameter

$$N^2 \equiv \frac{g}{\bar{\alpha}} \frac{\partial \bar{\alpha}}{\partial z} \quad (2.3)$$

The quantity N has the dimensions of $1/t$ and is known as the Brunt-Väisälä frequency. It corresponds to the frequency of oscillations of gravity waves, i.e., waves whose restoring force is due to buoyancy variations. There is now an external time scale $t \sim 1/N$, and hence similarity solutions like those above derived from dimensional analysis may not exist.

Now return to the case of a thermal, but this time embed it in a stratified medium. A length scale based on the two relevant dimensional parameters may be found for the problem: $L \sim (Q/N^2)^{1/4}$. This is related to the height the thermal will reach before it becomes neutrally buoyant (i.e., how high the mushroom cloud goes).

The seminal paper on this subject was written by Morton, Taylor and Turner in 1956, and the following approach is based on that work. Borrowing from the results of dimensional analysis, we assume first that the radial profiles of the thermal are geometrically similar at all heights z (i.e., the plume behaves *locally* as a true similarity plume). Second, we define entrainment as a horizontal influx of ambient fluid moving at speed \bar{u} , and assume

$$\bar{u} = -\alpha w \quad (2.4)$$

where α is an entrainment coefficient.

Characterize the thermal by some mean radius $R(z)$, and assume spherical geometry. Also make the Boussinesq approximation that density contrasts are negligible unless multiplied by g . Then the rate at which mass increases is

$$\begin{aligned} \frac{d}{dt} \left(\frac{4}{3} \pi R^3 \right) &= (4\pi R^2)(-\bar{u}) \\ &= (4\pi R^2)(\alpha w) \end{aligned} \quad (2.5)$$

We may write the momentum equation as:

$$\frac{d}{dt} \left(\frac{4}{3} \pi R^3 w \right) = \frac{4}{3} \pi R^3 B \quad (2.6)$$

Finally, conservation of heat yields:

$$\frac{d}{dt} \left(\frac{4}{3} \pi R^3 T_b \right) = (4\pi R^2)(\alpha w) T_a \quad (2.7)$$

where T_a and T_b are the temperatures of the ambient fluid and the thermal, respectively. By combining equations (2.5) and (2.7) we can find an expression for the time rate of change of buoyancy B :

$$\begin{aligned} \frac{d}{dt} \left(\frac{4}{3} \pi R^3 T_b \right) &= T_a \frac{d}{dt} \left(\frac{4}{3} \pi R^3 \right) \\ &= \frac{d}{dt} \left(\frac{4}{3} \pi R^3 T_a \right) - \frac{4}{3} \pi R^3 \frac{dT_a}{dt} \\ \Rightarrow \frac{d}{dt} \left(\frac{4}{3} \pi R^3 [T_b - T_a] \right) &= -\frac{4}{3} \pi R^3 w \frac{dT_a}{dz} \end{aligned} \quad (2.8)$$

where we have used $\frac{d}{dt} = w \frac{d}{dz}$. Multiply eqn. (2.8) by g/\bar{T}_a , use $B = g\beta\Delta T = g(T_b - T_a)/\bar{T}_a$ (with $\beta \approx 1/\bar{T}_a$ for an ideal gas). This gives

$$\frac{d}{dt} \left(\frac{4}{3} \pi R^3 B \right) = -\frac{4}{3} \pi R^3 w N^2 \quad (2.9)$$

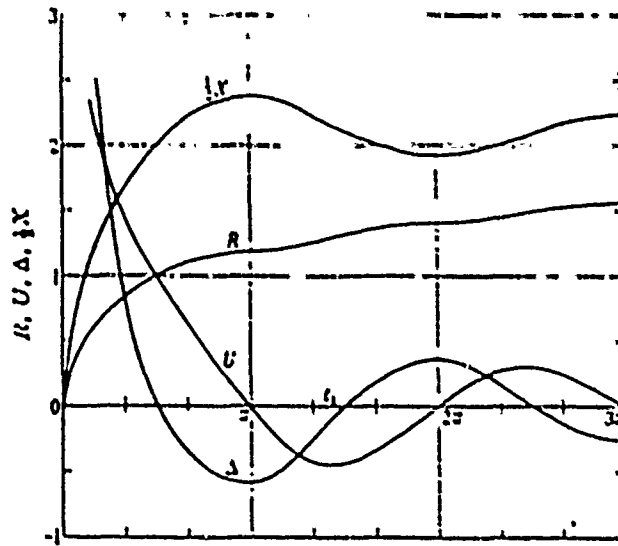
with

$$N^2 = \frac{g}{\bar{T}_a} \frac{\partial T_a}{\partial z}$$

To solve the set of equations (2.5), (2.6) and (2.9) make the substitution $\frac{d}{dt} = w \frac{d}{dz}$. The results are as follows:

$$\begin{aligned} R &= \alpha z \\ B &= -\frac{1}{4}N^2 z + \frac{3Q}{4\pi\alpha^3} z^3 \\ w &= -\frac{1}{16}N^2 z^2 + \frac{3Q}{8\pi\alpha^3 z^2} \end{aligned} \quad (2.10)$$

Note that we recover the unstratified results if $N = 0$.



The solutions for the dimensionless radius (R), height (z), buoyancy (Δ), and vertical velocity (u) of a thermal in a uniform stably stratified fluid (from Morton, Taylor, and Turner, 1956)

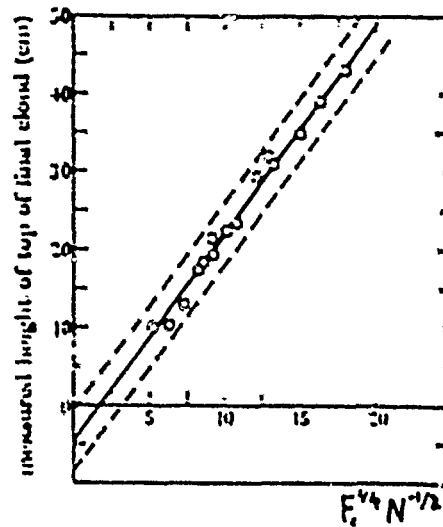
The maximum height reached by the thermal, z_{\max} , is given by

$$z_{\max} \equiv z(w = 0) = \left(\frac{6Q}{\pi\alpha^3 N^2} \right)^{1/4} \quad (2.11)$$

The height at which the buoyancy of the thermal drops to zero, z_{final} , is given by

$$z_{\text{final}} \equiv z(B = 0) = \left(\frac{3Q}{\pi\alpha^3 N^2} \right)^{1/4} = 0.84 z_{\max} \quad (2.12)$$

[Note the presence of the length scale $L \sim (Q/N^2)^{1/4}$.]



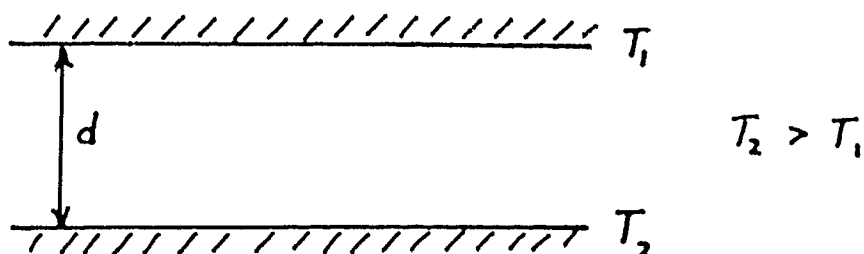
Measurements of the final height above the release point of a buoyant thermal in a stably stratified ambient fluid. The linear regression line is drawn in and the dashed lines represent twice the standard deviation. (from Morton, Taylor, and Turner, 1956)

Since $z_{max} > z_{final}$, we see that the thermal initially overshoots its equilibrium height. It then executes a damped oscillation about z_{final} .

The entrainment coefficient α may be deduced from observations using either eqns. (2.11), (2.12), or (2.10a). Woodward (1959) performed experiments with laboratory thermals and found that the thermals transverse a cone of half angle 15° , corresponding to $\alpha = 0.27$. Using eqn. (2.12) Morton, Taylor, and Turner determined experimentally that $\alpha = 0.285$, which is consistent with the value of Woodward and seems to be representative of most buoyant thermals.

To summarize, the main features of dry local convection include entrainment, linear (conical) expansion of radius with height, and a limiting height in the case of stratification. Later, when we examine the nature of cumulus convection, we will observe dramatically different phenomena.

We now move on to the topic of global convection. The paradigm is the convection of a homogeneous fluid between parallel plates, known as Rayleigh convection. The plates are assumed to be held at constant temperatures T_1 and T_2 (this assumes infinite heat conductivity for the plates) and separated by a distance d :



We specify the lower plate temperature T_2 to be hotter than the upper plate temperature T_1 . For small $\Delta T \equiv T_2 - T_1$, heat is transported by molecular diffusion and there is no convection. Above a certain critical ΔT convection begins. The basic parameters of the problem are the buoyancy $g\beta\Delta T$, d , ν , and κ , where the latter two variables are the viscosity and thermal diffusivity. The problem has two independent non-dimensional parameters, conventionally taken to be

$$Ra = \frac{g\beta\Delta T d^3}{\nu\kappa}, \quad \text{the Rayleigh number} \quad (2.13)$$

and

$$\sigma = \nu/\kappa, \quad \text{the Prandtl number} \quad (2.14)$$

The Ra can be interpreted as the ratio of convective heat flux to molecular heat flux, while σ is the ratio of the characteristic time scales for the diffusion of heat versus the diffusion of momentum by molecular processes.

The ratio of Ra and σ is

$$\frac{Ra}{\sigma} = \frac{g\beta\Delta T d^3}{\nu^2} \quad (2.15)$$

For laminar flow, where there is a balance between buoyancy and viscosity, $B = g\beta\Delta T$ scales as $w_0\nu/d^2$, which implies:

$$\frac{Ra}{\sigma} \sim \frac{w_0 d}{\nu} \equiv Re, \quad \text{the Reynolds number} = \frac{g\beta\Delta T d^3}{\nu^2} \quad (2.16)$$

References

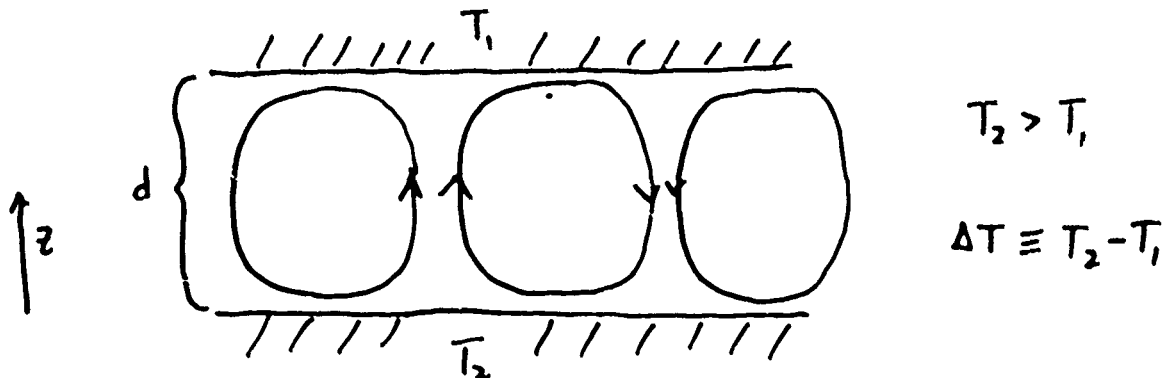
- Morton, B.R., Sir G. Taylor, and J.S. Turner (1956). Turbulent gravitational convection from maintained and instantaneous sources. *Proc. Roy. Soc.*, A243, 1-23.
- Rouse, H., C.-S. Yih, and H.W. Humphreys (1952). Gravitational convection from a boundary source. *Tellus*, 4, 201-210.
- Woodward, B. (1959). The motion in and around isolated thermals. *Quart. J. Roy. Met. Soc.*, 85, 144-151.

Notes by Tim Dowling and Mat Maltrud

3. GLOBAL CONVECTION

Rayleigh - Benard Convection

We will examine a thin, horizontal layer of fluid between two infinite plates. The lower plate is at a higher temperature than the upper boundary so that a negative heat gradient exist through the fluid. At weak enough values of the gradient the heat exchange is carried by molecular diffusion. As the gradient is increased in magnitude, con-ective cells form.



Empirically, it has been found that the aspect ratio of the depth of the fluid to the width of the convective cells is of the order of 1:1; while atmospheric convection has aspect ratios ranging from 1:30 up to 1:60. This, to date, has not been explained satisfactorily.

The problem of Rayleigh-Benard convection can be completely specified through the four physical parameters of the problem;

- d — depth of the layer
- ν — molecular diffusivity
- κ — thermal diffusivity
- $g\beta\Delta T$ — maximum buoyancy differential

It is assumed that parallel plates are perfectly conducting so that T_1 and T_2 remain uniformly constant with $T_1 < T_2$. By the Buckingham Pi theorem, the problem may be described by two independent non-dimensional parameters. Classically these are:

$$Ra \equiv \frac{g\beta\Delta T d^3}{\nu\kappa} \quad \text{--- Rayleigh number} \quad (3.1)$$

$$\sigma \equiv \frac{\nu}{\kappa} \quad \text{--- Prandtl number} \quad (3.2)$$

Experimentally, it has been shown that the fluid remains stationary until the Rayleigh number exceeds a critical number, at which point steady, convective overturning begins.

The Rayleigh number may be interpreted in various ways. For a laminar flow it is identical to the Nusselt number, Nu , the ratio of convective to conductive heat flux. Since

the flow is laminar, convective motions will be on the same scale as molecular diffusion motions. The equivalence of these buoyant forces B is made here:

$$B \sim g\beta\Delta T \sim w_c \frac{\nu}{d^2} \quad (3.3)$$

$$H_{\text{conv}} = Bw_c \quad \text{convective flux} \quad (3.4)$$

$$H_{\text{cond}} = \kappa \frac{B}{d} \quad \text{conductive flux} \quad (3.5)$$

$$Nu = \frac{w_c d}{\kappa} = \frac{g\beta\Delta T d^3}{\nu\kappa} = \text{Rayleigh number} \quad (3.6)$$

One may also define the Reynolds number for a measure of the local hydrodynamic stability of the cells.

$$R_l = \frac{w_c d}{\nu} = \frac{Ra}{\sigma} \quad (3.7)$$

Although Rayleigh-Benard convection is not a new problem, it is still the focus of current research especially for the transition to chaos and turbulence. One is referred to *Physics Today*, June, 1988. A group at the Univ. of Chicago [Heslot et. al. 1987] has obtained a Rayleigh number on the order of 10^{11} .

The problem is too complicated to have an exact analytic solution. Different approaches have been made to provide limited insight into the behavior of the convection. Linear analysis about the steady gradient solution has been valuable in determining the critical Rayleigh number and the initial motions of convection. Finite amplitude nonlinear theory can predict the first few transitions, and finally, a highly truncated spectral method may illuminate the general nature of the system although it isn't overly accurate. Since the interactions within the system are highly non-linear, there is a breakdown in the analysis with any of these simple methods.

A Brief Review of the Linear Analysis

As mentioned earlier, linear analysis entails expanding the variables about a known solution. The steady, diffusive solution is:

$$\mathbf{v} = 0 \quad (3.8a)$$

$$T = T_1 + (T_2 - T_1) \left(\frac{z}{d} \right) \quad (3.8b)$$

The expanded variables are placed in the Boussinesq equations. The steady state equations are then subtracted off leaving:

$$\frac{\partial \mathbf{v}'}{\partial t} = -\alpha_0 \nabla p' + B' \hat{k} + \nu \nabla^2 \mathbf{v}' \quad (3.9a)$$

$$\frac{\partial B'}{\partial t} - w \frac{\partial \bar{B}}{\partial z} = \kappa \nabla^2 B' \quad (3.9b)$$

$$\nabla \cdot \mathbf{v}' = 0 \quad (3.9c)$$

where $\bar{B} = [g(T_2 - T_1)z]/[0.5(T_2 + T_1)d]$ is the steady state buoyancy.

A diffusive scaling is then introduced.

$$\begin{aligned} (x^*, y^*, z^*) &= d(x, y, z) \\ t^* &= (d^2/\nu)t \\ \mathbf{v}'^* &= (\nu/d)\mathbf{v} \\ \alpha_0 p'^* &= (\nu^2/d^2)p \\ B'^* &= g\beta\Delta T\sigma B \end{aligned} \quad (3.10)$$

The domain is $0 < z < 1$ and $t > 0$.

The equations may now be simplified to contain the two non-dimensional parameters.

$$\begin{aligned} \frac{\partial \mathbf{v}}{\partial t} &= -\nabla p + Ra B \hat{k} + \nabla^2 \mathbf{v} \\ \sigma \frac{\partial B}{\partial t} - w &= \nabla^2 B \\ \nabla \cdot \mathbf{v} &= 0 \end{aligned} \quad (3.11)$$

By eliminating p and B , the problem may be further reduced to the sixth order equation:

$$(\sigma \frac{\partial}{\partial t} - \nabla^2)(\frac{\partial}{\partial t} - \nabla^2)\nabla^2 w = Ra \nabla_2^2 w \quad (3.12)$$

where

$$\nabla_2^2 \equiv \frac{\partial^2}{\partial x^2} + \frac{\partial^2}{\partial y^2}$$

Two different sets of boundary conditions may be imposed as either a free-slip condition at the two plates, or no-slip boundaries.

$$w(0) = 0, \quad w(1) = 0 \quad (3.13)$$

$$B(0) = 0, \quad B(1) = 0 \quad (3.14)$$

Free-slip:

$$u_x(0) = v_x(0) = 0, \quad u_x(1) = v_x(1) = 0 \quad (3.15)$$

No-slip:

$$u(0) = v(0) = 0, \quad u(1) = v(1) = 0 \quad (3.16)$$

The order of the problem is reduced from eighth order to sixth by the symmetry in the horizontal plane.

A Fourier series solution is sought for (3.12) with normal modes of the form:

$$w = \text{Re} \left(\int \int_{-\infty}^{\infty} w_1(z) \exp[\omega(K_x, K_y)t + i(K_x x + K_y y)] dK_x dK_y \right) \quad (3.17)$$

with a complex ω . Note if $\omega_r = 0$ then the solution is marginally stable. If $\omega_r > 0$ then the convection is characterized by unstable growth. If $\omega_i = 0$ then the solution has the form of stationary convection; otherwise the convection is oscillatory. In this problem, it may be shown that $\omega_i = 0$, for $\omega_r > 0$.

To prove this, the Fourier solution is substituted into (3.12). The resulting equation for w_1

$$(\sigma\omega + K^2 - D^2)(\omega + K^2 - D^2)(K^2 - D^2)w_1 = RaK^2w_1 \quad (3.18)$$

where

$$K^2 \equiv K_x^2 + K_y^2 \quad D^2 \equiv \frac{\partial^2}{\partial z^2}$$

is multiplied by w_1^* , the result is integrated over the vertical extent, making use of integration by parts and the boundary conditions, and the imaginary part is taken. The result is

$$\omega_i \int_0^1 K^2 [2\sigma\omega_r + K^2(1+\sigma)] |w_1|^2 + [2\sigma\omega_r + 2K^2(1+\sigma)] |Dw_1|^2 + (1+\sigma) |D^2w_1|^2 = 0 \quad (3.19)$$

Thus $\omega_i = 0$. One then goes back to (3.12) and examines the case $\omega_i = 0$ to find the marginal Rayleigh number from:

$$(K^2 - D^2)^3 w_1 = RaK^2 w_1 \quad (3.20)$$

A solution that satisfies free-slip boundaries is $w_1 = \sin(n\pi z)$. Make the substitution to find

$$Ra = \frac{(K^2 + n^2\pi^2)^3}{K^2} \quad (3.21)$$

then minimize with respect to n and K .

The minimum Rayleigh number occurs when n equals 1. Thus,

$$K_m^2 = \pi^2/2 \quad \text{i.e., } K_m = 2.22, \quad \pi/K_m = 1.42, \quad Ra_{\text{crit}} = \frac{27}{4}\pi^4 \approx 657.5 \quad (3.22)$$

Similarly one may work through the no-slip boundary conditions (see Chandrasekhar, 1962) to get

$$Ra_{\text{crit}} \simeq 1708, \quad K \simeq 3.12, \quad \text{and} \quad \pi/K \simeq 1.01 \quad (3.23)$$

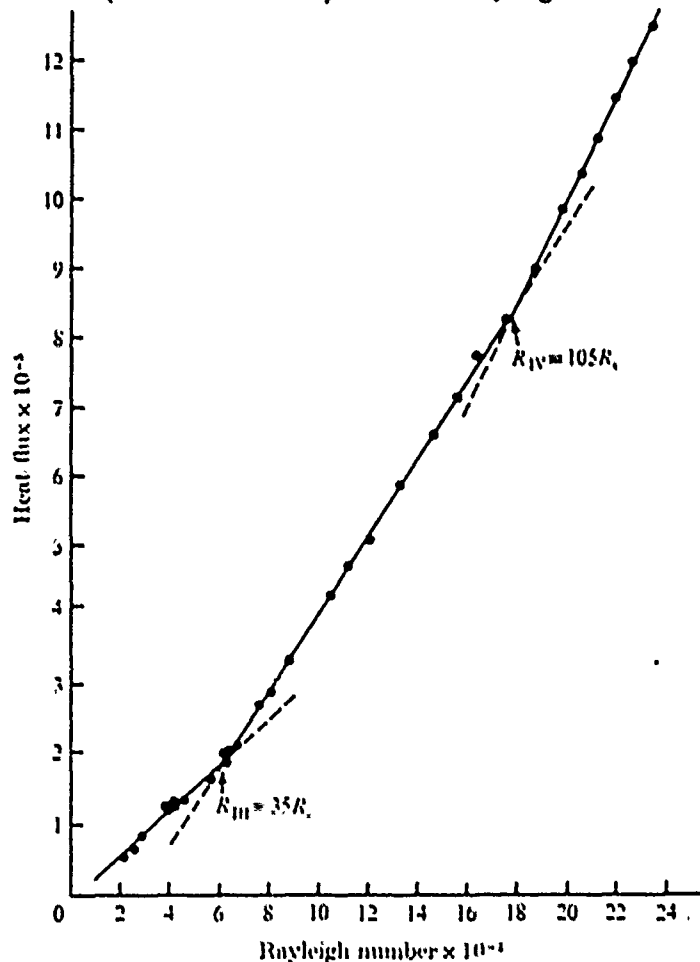
Here K is fixed but K_x and K_y may vary accordingly. Note that for the rigid boundaries the aspect ratio is closer to 1:1, with a higher critical Rayleigh number.

The cells formed should fill the plane. Two-dimensional rolls are common. To have a regular polygon evenly fill the surface one must have an internal angle of $\pi(1 - 2/N)$ where N is the number of sides of the polygon. If M such angles must fit together at a point then:

$$2\pi = M2\pi(1 - 2/N)$$

$$\left\langle \right\rangle \pi \left(1 - \frac{2}{N}\right)$$

The only integral solutions to this equation are $N = 3, 4$ & 6 . In convection, regular hexagons ($N = 6$) are usually observed. The range of validity of this solution is limited. Results of Krishnamurti [1970] show distinct transitions in the relation between the non-divergent heat flux (Nusselt number) and the Rayleigh number.

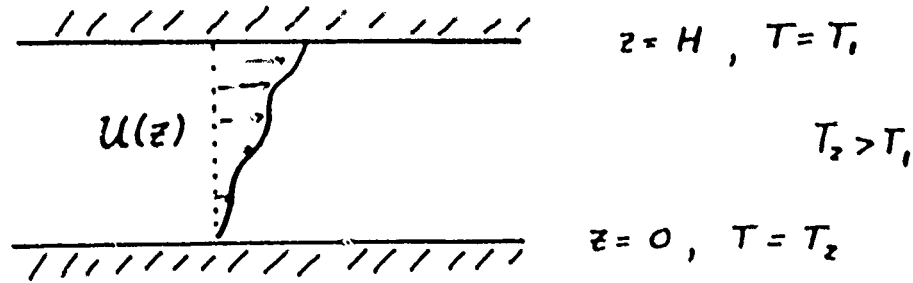


For high Rayleigh numbers the flow is highly turbulent and a relation of $Nu \sim Ra^{1/3}$ has been observed.

For Rayleigh numbers beyond this range coherent structures have been observed.

The Effect of Mean Shear Upon Convection

The Rayleigh-Benard problem may be extended to include mean vertical shear. Here we consider the inviscid problem for simplicity. Consider a basic flow between two horizontal plates with velocity $U(z)$ in the x -direction and imaginary buoyancy frequency $N(z)$ (so that $N^2 > 0$ corresponds to unstable stratification).



For small perturbations to this state the linearized equations governing Boussinesq, inviscid, adiabatic motions are

$$u_t + Uu_z + wU_z = -\alpha_0 p_x \quad (3.24a)$$

$$v_t + Uv_z = -\alpha_0 p_y \quad (3.24b)$$

$$w_t + Uw_z = -\alpha_0 p_z + B \quad (3.24c)$$

$$B_t + UB_z = N^2 w \quad (3.24d)$$

$$u_x + v_y + w_z = 0 \quad (3.24e)$$

where u , v , and w are the eastward, northward and upward velocities and p and B are the pressure and buoyancy perturbations. α_0 is a mean specific volume. From these we can derive some integral relations which show that the horizontally divergent part of the flow cannot extract energy from the mean shear when $N^2 > 0$ unless U_{zz} is non-zero.

We divide the horizontal motion into an irrotational part (subscript i) and a non-divergent part (subscript n) as follows:

$$u = u_i + u_n \quad (3.25)$$

$$v = v_i + v_n$$

where

$$\frac{\partial v_i}{\partial x} - \frac{\partial u_i}{\partial y} = 0 \quad (3.26)$$

and

$$\frac{\partial u_n}{\partial x} + \frac{\partial v_n}{\partial y} = 0 \quad (3.27)$$

By multiplying (3.24a), (3.24b) and (3.24c) by u_i , v_i and w respectively, adding, then averaging vertically between the plates and horizontally over one full period of the disturbance in x and y , we obtain

$$\frac{1}{2} \left(\overline{u_i^2} + \overline{v_i^2} + \overline{w^2} \right)_t = \overline{wB} - \overline{U_x u_i w} \quad (3.28)$$

where an overbar indicates a volume average. Similarly, multiplying (3.24a) and (3.24b) by u_n and v_n , adding, and averaging gives

$$\frac{1}{2} \left(\overline{u_n^2} + \overline{v_n^2} \right)_t = -\overline{U_x u_n w} \quad (3.29)$$

These are the energy equations for the divergent and non-divergent parts of the flow respectively. Note (3.28) does not depend on the non-divergent part of the flow and (3.29) does not depend on the buoyancy.

We can also derive an expression for the shear energy generation term $-\overline{U_x u_i \hat{w}}$. The solution to the linear system (3.24a) to (3.24b) will be a superposition of modes of the form:

$$\eta = \text{Re}[\hat{\eta}(z)e^{\sigma t}e^{ik(z-ct)+il y}] \quad (3.30)$$

for each dynamical variable η . After eliminating \hat{u} , \hat{v} , \hat{p} , and \hat{B} we are left with an equation for \hat{w} :

$$s \left(\frac{d^2 \hat{w}}{dz^2} - \lambda^2 \hat{w} \right) = -\frac{\lambda^2 N^2 \hat{w}}{s} + ik U_{xx} \hat{w} \quad (3.31)$$

Here $\lambda^2 \equiv k^2 + l^2$ is the total wavenumber squared and $s \equiv \sigma + ik(U - c)$.

Now we follow Howard (1961) in defining a new complex variable

$$h \equiv s^{n-1} \hat{w} \quad (3.32)$$

n is any real number. Substitute this in (3.31) and multiply by h^*/s^n , where $*$ means complex conjugate, then integrate vertically between the plates. Integrating by parts where appropriate and using the boundary condition that \hat{w} and hence h vanish at $z = 0$ and $z = H$, we obtain

$$\int_0^H \left[s^{2(1-n)} \left| \frac{dh}{dz} \right|^2 + \{n(1-n)s^{-2n} \left(\frac{ds}{dz} \right)^2 + ns^{1-2n} \frac{d^2 s}{dz^2} + \lambda^2 s^{2(1-n)} - \lambda^2 N^2 s^{-2n}\} |h|^2 \right] dz = 0 \quad (3.33)$$

In the particular case when $n = 1$ so that $h = \hat{w}$ the real part of this integral gives

$$\int_0^H \left[|\hat{w}_x|^2 + \lambda^2 |\hat{w}|^2 + \frac{|\hat{w}|^2}{|s|^2} \left\{ k^2 (U - c) U_{xx} - \frac{\lambda^2 N^2 (\sigma^2 - k^2 (U - c)^2)}{|s|^2} \right\} \right] dz = 0 \quad (3.34)$$

We can obtain a second integral relation by multiplying equation (3.31) by \hat{w}^* and integrating between the plates:

$$\int_0^H \left[\frac{ds}{dz} \hat{w}^* \frac{d\hat{w}}{dz} + s \left| \frac{d\hat{w}}{dz} \right|^2 + \left(\lambda^2 s + ik U_{xx} - \frac{\lambda^2 N^2}{s} \right) |\hat{w}|^2 \right] dz = 0 \quad (3.35)$$

Using the mass continuity equation (3.24e) and the irrotational relation (3.26) the first term in the integral can be expressed as

$$\begin{aligned} \hat{w}^* \frac{ds}{dz} \frac{d\hat{w}}{dz} &= -\hat{w}^* ik U_x (ik \hat{u}_i + il \hat{v}_i) \\ &= U_x \lambda^2 \hat{w}^* \hat{u}_i \end{aligned} \quad (3.36)$$

But, using (3.30), the shear generation term in (3.28) can be written

$$-\overline{U_z u_i w} = -\frac{1}{2H} \operatorname{Re} \left[\int_0^H U_z \hat{w}^* \hat{u}_i dz \right] \quad (3.37)$$

Substituting from (3.36) and (3.35) gives

$$-\overline{U_z u_i w} = \frac{\sigma}{2H\lambda^2} \int_0^H \left[\left| \frac{d\hat{w}}{dz} \right|^2 + \lambda^2 |\hat{w}|^2 - \frac{\lambda^2 N^2 |\hat{w}|^2}{|s|^2} \right] dz \quad (3.38)$$

Combining this with (3.34) to eliminate the first two terms in the integral yields

$$-\overline{U_z u_i w} = -\frac{\sigma k^2}{2H} \int_0^H \frac{|\hat{w}|^2}{|s|^2} \left[\frac{U_{zz}}{\lambda^2} (U - c) + \frac{2N^2 (U - c)^2}{|s|^2} \right] dz \quad (3.39)$$

From this we can conclude that for growing disturbances ($\sigma > 0$) in constant shear flow ($U_{zz} = 0$) with unstable stratification everywhere ($N^2 > 0$) the divergent circulation always gives up kinetic energy to the mean flow (unless convection occurs in rolls aligned with the shear so that there is no transfer of kinetic energy to or from the divergent circulation).

We can derive a similar expression for the generation term in the non-divergent kinetic energy budget. Start by taking the curl of the horizontal momentum equations (3.24a) and (3.24b) to eliminate the irrotational velocity:

$$s(k\hat{v}_n - l\hat{u}_n) = l\hat{w}U_z \quad (3.40)$$

Then eliminate \hat{v}_n using (3.27):

$$\hat{u}_n = -\frac{l^2}{s\lambda^2} \hat{w}U_z \quad (3.44)$$

Then the shear generation term in (3.32) can be written

$$\begin{aligned} -\overline{U_z u_n w} &= -\frac{1}{2H} \operatorname{Re} \left[\int_0^H U_z \hat{u}_n \hat{w}^* dz \right] \\ &= \frac{\sigma}{2H} \int_0^H \frac{l^2}{\lambda^2} \frac{|\hat{w}|^2}{|s|^2} U_z^2 dz \end{aligned} \quad (3.42)$$

So the non-divergent part of a growing disturbance always extracts energy from a mean flow with shear. However, from (3.28), this can never find its way into the vertical circulation.

References

- Chandrasekhar, S. (1962) *Hydrodynamic and Hydromagnetic Stability*. Oxford University Press, London, 652pp.
- Heslot F., B. Castaing and A. Libchaber (1987) Transitions to turbulence in helium gas. *Phys. Rev. A.*, **36**, 5870-5873.
- Howard, L. N. (1961) A note on a paper of John W. Miles. *J. Fluid Mech.*, **10**, 509-512.
- Krishnamurti, R. (1970) On the transition to turbulent convection. *J. Fluid Mech.*, **42**, 295-320.

Notes by Steve Siems and John Thuburn

4. MOIST THERMODYNAMICS.

This lecture introduces the definitions and basic concepts involved in moist thermodynamics. This includes the definition of the cloud specific volume and virtual temperature. The first law of thermodynamics is used to derive a buoyancy variable called θ_v which is conserved in the absence of phase changes. By considering phase equilibria a criterion for condensation to occur on displacing a parcel of air is developed from the Clausius-Clapeyron equations. A conserved entropy in the case in which phase changes may occur is also defined.

In this lecture we assume that all condensed water is falling at its terminal velocity and so we can ignore the acceleration of condensate relative to the air. We now define a number of properties of the system which will be useful in describing moist thermodynamics.

Thermodynamic Quantities

Specific Volume

We define the specific volume of the material, α , to be the ratio of the volume, V , to the mass M of the moist and cloudy air,

$$\alpha = \frac{V}{M}$$

where $M = M_d + M_v + M_c$ with the subscripts d =dry air, v =vapor and c =condensate.

Similarly, we define α_d to be the specific volume of dry air and α_l to be the specific volume of the water condensate to give

$$\alpha = \frac{\alpha_d + l\alpha_l}{1 + m + l}$$

where m is the ratio of the mass of water vapor to that of dry air and l is the ratio of the mass of condensate to that of dry air. The quantity $Q = m + l$ is the total water (vapor and condensate) and this is conserved in a reversible process. We note here that the ratio $l\alpha_l/\alpha_d$ is very small, of order 10^{-6} , and so the partial volume of the water condensate is negligible.

Virtual Temperature

We may write the specific volume in terms of p_d , the partial pressure of the dry air, as $\alpha_d = R_d T / p_d$ where R_d is the gas constant for the dry air and T the temperature. This alternative definition gives rise to the concept of a virtual temperature, T_v , which is the temperature giving the atmospheric density when used in conjunction with the perfect gas law for dry air. If we choose α to satisfy

$$\alpha = \frac{R_d T_v}{p}$$

then

$$T_v = T \frac{p}{p_d} \frac{1}{1 + Q}$$

where p is the total pressure in the cloud. If e is the partial pressure of the water vapor then

$$\frac{p}{p_d} = \frac{p}{p - e} = \frac{p_d + e}{p_d}$$

Since the ratio of the mass of water vapor to the mass of dry air $m = M_v/M_d = \alpha_d/\alpha_v = \epsilon c/p_d$ where $\epsilon \equiv R_d/R_v = 0.622$ for the atmosphere, we have $p/p_d = 1 + (m/\epsilon)$ and the expression for the virtual temperature becomes

$$T_v = T \frac{1 + (m/\epsilon)}{1 + Q}$$

Moist air without condensate is thus less dense than dry air at the same temperature. This has important consequences. For example, the buoyancy flux from the ocean in the tropics is introduced by moistening not by heating.

Buoyancy Variable θ_v

For moist air without condensate, the first law of thermodynamics gives us

$$(M_v + M_d)dq = (M_d c_{pd} + M_v c_{pv})dT - vdp$$

and so

$$dq = c'_p dT - \alpha dp$$

where

$$c'_p = c_{pd} \frac{1 + m(c_{pv}/c_{pd})}{1 + m}$$

We may write this in terms of virtual temperature as

$$dq = c''_p dT_v - \alpha dp$$

where

$$c''_p = c_{pd} \frac{1 + m(c_{pv}/c_{pd})}{1 + (m/\epsilon)} = c_{pd}(1 + 0.24m)$$

where we have ignored the volume occupied by the condensate.

Now, in an adiabatic process $dq = 0$ and so

$$c''_p dT_v = R_d T_v d \log(p)$$

from which we may define the variable θ_v ,

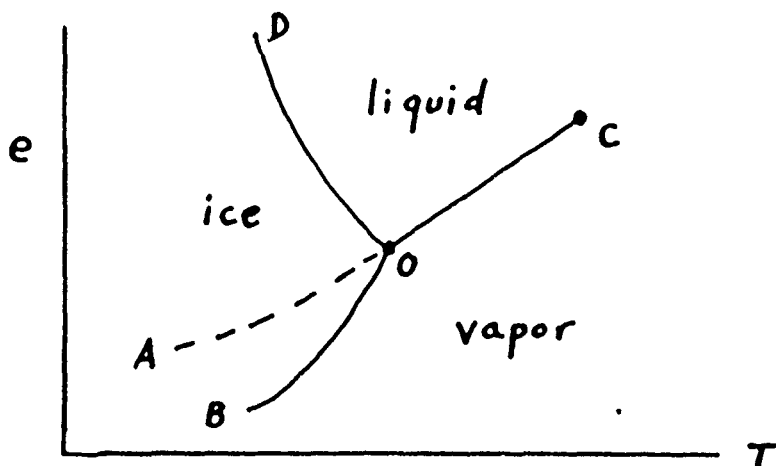
$$\theta_v = T_v \left(\frac{p_0}{p} \right)^{(R_d/c''_p)}$$

which is a constant along an adiabat. Note that c''_p is similar to c_{pd} as $m \leq 0.025$, even in the tropics.

We may interpret θ_v as a buoyancy variable. In the tropics it is observed that θ_v is approximately constant in the region 10 - 500 m above the ocean. This layer is convectively adjusted, and although other conserved properties may not be constant, θ_v is fixed because it is a buoyancy variable. Thus the fluid arranges itself to be in a state of neutral static stability.

Phase Equilibrium

We now consider the phase equilibria of an ice/water/vapor system. The diagram below shows the partial pressure of water vapor plotted as a function of the temperature along the equilibrium curves for (1) BO - ice and vapor, (2) CO - liquid and vapor, (3) DO - liquid and ice and (4) AO - supercooled liquid and ice. O is the triple point at which $T = 273.16^\circ K$ and the partial pressure, $e = 6.11 mb$. (Note that 1 millibar represents 100 mks units of pressure). C is the critical point at which the vapor/liquid equilibrium curve ends. At this point $T = 647^\circ K$ and $e = 221,000 mb$. An important feature of the phase relations for H_2O is that ice melts under pressure and this allows for a variety of phenomena including ice-skating.



The phase equilibrium curves may be derived from the differential form of the laws of thermodynamics to give the Clausius-Clapeyron equation. This has the form

$$\left(\frac{dp}{dT}\right)_e = \frac{L_I - L_{II}}{T(\alpha_I - \alpha_{II})}$$

where L is the latent heat of condensation or fusion. We note that the heat of fusion is an order of magnitude smaller than the heat of condensation in the case of water vapor.

Since the specific volume of vapor $\alpha_v \gg \alpha_l$, the specific volume of condensed water, we have from the equation of state

$$\frac{de_s}{dT} \approx \frac{L_v}{T\alpha_v} = \frac{L_v e_s}{R_v T^2}$$

where e_s is the partial pressure at saturation. If we neglect the dependence of L_v upon T then we can find the approximate solution

$$e_s = e_o \exp\left(\frac{L_v}{R_v} \left(\frac{1}{T_o} - \frac{1}{T}\right)\right)$$

where $e_0 = 6.11 \text{ mb}$; $T_0 = 273.16^\circ \text{K}$. Experimental data take into account the temperature dependence of L_v and other factors. An excellent empirical fit for atmospheric conditions is

$$e_s = 6.11 \exp \frac{17.67(T - 273.16)}{T - 29.66}$$

Phase Change Micro-Physics

The following micro-scale factors can modify the phase equilibrium curves for condensation of water vapor.

- (i) Surface tension increases the saturation vapor pressure. This effect becomes important as the water droplet size decreases.
- (ii) Salt lowers the saturation vapor pressure.
- (iii) Certain particles in suspension assist condensation; they are called condensation nuclei. These include dust, smoke, soot and salt particles. Note that maritime clouds are more likely to precipitate than land clouds because the spectra of condensation nuclei in continental clouds are more sharply peaked than the spectra of particles in maritime clouds. This more uniform size distribution increases the coalescence rate.

When the water vapor temperature lies between 0 and -40°C heterogeneous freezing can occur and there may be a mixture of water and ice in the cloud. In contrast to the process of condensation of water vapor, heterogeneous freezing of the condensed water does not occur as readily, since there is a shortage of nuclei with the same crystalline structure as ice. However, if the temperature falls below -40°C then ice forms homogeneously and spontaneously. If ice crystals fall into a supercooled water cloud, rapid growth of the crystals will occur at the expense of the water droplets since the saturation vapor pressure over ice is less than that over water.

Mixing and criterion for condensation:

When two masses of air at different positions on the water vapor/condensate equilibrium curve mix, the concavity of the curve may cause the mixture to be supersaturated since e (the vapor pressure) and T mix linearly. If we displace a parcel of (moist) saturated air and allow it to evolve adiabatically as the background e changes, condensation may occur if the change in saturation vapor pressure is greater than the change of saturation vapor pressure at constant mixing ratio in the parcel. We may quantify this criterion for condensation as follows

$$\left(\frac{\partial e}{\partial T} \right)_s > \left(\frac{\partial e}{\partial T} \right)_m$$

where the subscript s and m denotes a derivative along the saturation curve and at constant mixing ratio respectively. This equation gives the criterion for condensation as

$$T < \frac{\epsilon L_v}{C_{pd}} \approx 1500^\circ \text{K}$$

where we have used the Clausius-Clapeyron equation

$$\left(\frac{dp}{dT} \right)_s = \frac{L_v p_s}{R_v T^2}$$

for the evolution along the saturation equilibrium curve and the expression

$$\left(\frac{\partial p}{\partial T}\right)_m = \frac{\partial e}{\partial p_d} \left(\frac{\partial p_d}{\partial T}\right)_m = \frac{p C_{pd}}{T R_d}$$

gives the change of vapor pressure at constant mixing ratio.

Reversible Thermodynamics including Vapor/Condensation Phase Changes.

The specific entropy of a mixture of dry air, water vapor, and liquid water may be defined as

$$M_d S = M_d S_d + M_v S_v + M_l S_l$$

where M_l is the mass of liquid water, and so

$$S = S_d + m S_v + l S_l$$

where

$$S_v = C_{pv} \log(T) - R_v \log(e)$$

$$S_l = C_l \log(T)$$

and

$$S_d = C_{pd} \log(T) - R_d \log(p_d)$$

In phase equilibrium,

$$S_v - S_l = \frac{L_v}{T}$$

and so we may rewrite the entropy as

$$\begin{aligned} S &= S_d + \frac{L_v m}{T} + Q S_l \\ &= (C_{pd} + Q C_l) \log(T) + \frac{L_v m}{T} - R_d \log\left(\frac{p_d}{p_o}\right) - m R_v \log\left(\frac{e}{e_s}\right) \\ &= (C_{pd} + Q C_l) \log(\theta_e) \end{aligned}$$

where we have defined θ_e to be the equivalent potential temperature. The term involving the water vapor pressure is included to account for the effects when the air is unsaturated - it matches the non-saturated entropy to the saturated entropy. We may solve the above differential relation to give the expression for equivalent potential temperature

$$\theta_e = T \left(\frac{p_o}{p_d}\right)^{(R_d/[C_{pd}+QC_l])} \left(\frac{e}{e_s}\right)^{(m R_v/[C_{pd}+QC_l])} \exp\left(\frac{L_v w}{[C_{pd}+QC_l]T}\right)$$

This quantity is conserved under phase changes of water substance and in unsaturated air.

Processes which cause non-equilibrium effects include radiational cooling, freezing, melting and evaporation of rain falling into unsaturated air all produce non-equilibrium effects. We neglect rain evaporation as it only produces at most 0.2°C change of θ_e in heavy rain. However, as mentioned earlier, evaporation from an ocean or lake does change the moist entropy and is the dominant mechanism of heat transfer from the ocean in the tropics.

Notes by Fabian Waleffe and Andrew Woods

5. NON PRECIPITATING CLOUD

We now look at the thermodynamic and kinematic structure of the clouds. We will not try to explain their spatial distribution, i.e. size and the spacing between them. For instance, we will consider the clouds far enough apart to be independent, which is not completely valid if they are created from a source having a much larger scale.

A simple definition of the cloud corresponds to the water content of the air. When a plane goes into a cloud, it finds a near discontinuity as the water content jumps from zero to its maximum value (Warner, 1955)

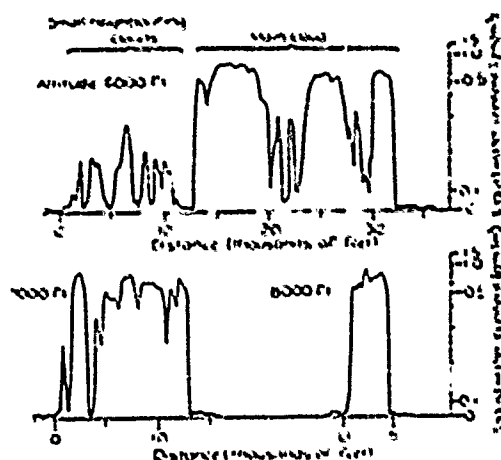


Fig. 3. Successive traverses through cumulus cloud at 6,000, 7,000 and 8,000 ft. Cloud base 3,000 ft, temperature 15.3° C, top 9,300 ft, -2° C.

This delineation corresponds to the sharp visual appearance of the cloud boundary.

The measurements are not very easy. In the 50's, the instruments had low precision. Now, the instruments are better, but the planes go through the cloud quickly, so the final resolution is also low, about 100m horizontally. The following figure from Malkus (1954) shows wind and turbulence levels. Note the strong shears at the edge of the cloud.

Another observing problem is the short life-time of each stage of a cumulus cloud, and our inability to predict the future of a given growing cloud, so that it is difficult to observe the whole life cycle. Also, fluctuations are much larger than the cloud mean values, as the convection is turbulent.

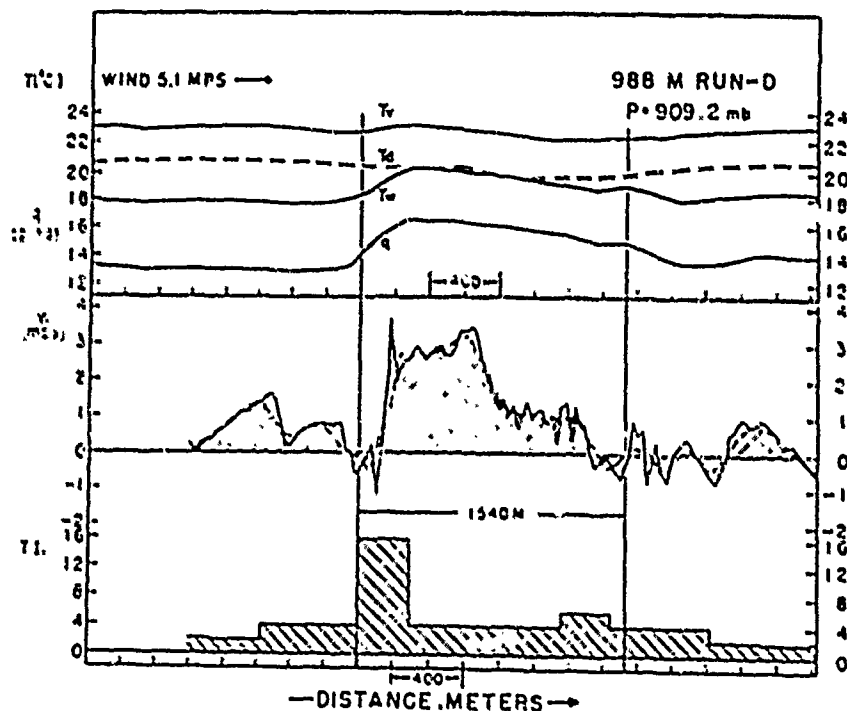


FIG. 7. 988-m run through cloud I. Notation same as in fig. 4.

For instance the mean vertical velocity can be of order 4 m/s, averaged in space (an average in time would give a much smaller value), and the noise is then typically 6 to 7 m/s. The variation of virtual temperature is also very small, of the order of the instrumental precision, 1 or 2°C. So it is very difficult to make buoyancy measurements in the cloud.

The convection occurs in response to local instability. The instability can be of finite amplitude, and this could explain the spacing and the structure of the cloud, but here we will only consider the case when a cloud is already formed. Since non-precipitating clouds do not produce net heating, the only way they can stabilize the atmosphere is to reduce the subcloud entropy by entrainment of dry air from aloft.

Mixing diagrams depict the composition of the clouds in terms of conserved variables $Q = l + m$, the total water content, and θ_e , the total entropy variable. These are nearly linearly mixing in the range of atmospheric conditions. The mixing diagram for the air near, but not in, the cloud looks like the following figure (Paluch, 1979).

This measurement serves as a reference to interpret where the air comes from in the next figure, which shows the measurements within a towering cumulus cloud, superimposed on the preceding diagram.

The in-cloud measurements nearly fall along a straight line connecting cloud base (near 1.5 km) with cloud top (near 8 km).

A straight line between two points on a diagram of two conserved quantities signifies that the air at a given height is a mixture of the air of the two extreme points only. Thus the cloud can be interpreted as a volume of air coming from near cloud base mixed only

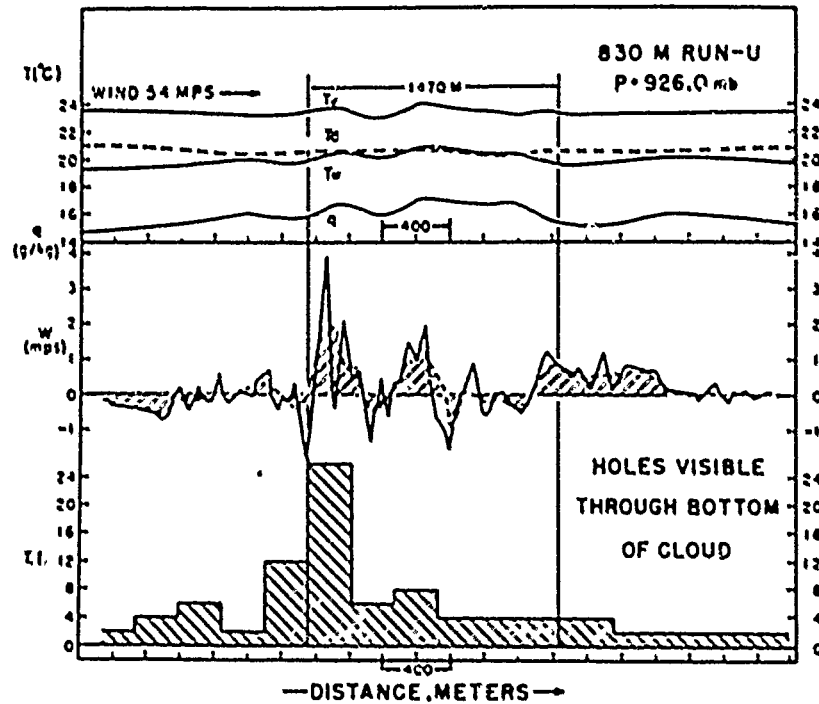


FIG. 8. 830-m run through cloud I. Notation same as in fig. 4. Note that updrafts are separated into smaller individuals at this level, and so are peaks in temperature and moisture records. Note also greater "waviness" of latter records outside cloud boundaries. Value "24" of turbulence index associated with left-hand cloud draft is one of highest values observed during 1952 trip.

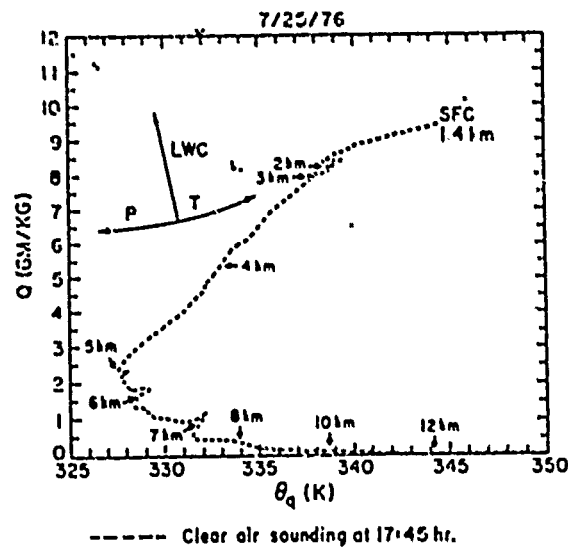


FIG. 2. Total mixing ratio Q (dashed curves) plotted against the wet equivalent potential temperature θ_q for the sounding in Fig. 1. The arrows indicate altitude. The three arrows in the upper left corner, labeled LWC, T and P , show how changes in liquid water, temperature or pressure appear on this type of plot. For further explanation see text.

with some air coming from the top of the cloud. The environmental air between these two regions does not seem to appear inside the cloud. A simple picture is thus a region with mixing of two layers, disconnected from the ambient air:

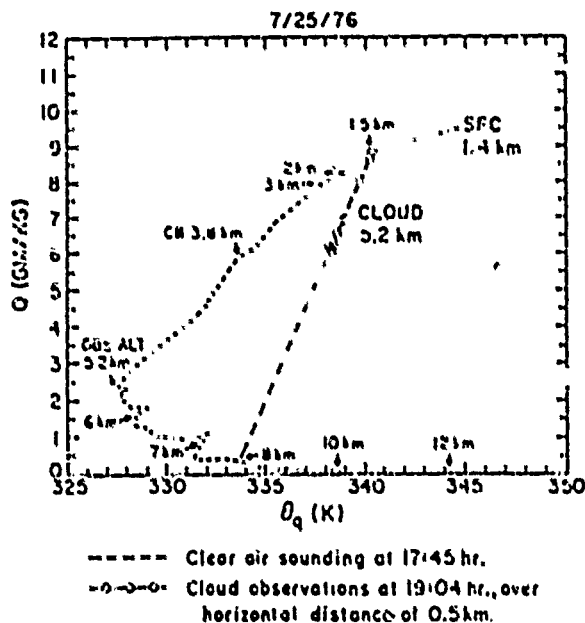
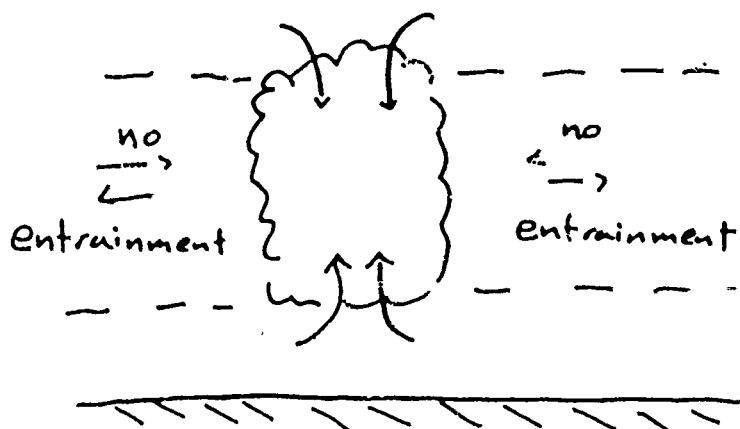


Fig. 4. Comparisons of the total mixing ratio Q and the wet equivalent potential temperature θ_q , computed from data collected inside a growing cumulus cloud with Q and θ_q values of a representative sounding. The dashed line refers to the sounding; the points connected by lines represent the in-cloud observations. The data correspond to the first half-kilometer shown in Fig. 3. Air with the observed properties could have been formed by mixing air from the surface levels with air from ~ 8 km as indicated by the dot-dashed line. The observation level was 3.2 km ($\sim 2^\circ\text{C}$). Cloud base (CB) was at 3.8 km.

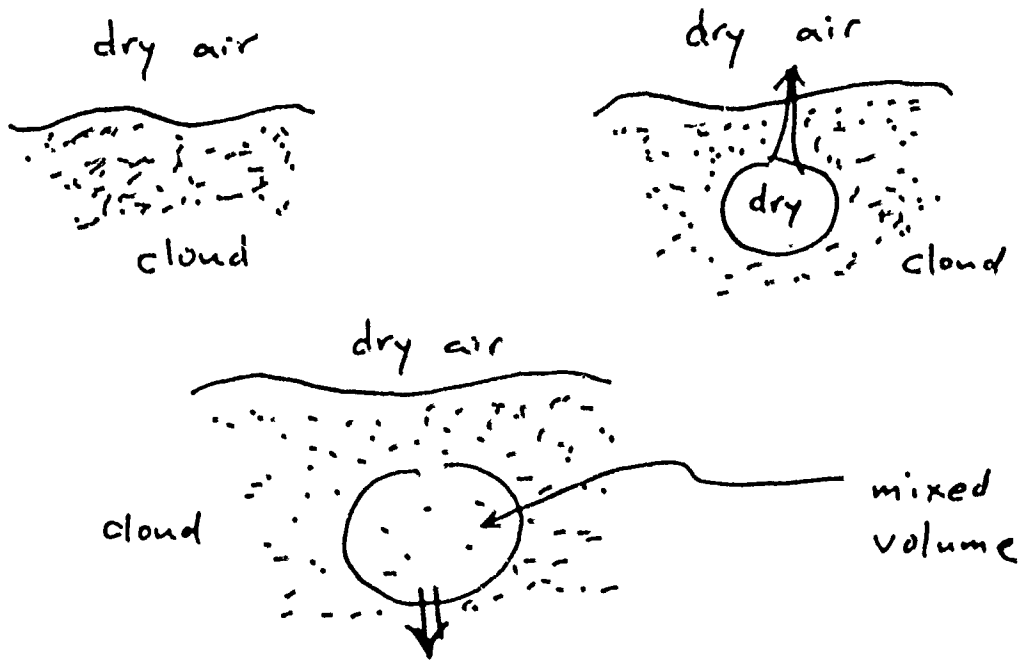


The presence of the air coming from the subcloud layer is natural, but explanation of the presence of the air coming from the top of the cloud requires discussion of a new mechanism: cloud top instability.

Cloud Top Instability

We study next an instability which occurs only in clouds. Consider the top of a cloud. We suppose that this interface is buoyantly stable, i.e. that a volume of dry air pushed into the cloud without any mixing is positively buoyant and vice-versa.

But an instability occurs when we allow the displaced volume to mix with surrounding air (the cloud is turbulent). When a volume of dry air is mixed into the cloud, and mixed, or some of the water of the cloud volume is evaporated. This evaporation makes the mixed volume colder, and, under some conditions, it will be negatively buoyant and accelerate downwards.



We assume that the mixed volume moves slowly compared to the time scale of evaporation, so it always remains in thermodynamic equilibrium. This is no longer true if it is raining or snowing, as the evaporation time for these particles is not small compared to mixing time scales.

Criterion for instability

We take the pressure to be hydrostatic and we neglect its fluctuations in the buoyancy. The heat equation becomes

$$\begin{aligned} dq &= 0 \\ &= c_p dT - \alpha dp + L_v dm \\ &= c_p dT + g dz + L_v dm \end{aligned}$$

with our assumption. So we define

$$h_v = c_p T_v + gz + L_v m$$

(corrected for the presence of vapor by using T_v rather than T , since $c_p T_v$ is closer to $c'_p T$ than $c_p T$) as the moist static energy. The inertial energy is neglected. This quantity is nearly conserved and linear with the mixing. We also define the virtual static energy:

$$\begin{aligned} S_v &= c_p T_v + gz \\ &= h_v - L_v m \end{aligned}$$

The buoyancy may be expressed:

$$B = \frac{g}{c_p \bar{T}_v} (S_{vm} - S_{vc}) + g(l_m - l_c) \quad (5.1)$$

where m refers to the mixed volume and c to the surrounding cloud. For a simplified treatment we first neglect the effect of the condensed water l . Thus

$$B = \frac{g}{c_p \bar{T}_v} [h_{vm} - h_{vc} - L_v(m_m - m_c)] \quad (5.2)$$

In order to obtain the greatest magnitude of negative buoyancy with the smallest mixing ratio, we suppose that all the water is just evaporated so that the mixed volume is at saturation.

Since we assume that the mixed volume is at equilibrium, we can use the Clausius-Clapeyron relation:

$$\begin{aligned} m_m &= m_c \exp \left(\frac{L_v}{R_v \bar{T}_g} B \right) \\ &\simeq m_c \left[1 + \frac{L_v}{R_v \bar{T}_g} B \right] \end{aligned} \quad (5.3)$$

as we assume that we are near the threshold of the instability, i.e., B is small.

As h_v is nearly conserved in mixing, we have:

$$h_{vm} = (h_{vc} + \delta h_{vc}) / (1 + \delta) \quad (5.4)$$

where δ is the mixing fraction, and c denotes the air just above the cloud top. Thus we obtain, using (5.2), (5.3) and (5.4)

$$B = \frac{g}{c_p \bar{T}_v} \frac{h_{vc} - h_{vc}}{(1 + \delta)[1 + mL_v^2/(R_v c_p \bar{T}_v^2)]} \quad (5.5)$$

The criterion for the instability is reached when B becomes negative; this happens when

$$h_{vc} < h_{vc} \quad \text{or} \quad \Delta h_v < 0$$

In a complete treatment, without neglecting the term $g(l_m - l_c) = -gl_c$ (as the mixed volume contains no condensate), we need a new relationship to find δ . Since total water mixes linearly,

$$m_m = \frac{m_c + \delta(m_c + l_c)}{1 + \delta}$$

The treatment is the same, just changing B to $(B - gl_c)$ in the Clausius Clapeyron equation.

Then we obtain $B < 0$ for:

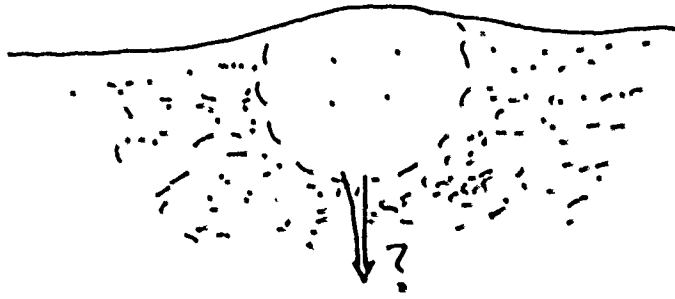
$$\Delta h_v < \Delta(l + m)c_p \bar{T}_v \frac{1 + q_c L_v^2/(c_p R_v \bar{T}_v^2)}{1 + q_c L_v/(R_v \bar{T}_v)}$$

Since $\Delta(l + m)$ is negative, Δh_v must be smaller than a finite negative value to obtain the instability.

Structure and Magnitude of the Instability

As a means of getting a rough estimate of the magnitude and form of the convection, we apply similarity theory, under the assumption that the plumes generated by the instability are highly local in character. See Emanuel (1981) for more details.

We are now interested in the future of a very local mixed region:



We assume that the mixed volume remains always saturated. The conservation equations for a spherical thermal are:
(Volume in Boussinesq approx.):

$$\frac{d}{dt}R^3 = -3R^2\alpha w \quad (5.6)$$

(Momentum):

$$\frac{d}{dt}(R^3 w) = R^3(B + gl_c) \quad (5.7)$$

where we discriminate between the thermal buoyancy B and the buoyancy due to the liquid content gl_c .

(Thermal buoyancy):

$$\frac{d}{dt}(R^3 B) = -N^2 R^3 w - \Gamma l_c \frac{d}{dt}R^3 \quad (5.8)$$

where $N^2 = (g/\theta_v)(d\theta_v/dz)$, θ_v is the virtual temperature of the dry atmosphere, and $\Gamma = L_v g/c_p \bar{T}_c$. The second term assumes the form above if the vapor evaporates instantaneously.

(Total water):

$$\frac{d}{dt}(R^3[Q - Q_c]) = -R^3 w \frac{dQ_c}{dz} \quad (5.9)$$

This is derived in the same way as the conservation equation for θ in a dry thermal.

The self similar solutions are

$$R = -\alpha z$$

$$w = \frac{1}{2}\alpha^{-3}F_0 z^{-2} - \frac{2}{7}(\Gamma - g)l_c z - \frac{1}{16}N^2 z$$

$$B = -f_0\alpha^{-3}z^{-3} - \Gamma l_c - \frac{1}{4}N^2 z$$

$$Q_s - Q = Q_0\alpha^{-3}z^{-3} - l_c + (Q - l_c) \left[\exp\left(\frac{L_v B}{R_v \bar{T}_v g}\right) - 1 \right] - \frac{1}{4} \left[-\frac{d}{dz}(Q_c - l_c) \right] z$$

i

ii

iii

iv

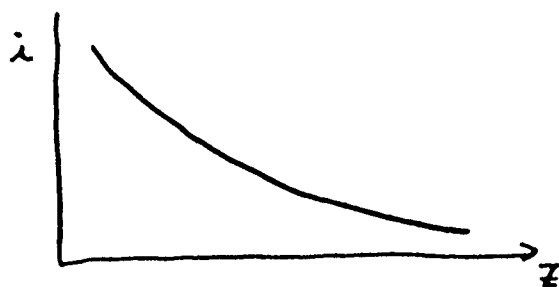
where Q_s = saturation mixing ratio ($= m_s$)

$$Q_0 \equiv [R^3(Q_m - Q_c)]_{z=0}$$

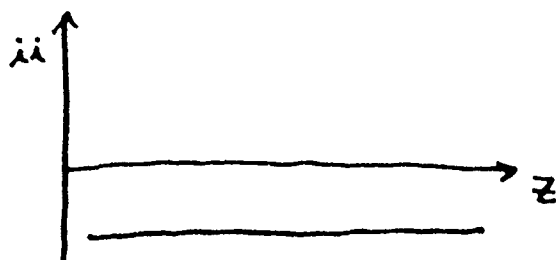
$$F_0 \equiv (R^3 B)_{z=0}$$

and z decreases downwards. We now check that the cloud remains unsaturated, i.e. $Q_s - Q > 0$. In the expression for $Q_s - Q$, we neglect the third term which is negative but small and find that

i is positive



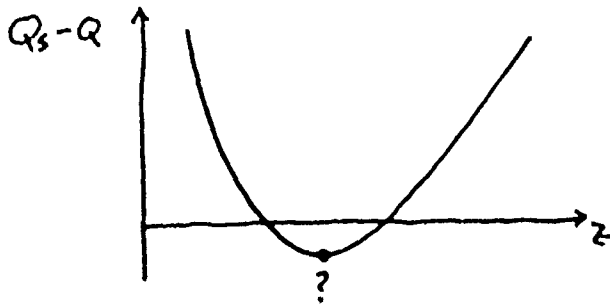
ii is negative



iv is positive



so that $Q_s - Q$ varies like



at first decreasing and then increasing. We ask that the minimum be positive. This leads to the approximate condition

$$-Q_0 > 6.75 l_c^4 \alpha^3 \left[-\frac{d}{dz}(Q_c - l_c) \right]^{-3}$$

In the atmosphere, this condition is easy to satisfy.

The mixed volume stops descending when $w(z) = 0$. At this depth, the first term in w is negligible; thus

$$-z_{\max} \simeq \frac{32}{7}(\Gamma - g)N^{-2}l_c$$

The maximum velocity is obtained at half this distance:

$$-w_{\max} = \frac{4}{7}(\Gamma - g)N^{-1}l_c \quad \text{at} \quad -z = \frac{16}{7}(\Gamma - g)N^{-2}l_c$$

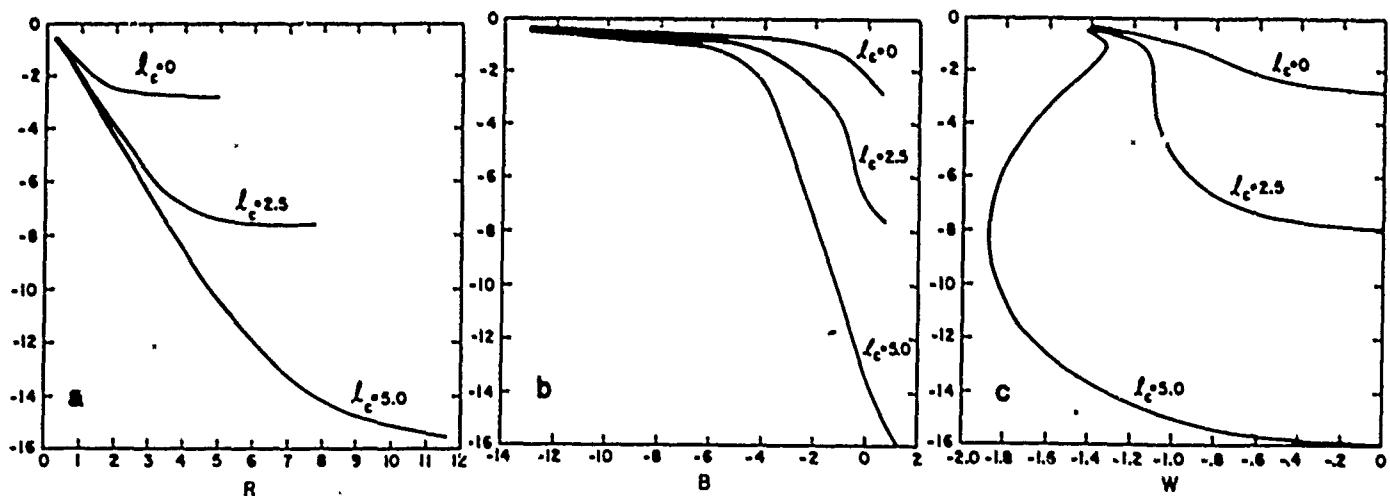


FIG. 1. Nondimensional plume radius R , buoyancy B and vertical velocity W as functions of dimensionless depth, for three values of the normalized cloud water content (l_c).

The important length scale here is $(\Gamma - g)N^{-2}l_c$, around 8 km for a 2 gm/km water content cloud. Note that this is independent of the entrainment parameter α . Corresponding vertical velocities reach 10 m/s. Also note that the plume is still unsaturated when it stops. As the thermal descends and expands, it gradually loses buoyancy and would eventually come to rest. But since it is still unsaturated at this point (when $Q_s - Q$ is everywhere positive), its base would be unstable for the same reason that the cloud top itself is. Were this to happen, new thermals would be formed from older ones. This implies either that the thermals would split on their descent or that they would maintain a nearly constant radius; in either case, similarity breaks down because of the importance of the length scale $(\Gamma - g)N^{-2}l_c$.

Despite the invalidity of similarity theory, we may conclude that cloud top instability produces downdrafts of at least the magnitude of ordinary cumulus updrafts. It is likely that this mechanism dominates the dynamics of non-precipitating clouds.

References

- Emanuel, K.A. (1981) A similarity theory for unsaturated downdrafts within clouds. *J. Atmos. Sci.*, **38**, 1541-1557.
- Malkus, J.S. (1954) Some results of a trade-cumulus cloud investigation. *J. Met.*, **11**, 220-237.
- Paluch, I.R. (1979) The entrainment mechanism in Colorado cumuli. *J. Atmos. Sci.*, **36**, 2467-2478.
- Warner, J. (1955) The water content of cumuliiform cloud. *Tellus*, **7**, 449-457.

Notes by Jim Countryman and Stephane Douady

6. TAXONOMY OF PRECIPITATING CLOUDS

In this lecture we will review some observations of different cloud systems. The first type of precipitating cloud system to become fairly well understood is known as an air mass thunderstorm. These relatively common storms (typical of Florida) tend to form in areas where there is little background horizontal wind, and move in the direction of that wind. A system of this type is made up of a random conglomeration of smaller individual cloud cells, in various states of growth and decay. These cells typically exist for about 30 minutes, although the storm system itself can last many hours. Air mass thunderstorms are about 5 to 10 km in height, with an order one aspect ratio. The evolution of individual cells can be characterized by three stages: the cumulus stage, the mature stage, and the dissipating stage.

The early stage of a single air mass thunderstorm cell is known as the cumulus stage, shown schematically in Fig. 6.1. During this stage, there is a net upward mass flux due to a mean upward vertical velocity at all levels in the cloud. There is little or no precipitation falling to the ground, but there is formation of precipitation-sized droplets inside the cloud. The second phase of a cell's life is the mature stage (Fig. 6.2). Cloud-scale downdrafts appear, along with surface rain. The final, dissipating, stage is characterized by weak downward motion and light surface rain (Fig. 6.3).

The dynamical consequences of the surface rain that appears during the mature stage can be very important, and will be the subject of a subsequent lecture, but one aspect should be mentioned in this context. As the rain falls into the relatively dry air below the cloud, some of the water is evaporated, thus cooling the air and increasing its density. This heavy air falls and spreads as a density current (gust), lifting light air as it moves. It is possible that this process of uplifting could initiate the growth of new convection cells, and hence explain why these cells tend to conglomerate into large systems (Fig. 6.4).

A second type of precipitating cloud system is known as an organized multi-cell storm. In contrast with the air mass thunderstorm, these relatively rare storms tend to form in areas with a fairly large vertical shear of the mean horizontal background wind, and do not move in the directions of the mean wind. In fact, they usually move at an angle to the right of the mean wind (in the Northern Hemisphere), with new cells forming preferentially on the right side of the storm (Fig. 6.5, 6.6ab). Unlike an Ekman layer, this symmetry breaking is not due directly to the earth's rotation, since the storms are too small and too short-lived. Instead, it is due to the shear of the mean wind veering to the right with height. Occasionally, the mean shear progresses to the left with height, resulting in preferential motion to the left of the mean wind (Fig. 6.6c).

In areas of even larger vertical shear, a third class of storm may develop, known as a supercell. As the name implies, this is a quasi-steady, single cell storm that is extremely energetic. In fact, they can be so violent that they can lead to the formation of tornados. They are typically about 10 km in horizontal extent, and can last several hours and produce a great deal of precipitation. Supercells are usually continental, and are seen mostly in the midwest of the United States and sometimes in Australia. A schematic of a supercell is shown in Fig. 6.7, and an actual radar image in Fig. 6.8. Note in the radar image that there is no signal from the "vault" region, and therefore no rain there. This reflects

the fact that upward velocities in the vault are typically 50 m/s, resulting in an advective time scale that is much shorter than the water droplet coalescence time scale. Most of the energetic motions in a supercell occur on the scale of the cloud radius, as opposed to the nonprecipitating case where most of the motion seems to appear at scales much smaller than the cloud. As a result, numerical models have been quite successful (in this instance) in helping to understand such systems.

A fourth type of precipitating cloud system is the squall line (Fig. 6.9). Like an air mass thunderstorm, a squall line is a group of individual convection cells, but the cells are arranged in a line that typically propagates at a speed of a few to as many as ten m/s. Broadly speaking, there are two types of squall lines. The first type is the so-called "slow" squall line (fig. 6.10), which is more common in the tropics, and lines up in the direction of the vertical shear of the mean horizontal background wind. There is relative flow into the squall line at all heights since $V_n - V_c$ is always positive, where V_c is the composite line speed and V_n is the wind speed normal to the line. The second type is called a "fast" squall line (Fig. 6.11), and is more common in mid-latitudes. As opposed to the "slow" case, these lines are oriented perpendicular to the mean shear. Again, there is relative flow into the line at all heights, except for a small range around a height of 4km. It is interesting to note that dry convection theories, even nonlinear formulations, predict squall lines forming only along the mean shear, as in the case of slow squall lines, but in contrast to the case of fast squall lines.

This concludes our brief look at examples of precipitating storm systems in the earth's atmosphere. Next, we will turn to the dynamics of precipitating convection.

References

- Barnes, G.M., and K. Sieckman (1984) The environment of fast- and slow-moving tropical mesoscale convective cloud lines. *Mon. Weath. Rev.*, 112, 1782-1794. (6.10-6.11)
- Browning, K.A. (1964) Airflow and precipitation trajectories within severe local storms which travel to the right of the winds. *J. Atmos. Sci.*, 21, 634-639. (6.7)
- Browning, K.A. (1965) Some inferences about the updraft within a severe local storm. *J. Atmos. Sci.*, 22, 669-677. (6.8)
- Byers, H.R., and R.R. Braham, Jr. (1948) Thunderstorm structure and circulation. *J. Met.*, 5, 71-86. (6.1-6.4)
- Houze, R.A., Jr., and A.K. Betts (1981) Convection in GATE. *Rev. Geophys. Space Phys.*, 19, 541-576.
- Marwitz, J.D. (1972) The structure and motion of severe hailstorms. Part II: Multi-cell storms. *J. Appl. Met.*, 11, 180-188. (6.5-6.6)
- Zipser, E.J., R.J. Meitin, and M.A. LeMone (1981) Mesoscale motion fields in association with a slow-moving GATE convective band. *J. Atmos. Sci.*, 38, 1725-1750. (6.9)
- See also Houze and Betts (1981).

Notes by Tim Dowling and Mat Maltrud

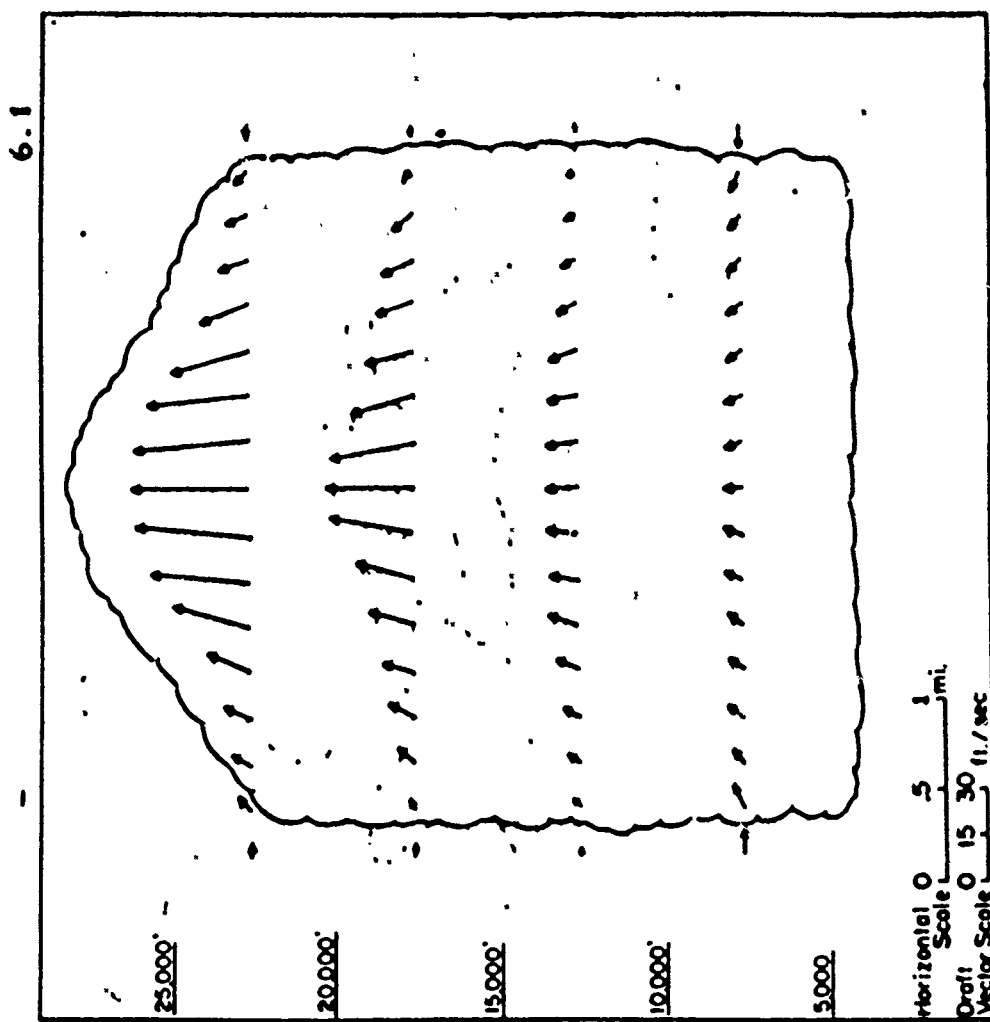


FIG. 6. Circulation within a typical cell in cumulus stage. Inflow and vertical motion beneath the cloud is light and is not shown.

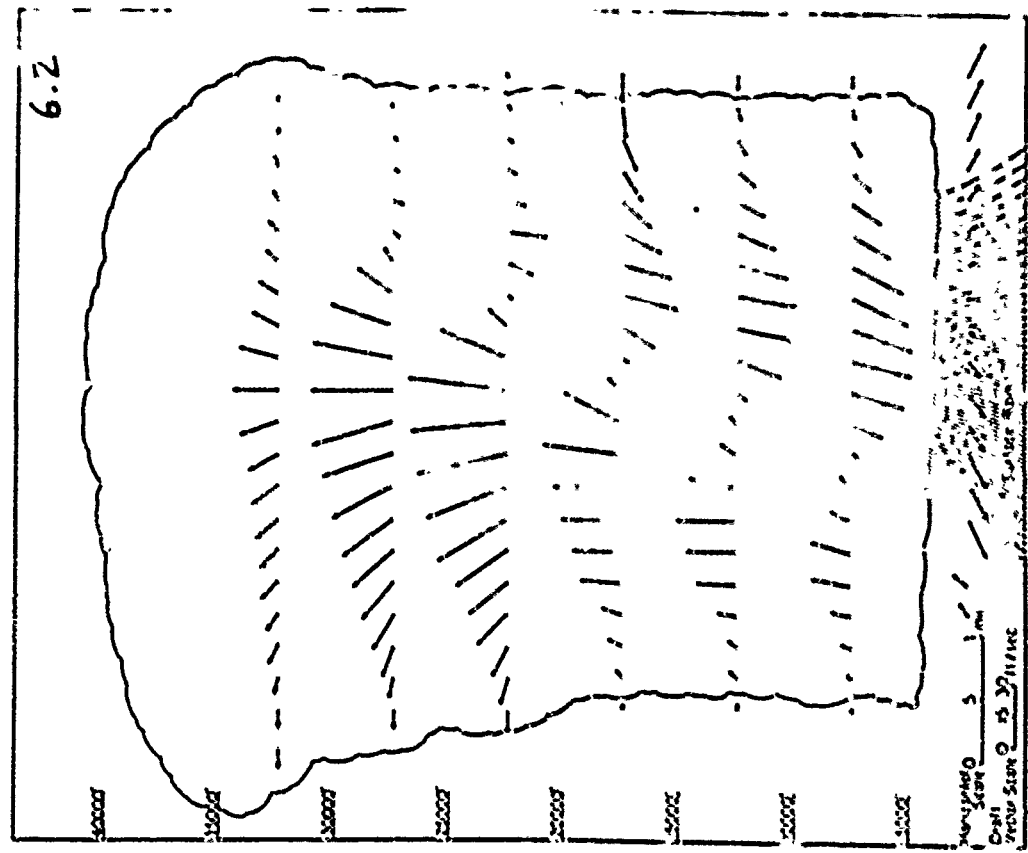


FIG. 11. Circulation within a typical cell in mature stage

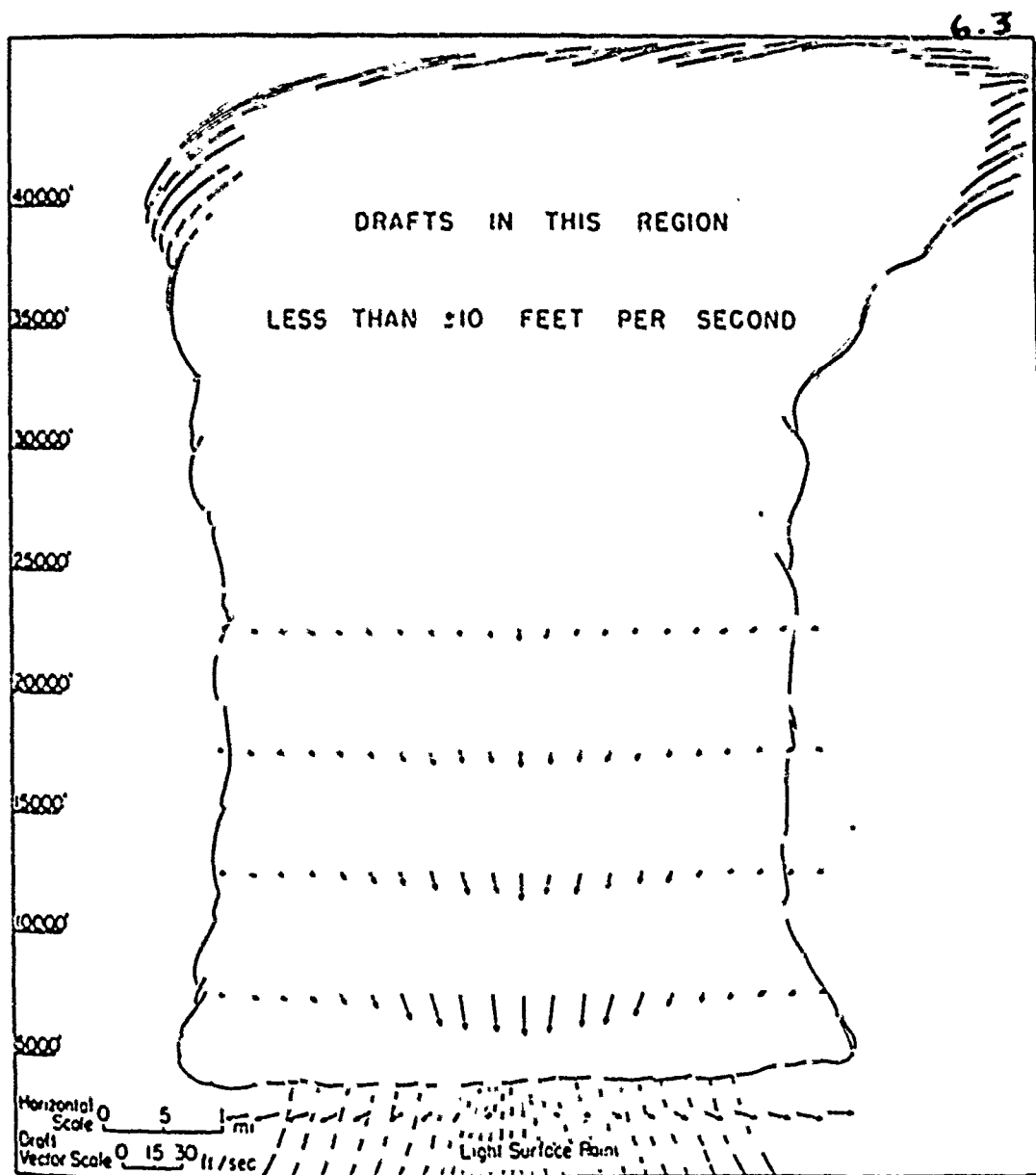


FIG. 12. Circulation within a typical cell in dissipating or anvil stage.

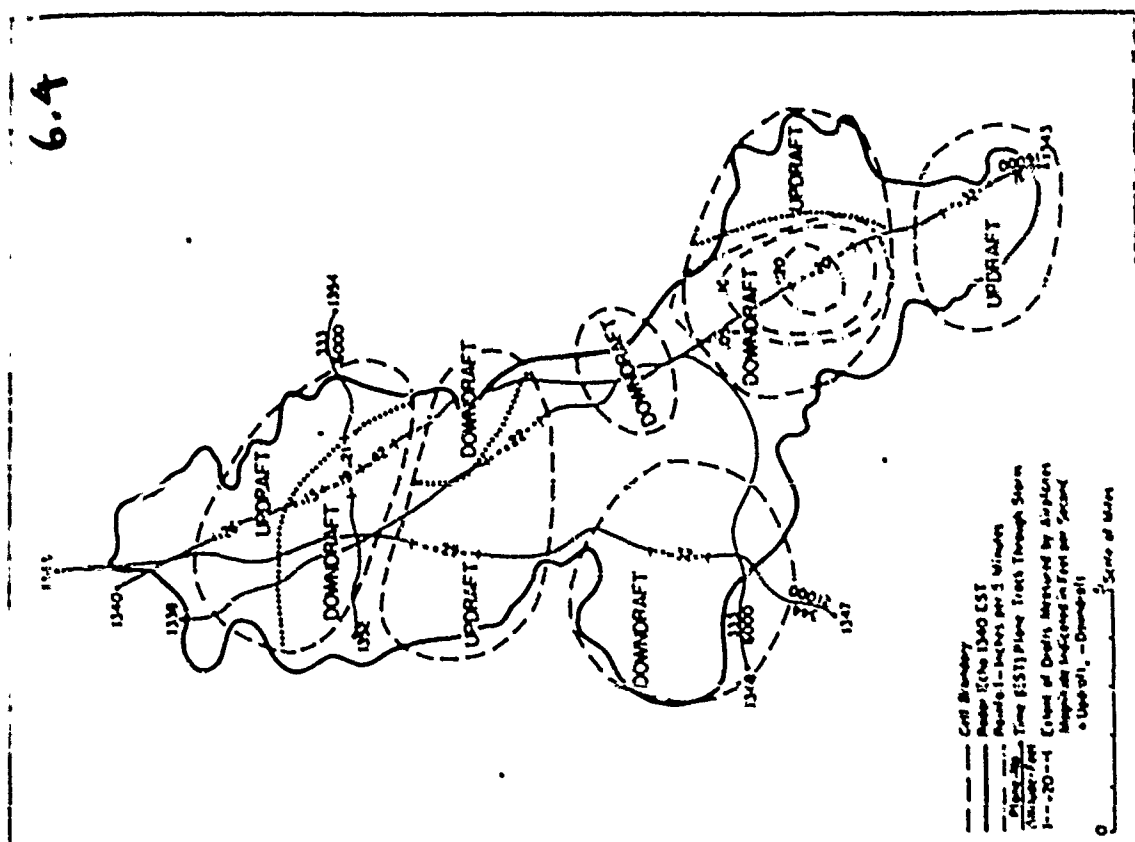
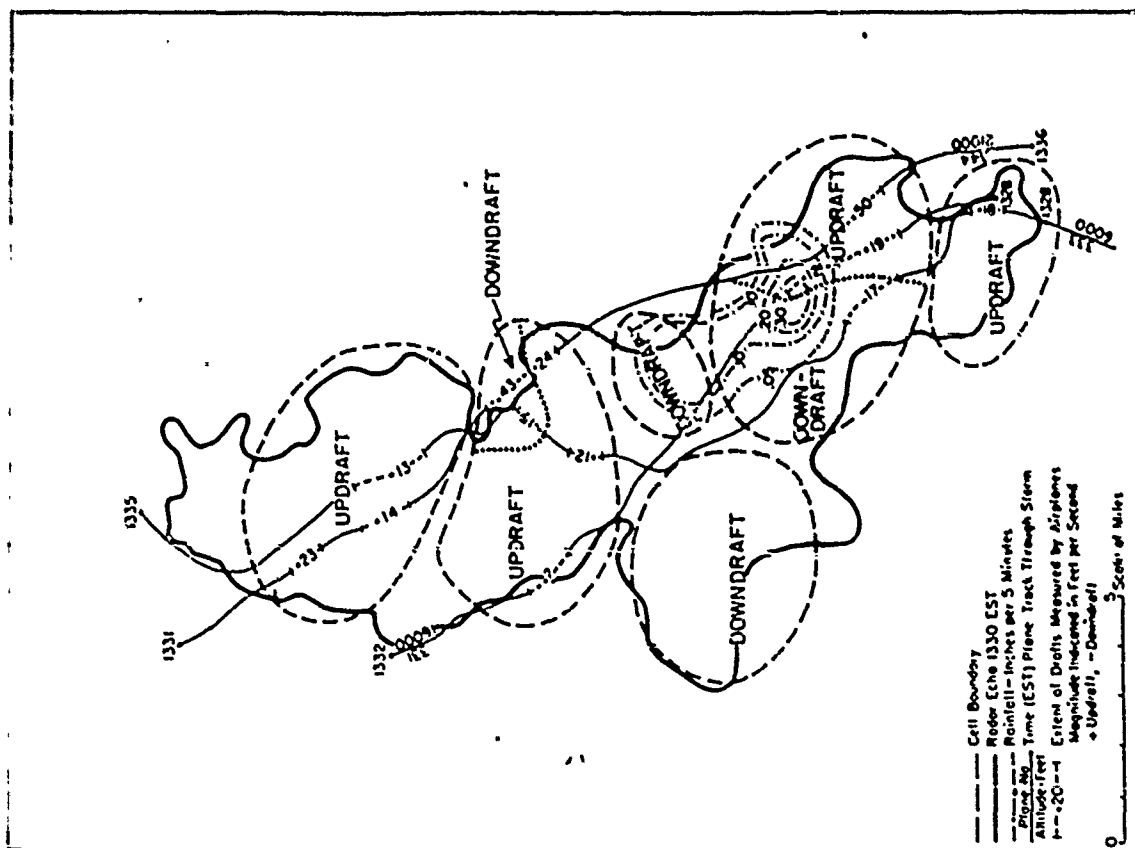


FIG. 18. Radar echo, plane paths, measured draft data, and cell outlines, 1340 EST 9 July 1946.



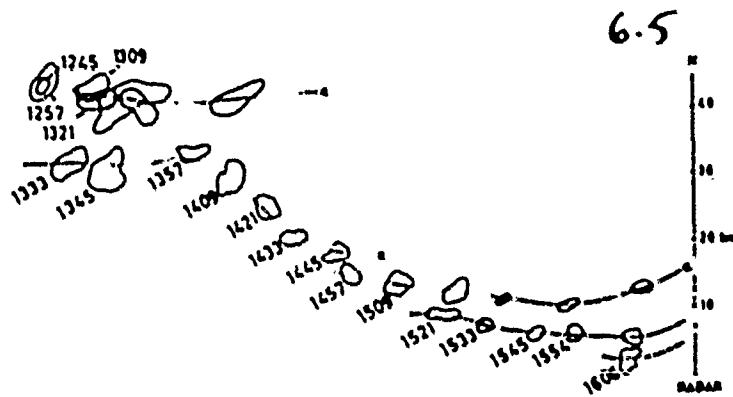
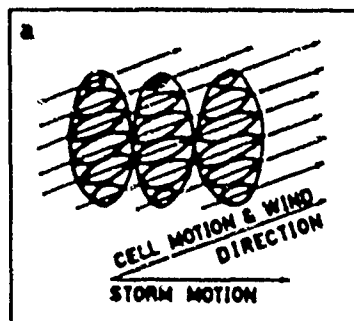


FIG. 8. Echo outlines of individual cells near the top of the Alhambra storm.



6.6

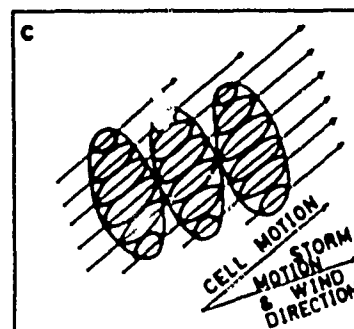
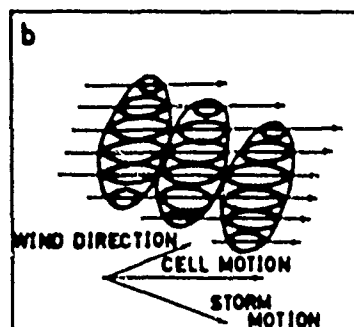


FIG. 18. Schematic diagrams of the Wokingham, Alhambra and Rimbey storms.

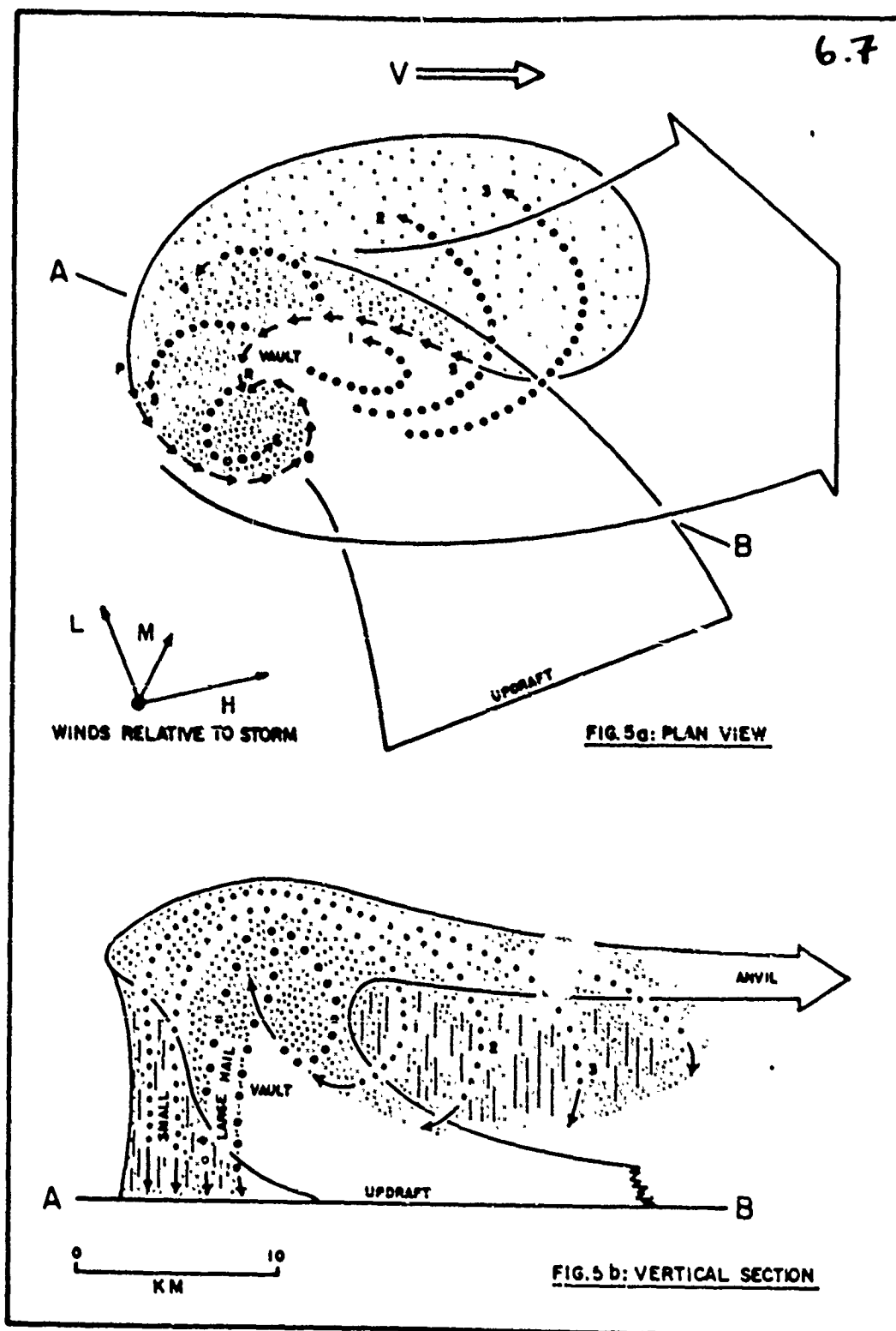


FIG. 5. Schematic horizontal (Fig. 5a) and vertical (Fig. 5b) sections qualitatively illustrating precipitation trajectories in different parts of an SK storm traveling at a velocity V . In both figures the extent of the updraft is represented by solid curves and precipitation trajectories are represented by dotted curves. In the horizontal section the extents of rain and hail close to the surface are represented by light and heavy shading, respectively, and the arrows around PQRS indicate the direction of motion of protuberances on the edge of the low-level radar echo. The vertical section along AB is oriented in the direction of the mean wind shear, into which the updraft is inclined at low and medium levels. In the vertical section the presence of downdrafts with strong normal components of motion is indicated by broken vertical hatching. On the downshear side of the updraft (right side of page) these components are directed into the page; beneath the updraft, on its upshear side, they are directed out of the page (cf. Fig. 2).

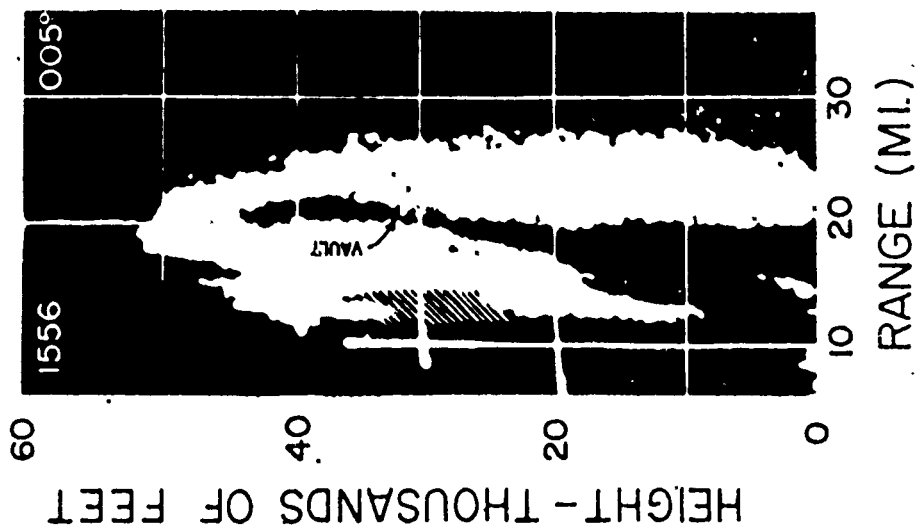


FIG. 7a. Vertical section through Storm E and the curtain obtained with the FPS-6 along 005 deg at 1556 CST. Fig. 7a shows an original RHI photograph with exaggerated vertical scale for which $Z_e = 10^4 \text{ mm}^4 \text{ m}^{-3}$ at 20 mi range.

6.8

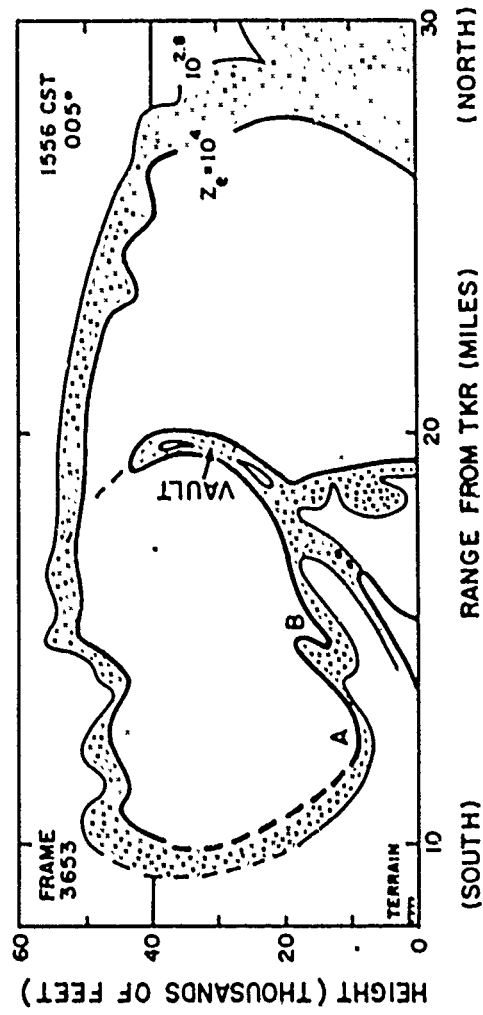


FIG. 7b. Vertical section from Fig. 7a drawn in true scale together with another intensity contour for $Z_e = 10^4 \text{ mm}^4 \text{ m}^{-3}$. Note the curtain of precipitation from Storm G entering the section at 15 mi range and then being borne upward into Storm E's vault.

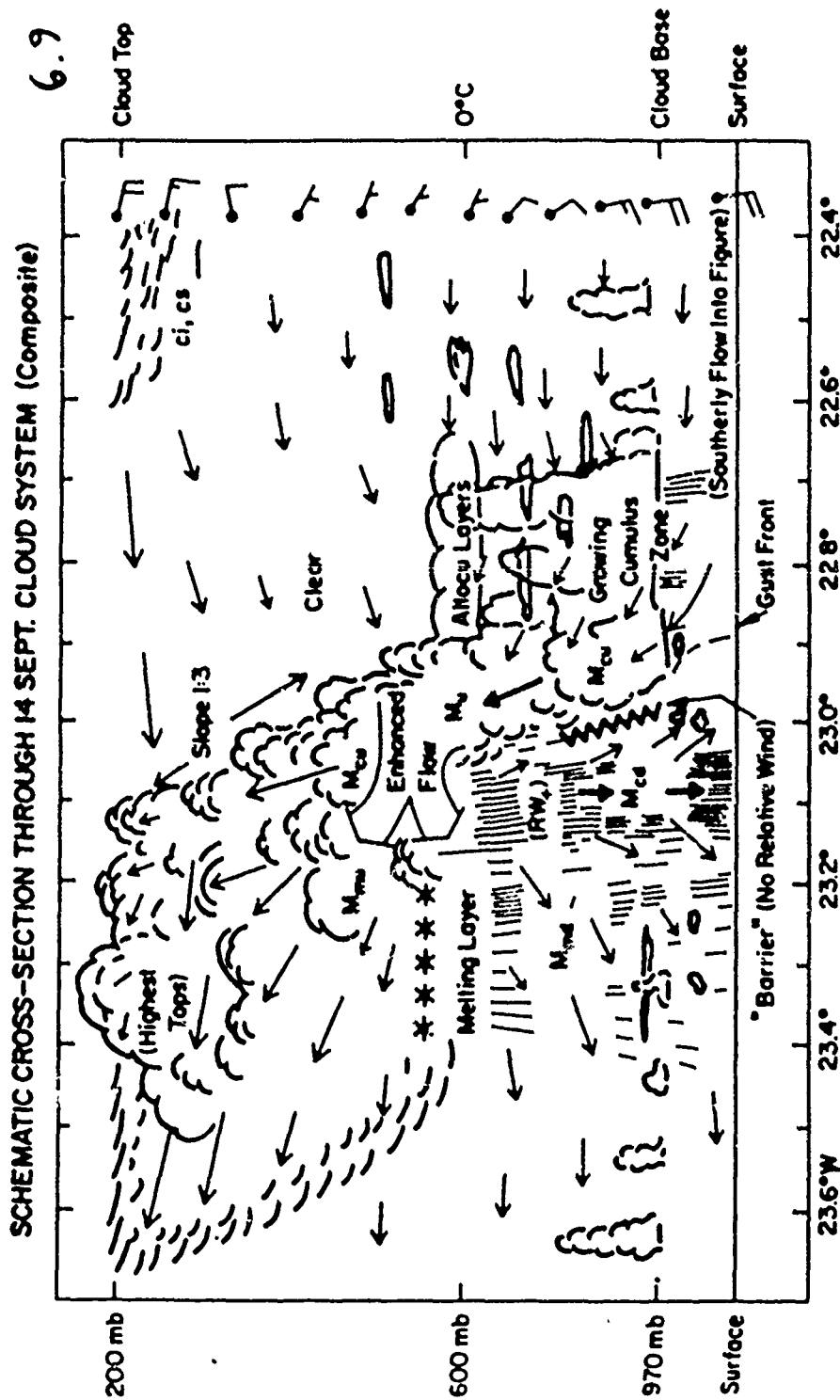


FIG. 8. Cross section through the north-south convective band constructed as a composite, representing best the time period of leg 5 (~1333 GMT). System motion is left to right at 2.5 m s^{-1} . The wind arrows along the right margin represent the large-scale flow field; each full barb is 5 m s^{-1} . The small arrows throughout the system represent flow relative to the system in the normal and vertical directions, based on Figs. 3 and 4 but partially schematic. See text.

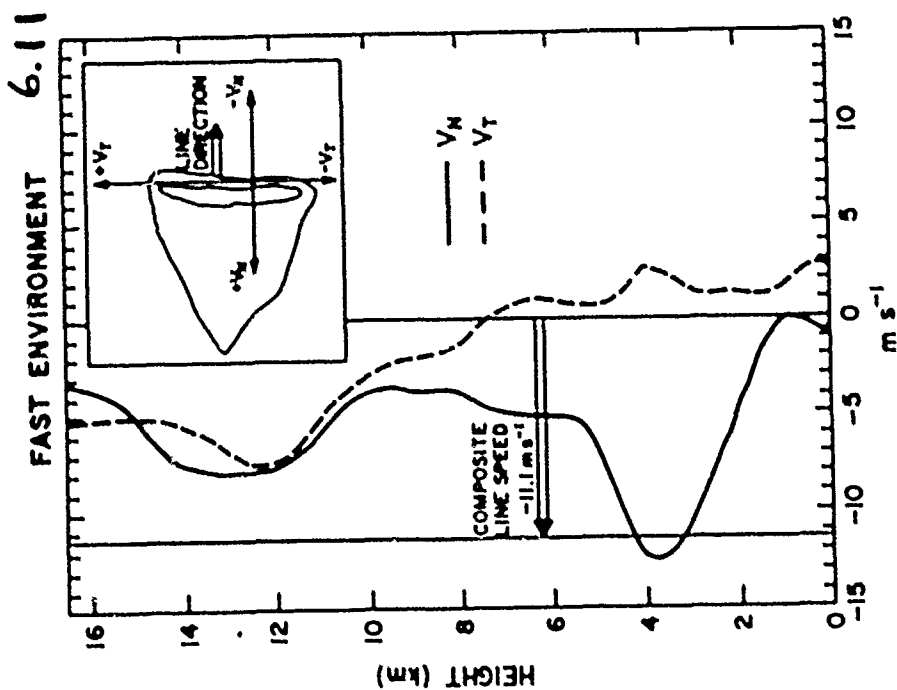


FIG. 7. Composite profile of the wind component normal (V_N , solid) and parallel (V_T , dashed) to the leading edge of a squall line for the environment. The mean line speed is shown by a thin vertical line.

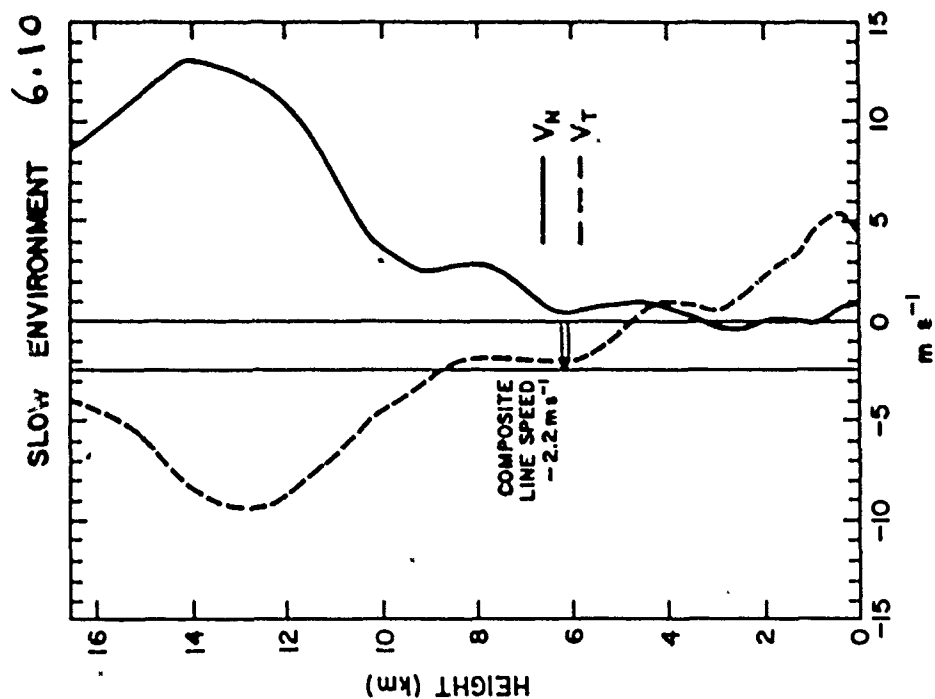


FIG. 8. As in Fig. 7 but for the slow-moving cloud line.

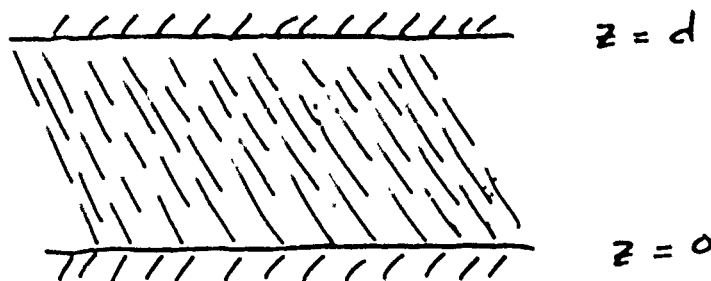
7. THE DYNAMICS OF PRECIPITATING CONVECTION

Four main points distinguish precipitating convection from non-precipitating convection:

- i) If precipitation reaches the ground there is a net vertically integrated latent heat release over the cloud lifetime.
- ii) The thermodynamics of precipitating convection is irreversible (although this is a small effect: for practical purposes 'conserved' quantities are approximately conserved).
- iii) There are buoyancy sinks and sources due to a) the weight of liquid water and b) latent heating (cooling) due to evaporation in unsaturated air, which are uncoupled from the vertical displacement. This enables disturbances to propagate.
- iv) Condensate may accumulate locally where $w \simeq v_T$ where v_T is the velocity at which rain drops fall, assumed to be their terminal velocity.

A Model Problem

As a means of appreciating the dynamical effects of falling precipitation, we formulate a very simple, linear, parallel-plate convection problem. Consider a flow between two horizontal plates. Assume that the air is saturated and is unstably stratified. There is a constant flux of liquid water through the top boundary, (its exact rate is irrelevant so long as it is enough to keep the condensate content finite): a so called 'shower head' boundary condition.



Also assume that the time scale of evaporation is negligibly small compared to the time scale of raindrop motions and that all drops of liquid water fall at the same fixed terminal velocity v_T . We consider only two-dimensional motions in the x, z plane.

The linearised equations governing inviscid, Boussinesq motions are:

$$u_t = -\alpha_0 p_x \quad (7.1)$$

$$w_t = -\alpha_0 p_z + B - gl \quad (7.2)$$

$$B_t + w\bar{B}_z = \dot{Q} = -\frac{L_v g}{c_p T_0} w\bar{q}_{sz} \quad (7.3)$$

$$l_t - v_T l_z = -w\bar{q}_{sz} \quad (7.4)$$

$$u_x + w_z = 0 \quad (7.5)$$

where u and w are the horizontal and vertical velocities, B is the buoyancy perturbation due to all effects other than liquid water loading and $\bar{B}(z)$ is a mean buoyancy. l is the perturbation mass mixing ratio of liquid water and $\bar{q}_s(z)$ is a mean saturation water vapor mixing ratio. We can rewrite the buoyancy equation as

$$B_t = w\bar{N}^2 \quad (7.6)$$

where

$$\bar{N}^2 \equiv -\frac{g}{c_p T_0} \bar{h}_{v,z} \quad (7.7)$$

and

$$\bar{h}_v = \bar{B} + \frac{L_v g}{c_p T_0} \bar{q}_s \quad (7.8)$$

\bar{h}_v is a mean virtual moist static energy. We can use (7.5) to define a stream function:

$$w \equiv \psi_z, \quad u \equiv -\psi_x \quad (7.9)$$

and combine (7.1) and (7.2) to eliminate pressure and form a vorticity equation, reducing the system to three equations.

$$(\nabla^2 \psi)_t = B_x - gl_x \quad (7.10)$$

$$B_t = \bar{N}^2 \psi_x \quad (7.11)$$

$$l_t - v_T l_x = -\psi_x \bar{q}_{s,x} \quad (7.12)$$

First consider the case where there are no top and bottom boundaries. The only length scale in the problem is $L = v_T / \bar{N}$. We use the following non-dimensionalization (where now a * indicates a dimensional variable):

$$\begin{aligned} (x^*, z^*) &= (v_T / \bar{N}) (x, z) \\ B^* &= N v_T B \\ \psi^* &= (v_T^2 / \bar{N}) \psi \\ t^* &= \bar{N}^{-1} t \\ l^* &= -\bar{q}_{s,x} v_T \bar{N}^{-1} l \end{aligned} \quad (7.13)$$

Then (7.10) to (7.11) become

$$(\nabla^2 \psi)_t = B_x - \alpha l_x \quad (7.14)$$

$$B_t = \psi_x \quad (7.15)$$

$$l_t - l_x = -\psi_x \quad (7.16)$$

where $\alpha \equiv -g \bar{q}_{s,x} / \bar{N}^2$ is the only parameter remaining in the problem. (α may be interpreted as the ratio of buoyancy due to liquid water loading to buoyancy due to temperature

changes.) We first consider the unbounded problem. Seeking normal mode solutions of the form

$$\psi = \text{Re} \left[\hat{\psi} e^{\sigma t + i(kx + rz)} \right] \quad (7.17)$$

etc., we obtain a cubic equation for the growth rate, σ :

$$\sigma^2 \left(1 + \frac{r^2}{k^2} \right) = 1 - \frac{\sigma \sigma}{\sigma - ir} \quad (7.18)$$

In general σ is complex implying both growth/decay and propagation. The growth rate σ_r and phase speed $-\sigma_i/k$ are shown as functions of $\beta \equiv 1/(1 + r^2/k^2)$.

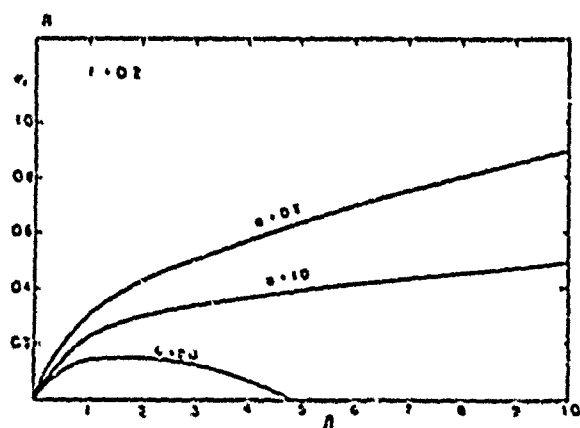


FIG. 1. Dimensionless growth rates of unbounded modes as a function of β for several values of α . Vertical wavenumber (a) $r = 0.2$ and (b) $r = 0.8$.

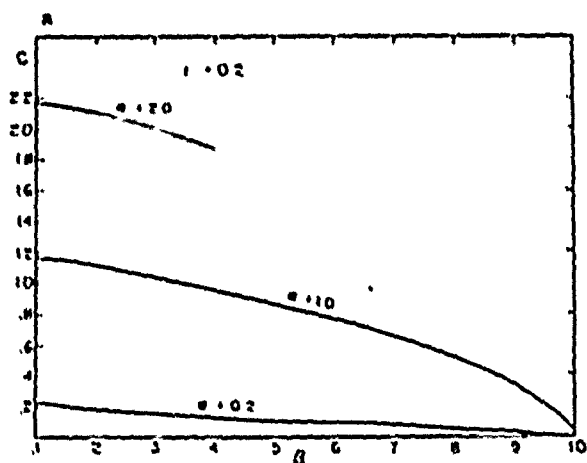
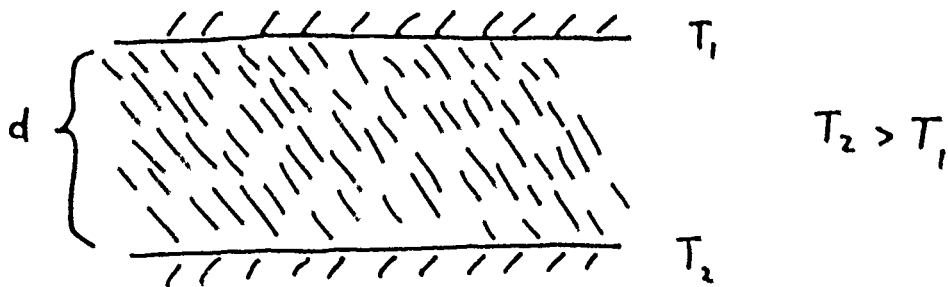


FIG. 2. As in Fig. 1 but showing dimensionless phase speeds.

The effect of falling water in this case is to cause the convection to propagate (oscillate), although the propagation direction is arbitrary. This effect was first explained by Seitter and Kuo (1983) who demonstrated that the phase-lagged buoyancy effects of falling rain lead to vorticity generation that is out of phase with the vorticity itself.

Precipitating Convection Between Two Plates

The domain for this dynamical model is now set to be that of the classical global convection problem between two parallel plates. This introduces a length scale, d , the separation length between the two plates.



One may now non-dimensionalize the problem in the following manner:

$$\begin{aligned}
 (x^*, z^*) &= d(x, z) \\
 B^* &= \tilde{N}^2 dB \\
 \psi^* &= \tilde{N} d^2 \psi \\
 t^* &= \tilde{N}^{-1} t \\
 l^* &= -\bar{q}_{zz} dl \\
 v_T^* &= \tilde{N} dv_T
 \end{aligned} \tag{7.19}$$

This will prove to be convenient in developing the governing equations. One still assumes a periodic solution in x similar to (7.17).

$$\psi = \Psi(z) e^{\omega t + i k x} \tag{7.20}$$

One now goes back to the governing equations and eliminates B and l in favor of Ψ to get:

$$\omega^2 v_T \Psi_{zzz} - \omega^3 \Psi_{zz} + v_T k^2 (1 - \omega^2) \Psi_z + \omega k^2 (\omega^2 + \alpha - 1) \Psi = 0 \tag{7.21}$$

This third order equation in z requires three boundary conditions. Along with assuming that the plates are rigid, it also assumed that the liquid water perturbation cannot exist over the top boundary. When combined with governing equations of conservation of momentum and buoyancy, one gets:

$$l = 0 \quad \text{at} \quad z = 1 \quad \Rightarrow \quad \Psi_{zz} = 0 \quad \text{at} \quad z = 1 \tag{7.22}$$

along with

$$\Psi = 0 \quad \text{at} \quad z = 0, 1 \tag{7.23}$$

This now constitutes an eigenvalue problem for the growth rate ω , as a function of α , v_T and k . A periodic solution of $\Psi(z) = \exp(iz)$ is assumed leading to another cubic dispersion relation. This equation is singular in v_T ; however, a diffusion term will correct this. The solutions of this cubic relation in r are found numerically, leading to 2 general classifications: propagating modes and non-propagating modes as shown:

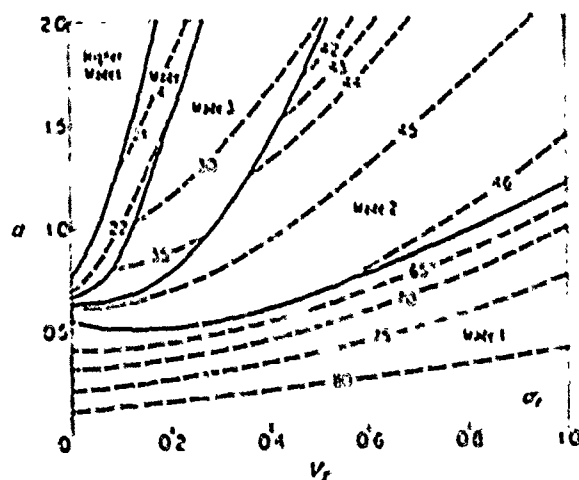


FIG. 3. Dimensionless growth rates of parallel-plate bounded stationary modes as a function of α and V_T for the case $k = 5$. Heavy solid lines denote mode transitions.

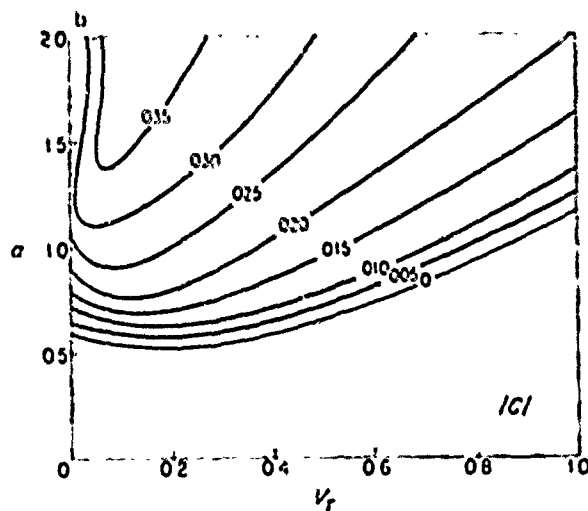
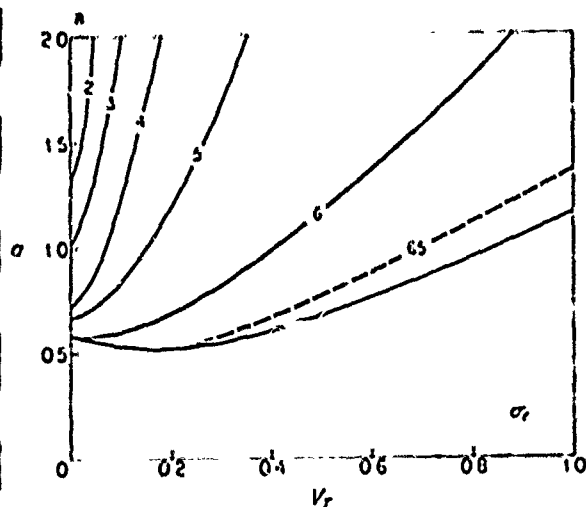


FIG. 4. As in Fig. 3 but (a) for gravest propagating modes. Heavy solid line at bottom shows limit of existence of propagating modes; (b) dimensionless phase speeds.

The symmetry of the problem prevents a favored direction of propagation. The phase speed may also be represented as a function of v_T and α

Finally, we present the stream functions for a propagating mode:

One of the important features to come out of this model is the lag between the updrafts and rainwater in the propagating mode. Propagating convection is favored for the system when the drag exerted by the falling liquid water from a vertical motion is comparable to the thermal buoyancy.

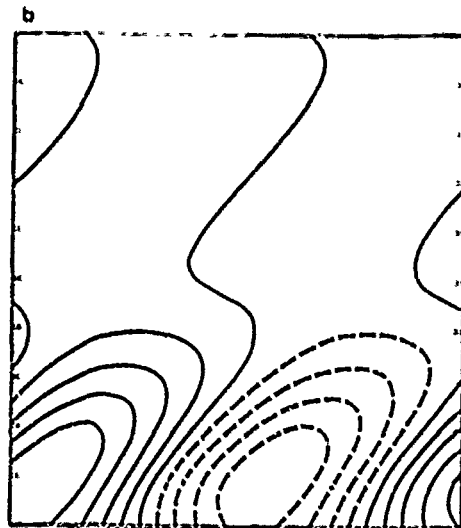
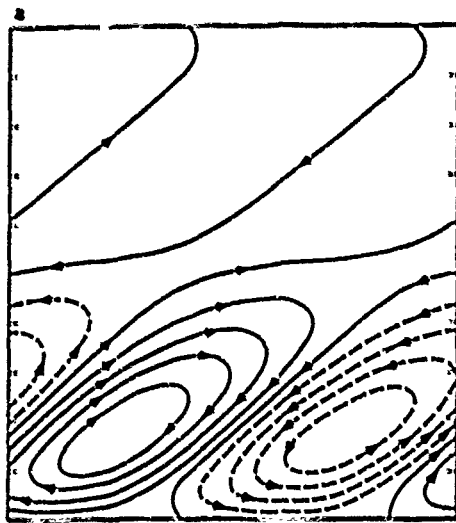
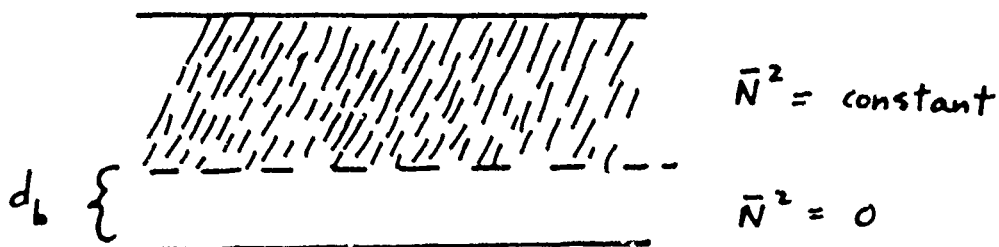


FIG. 7. (a) Streamfunction (normalized to have an amplitude of 1.0) associated with mode dominated by internal vertical scale l'/N , for $n = 2.0$; $l'_r = 0.032$ and $k = 2.1$; modes shown move from right to left at a dimensionless speed of 0.026; growth rate is 0.112. (b) Liquid water perturbation associated with mode shown in (a); dimensionless amplitude is 3.0 times the streamfunction amplitude

Precipitating Convection with a Sub-cloud Layer

One may study some of the aspects of sub-cloud evaporation by breaking the vertical domain to include a dry lower level.



Now the formed condensate from the moist convection falls into the dry level and may evaporate. It is assumed that the rate of evaporation is proportional to the amount present. The governing equations for the upper cloud layer remain the same while the equations governing the lower level are:

$$(\nabla^2 \psi)_t = B_z - \alpha l_z \quad (7.24)$$

$$B_t = -\alpha E M l \quad (7.25)$$

$$l_t - v_T l_z = -E l \quad (7.26)$$

where E is the evaporation rate normalized by \bar{N} , and M is proportional to the heat of vaporization:

$$M \equiv \frac{L_v}{c_p \bar{T}} \quad (7.27)$$

Solutions are found by matching vertical displacement, pressure and condensate across the boundary. Similarly, a dispersion relation is found which must be solved numerically. This now leaves a parameter space of α , v_T , E , and d which is too large to explore thoroughly. Solutions are found to fall into 2 categories. The first are "cloud" modes which are similar to the previous system. The second classification is the "sub-cloud" mode which is believed to be an artifact of the model. The stream function, perturbation liquid water and pressure perturbation fields are given for the "cloud" mode. It is noted that the pressure perturbation field shows strong similarity to the field produced by LeMone et al. (1984b) for a tropical squall line.

Precipitating Convection with a Mean Wind Shear

A final model of precipitating convection is explored in which the effects of a mean wind shear are roughly included. For simplicity, it has been assumed that the sub-cloud layer is at rest while the cloud layer is moving with a uniform velocity U . The governing equations are identical to the previous sections' with the exception that the normal mode solutions are Doppler-shifted (the growth rate is replaced by the complex expression $\sigma + ikU$) for the cloud layer. One then must again match the pressure, liquid water, and vertical displacement across the interface. It is noted that the stream function is no longer continuous across the layers. We avoid the usual shear modes by considering those modes whose phase speed lies outside the "Howard semi-circle", i.e. $c > U$ or $c < 0$. The effect of the shear on the growth rate and phase speed is shown below

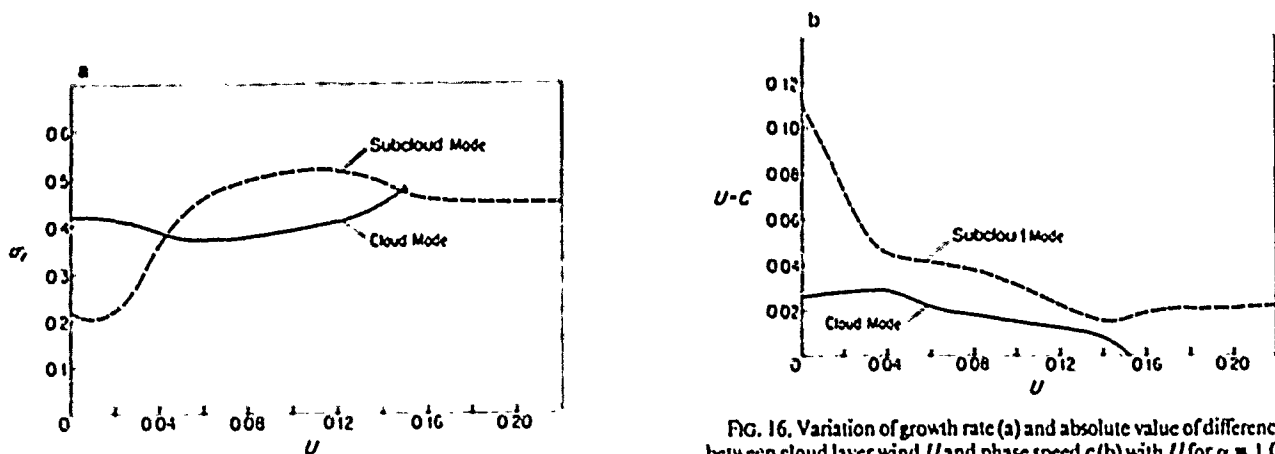


FIG. 16. Variation of growth rate (a) and absolute value of difference between cloud layer wind U and phase speed c (b) with U for $\alpha = 1.0$, $v_T = 0.1$, $E = 0.5$, $z_b = 0.2$ and $k = 5.0$.

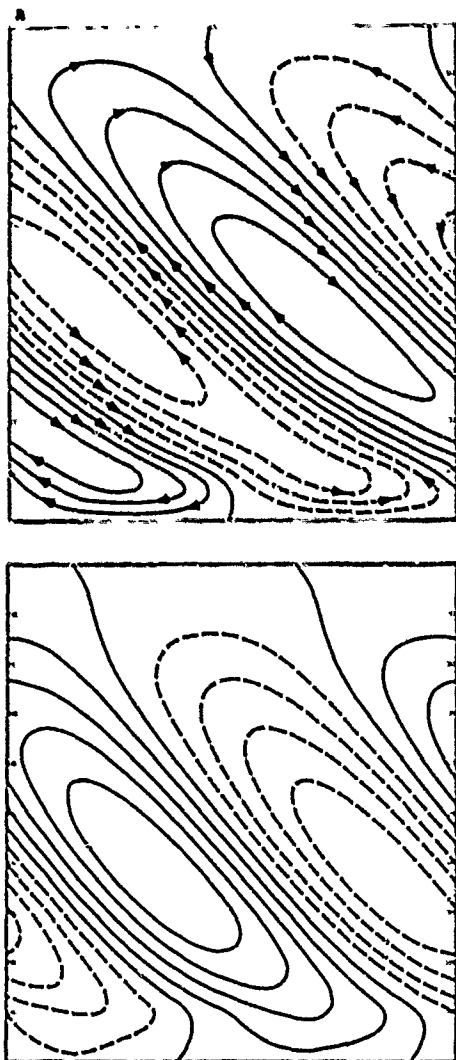


FIG. 12. (a) Streamfunction (normalized to have an amplitude of 1.0) associated with "cloud mode" for $\alpha = 1.0$, $V_r = 0.1$, $F = 0.5$ and $k = 8.0$; mode moves from left to right with a dimensionless speed of 0.022 and growth rate of 0.535; depth of subcloud layer is 0.1. (b) Perturbation liquid water associated with mode shown in (a); amplitude = 8.45.

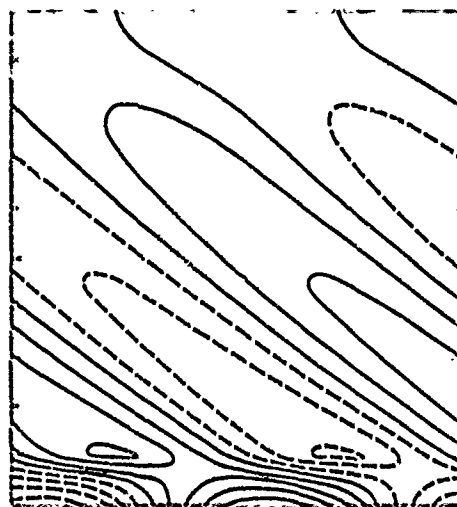


FIG. 13. Pressure perturbation associated with mode shown in Fig. 12; amplitude = 1.14 times the streamfunction amplitude.

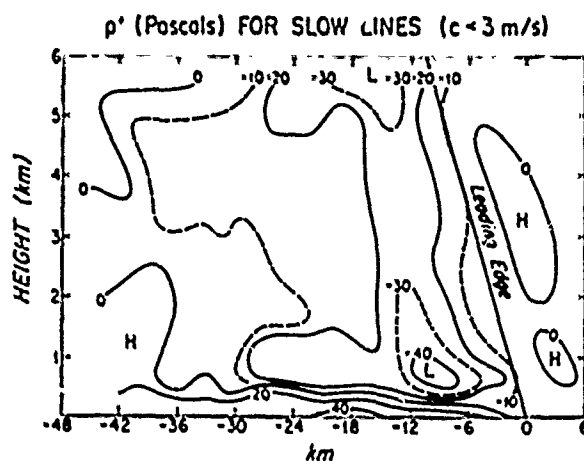


FIG. 14. Composite pressure perturbation (P') relative to inflow environment for slow-moving tropical squall lines. Sloping line indicates position of leading edge of clouds associated with squall. Dotted lines at left indicate average flight levels of aircraft. Note vertical scale exaggeration of 5:1. [From LeMone et al. (1982b)].

Next the growth rate is shown as a function of the evaporation constant E and the mean shear. For a given evaporation rate there is seen to be an optimal shear velocity. For weaker shear velocities convection parallel to the shear is preferred while for stronger shears perpendicular convection is the preferred form.

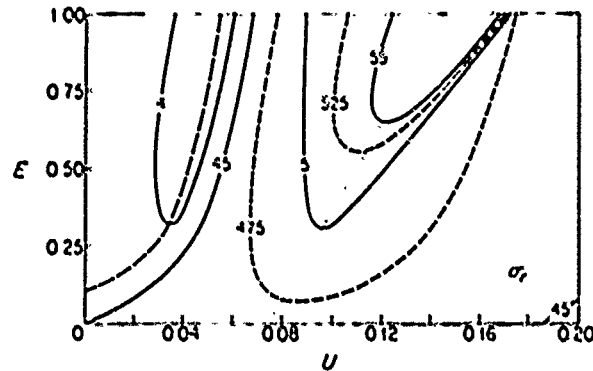


FIG. 18. Dimensionless growth rate as a function of evaporation rate E and cloud-layer/subcloud-layer shear U for $\alpha = 1.0$, $1/r = 0.1$, $z_A = 0.2$ and $k = 5.0$. Growth rates to left of heavy dashed line at left are associated with the "cloud mode"; all others pertain to "sub-cloud" mode. Dotted line denotes growth rate maximum.

Finally the dominant convective form as a function of the mean shear is shown:

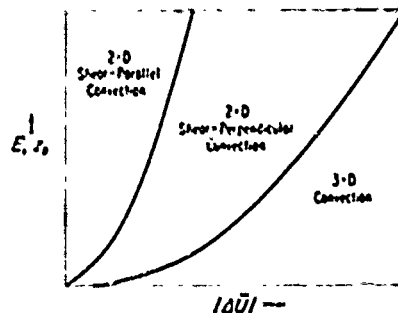
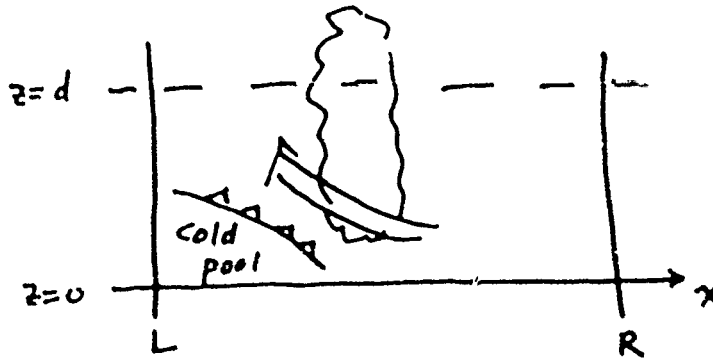


FIG. 19. Qualitative model regime diagram. Evaporation rate and/or subcloud-layer depth shown on ordinate while cloud-layer/subcloud-layer shear appears on abscissa.

A principal observation of this model is that precipitating convection can extract energy from the mean shear unlike non-precipitating convection.

The Optimal Low Level Shear

Rotunno et al. [1988] derive an expression for the optimal low-level shear: that which allows the updraft to be vertical.



Consider the region shown of depth d extending in the x direction from L to R . The vorticity equation for an incompressible Boussinesq fluid in two-dimensional motion may be written:

$$\frac{\partial \eta}{\partial t} + \nabla \cdot (\mathbf{v} \eta) = -\frac{\partial B}{\partial x} \quad (7.28)$$

In a frame of reference moving with the gust front the velocity is steady, so $\partial \eta / \partial t$ vanishes. Integrating (7.28) over the region shown we obtain:

$$\int_0^d [(u\eta)_R - (u\eta)_L] dz + \int_L^R (w\eta)_d dx = \int_0^d (B_R - B_L) dz \quad (7.29)$$

Assume the left and right boundaries are far enough away so that $\eta \simeq \partial u / \partial z$ there. Then

$$\frac{1}{2} [(u_{Rd}^2 - u_{R0}^2) - (u_{Ld}^2 - u_{L0}^2)] = - \int_L^R (w\eta)_d dx - \int_0^d (B_R - B_L) dz \quad (7.30)$$

Also assume there is negligible buoyancy in the air approaching the cold pool: $B_R = 0$, and demand that there is negligible advection of vorticity across the top boundary. Consider two cases;

Case i) No pre-frontal shear

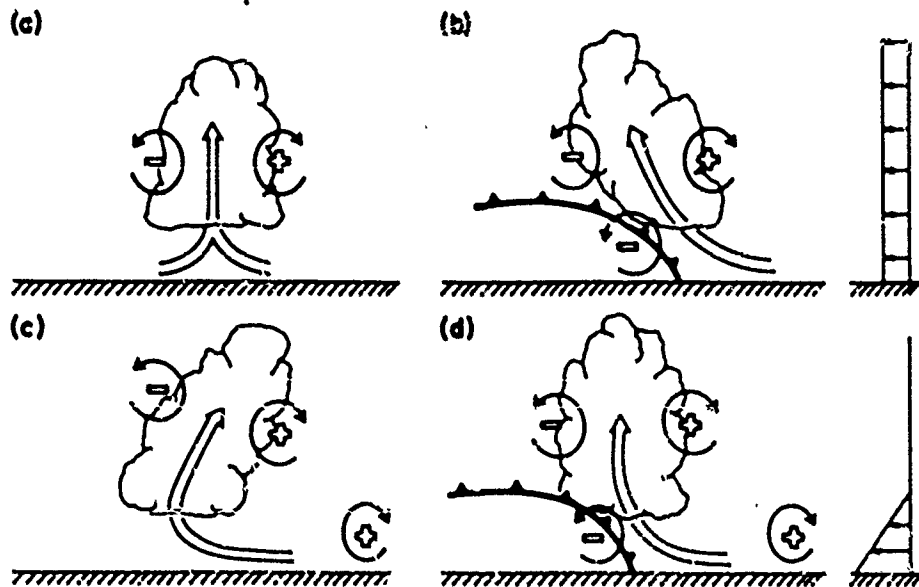
$u_{Rd} = u_{R0}$ and $u_{L0} = 0$ so (7.30) becomes

$$u_{Ld}^2 = -2 \int_0^d B_L dz \quad (7.31)$$

Note $\int_0^d B_L dz < 0$ because of the cold pool. Returning to a frame in which $u_{Ld} = 0$, we recover $(\int_0^d B_L dz)^{1/2}$ as the phase speed: just that of the classical gust front.

Case ii) Assume there is some incoming low-level shear Δu and ask what value of this shear will cause the low-level inflow to exit as a vertically oriented jet ($\int_L^R (w\eta)_d dx = 0$).

CASE 1)



CASE 2)

FIG. 18. Schematic diagram showing how a buoyant updraft may be influenced by wind shear and/or a cold pool. (a) With no shear and no cold pool, the axis of the updraft produced by the thermally created, symmetric vorticity distribution is vertical. (b) With a cold pool, the distribution is biased by the negative vorticity of the underlying cold pool and causes the updraft to lean upshear. (c) With shear, the distribution is biased toward positive vorticity and this causes the updraft to lean back over the cold pool. (d) With both a cold pool and shear, the two effects may negate each other, and allow an erect updraft.

Set $u_{Ld} = u_{Rd} = 0$ and $\int_L^R (w\eta)_d dx = 0$. Then equation (7.30) implies

$$\Delta u^2 = u_{R0}^2 = -2 \int_0^d B_L dz \quad (7.32)$$

Δu is the optimal shear. In this case the imported positive vorticity is just balanced by the generation of negative vorticity by the cold pool.

References

- Emanuel, K. A. (1986) Some dynamical aspects of precipitating convection. *J. Atmos. Sci.*, 43, 2183-2198.
 LeMone, M. A., and E. J. Zipser (1984) Momentum flux by lines of cumulonimbus over the tropical oceans. *J. Atmos. Sci.*, 14, 1914-1932.

- Rotunno, R., J. B. Klemp, and M. L. Weisman (1988) A theory for strong, long-lived squall lines. *J. Atmos. Sci.*, **45**, 463-485.
- Seitter, K.L., and H.-L. Kuo (1983) The dynamical structure of squall-line type thunderstorms. *J. Atmos. Sci.*, **40**, 2831-2854.

Notes by Steve Siems and John Thuburn

8. TROPICAL CYCLONES: OBSERVATIONS AND ENERGETICS

In this lecture we will begin the study of tropical cyclones, not only for their intrinsic interest, but also because tropical cyclones can be used as a laboratory for understanding the interaction between convection and large scale flows. After taking a look at the typical atmospheric state in the tropics, we will review some observational facts about tropical cyclones. This presentation will end with a look at the energetics of these storms. Their dynamics will be investigated in the next lecture.

The observations made by Jordan in 1958 (next page) are often regarded as typical of the tropical atmosphere. The solid line is the environmental virtual temperature. The dotted line on this diagram represents the virtual temperature of a parcel of fluid lifted pseudo-adiabatically from the boundary layer (that is without including the contribution from liquid water loading). This does not mean that rain falls, it is simply ignored! From this curve one would conclude that there is a strong potential for convective instability. However by looking at the dashed line, which includes liquid water loading in the definition of virtual temperature, the atmosphere seems nearly neutral.

According to the CISK (Conditional Instability of the Second kind) hypothesis, originally advanced by Charney and Eliassen, the initial development of the cyclone would result from the release of convective potential energy. This would imply that weak tropical cyclones would not necessarily be confined to maritime environments. However, contemporary numerical simulations reveal the essential importance of evaporation from the sea surface, and this suggests a quite different mechanism. In the remainder of this lecture and the next one it will be shown that intense storms can be maintained without any contribution from conditional instability. This is consistent with Riehl's (1954) early assumptions and estimates. The basic idea is that tropical cyclones result from a finite amplitude air-sea interaction instability. Thus origin and amplification of these storms are two different questions.

Observational Facts:

In nature some kind of disturbance is almost always observed to precede the occurrence of a tropical cyclone. This disturbance can be an easterly wave for instance, as illustrated in the following sequence of diagrams showing the genesis of hurricane Hilda.

To interpret these diagrams one should know that the thickness of the 500-200 mb layer is related to the average virtual temperature of that layer. For a hydrostatic atmosphere one can write

$$g \frac{\partial z}{\partial p} = -R \frac{T_v}{p},$$

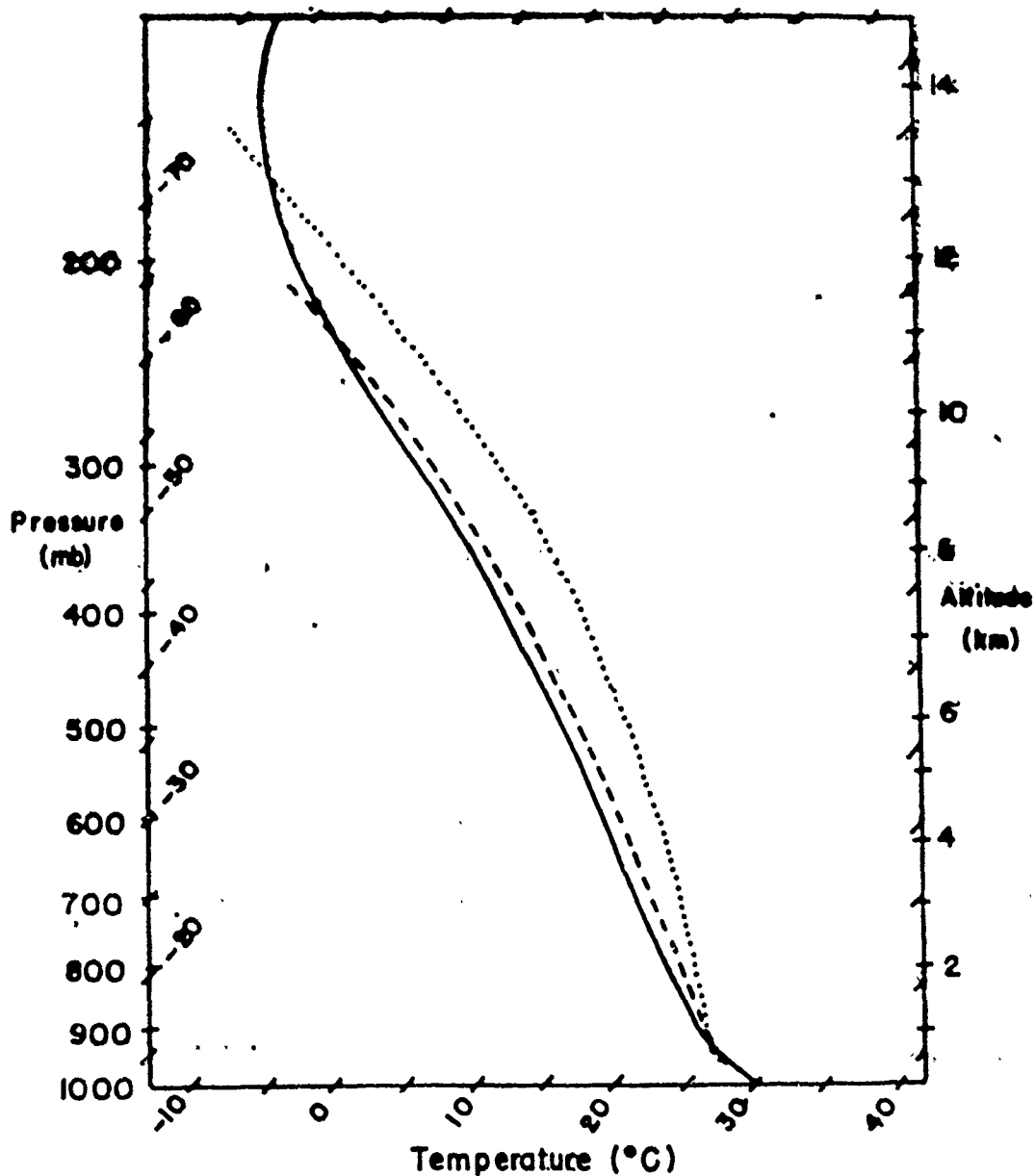
and thus

$$g \Delta z = -R \bar{T}_v \ln \frac{p_2}{p_1}$$

The next series of figures, constructed from observations of hurricane Inez, illustrates the inner structure of a hurricane.

The general picture is that of low-level air spiraling cyclonically toward low pressure, and speeding up due to the partial conservation of angular momentum.

Fig. 8.1



1. Mean thermodynamic conditions over the Caribbean region during hurricane season from rawinsonde observations composited by Jordan (1958). The solid line shows the environmental virtual temperature, and the dotted and dashed lines show the virtual temperature of a parcel lifted adiabatically from 1000 mb, not including and including the contribution from adiabatic liquid water loading, respectively.

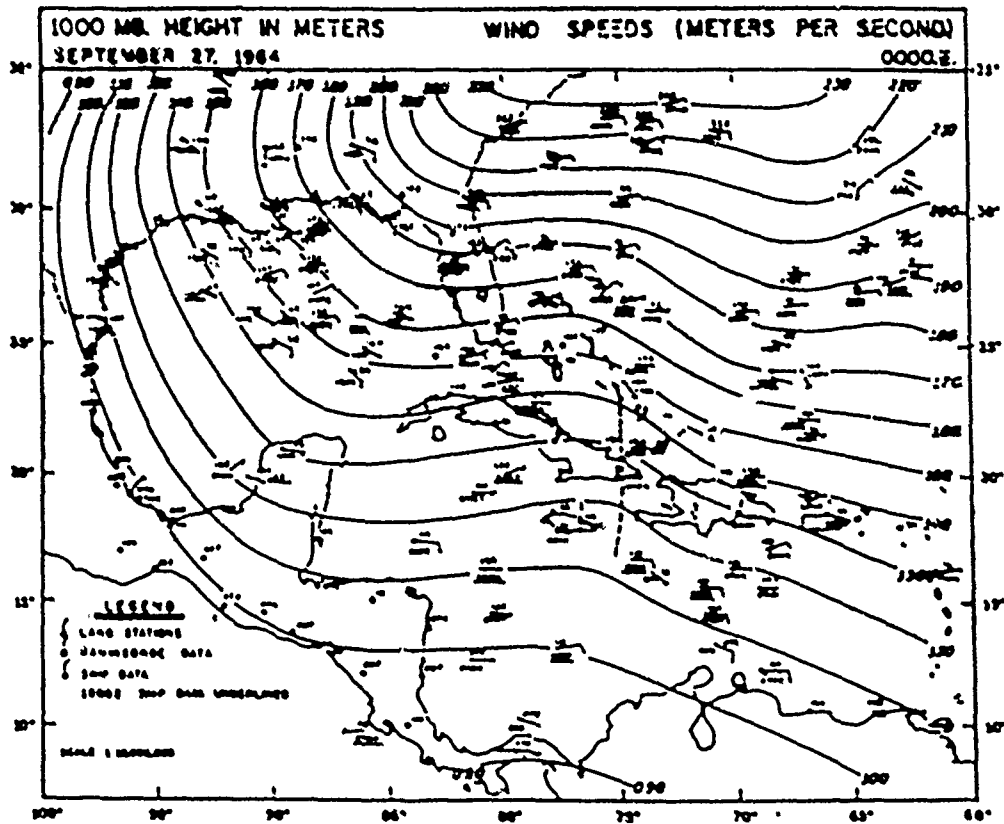


FIGURE 5.—1000-mb. contours for 00 GMT, September 27 showing a barely perceptible easterly wave over eastern Cuba, the first low level evidence of the disturbance that became hurricane Hilda.

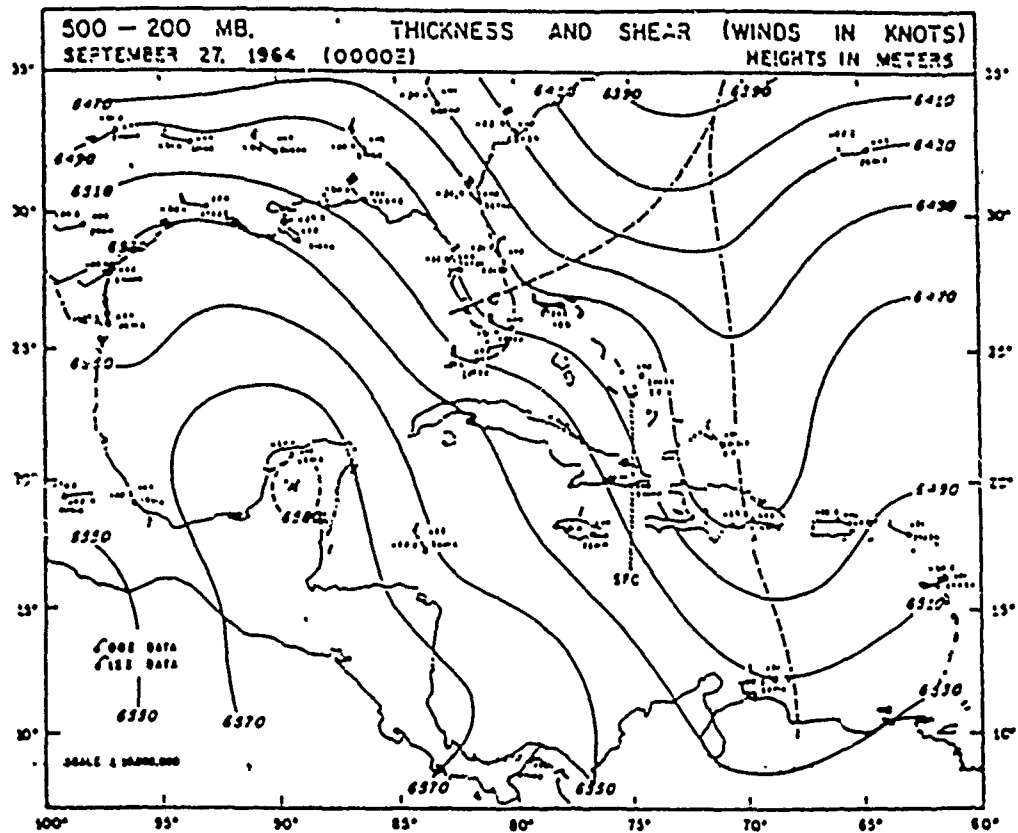


FIGURE 6.—The surface trough (dotted) almost midway between the trough-ridge system in the 500- to 200-mb. thickness.

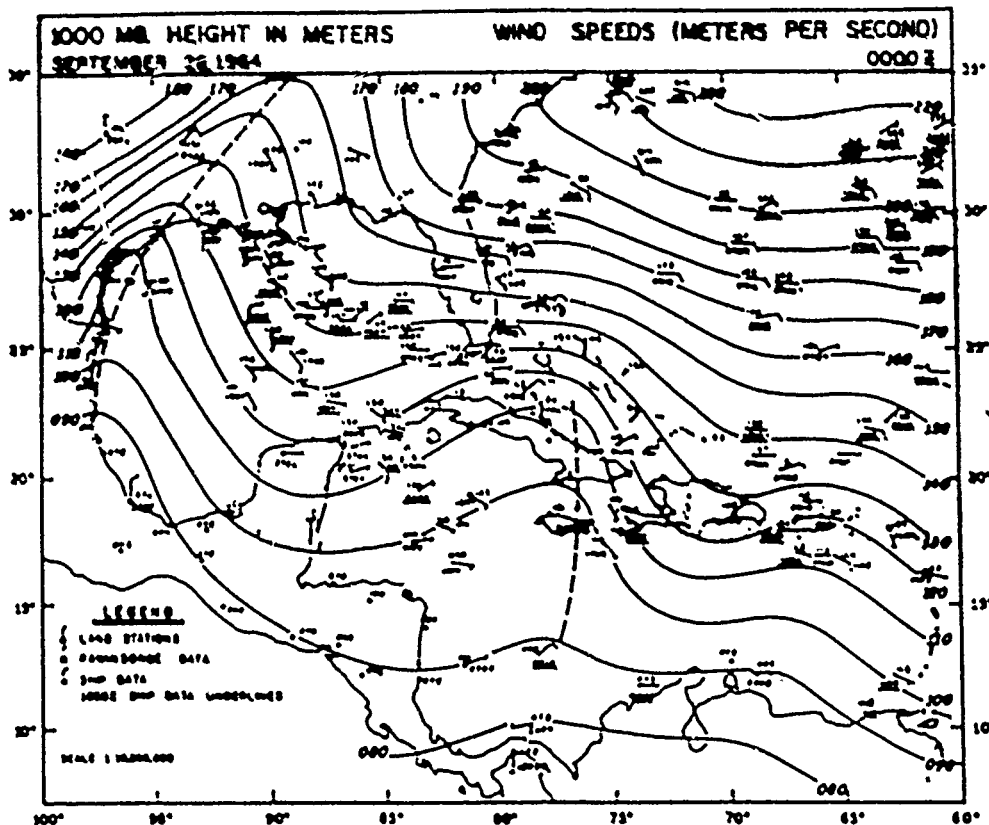
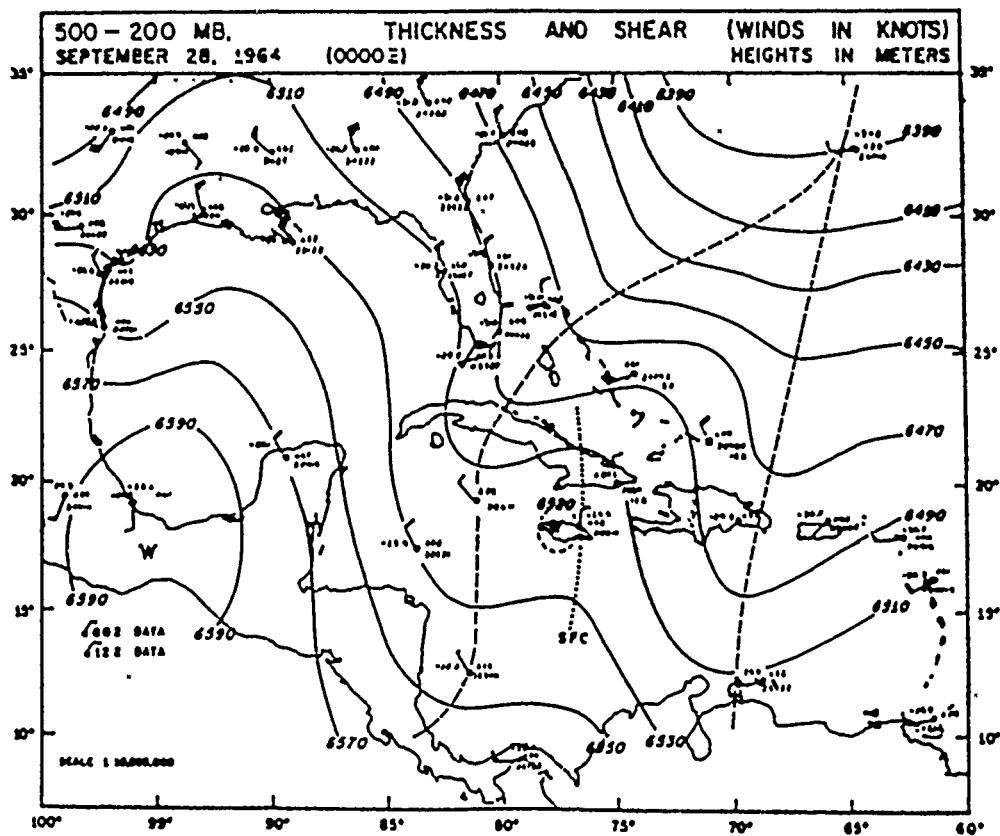
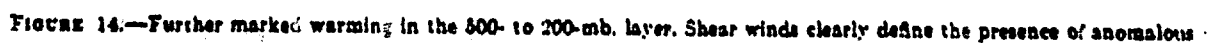
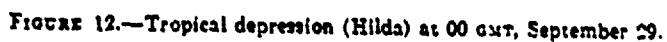


FIGURE 8.—Developing easterly wave over eastern Cuba and Jamaica.





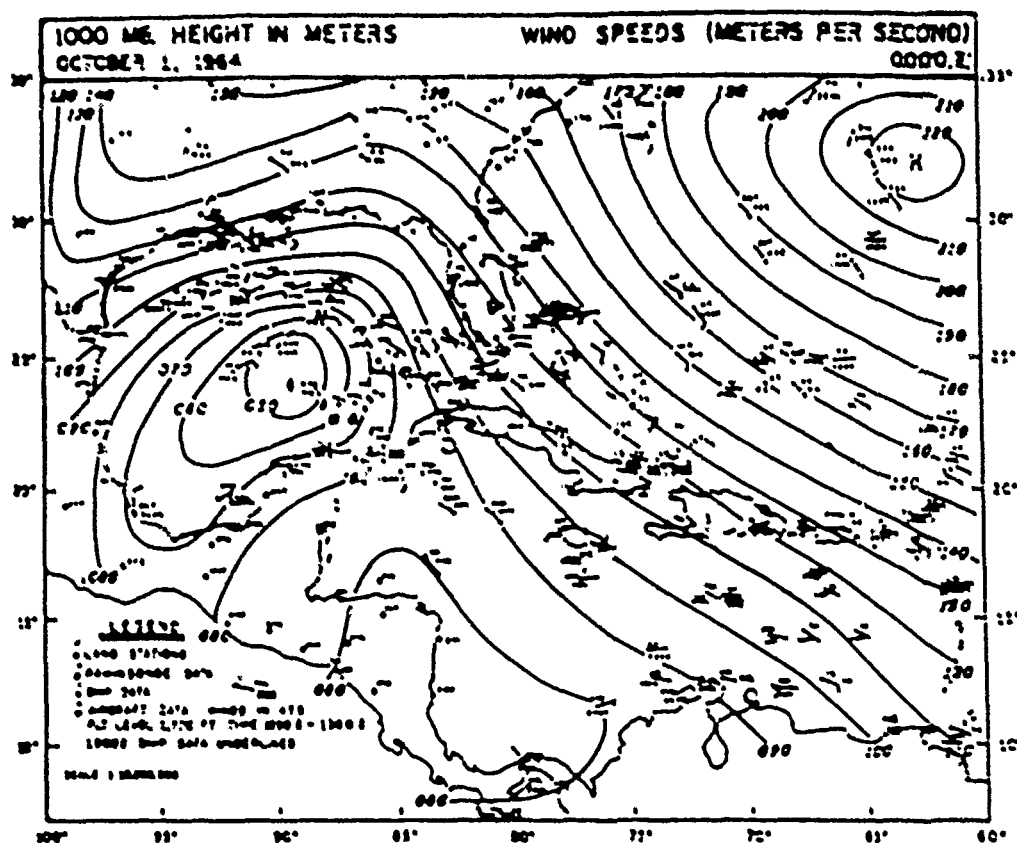


FIGURE 23.—Hurricane Hilda deepening rapidly near the center of the Gulf of Mexico.

Harry F. Hawkins and Deryl T. Rubsam

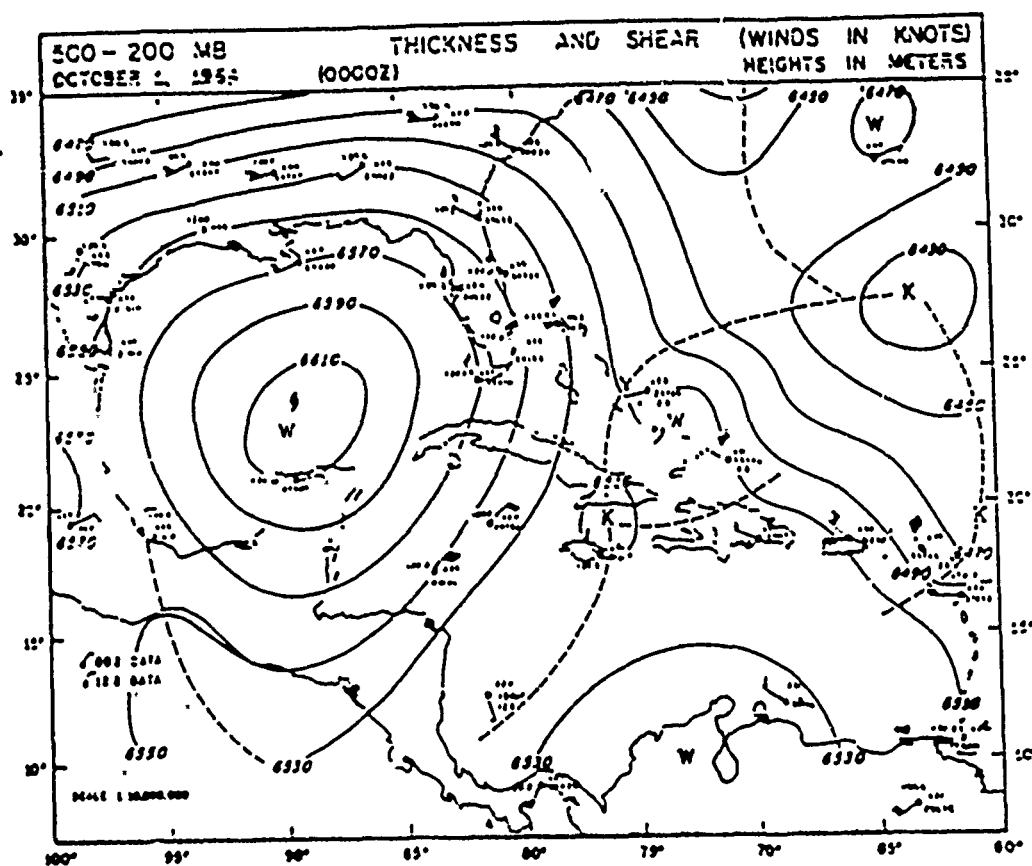


Fig. 8.7

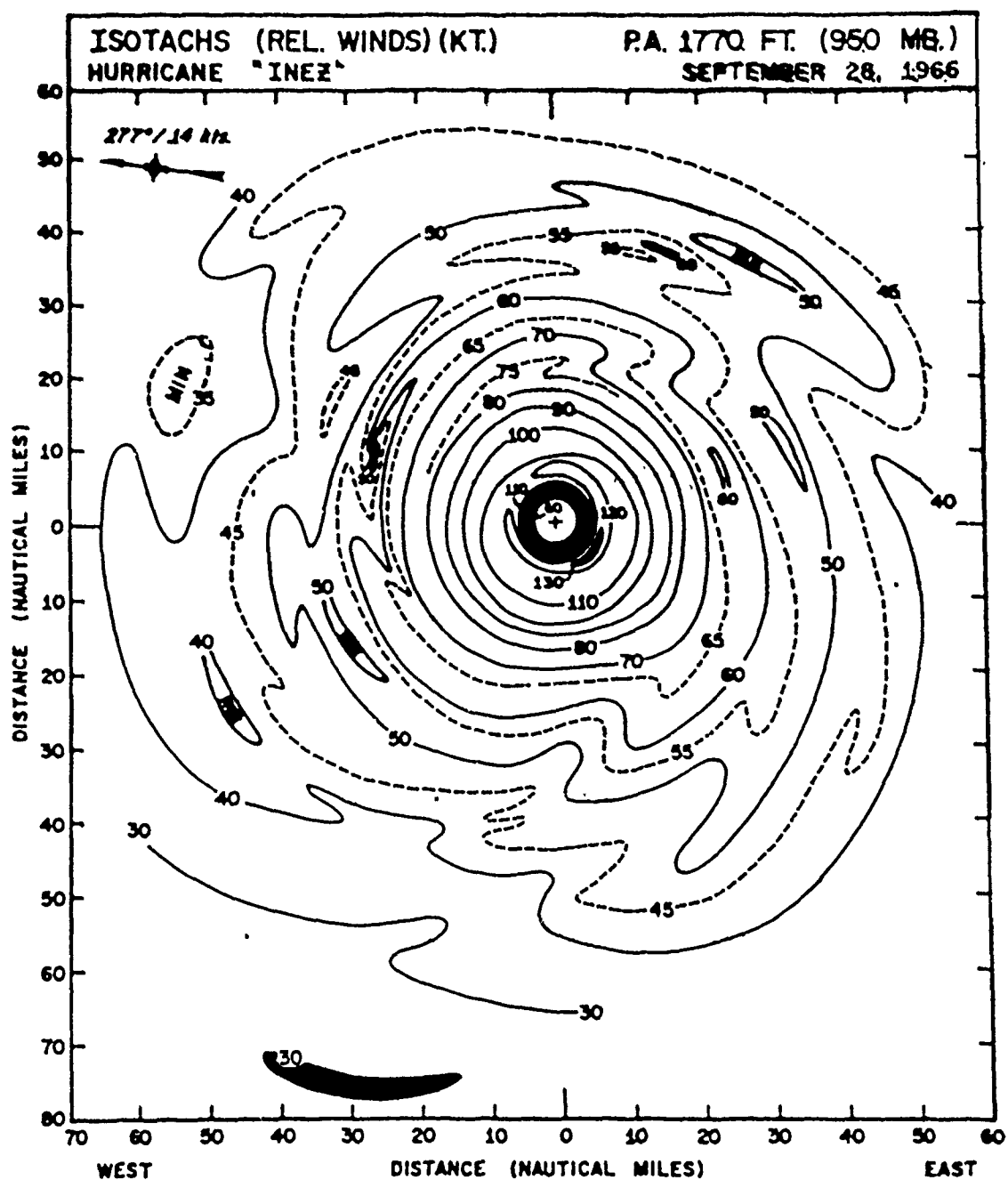


FIG. 2.4b. Low-level (950 mb) isotachs (kt) in Hurricane Inez (1966) (Hawkins and Imbembo, 1976).

75



According to Anthes (1982) the strongest sustained (1 min. average) winds ever recorded were 88 m/sec (317 km/h) for hurricane Inez precisely. The average maximum speed is about 50 m/sec.

These maximum winds occur at the "eye wall" where the inflowing convergent air suddenly turns upward. This is also the region of heaviest rainfall (up to 50 cm/day). The clouds are not distributed uniformly outside the eye wall, instead they organize into bands (?) spiraling toward the center. This is visible on the 2 satellite photographs.

The fluid is nearly in rigid body rotation inside the eye, and the velocity drops off as roughly $r^{-1/2}$ outside of it. There does not seem to be any typical length scale: the smallest storms can fit entirely within the eyes of the largest. The radius of the eye varies between 10 to 100 km. The vertical structure of hurricane Inez is displayed next. One will notice the relatively small variation with height, in the 900-400 mb layer especially, and an anticyclonic flow in the upper troposphere.

The figure above shows a warm core with a strong horizontal temperature gradient at the eye wall. Colder air is present from the surface to about 600 mb, between about 3 to 6 eye wall radii. That is the region where precipitation occurs. The figures below present a similar diagram for the equivalent potential temperature. It differs markedly from the temperature distribution. Notice for instance the pool of small equivalent potential temperature in the core around 500 mb, while the temperature increases to the center. The general inward increase of θ_e arises because moist entropy is transferred from the sea surface by evaporation. Finally let us mention that there is subsidence in the eye. This is related to the large temperature excess in the core. Air is sinking and warming up adiabatically.

There is a distinct seasonal cycle for the occurrence of tropical cyclones and they are generated only in regions of warm sea surface temperatures. These observations support the important role of air-sea interaction in hurricane dynamics.

Energetics

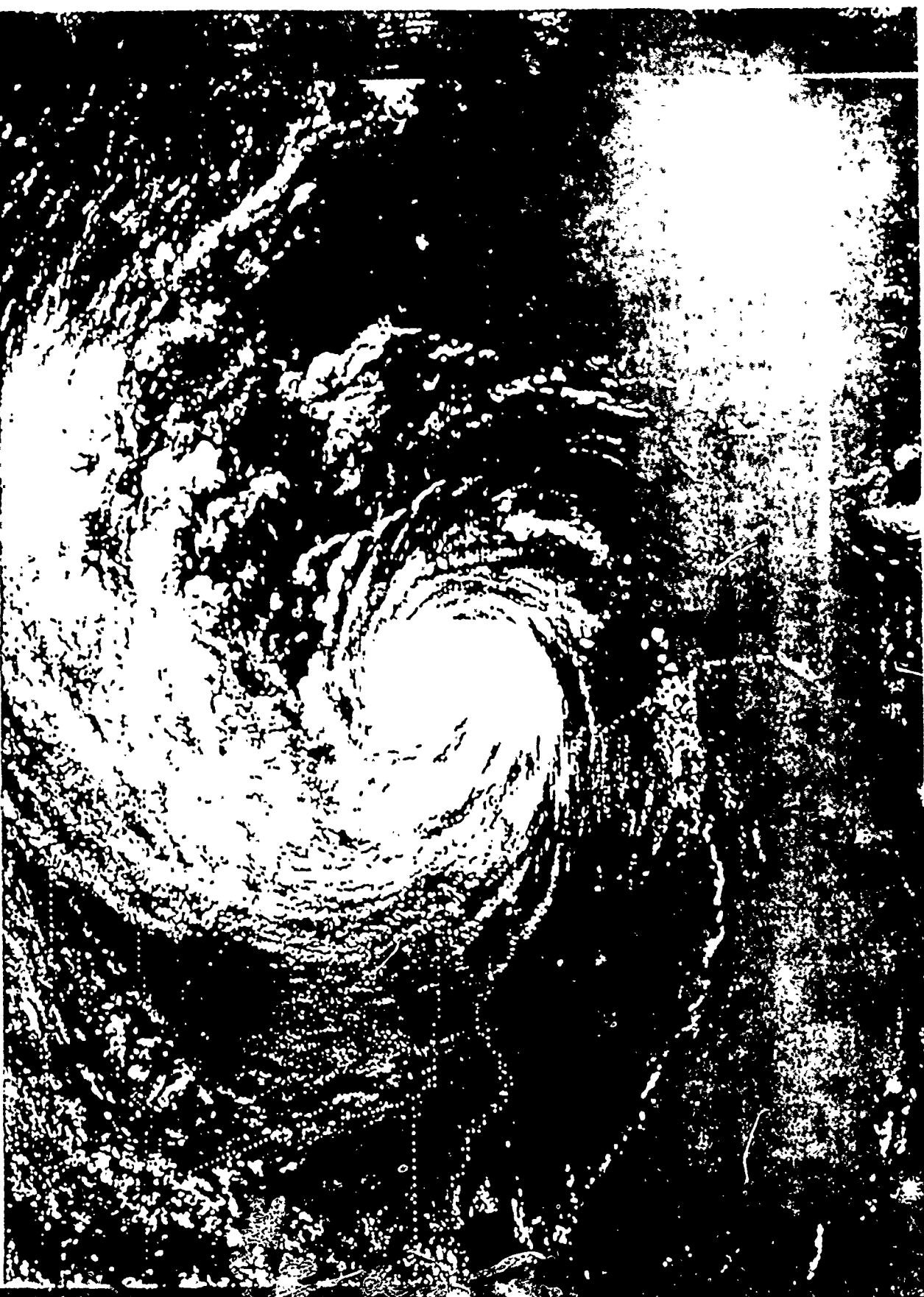
As stated earlier, our working assumption is that of no convective available potential energy. But then where does the energy necessary to maintain the tropical cyclone come from? The answer is that the near-surface air is sub-saturated (75 - 80 % humidity) and thus there is a large thermodynamic disequilibrium with the ocean. This is shown on the following figure where curve A is the virtual temperature (including condensate loading) of a parcel of air lifted adiabatically from the surface, which has first been saturated at sea level. Curve B corresponds to a parcel which has been saturated, then brought to 950 mb (a typical surface pressure in the eye of the hurricane) through an isothermal expansion.

This is the mechanism for the transfer of energy between the air and the ocean. Air is sucked in from large radius along the sea surface toward the eye. It acquires moist entropy by moisturizing and isothermal expansion. (about 1/2 the heat flux is due to isothermal expansion and 1/2 to increased humidity). It then rises adiabatically to high altitudes where it eventually loses heat by radiation.

Remark: the transfer of heat in the boundary layer is of course turbulent. This is "mechanically-driven" turbulence. The standard parameterization formula is for instance:

$$\overline{w'q'} = C_D V (q_s - q),$$

1800 10SE84 38A-1 02994 24494 MA30N80W-1



2130 11-094 38A-1 02775 24713 MA32N79W-1

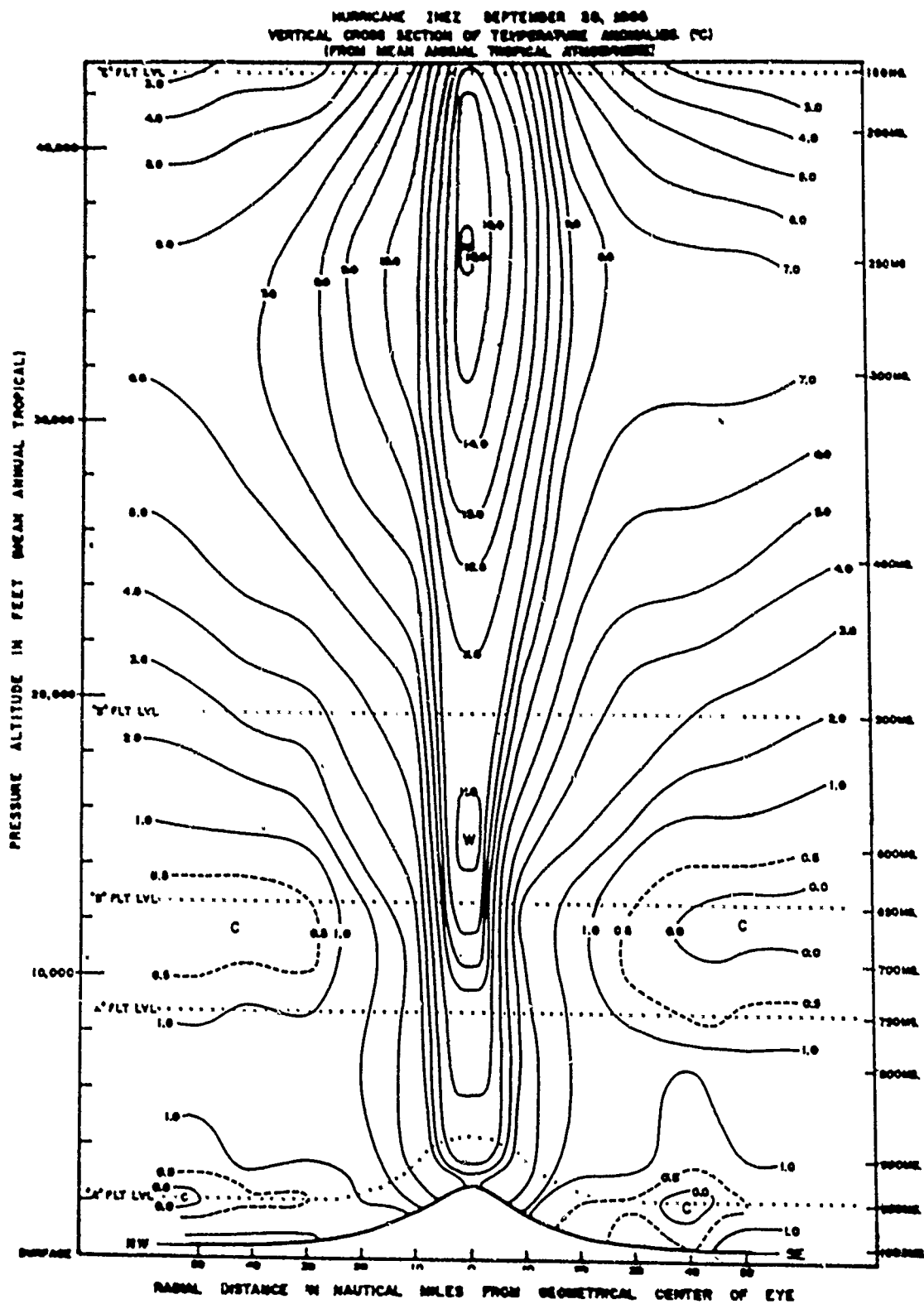
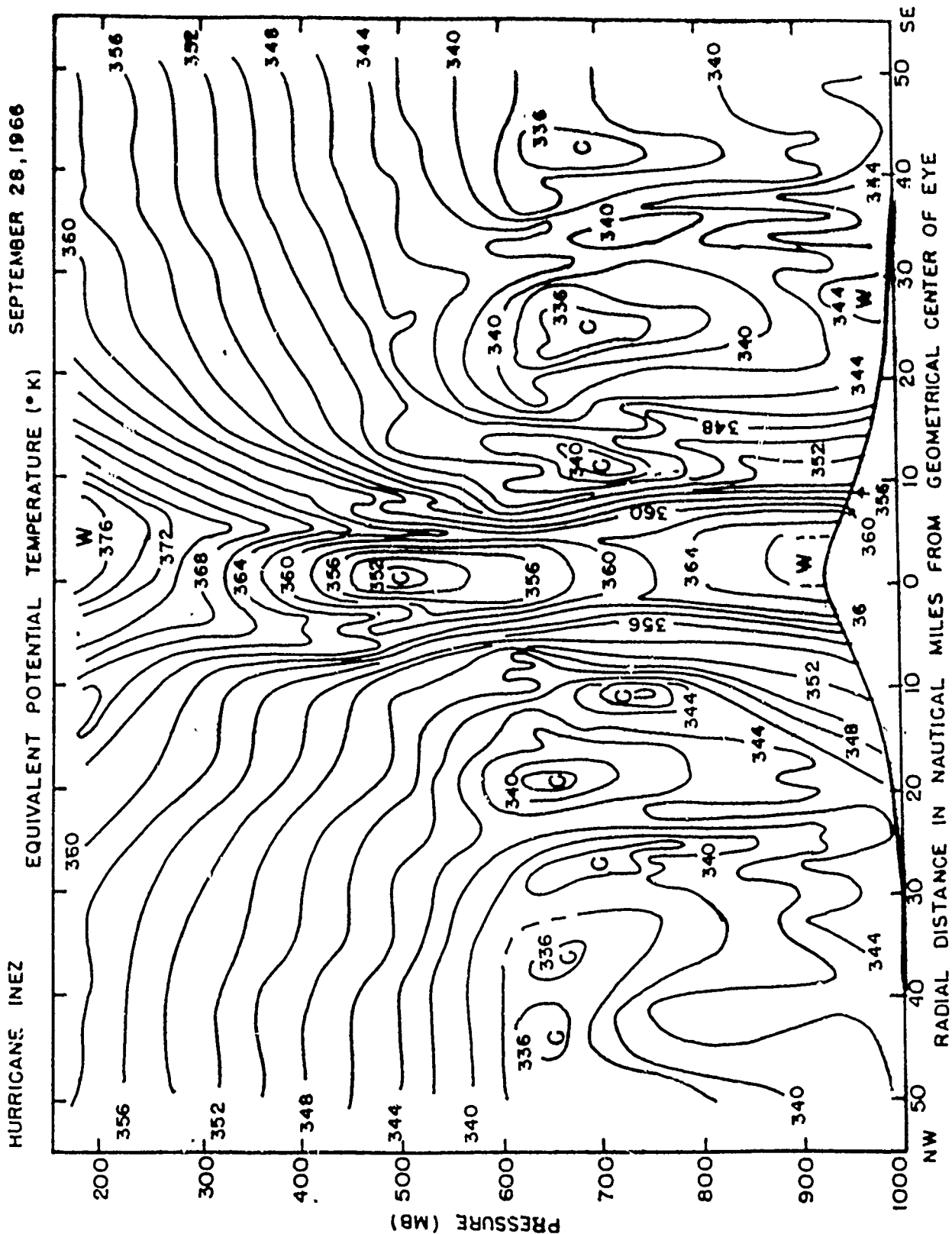
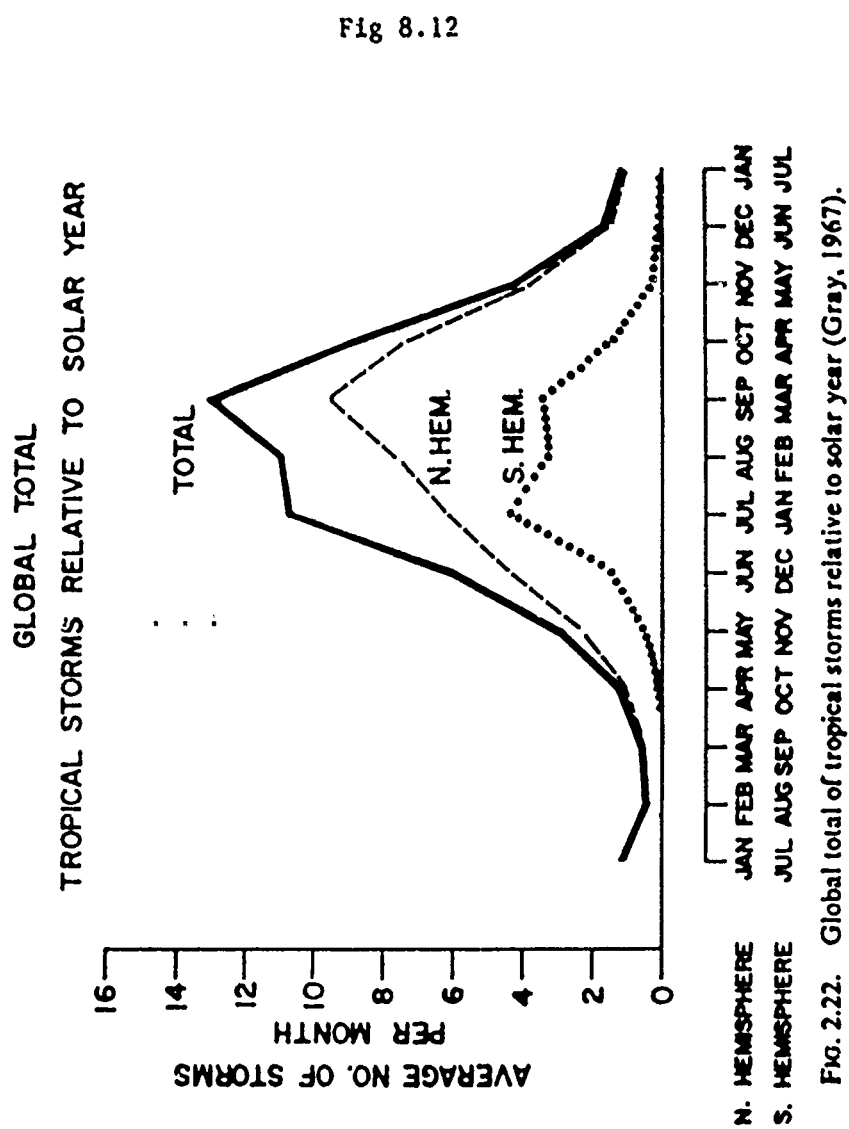


FIG. 2.11. Vertical cross section of temperature anomaly for Hurricane Inez on 28 September 1966 (Hawkins and Imbembo, 1976).





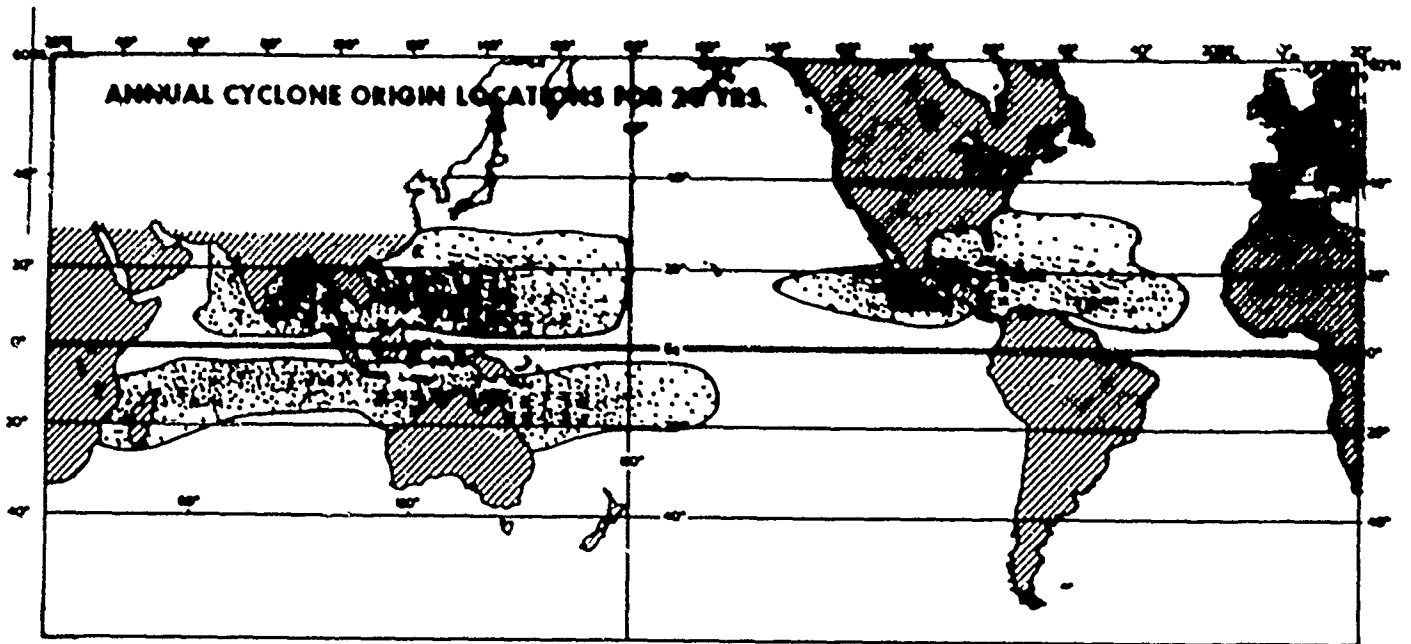


FIG. 2.21. Location of initial genesis points of tropical cyclones for a 20-year period (Gray, 1979)

where V is the modulus of the velocity and

$$q_s = \epsilon \frac{c_s(T)}{p_d}$$

This is very important and is the reason behind the finite amplitude behavior of a hurricane. The fluxes depend on the velocity, which depends on the pressure gradient, which in turn increases as the moist entropy increases as a result of the flux of water vapor. On the other hand, the turbulent flux of momentum in the boundary layer is the main sink of energy.

One can make the above description more quantitative. A tropical cyclone can in fact be represented by a simple Carnot cycle:

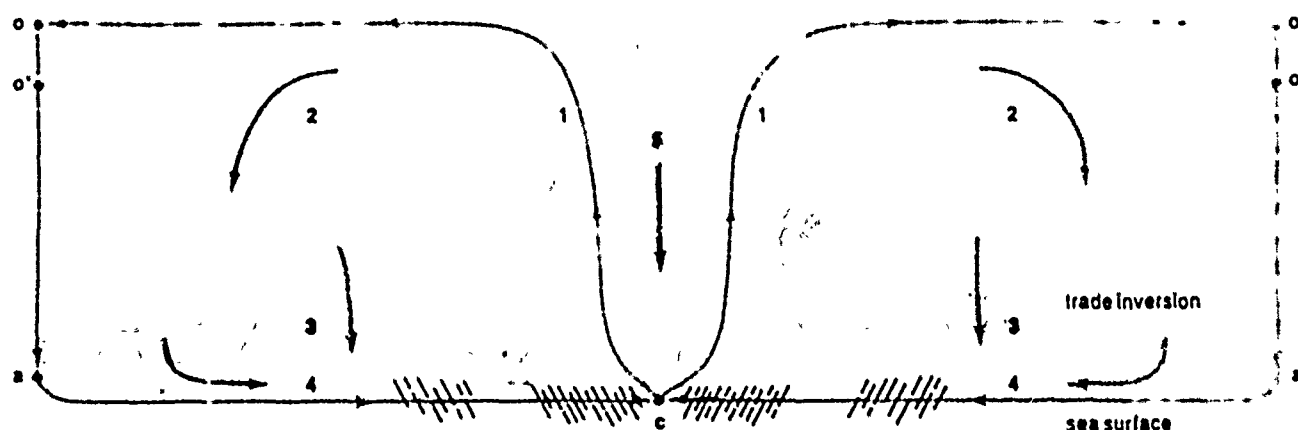


Figure 6. The structure and airflow of a mature hurricane are shown in this cross section, which spans a width of about 1,600 km and a height of 15 km. The regions correspond closely to those of the overall tropical atmosphere shown in Figure 4, but with an additional region of subsiding air in the eye (Region 5). In this case, the sea-surface temperature may be considered constant, but the total entropy content of the subcloud layer (Region 4) increases inward toward the eye as the increasing surface wind speed leads to greater evaporation rates, causing the near-surface air to approach

saturation. The total entropy increases from point u to point c and is approximately conserved during ascent through the eye wall to point o . Heat is lost by infrared radiation to space, symbolically between points o and o' . Because heat is acquired at a much higher temperature than it is lost at, the Carnot heat engine, which converts heat into mechanical energy, is very efficient ($\epsilon \approx 1/5$). In the steady state, this energy is mostly balanced by frictional dissipation at the surface.

The Hurricane Carnot cycle

The two essential laws are:

Bernoulli's relation: $d(\frac{1}{2}v^2) + gdz + \alpha dp + \vec{F} \cdot \vec{dl} = 0$

First law of thermodynamics: $Tds = c_p dT - \alpha dp + d(L_v w)$

where \vec{F} is the frictional force and \vec{l} is a unit vector along the motion vector.

Integrating Bernoulli's law over a closed loop one gets:

$$\oint \alpha dp = - \oint \vec{F} \cdot \vec{dl}$$

also

$$\int_a^c \alpha dp = - \int_a^c \vec{F} \cdot d\vec{l}$$

by integrating along the boundary layer which is assumed to be isothermal. The indice a corresponds to a point outside the cyclone, and c to the eye as shown in the figure above. Then assuming that all the frictional dissipation is in the boundary layer one gets:

$$\oint \alpha dp = \int_a^c \alpha dp$$

and from the first law of thermodynamics:

$$\oint T ds = - \oint \alpha dp = - \int_a^c \alpha dp$$

which gives:

$$(T_B - \bar{T}_{out})(S_c - S_a) = -R_d T_B \ln \frac{p_c}{p_a}$$

where T_B is the (uniform) temperature in the boundary layer, \bar{T}_{out} is the average temperature along o-o' (see fig. above), S is the specific entropy defined by:

$$S = C_p \ln T - R_d \ln p + L_v \frac{w}{T}$$

This relation states that the amount of heat in - heat out = the work done against dissipation in the boundary layer.

Using the definition of S in the boundary layer we can rewrite the above relation as :

$$\bar{T}_{out} R_d \ln \frac{p_a}{p_c} = L_v (w_c - w_a) \frac{T_B - \bar{T}_{out}}{T_B}$$

where

$$\frac{T_B - \bar{T}_{out}}{T_B}$$

is the thermodynamic efficiency. But now

$$w = \frac{M_v}{M_d} = \frac{\alpha_d}{\alpha_v} = \frac{R_d T}{R_v T} \frac{e}{p_d} = \epsilon RH \frac{e_s(T)}{p_d}$$

where RH stands for Relative Humidity, $\epsilon = R_d/R_v = 0.622$, and $e_s(T)$ is the saturation vapor pressure. p_d is the partial pressure of dry air.

Thus one gets :

$$\ln \frac{p_a}{p_c} = \frac{L_v w_a}{\bar{T}_{out} R_d} \frac{T_B - \bar{T}_{out}}{T_B} \frac{RH_c}{RH_c} \left(\frac{p_a}{p_c} - \frac{RH_a}{RH_c} \right)$$

or

$$\ln y = A(y - B)$$

where

$$y = \frac{p_a}{p_c}$$

This equation does not have solutions for all values of A and B . There is a limiting curve in the A - B parameter space.

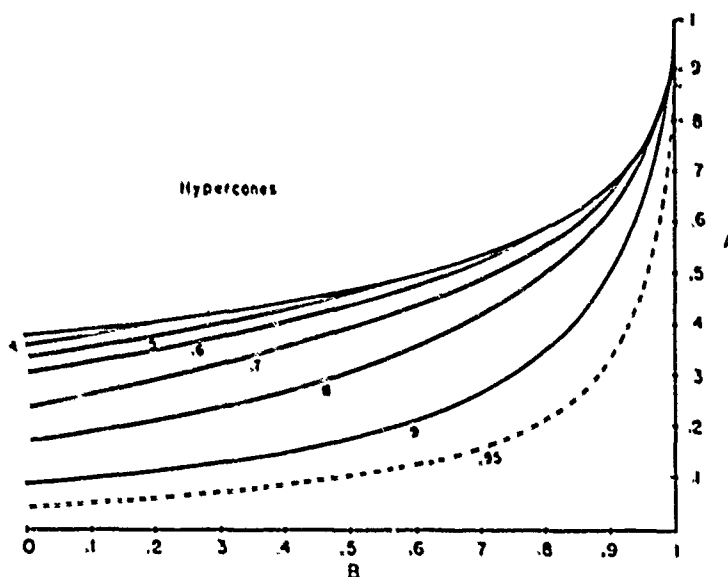


FIG. 2. General solutions of (18) for x ($\propto p_A/p_L$), as a function of A and B . The heavy solid curve denotes the critical condition beyond which no solutions exist.

The domain beyond that curve corresponds to "hypercanes", i.e. extremely intense hurricanes. In this regime, the isothermal expansion is so strong that the heating it causes cannot be balanced by dissipation in the boundary layer. If they existed (and they might in some different place or time) they would be supported by a quite different physics.

The figure below shows the minimum sustainable central pressures computed from the formula above [$\ln y = A(y - B)$] with $RH_c = 1$ assuming September mean climatological conditions.

Epilog

A couple of weeks after the end of the summer program, hurricane Gilbert was born and recorded as the most powerful ever in the Atlantic ocean. The following article appeared in *The Boston Globe*, Friday September 16, 1988.

Hurricane Gilbert is not only the most powerful Atlantic hurricane ever recorded, it may well be the most gigantic storm that ocean is capable of producing, weather scientists said yesterday.

However, the researchers said, they are mystified as to why Gilbert, alone of several storms this season, grew to such awesome proportions.

(...)[Robert Burpee, of NOAA] noted that the storm season has seen a dozen tropical depressions - low-pressure systems that spawn storms- "and five or six have followed nearly

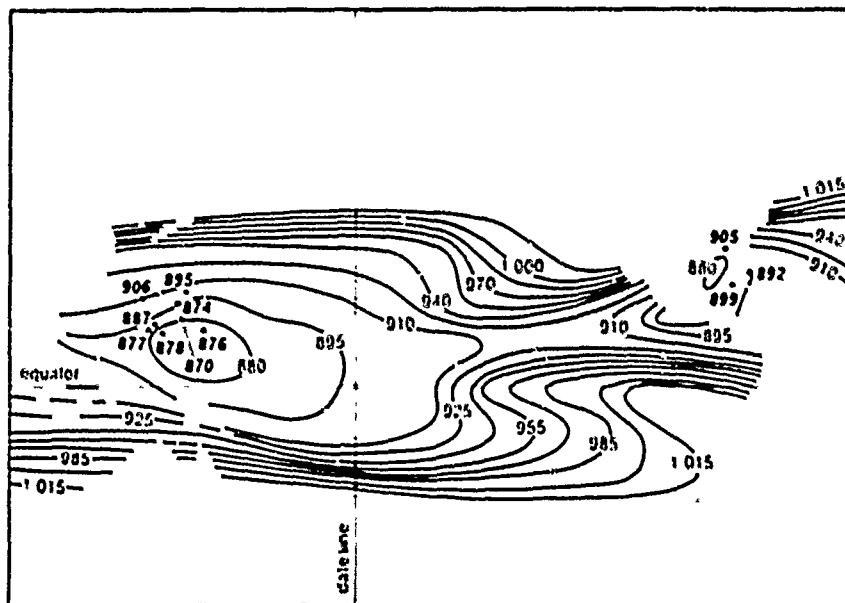


Figure 7. Hurricanes are areas of very low pressure. The tropical oceans are ideal spawning grounds for them, as demonstrated by this map, which shows the minimum sustainable central pressures in tropical storms under September mean climatological conditions over the Pacific Ocean and the Caribbean Sea. The pressures, which have been calculated using Eq. 5, are expressed in millibars, with 1,015 mb assumed to be the normal surface pressure. The dots and italicized numbers show, respectively, the locations and central pressures of some of the most intense hurricanes on record. Tropical storms in the Australian region are not indicated, because they occur during the late Southern Hemisphere summer (February-April).

identical paths ... but we are wondering why most have remained very, very weak, while this one -following nearly the same path- has become in terms of minimum pressure" the strongest of the century.

(...) Tuesday the atmospheric pressure beneath Gilbert's central "eye" was 26.91 inches of mercury. Only in a hurricane in the Western Pacific in 1927 has a lower figure been measured.

Low atmospheric pressure develops with the rise of warm, moist air that drives a hurricane.

Theory puts limit on intensity

A recent theory that hurricanes have a theoretical limit of intensity has been proposed by Kerry A. Emanuel, Professor of Meteorology at the Massachusetts Institute of Technology.

Hurricanes, termed "the greatest storms on earth," are spawned in tropical oceans from atmospheric disturbances that create regions of low pressure.

Simply hurricanes are a kind of "engine" that converts heat into mechanical energy - destructive winds that can pulverize entire cities.

The fuel for the engine is the wide temperature difference between the warm ocean surface and the much colder atmosphere above it; a hurricane typically rises some nine miles above the Earth.

For a hurricane to be born, the ocean surface must be 80 degrees Fahrenheit or warmer, and the water must be warm for a considerable depth below the surface.

Moisture from the warm ocean evaporates into the surrounding air, and as the moist air rises, it carries heat which is released when water condenses at chilly high altitudes. The high altitude temperature was about 120 degrees below zero Fahrenheit at the time Gilbert matured, said Emanuel.

The upward flow of warm, moist air produces thick clouds, torrential thunderstorms, lightning, and strong winds that, because of the earth rotation, spiral around a clear, tranquil "eye".

Emanuel said the power of a hurricane, like that of an auto engine, is limited by the rate at which "fuel" can be poured into it and the efficiency of the engine. The fuel limit for a storm is the amount of moisture the air over the ocean surface can hold, and the efficiency of the hurricane's "engine" is determined by the temperature differences. Calculations showed that Gilbert had reached those limits.

Gilbert's eye small

In addition, the violence of a hurricane's spiraling winds is related to the size of the central "eye", and Gilbert's eye is strikingly smaller - about eight miles wide compared to the usual 20 miles, said scientists.

Somewhat stronger hurricanes are possible in the Pacific Ocean, say researchers, because they accumulate more energy as they travel across that ocean's greater expanses. (...)

The following diagrams are also taken from the *Globe*.

References Anthes, R.A. (1982) *Tropical Cyclones: Their Evolution, Structure, and Effects*, AMS Press, Boston, 208pp.

Emanuel, K.A. (1988) The maximum intensity of hurricanes. *J. Atmos. Sci.*, **45**, 1144-1155.

Charney, J.G., and A. Eliassen (1964) On the growth of the hurricane disturbance. *J. Atmos. Sci.*, **21**, 68-75.

Hawkins, H.H., and S.M. Imbembo (1976) The structure of a small, intense hurricane — Inez, 1966. *Mon. Weath. Rev.*, **104**, 418-442.

Hawkins, H.H., and D.T. Rubsam (1968) Hurricane Hilda, 1964: II Structure and budgets of the hurricane on Oct. 1, 1964. *Mon. Weath. Rev.*, **96**, 617-636.

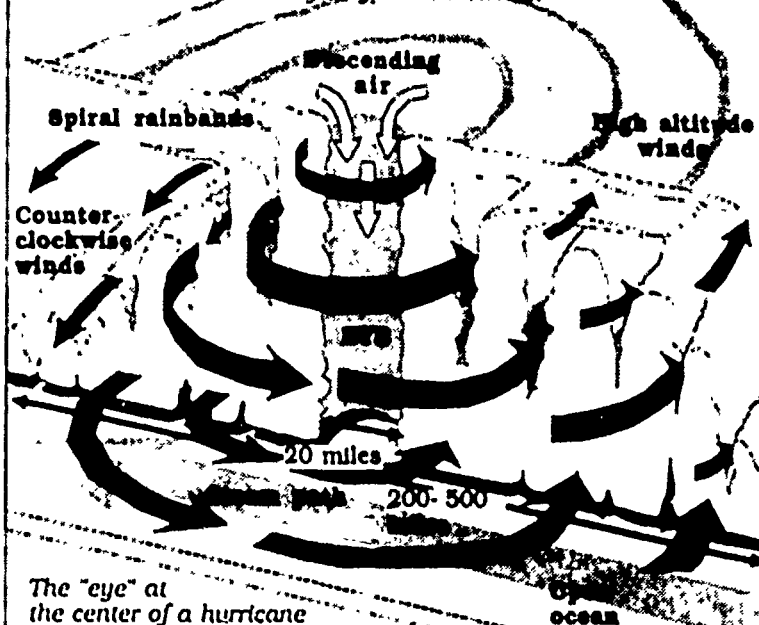
Jordan, C.L. (1958) Mean Soundings for the West Indies area. *J. Met.*, **15**, 91-97.

Riehl, H. (1954) *Tropical Meteorology*. McGraw-Hill, New York.

Notes by Fabian Waleffe and Andrew Woods

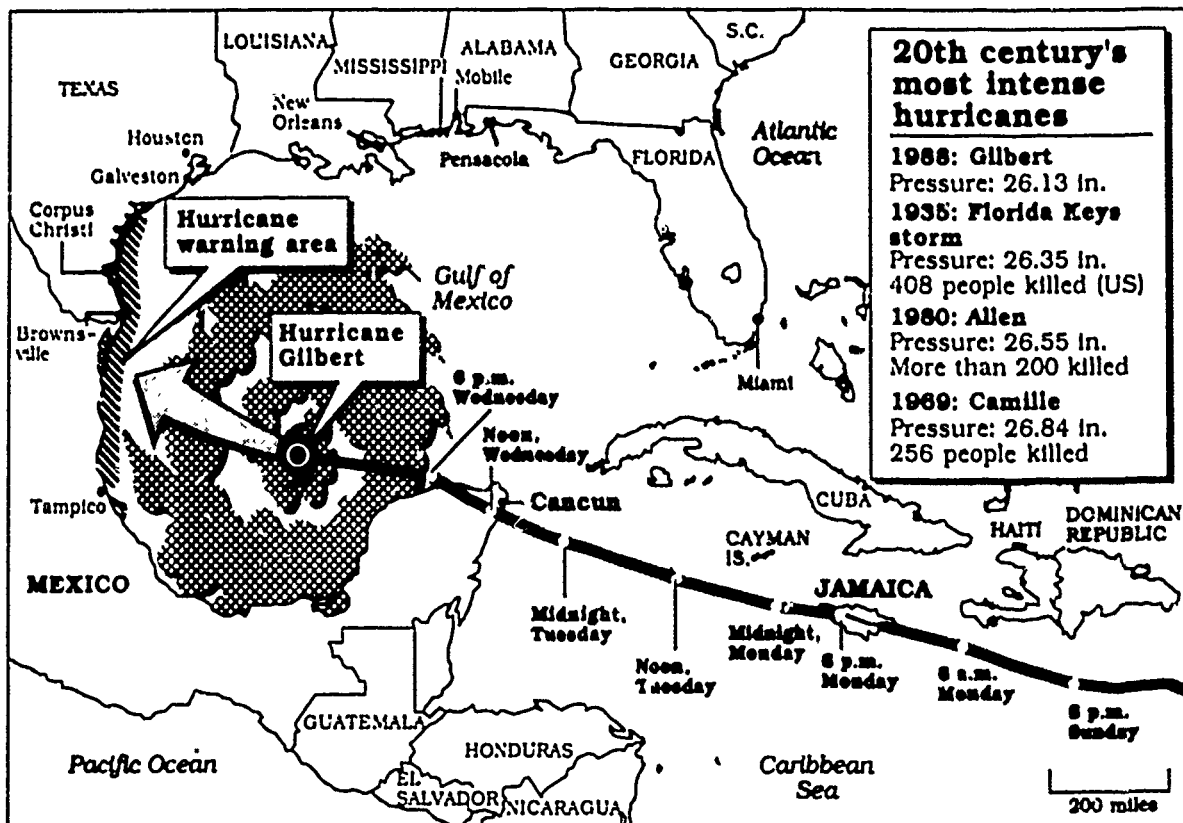
Anatomy of a hurricane

Here is a cross section of a typical hurricane.



The "eye" at the center of a hurricane is a zone about 20 miles across with little or no wind. The sky in the eye is clear or lightly clouded. Scientists believe the eye is created by two forces: the powerful centrifugal (outward) force due to the storm's rotation and the inward rush of wind toward the storm's low-pressure center. The wall of the eye forms where the two forces exactly balance.

Knight-Ridder



Source: National Hurricane Center

Knight-Ridder, Globe staff map

9. DYNAMICS OF TROPICAL CYCLONES

Numerical Simulation

In this lecture we first discuss an axisymmetric numerical hurricane model (Rotunno and Emanuel, 1987). Non-hydrostatic, primitive equations are used. The simulated region is 1500 km radially by 24 km vertically. Resolution is 15 km radially and 1.25 km vertically. A sponge layer is inserted between 19 and 24 km to absorb gravity waves and radiation lateral boundaries are used (i.e. waves propagate out ideally without reflection). Radiative relaxation is used $\dot{Q} = -(\theta - \bar{\theta})/\tau_r$. Highly simplified microphysics are used wherein basically $l > 1$ g/kg results in rain. The turbulence depends on the moist Richardson number. The sea surface temperature is fixed and the wind-dependent exchange coefficients are as follows:

$$\text{Momentum: } -c_D |\mathbf{v}| \mathbf{v} \quad c_D = c_{D0} + c_{Dv} |\mathbf{v}|$$

$$\text{Latent Heat: } c_\theta |\mathbf{v}| (\theta_s - \theta)$$

$$\text{Moisture Exchange: } c_q |\mathbf{v}| (q_s - q)$$

The model is initialized with a convectively neutral sounding. Results of the simulation follow.

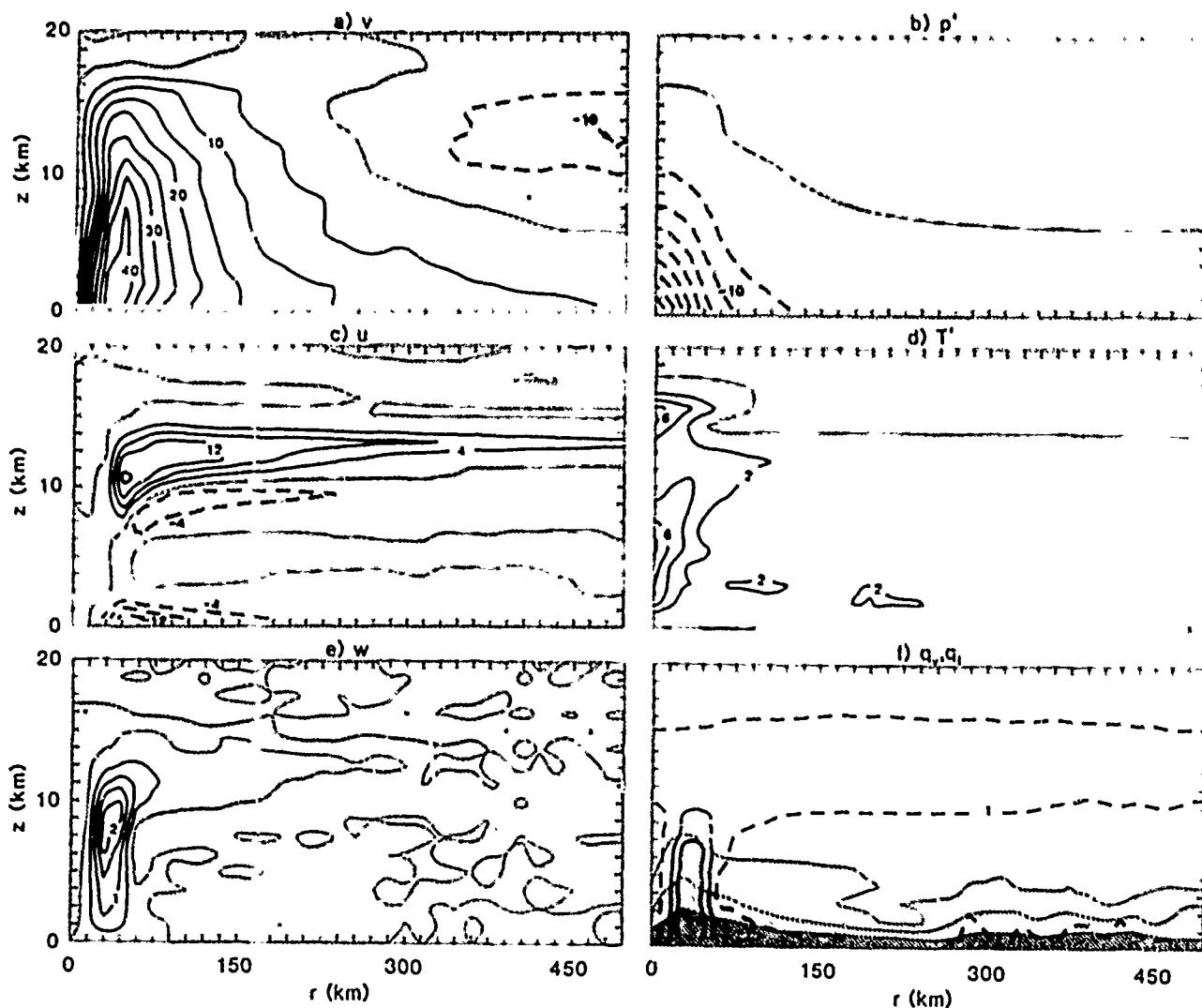


FIG. 5. The 160–180 h average fields for the nearly steady state reached in the control run. All stippled regions indicate negative values of the field. (a) Azimuthal velocity, contour interval, 5 m s^{-1} , (b) dimensional pressure deviation from the initial state, contour interval, 5 mb, (c) radial velocity, contour interval, 5 m s^{-1} , (d) temperature deviation from the initial state, contour interval, 2 K , (e) vertical velocity, contour interval, 0.5 m s^{-1} , (f) liquid water, contour interval, 1 g kg^{-1} , dashed line denotes the 0.1 g kg^{-1} contour, and water vapor, lightest shading indicates $3 < q_r < 8 \text{ g kg}^{-1}$, darker shading indicates $8 < q_r < 13 \text{ g kg}^{-1}$, and darkest shading indicates $q_r > 13 \text{ g kg}^{-1}$.

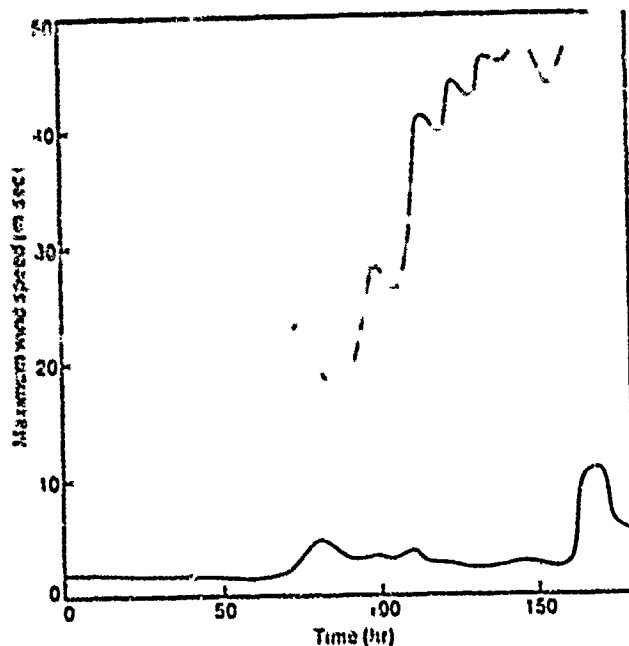


Figure 9. Computer models provide a partial answer to the question of why hurricanes are rare even though the tropical atmosphere has abundant energy to support them. This graph shows the evolution with time of the maximum surface wind speed produced by one such numerical model (Rotunno and Emanuel 1987). The red curve begins with a 12 m/sec amplitude vortex, while the maximum velocity in an experiment that starts with a 2 m/sec amplitude vortex, but is otherwise identical, is shown by the gray curve. The failure of the weak vortex to amplify demonstrates that hurricanes in this model cannot arise out of weak random noise; rather, a vortex of sufficient amplitude must be provided by independent means, such as a large-scale wave or a thunderstorm complex from a middle-latitude continent.

The upper line above shows the results of the control experiment which is initialized with a weak warm core vortex of amplitude 10 m/s. The lower line shows an identical experiment but with an initial amplitude of 2 m/s. The stronger initial vortex amplifies into a mature hurricane, while the weaker one never amplifies. This shows that the model storm results from a finite amplitude instability.

The above points are consistent with the observation that tropical cyclones only form when there is an initial disturbance and the theory that hurricanes are not manifestations of the release of convective instability but a finite amplitude air-sea interaction instability.

A simpler model

In this second part of lecture 9 we discuss a "simplified" numerical simulation. We assume that at all times the atmosphere is conditionally neutral defined in the general sense of being moist adiabatic along angular momentum surfaces. The model is axisymmetric and is expressed in the following coordinates:

Potential Radius R : $\frac{1}{2}R^2 = rV + \frac{1}{2}r^2$

Pressure P as vertical coordinate

Time τ

Assuming convection maintains a moist adiabatic lapse rate along R surfaces, the thermal wind equation can be shown to be:

$$r_b^{-2} = r_t^{-2} - \frac{2}{f^2 R^3} (T_b - T_t) \frac{dS^*}{dR}$$

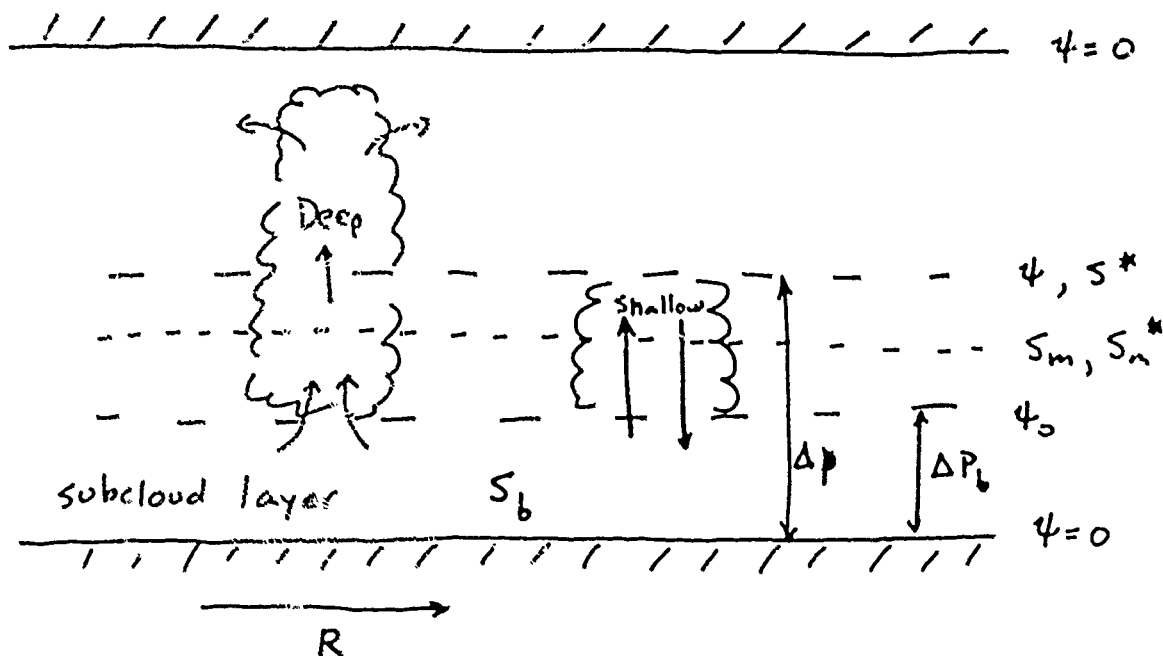
where

r_b — radius of R surface at top of PBL ($T = T_b$)

r_t — radius of R surface at tropopause ($T = T_t$)

S^* — saturation moist entropy

The saturation moist entropy is the entropy the atmosphere would have if it were saturated. This is a state variable but not a conserved quantity unless the air is saturated. The condition of conditional neutrality is equivalent to the specification of S^* constant along R surfaces.



ψ — mass stream function outside of clouds (zero at top and bottom)

S_b — moist entropy of BL.

ψ_0 — mass stream function at top of BL.

As indicated in the figure, the model distinguishes deep and shallow convection. This is an essential part of the model. The deep clouds precipitate and have a net mass flux. They represent a mass source at the top and correspondingly a mass sink at the bottom. The shallow clouds do not precipitate and have no net mass flux. They do act as a source of moist entropy in the middle layer and a sink of moist entropy in the BL.

A parameter of the system is α . In the equations that follow this will be seen to relate the vertical cloud velocities to the convective instability. However, the model is not sensitive to this parameter since the convective time scales are short compared to the system evolution time scales.

In the shallow clouds, the pressure velocities ($\omega \equiv dp/dt$) of the updrafts and downdrafts are

$$\omega_u = -\omega_d = -\alpha(S_b - S_m^*)^{(1/2)}$$

and the fractional areas covered by updrafts and downdrafts are equal. Thus there is no net mass flux by shallow clouds, but they do transport entropy.

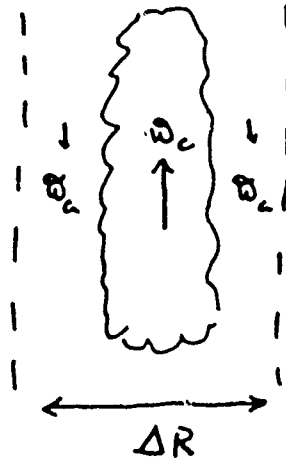
In the deep clouds

$$\omega_c = -\alpha(S_b - S^*)^{(1/2)}$$

and this does lead to a net mass flux.

With the definition of σ as the fractional area of a grid covered by a deep cloud and reference to the figure below, the mass continuity equation can be written:

$$\frac{1}{r} \frac{\partial}{\partial r}(ru) + (1 - \sigma) \frac{\partial \omega_a}{\partial P} = -\sigma \frac{\partial \omega_c}{\partial P}$$



Let

$$ru \equiv \frac{\partial \psi}{\partial P} + G$$

$$(1 - \sigma) r \omega_a \equiv -\frac{\partial \psi}{\partial r}$$

so that

$$\frac{1}{r} \frac{\partial G}{\partial r} = -\sigma \frac{\partial \omega_c}{\partial P}$$

and

$$G = -\frac{1}{2} \int_0^r \sigma \frac{\partial \omega_c}{\partial P} dr^2$$

Again, ψ is a mass streamfunction for flow excluding deep clouds. G represents the mass fluxes in deep clouds.

Lateral friction is included in the boundary layer. The equations for conservation of moist entropy complete the system.

The variables are now scaled as follows: Define

$$\chi \equiv (T_b - T_t)(S - S_a)$$

where S_a is the ambient PBL entropy, and

$$\chi_s \equiv (T_b - T_t)(S_{s0} - S_a)$$

where S_{s0} is the saturated entropy of sea surface at ambient pressure.

Note that χ_s is a measure of initial air-sea thermodynamic disequilibrium. We nondimensionalize as follows:

$$\begin{aligned}\chi &\rightarrow \chi_s \chi \\ \chi^* &\rightarrow \chi_s \chi^* \\ r &\rightarrow \chi_s^{(1/2)} f^{-1} r \\ R &\rightarrow \chi_s^{(1/2)} f^{-1} R \\ \tau &\rightarrow c_D^{-1} \frac{RT_s}{g} \left(\frac{P_0 - P_t}{P_0} \right) \chi_s^{-(1/2)} \tau \\ \psi &\rightarrow \frac{1}{2} c_D \rho_s g \chi_s^{(3/2)} f^{-2} \psi \\ P &\rightarrow P_0 \exp \left[\frac{\chi_0}{R_d T_s} P \right]\end{aligned}$$

From this nondimensionalization and values of the various parameters, we find typical scales:

$$\begin{aligned}\text{velocity} &= \chi_s^{(1/2)} \quad (60 \text{ m/s}) \\ \text{radius} &= \chi_s^{(1/2)} f^{-1} \quad (1000 \text{ km}) \\ \text{time} &= c_D^{-1} \frac{RT_s}{g} \left(\frac{P_0 - P_t}{P_0} \right) \chi_s^{-(1/2)} \quad (16 \text{ hours})\end{aligned}$$

Our equations are now:

conservation of angular momentum in boundary layer:

$$\frac{\partial r_b^2}{\partial \tau} = \psi_0 - \psi - \frac{1}{R} \frac{\partial}{\partial R} \left(r_b^3 \nu \frac{\partial}{\partial r_b} \left(\frac{R^2}{r_b^2} \right) \right)$$

with

$$\nu \equiv \ell^2 |r_b \frac{\partial}{\partial r_b} \left(\frac{R^2}{r_b^2} \right)|$$

conservation of angular momentum in top layer:

$$\frac{\partial r_i^2}{\partial \tau} = \psi - \int_0^{r_i^2} \omega_c \sigma dr^2$$

thermal wind:

$$r_b^{-2} = r_i^{-2} - \frac{2}{R^2} \frac{\partial \chi^*}{\partial R}$$

a diagnostic equation for the boundary layer streamfunction:

$$\psi_0 = (1 + c|v_b|)|v_b| \frac{1}{2R} \frac{\partial r_b^2}{\partial R} (R^2 - r_b^2) + \int_0^{r_i^2} \sigma \omega_c dr^2$$

temperature equations

$$\frac{\partial \chi^*}{\partial \tau} = Q\omega_a(1 - \sigma) + \frac{\partial}{\partial r_b^2} (r_b \nu \frac{\partial \chi^*}{\partial r_b}) - \text{rad}(\chi^*)$$

$$\frac{\partial \chi_m^*}{\partial \tau} = Q \frac{\omega_a + \omega_0}{2} (1 - \sigma) - \text{rad}(\chi_m^*)$$

with

$$(1 - \sigma)\omega_a \equiv -\frac{\partial \psi}{\partial r_m^2}$$

$$(1 - \sigma)\omega_0 \equiv -\frac{\partial \psi_0}{\partial r_b^2}$$

and

$$r_m^{-2} = \frac{T_s - T_m}{T_s - T_i} r_i^{-2} + \frac{T_m - T_i}{T_s - T_i} r_b^{-2}$$

the entropy conservation equations:

$$\gamma \frac{\partial \chi}{\partial \tau} = \psi_0 \frac{\partial \chi}{\partial r_b^2} - (1 - \sigma) \left(\frac{\omega_0 + |\omega_0|}{2} \right) (\chi - \chi_m) - \sigma_s \omega_d (\chi - \chi_m) + (1 + c|v|)|v|(\chi_s^* - \chi)$$

$$\begin{aligned} \frac{\partial \chi_m}{\partial \tau} = & -(1 - \sigma) \left(\frac{\omega_0 - |\omega_0|}{2} \right) (\chi - \chi_m) - (1 - \sigma) \left(\frac{\omega_0 + |\omega_0|}{2} \right) (\chi_i - \chi_m) \\ & - \sigma_s \omega_u (\chi - \chi_m) - \text{rad}(\chi_m) \end{aligned}$$

with

$$\chi_s^* = 1 - \frac{T_s - T_i}{T_s} P + \frac{1}{1 - RH_a} (e^{-\beta P} - 1)$$

$$\chi_i = 2\chi_{mi} + \chi^*$$

fractional coverage of convection

$$\sigma = \frac{f}{\sqrt{\chi_s}} (10 \text{ km}) \frac{1}{\Delta r_b}$$

$$\sigma_s = 0.5$$

surface pressure

$$\frac{\partial P}{\partial r_b} = v + \frac{v^2}{r_b}$$

These dimensionless equations are described as follows: the radius of R surfaces in the lower layer (r_b) changes according to the mass flow in the lower layer and viscous dissipation, with the latter proportional to the deformation multiplied by a length scale, ℓ , squared. The radius of R surfaces in the upper layer changes according to the total mass flow (including that due to deep convection) in the upper layer. The boundary layer flow is determined by the surface stress according to the aerodynamic drag formulation with a wind-dependent exchange coefficient and the mass sink due to deep convection.

The temperature equations for the middle and lower layer contain terms representing adiabatic compression, diffusion (to control the numerical integration), and radiative relaxation to the initial condition. The calculation of the vertical velocity at the middle level requires knowledge of the radius of R surfaces there (r_m) which is again determined from the thermal wind equation.

The boundary layer entropy conservation equation includes horizontal advection, vertical exchange through the boundary layer top by the mean flow and by shallow convection, and surface fluxes. χ_s^* is the (pressure-dependent) saturation entropy of the sea surface. Entropy conservation in the lower layer is controlled by mean fluxes through the top and bottom of the layer, shallow convective fluxes, and radiation. χ_t is the entropy in the upper layer which is assumed to be that of the initial state (χ_{mi} , an upward extrapolation from the boundary layer and lower layer) plus χ^* .

The fractional area covered by deep clouds is simply a constant cloud width (10 km) divided by the dimensional physical distance between adjacent R surfaces. This means that we permit only one deep cloud per grid volume. The fractional coverage of shallow clouds is fixed at 0.5. Surface pressure is diagnosed from the cyclostrophic relation.

The dimensionless parameters of the system are:

α — discussed previously

c — determines the wind-dependence of the surface exchange coefficient

ℓ — a diffusion length scale

Q — dry static stability

rad — a radiative relaxation rate

γ — the ratio of the boundary layer pressure depth to that of the lower and upper

layers

β — determines the magnitude of the isothermal expansion heating

RH_a — the ambient surface relative humidity

χ_{mi} — the initial entropy of the lower troposphere

$\frac{T_s - T_i}{T_i}$ — the thermodynamic efficiency

All the other dimensionless parameters describe the initial and boundary conditions.

Preliminary experiments with this model reveal the reasons for the finite amplitude nature of cyclogenesis in the model. The figure below shows two different experiments which are identical except that they are initialized with different amplitudes. The weak vortex decays while the stronger one amplifies, as in the more complete model. A third experiment is identical to the first except that shallow convection has been artificially turned off. The run with no shallow convection amplifies immediately but does not attain the same amplitude. Evidently the shallow convection plays a dual role: it prevents weak disturbances from amplifying but permits mature storms to reach a larger amplitude than they otherwise would.

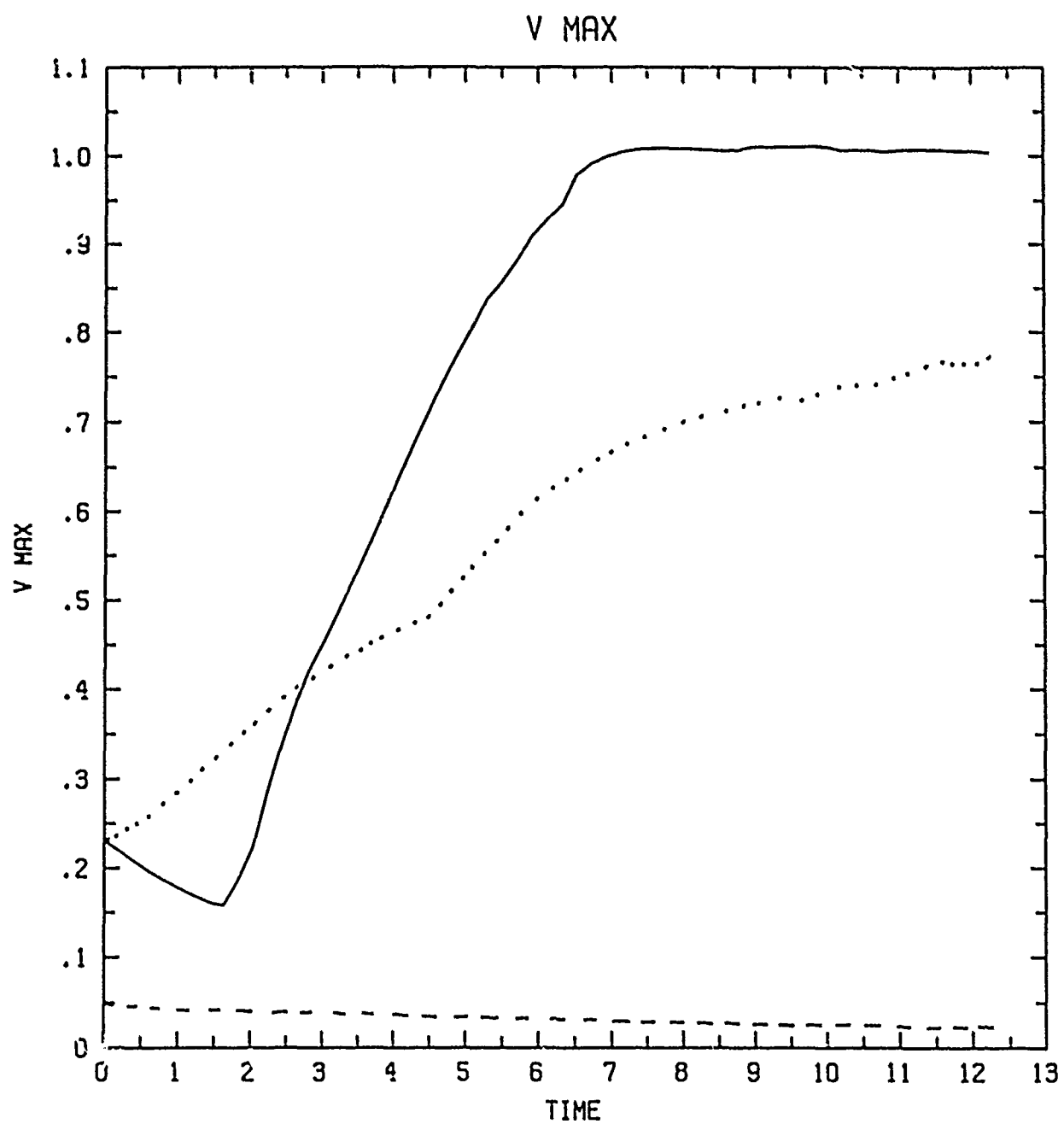
The reasons for this behavior are straightforward. When a weak vortex is placed in contact with the ocean, Ekman pumping cools the lower layer of the interior of the storm by adiabatic expansion. This leads to the development of shallow convection, which, because it does not precipitate, does not heat. But because the vertically integrated entropy is conserved in convective overturning, the boundary layer dries out as the lower layer moistens. Thus the vortex becomes cold core and weakens due to friction. Only if the initial vortex is sufficiently strong will the anomalously large surface entropy fluxes make up for the drying of the boundary layer by shallow clouds. Then deep convection can occur in the core, and the vortex intensifies.

If shallow convection is prevented, however, the boundary layer in the outer region of mature vortices moistens and deep convection breaks out. When this happens, the surface flow in the interior becomes divergent and the vortex weakens.

References

- Rotunno, R. and K.A. Emanuel, 1987. An air-sea interaction theory for tropical cyclones. Part II: Evolutionary study using a nonhydrostatic axisymmetric numerical model. *J. Atmos. Sci.*, 44, 542-561.

Notes by Jim Countryman and Stephane Douady



10. OSCILLATIONS IN CONVECTIVELY-ADJUSTED FLOWS

Today we will focus on a relatively new class of air-sea interactions. Observations have led to the discovery of a prominent mode of oscillation in the east-west winds of period 30-60 days in the tropical atmosphere, often called the 40-day oscillation. This mode usually has its maximum amplitude at the equator, is confined to within 30 degrees latitude of the equator, and is seen to have a planetary wave number of unity. The strongest signals in the zonal wind, found at heights of 850 mb and 150 mb in the troposphere, are out of phase, implying the oscillation is baroclinic in nature. Infrared images of cloud tops have shown that the wave moves toward the east at a speed of about 10 m/s.

Although this phenomenon hasn't been the subject of much investigation, some theoretical explanations have been offered. The first attempt was to explain the wave as an equatorial Kelvin wave, but phase speeds of Kelvin modes matching the observed atmospheric structure are many times larger than the observed speeds. The inclusion of strong dissipation can reduce Kelvin wave speeds to those that are observed, but the notable sensitivity of wave speeds to diffusion coefficients is disturbing, as is the problem of maintaining a wave subject to such dissipation. General circulation models (GCM's) using an ocean planet have produced wave modes with periods of about 30 days, whose structure closely resembles the observations, suggesting that the presence of land and zonal asymmetry may not be very important in explaining this phenomenon. However, the phase speeds produced by these models are generally too large by a factor of two.

Consider a new model based on the interaction of a moist atmosphere with a fixed ocean. The convection in this atmosphere is viewed as a means of redistributing heat from the ocean surface throughout the entire troposphere. On the time scale of the 30-60 day wave, convection can be treated as instantaneous, so that the atmosphere is considered to be convectively neutral. It is assumed that the moist adiabatic lapse rate characterizing this neutral atmosphere is determined by the moist entropy of the boundary layer i.e.,

$$S^* = S_b \quad (10.1)$$

where S^* is the saturation moist entropy of the troposphere above the subcloud layer, and S is the moist entropy of the subcloud layer itself. In addition, fluctuations in the moist entropy of the subcloud layer are assumed to be linearly proportional to fluctuations in the mean moist entropy of the troposphere above it, i.e.,

$$\delta S_b = \nu \delta \bar{S} \quad (10.2)$$

where δ denotes a fluctuation, ν is the proportionality constant and \bar{S} is defined as

$$\bar{S} \equiv \frac{1}{\Delta p} \int_{p_t}^{p_b} S dp$$

with p_b and p_t being the pressure at the top of the sub-cloud layer and at the top of the troposphere, respectively, and $\Delta p \equiv p_b - p_t$. The value of ν can be related to fluctuations in the relative humidity of the troposphere, or to the percentage of surface evaporation

anomalies realized as precipitation. Thus, in precipitating regions, ν is close to unity, while it can be quite small otherwise.

We are interested in forming a linear model that gives rise to growing baroclinic disturbances, as suggested by observations and GCM's. The anticipated wind-evaporation feedback instability is sketched schematically below:

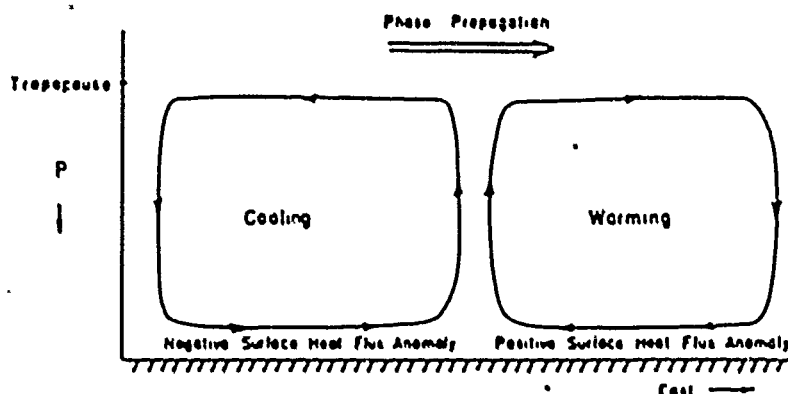


FIG. 1. Conceptual illustration of the 30-60 day wave as an air-sea interaction instability. Anomalously strong easterlies at right give rise to anomalous heat fluxes from the sea surface; the moist entropy is then rapidly redistributed aloft by convection. The resulting temperature anomaly leads the surface convergence by one quarter cycle, leading to wave growth and eastward propagation.

Since we want baroclinic disturbances, the mean state is chosen to be barotropically stable, and the vertically integrated velocity fluctuation must vanish to insure that there will be no barotropic disturbances. Using the hydrostatic relation and the equation of motion for horizontal velocity fluctuations, an expression can be derived relating fluctuations in surface pressure to fluctuations of moist entropy in the surface layer, and hence fluctuations in the mean moist entropy in the troposphere via equation 10.2:

$$\delta\phi_b = -T_b\epsilon\nu\delta\bar{S} \quad (10.3)$$

where ϕ_b and T_b are the geopotential and absolute temperature of the surface layer, respectively, and ϵ is the thermodynamic efficiency given by

$$\epsilon \equiv \frac{T_b - \bar{T}}{T_b} \quad (10.4)$$

with \bar{T} being the mean absolute temperature in the atmosphere,

$$\bar{T} \equiv \frac{1}{\Delta p_0} \int_{p_t}^{p_0} T dp \quad (10.5)$$

where p_0 is taken to be 1000 mb and $\Delta p_0 \equiv p_0 - p_t$. Equation 10.3 effectively constitutes our convective parameterization. Note that this parameterization allows no changes in the temperature of the atmosphere above the boundary layer as long as processes in the boundary layer occur at constant entropy. Thus, even if there is some amount of "moisture convergence" (which is necessary to drive other convection parameterizations), our parameterization implies that heating due to condensation exactly cancels adiabatic cooling, if the boundary layer entropy remains constant.

Now we are in a position to formulate the equations that are to be solved. On an equatorial β -plane, the horizontal momentum equations are

$$\frac{du}{dt} = -\frac{\partial \phi}{\partial x} + \beta y v - g \frac{\partial \tau^x}{\partial p} \quad (10.6)$$

$$\frac{dv}{dt} = -\frac{\partial \phi}{\partial y} - \beta y u - g \frac{\partial \tau^y}{\partial p} \quad (10.7)$$

where τ^x and τ^y are stresses. If we assume that the stresses vary linearly (with pressure) from the surface layer to the top of the sub cloud layer and if the standard bulk-aerodynamic stress relation is used, then the stresses are

$$\frac{\partial \tau^x}{\partial p} = \frac{\rho_a}{\Delta p_m} c_D |\mathbf{v}_a| u_a \quad (10.8)$$

$$\frac{\partial \tau^y}{\partial p} = \frac{\rho_a}{\Delta p_m} c_D |\mathbf{v}_a| v_a \quad (10.9)$$

where the subscript a denotes the top of the surface layer, Δp_m is the difference between the pressure at the surface and the top of the sub cloud layer, and c_D is the drag coefficient. The mean state is assumed to have a zonally and vertically constant zonal wind. If eqns. (10.6) and (10.7) are linearized about this mean state, and eqns. (10.8) and (10.9) are used, we get the following in the boundary layer:

$$\frac{\partial}{\partial t}(\delta u) + U \frac{\partial}{\partial x}(\delta u) = -\frac{\partial}{\partial x}(\delta \phi_b) + \beta y(\delta v) - 2 \frac{c_D}{h} U(\delta u) \quad (10.10)$$

$$\frac{\partial}{\partial t}(\delta v) + U \frac{\partial}{\partial x}(\delta v) = -\frac{\partial}{\partial y}(\delta \phi_b) - \beta y(\delta u) - \frac{c_D}{h} U(\delta v) \quad (10.11)$$

where δ denotes a fluctuation quantity, $h \equiv (\Delta p_m R T_a) / (p_a g)$ is a boundary layer scale height, and the factor of 2 difference in the stress terms arises due to the fact that the mean wind is purely zonal. Note that we have an expression for fluctuations in geopotential at the top of the boundary layer (eq. 10.3), so we will solve 10.10 and 10.11 there, along with a thermodynamic equation for $\delta \bar{S}$.

The relevant thermodynamic equation is

$$\frac{dS}{dt} = -gc_p \frac{\partial \tau}{\partial p} + \dot{R} \quad (10.12)$$

where c_p is the heat capacity at constant pressure, τ is the vertical entropy flux, and \dot{R} is the radiative cooling. Again, assume a bulk aerodynamic relation for the surface flux,

$$\tau_s = \rho_a c_\theta c_p |\mathbf{v}_a| (S - S_s) \quad (10.13)$$

where c_θ is the exchange coefficient and S_s the saturation moist entropy of the sea surface. If eqn. (10.12) is then linearized about a mean state of radiative convective equilibrium, we get

$$\frac{\partial}{\partial t}(\delta S) + U \frac{\partial}{\partial x}(\delta S) = -g \frac{\partial}{\partial p} \tau' + \delta \dot{R} \quad (10.14)$$

To get an expression for $\delta \bar{S}$, eqn. (10.14) is integrated from the top of the surface layer to the top of the troposphere,

$$\frac{\partial}{\partial t}(\delta \bar{S}) + U \frac{\partial}{\partial x}(\delta \bar{S}) = -\frac{g}{\Delta p} [\rho_a c_\theta U \delta \bar{S} - \rho_a c_\theta \text{sgn}(U)(S_s - S) \delta u] + \frac{1}{\Delta p} \int_{p_t}^{p_a} \delta \dot{R} dp \quad (10.15)$$

where $S_s - S$ is now the mean (time averaged) difference. If it is assumed that the radiative cooling term can be approximated by Newtonian cooling,

$$\frac{1}{\Delta p} \int_{p_t}^{p_a} \delta \dot{R} dp \simeq -\frac{1}{\tau_r} \delta \bar{S} \quad (10.16)$$

where τ_r is an appropriate time scale, then our set of linear equations is:

$$\frac{\partial}{\partial t}(\delta u) + U \frac{\partial}{\partial x}(\delta u) = T_b c_\nu \frac{\partial}{\partial x}(\delta \bar{S}) + \beta y(\delta v) - 2 \frac{c_D}{h} U(\delta u) \quad (10.17)$$

$$\frac{\partial}{\partial t}(\delta v) + U \frac{\partial}{\partial x}(\delta v) = T_b c_\nu \frac{\partial}{\partial y}(\delta \bar{S}) - \beta y(\delta u) - \frac{c_D}{h} U(\delta v) \quad (10.18)$$

$$\frac{\partial}{\partial t}(\delta \bar{S}) + U \frac{\partial}{\partial x}(\delta \bar{S}) = -\frac{c_\theta}{H} \nu U(\delta \bar{S}) + \frac{c_\theta}{H} \text{sgn}(U)(S_s - S)(\delta u) - \frac{1}{\tau_r}(\delta \bar{S}) \quad (10.19)$$

where $H \equiv (\Delta p R T_a / p_a g)$ and (10.3) has been used.

As a prelude to solving these equations, we will nondimensionalize as follows, with asterisks denoting dimensional variables:

$$\begin{aligned} x^* &= ax \\ y^* &= A^{1/4} \beta^{-1/2} a^{1/4} y \\ t^* &= A^{-1/2} a^{1/2} t \\ \delta u^* &= A^{1/2} a^{1/2} \delta u \\ \delta v^* &= A^{3/4} \beta^{-1/2} a^{-1/4} \delta v \\ \delta \bar{S}^* &= a H^{-1} c_\theta (S_s - S) \delta T \\ U^* &= A^{1/2} a^{1/2} U \end{aligned} \quad (10.20)$$

where a is the radius of the earth, and

$$A \equiv c_p T_a H^{-1} c_\theta (S_a - S).$$

Using the above scalings, the equations become

$$\frac{\partial}{\partial t}(\delta u) + U \frac{\partial}{\partial x}(\delta u) = \frac{\partial}{\partial x}(\delta T) + y(\delta v) - 2F(\delta u) \quad (10.21)$$

$$\frac{\partial}{\partial t}(\delta v) + U \frac{\partial}{\partial x}(\delta v) = P \frac{\partial}{\partial y}(\delta u) - P y(\delta u) - F(\delta v) \quad (10.22)$$

$$\frac{\partial}{\partial t}(\delta T) + U \frac{\partial}{\partial x}(\delta T) = -\gamma(\delta T) + \text{sgn}(U)(\delta u) \quad (10.23)$$

where $F \equiv c_p U a h^{-1}$, $P \equiv \beta A^{-1/2} a^{3/2}$, and $\gamma \equiv a^{1/2} A^{-1/2} \tau_r^{-1} + F v(c_\theta h)/(c_p H)$. Since we have a closed set of linear equations with constant coefficients, we will try solutions of the form

$$\delta u = u(y) e^{ikx + \sigma t} \quad (10.24)$$

where σ is complex. Similar expressions are used for δv and δT , resulting in the following linear equations:

$$(D + 2F)u = ikT + yv \quad (10.25)$$

$$(D + F)v = P \left(\frac{dT}{dy} - yu \right) \quad (10.26)$$

$$(D + \gamma)T = u \text{sgn}(U) \quad (10.27)$$

where $D = \sigma + ikU$. First we search for some solutions of simplified equations. Note that if $v = 0$ eqns. (10.25) and (10.27) can be used to find the dispersion relation:

$$(D + 2F)(D + \gamma) = ik \text{sgn}(U) \quad (10.28)$$

If P is large, then the geostrophic approximation, $dT/dy = yu$, can be made. In this case the dispersion relation implies $v = 0$ everywhere. From eqns. (10.26) and (10.27), the temperature structure is seen to be

$$T = B \exp \left[\frac{1}{2} y^2 (D + \gamma) \text{sgn}(U) \right] \quad (10.29)$$

where B is a constant. To have well-behaved solutions, the exponential must decay with increasing y . Thus if we assume that the real part of D is positive, resulting in growing disturbances, we conclude that $\text{sgn}(U)$ must be negative. Therefore, consideration will be limited strictly to mean easterly winds.

The following figure shows the horizontal structure of the solutions for the moist entropy, zonal wind, vertical velocity, and cumulus mass flux perturbations for $k = 1$.

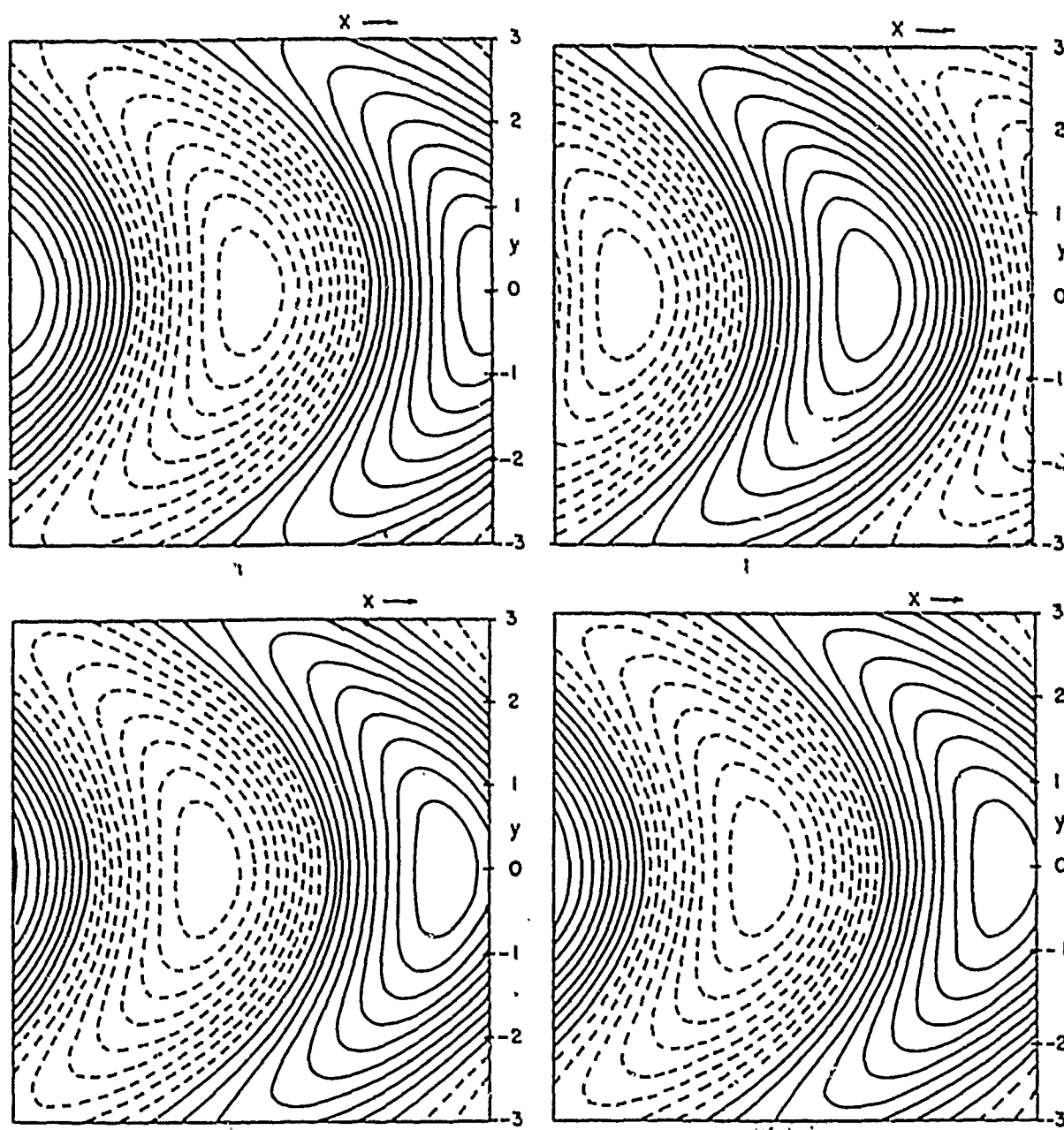


FIG. 2. Horizontal distributions of the dimensionless (a) moist entropy perturbation T , (b) zonal velocity perturbation u , (c) vertical velocity w , and (d) cumulus mass flux, calculated at the top of the mixed layer for wavenumber 1 for the case $F = 0.9$ and $\gamma = 0.2$. Dashed lines denote negative values. For a zonal velocity amplitude of 1, the amplitudes of T , w , and the cumulus mass flux are 1.71, 0.99 and 0.95, respectively. The ordinate is dimensionless meridional distance with one unit representing approximately nine degrees latitude.

The vertical velocity, w , is calculated using mass continuity,

$$w = -ik u \quad (10.30)$$

where the dimensional w has been normalized by $h' A^{1/2} a^{-1/2}$ and h' is half the depth of the wave. The mass flux is calculated by requiring that the subsidence outside the wave

account for the temperature changes in the wave. This estimate results in an expression for the (non-dimensional) cumulus mass flux perturbation, M_c :

$$M_c = w + i2DT \quad (10.31)$$

Note that the w field is almost identical to the M_c field and that the negative peaks in u (anomalously high total wind) lead the positive peaks in T by a little less than 45° .

Estimates of the thermal damping, γ , indicate that it is at least an order of magnitude smaller than F , and is neglected. The dispersion relation (10.29) is then investigated in two limits. In the limit of large friction, $F^2 \gg k$, the growth rate is

$$\sigma_r = 0.125k^2/F^3 \quad (10.32)$$

while the phase speed is

$$c = U + 0.5/F \quad (10.33)$$

Note that the phase speed is independent of wavenumber. In the opposite limit, $k \gg F^2$, we get

$$\sigma_r = 0.5^{1/2}k^{1/2} \quad \text{and} \quad c = 0.5^{1/2}k^{-1/2} \quad (10.34)$$

In this case, which may be more applicable to the real atmosphere, a growth rate $\sigma_r = 0.27 \text{ day}^{-1}$ and wave period of 23 days is obtained for a wavenumber unity disturbance. In both limits, the linear theory fails to choose the longest waves to be most unstable.

There are some possible explanations why the real atmosphere may nevertheless choose the longest wave. First, the meridional scale should be comparable to the equatorial deformation radius, $(NH/2\beta)^{1/2}$ where N is the buoyancy frequency. Using the y normalization from eqn. (10.20), and using eqn. (10.29) to define a meridional length scale, it is found that only disturbances of very low wavenumber can have a scale greater than or equal to the deformation radius. Another possibility for why the atmosphere chooses the longest waves is the effect of finite amplitude waves. Waves will tend to be damped if subsidence warming exceeds radiational cooling in the descending wave motions. It is estimated that the least amount of damping will occur for the longest waves.

Equations (10.25) – (10.27) also permit a set of nongeostrophic modes characterized by u and T vanishing at the equator. Proceeding as before, it is found that these modes can have quite large growth rates, but also have both eastward and westward phase speeds of 70 to 80 m/s for $k = 1$, and are thus not directly related to the problem of the 30–60 day oscillation. However, these modes do have periods (5–6 days) that are similar to observations of higher wavenumber tropical waves.

We have seen what the perturbation fields look like for constant sea surface temperature (SST) and constant mean zonal wind. It is of interest to vary these quantities in the meridional direction to see how the structure of the perturbation fields changes.

If we vary the SST in the meridional direction, the only change in eqns. (10.25) – (10.27) is that eqn. (10.27) becomes

$$(D + \gamma)T = -uB(y) \quad (10.35)$$

where it is assumed that $\text{sgn}(U) = -1$. $B(y)$ is nondimensional and is interpreted to be the meridional variation of either the mean air-sea moist entropy difference or the thermodynamic efficiency. Just as in the constant SST case, the equations decouple at $y = 0$, and we get the dispersion relation

$$(D + 2F)(D + \gamma) = -ikB(0) \quad (10.36)$$

Thus, we see that although the form of $B(y)$ will affect the structure of the modes, the dispersion relation depends only on its value at the equator. Below are shown the horizontal structure of the T , u , v and w fields for the case $B(y) = 1/(1 + y^2)$.

The cumulus mass flux is henceforth not plotted because it strongly resembles the w field. It can be seen that the eddy angular momentum flux, $\frac{1}{2}\text{Re}[u^*v]$, is always directed away from the SST maximum at the equator, and perhaps helps to sustain equatorial easterlies. We show a similar case with $B(y) = 1/[1 + 0.5(y - 0.5)^2]$.

The asymmetry in the wind fields is due to the fact that higher winds are needed south of the equator to balance the heat flux due to the higher temperature in the north. Again, note that the eddy angular momentum flux is directed away from the SST maximum.

Now consider the case where the mean zonal wind varies in the meridional direction, but does not vary with height (i.e., barotropic), and $U(y) < 0$ for all y where the solutions have a significant amplitude. The existence of the mean zonal wind affects the damping and advection terms, so eqns. (10.25) - (10.27) become

$$(\sigma + ikU + 2F'U)u = ikT + v(y - \frac{dU}{dy}) \quad (10.37)$$

$$\frac{dT}{dy} = yu \quad (10.38)$$

$$(\sigma + ikU + G'U + \gamma)T = -u \quad (10.39)$$

where the geostrophic approximation has been made, and $F' = c_D a h^{-1}$, and $G' = c_g a H^{-1}$. Once again, the equations decouple at $y = 0$, provided $dU/dy = 0$ there, so the dispersion relation depends only on the value of U at the equator. We show the various fields for $U(y) = -0.05/(1 + y^2)$.

Note that, in this case, the eddy angular momentum flux is toward the equator. Next are the fields for $U(y) = 0.25 \cos(\pi y) - 0.075$.

Again, the vertical velocity is strongly peaked at the equator, while the angular momentum flux is toward the equator.

Neelin, et al. (1987) independently introduced an almost identical model. In addition, GCM experiments were made in an attempt to confirm the wind-evaporation feedback mechanism. Experiments that inhibit this feedback show a marked reduction in energy at periods characterizing the 30-60 day wave. However, they also find that this may not be the only mechanism at work, suggesting that wave-CISK or some other instability could also be a factor.

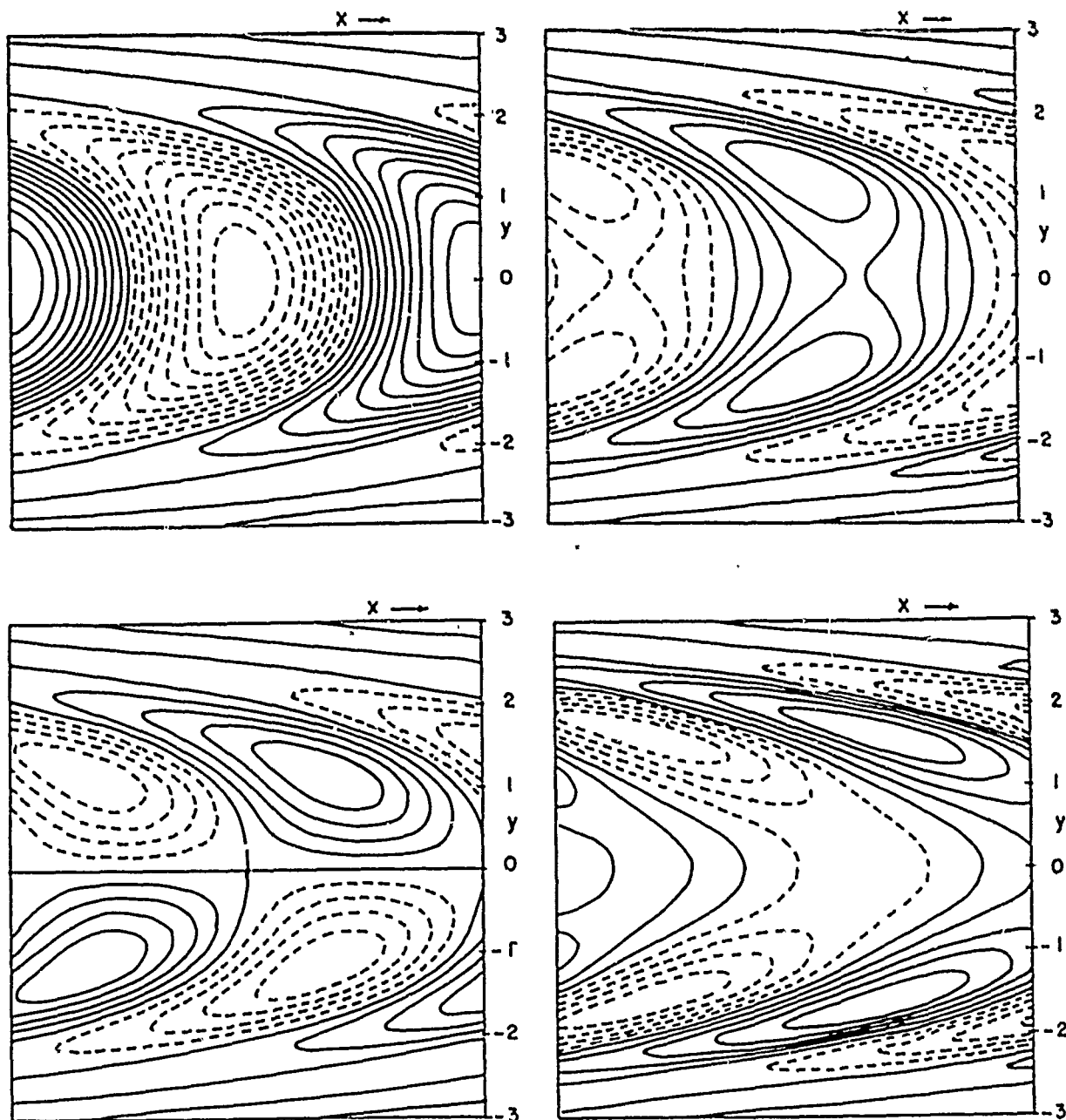


FIG. 3. Horizontal distributions of (a) T , (b) u , (c) v and (d) w as in Fig. 2, but for the quantity A defined by (26) varying according to $A = 1/(1 + y^2)$. For a zonal velocity amplitude of 1 the amplitudes of T , v and w are 1.04, 0.84 and 2.81, respectively.

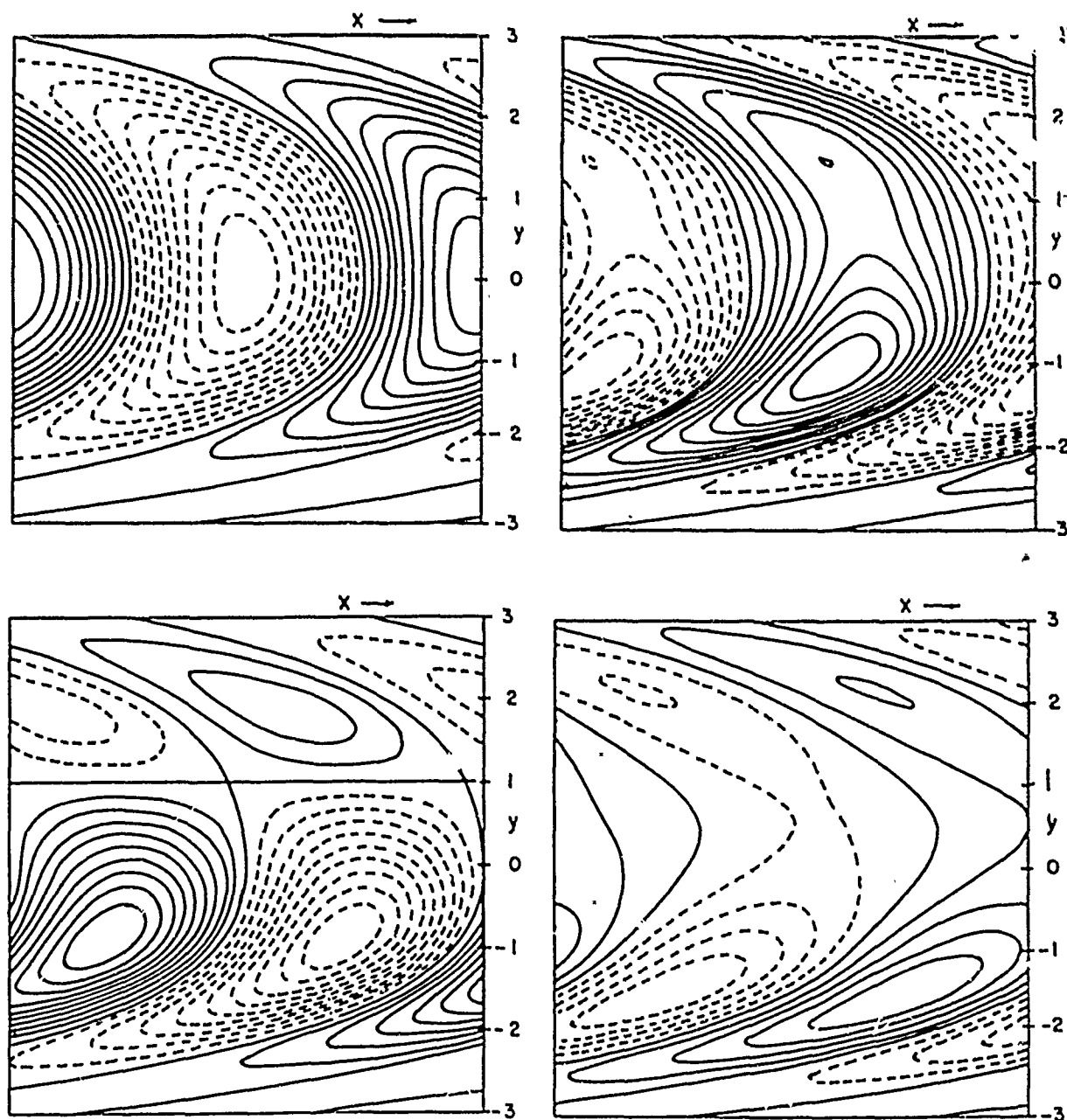


FIG. 4. As in Fig. 3, but for A varying according to $A = 1/[1 + 0.5(y - 0.5)^2]$. For a zonal velocity amplitude of 1 the amplitudes of T , v and w are 1.13, 0.79, and 2.19, respectively.

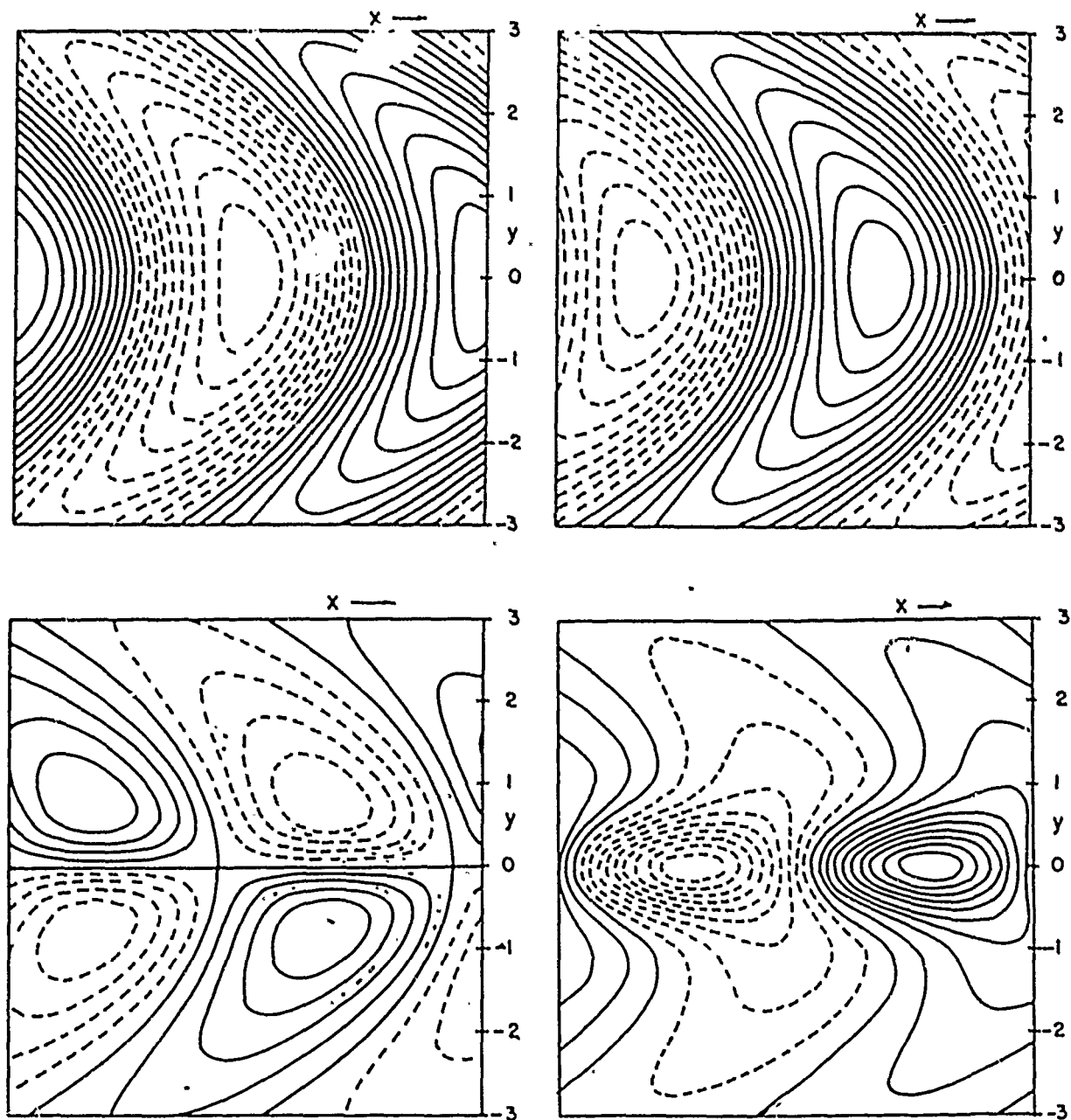


FIG. 5. Horizontal distributions of (a) T , (b) u , (c) v and (d) w for $\gamma = 0$, $F' = 12$, and $G' = 1$ for mean zonal wind varying according to $[U] = -0.05/(1 + y^2)$. For a zonal velocity amplitude of 1.0 the amplitudes of T , v , and w are 1.53, 0.62 and 1.83, respectively.

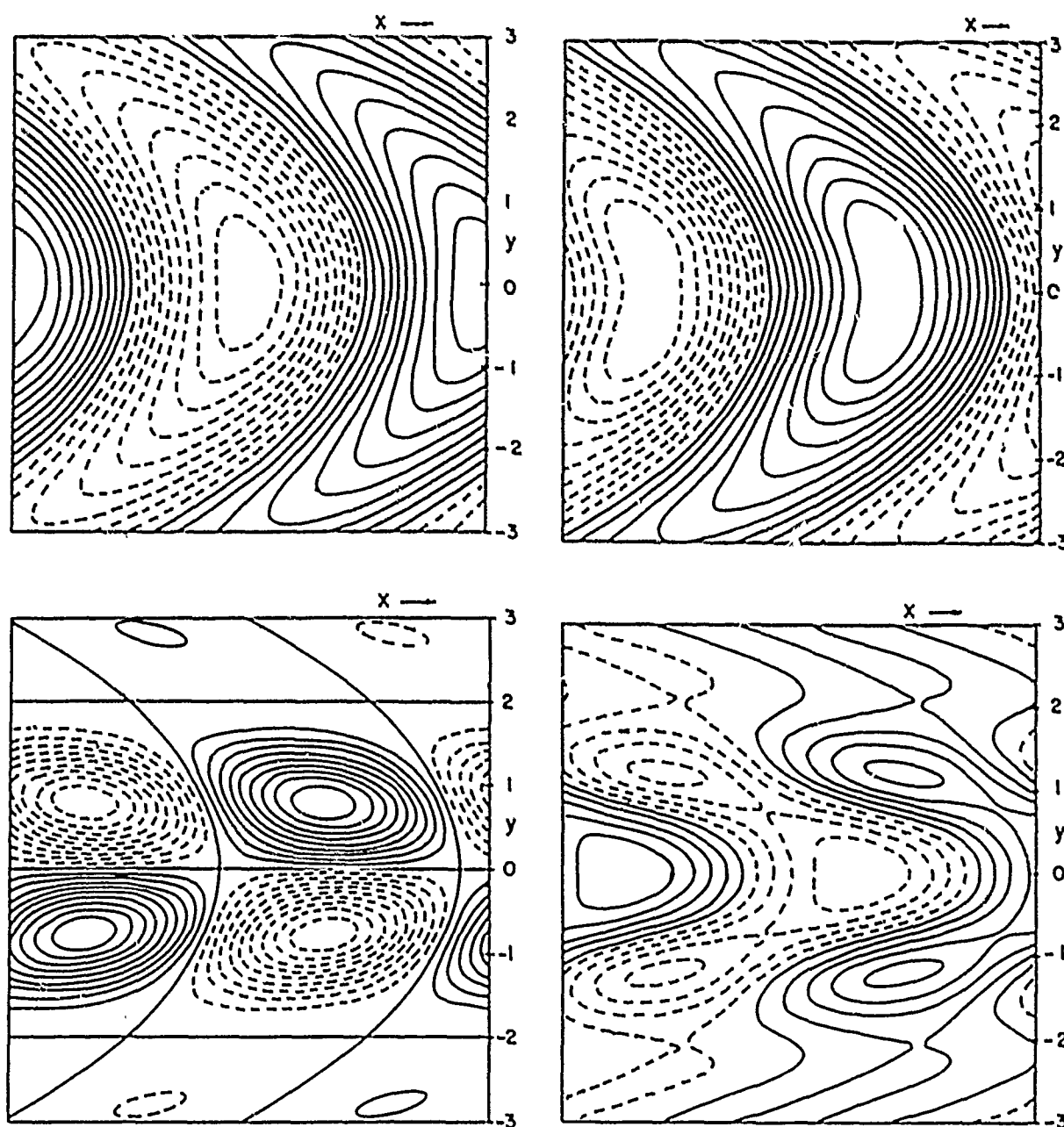


FIG. 6. As in Fig. 5 but for $[U] = 0.025 \cos \pi y - 0.075$. For a zonal velocity amplitude of 1.0, the amplitudes of T , v and w are 1.51, 1.42 and 2.80, respectively.

References

- Emanuel, K.A., 1987: An air-sea interaction model of intraseasonal oscillations in the tropics. *J. Atmos. Sci.*, **44**, 2324-2340.
- Neelin, J.D., I.M. Held and K.H. Cook, 1987: Evaporation - wind feed back and low frequency variability in the tropical atmosphere. *J. Atmos. Sci.*, **44**, 2341-2348.

Notes by Tim Dowling and Mat Maltrud

1988 Summer Study Program

in

Geophysical Fluid Dynamics

ABSTRACTS OF PARTICIPANTS

INTERACTION OF OCEANIC CONVECTIVE BOUNDARY LAYER AND TROPICAL CLIMATE

Alan K. Betts
Middlebury, Vermont

Observational analysis of FGGE dropwindsonde data using conserved thermodynamic variables showed mixing line structures for the convective boundary layer over the equatorial Pacific. Deeper boundary layers show a double structure. Reversals of the gradients of mixing ratio and equivalent potential temperature above the boundary layer top are present in all the averages and suggest that the origin of the air sinking into the boundary layer needs further study. (Betts and Albrecht, 1987)

Betts and Ridgway (1988) used an idealized energy-balance model for a closed tropical circulation to illustrate the coupling between the net tropospheric radiative cooling, the surface fluxes and the mean subsidence away from the precipitation zones. Then a one-dimensional diagnostic model and radiation mode with boundary layer clouds were combined to explore this coupling for a specific region using mean sounding data over the tropical Pacific from Betts and Albrecht (1987). The radiatively driven subsidence rate at the top of the convective boundary layer is approximately 35 mb/day (0.04 Pa/s) and is largely independent of boundary layer cloud fraction. The sensitivity of the corresponding convective heat flux profiles to the mass divergence profile and cloud fraction within the boundary layer is explored. Reasonable assumptions give realistic surface sensible and latent heat fluxes for this region of approximately 10 and 130 W m². The work illustrates the important background climatic control of the radiation field on the tropical surface fluxes.

A one-dimensional, thermodynamic model for a partially mixed, partly cloudy, convective boundary layer (CBL) is coupled to a radiation model to compute equilibrium solutions for a tropical CBL and troposphere in energy balance over the ocean (Betts and Ridgway 1989). The model gives the climatic equilibrium cloudbase (950mb) and CBL top (800mb) and low level (347K) and shows the deepening of the CBL and rise of low level with increasing wind speed and sea surface temperature (SST). One extension of the model gives the equilibrium SST as a function of surface wind speed and CBL cloudiness.

References

- Betts, A.K., and B.A. Albrecht, 1987: Conserved variable analysis of boundary layer thermodynamic structure over the tropical oceans. *J. Atmos. Sci.*, 44, 83-99.
- Betts, A.K. and W. Ridgway, 1988: Coupling of the radiative, convective and surface fluxes over the equatorial Pacific. *J. Atmos. Sci.*, 45.

Betts, A.K. and W. Ridgway, 1989: The equilibrium convective boundary layer over the tropical oceans. MS in preparation.

CONVECTIVE PARAMETERIZATION IN LARGE-SCALE MODELS

Alan K. Betts
Middlebury, Vermont

Betts (1986) and Betts and Miller (1986) outlined a new convective adjustment scheme, based on the lagged adjustment of temperature and moisture fields towards reference quasi equilibrium thermodynamic structures.

The shallow convection reference profile was based on a mixing line, and that for deep convection used a moist virtual adiabat up to the freezing level, and a specified constraint on the moisture profile.

Subsequent work with this scheme in progress at ECMWF (Heckley et al, 1987; Betts and Miller, 1985) has shown the complexity of the interactions between convection, clouds, radiation and the tropical climate. Work in progress at NMC has shown the importance of the convective parameterization to summer rainfall forecasts.

References

- Betts, A.K., 1986: A new convective adjustment scheme. Part I: Observational and theoretical basis. *Quart. J. Roy. Meteor. Soc.*, 112, 677-692.
- Betts, A.K. and M.J. Miller, 1985: A new convective adjustment scheme for global models. *Seventh Conf. on N.W.P.* Montreal, June, 1985, 7pp. (preprint)
- Betts, A.K. and M.J. Miller, 1986: A new convective adjustment scheme. Part II: Single Column tests using GATE-wave, BOMEX, ATEX, and Arctic Airmass data sets. *Quart. J. Roy. Meteor. Soc.*, 112, 693-710.
- Heckley, W.A., M.J. Miller, and A.K. Betts, 1987: An example of hurricane tracking and forecasting with a global analysis/forecasting system. *Bull. Amer. Meteor. Soc.*, 68, 226-229.

ENERGY EXTREMIZATION BY PSEUDO-ADVECTION

G.F. Carnevale
G.K. Vallis
W.R. Young
Scripps Institution of Oceanography
La Jolla, CA, 92093, U.S.A.

A new method for finding stable stationary flows is presented along with demonstrations of its implementation by numerical simulation. This method can be applied to any system in which advection plays a role. Algorithms are constructed which can smoothly deform any flow into a flow of extremal energy while preserving all topological invariants. The algorithms are based solely on advection with an artificially crafted velocity field, chosen at each instant in such a way that the energy changes monotonically for all time. Specific pseudo-advection algorithms have been derived for a wide variety of systems including quasigeostrophic flow, three-dimensional Euler flow, and magnetohydrodynamics have been derived. There are actually many ways of accomplishing this as described in Vallis et al. (1989). We have successfully applied this pseudo-advection technique numerically in two-dimensional Euler flow and one-layer quasigeostrophic flow over topography. For example, consider the case of two-dimensional Euler flow. The dynamical evolution of the flow is simply the advection of relative vorticity, ω , by the incompressible velocity field derived from a streamfunction which satisfies $\omega = \nabla^2 \psi$:

$$\frac{\partial \omega}{\partial t} = -J(\psi, \omega) \quad (1)$$

An algorithm which monotonically changes the energy of the flow while preserving the value of ω on all particles evolves the vorticity field according to the following artificial dynamics:

$$\frac{\partial \omega}{\partial t} = -J(\psi - \alpha J(\psi, \omega), \omega) \quad (2)$$

where α is an arbitrary constant. That is, all of the particles carrying their original values of ω are simply advected with a new velocity field that is derived from an artificial streamfunction, $\hat{\psi}$, which is related to the physical streamfunction by

$$\hat{\psi} = \psi - \alpha \nabla^2 J(\psi, \omega) \quad (3)$$

The vorticity field evolving according to the modified dynamics (2) continually gains or loses energy depending on the sign of α according to

$$\frac{dE}{dt} = \alpha \int [J(\psi, \omega)]^2 dx dy \quad (4)$$

Thus any state is driven toward an extremal energy state, which since it is extremal must be stationary and stable. Consequently, this method seeks and where possible finds the stable stationary flow isovortical to any given flow. An example of this algorithm simulated numerically is provided in the accompanying figure.

A NONLINEAR, TIME DEPENDENT THERMOCLINE THEORY

William K. Dewar
Department of Oceanography
Florida State University
Tallahassee, FL 32306

A non-eddy resolving, time dependent, nonlinear theory of the large-scale ocean circulation is discussed. The variability in this theory occurs as a response to variability in forcing. Baroclinic and barotropic evolution is computed using a two-layer, quasigeostrophic, wind-driven model. Both analytical and numerical solutions are obtained.

Attention is focussed on the low-frequency, basin scale fluctuations of the wind. Based on these restrictions, the various modes of response are separated by means of a multiple time scale analysis. The barotropic response is found to be effectively instantaneous, and a relatively simple advection-diffusion equation is shown to govern the baroclinic response. Analytical solutions of the baroclinic equation are obtained under the assumption that the time scales of the wind variability are short compared to the cross-basin baroclinic wave propagation time. Numerical solutions are obtained in more general cases.

The baroclinic large-scale response is fundamentally nonlinear in that baroclinic waves propagate in the presence of the Sverdrup flow, which is itself time dependent. This nonlinearity results in at least two effects. First, the characteristics of wave propagation are significantly altered from pure zonality. This leads to the formation of homogenized zones, within which directly forced thermocline variability vanishes. Second, thermocline fluctuations are produced which have variance at frequencies other than those of the forcing. Thus, forcing the model with an annually varying wind stress yields contributions to the thermocline spectrum at one year and all its superharmonics (i.e., 6 months, 4 months, 3 months, etc.). The amplitudes of the superharmonics increase with distance from the eastern boundary. Mean baroclinic circulation on the scale of the thermocline waves is also found. The above features are predicted by analytical theory and confirmed by numerical experimentation.

Observations of the geographical distribution of thermocline variability in the North Pacific and North Atlantic Oceans and of first mode variance at "inadmissible" planetary wave frequencies are discussed in light of the theory.

FARADAY INSTABILITY

Stephane Douady

Laboratoire de Physique de l'Ecole Normale Supérieure de Lyon
46 Allée d'Italie 69364 Lyon Cedex 07 France

Faraday discovered in 1831 that the free surface of a vertically oscillating layer of fluid is unstable to surface waves. An experimental study of these parametrically excited surface waves is presented. The shape of the eigenmodes in a closed basin is discussed, and the importance of boundary conditions and of the meniscus wave is proved by a study of the modes. Stability boundaries, wave amplitude, and characteristic perturbation decay times are measured and found to be in accordance with an amplitude equation derived from symmetry. The measurement of the amplitude equation coefficients allow us to explain the observed supercritical transitions and to show the effects of the edge constraint on the dissipation and eigenfrequency of the various modes. The fluid surface tension is obtained from the dispersion relation measurement. Several visualization methods in large aspect ratio cells are presented, and the existence of many stationary wave patterns above the instability onset is shown. In a square cell, patterns with different symmetries are observed and understood as superpositions of linearly unstable modes of the fluid free surface.

JUPITER'S GREAT RED SPOT AS A SHALLOW WATER SYSTEM

Tim Dowling

California Institute of Technology

The Voyager spacecraft have provided us with high resolution photographs of Jupiter's Great Red Spot (GRS) and other long-lived atmospheric vortices. From these we have derived detailed horizontal velocity fields for the cloud-top level, but information about the deep motions is not directly observable. Lack of vertical information leaves open many fundamentally different possibilities for the dynamics of Jupiter's deep atmosphere and its effect on the vortices.

Most models of the GRS drastically simplify the vertical structure of the atmosphere due to lack of information. The so-called 1-1/2 layer model is popular, where the thin upper weather layer, which contains the vortex, overlies a much deeper layer, which is meant to represent the neutrally stratified deep atmosphere. Any motions in the deep layer are assumed to be zonal and steady, and result in meridional topography at the fluid layer interface. Specifying the deep motions is equivalent to specifying the bottom topography of the upper layer, and hence the background potential vorticity field. Current

models of the GRS start by guessing the deep motions and then proceed to study vortices using the implied bottom topography.

By making the same 1-1/2 layer model assumptions as above, we can derive the correct bottom topography from the GRS cloud-top velocity data, up to a constant which depends on the unknown radius of deformation. A quasi-geostrophic analysis of the data is presented in Dowling and Ingersoll (1988), and a more complete shallow water (SW) analysis is in preparation. In the SW analysis we start by calculating the Bernoulli function B from the GRS velocity data, which is observed to be nearly steady in the reference frame of the vortex. We also calculate the kinetic energy per mass K , and the absolute vertical vorticity field, $(\zeta + f)$. The bottom topography gh_2 is related to the observations by $gh_2 = B - K - (\zeta + f)/q$, where the potential vorticity q , is the only unknown. Since for steady motions a B contour (known) is equivalent to a q contour, we can model q by some function $q(B)$. The procedure is to specify $q = q_0$ on $B = B_0$, and then solve by least squares for the bottom topography and for $q(B)$.

The results yield the bottom topography, and hence the deep velocity field and background potential vorticity, consistent with the GRS velocity data. None of the current models is qualitatively correct over the entire latitude range of the GRS. The results show that the deep atmosphere is in differential motion and that the background potential vorticity field is not uniform.

We are currently studying a numerical 1-1/2 layer SW model with the derived bottom topography. A model run which starts with the observed cloud top winds produces several eddies. These eddies merge over time to form a single, long-lived eddy, closely resembling the GRS. Notable features, like the large filamentary region extending to the west of the GRS, appear in the runs but do not persist. The initial system is unstable, leading naturally to the genesis of vortices, but the upper layer velocity field tends to smooth out with time. How the cloud top winds on Jupiter are maintained in an unstable state is a crucial unanswered question.

References

- Dowling, T.E., and A.P. Ingersoll (1988). Potential vorticity and layer thickness variations in the flow around Jupiter's Great Red Spot and White Oval BC. *J. Atmos. Sci.*, 45, 1380-1396.

LARGE-SCALE DYNAMICS AND TOPOLOGY NEAR THE ONSET OF CONVECTION

Christian Elphick and E. A. Spiegel
Department of Astronomy
Columbia University

I. Evolution Equations

There has been a renewed concentration of interest lately on the developments near to the onset of sustained convective motion for a variety of reasons (as explained in a review in preparation with S. Zaleski). Though much of the theoretical work on these questions is based on the mildness of the instability, the evolution equations for convection near to onset are as nonlinear as the Navier-Stokes equations themselves, and give rise to phenomena of great complexity, if in lower dimensionality than the original fluid equations. Moreover, a great number of controlled experiments in the regime of mild instability parameter are being conducted. These render the subject interesting in its own right and also make it a crucible for general ideas on the nature of nonlinear dynamics. We will sketch some features of the basic theory as background for a discussion of those aspects of present interest to us, namely the development of spatio-temporal structures.

We assume an acceptance of the Boussinesq equations for basic convection. It is convenient to write these equations as evolution equations for a state vector $U(x, z, t)$ where x is the horizontal coordinate vector and the components of U are all scalars or pseudoscalars. In the case of basic Boussinesq convection, we have

$$U = \begin{pmatrix} w \\ \theta \\ \zeta \end{pmatrix}, \quad (1)$$

where w , θ and ζ are the vertical velocity, deviation of the temperature from its local static value and the vertical component of vorticity. The equations have this general form:

$$\partial_t \mathcal{M}U = \mathcal{L}U + \mathcal{N}(U). \quad (2)$$

Here \mathcal{L} and \mathcal{M} are linear, partial differential operators, depending on the parameters of the system (Rayleigh number, Prandtl number and aspect ratio) and \mathcal{N} is a nonlinear operator, which also involves spatial derivatives. This equation possesses the usual symmetries, such as invariance under translation in x and t , Galilean invariance and *Boussinesq symmetry*. With the latter symmetry, if $U(X, t)$ is a solution, where $X = (x, z)$, then so is $-BU(BX)$ a solution, where $B = \text{diag}(1, 1, -1)$.

In the case of finite box size, the linearization of (2) gives rise to a discrete spectrum of growth rates. Let there be N modes with slow growth or decay

and suppose that all the other modes are very stable in linear theory. Then we write

$$U(x, z, t) = \sum_{I=1}^N A_I(t) \phi(z; k_I, n_I) e^{i k_I \cdot x} + \dots \quad (3)$$

where k_I and n_I represent the horizontal wave vectors and the vertical mode numbers of the modes and the dots replace the terms containing the highly stable modes. Amplitude equations may be derived for $A \equiv (A_I)$ by known means. These equations are of the form

$$\dot{A} = MA + g(A) \quad (4)$$

where g is a nonlinear, vector-valued function. The $N \times N$ matrix M has as eigenvalues all the (possibly complex) linear eigenvalues of the slow modes. The only instability that a mode can have in basic Boussinesq convection is a direct (monotonic) growth when the Rayleigh number increases through a critical value. But if we enrich the problem with rotation or other such influences on stability, we may introduce new parameters and, with them, the possibility of instability by growing oscillations — overstability. With two stability parameters, we can even arrange for the frequency of the overstable mode to pass through zero as the growth rate does. All such vagaries of the spectrum of possible instabilities are expressed in the eigenvalues of M .

When the order of the amplitude equation (4) is three or more, we can have chaotic solutions. Of course such results can be derived by analysis only asymptotically as we approach marginality. An amplitude equation, when three dynamical effects operate on the stability of the fluid, occurs with

$$M = \begin{pmatrix} 0 & 1 & 0 \\ 0 & 0 & 1 \\ \alpha & \beta & \gamma \end{pmatrix} \quad g = \begin{pmatrix} 0 \\ 0 \\ A_1^3 \end{pmatrix}$$

where α , β and γ are parameters of the linear theory (Arneodo, et al. GAFD 1985). Though one gets chaos from such equations, some of the fun goes out of it when we remember that they can be derived by respectable methods only in very carefully tuned conditions. It would be nice to encounter rich behavior with less contrivance. One way to do that is to increase the box size and thus allow more modes to be slow near onset, without special pleading about the parameters. In the limit of infinite horizontal extent, we encounter continua of modes becoming slightly unstable together through the tuning of a single parameter.

In the continuous case, when there is translational invariance in x , it is often helpful to write

$$U(x, z, t) = \int U_k(z, t) d_2 k. \quad (5)$$

The case of a band of modes becoming directly unstable has been widely studied. Proceeding in parallel as in the discrete case ¹

$$U_k(z, t) = A_k(t)\phi(z; k, n) + \dots, \quad (6)$$

where the higher terms are nonlinear in A_k . To proceed, we need to suppose that A_k vanishes for k lying outside of a thin ring in the k -plane containing $|k| = k_c$ where k_c is the magnitude of the wave vector for which instability first becomes possible as the Rayleigh number increases through its control value. Then we can seek, in analogy with (4), an evolution equation like

$$\partial_t A_k = \sigma_k A_k + \iiint G_k(p, q, r) A_p A_q A_r d_2p d_2q d_2r, \quad (7)$$

where $k = |k|$, σ is the growth rate of the mode with the appropriate k , and the kernel G_k contains a factor $\delta(k - p - q - r)$. Since the wave vectors in G_k all lie on the critical circle $|k| = k_c$, the wave vectors $p, q, r, -k$ are colinear in pairs. Hence the rest of G_k , apart from the δ -function, depends only on a single angle. When the convection is two-dimensional, that angle is constant and the kernel is just a constant times the δ -function. If the kernel that applies for two-dimensional convection is used generally, we have the model proposed by Swift and Hohenberg.

It is also good to use the x -representation, so we define the nonlinear planform function

$$A(x, t) = (2\pi)^{-1} \int A_k(t) e^{ik \cdot x} d_2k, \quad (8)$$

with

$$\sigma_k = \epsilon^2 - \xi(k^2 - k_c^2)^2, \quad (9)$$

where ξ is a real constant of order unity. Then, we get

$$\partial_t A = [\epsilon^2 - \xi^2(\nabla^2 + k_c^2)^2]A + \mathcal{F}\{A\}, \quad (10)$$

where \mathcal{F} is a cubic functional. (For suggestions about how to derive such an equation see Cross, *Phys. Fluids*, 1980 or Coulet & Spiegel 1988.) The same kind of thing arose in work on melting in layers and it was apparently that inspiration that led to the proposal of the S-W model with $\mathcal{F}\{A\} = \text{const.} \times A^3$. In the 2-d case, we have, approximately, $(k^2 - k_c^2)^2 = 4k_c^2(k - k_c)^2$, with $k - k_c = O(\epsilon)$. Then we are led to the Ginzburg-Landau equation, calculated for convection by Newell and Whitehead and by Segel (both in JFM 1969). We should add that if the boundaries do not sustain tangential shears, we find that the vertical vorticity modes for $|k|$ close to zero are very weakly damped. They should be

¹ Coulet & Spiegel in "Energy stability and convection," Galdi & Straughan, eds. Pitman Res. Note 168 (1988).

included in the dynamics as Zippelius and Siggia have done in *Phys. Fluids* 1983.

The derivation of an evolution equation for the planform function $A(x, t)$ starting from an ansatz like (6) is suggested by the procedures used by Bogoliubov and collaborators in statistical physics. This approach is advantageous for complicated situations with more than one band of unstable wavenumbers. But the explicit calculations can become burdensome. If you just want the form of the equations, you may be willing to get these more directly, using symmetry arguments. Physicists have been doing this for some time. In fluid dynamics, H.P. Robertson used symmetry arguments to deduce the Karman-Howarth equations. The popularity of using symmetry arguments to derive evolution equations for bifurcations in systems with continuous spectra seems to have begun when Fauve proposed doing this in his 1982 Fellow's lecture. Just to give the flavor of this kind of approach, let us sketch it here for the case of overstability in the full three-dimensional case, starting from the Bogoliubov type of ansatz. This constitutes part of the thesis work of Z. Qian. A full treatment would also include vertical vorticity in the free slip case, but we leave that out here.

For the stationary bifurcation, we modulated $\phi(z; k, n) \exp(ik_c \cdot x)$ with an amplitude function $A_k(t)$. After finding the evolution equation, it seemed more revealing to leave the wave vector representation and go over to an $A(x, t)$, as in (8). But now, in the overstable case, we are going to modulate something like $\phi(z; k, n) \exp(ik_c \cdot x + i\omega_c t)$. Hence, we expect that the analogue of $A(x, t)$ will be complex. To stress this feature, we will call the modulational amplitude in x -representation $\Psi(x, t)$. We expect this to be written as in (8):

$$\Psi(x, t) = (2\pi)^{-1} \int A_k(t) e^{ik \cdot x} d_2 k. \quad (11)$$

But now, we have also

$$\Psi^*(x, t) = (2\pi)^{-1} \int A_{-k}^*(t) e^{ik \cdot x} d_2 k. \quad (11a)$$

So corresponding to Ψ and Ψ^* we have in k -representation $A_k(t)$ and $A_{-k}^*(t)$, which may look familiar to those acquainted with the formalism of second quantization.

With Qian, we seek solutions of the form

$$U_k(z, t) = A_k(t) \phi(z; k, n) + A_{-k}^*(t) \phi(z; k, n) + \dots \quad (12)$$

Let $A_k^\mu = (A_k, A_k^*)$, with $\mu = 1, 2$. We look for an evolution equation of the form

$$\partial_t A_k^\mu = \sigma_k A_k^\mu + \int \int {}^\mu \Gamma_{\alpha\beta}^{pq} A_p^\alpha A_q^\beta d_2 p d_2 q + \dots, \quad (13)$$

where, for the case of overstable convection,

$$\sigma_k = \epsilon^2 + i\omega_1(k^2 - k_c^2) - \xi(k^2 - k_c^2)^2. \quad (14)$$

where ω_1 is a real constant and ξ is complex. The dots in (13) stand for cubic and higher nonlinearities and for corrections to the frequency of the overstable mode. The tensor kernels can be given forms dictated by the theory of isotropic tensors, as in the work of Robertson. Here, we sketch the simplest approach to the guessing of equations of the right form.

Since we have invariance under the transformation $t \rightarrow t + t_0$, we require that under the transformation,

$$A_k^\mu \exp[i(-1)^{\mu+1}t\omega_c] \rightarrow A_k^\mu \exp[i(-1)^{\mu+1}(t + t_0)\omega_c],$$

the evolution equation should not change. With $\varphi_0 = \omega_c t_0$ we write this as invariance under $A_k^\mu \rightarrow A_k^\mu \exp[i(-1)^{\mu+1}\varphi_0]$. This implies that ${}^\mu\Gamma_{\alpha\beta}^{pq} = 0$; indeed, it implies that ${}^\mu\Gamma_{\alpha_1\alpha_2\ldots}^{p_1p_2\ldots} = 0$ unless $\sum_{i=1}^N (-1)^{\alpha_i+1} = (-1)^\mu$. Similarly, invariance under the transformation $\mathbf{x} \rightarrow \mathbf{x} + \mathbf{a}$, that is, $U_k \rightarrow U_k \exp(i\mathbf{k} \cdot \mathbf{a})$, gives

$${}^\mu\Gamma_{\alpha_1\ldots\alpha_N}^{p_1\ldots p_N} = {}^\mu G_{\alpha_1\ldots\alpha_N}^{p_1\ldots p_N}(\mathbf{k}) \delta(\mathbf{k} + p_1(-1)^{\alpha_1} + \ldots + p_N(-1)^{\alpha_N}).$$

To leading order then

$$\partial_t A_k^\mu = \sigma_k A_k^\mu + \iint {}^\mu\Gamma_{\alpha\beta\gamma}^{pqr} A_p^\alpha A_q^\beta A_r^\gamma d_2p d_2q d_2r, \quad (15)$$

with the side condition that $-\mu + \alpha + \beta + \gamma$ should be even. Without pursuing this to the bitter end, we may simply report that many of the same properties of the stationary bifurcation case are recovered: the kernel is simplified in the two-d case and, if we use that simplification in general, we get the Hopfian analogue of the S-W model. The one-d limit of this equation is asymptotically the pair of coupled complex Ginzburg-Landau equations known to be appropriate for this problem.

These equations for real and for complex planform functions, or order parameters, have not been well studied, though simulations have been done for the stationary case. We want to see whether the amplitude-evolution equations for the overstable case admits in its repertory fields of solutions of coherent structures as the G-L equation does. The interacting coherent structures for the one-d case have been studied in a manner used by some particle physicists. We describe this method here.

II. Dynamics of Interacting Structures

Equations like the G-L equation become ordinary differential equations when we try traveling wave solutions. There often exist wave velocities for which these ODEs admit heteroclinic or homoclinic trajectories. In terms of the

original PDEs, these trajectories correspond to shocks or pulses respectively. These are analogues of the coherent structures of turbulence, or so it has been claimed (in the the 1981 GFD course, for example). It ought to be possible to study the interactive dynamics of such structures, at least when they are widely spaced. The interaction of the shock-like domain walls that may arise in cellular convection has been especially studied by the group in Nice (see references in Lecture III).

One way to approach such a multi-structure theory is to use some of the ideas of statistical physics. We have in mind the example of a one-dimensional system such as that produced by two-dimensional convection. We are currently studying the two-dimensional extension for three-d convection with Qian. The work we describe next was done with Ehud Meron (PRL 1988). We are working on an astrophysical applications with Oded Regev. There is also work by Fowler (les Houches lecture, 1987) that attacks these problems from the standpoint of the homoclinic solutions of the PDE itself (a possibility also raised by Howard in a GFD lecture some years ago).

Suppose once again that we have an equation of the type

$$\partial_t U = \mathcal{L}U + \mathcal{N}(U), \quad (16)$$

where $U(x, t)$ is a state vector depending on x , $\mathcal{L}(\partial_x)$ is a linear differential operator and \mathcal{N} is a nonlinear operator. We shall suppose that (16) has translational invariance, but shall ignore other invariances in this treatment.

We look for a solution to (16) of the form

$$U(x, t) = H(\chi), \quad \chi = x - ct, \quad (17)$$

where c is a constant speed and where $H \rightarrow 0$ when $x - ct \rightarrow \pm\infty$. (Such solutions do exist for the G-I equation, both real and complex for a particular c , say c_0 .) For fiducial purposes, we arrange that when the first component of H , $H^{(1)}$ say, is largest, $\chi = 0$. Then $H^{(1)} \rightarrow 0$ when $\chi \rightarrow \pm\infty$.

We consider next the possibility of a solution to the PDE (16) containing N pulses located at the positions $\chi = \chi_j$ where $j = 1, 2, \dots, N$ and now $\chi = x - c_0 t$. The pulses will interact, so that, even in the frame of the single-pulse solution, they move; hence the χ_j depend on t . These pulse drifts are to be given by equations of motion that come out of a solvability condition based on the multi-pulse ansatz. That happens in a way that we shall describe elsewhere, with epsilons and all that. Here, we offer a shorter, somewhat postulational derivation.

Let us assume that

(A) There is an N -pulse solution of (16):

$$U(x, t) = V_N(\chi, \{\chi_\ell\}), \ell = 1, 2, \dots, N. \quad (18)$$

Here $\{\chi_\ell\}$ means the set of all pulse positions, χ_ℓ , which depend on t . If we put (18) back into (16), we get

$$(c\partial_\chi - \mathcal{L})V_N = \mathcal{M}(V_N) - \sum_{\ell=1}^N \dot{\chi}_\ell \partial_{\chi_\ell} V_N. \quad (19)$$

(B) There exists a $V_1(\chi, \chi_k)$ for any of the N χ_k such that

$$(c\partial_\chi - \mathcal{L})V_1 = \mathcal{M}(V_1) \quad (20)$$

and $V_1(\chi, \chi_k) = H(\chi - \chi_k)$. We shall write $H_\ell = H(\chi - \chi_\ell)$.

Now we make the basic approximation that we expect to hold when the gas of pulses is very dilute:

$$(C) \quad V_N(\chi, \{\chi_\ell\}) = \sum_{\ell=1}^N V_1(\chi, \chi_\ell). \quad (21)$$

More generally, we would express V_N in terms of all the lower order V_K , $K < N$. That is, (21) is a first approximation to a series in which V_N is expressed in terms of the other V_K with $K < N$. That sort of series is what leads to the famous hierarchy of approximations of statistical mechanics.

By combining (19) and (20) we obtain the lowest order approximation:

$$-\sum_{\ell=1}^N \dot{\chi}_\ell H'_\ell = \mathcal{M}\left(\sum_{\ell=1}^N H_\ell\right) - \sum_{\ell=1}^N \mathcal{M}(H_\ell), \quad (22)$$

where prime means differentiation w.r.t. the argument. To go further, we need to define an inner product in the space of state vectors. This is the ordinary scalar product for the components and integration over χ . Once there is a scalar product, we can define an adjoint. The adjoint to H_ℓ satisfies

$$[-c\partial_\chi - \mathcal{L}(-\partial_\chi)]\tilde{H}_\ell = \mathcal{M}^\dagger(\tilde{H}_\ell). \quad (23)$$

We further assume that

(D) A solution of (23) exists with $\tilde{H}_\ell \rightarrow 0$ when $\chi \rightarrow \pm\infty$.

If we differentiate (23) w.r.t. χ_ℓ , we get

$$[-c\partial_\chi - \mathcal{L}(-\partial_\chi)]\tilde{H}'_\ell = \frac{\delta \mathcal{M}^\dagger}{\delta \tilde{H}_\ell} \cdot \tilde{H}'_\ell. \quad (24)$$

The idea is that we may use the operator $L = -c\partial_\chi - \mathcal{L}(-\partial_\chi) - \frac{\delta \mathcal{M}^\dagger}{\delta \tilde{H}_\ell}$ to define a set of basis functions and that the null vector \tilde{H}_ℓ is one of these. Naturally, that this is possible is also a mild assumption, (E) say.

Let

$$\langle \mathbf{H}'_\ell | \tilde{\mathbf{H}}'_m \rangle = \int \mathbf{H}'(\chi - \chi_\ell) \cdot \tilde{\mathbf{H}}'(\chi - \chi_m) = -g(\chi_\ell - \chi_m) = -g_{\ell m}. \quad (25)$$

Assuming that these homoclinic pulses drop off exponentially at $\pm\infty$ we conclude that $g_{mm} = g_0 \approx 1$ and that the off-diagonal $g_{\ell m}$ are exponentially small in separation of neighboring pulses. Hence, if we multiply by $\tilde{\mathbf{H}}'_m$, we get

$$g_0 \dot{\chi}_k = \left\langle \tilde{\mathbf{H}}'_k \left| \mathcal{N} \left(\sum_{n=1}^N \mathbf{H}_n \right) - \sum_{n=1}^N \mathcal{N}(\mathbf{H}_n) \right. \right\rangle. \quad (26)$$

This then is the equation of motion of the interacting pulses, up to terms that are exponentially small in the separation of pulses. So long as the gas of pulses remains dilute, these terms continue to be small.

Eq. (26) is the equation of motion for the N pulses. We have here what is sometimes called a lattice gas, but it is a highly dissipative one for there is no second derivative of pulse position. That lack is inevitable for we did not allow the gas to be Galilean invariant. (That is another story that we save for another occasion.) We have also to calculate the right hand side, but we won't go into all that here either. In the dilute case, we expect only nearest neighbor interaction, so the velocity of the k^{th} particle can depend only $\chi_k - \chi_{k-1}$ and $\chi_{k+1} - \chi_k$, because of translational invariance.

In one dimensional dynamics, the force law between pulses is not expected to depend on powers of pulse separation. However, the force law may have a range. In the case of pulse gases, two funny things can happen. The pulse pushes (or pulls) on the one ahead differently than on the one behind. So we have an anisotropy and Newton's third law does not apply. The second thing is that, in the force law, the range can be complex; that is the force can be both exponential and trigonometric in its dependence on pulse separation. This gives a pulse dynamics that can produce rather complicated pulse trains where the pulses bunch up together and then leave goodly gaps. Next time you look at a train of "solitary" waves, you should be aware that it may be possible to give such a simple description of the structure of the train. But the paradigm for this game remains convection near to threshold and we hope to be able to apply these notions in some detail for that case. To show how that may go, we describe next the collective structures known as defects of the convective patterns.

III. Defect Theory

We conclude with a brief discussion of topological defects in the solutions of the nonlinear planform equations. Suppose such an evolution equation has the form $\partial_t A = F(\nabla, A)$, which is a simplified form of (13). We shall call a stable solution of this equation that is localized to a small region of physical space

(called the defect's core) a topological defect of a macroscopic system, where the medium is found to be in an unbroken symmetry phase. Examples such as dislocations, grain boundaries and sources and sinks of traveling waves in convective structures have attracted considerable attention (e.g. Cellular Structures in Instabilities, 210 of *Lecture Notes in Physics* eds. J. Wesfried and S. Zaleski; Couillet, Elphick, Gil and Lega, *Phys. Rev. Lett.*, 59 1987); in particular they are thought to play a role in the transition to turbulence (Cross and Newell, *Physica D*, 10, 1984; Pocheau, Croquette and Le Gal, *Phys. Rev. Lett.*, 55, 1986). In general these topological structures are expected to appear whenever a system suffers a phase transition associated with the breaking of fundamental symmetries.

Far enough from the defect's core the medium is an ordered state or in a broken symmetry phase. In this region the defect solution takes values on a manifold \mathcal{M} hence the name topological defect. Let us illustrate these concepts in the case of a dislocation in Rayleigh-Bénard convection (See Fig. 1). In this case we can represent the defect's core as the interior of a small circle enclosing a point D , where the roll amplitude vanishes while its phase turns by 2π around it. (D is referred to as a point defect.) Physically this corresponds to the insertion of an extra wavelength into a pattern of rolls. In this example, the ordered state corresponds to the perfectly periodic roll structure (breaking translational invariance) and \mathcal{M} is a circle with radius $\left(\frac{R-R_c}{R_c}\right)^{\frac{1}{2}}$ parametrized by the roll phase, where R is the Rayleigh number.

We now introduce some mathematical tools (a readable introduction to this topic is Mermin, *Rev. Mod. Phys.*, 51 1979) that are useful to understand the topological aspects of these localized structures. Let us assume that our physical system occupies some continuous region \mathcal{R} and suppose that the system is an ordered state (broken symmetry situation) except in certain defect-regions (points, lines, surfaces) where some broken symmetries are restored. (E.g. in Fig. 1 since the roll amplitude vanishes at D , translational invariance is locally restored in a small neighborhood of D .) We can describe this situation by introducing an order parameter A defined in $\mathcal{R} - \{\text{defects}\} = V$. Let us define \mathcal{M} (sometimes called the "manifold of internal states") to be the manifold where A takes its values (in some cases \mathcal{M} can be identified with the set of equilibria of the system). So we have a mapping $A : V \rightarrow \mathcal{M}$.

Having defined this mapping it is natural to ask whether the singular regions (the defect cores) where A is not defined can be removed or not by purely local alteration of the order parameter configuration. To answer this question we have to study the topological stability of a defect. To do this we surround the defect-region by a subspace $v \subset V$. For simplicity we choose v to be a hypersphere. If $d = \dim(\mathcal{R})$, $d' = \dim(\text{defect})$, then $\dim v = d - d' - 1 := r$. This leads to a mapping $A : S^r \rightarrow \mathcal{M}$. The defect under consideration is topologically stable if this mapping has some non-trivial topological aspect (such as a non zero winding number) or in, other words, if there exists some topological obstruction that prevents the disappearance of the defect. In our example of

Fig. 1 we are led to study mappings $S^1 \rightarrow S^1$. It is a mathematical result that mappings from $S^1 \rightarrow S^1$ (see Fig. 2) can be classified into homotopy sectors. Mappings within one sector can be continuously deformed into one another, whereas mappings from two different sectors cannot be continuously deformed into one another. Furthermore, each homotopy sector is characterized by an integer N (the winding number of a mapping in that sector). The dislocation shown in Fig. 1 corresponds to a topological defect belonging to the $N = 1$ sector and its stability follows from the following reasoning: Suppose we were able to make it disappear. Then we could continuously deform the loop L to a point. But then the winding number would have to make an abrupt jump from $N = 1$ to $N = 0$, which would contradict the assumed continuity. A similar reasoning gives the result that topological defects with vanishing winding number are topologically unstable.

For a kink-like topological defect (the defect's core has dimension $d' = d - 1$ and is sometimes called a domain wall; it corresponds to a surface in 3-d, a line in 2-d and a point in 1-d) what we have said so far leads us to consider mappings $S^0 \rightarrow \mathcal{M}$. S^0 , the unit sphere in \mathbb{R} , consists of the two points ± 1 . One of the points, $+1$, corresponds to a point on one side of the domain wall, and the other, -1 , to a point on the other side. It is fairly clear that topologically nontrivial mappings from S^0 to \mathcal{M} exist only if \mathcal{M} is a disconnected space, that is, if the set of equilibria of the system are related to each other by a discrete symmetry group.

To illustrate these concepts we consider the case of a grain boundary in Rayleigh-Bénard convection (see Fig. 3). This is a system of rolls that meet at a right angle.

A typical thermohydrodynamic field ϕ can be expressed in terms of the complex amplitudes A and B as $\phi = Ae^{ik_c x} + Be^{ik_c y} + cc$. From the expression for ϕ and Fig. 3 we see that this system possesses the discrete symmetry $x \rightarrow y$, $A \rightarrow B$. In this case, \mathcal{M} can be identified with the equilibria of the system that correspond to two disconnected circles, one circle parametrized by the phase of rolls A and the other by the phase of rolls B . The two circles are related to each other by the discrete symmetry group of the grain boundary. Our topological considerations lead us to expect the appearance in this system of stable kink-like topological defects. In fact, we can obtain these localized structures by solving the amplitude equations for A and B (see Fig. 4),

$$\partial_t A = \mu A + \xi \left(\partial_x - \frac{i}{2k_c} \partial_{yy} \right)^2 A - (|A|^2 + g|B|^2) A$$

$$\partial_t B = \mu B + \xi \left(\partial_y - \frac{i}{2k_c} \partial_{xx} \right)^2 B - (|B|^2 + g|A|^2) B$$

where ξ and g are real constants and $\mu = (R - R_c)/R_c$. For stability of rolls, $g > 1$.

So far our considerations have been purely topological. For a complete description of topological defects we have to address also the dynamical aspects

of these localized structures. For example using a method very similar to that presented in the first part of this work we can study the interaction of many kink-like topological defects. We are currently studying these issues (in collaboration with J. Milovich) for the grain boundary system.

This work has been supported by the NSF under grant PHY 87-04250 to Columbia University. We would like to mention once again that our coworkers in various aspects of this work are E. Meron, Z. Qian and O. Regev.

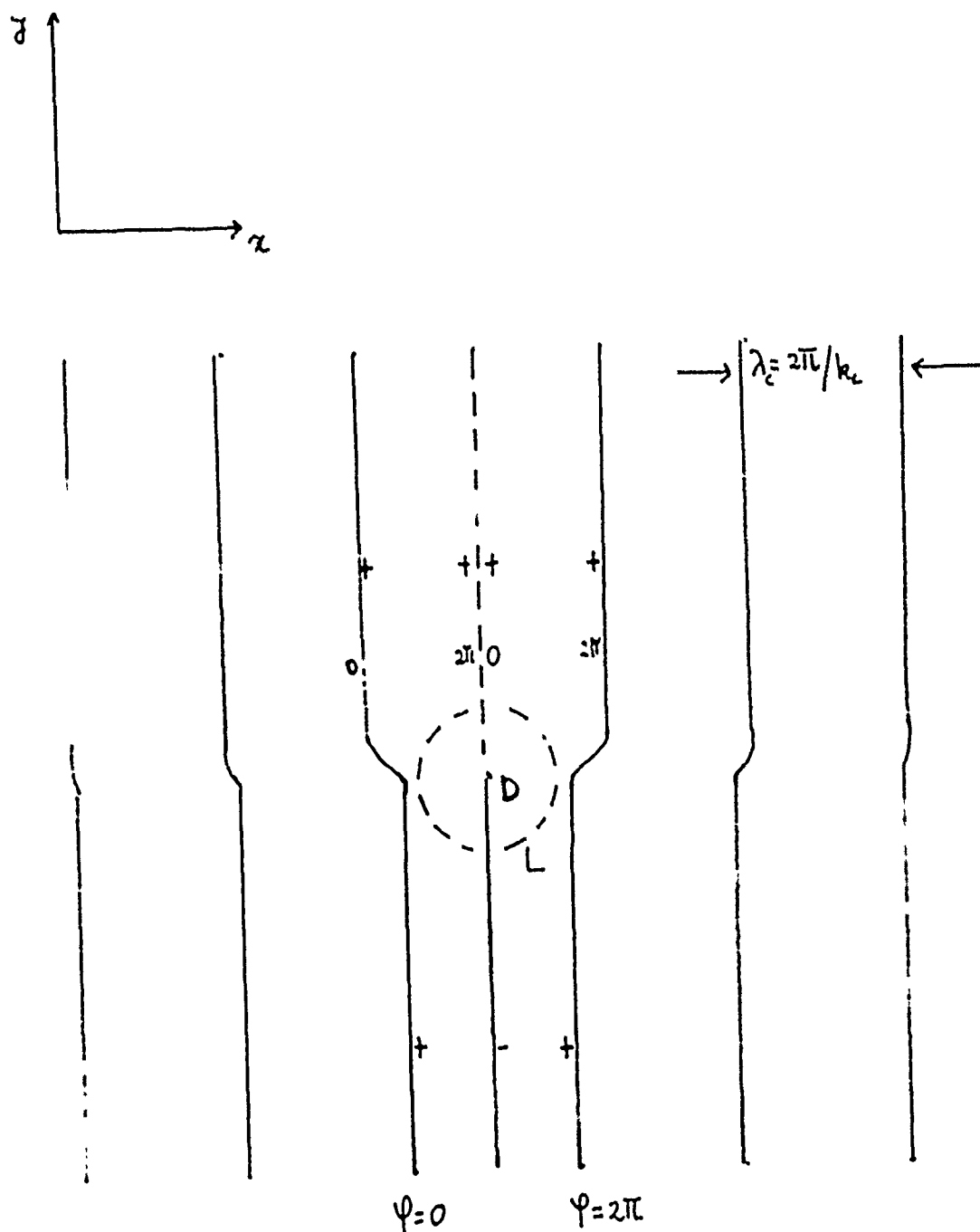


Fig. 1 A top view of a dislocation in R-B convection. The lines represent roll equiphases. The $+$ (resp $-$) sign indicates upward (resp. downward) fluid motion. Turning once around the loop L makes a jump of 2π in the roll's phase. This corresponds to a dislocation with winding number $N = 1$. Physically this corresponds to the insertion of an extra wavelength λ_c . An anti-dislocation has winding number $N = -1$ and can annihilate a dislocation leaving the medium in a state with net winding number $N = 0$. The state $N = 0$ is topologically equivalent to a perfectly periodic roll structure.

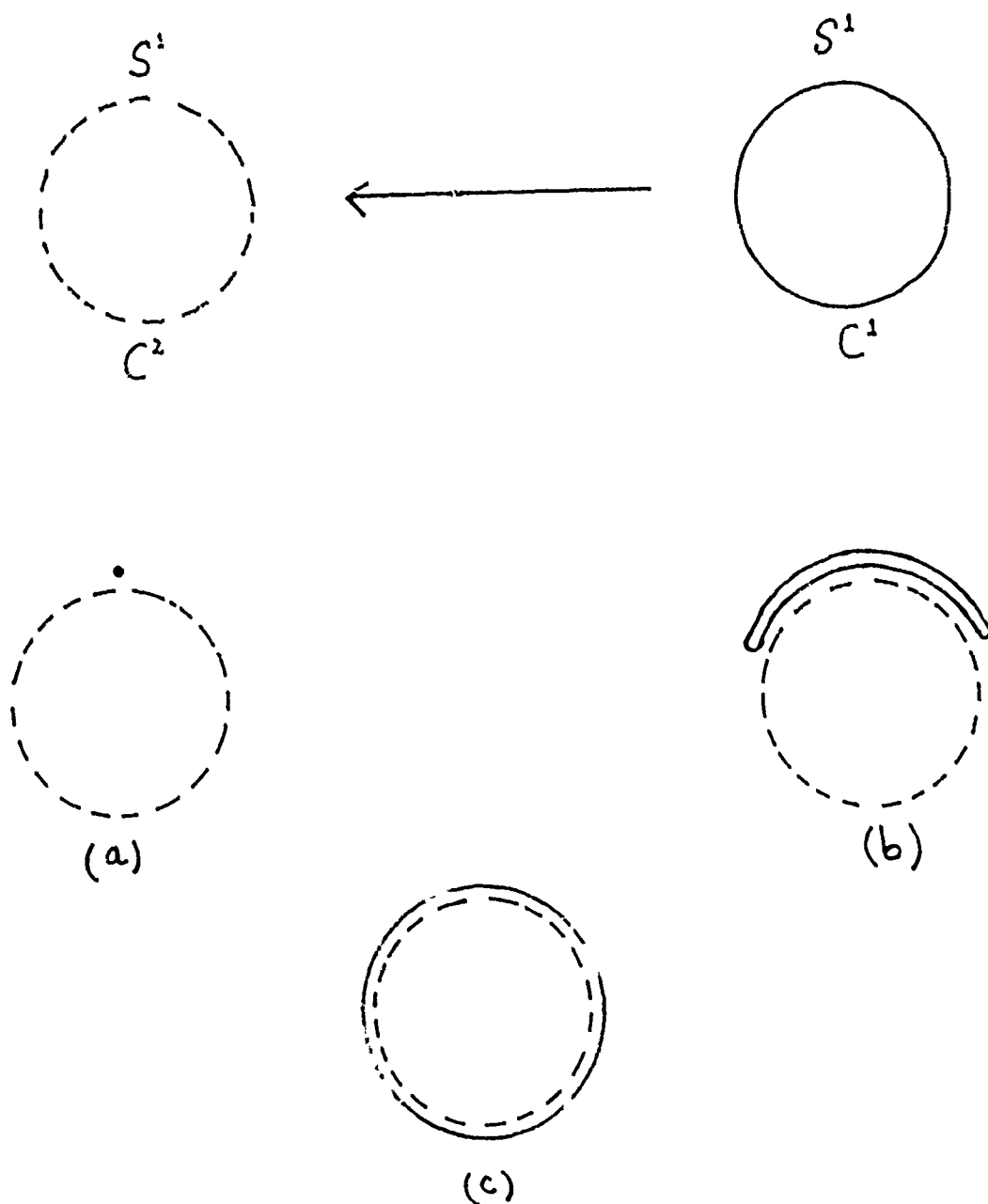


Figure 2. Mappings from $S^1 \rightarrow S^1$. In (a) the trivial mapping is given where the circle C^1 maps into one point in the circle C^2 . In (b) a non trivial mapping is given. Both (a) and (b) have $N = 0$ and can be continuously deformed into one another by shrinking the undashed loop. In (c) a non trivial mapping with $N = 1$ is shown; it cannot be deformed into (a) or (b).

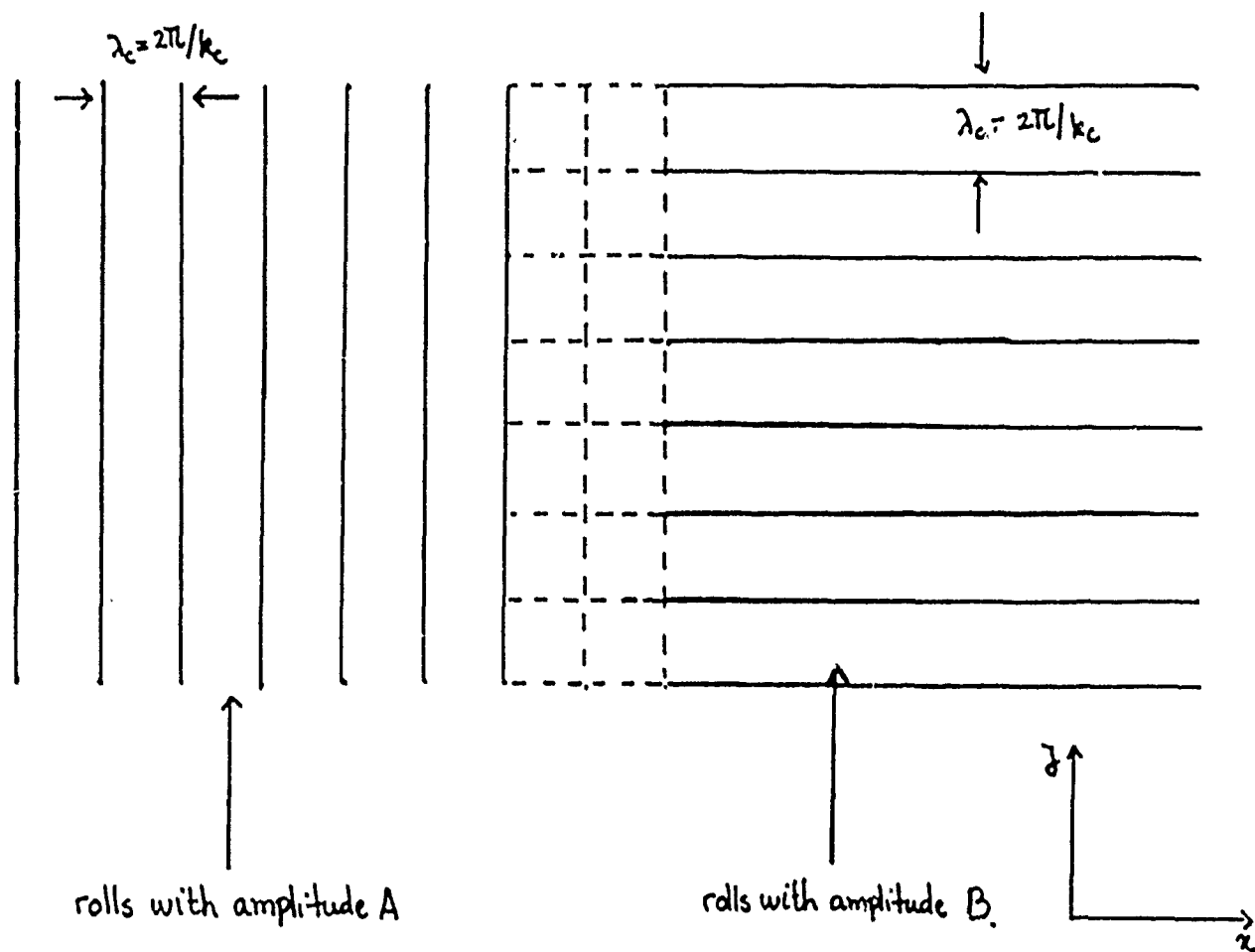


Figure 3. A grain boundary in Rayleigh-Bénard convection (top view).

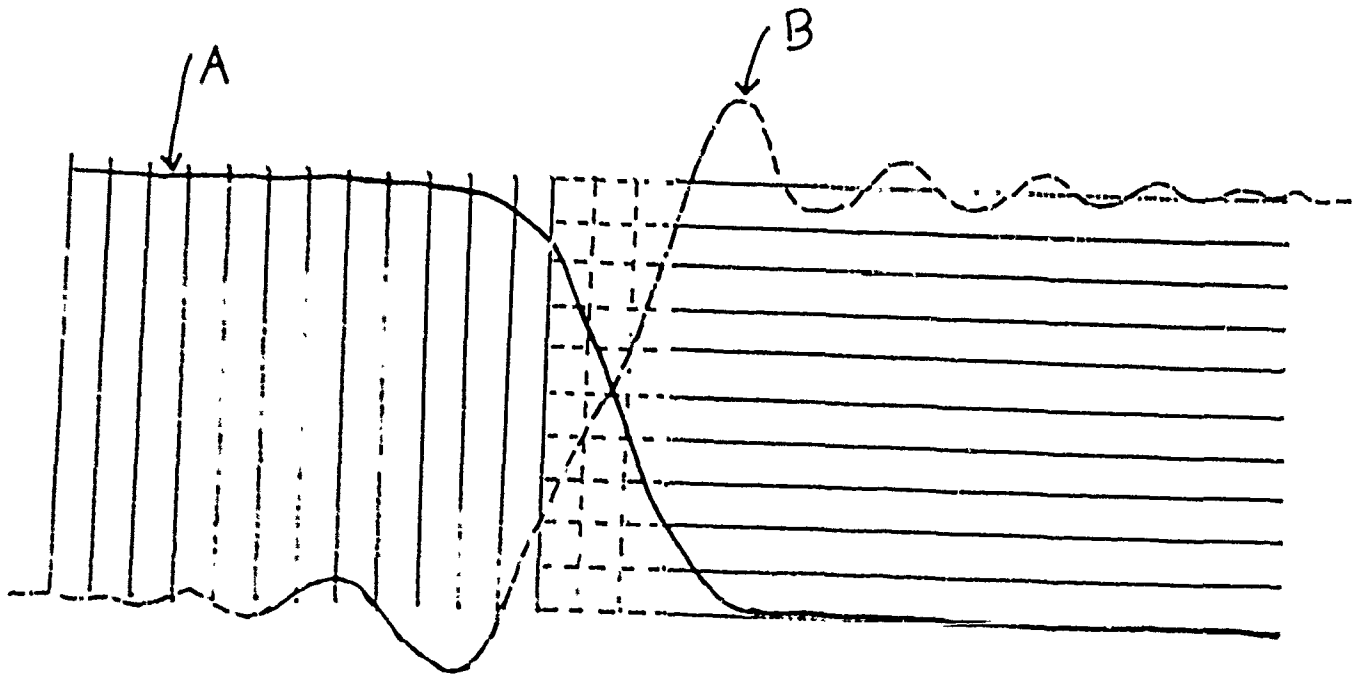


Figure 4. Sketch of kink-like solutions of the amplitude equations associated with a grain boundary. For pedagogical purposes we have enlarged the defect's core (experimentally one observes an abrupt transition from rolls *A* to rolls *B*) and the resulting pattern is made up of squares restoring the broken symmetry $x \rightarrow y$, $A \rightarrow B$.

GENERATION OF BAROCLINIC MOTIONS FROM BAROTROPIC EDDIES

Glenn R. Flierl

Center for Meteorology and Physical Oceanography
MIT

1. Circular Eddies

Barotropic circular eddies can be unstable to baroclinic modes which cause vertically-varying shifts in the axis of the eddy. McWilliams and Gent (1986) first demonstrated this by numerical solution of the instability problem, showing that an $m = 1$ baroclinic mode could appear in regions stable to barotropic disturbances. Flierl (1988) studied this problem analytically using vortices with piecewise constant potential vorticity fields. When the basic vortex has no flow outside of a radius $r > b$ with peak velocities at $r = 1$, the baroclinic "twisting mode" (the $m = 1$ mode, corresponding to tilting the axis in the vertical) appeared in barotropically stable regimes when $b > 2$ and γ (the nondimensional inverse deformation radius) is smaller than $1.2/(b - 1)$. The instability only appeared when the circulation in the deep fluid was in the same sense as that in the upper fluid. The mechanism for this instability could be interpreted as a combination of two effects: shifting of the inner and outer centers leads to dipolar propagation as in Blebuyc's summer fellowship lecture (1986); tilts in the vertical axis lead to a rotational tendency. If these two have the proper phase relationships they will reinforce an initial tilt and center shifts.

Note that Squire's theorem does not hold because the azimuthal wavenumber is quantized; one can show that a barotropic jet in a periodic domain can likewise have the most rapidly growing mode be baroclinic. The circular eddy geometry makes quantization natural; in addition, the $m = 1$ mode is, unlike the zonal jet problem, not stationary.

2. Elliptical Eddies

We next consider the case of elliptical barotropic flow, generalizing the results of Pierrehumbert and Bayly for infinite elliptical streamline patterns $\Psi = (\gamma - \epsilon)x^2/2 + (\gamma + \epsilon)y^2/2$ to rotating and stratified flows. Following Bayly's procedure of setting all fields proportional to $\exp(i(k(t)x + \ell(t)y + mz))$ and choosing appropriate time dependence for k and ℓ yields a Floquet problem for a three vector of horizontal velocity amplitudes and z times the buoyancy amplitude. We find a resonance point for $\epsilon = 0$ when the wavenumbers are related by

$$m^2 = \frac{s^2(\gamma^2 - N^2)}{(f + 2\gamma)^2 - \gamma^2} \quad (1)$$

with $s^2 \approx k^2 + \ell^2$, which is constant to the appropriate order in $|c| \ll 1$. As c increases (the flow becomes more elliptical), a band of instability will open for m values around the resonant point.

For nonrotating, homogeneous flows, the above equation is satisfied for $m/s = 3^{-1/2}$; but for the geophysically interesting case, with $\gamma < f \ll N$, we find instability for

$$-f < \gamma < -f/3$$

Thus the vortex must be anticyclonic and have a Rossby number greater than $1/3$. Then the vortex can feed energy into internal gravity waves with an m/s value derived from the expression (1). Strong, anticyclonic, elliptical flows may be a source for internal wave motions.

We also considered bounded regions of elliptical flows, taking the Kirchhoff vortex as case of an barotropic exact solution with elliptical streamlines. When the ellipticity is weak, the ellipse can be thought of as an azimuthal mode 2 disturbance upon a Rankine vortex. We used weakly nonlinear contour dynamics methods to solve for the evolution of a mode 2 barotropic disturbance and a baroclinic mode 1 disturbance. The latter corresponds to a depth-dependent shift in the position of the axis of the vortex. The coupled equations for the amplitudes of these two modes are then treated as a perturbation problem with the baroclinic disturbance being much weaker than the barotropic amplitude. A critical value of the ratio of the deformation radius for the vertical structure in question to the vortex radius of $1.7^{-1/2}$ was derived. (This can also be thought of as $mR = 1.7^{1/2}N/f$ in analogy to the expression above for m/s ; now, however, the perturbations are geostrophic rather than internal waves.) Again, as the ellipticity increases, we expect their to be a wider range of unstable vertical wavenumbers. Numerical computations with a two layer contour dynamics code initialized with a barotropic ellipse with a 2:1 aspect ratio (stable to barotropic perturbations) demonstrate that the instability indeed shifts energy from the elliptical mode into displacement of the centers in the two layers (with the eddies becoming more circular). The instability seems to vacillate, but it may be that the contour will steepen and break off filaments at some point in the evolution, causing an effectively irreversible change in the eddy structure.

References

- Bayly, B. (1988) Three-dimensional instability of elliptical flows. *Phys. Rev. Lett.*, 57, 2160-2163.
- Gent, P.R. and J.C. McWilliams (1986) The instability of circular vortices. *Geophys. and Astrophys. Fluid Dyn.*, 35, 209-233.
- Pierrehumbert, R. (1988) Universal short-wave instability of two-dimensional eddies in an inviscid fluid. *Phys. Rev. Lett.*, 57, 2157-2159.

SOME STRAIT TALK

Chris Garrett
Dalhousie University

The Strait of Gibraltar is an exciting and important place oceanographically and raises many interesting problems in geophysical fluid dynamics.

A key question is whether the exchange through the Strait, that is required by an excess of evaporation over precipitation in the Mediterranean, has been driven to a maximum "overmixing" limit by strong mixing in the Mediterranean. This has been proposed by Bryden and Stommel (1984), and elaborated upon by Farmer and Armi (1986) using their two layer hydraulic theory. Historical data cannot be easily interpreted in terms of these idealized theories, so Myriam Bormans and I have been concerned with the importance of non-rectangular cross-sections, the earth's rotation, friction and barotropic fluctuations. Details are given in the papers cited below, but one elementary general consequence of simple scaling arguments is that the importance of the earth's rotation depends not only the ratio of the strait width to internal Rossby radius, but also on the Froude number.

As assessment of a wide variety of data sets in the light of the models leaves the question of maximal or submaximal exchange unresolved; maybe the exchange alternates between the two states on time scales that we do not know and for reasons that we do not understand. The problem is worth pursuing in view of the potential of the Strait of Gibraltar as a "choke point" for monitoring changes in the Mediterranean.

References

- Bormans, M. and C. Garrett, 1988; The effects of non-rectangular cross-section, friction and barotropic fluctuations on the exchange through the Strait of Gibraltar. *J. Phys. Oceanogr.* (submitted).
- Bormans, M. and C. Garrett, 1988; The effect of rotation on the surface inflow through the strait of Gibraltar. *J. Phys. Oceanogr.* (submitted).
- Bryden, H.L., and H.M. Stommel, 1984; Limiting processes that determine basic features of the circulation in the Mediterranean Sea. *Oceanologica Acta*, 7, 289-296.
- Farmer, D.M., and L. Armi, 1986; Maximal two-layer exchange over a sill and through the combination of a sill and contraction with barotropic flow. *J. Fluid Mech.*, 164, 53-76.
- Garrett, C., J. Akerley, K.R. Thompson, 1988; Low frequency fluctuations in the Strait of Gibraltar from MEDALPEX sea level data. (in preparation).

NONLINEAR WAVES, SOLITONS AND WAVE TRANSPORT IN BUOYANT CONDUITS

Karl R. Helfrich and John A. Whitehead
Department of Physical Oceanography
Woods Hole Oceanographic Institution

Fluid of a lower density and viscosity can buoyantly rise through a viscous fluid in a field of gravity through conduits. These conduits support simple pipe, or Poiseuille, flow. However, the conduits are surprisingly rich in their behavior because of the movement of the pipe wall which may be expressed as a nonlinear partial differential equation having propagating wave solutions, including solitary waves. There is interest in the conduits for several reasons. One is that geological and geophysical counterparts of conduits may actually exist in the Earth as rising plumes of low viscosity material. Secondly, the conduits are a simple analog of compaction driven flow in a porous viscous matrix. Thirdly, the conduits support solitary waves which exhibit soliton-like behavior.

Laboratory experiments on the characteristics of the solitary waves and their interactions have been conducted and compared with theory. The observations of shape and phase speed of individual waves show good agreement with the theoretical predictions. Large amplitude waves traveled slightly faster than the theoretical predictions. The discrepancy is probably due to higher order effects associated with wave slope not accounted for in the theory. Individual wave characteristics (shape, amplitude and speed) were very nearly preserved after collision with another wave. A phase jump of each wave was the main effect of a collision. The larger (faster) waves increased in amplitude by an average of 5 percent after collision and their phase speeds decreased by an average of 4 percent. The small wave was unchanged. Numerical solutions over-predicted the magnitude of the observed phase jumps by about 40 percent when compared to the experiments.

It is also shown theoretically and confirmed experimentally that all solitary waves have closed streamlines in a frame moving with the waves. Thus, isolated parcels of material will be trapped within the closed streamlines and transported upward over large distances. Calculations indicate that material in these parcels will be far less contaminated by diffusion from the surroundings than material in ordinary pipe flow where longitudinal stretching and lateral diffusion dominate. We suggest such waves might exist in the mantle of the Earth and convey uncontaminated deep mantle material to the surface of the Earth.

EXACT NON-REFLECTING BOUNDARY CONDITIONS

Joseph B. Keller and Dan Givoli

Department of Mathematics and Mechanical Engineering
Stanford University

An exact non-reflecting boundary condition is devised for use in solving the reduced wave equation in an infinite domain. The domain is made finite by the introduction of an artificial boundary on which this exact condition is imposed. In the finite domain a finite element method is employed. Although the boundary condition is non-local, that does not affect the efficiency of the computational scheme. Numerical examples are presented which show that the use of the exact non-local boundary condition yields results which are much more accurate than those obtained with various approximate local conditions. The method can also be used to solve problems in large finite domains by reducing them to smaller domains, and it can be adapted to other differential equations.

Introduction

To solve the reduced wave equation numerically in an unbounded domain, it is usual to introduce an artificial boundary \mathcal{B} to make the computational domain finite. Then some boundary condition must be imposed on \mathcal{B} . We shall show how to obtain an exact boundary condition there, and how to combine it with the finite element method in the computational domain. This leads to an efficient method which eliminates the defects, such as spurious reflections from \mathcal{B} , which arise in other procedures.

We shall also show how to solve a problem in a large finite domain by cutting out a large regular subdomain, thus introducing an artificial boundary \mathcal{B} . This leaves a smaller computational domain bounded in part by \mathcal{B} . On \mathcal{B} we shall again obtain an exact boundary condition and use it with the finite element method in the computational domain.

Naturally there has been a great deal of previous work on these subjects. In order to see how the present work is related to it, and to what extent the present work is novel, we shall describe some of the previous methods. The simplest and most usual boundary condition is

$$u_\nu(x) = iku(x), \quad x \text{ on } \mathcal{B}. \quad (1)$$

Here $u(x)$ is the unknown scattered field, u_ν is its outward normal derivative, and k is the wave number. This condition is of the same form as the Sommerfeld radiation condition, which is exactly correct when imposed at infinity but only approximately correct when imposed at a finite boundary \mathcal{B} . As a consequence the use of (1) leads to the spurious reflection of waves from \mathcal{B} . The magnitude of the reflected wave increases the more the direction of the wave u deviates

from the direction normal to ∂ , so it increases as ∂ is moved closer to the scattering region.

In order to diminish the spurious reflection, various authors have devised improved local boundary conditions. Engquist and Majda [1] did so by expressing u_ν exactly as a pseudodifferential operator applied to u on ∂ , and then approximating this operator by the local differential operators given in (65) and (66) below. Bayliss and Turkel [2] used the asymptotic expansion of u far from the scatterer to obtain similar approximate local boundary conditions. Feng [3] obtained an exact non-local condition involving an integral over ∂ of u multiplied by a Green's function, and then he approximated it by various local conditions, such as (67) below. However all these local boundary conditions still lead to spurious reflection.

Gustafsson and Kreiss [4] considered a hyperbolic system of equations for two functions of x , y and t in a waveguide. They obtained an exact non-local boundary condition involving the Fourier coefficients of the solution, and discussed its use in a finite difference method. Hagstrom and Keller [5] formed an exact boundary condition in a cylindrical domain in terms of the eigenfunctions and eigenvalues of a problem in the cross-section of the cylinder. They also proved the existence of an exact boundary condition for certain nonlinear problems, and gave an asymptotic expansion for it. Ting and Miksis [6] obtained an exact boundary condition by expressing u on ∂ as an integral of u and u_ν over a surface interior to ∂ , using the free space Green's function.

The work most closely related to ours is contained in Fix and Marin [7], MacCamy and Marin [8], Marin [9], [10] and Goldstein [11]. In all of them an exact boundary condition is imposed on ∂ and the finite element method is employed in the computational domain. In [7] this boundary condition is found analytically for a waveguide and some numerical results are given. In [8] two dimensional exterior domains are considered. The boundary condition involves the solution of an integral equation on ∂ for which numerical methods of solution are given. The convergence of the finite element method with this boundary condition is proved. A summary of these results and a numerical example are presented in [9]. Goldstein [11] presents a survey of previous work, and gives a convergence proof for the finite element method with an exact boundary condition on ∂ in the case of two dimensional exterior problems and waveguides.

In contrast with the method of MacCamy and Marin [8] and Marin [9], we choose ∂ to be a circle in two dimensional exterior problems and a sphere in three dimensional ones. As a consequence we can express the exact boundary condition explicitly in terms of known functions rather than in terms of the solution of an integral equation which is obtained numerically. This results in a simpler and more accurate method, which is similar to that used by Fix and Marin [7] for waveguides. It enables us to discuss the bandedness of the finite element stiffness matrix, the separability of the integrals in the boundary

condition, and the best choice of the radius of B in terms of the computational accuracy and cost.

We shall present the solutions of some test problems obtained by our method. We shall compare them with exact solutions and with numerical solutions involving the Sommerfeld condition (1), the Engquist-Majda conditions (65) and (66) and the Feng condition (67).

We shall also obtain the exact boundary condition explicitly for Laplace's equation in both exterior and interior domains. Then we shall present a simple convergence proof of the finite element method with this boundary condition.

At first sight it seems that the non-locality of the exact boundary condition might spoil the banded structure of the finite element matrix, and the complexity of this condition might require a great deal of computation. However neither of these difficulties occurs. In fact our results using the non-local conditions are more accurate than those obtained by using approximate local conditions, and they require about the same computational work.

We present the finite element formulation for the reduced wave equation in a infinite domain. The exact boundary condition is formulated, and we also show how the method can be applied to large finite domains. The convergence of the scheme and some computational aspects is discussed and we present some numerical results and compare them to those obtained by using the approximate local boundary conditions proposed by other authors.

Acknowledgments

This work was supported in part by ONR, AFOSR and NSF. It will appear in the *Journal of Computational Physics*.

References

1. B. Engquist and A. Majda, *Math. Comput.*, **31**, 629 (1977).
2. A. Bayliss and E. Turkel, *Commun. Pure Appl. Math.*, **33**, 707 (1980).
3. K. Feng, in *Proceedings of the International Congress of Mathematicians*, Warsaw, Poland, 1983, p. 1439.
4. B. Gustafsson and H.O. Kreiss, *J. Comput. Phys.*, **30**, 333 (1979).
5. T. Hagstrom and H.B. Keller, *SIAM J. Math. Anal.*, **17**, 322 (1986).
6. L. Ting and M.J. Miksis, *J. Acoust. Soc. Am.*, **80**, 1825 (1986).
7. G.J. Fix and S.P. Marin, *J. Comput. Phys.*, **28**, 253 (1978).
8. R.C. MacCamy and S.P. Marin, *Int. J. Math. Math. Sci.*, **3**, 311 (1980).
9. S.P. Marin, *IEEE Trans. Antennas and Propagat.*, AP-30, 1045 (1982).
10. S.P. Marin, Thesis, Carnegie-Mellon University, 1978.
11. C.I. Goldstein, *Math. Comput.*, **39**, 309 (1982).
12. G. Strang and G.J. Fix, *An Analysis of the Finite Element Method*, Prentice-Hall New Jersey, 1973.

DEEP CONVECTION IN THE WORLD OCEAN

Peter D. Killworth

Deacon Lab. of the Institute of Oceanographic Sciences
Hooke Institute for Atmospheric Research
Department of Atmospheric Physics
Clarendon Laboratory, Parks Road
Oxford OX1 3PU, England

The observational background to deep oceanic convection is discussed, taking two main scenarios as paradigms. The first is the "classic" sinking of dense water down and around a continental slope. Five separate ingredients appear to be involved. The first is a reservoir on which dense water can form; in the paradigm, this would be a wide, shallow continental shelf. The second is a source of dense water within the reservoir, frequently the efflux of dense brine by the freezing of sea ice. The third is a reason for dense water to descend to depth (since dense shelf water can be geostrophically balanced against lighter sea water); instabilities or pre-existing wind- or buoyancy-driven circulations can serve as this mechanism. Observations suggest that a multiplicity of water masses always seems to be a fourth ingredient. The last ingredient is merely that the densities, dynamics, and geography do permit the dense water to sink; for example, it appears that the variation of expansion coefficient with depth plays an important role in the energetics of the descent of Weddell Sea Bottom Water.

The second scenario is open-ocean convection, of which the classic example is wintertime deep convection in the Mediterranean. Again, certain ingredients are necessary. First, a background cyclonic circulation, to produce an upward "doming" of isopycnals is necessary. Second, a "preconditioning" mechanism, usually ill-defined, is needed to select an area for future convection. Third, in common with slope convection, more than one water mass appears always to be involved. Fourth, a sufficiently strong surface forcing is involved. These ingredients combine to yield a narrow violent mixing region, followed by a poorly understood sinking and spreading phase.

Observations have historically concentrated upon the convective events themselves, and much less upon the interaction between the larger scale flows (in which the convection is embedded) and the convective events. In particular, the way in which convection modifies its own environment — and hence alters future convective events — is poorly understood.

FLOWS PRODUCED BY DISCRETE SOURCES OF BUOYANCY

Peter D. Killworth

Deacon Lab. of the Institute of Oceanographic Sciences
Hooke Institute for Atmospheric Research
Department of Atmospheric Physics
Clarendon Laboratory, Parks Road
Oxford OX1 3PU, England

(Work joint with M.K. Davey of the U.K. Met. office is reported)

The response of an ocean with a single active dynamical layer (notionally with an infinitely deep upper layer above it, of slightly less density) to localised buoyancy forcing on a beta-plane is considered. The archetypal oceanic problem would be a localised source of dense water (indeed, some discussion of the Mediterranean outflow was given in the talk).

It is shown that three regimes exist. When the forcing is very weak, the response is linear, and consists of a quasi-steady "tube" of fluid stretching westward from the forcing region, with a front advancing at the long Rossby wave speed, and some transient structure in the vicinity of the forcing. (It has not been possible to find an equivalent solution for the case of an f-plane with a sloping bottom, so that the experiments of Whitehead, and of Linden, may be intrinsically nonlinear). When the amplitude of the forcing is increased, potential vorticity contours are sufficiently deformed to permit instability both in the forced region and to its west. The response becomes a series of shed eddies, each of which propagates westward almost independently of its neighbours. Further increase in forcing amplitude yields a completely unsteady response.

LARGE SCALE FLOW IN TURBULENT RAYLEIGH-BENARD CONVECTION

Ruby Krishnamurti
Florida State University

Laboratory experimental data was reviewed which showed the occurrence, at certain Rayleigh numbers of a large scale horizontal shear flow $\bar{u}(z)$ in turbulent Rayleigh-Benard convection. Measurements of turbulent velocities and their correlations show that, in the horizontally-averaged horizontal momentum equation, the balance is between the Reynolds stress divergence $\partial/\partial z(\bar{u}\bar{w})$ and the divergence of the viscous stress on the mean flow $\nu\partial^2\bar{u}/\partial z^2$ where \bar{u} is the horizontally averaged u , which is the horizontal velocity component, w is the vertical velocity component, z the vertical coordinate and ν the kinematic

viscosity. A nonzero averaged stress \overline{uw} is associated with the vertical tilting of convective plumes, and leads to a vertical transport of horizontal momentum up the gradient of \bar{u} .

In a low order model of Rayleigh-Benard convection it was found that *tilted* cellular flows arise as an instability of the usual upright cells. A further bifurcation to tilted *transient* plumes results in many of the laboratory-observed features such as a large scale shear flow $\bar{u}(z)$ and countergradient momentum transport of horizontal momentum by the tilted plumes.

These ideas were applied to the numerical weather prediction problem of "systematic errors" in the forecast, i.e. a secular drift to a different climatology after long time integration. In spite of our lack (to date) of laboratory data on the parameter dependence of this momentum transport by convective plumes, we nevertheless attempted to incorporate these ideas in a parameterized countergradient transport of horizontal momentum by shallow cumulus convection in the tropical troposphere. Using the FSU global spectral model truncated at T42, and ECMWF global data from February 1979, we found a marked decrease in the systematic error of a 15-day integration, particularly through better maintaining the strength of the Trades in the region of the Pacific ITCZ.

UPPER BOUNDS ON FUNCTIONS OF THE DISSIPATION RATE IN TURBULENT SHEAR FLOW.

W.V.R. Malkus and L.M. Smith
Department of Mathematics, MIT

The search for a statistical stability criterion characterizing steady state turbulent shear flows has led us to the study of a function we call the dissipation rate Nusselt number. It is proportional to the ratio of the fluctuation dissipation rate and the dissipation rate of the mean. The first Euler-Lagrange equations for an upper bound of this function have optimal solutions with the observed scaling laws and an asymptotic velocity defect for turbulent channel flow. As in the case of maximum transport, the optional solution for the model equations is a discrete spectrum of stream-wise vortices. It is shown how these solutions can be brought closer to the realized flow with additional constraints on the smallest vortex.

A second test of the generalizability of the dissipation rate Nusselt number is sought in comparing the predicted extremes for Couette flow with the (limited) observations. Both extrema and observations indicate that the velocity defect will vanish at large Reynolds number in Couette flow. New data is needed to evaluate this unexpected conclusion.

Lastly, steps to deduce this remarkably simple statistical stability criterion from relative stability arguments lead to just those integrals which appear in the criterion — yet to date, not in the correct configuration.

EDDY-WALL INTERACTIONS

Doron Nof

Department of Oceanography
Florida State University
Tallahassee, Florida 32306

A nonlinear one and a half-layer model was considered to examine the collision of isolated eddies with vertical walls. The round undisturbed eddies were allowed to have relatively large amplitudes; they were bounded by a free streamline beyond which the ocean is stagnant. The inviscid interaction was described by, conceptually, "cutting" the eddies with a straight vertical wall. The resulting events were studied using a perturbation expansion in , the nondimensional penetration of the wall into the vortices, i.e., "weak" interactions are examined. Two class of eddies were considered. The first consists of linear quasi-geostrophic eddies (i.e., small amplitude and slow circulation) that were weakly interacting with a wall whereas the second involved moderately nonlinear eddies (i.e., relatively high amplitude and fast speed) that again were weakly interacting with the wall. Analytical solutions for times of (where f is the Coriolis parameter) and an infinitely deep lower layer were constructed by applying the conservation of potential vorticity, energy and integrated momentum.

It was found that the first class of eddies (linear quasi-geostrophic eddies) leak fluid as they interact with the wall. When a quasi-geostrophic anticyclonic vortex interacts with a wall, it leaks fluid from its right-hand side (looking offshore in the northern hemisphere) whereas a quasi-geostrophic cyclonic vortex leaks from its left-hand side.

Surprisingly, the second class of eddies (moderately nonlinear eddies) behave in a very different way. Due to the high inertia of these eddies, the leakage associated with a weak interaction is completely blocked and the adjustment to the presence of the wall is confined to the contact area. This bizarre behavior stems from the high speeds along the eddy's rim which choke the leaked flow. When these high speeds are relaxed the leakage re-appears.

Simple qualitative experiments on a rotating table support the conclusion that eddies with small speeds along the edge leak. It was speculated that the interaction of warm-core rings with the Gulf Stream has some similarities to the interaction of an anticyclonic vortex with a solid wall. Furthermore, it was speculated that the loss of mass observed during such ring-Stream interactions is a result of the leakage predicted by our theory and experiment.

MESOSCALE CONVECTION IN THE OCEAN

Donald B. Olson

Rosentiel School of Marine and Atmospheric Science

Observations of convective modification within mesoscale ($L \sim R_d$) field in the oceans are reviewed. The role buoyancy generated convection plays in water mass modification is considered with simple one dimensional and θ/S space models. It is concluded that mesoscale rings formed from western boundary currents are natural sites for intermediate depth convection because of the tendency for anticyclonic or warm ring production to introduce high temperature surface waters to climatologically cooler atmospheric conditions. This air-sea interaction anomaly is responsible for convective mixing of surface waters to greater density horizons than is possible in the parent water masses in the subtropical gyres of the ocean. Observed convected cells in a Gulf Stream warm core ring are described. These features found in a survey of ring 82B (second ring of 1982) are approximately 10 – 12 km in diameter compared to the ring length scale, as measured by the radius of its velocity maximum of 60 km. This recently convected patch of fluid is 0.02 kg m^{-3} denser than the rest of the ring's adiabatic core. This density anomaly and the 300 m thickness of the layer gives the feature a perturbation radius of deformation of $R_d = \sqrt{g'h}/f = 2.5 \text{ km}$. The feature is expected to produce velocity anomalies based on a perhaps questionable geostrophic scaling of 0.10 m s^{-1} as compared to ring velocities of 0.60 m s^{-1} . Observations of the temporal evolution of the convected region in ring 82B using satellite imagery suggests it was advected around the ring by the ring's swirl velocity, and slowly sheared out into a thin filament; i.e. the shear in the ring destroyed any tendency for the region to maintain its identity for more than a week. Observations in both this Gulf Stream ring and a ring from the Agulhas Current show, however, that the ring cores remain inhomogeneous over time scales of several months. Colder more dense well mixed layers are often found underlying the main convectively mixed region or stad in these rings. It is speculated that these sub-thermostad layers are derived from the ring edge. A nonlinear mixed layer model coupled with the conservation of angular momentum is formulated to further consider this problem. Finally estimates are made of the importance of convection within mesoscale features to the larger scale distribution of properties in the ocean. It is found that although rings in the Gulf Stream system are not important in terms of their contribution to the planetary heat and salt fluxes they can dominate the character of the near surface water masses and play an important role in the ventilation of a portion of the subtropical gyre thermocline. Convective modification of waters in the mesoscale field contributed to the South Atlantic by the Agulhas may dominate the central water properties of its subtropical gyre.

ENTRAINMENT AND DETRAINMENT IN CUMULUS CLOUDS

David J. Raymond
 Physics Department and Langmuir Laboratory
 for Atmospheric Research
 New Mexico Institute of Mining and Technology
 Socorro, NM 87801

1. Introduction

In this talk we first lay out a framework in which the effect of cumulus clouds on large scales may be discussed. We then present current ideas as to what cumulus clouds actually do to large scales. Emphasis here is on non-precipitating clouds.

2. Framework

The basic equations are

$$\nabla \cdot (\rho_0 \mathbf{v}) = 0 \quad (1)$$

for mass continuity, where ρ_0 is the ambient density as a function of height,

$$\frac{\partial \theta}{\partial t} + \mathbf{v} \cdot \nabla \theta = H^* \quad (2)$$

for potential temperature, where H^* is the rate of change of θ due to condensation and evaporation of water, and

$$\frac{\partial \theta_c}{\partial t} + \mathbf{v} \cdot \nabla \theta_c = 0 \quad (3)$$

for equivalent potential temperature.

We define a horizontal low pass filter operator $\langle \rangle$ and divide θ and θ_c into slowly and rapidly varying parts:

$$\begin{aligned} \theta &= \langle \theta \rangle + \theta' \\ \theta_c &= \langle \theta_c \rangle + \theta'_c. \end{aligned} \quad (4)$$

The low pass filter is assumed to have the property that $\langle \theta' \rangle = \langle \theta'_c \rangle = 0$.

Applying the low pass filter operator to the potential temperature equation results in

$$\frac{\partial \langle \theta \rangle}{\partial t} + \langle \mathbf{v} \rangle \cdot \nabla \langle \theta \rangle = \langle H^* \rangle - \frac{1}{\rho_0} \nabla \cdot (\rho_0 \langle \mathbf{v} \theta' \rangle) \equiv \langle H \rangle. \quad (5)$$

Note that we have not performed a conventional Reynolds separation, because the velocity has not been split into smoothed and fluctuating parts. This

is because the fluctuating velocity associated with a cumulus cloud does not necessarily average to zero as required by a Reynolds separation.

We now define a quantity

$$\langle m \rangle \equiv \langle H \rangle / (\partial \langle \theta \rangle / \partial z), \quad (6)$$

and further define

$$\langle v_a \rangle = \langle v \rangle - k \langle m \rangle. \quad (7)$$

Equation (5) simplifies to

$$\frac{\partial \langle \theta \rangle}{\partial t} + \langle v_a \rangle \cdot \nabla \langle \theta \rangle = 0 \quad (8)$$

when $\langle v \rangle$ is eliminated in favor of $\langle v_a \rangle$. The quantity $\langle v_a \rangle$ is actually the velocity of the air in the dry environment surrounding any cumulus clouds that may exist. Since the motion of the environment is adiabatic, we call this the *adiabatic velocity*. Notice that the adiabatic velocity by itself doesn't satisfy the continuity equation. Physically, this is because air is continually flowing back and forth between the environment and cumulus clouds.

Eliminating $\langle v \rangle$ from (1) and low pass filtering results in

$$\nabla \cdot (\rho_0 \langle v_a \rangle) = - \frac{\partial \rho_0 \langle m \rangle}{\partial z} \equiv \rho_0 \langle S \rangle. \quad (9)$$

Clearly, $-\partial \rho_0 \langle m \rangle / \partial z$ plays the role of a source term for the mass continuity equation. The quantity $\rho_0 \langle m \rangle$ is thus the horizontally smoothed vertical flux of mass due to cumulus clouds. Since $\langle v_a \rangle$ describes only adiabatic motions, $\rho_0 \langle m \rangle$ must include all diabatically induced vertical motions, including those due to the evaporation of liquid water as cloud material is injected into the environment.

A similar treatment for the equivalent potential temperature equation results in

$$\frac{\partial \langle \theta_e \rangle}{\partial t} + \langle v_a \rangle \cdot \nabla \langle \theta_e \rangle = - \langle m \rangle \frac{\partial \langle \theta_e \rangle}{\partial z} - \frac{1}{\rho_0} \nabla \cdot (\rho_0 \langle v \theta'_e \rangle) \equiv \langle E \rangle, \quad (10)$$

which may not immediately look like a simplification, as equivalent potential temperature has acquired a rather complex source term, $\langle E \rangle$. However, many models of convection treat $\langle v \theta'_e \rangle$ as a sum of currents carrying air vertically from one level to another, i. e.,

$$\langle v \theta'_e \rangle \approx k \sum_i m_i [\theta_{ei} - \langle \theta_e \rangle], \quad (11)$$

where θ'_e in each current has been equated to the actual equivalent potential temperature in that current, θ_{ei} , minus the mean equivalent potential temperature. The total mass flux is the sum of the partial mass fluxes, i. e.,

$$\langle m \rangle = \sum_i m_i, \quad (12)$$

so E simplifies to

$$\langle E \rangle = -\frac{1}{\rho_0} \sum_i \frac{\partial \rho_0 m_i}{\partial z} (\theta_{ei} - \langle \theta_e \rangle) - \sum_i m_i \frac{\partial \theta_{ei}}{\partial z}, \quad (13)$$

and the determination of $\langle E \rangle$ reduces to the determination of $m_i(z)$ and $\theta_{ei}(z)$ for each current. If no entrainment or detrainment occurs between the beginning and end of each current, (13) simplifies even further. Since equivalent potential temperature is then conserved in transport along the current, the last term in (13) vanishes and the derivative $\partial(\rho_0 m_i)/\partial z$ reduces to delta functions at the top and bottom limits.

If a chemical species with mixing ratio χ and source function C^* exists in the environment, it obeys the equation

$$\frac{\partial \chi}{\partial t} + \mathbf{v} \cdot \nabla \chi = C^*. \quad (14)$$

Similar treatment results in a smoothed equation for the mixing ratio of the species,

$$\frac{\partial \langle \chi \rangle}{\partial t} + \langle \mathbf{v}_a \rangle \cdot \nabla \langle \chi \rangle = \langle C \rangle \quad (15)$$

where

$$\langle C \rangle = \langle C^* \rangle - \frac{1}{\rho_0} \sum_i \frac{\partial \rho_0 m_i}{\partial z} (\chi_i - \langle \chi \rangle) - \sum_i m_i \frac{\partial \chi_i}{\partial z}. \quad (16)$$

This is a way to describe the effects of cloud chemistry on the environment.

The above framework was first proposed by Ooyama (1971) for the special case in which the currents took the form of entraining plumes, and was later generalized by Raymond (1987).

3. The coupled current model

We now investigate an approximation scheme in which a cloud is characterized as a system of coupled mass currents, each of which neither entrains or detrains along its length. Each current originates from some mixture of the environment and the output of other currents, and each current discharges into other currents, the environment, or some combination thereof. Since the mass flux along a current is constant under these assumptions, we have

$$\frac{\partial \rho_0 m_i}{\partial z} = \mu_i [\delta(z - a_i) - \delta(z - b_i)], \quad (17)$$

where a_i is the starting level for the i 'th current and b_i is its ending level. The constant mass flux associated with that current is μ_i .

Under these conditions, (13) reduces to

$$\langle E \rangle = -\frac{1}{\rho_0} \sum_i \mu_i [\delta(z - a_i) \theta'_{eai} - \delta(z - b_i) \theta'_{ebi}], \quad (18)$$

where

$$\theta'_{eai} = \theta_{ei}(a_i) - \langle \theta_e(a_i) \rangle \quad (19)$$

and

$$\theta'_{ebi} = \theta_{ei}(b_i) - \langle \theta_e(b_i) \rangle. \quad (20)$$

Thus, only the values of the equivalent potential temperature at the beginning and end of the channel relative to the environment at those levels are important. In a finite difference model the delta functions could be spread out over a single grid interval.

For a chemical species the corresponding equation is complicated by the presence of an intrinsic source function C^* , and the possibility that the mixing ratio might change along a current due to chemical processes. However, these two effects nearly cancel each other out. This may be seen by noting that

$$\langle C^* \rangle = \langle C_{env} \rangle + \sum_i C_i^*, \quad (21)$$

where we have divided the smoothed source term into a part occurring in the environment and a part occurring in each current. As long as a statistically steady state exists, the time rate of change of the concentration of a chemical species in a parcel moving up or down a current should equal the vertical velocity times the z -derivative of the concentration along the current. When appropriate smoothing is done, this results in

$$C_i^* = m_i \frac{\partial \chi_i}{\partial z}, \quad (22)$$

whence

$$\langle C \rangle = \langle C_{env} \rangle - \frac{1}{\rho_0} \sum_i \mu_i [\delta(z - a_i) \chi'_{ai} - \delta(z - b_i) \chi'_{bi}], \quad (23)$$

where the definitions of χ'_{ai} and χ'_{bi} are analogous to (19) and (20).

4. Graphical notation and examples

It is possible to represent the currents in a cumulus cloud by arrows in a graphical notation. We adopt the convention that arrows entering from the bottom represent pure cloud base air, while those entering from the left side represent environmental air. Arrows either terminate at a junction of currents

or exit into the environment, depending on the disposition of the contents of that current.

Figure 1 shows diagrams describing unmixed parcel ascent, an entraining plume, and a detraining plume. Unmixed parcel ascent requires no explanation, but the other two do. Because individual currents cannot entrain, the entrainment in the entraining plume must be represented as a sequence of discrete events in which the current representing a segment of the plume mixes with a current from the environment, the mixture feeding the next plume segment.

The detraining plume is even more complex. The initial current from cloud base splits into two currents, one of which mixes with a current from the environment and exits to the environment. The other branch ascends, again bifurcates, and the two sub-currents repeat what happened in the first step. This goes on until the last bit of cloud base air is used up.

These diagrams make it clear that a *detraining* system is much more complex than an *entraining* system because multiple currents containing cloud base air have to be accounted for.

It is possible to translate the above diagrams directly into mathematical expressions by entering the properties of each stream into the sums of (18) and (23). For example, the case of unmixed ascent has only one current with $\theta'_{cui} = 0$, since it is picking up environmental cloud base air at that point. At the upper level $\theta'_{cli} = \theta_c(\text{cloudbase}) - \theta_c(\text{cloudtop})$, and

$$\langle E \rangle = \frac{\mu}{\rho_0} \delta(z - z_{top}) [\theta_c(\text{base}) - \theta_c(\text{top})]. \quad (24)$$

For an entraining plume with one entrainment event, we find

$$\langle E \rangle = \frac{\mu_1}{\rho_0} \delta(z - z_{mid}) \theta_{c1} - \frac{\mu_1 + \mu_{env}}{\rho_0} [\delta(z - z_{mid}) \theta_{c2} - \delta(z - z_{top}) \theta_{c3}], \quad (25)$$

where $\theta_{c1} = \theta_c(\text{base}) - \theta_c(\text{mid})$, $\theta_{c2} = \theta_c(\text{mix}) - \theta_c(\text{mid})$, and $\theta_{c3} = \theta_c(\text{mix}) - \theta_c(\text{top})$. The value of θ_c in the upper current is given by linear mixing with the environment in proportion to the mass flux, i. e.,

$$\theta_c(\text{mix}) = \frac{\mu_1 \theta_c(\text{base}) + \mu_{env} \theta_c(\text{mid})}{\mu_1 + \mu_{env}}. \quad (26)$$

A bit of algebra shows that the mid-level terms in (25) cancel, resulting in

$$\langle E \rangle = \frac{\mu_1 + \mu_{env}}{\rho_0} \delta(z - z_{top}) \theta_{c3}. \quad (27)$$

In other words, an entraining plume only modifies the environmental θ_c at the level of final detrainment.

5. What actually happens in cumulus clouds

Raymond and Blyth (1986) present observations of the detrained mass flux of cumulus clouds F as well as the results of corresponding model calculations. (F is the mass source term $\langle S \rangle$, defined in (9), divided by the number of cumulus clouds per unit area.) The model is equivalent to a detraining thermal model with the proviso that detrained material mixes in varying proportions with environmental air and then rises or sinks to its level of neutral buoyancy before exiting the cloud.

Figures 2-4 show the computed and measured $F(z)$ for four different cases. The observed detrained mass flux in figure 2 is from a composite of cumulus congestus clouds that occurred during the summer of 1982 over the Magdalena Mountains in central New Mexico. Note that even though cloud top was near 500 mb, air was detrained primarily near cloud base, or between 600 and 700 mb. In other words, cloud base air that reached cloud top typically sank almost back to cloud base after mixing with environmental air. The model shows quite similar results.

Figures 3 and 4 show two cases (also observed over the Magdalena Mountains) in which thin detrainment layers aloft occurred. These layers were at least qualitatively predicted by the the model. Note that in both these cases substantial detrainment also occurred near cloud base. More details on these studies may be obtained from the above-referenced paper.

Note that the observed cloud tops in figures 2 and 4 actually exceeded the predicted cloud tops, which were simply the equilibrium levels for a non-entraining parcel. This definitively eliminates the entraining plume as a possible model for these clouds, since entrainment would imply a maximum cloud top height much less than the undilute equilibrium level.

6. Summary

In this talk I have attempted to develop the conceptual and mathematical basis for describing cumulus models with a multitude of interconnected flows. I then showed that entraining and detraining models were conceptually very different in spite of the symmetry in terminology. Finally, I presented observational results that can only be explained by a flow that is functionally equivalent to a detraining thermal. Whether cumulus clouds actually take the form of detraining thermals, or whether some more complex flow is mimicking this behavior is unknown at this point.

References

- Ooyama, K., 1971: A theory on parameterization of cumulus convection. *J. Meteor. Soc. Japan*, 49 (special issue), 744-756.
- Raymond, D. J., and A. M. Blyth, 1986: A stochastic mixing model for non-precipitating cumulus clouds. *J. Atmos. Sci.*, 43, 2708-2718.

Raymond, D. J., 1987: A forced gravity wave model of self-organizing convection. *J. Atmos. Sci.*, **44**, 3528-3543.

Figure Captions

Figure 1. Coupled current diagrams describing models of mixing, entrainment, and detrainment. a) The unmixed parcel is represented by a single current. b) The entraining plume is split into segments of no entrainment separated by impulsive entrainment events. c) The detraining plume splits off sub-currents which mix with environmental air.

Figure 2. Observed and predicted detrained mass fluxes for a composite case of cumulus congestus clouds over the Magdalena Mountains of central New Mexico. Note that even though cloud top exceeded 500 mb, most mass detrained between 600 and 700 mb.

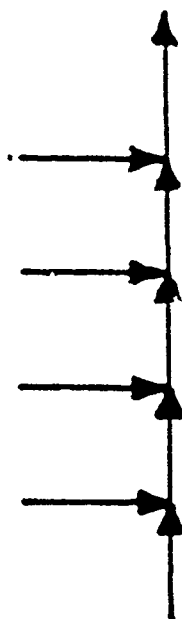
Figure 3. As in figure 2, except a single case on 24 July 1980. In this case detrainment occurred both below cloud base and at middle levels. The two different curves on the left indicate two different imposed cloud base temperatures.

Figure 4. As in figure 3, but case of 23 July 1984. Note again the strong detrainment well below cloud top.

a) Unmixed parcel



b) Extraining Plume



c) Detraining Plume

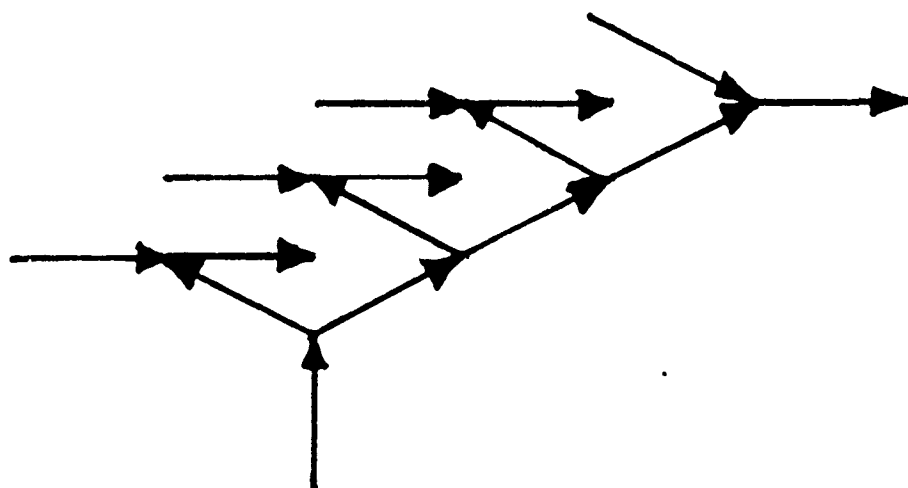
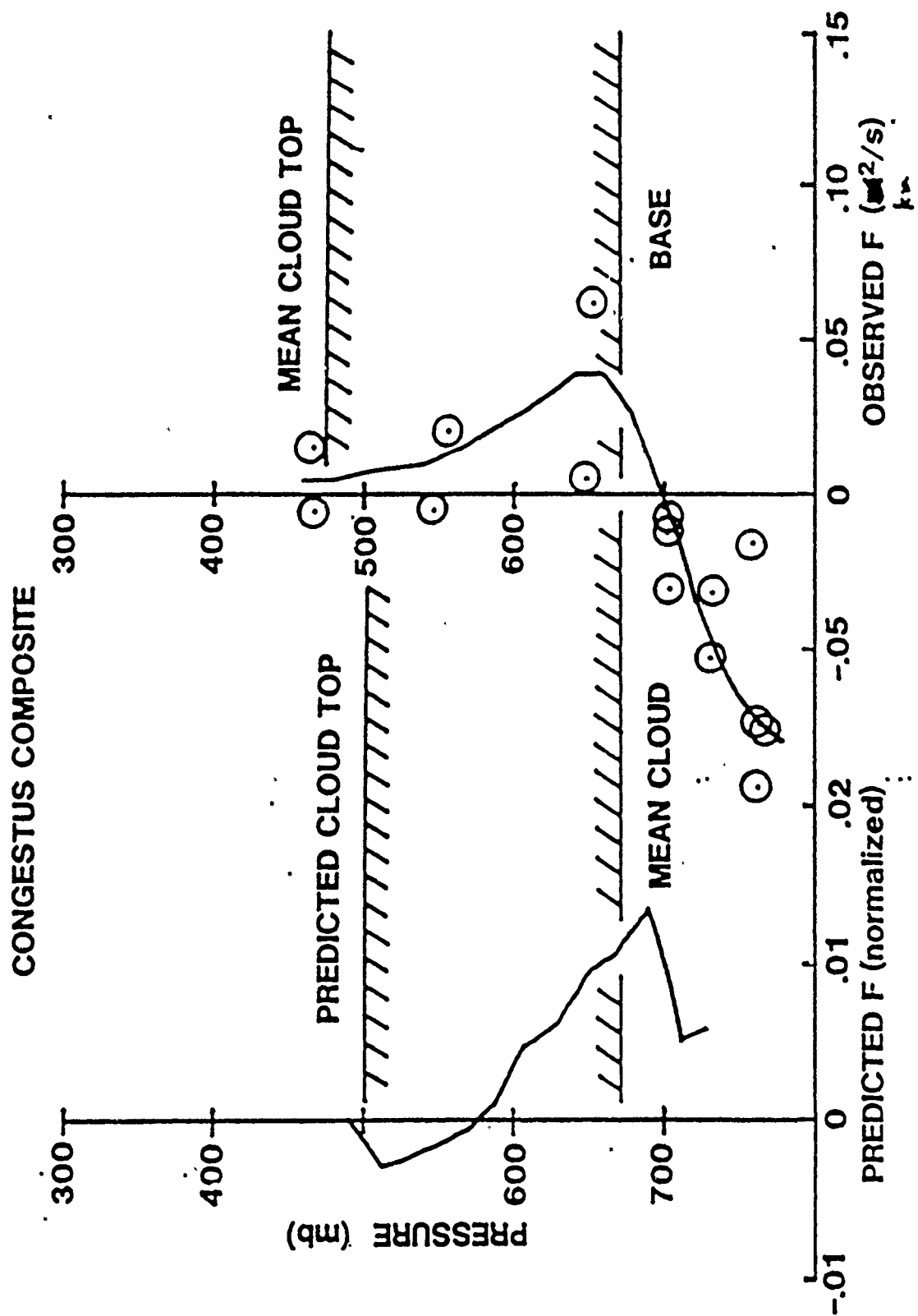
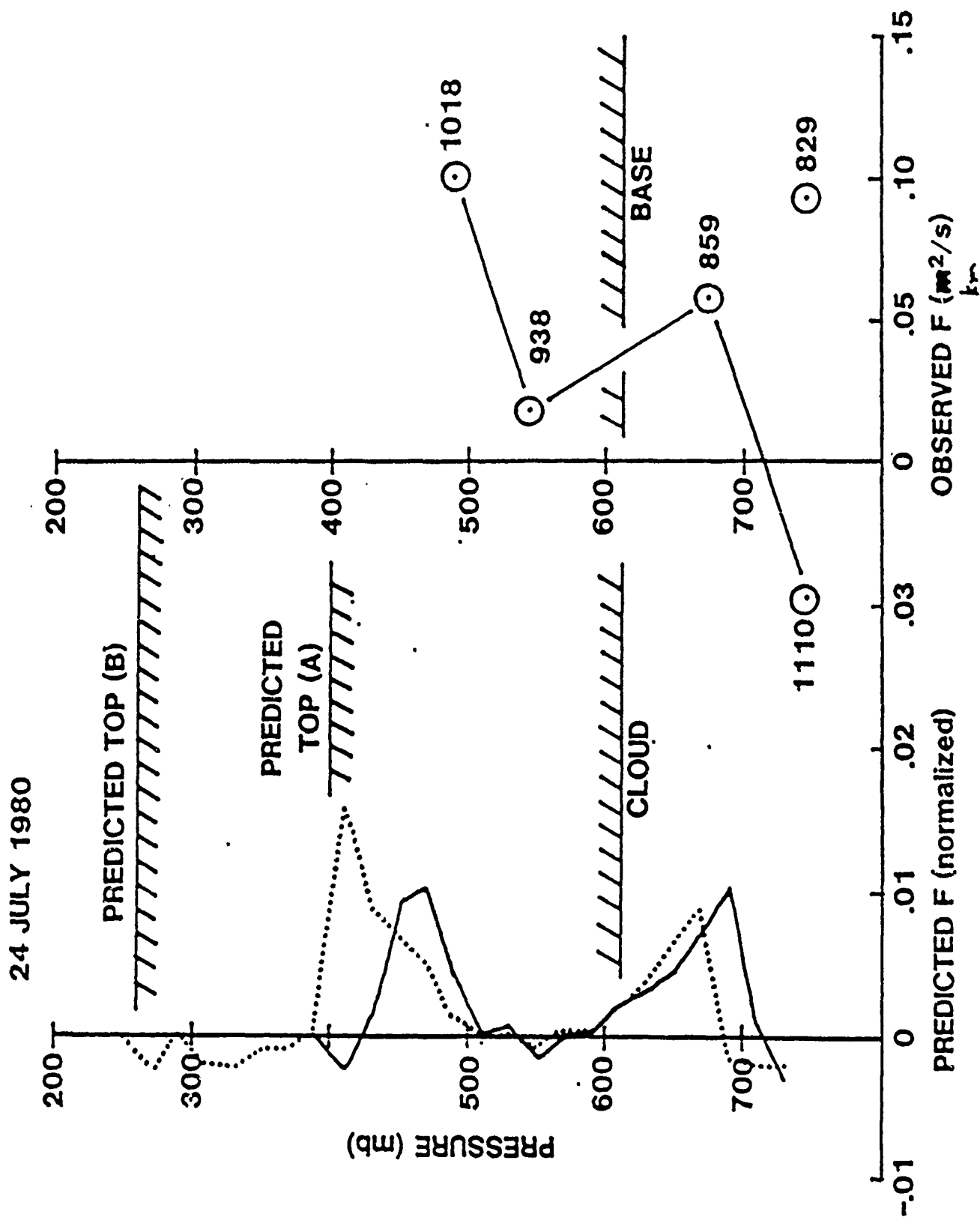


Fig. 2





23 JULY 1984

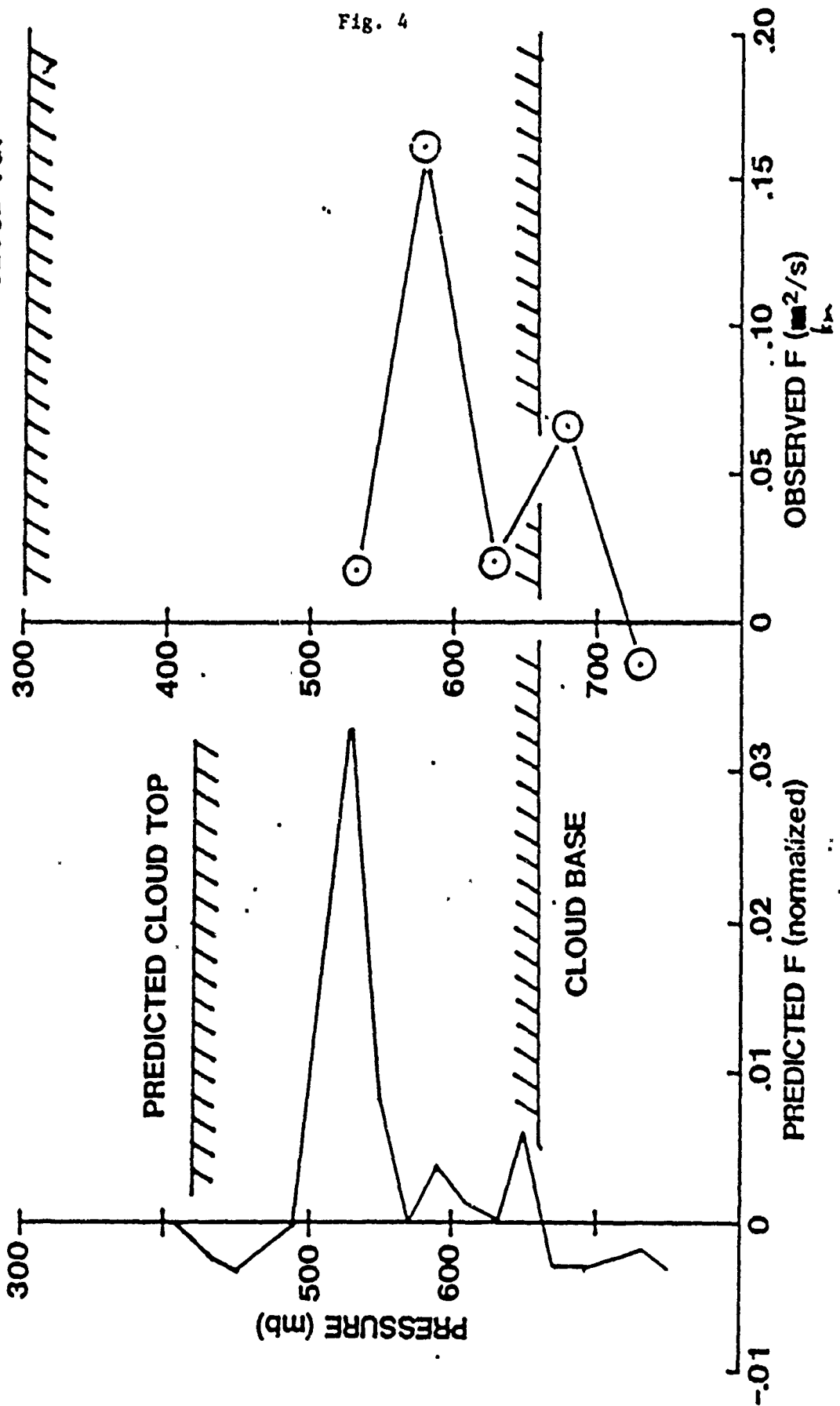


Fig. 4

DYNAMICAL MODELS FOR MELT SEGREGATION

Frank M. Richter
University of Chicago

The most pervasive form of melting in the earth is due to decompression, as in the case of mid-ocean ridges where the surface divergence of the plates forces adiabatic upwelling and partial melting of order 20%. Since the oceanic crust is made up of pure melt phase, there must exist a mechanism for separating melt from residual solids, which in turn implies that the residual solids must themselves be deformable.

McKenzie has developed a formalism for describing the process of melt segregation from a deformable residual matrix in terms of a compacting porous medium, and in this talk I will consider some of the solutions that have been found. The simplest situation involves the one-dimensional compaction by gravity of a melt-matrix mixture resting on an impermeable base. If the melt fraction is given as an initial condition the subsequent evolution of the system involves a compaction boundary layer at the base where the matrix deforms to invade the interstitial pore spaces and push out the melt. Above this boundary layer is an interior regime where the pressure gradient due to the flow of melt is sufficient to balance the tendency of the matrix to deform. As melt is exhausted from the boundary layer, the boundary layer grows at the expense of the interior regime and eventually dominates the system.

Another class of solutions to the McKenzie equations is solitary waves of excess melt fraction. Such waves will arise if the rate of melting is heterogeneous in the sense of there being local regions characterized by more rapid melting. These waves can be one, two, or three-dimensional. We can show that the one-dimensional solitary waves are unstable to the two-dimensional waves and expect that two-dimensional waves are themselves unstable to three-dimensional perturbations.

EFFECTS OF GEOTHERMAL HEAT FLUX AND TOPOGRAPHY ON THE CONVECTIVE VENTILATION OF CONFINED BASINS

Claes G.H. Rooth
RSMAS, University of Miami

Convective ventilation of confined ocean basins requires, in steady state, a compensating buoyancy flux which can be supplied either by downward forced convection (mixing/eddy diffusion) of buoyancy, or by geothermal heating effects. The latter are usually considered dynamically negligible in deep ocean

circulation analysis but isolated deep basins tend to develop almost adiabatic stratification in their deepest layers, allowing even weak interior buoyancy sources to become significant.

The intensity of the geothermal heat flux can be taken as uniformly distributed over the horizontal projection of the basin area. The heat input per unit depth is then proportional to the gradient of cross sectional area with depth, dA/dz . This provides a dynamic link between the basin topography and the convective ventilation, since the stratification will be modified by any buoyancy flux imbalances in such a way as to minimize them.

Killworth and Turner (1982) demonstrated that a transient basin filling experiment with a time-modulated buoyancy source could be effectively modelled based on a triple time scale mean field interaction approximation. The convective process is treated as a quasi-stationary response to a slowly varying buoyancy source, while the time scale of latter is in turn taken as fast compared to rate of evolution of the interior basin state. For this case, one or several time-variable convective sources can be treated as an ensemble of simultaneously acting (parallel) sources. For such an ensemble, let the integrated buoyancy flux across a level surface be B . Then it is easily seen that $dB/dz = NV$, where N is the buoyancy (Brunt-Vaisala) frequency for the interior domain, and V is the integral volume flux for the convective plume ensemble (z is taken as positive upwards). An identical relation couples the buoyancy flux gradient for any individual plume to its volume flux and the interior stratification. An interesting consequence of this is that the deep basin stratification is expected to approximately mirror the hypsographic curve.

To close the problem, we must formulate a predictor for the mass flux variations for the convective plumes. This has been done for the limiting cases of free plumes and of shallow flows on sloping boundaries, in either case neglecting rotation effects (Turner, 1973). Numerical experiments with a free plume ensemble and a series of different bottom topography forms bear out the prediction of a close tie between the bottom shape and the probability distribution for the depth of penetration of individual elements of a plume ensemble. In the seminar, computations were presented for a plume ensemble with a uniform distribution of initial buoyancy flux over a 40:1 range of intensity, with the total negative buoyancy flux input ten times the geothermal heating effect. Approximately 40% of the ensemble (the weakest elements, representing about 16% of the total original buoyancy flux input relative to the reference density at the source level in the basin) terminate within the diffusive thermocline range, while the rest reach the bottom in the case of a square (flat bottom) basin, or exhibit a distributed termination pattern which roughly mirrors the basin hypsography. Note that while the latter subset carries over 80% of the initial buoyancy flux relative to the density at the upper basin boundary, an approximate balance with the geothermal heat flux in the deeper basin part has been reached at the bottom of the thermocline. This happens mostly because of

the entrainment of thermocline waters, but in part also because of this point a greater reference density enters in the buoyancy flux definition.

Tracer based ventilation diagnostics for the deep Caribbean basin, and for the Cariaco basin, off the coast of Venezuela (Holmen and Rooth, 1988) support the theoretical expectation of a bimodal ventilation effect in deep natural basins.

References

- Holmen, Kim J. and Claes G.H. Rooth (1988), Ventilation of the Cariaco Trench, a case of Multiple Source Competition? Submitted to *Deep Sea Research*.
- Killworth, Peter D. and J. Stewart Turner (1982), Plumes with time variable buoyancy in a confined region. *Geophysical and Astrophysical Fluid Dynamics*, 20, 265-294.
- Turner, J. Stewart (1973) *Buoyancy Effects in Fluids*, Cambridge University Press, Cambridge, U.K., 367 pp.

A THEORY FOR STRONG, LONG-LIVED SQUALL LINES

Richard Rotunno
NCAR
Boulder, Colorado

I discuss a study of the mechanics of long-live, line-oriented, precipitating cumulus convection (squall lines) using two- and three-dimensional numerical models of moist convection (Rotunno, Klemp and Weisman, 1988). These models, used in juxtaposition, enable us to address the important theoretical issue of whether a squall line is a system of special, long-lived cells, or whether it is a long-lived system of ordinary short-lived cells. Our review of the observational literature indicates that the latter is the most consistent paradigm for the vast majority of cases, but, on occasion, a squall line may be composed of essentially steady, supercell thunderstorms. The numerical experiments presented show that either type of squall line may develop from an initial line-like disturbance depending on the magnitude and orientation of the environmental shear with respect to the line. With shallow shear, oriented perpendicular to the line, a long-lived line evolves containing individually short-lived cells. Our analysis of this type of simulated squall line suggests that the interaction of a storm cell's cold surface outflow with the low-level shear produces much deeper and less inhibited lifting than is possible without the low-level shear, making it easier for new cells to form and grow as old cells decay. Through intercomparison of two- and three-dimensional squall line simulations, we conclude that the essential physics of this type of squall line is contained in the

two-dimensional framework. We argue that these results describe the physics of both midlatitude and tropical squall lines. Under conditions of deep strong shear at an angle to the supposed line, a line of supercells develops in which their respective three-dimensional circulations do not interfere with one another.

References

Rotunno, R., J.B. Klemp and M.L. Weisman, 1988. A theory for strong, long-lived squall lines. *J. Atmos. Sci.*, 45, 463-485.

A GEOMETRIC VIEW OF DYNAMICAL APPROXIMATIONS

Rick Salmon

University of California-Scripps
Institute of Oceanography

This lecture presents a method for deriving approximate dynamical equations that satisfy a prescribed constraint typically chosen to filter out unwanted high-frequency waves. Although the method proposed is very general, we are mainly interested in the case of a rotating fluid in which the prescribed constraint is geostrophic balance.

Let R be the (infinite-dimensional) phase space of the fluid, with general coordinates x^i . Every point $x \equiv (x^1, x^2, x^3, \dots)$ of R corresponds to a possible state of the fluid system as a whole. The exact dynamics

$$dx^i/dt = v^i(x) \quad (1)$$

corresponds to the vector field v^i in phase space.

Consider the phase-space submanifold composed of states in which the fluid is everywhere in geostrophic balance. We call this submanifold the slow manifold. The slow manifold is defined by the (infinitely many) equations

$$\phi_{(\ell)}(x) = 0, \quad \ell = 1, 2, 3, \dots \quad (2)$$

expressing geostrophic balance at every point of physical space. We seek "balanced" dynamical approximations in which systems on the slow manifold remain there. Such approximations obviously consist in replacing the exact vector field v^i in (1) by a vector field tangent to the slow manifold (2).

The quasigeostrophic approximation (QG) corresponds to an "ordinary projection" of v^i onto the slow manifold, in which the normal mode amplitudes of the linearized dynamical equations are treated like Cartesian coordinates in phase space.

In more geometrical language, QG is equivalent to the metric projection

$$dx^i/dt = v^i + \mu_{(\ell)} g^{ij} \partial \phi_{(\ell)} / \partial x^j \quad (3)$$

of the exact dynamics (1) onto the slow manifold (2) of geostrophic states. The coefficients $\mu_{(\ell)}$ are chosen such that (3) satisfies

$$d\phi_{(\ell)}/dt = 0 \quad (4)$$

and the metric g^{ij} is related to the exact dynamics as follows: If the exact equations are linearized about a state x_0 of rest with flat isopycnals, then the linear equations conserve the energy

$$H_0 = \frac{1}{2} g_{ij} \Delta x^i \Delta x^j \quad (5)$$

where $\Delta x \equiv x - x_0$ is the phase space displacement from the fixed point x_0 , and the constant tensor g_{ij} is the inverse of g^{ij} .

Unfortunately, phase-space has no natural metric, and g^{ij} is therefore an artificial component of the quasigeostrophic approximation. Its presence explains why QG is valid only near a state with flat isopycnals.

If the exact dynamics are Hamiltonian, then v^i takes the particular form

$$v^i = J^{ij} \partial H / \partial x^j \quad (5)$$

where J^{ij} is the symplectic tensor and H is the Hamiltonian. J^{ij} and g^{ij} have completely different properties. However, the semigeostrophic equations are obtained by replacing g^{ij} by J^{ij} in (3) and (4). The resulting equations, which can also be derived in several motivated ways, lie at the heart of a beautiful theory developed by Dirac.

The constraints (2) defining the slow manifold are the only arbitrary components of this theory. These constraints are "consistent" if the coefficients $\mu_{(\ell)}$ are uniquely determined. A simple iterative procedure tests and (if necessary and possible) augments an arbitrary set of trial constraints to produce a consistent set. If the constraints are consistent, then the approximate dynamics is itself a Hamiltonian dynamics, and canonical coordinates exist. The various forms of the semigeostrophic equations correspond to slightly different definitions of the slow manifold. The optimal form is that for which canonical coordinates are easiest to find.

The most important lesson from this work may be that any approximation takes its most transparent form when written in a covariant form in general phase space coordinates.

References

- Salmon, R. Semigeostrophic theory as a Dirac-bracket projection. *J. Fluid Mech.* (in press)

SEPARATION OF A BOUNDARY JET IN A ROTATING FLUID

Melvin Stern
Florida State University

A jet flows from a source along a vertical wall of a large rotating tank containing water of the same density. The flow approaches a sharp corner where the vertical wall turns through an angle A . If A is less than a critical value the current flows past the corner and continues down the wall. If A exceeds the critical angle, then the jet separates at the corner by flowing into a dipolar vortex, which carries the mass away from the wall and into a large recirculating gyre. The main significance of the rotation is to make the flow two dimensional, and to conserve vertical vorticity. The critical A is computed by contour dynamics (using a conformal mapping) for a piecewise uniform vorticity jet. The results compare favorably with laboratory measurements.

VORTEX DYNAMICS OF STRATIFIED FLOWS

Gretar Tryggvason
Department of Mechanical Engineering and Applied Mechanics
The University of Michigan
Ann Arbor, MI 48109

Two recent applications of vortex methods to stratified, vortical flows are discussed. One is the deformation of a free surface due to the large amplitude Kelvin-Helmholtz instability of a submerged vortex sheet. The roll-up of the vortex sheet causes a deformation of the free surface and leads to a breaking wave, the entrainment of air, or the generation of relatively short waves, depending on the strength and depth of the vortex sheet. The other example considers the collision of a vortex pair, or a ring, with a relatively weak density interface. In the limit of weak density stratification, this problem is governed by only one nondimensional parameter combining the effect of the vortex strength and the stratification. Weak rings behave as if the interface were a solid boundary, but strong rings penetrate deep into the other fluid. For intermediate strength, the vortex pair penetrates partly and is then pushed back by baroclinically generated vorticity at the interface. The back flow generates a complicated system of secondary vortices. The calculated behavior correlates well with recent experimental results of Willmarth and Hirs for free surface flows, and Dahm and Scheil for the interaction of vortex rings with a weak density interface.

We then discuss the extension of generalized vortex methods to three-dimensional free surface problems. As in two dimensions, the dynamics is governed by the condition that the pressure is constant at the interface (in

the absence of surface tension). This allows us to write an evolution equation for either the tangential velocity or the velocity potential. The normal component is determined by the conditions of incompressibility and irrotationality which leads to an integral equation over the free surface. By an application of the formulas of classical vector analysis it is possible to formulate several alternative boundary integral equations for the normal velocity or the vector stream function. We list the various possibilities and discuss which are suitable for numerical implementation. In conclusion, some general comments on the vorticity formulation of stratified flows are presented.

DIFFUSION COEFFICIENTS AND VELOCITIES FROM TRACERS

George Veronis
Yale University

An investigation into the feasibility of solving the inverse problem for (eddy) mixing coefficients, κ , along with the velocity field, v from distributions of tracers was based on solving the 2D forward problem first (given κ and v determine tracer distributions). Since the known κ and v of the forward problem are the unknowns of the inverse problem, the exact solution is known and can be used to measure the accuracy of the results obtained.

The forward problem involved flow, either rectilinear or with embedded eddies, in a channel with fixed tracer concentrations at the boundaries. The tracer distributions were obtained on a network of gridpoints. The inverse problem was first solved in portions of the channel where the tracer field was given on the same network. With enough error-free tracer data the exact κ and v could be obtained, so the inverse problem is well posed. Most of the inverse calculations made use of tracer data with errors due to either truncation or added noise.

It comes as no surprise that if enough data are available (sufficiently many tracers and/or sufficiently many gridpoints), the accuracy in the derived values of κ and v is limited only by the accuracy of the given tracer data. Generally speaking, satisfactory results were obtained only if the system to be solved was overdetermined, either by enough data or via approximations that limited the number of unknowns.

An encouraging sign is that using a limited representation for κ (either constant in blocks of cells or a low-order polynomial) yielded values of κ and v that were as accurate as, and sometimes more accurate than, the values obtained with a more complete representation for κ . The approximate form for κ gave better results than a fully variable κ even when the velocity field included a small scale eddy that was only marginally resolved by the grid network.

The success obtained with approximate forms for κ and v is very encouraging since one of the most serious problems confronting observers who try to interpret the record is paucity of data. The anisotropy of mixing (at least, horizontal and vertical) plus the low vertical velocity of the mean flow render the 3D problem a difficult one where the demands on data can be met only marginally if at all. It is here that the approximate forms for κ and v may make an otherwise hopeless task one that is tractable.

THE FLUID DYNAMICS AND THERMODYNAMICS OF ERUPTION COLUMNS

Andrew W. Woods
University of Cambridge

This talk considers modelling the fluid dynamics and the thermodynamics of Plinian eruption columns (Woods, 1988). Plinian eruptions involve the continuous discharge of a mixture of gas and solid fragments from volcanic vents at speeds on the order of hundreds of metres per second, generating a continuous column of hot pyroclasts, rocks, and entrained air which rises to a few tens of kilometres (Walker 1981). The lower part of the eruption column in which the initially dense material from the vent is carried a few kilometres upwards by its momentum is called the gas-thrust region (Sparks and Wilson 1976). Air is entrained as the material rises; the air expands due to heating from the hot pyroclasts and can eventually cause the material in the column to become buoyant. If there is sufficient thermal energy in the column, it then behaves as a buoyancy-driven convective plume in which the plume material is significantly hotter than the ambient fluid. This effect causes the column to continue rising to as much as a few tens of kilometres, until the column material ceases to be buoyant. Above this neutral buoyancy height, an umbrella cloud, of a few kilometres thickness, grows radially. Alternatively, if the initial momentum (or other properties controlling the process, e.g. temperature) is insufficient for the material to reach the point at which the upwards buoyancy forces begin to dominate, then the column will collapse at a much lower height, typically a few kilometres.

Various models of Plinian eruptions have been presented (particularly Wilson 1976; Sparks 1986; Wilson and Walker 1987), and the results have been compared with observational data (Settle 1978; Wilson et al. 1978). A number of these models are based on the classical work of Morton et al. (1956) who introduced models for convecting plumes in both uniform and stratified environments in which density differences between the constituent fluids are small. Their model incorporated a Boussinesq approximation and did not consider any of the large thermal effects which are present in a volcanic eruption.

However, the models of Morton et al. have been applied to volcanic eruption columns by modifying the buoyancy term in the governing equations or by including an additional expansion of the air due to internal heating, but retaining the basic approximations which were made in the original model. The resulting models are not always consistent with the basic laws of thermodynamics and fluid dynamics which govern the eruption column motion because of the large density and temperature changes which can occur in an eruption column.

A major purpose of this talk is to develop a physical model of Plinian eruption columns from first principles. This work derives and investigates the fluid dynamic and thermodynamic constraints in the basic governing equations which describe an eruption column. The column is modelled as being in a steady state in both the gas-thrust region and buoyancy-driven region with a constant, continuous supply of material from the vent. The steady-state approximation is a good model of the eruption process when the column has become established, after the initial explosion (Carey and Sigurdsson 1985). The thermal interactions in the column are modelled using the steady flow energy equation. A closure hypothesis is required to complete the model. Some previous models of plume rise (for example Schatzmann 1979) have attempted to derive a universal closure hypothesis encompassing both buoyancy-driven and momentum-driven plumes. This approach has been successful in modelling laboratory experiments; however, it necessitates the introduction of (up to) five empirical constants. In contrast, the present study proposes separate closure hypotheses for the gas-thrust and buoyancy-driven regions by considering the dynamics particular to each region. In the gas thrust region we use a modification of Prandtl's model of a jet (1954) while in the buoyancy driven region we use the entrainment assumption, (Morton et al.) 1956. This requires only one empirical constant for each of the regions and the regions are merged where the column becomes buoyant. The laterally spreading umbrella cloud at the top of the column, which has been modelled by Sparks (1986), is considered as part of the convective region in order to determine the total column height, as in Morton et al. (1956). The important effects on the column height and structure resulting from the ambient stratification in both the troposphere and the stratosphere have also been investigated.

Numerical calculations have yielded the following conclusions for the parameter ranges of interest:

1. In the upper region of the column the rate of change of the enthalpy flux with height is principally governed by the rate of change of the potential energy flux. This reduces the column temperature in the upper region, and so the column becomes less buoyant, until it comes to rest. This effect reduces the vertical extent of the column. Thus the steady-flow-energy equation which incorporates the interaction of the enthalpy with the potential energy plays an important role in determining where the top of the column is located.

2. The radius of the column increases rapidly in the gas-thrust region as the entrained air is heated to a very great temperature. This is followed by a more gradual column radius increase in the buoyancy-driven region when the entrained air is not heated to such great temperatures. Above the neutral buoyancy point, the radius increases more rapidly into the radially spreading umbrella cloud.

3. The phenomenon of column collapse is critically dependent on the vent velocity. It is predicted to occur only for much smaller velocities than found previously by Wilson (1976) ($U \simeq 100$ m/s whereas Wilson found collapse when $100 \text{ m/s} < U < 400 \text{ m/s}$). This greatly increases the range of eruption conditions which can generate a Plinian column, as well as extending the range of heights of Plinian columns to smaller values.

4. If the vent radius is large or the initial gas mass fraction small, the column can become so buoyant once above the gas-thrust region, because of the large amount of thermal energy, that the column velocity can actually increase with height in the column.

5. The gas-thrust region height decreases with initial temperature, initial gas content and initial velocity because these increase the buoyancy of the column. It increases with increasing vent radius because the volume of air entrained relative to the column volume (per unit height) decreases with radius.

6. As anticipated, the column height increases with the initial temperature, initial velocity and vent radius but decreases with the initial gas content.

7. In the troposphere the temperature decreases with height and so columns rise somewhat higher than they would in an isothermal environment because of their increased buoyancy. However, once in the stratosphere, the temperature gradient reverses, and so this effect is reversed.

References

- (Main Ref.) Woods, A.W. (1988) The Fluid Dynamics and Thermodynamics of Volcanic Eruptions, *Bull. Volcanol.*, v.50, p.169-193.
- Carey, S. Sigurdsson, H. (1985) The May 18, 1980 eruption of Mt. St. Helens. 2. Modelling of the dynamics of the Plinian phase. *Jour. Geophys. Res.*, 90, 2948.
- Morton, BR, Taylor, G. Turner, J.S. (1956) Turbulent gravitational convection from maintained and instantaneous sources. *Proc. Roy. Soc.*, A234, 1-23.
- Prandtl, L. (1954) *Essentials of Fluid Mechanics*, Blachie, Glasgow pp.1-452.
- Settle, M. (1978) Volcanic eruption clouds and the thermal power output of explosive eruptions. *J. Volcanol. Geotherm. Res.*, 3,309-324.
- Sparks, R.S.J., (1986) The dimensions and dynamics of volcanic eruption columns. *Bull. Volcanol.*, 48, 3-15.
- Sparks, R.S.J., Wilson, L. (1976) A model for the formation of ignimbrite by the gravitational column collapse. *J. Geol. Soc. London.*, 132, 441-451.

- Walker, G.P.L. (1981) Plinian eruptions and products. *Bull. Volcanol.*, **44**, 223–240.
- Wilson, L. (1976) Explosive volcanic eruptions — III Plinian eruption columns. *Geophys. Jour. Astron. Soc.*, **45**, 543–556.
- Wilson, L. Sparks, R.S.J., Huang, T.C. Watkins, N.D. (1978) The control of volcanic column height dynamics by eruption energetics and dynamics. *Jour. Geophys. Res.*, **83** [B4], 1829–1836.
- Wilson, L. Walker, G.P.L. (1987) Explosive volcanic eruptions VI — Ejecta dispersal in plinian eruptions: the control of eruption conditions and atmospheric properties. *Jour. Astron. Soc.*, **89**, 657–679.

ARRESTED SHEAR DISPERSION AND OTHER MODELS OF ANOMALOUS DIFFUSION

W.R. Young
University of California–Scripps

The macroscopic dispersion of tracer in microscopically disordered fluid flow can ultimately, at large times, be described by an advection–diffusion equation. But before this asymptotic regime is reached there is an intermediate regime in which first and second spatial moments of the distribution are proportional to t^v . Conventional advection–diffusion (which applies at large times) has $v = 1$ but in the intermediate regime $v < 1$. This phenomenon is referred to as “anomalous diffusion” and we discuss the special case $v = 1/2$ in detail. This particular value of v results from tracer dispersion in a central pipe with many stagnant side branches leading away from it. The tracer is “held up” or “arrested” when it wanders into the side branches and so the dispersion in the central duct is more gradual than in conventional advection–diffusion (i.e. $v = 1/2 < 1$).

This particular example serves as an entry point into a more general class of models which describe tracer arrest in closed pockets of recirculation, permeable particles, etc. with an integro–differential equation. In this view tracer is arrested and detained at a particular site for a random period. A quantity of fundamental importance in formulating a continuum model of this interrupted random walk is the distribution of stopping times at a site. Distributions with slowly decaying tails (long sojourns) produce anomalous diffusion while the conventional model results from distributions with short tails.

RECENT RESULTS ON VORTEX RECONNECTION IN 3D FLOWS

Norman J. Zabusky
University of Pittsburgh

We review recent results obtained from Biot-Savart filament codes (E. Siggia, A. Pumir and K. Schwarz) and spectral codes (S. Kida, R. Kerr, A. Pumir) with varying initial conditions. In particular, we emphasize the recent results of Melander and Zabusky, where the initial condition consists of orthogonally-offset gaussian vortices. For two vortices we see three stages for a reconnection.

The early phase is where the primary configuration evolves into a locally antiparallel bound vortex pair. At the same time, one observes secondary "hairpin-like" structures being "pulled" from weak regions of the vortex tube. These are intensified.

During the second phase, the primary bound structures are intensified while tertiary vortex structures are entangled around the primary tubes. In the final phase there seems to be local and sudden dissipation and reconnection. The primary vortices move apart, mainly as a result of the curvature of the entangled "hairpins."

We also examine the collision of translating dipolar vortex tubes and dipolar-dipolar vortex systems. A common feature is the formation of ring-like structures.

1988 Summer Study Program

in

Geophysical Fluid Dynamics

REPORTS OF FELLOWS

Baroclinic Models and Hurricane Motion

J.R. Countryman

Summer 1988

Abstract

This project marks the beginning of work which will investigate the causes of hurricane motion. The dominant causes of motion, steering wind and beta-drift have been primarily studied in barotropic models. Both the large scale environment of a hurricane and the storm itself are baroclinic. The bulk of this project has been to document vortex pair solutions in a 2-layer quasi-geostrophic model with varying effective beta (mean gradient of potential vorticity) and vertical shear. These do not resemble cyclones, but represent non-linear solutions in a model that I will further investigate with regards to hurricanes.

1 Introduction:

The generally accepted dominant causes of hurricane motion are advection by a steering wind and beta-drift. Both empirical forecasting and analytic models have primarily considered these barotropically. It is undeniably true that both the large scale environment surrounding a hurricane and the cyclone itself are baroclinic. Following is a speculative list of some baroclinic factors:

- Vertical sheering of the steering (or ambient) wind.
- The effective beta (defined as the horizontal gradient of ambient potential vorticity) is height dependent.
- The baroclinic internal structure of the hurricane has dynamics that influence the storm motion and these dynamics are dependent on the above two factors.

Furthermore, the simplifying assumption that the hurricane does not alter the ambient environment is usually made. If you want to drop this assumption, and consider the hurricane and the large scale as coupled, then baroclinicity is important.

We have considered the simplest baroclinic model; a quasi-geostrophic two layer model. This is in no way quantitatively adequate, but is a tractable model

and can provide insight and direction for the research of more complicated and realistic models. First, the general form of propagating solution modes for this model are derived and then specific coupled vortex pair solutions are developed. Essentially, this work is the logical way to start to systematically consider propagating solutions in this model. The solutions little resemble hurricanes. However, our solutions are always cyclonic in the bottom layer and anticyclonic above with the following rationale.

Diagnosis of potential vorticity vs. theta profiles of hurricanes show a concentrated deep region of significantly positive potential vorticity "below" and a larger, shallower and weaker region of relatively low potential vorticity "above" (Schubert and Alworth, 1987). The quotes are to stress that potential vorticity is plotted against theta. Theta always increases with height, but surfaces of constant theta are far from horizontal. Dynamical equations can be written with theta as the vertical coordinate and potential vorticity as the dependent variable. The invertibility principle allows determination of velocity and mass fields. Our belief is that the two-layer QG model with invertibility by geostrophic wind is qualitatively analogous to a more realistic model with potential vorticity, theta coordinates and invertibility by the non-linear balance equation.

In section 2 the two-layer QG model is presented. The fields are partitioned into ambient (no time dependence) and disturbance (time varying) parts to allow consideration of solutions in different large scale conditions. In section 3 the general form of zonally propagating solution modes is derived. And in section 4 isolated, dipole solutions are presented. Section 5 is a discussion of dipole solution results and in section 6 concluding comments are made.

2 Two-Layer Model:

2.1 Quasi-geostrophic two layer equations:

The quasi-geostrophic equations for two layers with sloping boundaries are:

$$\omega q_1 / \partial t + J(\psi_1, q_1) = 0 \quad (1)$$

$$\partial q_2 / \partial t + J(\psi_2, q_2) = 0 \quad (2)$$

where subscripts 1 and 2 denote the top and bottom layers respectively (Pedlosky, 1979). The quasi-geostrophic potential vorticities are defined:

$$q_1 = \nabla^2 \psi_1 + \lambda_1^2 (\psi_2 - \psi_1) + \beta_1 y \quad (3)$$

$$q_2 = \nabla^2 \psi_2 + \lambda_2^2 (\psi_1 - \psi_2) + \beta_2 y \quad (4)$$

$$\lambda_1^2 = f_0^2 / g' D_1 \quad \text{and} \quad \lambda_2^2 = f_0^2 / g' D_2$$

are the inverses of the Rossby radii of deformation squared. And

$$\beta_1 = \beta(\text{planetary}) + \beta_{1s}(\text{sloping top boundary}) \quad (5)$$

$$\beta_2 = \beta(\text{planetary}) + \beta_{2s}(\text{sloping bottom boundary}) \quad (6)$$

By including sloping boundaries, the velocity shear and potential vorticity gradients can be independently varied.

2.2 Partitioning into ambient (function of y only) and disturbance fields:

The fields are partitioned into ambient (barred) and disturbance (primed) parts. Note that the disturbance is generally non-linear. We restrict the ambient fields to be functions of y only. Thus:

$$\psi_1 = \bar{\psi}_1(y) + \psi_1'(x, y, t) \quad (7)$$

$$\psi_2 = \bar{\psi}_2(y) + \psi_2'(x, y, t) \quad (8)$$

$$q_1(y) = \nabla^2 \bar{\psi}_1(y) + \lambda_1^2(\bar{\psi}_2 - \bar{\psi}_1) + \beta_1 y = -(u_1)_y + \lambda_1^2(\bar{\psi}_2 - \bar{\psi}_1) + \beta_1 y \quad (9)$$

$$q_2(y) = \nabla^2 \bar{\psi}_2(y) + \lambda_2^2(\bar{\psi}_1 - \bar{\psi}_2) + \beta_2 y = -(u_2)_y + \lambda_2^2(\bar{\psi}_1 - \bar{\psi}_2) + \beta_2 y \quad (10)$$

$$q_1' = \nabla^2 \psi_1' + \lambda_1^2(\psi_2' - \psi_1') \quad (11)$$

$$q_2' = \nabla^2 \psi_2' + \lambda_2^2(\psi_1' - \psi_2') \quad (12)$$

2.3 Disturbance equations:

We now define:

$$\bar{\beta}_1 = (q_1)_y = -(u_1)_{yy} + \lambda_1^2(u_1 - u_2) + \beta_1 \quad (13)$$

$$\bar{\beta}_2 = (q_2)_y = -(u_2)_{yy} + \lambda_2^2(u_2 - u_1) + \beta_2 \quad (14)$$

Note that $\bar{\beta}_1$ and $\bar{\beta}_2$ are simply the meridional gradients of ambient quasi-geostrophic potential vorticity. Recall that we are restricting all ambient variables to be functions only of y . Thus, $\bar{\beta}_1$ and $\bar{\beta}_2$ depend only on y . Equations 1 and 2 can now be written:

$$\left(\frac{\partial}{\partial t} + u_1 \frac{\partial}{\partial x} \right) q_1' + J(\psi_1', q_1' + \bar{\beta}_1 y) = 0 \quad (15)$$

$$\left(\frac{\partial}{\partial t} + u_2 \frac{\partial}{\partial x} \right) q_2' + J(\psi_2', q_2' + \bar{\beta}_2 y) = 0 \quad (16)$$

2.4 Scaling:

In this section, and hereafter, dimensional variables will be denoted with a * superscript and dimensionless variables will have no * superscript. We now define the Rossby radius of deformation for the baroclinic mode:

$$R^* = \sqrt{\frac{g^* H_1^* H_2^*}{f_0^2 (H_1^* + H_2^*)}}$$

We define dimensionless variables:

$$\begin{aligned} (x^*, y^*) &= [R^*] (x, y) & t^* &= [1/\beta^* R^*] t \\ (u^*, v^*) &= [\beta^* R^{*2}] (u, v) & (\psi_1^*, \psi_2^*) &= [\beta^* R^{*2}] (\psi_1, \psi_2) \end{aligned}$$

And we also define dimensionless $\bar{\beta}_1$ and $\bar{\beta}_2$.

$$(\bar{\beta}_1^*, \bar{\beta}_2^*) = [\beta^*] (\bar{\beta}_1, \bar{\beta}_2)$$

Finally, we define F_1 and F_2 , whose square roots are the ratios of the length scale to the Rossby radii of each layer. With R^* as the length scale, F_1 and F_2 considerably simplify:

$$F_1 = \lambda_1^{*2} R^{*2} = \frac{H_2^{*2}}{H_1^{*2} + H_2^{*2}} \quad F_2 = \lambda_2^{*2} R^{*2} = \frac{H_1^{*2}}{H_1^{*2} + H_2^{*2}}$$

With the above, $\bar{\beta}_1$ and $\bar{\beta}_2$, the meridional-gradients of ambient potential vorticity are:

$$\bar{\beta}_1 = 1 + \beta_{1s} + F_1 (u_1 - u_2) - (u_1)_{yy}$$

$$\bar{\beta}_2 = 1 + \beta_{2s} + F_2 (u_2 - u_1) - (u_2)_{yy}$$

where β_{1s} and β_{2s} are the scaled "slope betas", ie. $\beta_{1s} = \beta_{1s}^*/\beta^*$ and similarly for β_{2s} .

2.5 Scaled two layer equations:

With the scaling of the previous section and the restrictions that the ambient currents have zero second derivative in the meridional direction, our final system is:

$$\left(\frac{\partial}{\partial t} + u_1 \frac{\partial}{\partial x} \right) q_1' + J(\psi_1', q_1' + \bar{\beta}_1 y) = 0 \quad (17)$$

$$\left(\frac{\partial}{\partial t} + u_2 \frac{\partial}{\partial x} \right) q_2' + J(\psi_2', q_2' + \bar{\beta}_2 y) = 0 \quad (18)$$

where the dimensionless variables are:

$$\begin{aligned}\psi_1 &= \bar{\psi}_1 + \psi_1' & \psi_2 &= \bar{\psi}_2 + \psi_2' \\ u_1 &= -(\bar{\psi}_1)_y & u_2 &= -(\bar{\psi}_2)_y\end{aligned}$$

$$q_1' = \nabla^2 \psi_1' + F_1(\psi_2' - \psi_1')$$

$$q_2' = \nabla^2 \psi_2' + F_2(\psi_1' - \psi_2')$$

and

$$\bar{\beta}_1 = 1 + \beta_1 + F_1(u_1 - u_2)$$

$$\bar{\beta}_2 = 1 + \beta_2 + F_2(u_2 - u_1)$$

3 Solution Modes:

In this section we consider the various modes that are possible in our system.

3.1 Two equivalent methods:

As way of example, we contrast two equivalent ways of obtaining solutions for a one-layer equivalent barotropic system. The first way is the common method of specifying the form of solution and plugging this into the governing equation. The second method, by considering the form of zonally propagating solutions, specifies the potential vorticity as an arbitrary function of $\Psi + cy - ay$.

In this section we are considering a one layer equivalent barotropic system with constant zonal current, u . The governing equation is:

$$\left(\frac{\partial}{\partial t} + u \frac{\partial}{\partial x} \right) q + J(\psi, q + \beta y) = 0 \quad (19)$$

where

$$q = \nabla^2 \psi - F\psi$$

We are looking for zonally propagating solutions and hence of the form:

$$\psi(x, y, t) = \Psi(X, y) \quad \text{where } X = (x - ct)$$

Applying the chain rule and simplifying:

$$\begin{aligned}\psi_x &= \Psi_X \\ \psi_y &= \Psi_y \\ \nabla^2 \psi &= \Psi_{XX} + \Psi_{yy} \\ \psi_t &= -c\Psi_X\end{aligned}$$

3.1.1 Method I:

Consider solutions where

$$\Psi_{xx} + \Psi_{yy} = K^2(\Psi)$$

Substituting in equation 19, we obtain:

$$\Psi_X [(u - c)(K^2 - F) + \beta] = 0 \quad (20)$$

relating c and K . If K is imaginary, (ie. $K^2 < 0$), and we define:

$$\tilde{K} = K/i$$

we obtain the familiar Rossby wave zonal phase speed relation:

$$c = u - \frac{\beta}{\tilde{K}^2 + F} \quad (21)$$

We call these the "wave" modes, and forms of solutions are:

$$\begin{aligned} \psi &= \Re \left(e^{i(k(x-ct)+ly)} \right) \quad \text{where } \tilde{K}^2 = k^2 + l^2 \\ \psi &= J_n(\tilde{K}r) \\ \psi &= J_n(\tilde{K}r)(c_1 \cos(n\theta) + c_2 \sin(n\theta)) \\ \psi &= Y_n(\tilde{K}r) \\ \psi &= Y_n(\tilde{K}r)(c_1 \cos(n\theta) + c_2 \sin(n\theta)) \end{aligned}$$

where $r = \sqrt{(x-ct)^2 + y^2}$, $\theta = \arctan(y/(x-ct))$, and J and Y are Bessel functions.

If K is real, we obtain what we will call the "exponential" modes. We obtain the following:

$$c = u + \frac{\beta}{K^2 - F} \quad (22)$$

Forms of solution are:

$$\begin{aligned} \psi &= e^{(k(x-ct)+ly)} \quad \text{where } K^2 = k^2 + l^2 \\ \psi &= K_0(Kr) \\ \psi &= K_n(Kr)(c_1 \cos(n\theta) + c_2 \sin(n\theta)) \\ \psi &= I_0(Kr) \\ \psi &= I_n(Kr)(c_1 \cos(n\theta) + c_2 \sin(n\theta)) \end{aligned}$$

where r and θ are defined as above and K and I are modified Bessel functions.

3.1.2 Method II:

With our definition of $\Psi(X, y)$ and the chain rule relations, equation 19 can be written:

$$J(\Psi + cy - ay, q + \beta y) = 0 \quad (23)$$

Hence, any Ψ satisfying:

$$q + \beta y = \mathcal{F}(\Psi + cy - ay) \quad (24)$$

is a solution. If Ψ and q approach zero, then the limiting form of equation 24 is:

$$\beta y = \mathcal{F}(cy - ay)$$

and thus the form of \mathcal{F} is simply a constant, b , multiplying its argument:

$$b = \frac{\beta}{(c - a)}$$

Our equation for Ψ , equation 24, simplifies to:

$$\underbrace{\Psi_{xx} + \Psi_{yy}}_r - F\Psi = b(\Psi) \quad (25)$$

Again, considering solutions where

$$\Psi_{xx} + \Psi_{yy} = K^2(\Psi)$$

we obtain:

$$K^2 = b + F$$

If $(b + F) > 0$, then we obtain the "exponential" modes of the previous section. If $(b + F) < 0$, then we obtain the "wave" modes.

The motivation for this second method is this. By considering equation 24 with \mathcal{F} of the linear form of $b(\cdot)$ it is clear that superpositions of solutions are solutions. We can add any number of the "wave" or "exponential" modes and still have an exact steadily propagating solution.

3.2 Solution modes in two-layer system:

In this section we use method I to obtain the solutions to the two layer quasi-geostrophic system. It should be stressed that the identical solutions could be obtained by method II and therefore a superposition of modes for one particular c are exact solutions. Henceforth, we will take the current in the bottom layer, u_2 , to be zero, and consider only cases where $u_1 \stackrel{\text{def}}{=} U$ is a constant. With these restrictions and dropping primes we have from section 2.5:

$$\left(\frac{\partial}{\partial t} + O \frac{\partial}{\partial x} \right) q_1 + J(\psi_1, q_1 + \bar{\beta}_1 y) = 0 \quad (20)$$

$$\left(\frac{\partial}{\partial t} \right) q_2 + J(\psi_2, q_2 + \bar{\beta}_2 y) = 0 \quad (27)$$

where

$$q_1 = \nabla^2 \psi_1 + F_1(\psi_2 - \psi_1)$$

$$q_2 = \nabla^2 \psi_2 + F_2(\psi_1 - \psi_2)$$

and

$$\bar{\beta}_1 = 1 + \beta_1 + F_1(O)$$

$$\bar{\beta}_2 = 1 + \beta_2 - F_2(O)$$

Again, we are considering steady, zonally propagating solutions where:

$$\begin{aligned} \psi_1(x, y, t) &= \Psi_1(X, y) \quad \text{and} \\ \psi_2(x, y, t) &= \Psi_2(X, y) \quad \text{where } X = (x - ct) \end{aligned}$$

For a particular mode we take:

$$\Psi_1 = A_1 \Psi(X, y) \quad \Psi_2 = A_2 \Psi(X, y)$$

where

$$(\Psi)_{xx} + (\Psi)_{yy} = K^2(\Psi)$$

Plugging this into equations 26 and 27 and using the chain rule relations we obtain:

$$\begin{pmatrix} (O - c)(K^2 - F_1) + \bar{\beta}_1 & (O - c)F_1 \\ -cF_2 & -c(K^2 - F_2) + \bar{\beta}_2 \end{pmatrix} \begin{pmatrix} A_1 \Psi_X \\ A_2 \Psi_X \end{pmatrix} = \begin{pmatrix} 0 \\ 0 \end{pmatrix} \quad (28)$$

For the above system of equations to hold for non-trivial solutions the determinant of the matrix must be zero. To satisfy this, for a given K^2 , we obtain a quadratic equation in c and hence two possible modes (two different c 's). After the appropriate algebra:

$$c = \frac{O}{2} + \frac{\left((K^2 - F_1)\bar{\beta}_2 + (K^2 - F_2)\bar{\beta}_1 \right) \pm \sqrt{ARG}}{2K^2(K^2 - F_1 - F_2)} \quad (29)$$

with

$$ARG = \left\{ (K^2 - F_2)\bar{\beta}_1 - (K^2 - F_1)\bar{\beta}_2 + OK^2(K^2 - F_1 - F_2) \right\}^2 + 4F_1F_2\bar{\beta}_1\bar{\beta}_2$$

Also, from equations 28 we obtain a relationship for A_2/A_1 for each mode.

In figures 1 - 5 are plotted the propagation speed (C) and A_2/A_1 vs K for the two modes. In each figure, the two plots to the left are the "exponential" modes (ie. $K^2 > 0$, K real). And to the right are the "wave" modes (ie. $K^2 < 0$, K imaginary). Note that the abscissas of the "wave" mode plots should really be labeled K , the imaginary part K .

In figure 1, note the "exponential" baroclinic mode (solid curve). As

$$K \rightarrow 1^+, \quad c \rightarrow +\infty$$

$$K \rightarrow 1^-, \quad c \rightarrow -\infty$$

This is associated with the fact that $\nabla^2\Psi$, the relative vorticity and $-F(\Psi)$, the stretching vorticity are of opposite sign and can cancel, unlike the "wave" modes where the relative vorticity and the stretching term are of same sign.

Figure 1 is the standard two-layer beta plane case. $\bar{U} = 0$ and both top and bottom boundary are flat. In this case, we clearly have barotropic modes ($A_2/A_1 = 1$) and baroclinic modes ($A_2/A_1 = -1$) for all K . In the subsequent cases, we see that the relative amplitude of the two layers is dependent on wave number, K .

The parameters for figures 2-4 correspond to increasing ambient baroclinicity with flat boundaries. In figure 4, $\bar{U} = 2.0$. For $\bar{U} > 2$ we have baroclinic instability (Phillips Model). The modes grow with time and there are no steady solutions. A highly idealized explanation for the $\bar{U} = 2.0$ limit is as follows: If you have heating in the tropics, the analog for the two layer model is to decrease the depth of the lower (denser) layer and increase the depth of the upper (lighter) layer. With the constraints of no bottom layer current, and rigid, level boundaries, the parameters of figures 2-4 obtain. In the same way that a dry atmosphere heated below ideally would equilibrate to a dry adiabat, the ambient two-layer state, ideally would equilibrate to $\bar{U} = 2$, $\bar{\beta}_1 = 2$, $\bar{\beta}_2 = 0$. Figure 5 is the case where the top boundary slopes. Going further out on a limb, one could draw the analogy to the tropopause, which does slope in the same sense as Fig. 5 parameters. The tropopause is not a rigid boundary but may act somewhat like one.

Note that figure 3 is included basically to illustrate the way that figure 4 is approached. The sharp corners of figure 4 are not so surprising when you consider that this case is just on the edge of baroclinic instability.

4 Dipole Solutions:

In this section we obtain solutions that are essentially point vortex pairs. The solutions are a superposition of K_0 "exponential" modes. There is a difficulty with superposing K_0 modes. The K_0 modes include a singularity at $r = 0$. To obtain valid solutions, an interior solution, valid for $r < \epsilon$, is matched to the K_0 exterior solutions, valid for $r > \epsilon$. In the limit as $\epsilon \rightarrow 0$ the interior solution approaches a point vortex and the matching condition becomes that the local velocity, at the point vortex, is equal to the propagation speed. (Flierl, Larichev, McWilliams, Reznik, 1980; Flierl, 1987)

4.1 Modal solutions for two layers, Method II:

Substituting Ψ_1 and Ψ_2 as defined in section 3.2 in equations 26 and 27 we obtain:

$$J(\Psi_1 + cy - Uy, q_1 + \tilde{\beta}_1 y) = 0 \quad (30)$$

$$J(\Psi_2 + cy, q_2 + \tilde{\beta}_2 y) = 0 \quad (31)$$

Hence, any Ψ_1, Ψ_2 satisfying:

$$q_1 + \tilde{\beta}_1 y = \mathcal{F}_1(\Psi_1 + cy - Uy) \quad (32)$$

$$q_2 + \tilde{\beta}_2 y = \mathcal{F}_2(\Psi_2 + cy) \quad (33)$$

is a solution. If Ψ_1, Ψ_2, q_1, q_2 approach zero, then the limiting form of equations 32 and 33 are:

$$\tilde{\beta}_1 y = \mathcal{F}_1(cy - Uy)$$

$$\tilde{\beta}_2 y = \mathcal{F}_2(cy)$$

Thus, the form of both \mathcal{F}_1 and \mathcal{F}_2 are constants, b_1, b_2 , multiplying their arguments:

$$b_1 = \frac{\tilde{\beta}_1}{(c-U)} \quad b_2 = \frac{\tilde{\beta}_2}{c}$$

Equations 32 and 33 simplify to:

$$\underbrace{\nabla^2 \Psi_1 + F_1(\Psi_2 - \Psi_1)}_{\eta_1} = b_1(\Psi_1) \quad (34)$$

$$\underbrace{\nabla^2 \Psi_2 + F_2(\Psi_1 - \Psi_2)}_{\eta_2} = b_2(\Psi_2) \quad (35)$$

where

$$\nabla^2 \equiv \left(\frac{\partial^2}{\partial X \partial X} + \frac{\partial^2}{\partial y \partial y} \right)$$

Again, we stress that equations 34 and 35 are linear and we can superpose solutions. Taking

$$\begin{aligned}\Psi_1 &= A_1 \Psi(X, y) & \Psi_2 &= A_2 \Psi(X, y) \\ \nabla^2 \Psi &= K^2 \Psi\end{aligned}$$

equations 34 and 35 can be written in matrix form:

$$\begin{pmatrix} ((K^2 - F_1 - b_1) & F_1 \\ F_2 & (K^2 - F_2 - b_2) \end{pmatrix} \begin{pmatrix} A_1 \Psi_N \\ A_2 \Psi_N \end{pmatrix} = \begin{pmatrix} 0 \\ 0 \end{pmatrix} \quad (30)$$

From the requirement that the determinant in 30 equal zero, we obtain a quadratic for K^2 and:

$$K^2 = \frac{(F_1 + F_2 + b_1 + b_2)}{2} \pm \sqrt{ARG} \quad (37)$$

where

$$ARG = (F_1 + F_2)^2 + (b_1 - b_2)^2 + 2.0(F_1 - F_2)(b_1 - b_2)$$

Also, for each K^2 we have:

$$\begin{aligned}A_2/A_1 &= (-1.0(K^2 - F_1 - b_1))/F_1 \\ &= (-1.0 F_2)/(K^2 - F_2 - b_2)\end{aligned} \quad (38)$$

4.2 Final form of Dipole Solutions:

From section 4.1, the specification of the propagation speed, c , determines b_1 and b_2 and subsequently two modes with

$$\begin{aligned}k_1 &\stackrel{\text{def}}{=} K & (\text{one value from eqn. 37}) \\ k_2 &\stackrel{\text{def}}{=} K & (\text{other value from eqn. 37})\end{aligned}$$

For each mode, the relative amplitudes of each layer are specified by equation 38.

We choose as our modal solutions K_n modified bessel functions. The governing equations are translation invariant and therefore we can arbitrarily specify the origin ($r=0$) of each mode. By the linearity of equations 34 and 35 we can superpose any number of modes, for one value of c . We define radial coordinates:

$$\begin{aligned}r^u &\stackrel{\text{def}}{=} \sqrt{(x - ct)^2 + (y + \Delta/2)^2} \\ r^l &\stackrel{\text{def}}{=} \sqrt{(x - ct)^2 + (y - \Delta/2)^2}\end{aligned}$$

The final form of the disturbance field is now written:

$$\begin{aligned}\Psi_1 &= s'' \left\{ u_1^{k_1} [K_0(k_1 r'')] + u_1^{k_2} [K_0(k_2 r'')] \right\} + s' \left\{ \mathcal{L}_1^{k_1} [K_0(k_1 r')] + \mathcal{L}_1^{k_2} [K_0(k_2 r')] \right\} \\ \Psi_2 &= s'' \left\{ u_2^{k_1} [K_0(k_1 r'')] + u_2^{k_2} [K_0(k_2 r'')] \right\} + s' \left\{ \mathcal{L}_2^{k_1} [K_0(k_1 r')] + \mathcal{L}_2^{k_2} [K_0(k_2 r')] \right\}\end{aligned}$$

We have written the solution in two parts with s'' multiplying the part comprised of modes with origin:

$$(x = ct, y = -\Delta/2) \quad \text{def} \quad \bar{U}$$

and s' multiplying the part comprised of modes with origin:

$$(x = ct, y = \Delta/2) \quad \text{def} \quad \bar{\mathcal{L}}$$

We choose the four coefficients, $u_1^{k_1}$, $u_1^{k_2}$, $u_2^{k_1}$, and $u_2^{k_2}$ such that in the limit $r'' \rightarrow 0$:

- The s'' part of the solution approaches a point vortex of strength s'' in the upper layer at point \bar{U}
- The lower layer singularities cancel.

The azimuthal velocity associated with $K_0(kr)$ is the radial derivative, $kK_1(kr)$, which in the small r limit approaches $-1/r$. Our criteria are thus:

$$u_1^{k_1} + u_1^{k_2} = -1/2\pi \quad (39)$$

$$u_2^{k_1} + u_2^{k_2} = 0 \quad (40)$$

Equation 38 for k_1 and k_2 determines $u_2^{k_1}/u_1^{k_1}$ and $u_2^{k_2}/u_1^{k_2}$. These four conditions determine the four U coefficients.

Similarly, the four \mathcal{L} coefficients are chosen so have a point vortex of strength s' in the lower layer at point $\bar{\mathcal{L}}$ and singularity cancellation in the top layer:

$$\mathcal{L}_1^{k_1} + \mathcal{L}_1^{k_2} = 0 \quad (41)$$

$$\mathcal{L}_2^{k_1} + \mathcal{L}_2^{k_2} = -1/2\pi \quad (42)$$

Again, equation 38 specifies $\mathcal{L}_2^{k_1}/\mathcal{L}_1^{k_1}$ and $\mathcal{L}_2^{k_2}/\mathcal{L}_1^{k_2}$.

Finally, s_u and s_l are determined by demanding that the local velocities at the singularities be equal to the propagation speed. Remember, Ψ_1 and Ψ_2 as defined in section 3.2 are the disturbance fields. The top layer, layer 1, includes O :

$$O = s' \left\{ \mathcal{L}_1^{k_1} [K_0(k_1 r')] + \mathcal{L}_1^{k_2} [K_0(k_2 r')] \right\}_y = c \quad (x = ct, y = -\Delta/2) \quad (43)$$

$$-s'' \left\{ u_2^{k_1} [K_0(k_1 r'')] + u_2^{k_2} [K_0(k_2 r'')] \right\}_y = c \quad (x = ct, y = \Delta/2) \quad (44)$$

where the y subscripts indicate that a partial derivative w.r.t y is to be taken. By aligning the two point vortices as we have there are only zonal currents at the singularities. The y derivatives are easily related to radial derivatives:

$$0 = s^l \left\{ \mathcal{L}_1^{k_1}(k_1) |K_1(k_1 \Delta)| + \mathcal{L}_1^{k_2}(k_2) |K_1(k_2 \Delta)| \right\} = c \quad (45)$$

$$s^u \left\{ \mathcal{U}_2^{k_1}(k_1) |K_1(k_1 \Delta)| + \mathcal{U}_2^{k_2}(k_2) |K_1(k_2 \Delta)| \right\} = c \quad (46)$$

We briefly review the solution method:

- The ambient state is specified by: F_1 , F_2 , \bar{U} , $\bar{\beta}_1$, and $\bar{\beta}_2$.
- The propagation speed, c , and the ambient state determine b_1 , b_2 , k_1 , k_2 and the \mathcal{U} and \mathcal{L} coefficients.
- The meridional distance between the two vortices, Δ , determines s^u and s^l and this completes the specification of a solution.

5 Dipole Solutions, Discussion:

5.1 Strengths of vortices vs. c and Δ :

In the top half of figures 6-11 are plotted the two vortex strengths as a function of propagation speed, c , and the meridional distance between the vortices, Δ . The values of Δ are written along the curves. In the bottom half, the wave numbers and corresponding values of $A2/A1$ for the two modes are plotted as a function of propagation speed.

Figures 6 and 7 are for the standard two layer case, $\bar{U} = 0$. In figure 6 curves are drawn for Δ between 0.5 and 3.5. In figure 7, Δ varies between 0.1 and 0.5. Figures 5 and 7 reflect the same parameter values as figure 1. Referring to fig. 6, we see that for larger values of c , the effect of β diminishes and we see the intuitive result that the propagation speed is greater for stronger vortices. And for a fixed strength, propagation speeds are larger for vortices close together. The solution bears similarities to vortex pairs in one layer, no β . For smaller c , the effect of β becomes important. For modes that propagate slowly, the relative vorticity must dominate the planetary vorticity. Thus, the wave numbers are large. The larger the wave number, the more quickly the velocities fall off away from the point vortex. From figure 1, we see that as $c \rightarrow 0$, $K \rightarrow \infty$. Thus, we see the vortex strengths growing arbitrarily large as $c \rightarrow 0$. Note that the leftmost propagation speed plotted in figures 6 and 7 is $c = .01$, and therefore k_1 and k_2 are finite.

Figure 8 is for $\bar{U} = 1.0$, $\bar{\beta}_1 = 1.5$, $\bar{\beta}_2 = 0.5$. The relevant previous figure is figure 2. Figures 9 and 10 are for the case $\bar{U} = 2.0$, $\bar{\beta}_1 = 2.0$, $\bar{\beta}_2 = 0.0$; refer to figure 4. For these cases the strength of the upper layer vortex is larger.

The upper layer vortex solution is the only current advecting the lower layer vortex, whereas the upper layer vortex is advected by U as well as the lower layer vortex solution. For small c , $\tilde{\beta}_1 > \tilde{\beta}_2$ becomes significant.

Figure 11 is for the case of no U , but sloping upper boundary and therefore $\tilde{\beta}_1 > \tilde{\beta}_2$. The vortex strength plots are very similar to figure 6, with double the strengths, yet equal strengths in each layer. In the next section, we will see that the structure of the vortices differ, however.

5.2 Streamlines and Streaklines:

In figures 12-17 are plotted Ψ and $\Psi + cy$ for some exemplary solutions. The Ψ field are streamlines and determine velocities in a fixed frame. The $\Psi + cy$ fields are called streaklines and determine the velocities relative to a frame moving at the propagation speed. In all cases the domain is 10 by 10 (non-dimensional length, see section 2.4). Note that all solutions have singularities. The solutions in regions near the singularities are clipped.

Figures 12 and 13 are for the standard two layer case, $U = 0$. These two solutions show that two propagation speeds are possible with the vortex strengths and Δ remaining equal. The wavenumbers and corresponding horizontal scale of the solutions are different.

Figures 14, 15 and 16 are for cases with U and consequently stronger vortices in the top layer. Comparison of figures 14 and 15 shows the general trend of more symmetric solutions for larger c .

Finally, figure 17 is the case of no U , but sloping upper boundary. The strengths of the vortices are equal but it can be seen that the upper and lower layer solutions are not exact reflections of each other. Compare to figure 13.

6 Conclusion:

As previously stated, the solutions presented have little to do with hurricanes. They do indicate dynamical interactions that are important in a model that will be further studied with regard to cyclone motion. Solutions that are propagating, steady, isolated and unforced in a β plane can be shown to be limited to east-west propagation.

A hurricane is certainly forced. A direction for future work is to include a parameterization of convective forcing and search for steady propagating solutions that are therefore not limited to zonal motion. This introduces the complication of Rossby wave radiation and associated radiation conditions, but we speculate that this is both realistic and an essential part of the dynamics.

Finally, we express the concern that the steady constraint may be unrealistic; it may be necessary to consider propagating solutions that vary with time. A related concern is that a realistic hurricane solution might slowly influence a

larger and larger region of the large scale environment.

ACKNOWLEDGMENTS

I would like to thank all who contributed to making the 1988 Summer Study Program at Woods Hole uniquely challenging and enlightening. I thank especially Glenn Flierl for his patient guidance regarding this project.

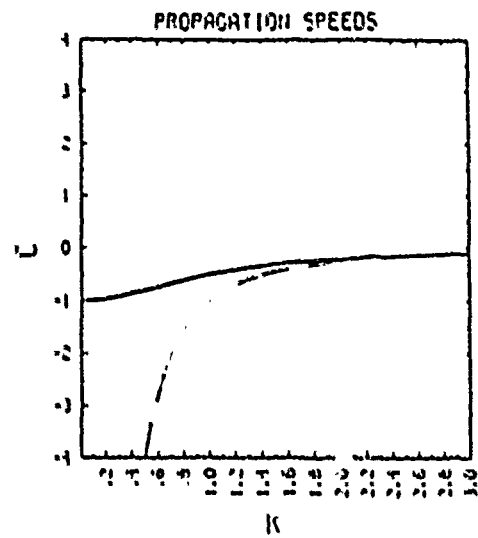
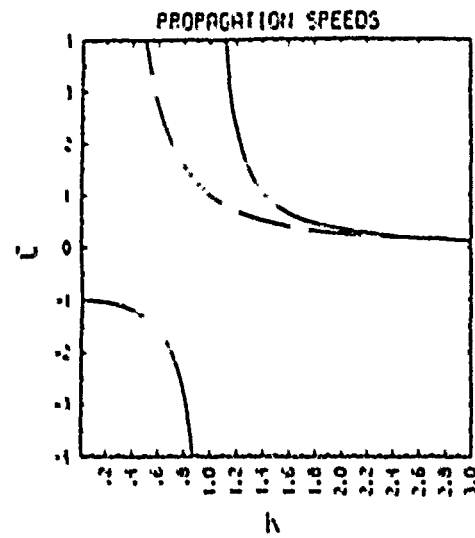
REFERENCES

- Flierl, G. R., Larichev, V. D., McWilliams, J. C., Resnik, G. M. 1980. The Dynamics of Baroclinic and Barotropic Solitary Eddies. *Dyn. Atmos. Oceans* 5: 1-41
- Flierl, G. R., 1987. Isolated Eddy Models in Geophysics. *Ann. Rev. Fluid Mech.* 19:493-530
- Pedlosky, J. 1979. *Geophysical Fluid Dynamics*. Berlin : Springer-Verlag. 629 pp.
- Schubert, W. H., Alworth, B. T. 1987. Evolution of Potential Vorticity in Tropical Cyclones. *17th Conference on Hurricanes and Tropical Meteorology* American Meteorological Society. pp. 324-328

"EXP." MODES

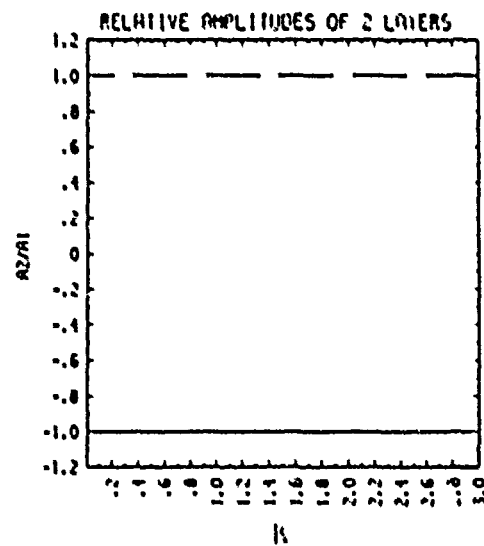
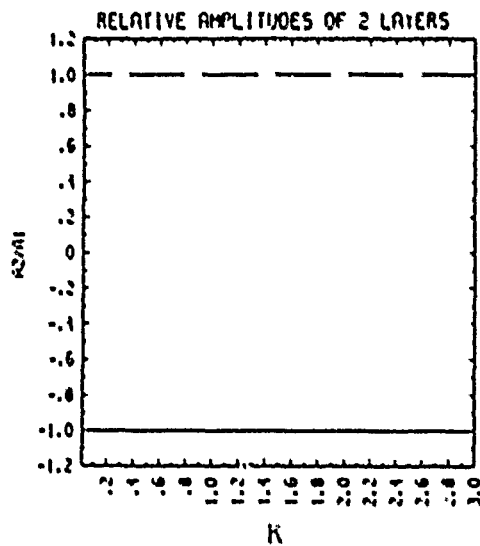
"WAVE" MODES

181



$$\begin{aligned}\bar{U} &= 0.00 \\ \bar{\beta}_1 &= 1.00 \\ \bar{\beta}_2 &= 1.00\end{aligned}$$

$$\begin{aligned}\bar{\beta}_{1y} &= 0.00 \\ \bar{\beta}_{2y} &= 0.00\end{aligned}$$



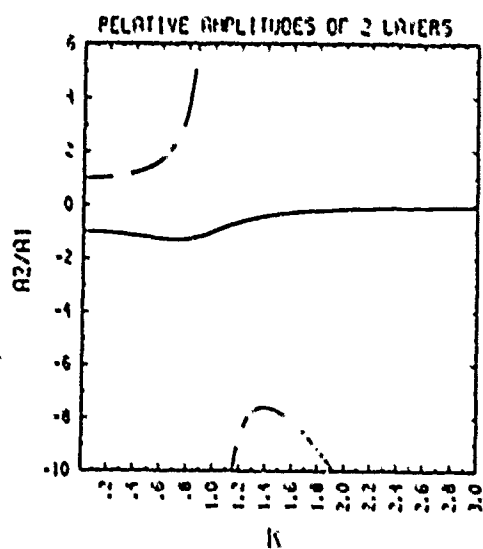
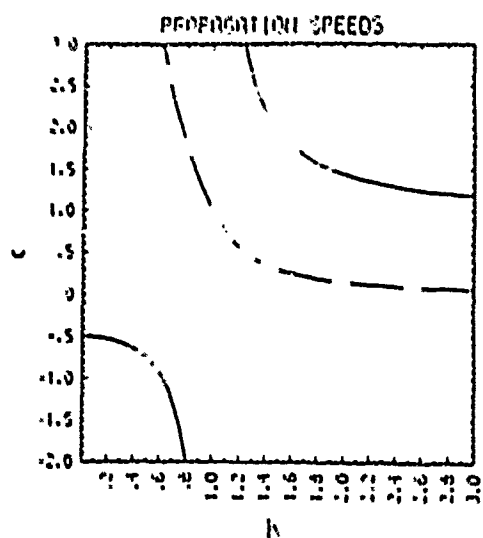
$$\begin{aligned}H_1 &= 1.00 \\ H_2 &= 1.00 \\ F_1 &= 0.50 \\ F_2 &= 0.50\end{aligned}$$

Fig. 1. Propagation Speed (C) and Relative Amplitude of the Solution in the Two Layers vs. "wave number" for steady, propagating modes.

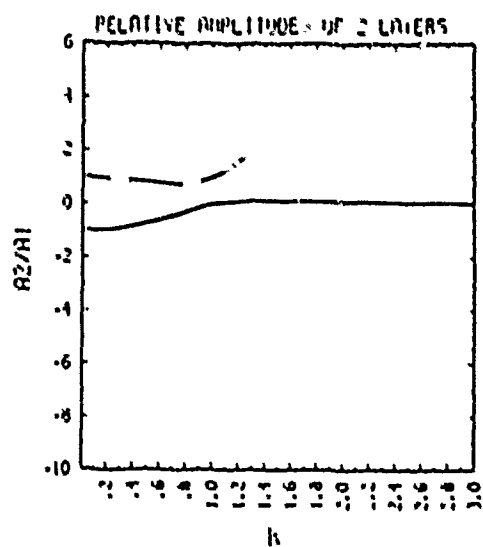
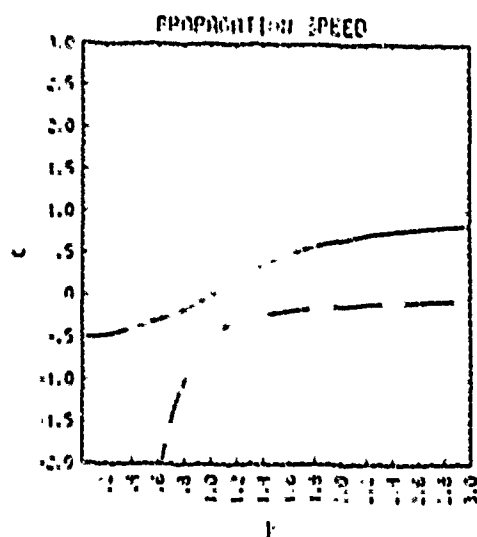
$\bar{U} = 0$ and the effective betas in both layers ($\bar{\beta}_1$ and $\bar{\beta}_2$) are equal to the planetary beta. Flat boundaries.

The wave modes are the familiar Rossby Waves for a QG two-layer model (Pedlosky, 1979)

EXP. MODES



WAVE MODES



$$\bar{U} = 1.0$$

$$\bar{\beta}_1 = 1.5$$

$$\bar{\beta}_2 = 0.50$$

$$\bar{\beta}_3 = 0.00$$

$$\bar{\beta}_4 = 0.0$$

$$H_1 = 1.0$$

$$H_2 = 1.00$$

$$\Gamma_1 = 0.50$$

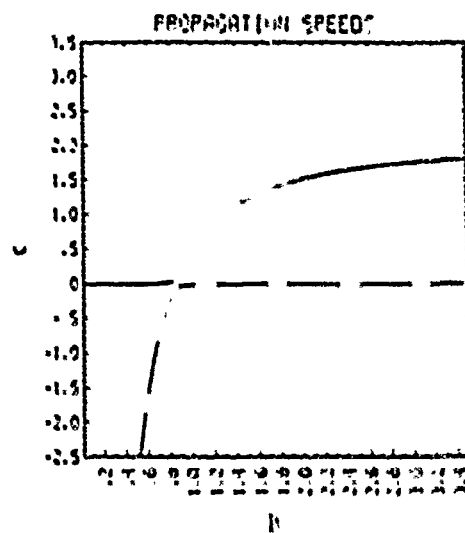
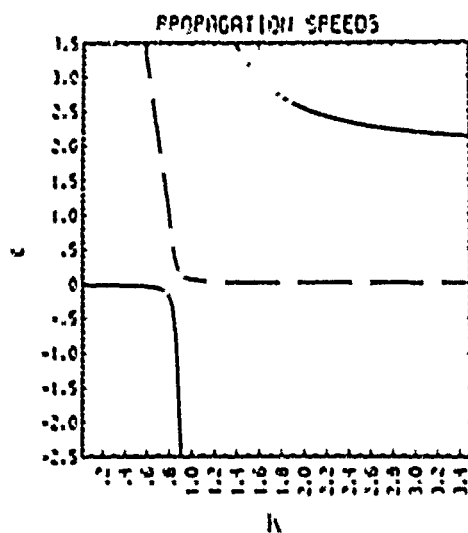
$$\Gamma_2 = 0.5$$

Fig. 2. Propagation Speed (C) and Relative Amplitude of the Solution in the Two Layers vs. "wave number" for steady, propagating modes.
 $\bar{U} = 1.0$ and the effective betas ($\bar{\beta}_1$ and $\bar{\beta}_2$) are 1.5 and 0.5. Flat boundaries.

"EXP." MODES

"WAVE" MODES

183



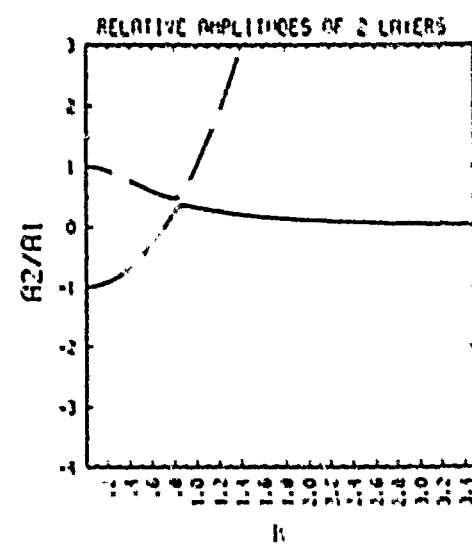
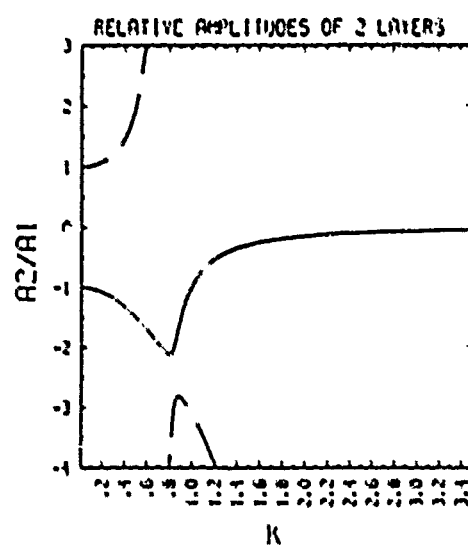
$$\bar{U} = 1.96$$

$$\bar{\beta}_1 = 1.98$$

$$\bar{\beta}_2 = 0.02$$

$$\bar{H}_1 = 0.00$$

$$\bar{H}_2 = 0.00$$



$$H_1 = 1.00$$

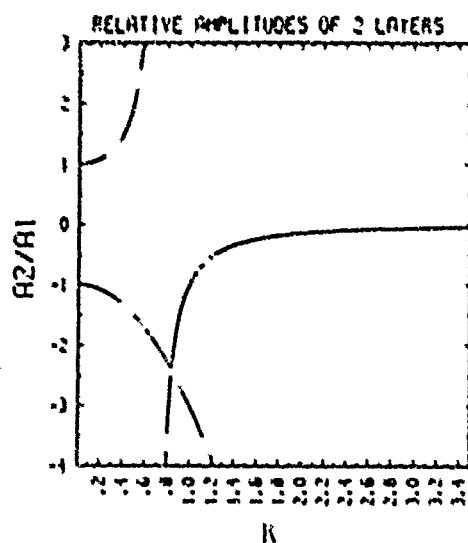
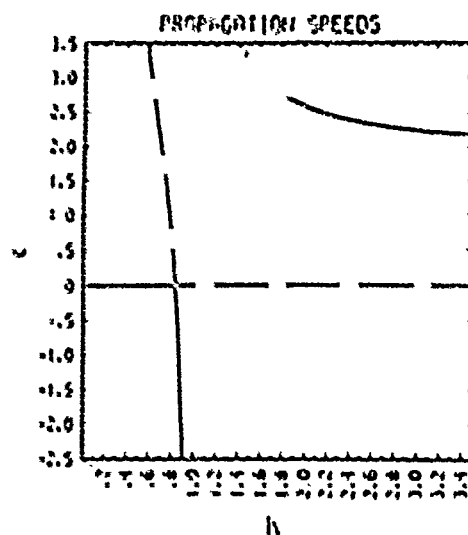
$$H_2 = 1.00$$

$$F_1 = 0.50$$

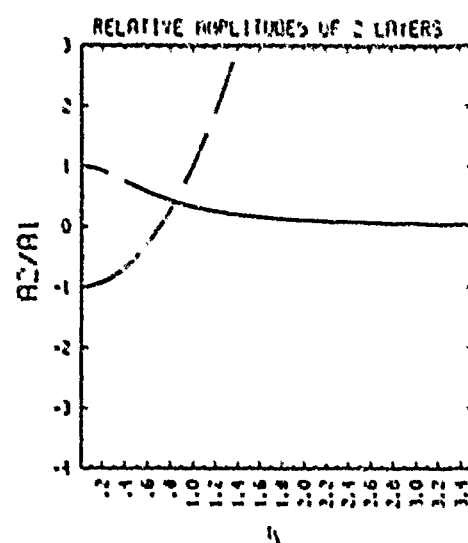
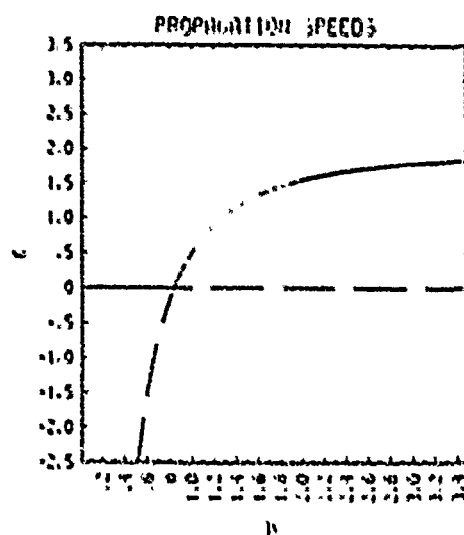
$$F_2 = 0.50$$

Fig. 3. Propagation Speed (C) and Relative Amplitude of the Solution in the Two Layers vs. "wave number" for steady, propagating modes. $\bar{U} = 1.96$ and the effective betas ($\bar{\beta}_1$ and $\bar{\beta}_2$) are 1.98 and 0.02. Flat boundaries. This figure should be compared to figure 4 where $\bar{U} = 2.0$. Recall that for $\bar{U} > 2.0$ the solutions are baroclinically unstable.

"EXP." MODES



"WAVE" MODES



$$\bar{U} = 2.00$$

$$\bar{\beta}_1 = 2.00$$

$$\bar{\beta}_2 = 0.00$$

$$\bar{U}_m = 0.00$$

$$\bar{U}_m = 0.00$$

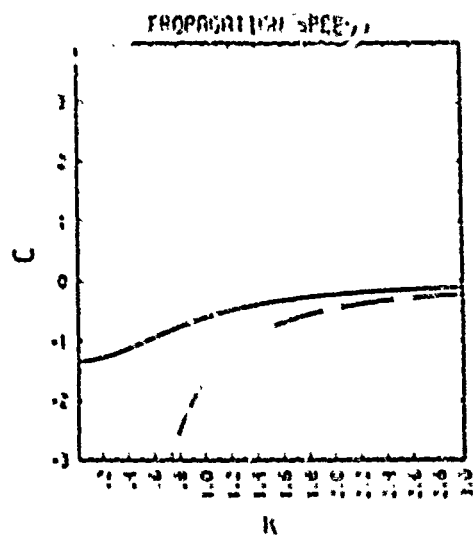
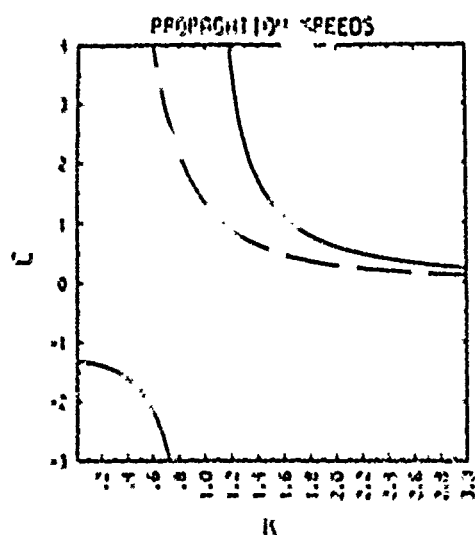
$$H_1 = 1.00$$

$$H_2 = 1.00$$

$$F_1 = 0.50$$

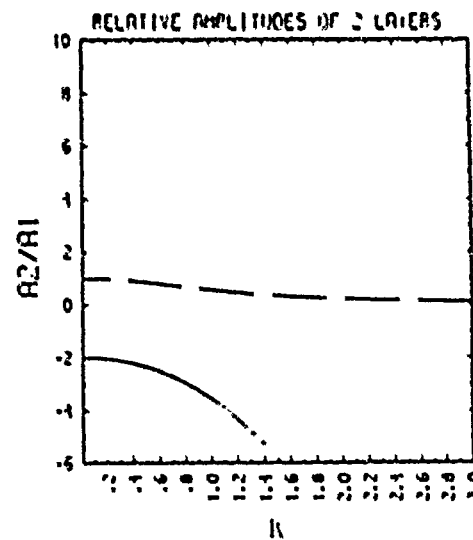
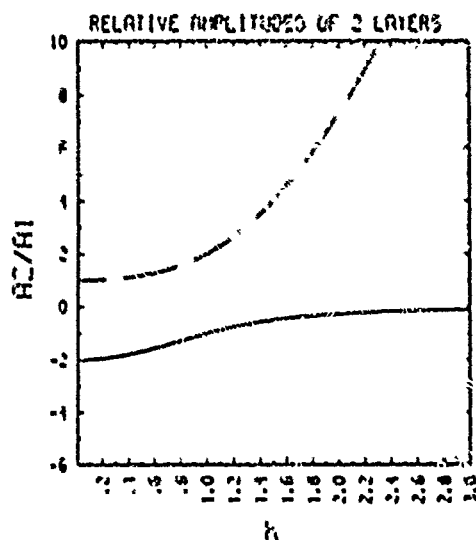
$$F_2 = 0.50$$

Fig. 4. Propagation Speed (C) and Relative Amplitude of the Solution in the Two Layers vs. "wave number" for steady, propagating modes.
 $\bar{U} = 2.0$ and the effective betas ($\bar{\beta}_1$ and $\bar{\beta}_2$) are 2.0 and 0.0. Flat boundaries.
 Recall, $\bar{U} > 2.0$ results in baroclinic instability.



$U = 0.00$
 $\tilde{\beta}_1 = 2.00$
 $\tilde{\beta}_2 = 1.00$

$\tilde{\beta}_1 = 1.00$
 $\tilde{\beta}_2 = 0.00$



$H_1 = 1.00$
 $H_2 = 1.00$
 $F_1 = 0.50$
 $F_2 = 0.50$

Fig. 5. Propagation Speed (C) and Relative Amplitude of the Solution in the Two Layers vs. "wave number" for steady, propagating modes. $U = 0.0$ and the effective betas ($\tilde{\beta}_1$ and $\tilde{\beta}_2$) are 2.0 and 1.0. Sloping top boundary.

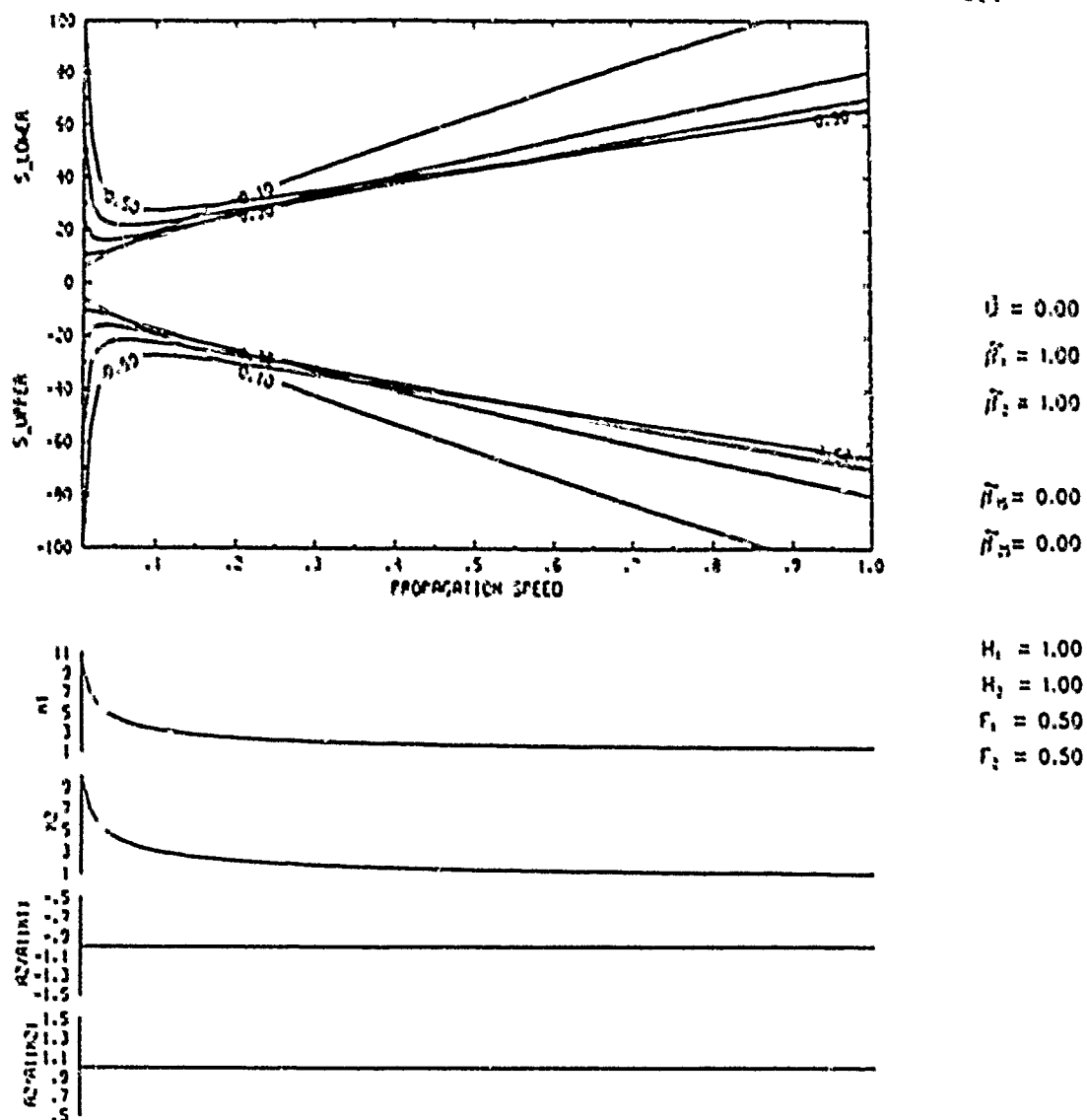


Fig. 7. TOP HALF: The upper and lower vortex strengths vs. propagation speed and Δ for steady, eastward propagating dipole solutions. The values written along the curves are Δ , the meridional distance between the vortices. BOTTOM HALF: Wave numbers and corresponding values of A_2/A_1 for the two modes vs. propagation speed.

$U = 0$ and the effective betas in both layers ($\bar{\beta}_1$ and $\bar{\beta}_2$) are equal to the planetary beta. Flat boundaries. Note that fig. 6 is for same parameter values except different Δ values. (Also, see fig. 1)

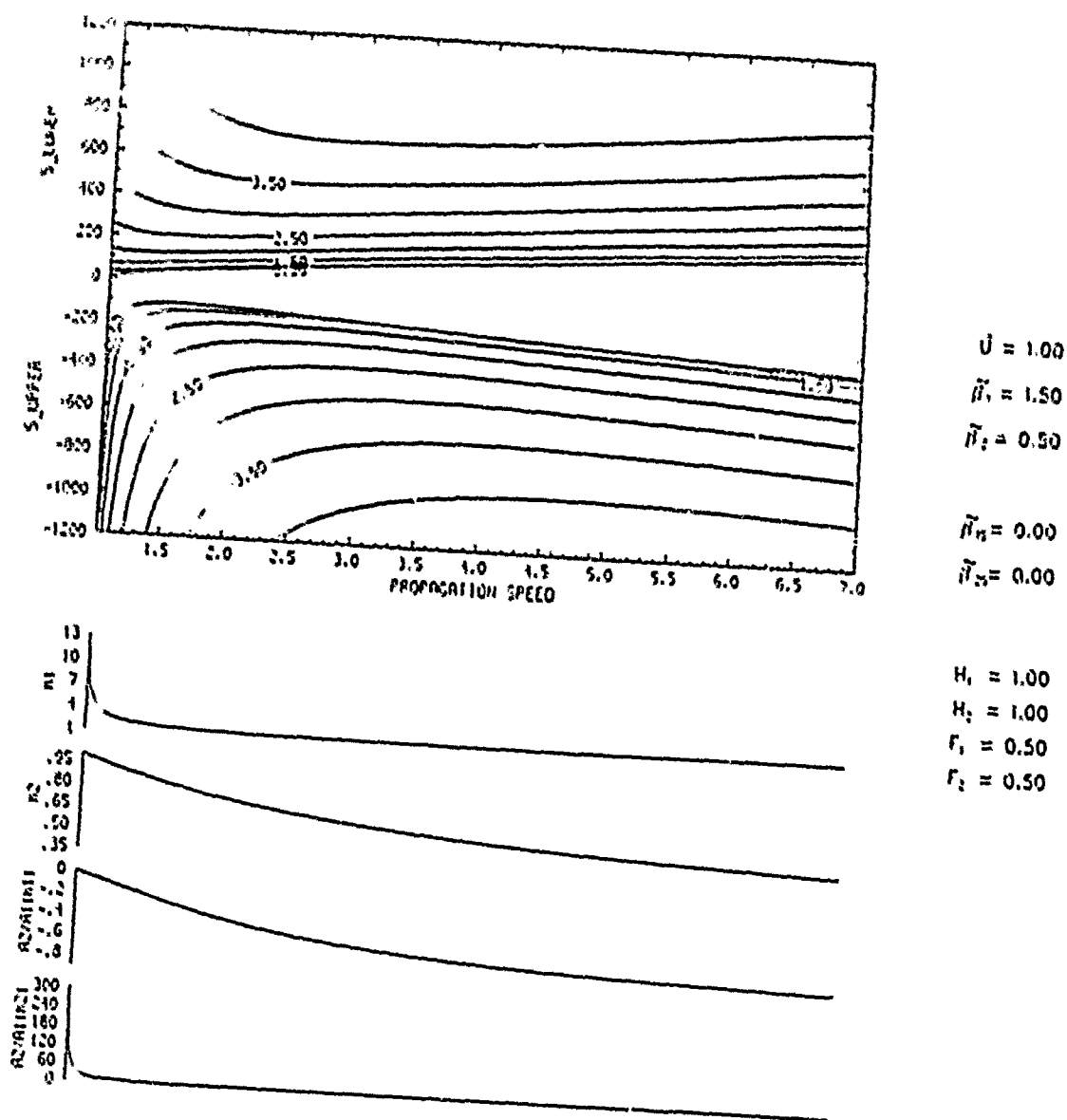


Fig. 8. TOP HALF: The upper and lower vortex strengths vs. propagation speed and Δ for steady, eastward propagating dipole solutions. The values written along the curves are Δ , the meridional distance between the vortices. BOTTOM HALF: Wave numbers and corresponding values of $A2/A1$ for the two modes vs. propagation speed.

$\bar{U} = 1.0$ and effective betas ($\bar{\beta}_1$ and $\bar{\beta}_2$) are 1.5 and 0.5. Flat boundaries. (Also, see fig. 2)

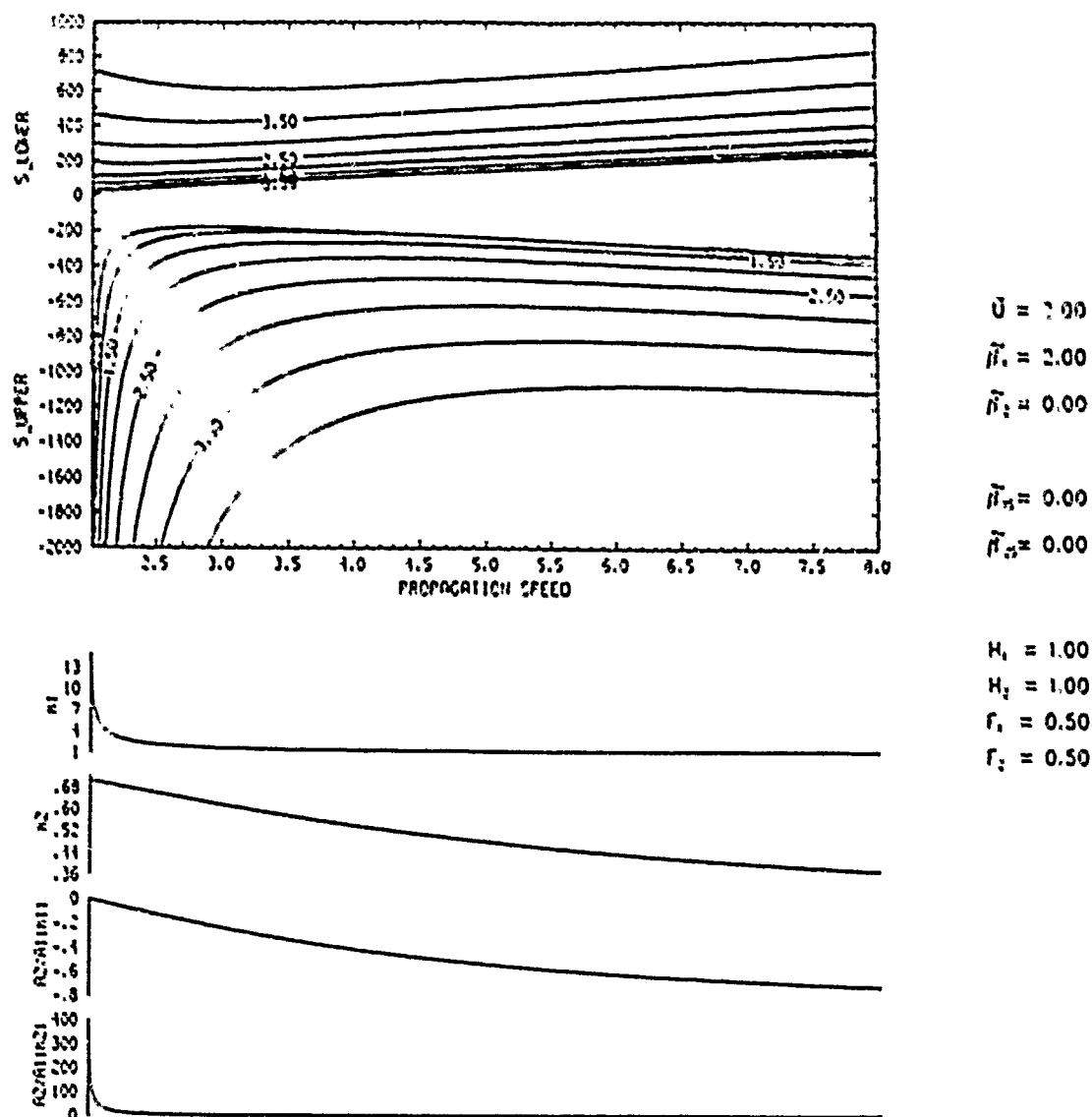


Fig. 9. TOP HALF: The upper and lower vortex strengths vs. propagation speed and Δ for steady, eastward propagating dipole solutions. The values written along the curves are Δ , the meridional distance between the vortices. BOTTOM HALF: Wave numbers and corresponding values of A_2/A_1 for the two modes vs. propagation speed.

$\bar{U} = 2.0$ and effective betas ($\bar{\beta}_1$ and $\bar{\beta}_2$) are 2.0 and 0.0. Flat boundaries. Note that fig. 10 is for same parameter values except different Δ values. (Also, see fig. 4)

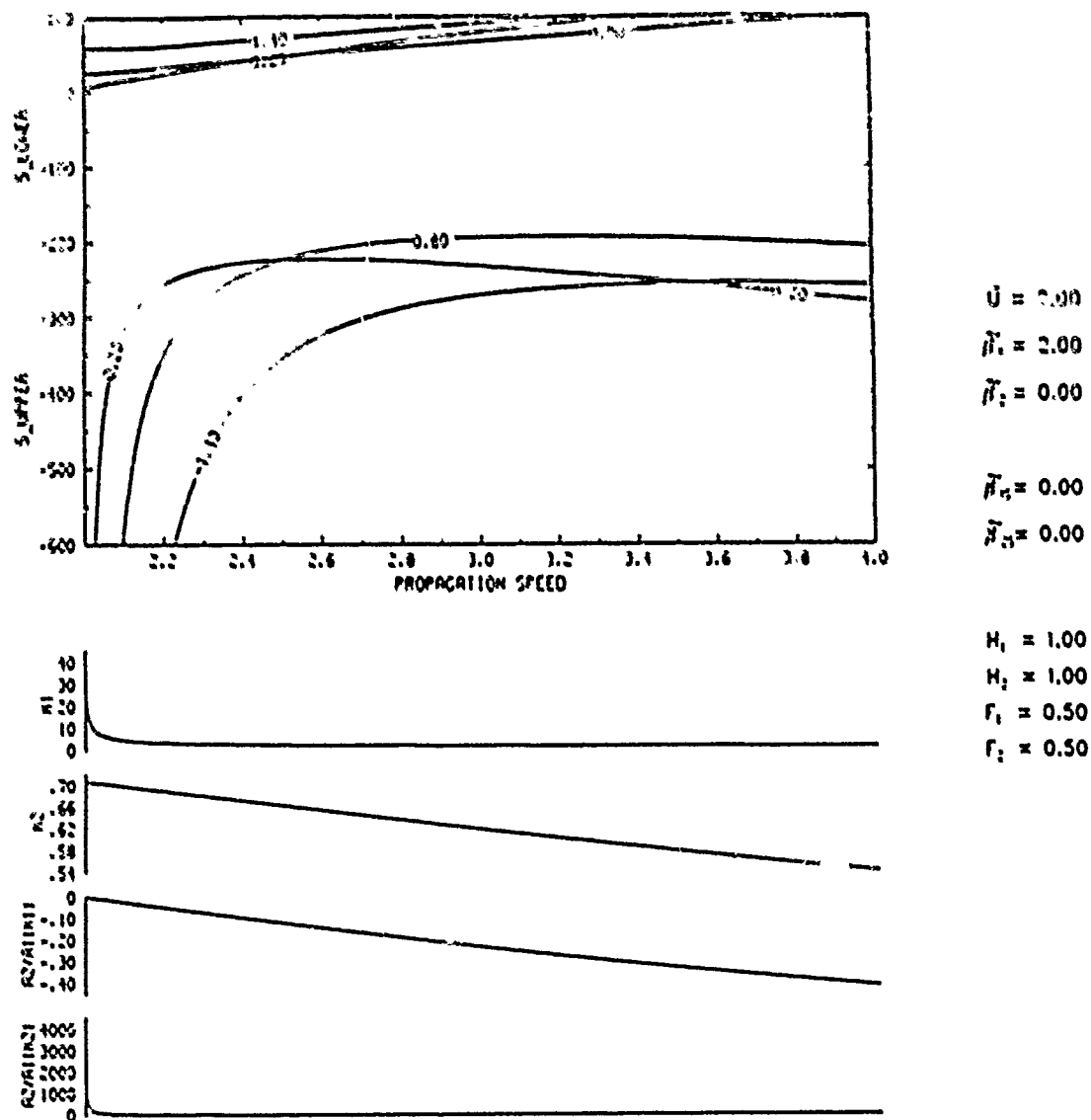


Fig. 10. TOP HALF: The upper and lower vortex strengths vs. propagation speed and Δ for steady, eastward propagating dipole solutions. The values written along the curves are Δ , the meridional distance between the vortices. BOTTOM HALF: Wave numbers and corresponding values of A_2/A_1 for the two modes vs. propagation speed.

$U = 2.0$ and effective betas ($\tilde{\beta}_1$ and $\tilde{\beta}_2$) are 2.0 and 0.0. Flat boundaries. Note that fig. 9 is for same parameter values except different Δ values. (Also, see fig. 4)

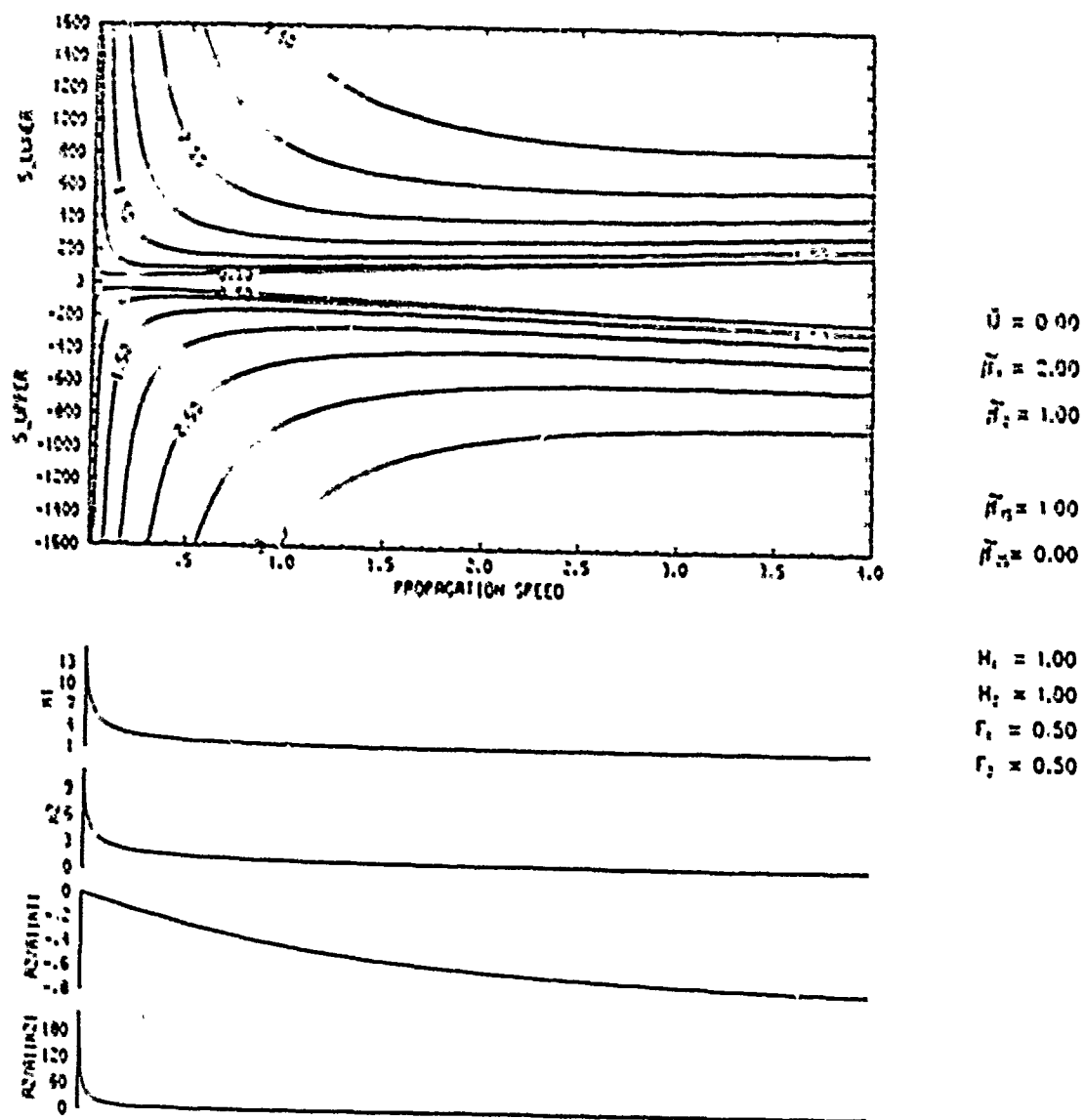


Fig. 11 TOP HALF: The upper and lower vortex strengths vs. propagation speed and Δ for steady, eastward propagating dipole solutions. The values written along the curves are Δ , the meridional distance between the vortices. BOTTOM HALF: Wave numbers and corresponding values of $A2/A1$ for the two modes vs. propagation speed.

$\bar{U} = 0.0$ and effective betas ($\bar{\beta}_1$ and $\bar{\beta}_2$) are 2.0 and 1.0. Sloping top boundary. (Also, see fig. 5)

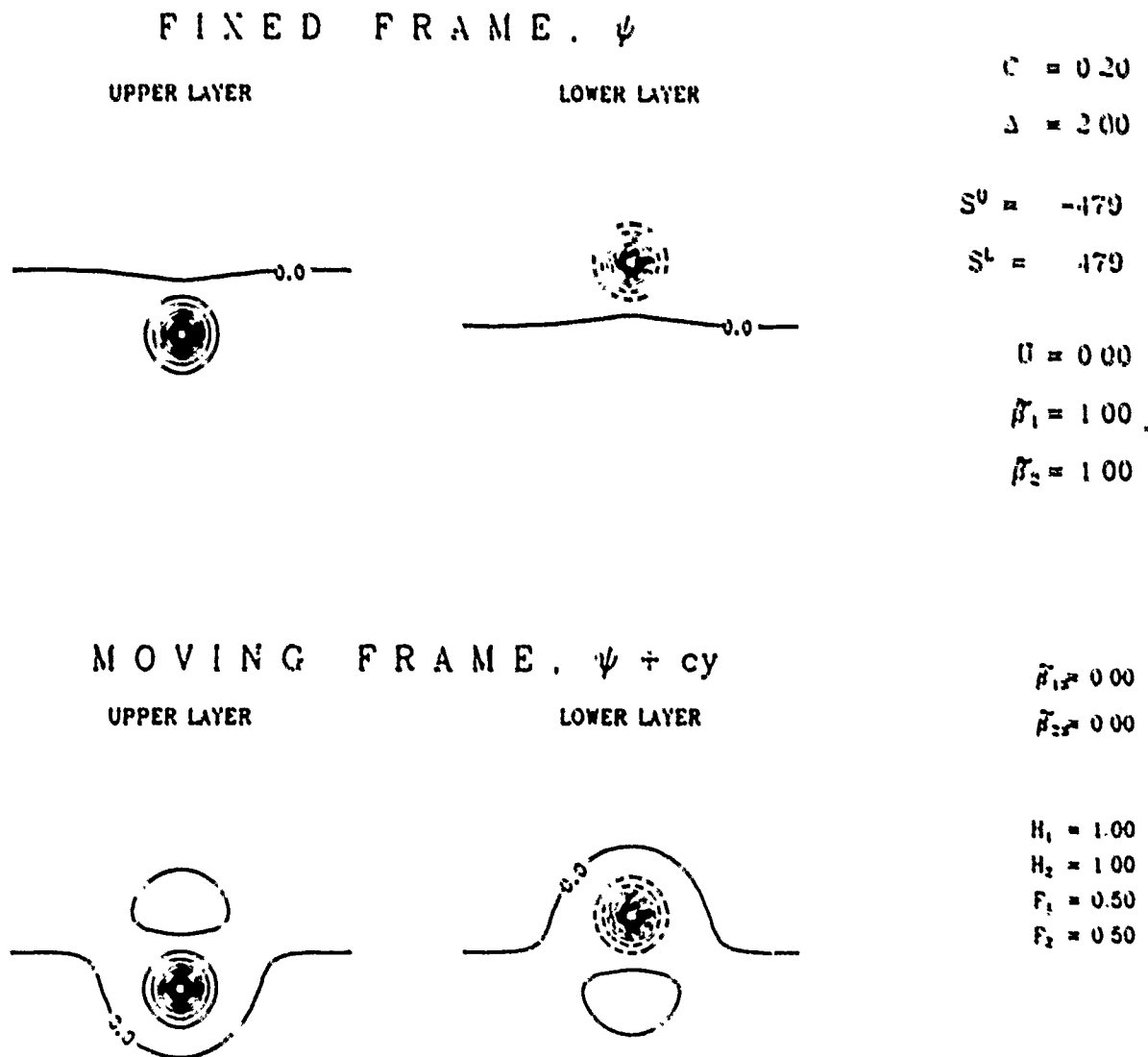


Fig. 12. Streamlines and Streaklines for the indicated parameter values. The domain is 10 by 10 non-dimensional lengths (see section 2.4). Solutions near singularities are clipped.

$U = 0.0$ and effective betas ($\tilde{\beta}_1$ and $\tilde{\beta}_2$) are both equal to the planetary beta. Compare with fig 13. All parameters including vortex strengths and Δ are equal but solutions are different.

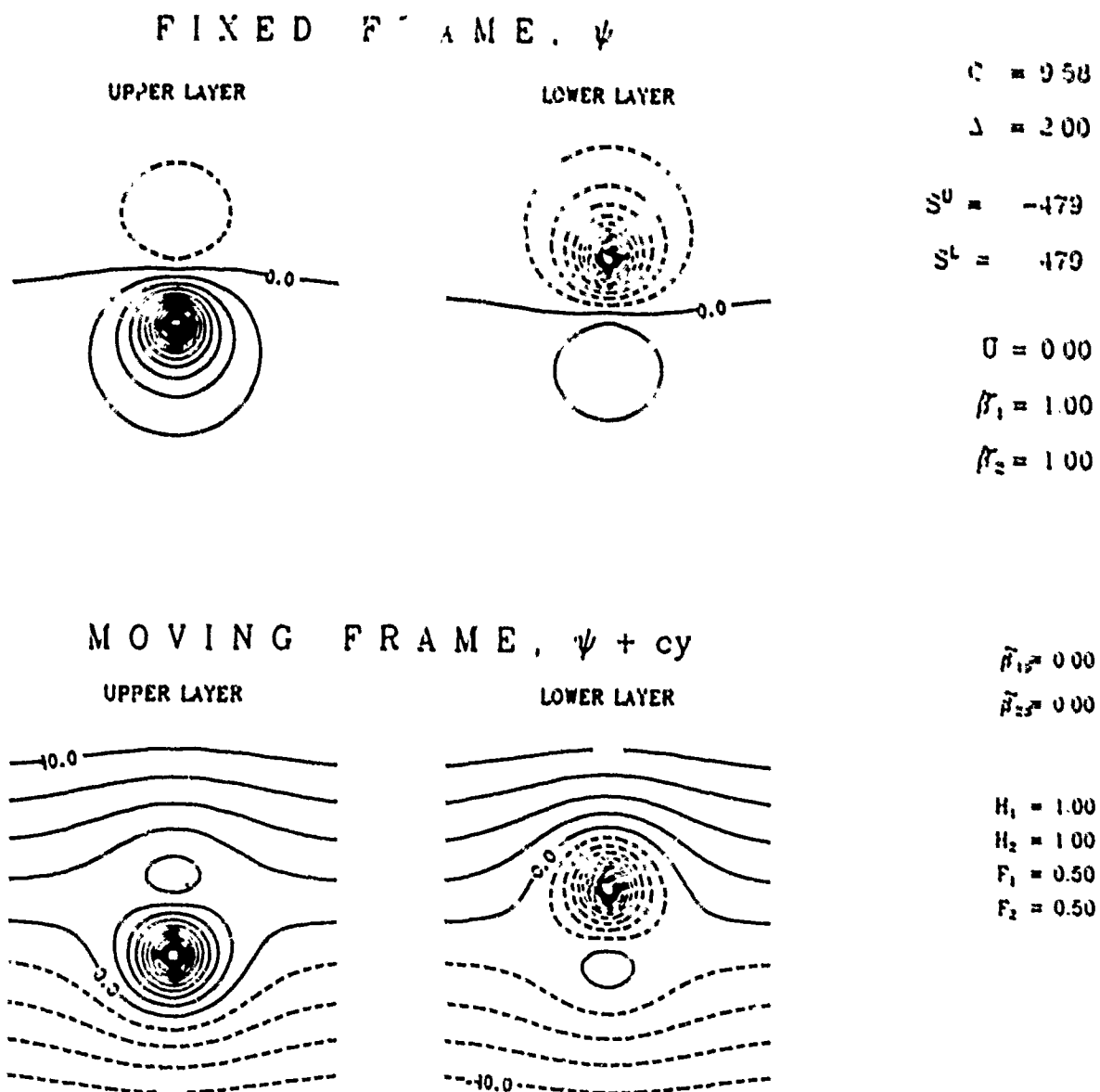


Fig. 13. Streamlines and Streaklines for the indicated parameter values. The domain is 10 by 10 non-dimensional lengths (see section 2.4). Solutions near singularities are clipped.

$U = 0.0$ and effective betas ($\tilde{\beta}_1$ and $\tilde{\beta}_2$) are both equal to the planetary beta. Compare with fig 14. All parameters including vortex strengths and Δ are equal but solutions are different.

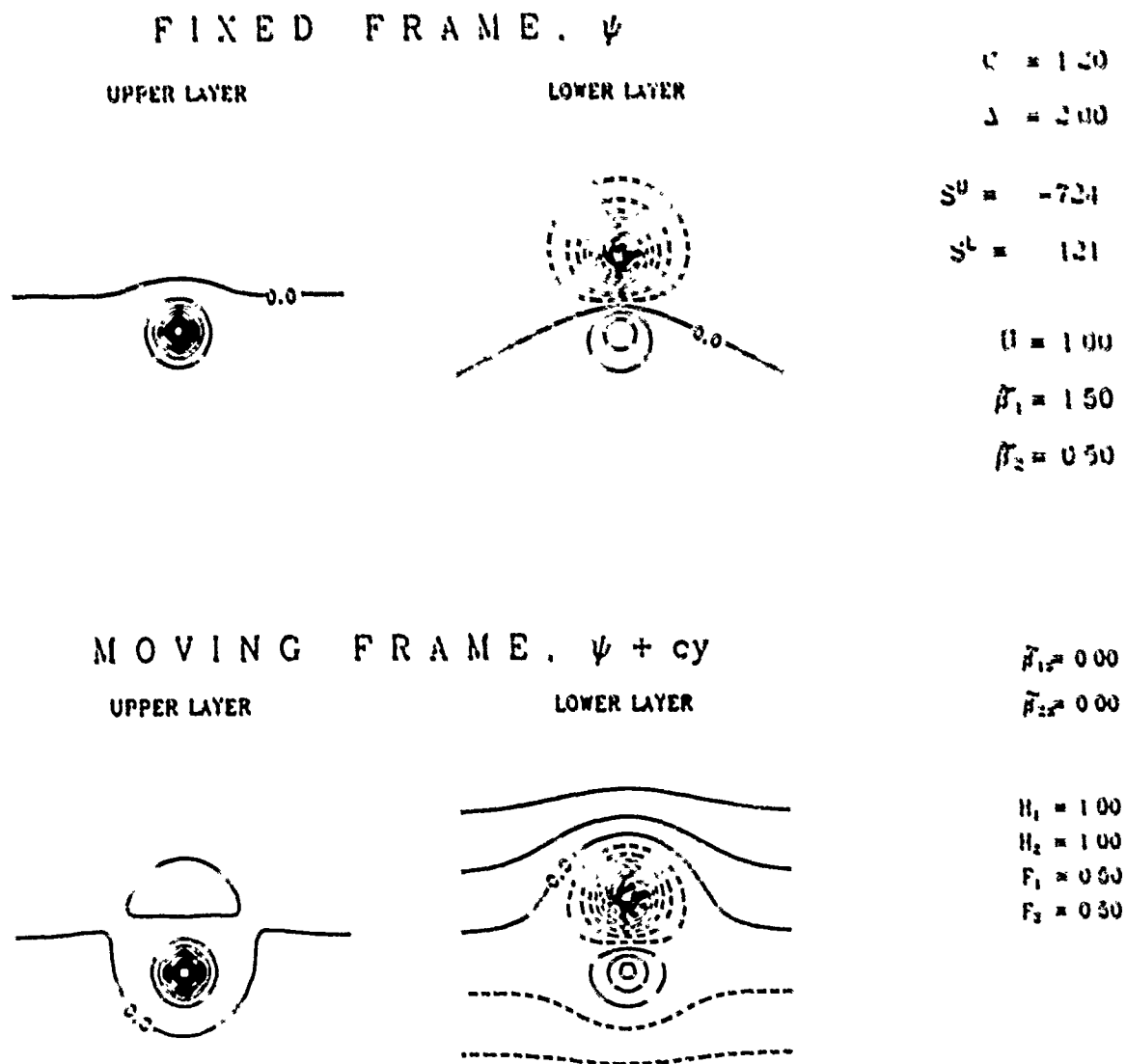


Fig. 14. Streamlines and Streaklines for the indicated parameter values. The domain is 10 by 10 non-dimensional lengths (see section 2.4). Solutions near singularities are clipped.

$U = 1.0$ and effective betas ($\tilde{\beta}_1$ and $\tilde{\beta}_2$) are 1.5 and 0.5. Flat boundaries. Note stronger vortex in top layer associated with U .

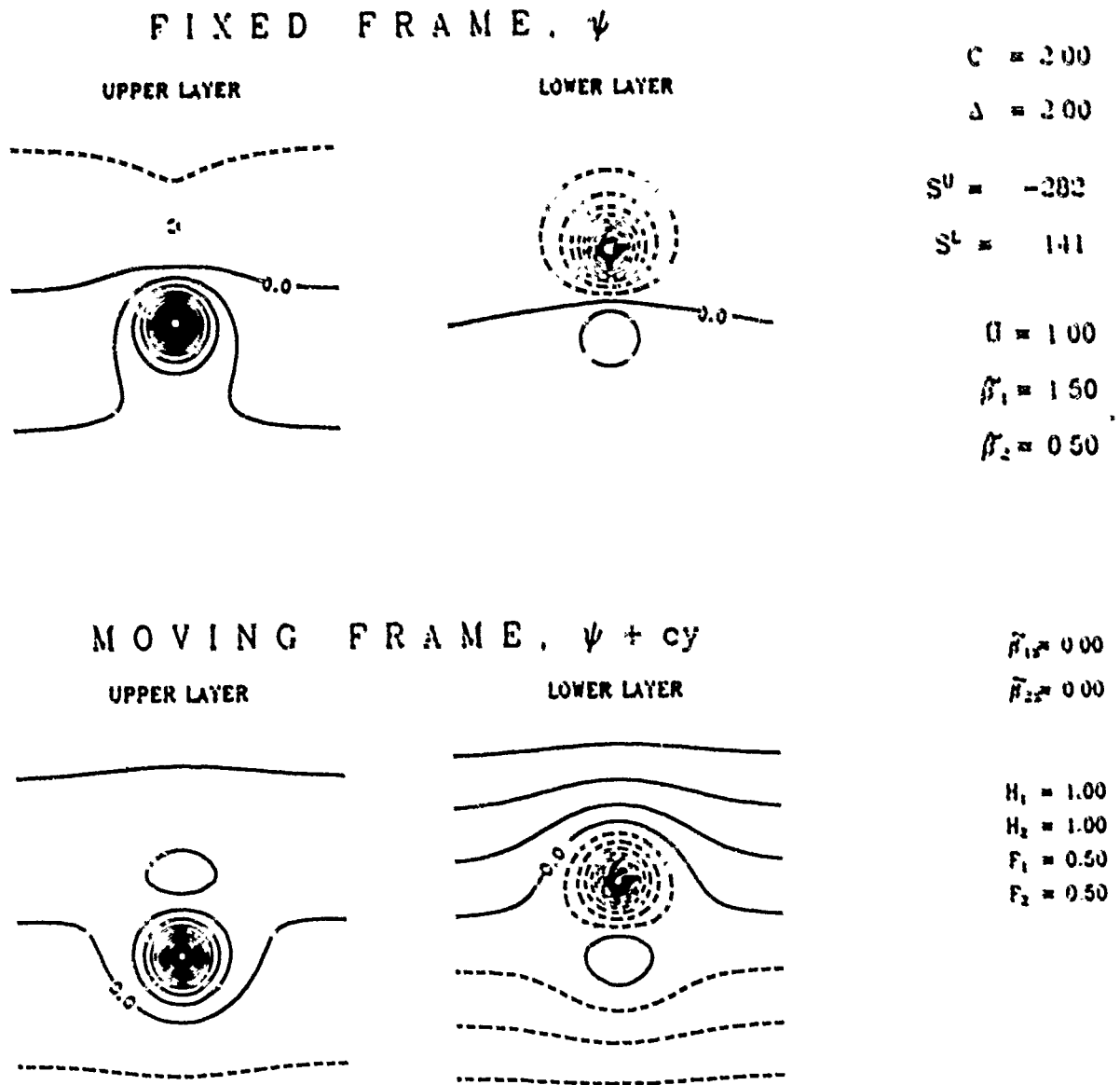


Fig. 15. Streamlines and Streaklines for the indicated parameter values. The domain is 10 by 10 non-dimensional lengths (see section 2.4). Solutions near singularities are clipped.

$\Omega = 1.0$ and effective betas ($\tilde{\beta}_1$ and $\tilde{\beta}_2$) are 1.5 and 0.5. Flat boundaries. Note stronger vortex in top layer associated with Ω .

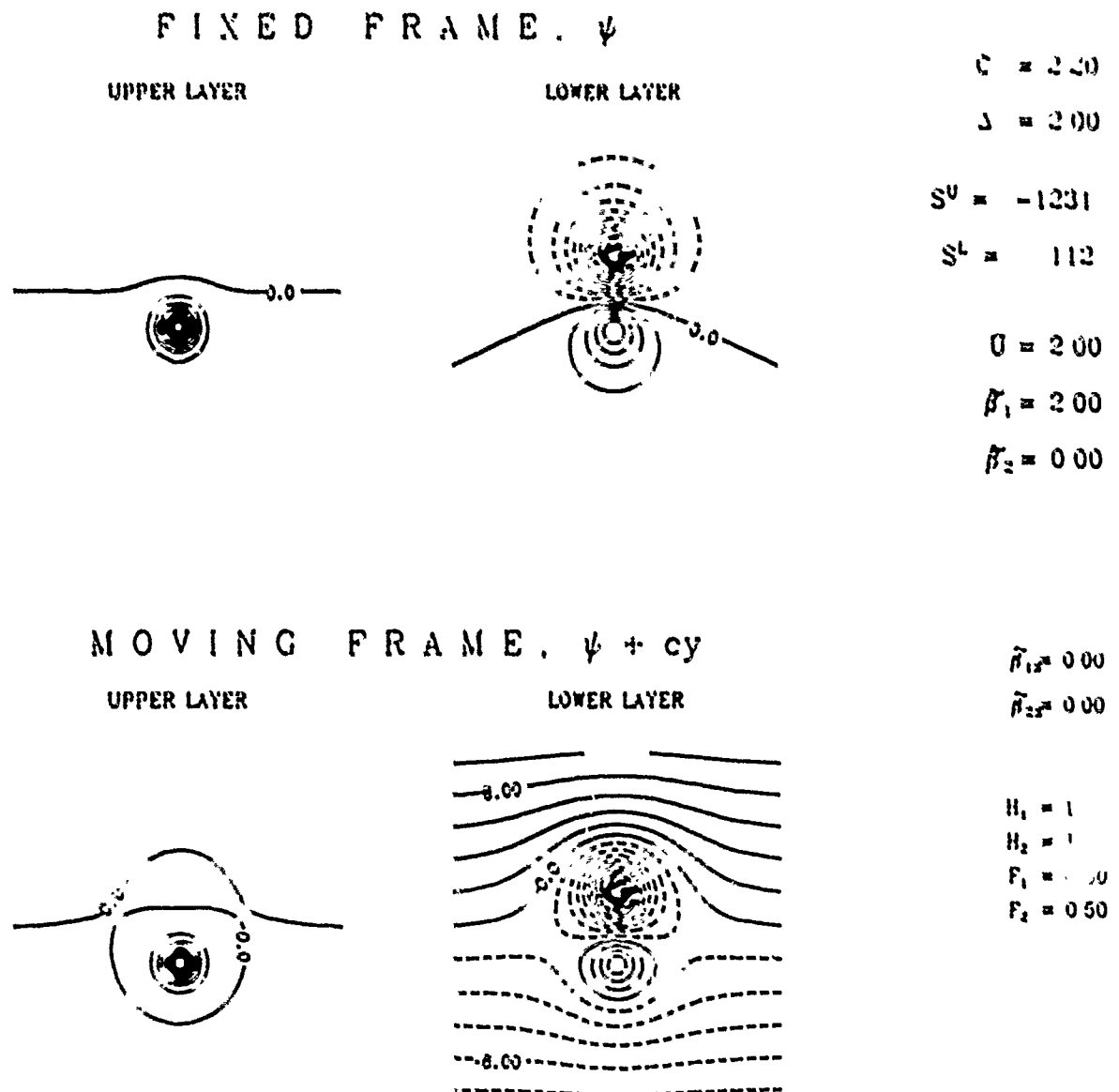
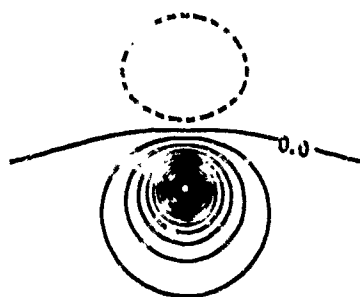


Fig. 16. Streamlines and Streaklines for the indicated parameter values. The domain is 10 by 10 non-dimensional lengths (see section 2.4). Solutions near singularities are clipped.

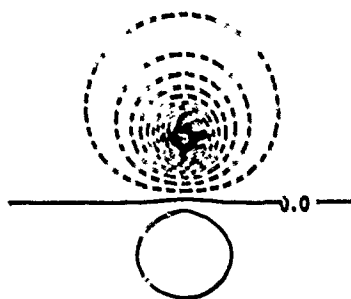
$U = 2.0$ and effective betas ($\tilde{\beta}_1$ and $\tilde{\beta}_2$) are 2.0 and 0.0. Flat boundaries. Note stronger vortex in top layer associated with U .

FIXED FRAME, ψ

UPPER LAYER



LOWER LAYER



$$C = 9.58$$

$$\Delta = 2.00$$

$$S^U = -538$$

$$S^L = 538$$

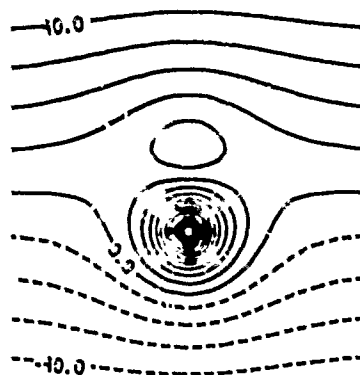
$$c = 0.00$$

$$\beta_1 = 2.00$$

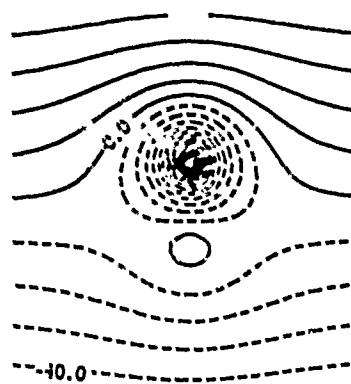
$$\beta_2 = 1.00$$

MOVING FRAME, $\psi + cy$

UPPER LAYER



LOWER LAYER



$$\tilde{\beta}_{1,2} = 1.00$$

$$\tilde{\beta}_{2,2} = 0.00$$

$$H_1 = 1.00$$

$$H_2 = 1.00$$

$$F_1 = 0.50$$

$$F_2 = 0.50$$

Fig. 17. Streamlines and Streaklines for the indicated parameter values. The domain is 10 by 10 non-dimensional lengths (see section 2.4). Solutions near singularities are clipped.

$U = 0.0$ and effective betas ($\tilde{\beta}_1$ and $\tilde{\beta}_2$) are 2.0 and 1.0. Sloping top boundary. Although the upper and lower vortices are of equal strength, the solutions are not reflections of each other. (compare to figs. 12 and 13)

CAPILLARY-GRAVITY SURFACE WAVE MODES IN A CLOSED VESSEL WITH EDGE CONSTRAINT : EIGEN-FREQUENCY AND DISSIPATION

Stephane DOUADY

INTRODUCTION	1
Summary of the previous experimental results.....	1
I GENERAL CONSIDERATIONS.....	3
1 Inviscid Problem.....	3
1.1 Boundary Conditions for the Free Surface.....	3
1.2 Structure of the Inviscid Problem.....	4
1.3 Dispersion relation and equipartition of energy	4
2 Viscous Fluid	5
2.1 scaling.....	5
2.2 First order.....	6
2.3 Second order : Rectified flow	7
3 Dissipation	7
3.1 Mathieu ,amplitude, and energy equations.....	7
3.2 Dissipation of the amplitude equation from Navier-Stokes	8
II INVISCID PROBLEM.....	10
1 Formal Solution	10
1.1 Formal Solution of the geometrical problem.....	10
1.2 Selection of the free surface and eigen frequency.....	11
2 Exemples on how to use the formal solution to obtain valid solutions.....	13
2.1 Bidimensionnal case, infinite depth.....	13
2.2 Bidimensionnal case with bottom.....	15
2.3 Lateral wall with bottom (step).....	16
2.4 Corner with botom.....	16
2.5 Infinite channel.....	18
2.6 Half infinite channel	18
2.7 Closed cell	19
3 Short study of the dispersion relation.....	21
4 Conclusion	21
III DISSIPATION.....	22
1 First boundary condition.....	22
2 Second boundary condition	23
2.1 Bidimensionnal case without bottom.....	23
2.2 Step (wall with bottom).....	23
2.3 Square cell and corner.....	25
4 conclusion.....	26
CONCLUSION.....	27

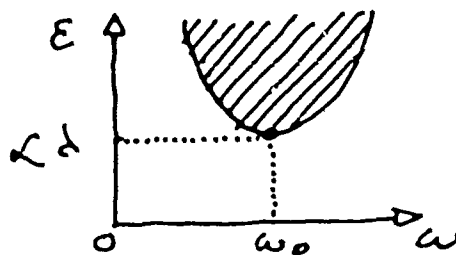
INTRODUCTION

Previous experiments on the Faraday instability had shown that it is a very simple and convenient way to observe the surface wave modes of a closed vessel. This instability allows us to measure their eigenfrequency and dissipation which, when the free surface is pinned at the edge of the lateral walls, appear to depend on the aspect ratio $\frac{k_x}{k_y}$ for a given wavenumber K . When we consider the linear problem, these effects come, of course, from the side walls, but the aim of this project was to show that they come only from this special boundary condition for the free surface.

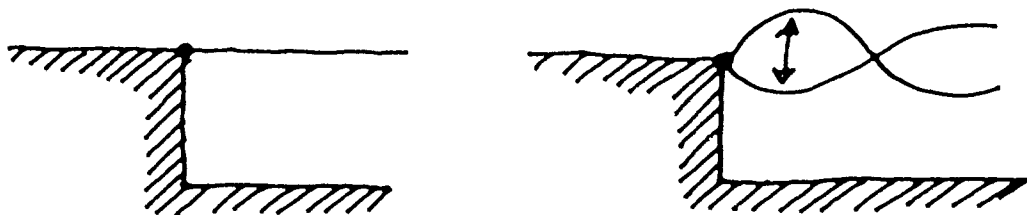
After a short summary of the previous experimental results, we first develop some general considerations about the boundary conditions of an inviscid problem, the general relation between the dispersion relation and the equipartition of the energy, the treatment of the viscosity by boundary layers (including the rectified flow), and how to found from Navier-Stokes the real coefficients (among them the dissipation) of the amplitude equation of the instability. These considerations show that we only need to know the free surface and the longitudinal velocity at the walls in the inviscid linear problem. In a second part, we try to solve the inviscid problem with this new boundary condition: for the free surface, by finding both the flow and the dispersion relation. We also discuss the work of Benjamin & Scott on the eigenfrequency problem. Finally, we present the induced results for the dissipation.

Summary of the previous experimental results

The Faraday instability is a parametrical excitation of surface waves in a vertically oscillating vessel of fluid. In the frame of the vessel, the gravity is modulated : $g \rightarrow g (1 + \epsilon \cos \omega t)$, and the modulation parametrically excites the surface waves through the gravity term of the dispersion relation of the waves. The threshold curves (the acceleration above which the waves appear as a function of ω) give directly the eigenfrequency and the dissipation of the mode :

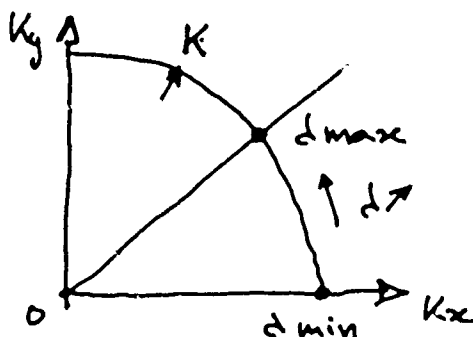


For practical reasons (to avoid the waves generated by the meniscus), we chose to pin the free surface at the edge of the lateral walls so that the surface is perfectly flat:



This is very simple to perform experimentally, with water for instance, and is the best way to obtain a perfectly flat surface with well-controlled and well-defined boundary conditions.

In a rectangular cell, with wave numbers k_x and k_y along each direction, the results give an eigenfrequency depending on the aspect ratio $\frac{k_x}{k_y}$ for a same total wave number $K = \sqrt{k_x^2 + k_y^2}$. Thus, this boundary condition induces a new dispersion relation, as the usual one depends only on K . In the same way, the dissipation depends on the aspect ratios $\frac{k_x}{k_y}$. In a square cell, we observed that the dissipation was increasing with $\frac{k_x}{k_y}$ ($\in [0, 1]$) at a same K :

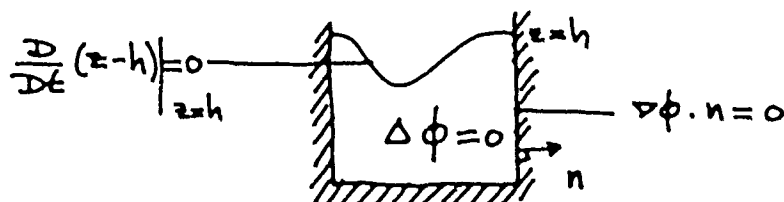


Another experimental observation is a constant flow with the structure of a Marangoni convection directly induced by the surface waves. Also, at high accelerations, we sometimes observe an important horizontal flow coming from the side walls. These effects can be explained as we will show by the rectified flow in the viscous boundary layer.

I GENERAL CONSIDERATIONS

1 Inviscid Problem

We consider an inviscid fluid in a closed vessel with a free surface :



The second boundary condition, at the first linear order is $\phi_t = -g h + \gamma \Delta h$

and the first one is $\phi_z = h_t$. We will look only at the first linear order problem.

We discriminate the vectors parallel to the wall, or horizontals, from the perpendicular, or vertical ones, by adding a slash at these variables (for instance ∇ is the horizontal gradient).

1.1 Boundary Conditions for the Free Surface

There are only two possibilities:

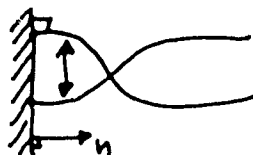
- If n , the vector normal to the wall, is defined at the boundary of the free surface, we can apply there both $\phi_z = h_t$ and $\nabla\phi \cdot n = 0$. This gives (at a vertical wall):

$$\frac{d}{dt} (\nabla h \cdot n) = 0$$

So, with the initial conditions of a flat surface:

$$\nabla h \cdot n = 0$$

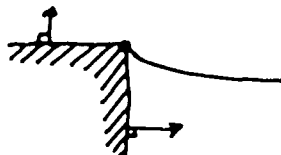
This is what we call the usual, or first, boundary condition. This equation means that the free surface is always perpendicular to the wall :



- If n is not defined, for example at the edge of the lateral walls, we have then condition on h . But this is only true at this particular line where n is not defined. Thus, if we want to always escape the preceding boundary condition, we now have the condition $h = c(l)$, where $c(l)$ is the edge line of the lateral walls. For an horizontal one, we thus have

$$h = 0$$

This is what we call the new, or second, boundary condition.



In conclusion, we can summarize the two possibilities by the general condition :

$$h \nabla h \cdot n = 0$$

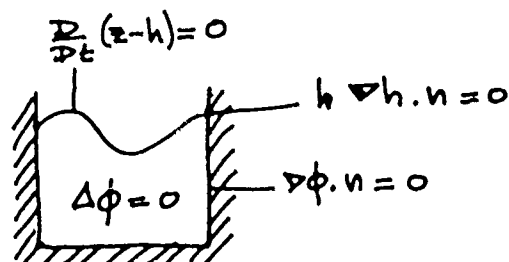
The first boundary condition makes the problem very easy to solve. But this condition cannot be preserved when one adds surface tension and viscosity to the problem. Moreover the boundary condition of an oscillating fluid near a vertical wall is very difficult to describe and solve. Thus, the derived inviscid solution cannot be used to directly find the real flow.

On the other hand, the new boundary condition makes the inviscid problem very difficult to solve. But this solution can be used to obtain directly the real flow when adding the surface tension and viscosity, as this boundary condition is still valid.

1.2 Structure of the Inviscid Problem

This problem is constituted in two parts :

- The geometrical one



does not depend on the properties of the fluid, except the incompressibility. It just expresses the flow ϕ as a function of any imposed surface $h(x, y, t)$.

- The physical one (the second boundary condition at the surface) :

$$\phi_t = -g h + \gamma \Delta h$$

where the physics of the fluid appears.

It expresses the fact that the surface displacement is an eigenmode.

Thus, we first solve the geometrical problem ; i.e., find ϕ as a functional of h , and report this solution in the physical boundary condition. This gives both the dispersion relation and the free surface eigenmodes.

1.3 Dispersion relation and equipartition of energy

To obtain the energy equation, one multiplies $\Delta\phi = 0$ by ϕ_t and integrates over the volume. After few transformations, using that $\frac{D}{Dt}(z-h) = 0$ is equivalent to $\nabla\phi \cdot \mathbf{n} = \frac{h_t}{\sqrt{1+(\nabla h)^2}}$ and $\frac{dA}{\sqrt{1+(\nabla h)^2}} = dx dy$, using also the physical condition at the surface and the general form of the boundary condition for the free surface, one finally obtains :

$$\frac{1}{2} \frac{d}{dt} \left[\int_{\text{Volume}} (\nabla\phi)^2 dv + \int_{\text{Projected Surface}} [g h^2 + \gamma (\nabla h)^2] dx dy \right] = 0.$$

One checks the conservation of energy in an inviscid fluid.

But another way to obtain the dispersion relation is by multiply the equation $\Delta\phi = 0$ by ϕ and integrating over the volume. After the same transformations, and using also the physical condition at the surface and the general form of the boundary condition for the free surface, and the Taylor theorem, one finally obtains :

$$\overline{\int (\nabla\phi)^2 dv} = \overline{\int_P \int_S [g h^2 + \gamma (\nabla h)^2] dx dy}$$

where the bar correspond to a time average over one oscillation period.

This equation can also be obtained by multiplying the physical condition at the surface by h and integrating over the surface.

By doing these integrations, we have lost the condition on h , and we only found the dispersion relation.

Under this form one recognize the equipartition of energy, the right term being the kinetic energy, and the left term the potential energy. But it is also the the dispersion relation as it gives ω^2 (the first term) as a function of the flow and surface properties.

This property of equivalence is in fact quite general for any oscillator, as it always can be written under the form $K \cdot h = \omega^2 M \cdot h$, where K is a stiffness operator and M an inertia operator ; so

$\omega^2 \int h^* \cdot M \cdot h = \int h^* \cdot K \cdot h$ or $\omega^2 = \frac{\int h^* \cdot K \cdot h}{\int h^* \cdot M \cdot h}$. Benjamin & Scott used this formulation with a variational principle, saying that the real eigen frequency correspond to the minima of this ratio.

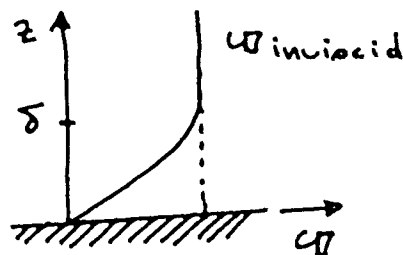
2. Viscous Fluid

We just summarize well-known results on the viscous boundary layer theory. The equations are :

$$\begin{aligned}\partial_t \mathbf{u} + (\mathbf{u} \cdot \nabla) \mathbf{u} &= -\nabla p + \nu \Delta \mathbf{u} \\ \nabla \cdot \mathbf{u} &= 0\end{aligned}$$

2.1 scaling

we assume that the viscosity is small, so that the inviscid solution is still valid except near the wall :



The scaling in the fluid is :

$$\begin{aligned}U &\sim W \sim U \\ \nabla &\sim \partial_z \sim \frac{1}{L} \\ \partial_t &\sim \omega \\ p &\sim U\omega L\end{aligned}$$

where L and ω are the wave length and pulsation of the surface waves.

The equations then reads :

$$\begin{aligned}\partial_t \mathbf{u} + \frac{U}{\omega L} (\mathbf{u} \cdot \nabla) \mathbf{u} &= -\nabla p + \frac{\nu}{\omega L^2} \Delta \mathbf{u} \\ \nabla \cdot \mathbf{u} &= 0\end{aligned}$$

with the assumptions of $\frac{U}{\omega L} \ll 1$, which corresponds to $h \ll L$, where h is the amplitude of the

waves ; and $\frac{\nu}{\omega L^2} \ll 1$.

The length scale δ where the viscosity starts to kill the tangential velocity is obtained by equilibrating the terms $\partial_t \mathbf{u}$ and $\nu \partial_z^2 \mathbf{u}$; so $\omega \sim \frac{\nu}{\delta^2}$, i.e. $\delta = \sqrt{\frac{\nu}{\omega}}$. One can notice that $\frac{\nu}{\omega L^2} = \left(\frac{\delta}{L}\right)^2$.

In the viscous boundary layer the scaling is then :

$$\begin{aligned}u &\sim U, \text{ but } w \sim \left(\frac{\delta}{L}\right) U \\ \nabla &\sim \frac{1}{L}, \text{ but } \partial_z \sim \frac{1}{\delta}\end{aligned}$$

and the equations read :

$$\begin{aligned}\partial_t \mathbf{u} + \frac{U}{\omega L} (\mathbf{u} \cdot \nabla) \mathbf{u} &= -\nabla p + \left(\frac{\delta}{L}\right)^2 \Delta \mathbf{u} + \partial_z^2 \mathbf{u} \\ \nabla \cdot \mathbf{u} &= 0\end{aligned}$$

The principal question is now to know the variation of pressure in the boundary layer. By taking the divergence of Navier-Stokes, one obtains $\Delta p = -\nabla \cdot (\mathbf{u} \cdot \nabla) \mathbf{u}$.

This gives in the fluid $\Delta p = -\frac{U}{\omega L} \nabla \cdot (u \cdot \nabla) u$

and in the boundary layer $\Delta p + \left(\frac{L}{\delta}\right)^2 \partial_z^2 p = -\frac{U}{\omega L} \nabla \cdot (u \cdot \nabla) u$.

Now to solve the problem we develop the velocity field and the pressure in orders of a small parameter ε , and we solve for each order. As there is two physical small parameters in the problem, we will need to compare both.

2.2 First order

For the pressure, we have, in the viscous boundary layer, $\partial_z^2 p_0 = 0$; so the pressure is the same than in the fluid. We have in the fluid :

$$U_0^i = -\nabla p_0$$

$$\nabla \cdot U_0 = 0$$

where U_0 is the inviscid boundary solution. In the boundary layer :

$$u_0^i = -\nabla p_0 + \nu u_{zz}^0 = -\nabla p_0 + \nu u_{zz}^0$$

$$= U_0^i + \nu u_{zz}^0$$

$$\nabla \cdot u_0 = 0$$

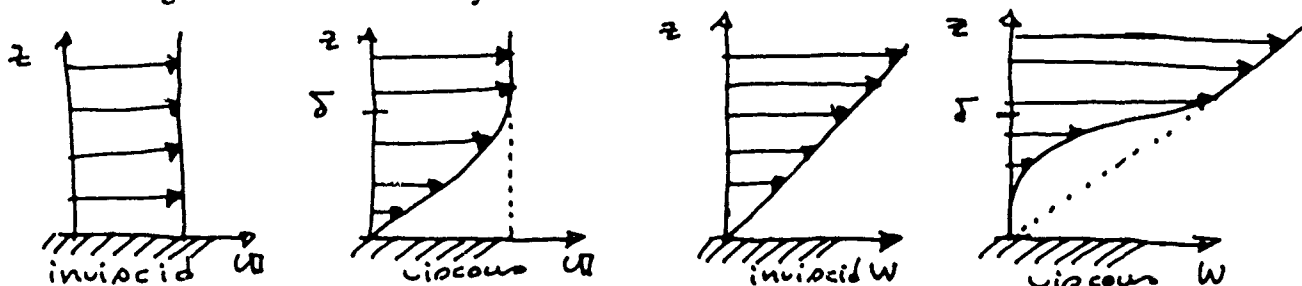
We match the two solution, i.e. we impose that $u^0 \rightarrow U^0$ when $\frac{z}{\delta} \rightarrow +\infty$. With the notations :

$U^0 \sim U^0(x,y) e^{i\omega t}$ when $z \rightarrow 0$, and $W^0 \sim -\nabla \cdot U^0(x,y) z e^{i\omega t}$ when $z \rightarrow 0$, the solution for u reads :

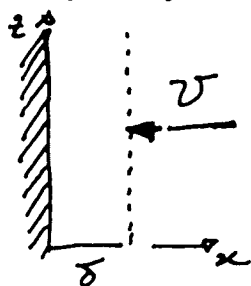
$$\begin{cases} u^0 = U^0(x,y) e^{i\omega t} f\left(\frac{z}{\delta}\right) \\ w^0 = -\nabla \cdot U^0(x,y) e^{i\omega t} \delta g\left(\frac{z}{\delta}\right) \end{cases}$$

where $\begin{cases} f\left(\frac{z}{\delta}\right) = \text{Real part} \left[1 - \exp\left(-\frac{1+i}{\sqrt{2}} \frac{z}{\delta}\right) \right] \\ g\left(\frac{z}{\delta}\right) = \text{Real part} \left[\frac{z}{\delta} - \frac{1-i}{\sqrt{2}} \left[\exp\left(-\frac{1+i}{\sqrt{2}} \frac{z}{\delta}\right) - 1 \right] \right] \end{cases}$

The physics correspond simply to kill the tangential velocity on a length δ ; but one can observe that it kills also the gradient of normal velocity :



One can here note that the first idea to solve the problem of a flow with a surface in sine by using only the viscosity to kill the normal velocity, is impossible. It can be seen by doing the same kind of scaling, mutatis mutandis :



Then one finds $w \sim \left(\frac{L}{\delta}\right) u$, so $w \gg u$ and infinite at the limit of a zero viscosity, what is rather unphysical. So we first have to solve the inviscid problem, and after use the result of the boundary layer theory.

2.3 Second order : Rectified flow

We now need to compare $\frac{U}{\omega L}$ and $\left(\frac{\delta}{L}\right)^2$. Physically, we prefer to still have the dissipation occurring only in the viscous boundary layer, so $\frac{U}{\omega L} \gg \left(\frac{\delta}{L}\right)^2$. This corresponds also to the experimental limit where $\delta \ll h \ll L$.

We then takes $\varepsilon = \frac{U}{\omega L}$, and a possible scaling $\sim \varepsilon^2$. This gives for the pressure :

$$\partial_z^2 p + \varepsilon^2 \Delta p = - \varepsilon^3 \nabla \cdot (u \cdot \nabla) u$$

So at the second order we still have no variation of the pressure when crossing the boundary layer. The equation for the flow in the viscous boundary layer is then :

$$u^1_t + (u^0 \cdot \nabla) u^0 = U^1_t + (U^0 \cdot \nabla) U^0 + \nu u^1_{zz}$$

The rectified flow U is the constant flow at the end of the viscous boundary layer, found by using

the trick : $\nu \int_0^{+\infty} z u_{zz} dz = - \nu U$. So we multiply by z , integrate and average in time the preceeding

equation. It gives the final result : $U = -\frac{3}{8} \frac{1}{\omega} U^0 U^0_x$

With the negative sign, one sees that this flow escape the maximum of velocity oscillation to converges to the minimum of velocity oscillation. This corresponds exactly to the constant flow observed in experiments in water, meaning that this flow is due to the friction of the surface wave flow on the bottom.

The physic of the rectified field flow is in fact very simple. For an oscillatory flow, the quadratic term, i.e., the advective term, of Navier-Stokes will always gives a constant term. The question is now why a viscous boundary layer is needed? Because in the fluid, the pressure is not imposed, so the constant part of the advective term is balanced by a constant pressure gradient. But on the contrary, in the boundary layer the pressure is imposed to be the pressure in the fluid. As the velocity decreases to go to zero at the wall, in the boundary the advective term cannot balance this constant pressure gradient, and thus a rectified flow is generated.

This property of the pressure in the boundary layer is general and always creates secondary flows, even in a non-oscillating system, for instance in curved system (the tea leaves in a cup of tea).

3 Dissipation

3.1 Mathieu ,amplitude, and energy equations

The studied instability is a parametrical one, governed at the first linear order by the Mathieu equation:

$$x_{tt} + 2\lambda x_t + \omega^2(t) x = 0$$

This equation, without the damping term in λ , can be obtained from the inviscid problem in the case of the first boundary condition (Benjamin & Ursell). If one takes the nonlinear problem, one can found the corresponding nonlinear terms.

The amplitude equation can be obtained from the preceeding by developing in ε all the quantities

$$x = \varepsilon (A e^{i\omega t} + c.c.) + h.o.t.$$

$$\omega^2(t) = \omega_0^2 (1 + \epsilon f(c i \omega t + c.c.) + h.o.t.)$$

$$\omega_0 = \frac{v}{2} + \epsilon \delta + h.o.t.$$

$$\Lambda_t = \epsilon F(\Lambda) + h.o.t.$$

All these developements have their physiscal meanings.

One obtains at the first order the 1/2 resonance, i.e. the dispersion relation. At the second order, one obtains the linear amplitude equation :

$$\Lambda_t = (-\lambda + i \delta) \Lambda + i \frac{fv}{4} \overline{\Lambda}$$

The energy equation is obtained by multiplying the Mathieu equation by x_t and integrating over one excitation period. If one then reports the same developement than before, one found the equation for the modula of the amplitude, i.e. only the real terms of the amplitude equation :

$$(\Lambda \overline{\Lambda})_t = -\lambda \Lambda \overline{\Lambda} + i \frac{fv}{4} (\overline{\Lambda}^2 - \Lambda^2)$$

From the nonlinear inviscid equation, one knows how to found the linear and nonlinear imaginary terms of the amplitude equation (the real parts correspond to the dissipative case). The idea is now to found the real linear and nonlinear real parts of the amplitude equation from the energy equation derived from Navier-Stokes. Practically this is possible accurately only for the first real term, usually called the dissipation.

3.2 Dissipation of the amplitude equation from Navier-Stokes

We first have to write the energy equation, always obtained by the same way and transformed with the same tricks :

$$\frac{d}{dt} \left[\int_V \frac{1}{2} (u)^2 dv + g \int_V z dv + \gamma \int_S dA \right] = \frac{d}{dt} g \int_V z dv - v \int_V (\omega)^2 dv - v \int_S u \times \omega \cdot n dA$$

where V and S refer to the volume and surface of the oscillating free surface volume of fluid.

We recognize in this equation that the energy source comes from the modulation of the gravity, and that the dissipation occurs only where $\omega \neq 0$, principally in the viscous boundary layer (here the surface dissipation will be neglected).

Now one just have to express u (and then ω), as a function of the free surface h. After, the same developement of h over one eigen mode of oscillating amplitude x and constant one A will give the equivalent of the energy equation for the amplitude equation.

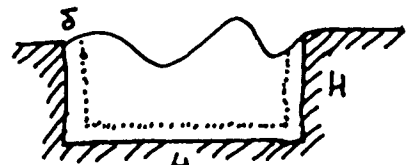
One must note that, at this point, this equation assumed no approximation, and thus is exact to all orders (including the nonlinear). But one sees that one would have to develop the integrals, which limits oscillate, but also to know u with the corresponding accuracy, i.e. to solve the nonlinear viscous problem for the flow of one free surface wave mode.

The first term is exactly the first term in the equation for the module of the amplitude, the second term coressond to the forcing, the energy source, and the third to the dissipative term.

We just need to compute the third one, but also the first as it gives a coefficient. To compute the first term, we first assume that the kinetic energy is very close to the inviscid one. The error can be estimated :

$$\int_V \frac{1}{2} (u)^2 dv \approx \int_V \frac{1}{2} (U^0)^2 dv \cdot [1 - \Delta]$$

$$\text{with } \Delta = \delta \left[\frac{U_{\text{bottom}}^2}{U_{\text{surface}}^2} \frac{1}{L} + \frac{4}{H} \right]$$



One can here note that the preceeding approximation explains why the eigen frequency is changed by viscosity, as for a same free surface, and thus potential energy, the kinetic energy is reduced. Thus the

eigen frequency is increased : $\omega_{\text{visc}}^2 \approx \omega_{\text{inv}}^2 \left[1 + \frac{\Delta}{2} \right]$.

Now we use the equivalence of dispersion relation and eigen frequency and transform the potential energy for h small, so :

$$\frac{d}{dt}(E) = \int_P \int_S [g h^2 + \gamma (\nabla h)^2] dx dy ,$$

which is very easy to compute for a given free surface wave mode (for a sinusoidal one this gives the usual factor $(g + \gamma K^2)$).

To compute the dissipative term, we use the preceeding scaling to simplify the expression of the vorticity : $\eta = u_z - w_x = u_z$ as $w_x \sim \left(\frac{\delta}{L}\right) u_z$. Now u_z has a simple expression as a function of the inviscid solution : $u_z = U^0(x,y) e^{i\omega t} \frac{1}{\delta} f\left(\frac{z}{\delta}\right)$ with $f'\left(\frac{z}{\delta}\right) = f_z\left(\frac{z}{\delta}\right) = \text{Real part} \left[\frac{1+i}{\sqrt{2}} \exp\left(-\frac{1+i}{\sqrt{2}} \frac{z}{\delta}\right) \right]$. Thus

$$\nu \int_V (\omega)^2 dV = \frac{\nu}{\delta} I \int_{\text{Wall Surfaces}} (U^0)^2 ds$$

where $I = \int_0^{+\infty} f\left(\frac{z}{\delta}\right)^2 \frac{dz}{\delta} = \frac{3\sqrt{2}}{8}$. Thus we just have to compute the integral of the module of the

inviscid velocity at the wall. With the usual adimensionnalization $U \sim \omega h$, this gives

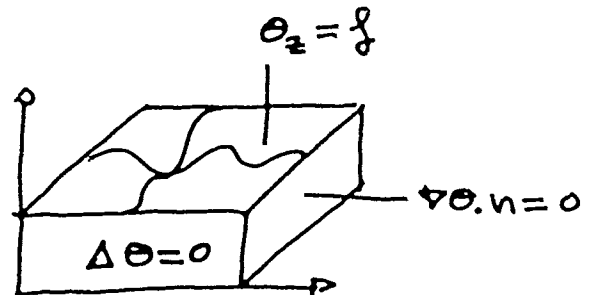
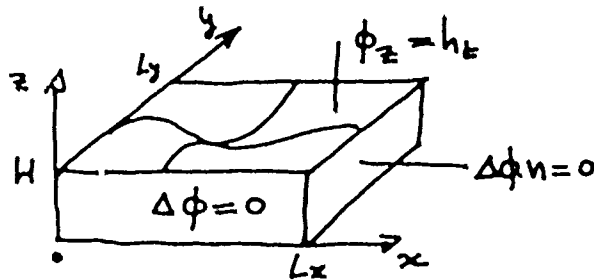
$$\lambda \sim \sqrt{\nu} \omega \frac{\omega^2}{[g + \gamma K^2]} \frac{2 I}{L_x L_y} G(KH, KL)$$

where $G(KH, KL) = \int_S (\underline{U}^0)^2 ds$ (the $\underline{\quad}$ denotes the adimensionnalization) is a geometrical factor corresponding to the structure of the inviscid flow.

II INVISCID PROBLEM

1 Formal Solution

1.1 Formal Solution of the geometrical problem



We note $h = h(x, y) e^{i\omega t}$
 $\phi = i\omega h \theta(x, y, z) e^{i\omega t}$

The first idea is to decompose θ on products of two cosines, which automatically satisfy the lateral boundary conditions.

Thus we note $\theta_{mn} = \int_0^{L_x} \int_0^{L_y} \theta \cos(k_m x) \cos(k_n y) dx dy$

where $k_m = \frac{m\pi}{L_x}$, $k_n = \frac{n\pi}{L_y}$; and

$$\theta = \sum_{m,n} \theta_{mn} \cos(k_m x) \cos(k_n y)$$

where the ' denotes a factor 2 for $(m, n) \neq (0, 0)$.

$$\text{Then } \int_0^{L_x} \theta_{xx} \cos(k_m x) dx = [\theta_x(L_x) - \theta_x(0)] - k_m^2 \int_0^{L_x} \theta \cos(k_m x) dx.$$

Thus one note that this transformation naturally takes into account the solid boundary conditions for θ ; and the new system reads:

$$\begin{aligned} \theta_{mn} z z - k_{mn}^2 \theta_{mn} &= 0 & \text{where } k_{mn}^2 &= k_m^2 + k_n^2 \\ \theta_{mn} z &= f_{mn} \text{ at } z = H, \\ \theta_{mn} z &= 0 \text{ at } z = 0 \end{aligned}$$

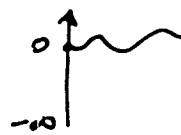
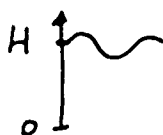
The solution of which is: $\theta_{mn} = \frac{\text{ch}(k_{mn} z)}{k_{mn} \text{sh}(k_{mn} H)} f_{mn}$

or

$$\theta = \sum_{m,n} f_{mn} \frac{\text{ch}(k_{mn} z)}{k_{mn} \text{sh}(k_{mn} H)} \cos(k_m x) \cos(k_n y)$$

If one lateral wall is at infinity it just corresponds to: $\sum_{m,n} \rightarrow \frac{2}{\pi} \int_0^{+\infty} dr$

and, for an infinite depth: $\frac{\text{ch}(k_{mn} z)}{k_{mn} \text{sh}(k_{mn} H)} \rightarrow \frac{e^{k_{mn} z}}{k_{mn}}$



This is not clear under this form that this solution is really one (problems of divergences). We will check that above.

1.2 Selection of the free surface and eigen frequency

The free surface boundary condition reads :

$$\phi_t = (-g + \gamma \Delta) h \rightarrow \omega^2 \theta = (g - \gamma \Delta) f \quad \text{at } z = H \quad (1)$$

• With the first boundary condition for the free surface, $\forall h, n = 0$, the free surface is naturally decomposed over the product of cosines :

$$f = \sum_{p, q} f_{pq} \cos(k_p x) \cos(k_q y)$$

and thus equation (1) gives :

$$\sum_{p, q} f_{pq} \left[\omega^2 \frac{\text{ch}(k_{pq} H)}{k_{pq} \text{sh}(k_{pq} H)} - (g + \gamma k_{pq}^2) \right] \cos(k_p x) \cos(k_q y) = 0$$

if we project along each product of cosines, we thus obtain :

$$\forall p, q, \quad f_{pq} \left[\omega^2 \frac{\text{ch}(k_{pq} H)}{k_{pq} \text{sh}(k_{pq} H)} - (g + \gamma k_{pq}^2) \right] = 0$$

The only solution with $f \neq 0$ is :

$$\boxed{\begin{aligned} f &= \cos(k_m x) \cos(k_n y) \\ \omega^2 \frac{\text{ch}(k_{mn} H)}{k_{mn} \text{sh}(k_{mn} H)} &= (g + \gamma k_{mn}^2) \end{aligned}}$$

Thus the eigen modes are simply the product of two cosines, and the usual dispersion relation is obtained.

• With the second boundary condition, $h=0$, the surface is naturally decomposed over the product of two sines :

$$f = \sum_{p, q} f_{pq} \sin(k_p x) \sin(k_q y)$$

$$\begin{aligned} \text{Now } \int_0^{L_x} \sin(k_p x) \cos(k_m x) dx &= 0, \text{ if } p \text{ and } m \text{ have the same parity} \\ &= \frac{2 k_p}{k_p^2 - k_m^2}, \text{ if } p \text{ and } m \text{ are of opposite parity.} \end{aligned}$$

This selection on m correspond exactly to the reflection symmetry at the middle of the cell. The formal solution thus reads :

$$\boxed{\theta = \sum_{m, n} \sum_{p, q} f_{pq} \frac{2 k_p}{k_p^2 - k_m^2} \frac{2 k_q}{k_q^2 - k_n^2} \frac{\text{ch}(k_{mn} z)}{k_{mn} \text{sh}(k_{mn} H)} \cos(k_m x) \cos(k_n y)}$$

where the " denotes also the selection on m and n .
The equation (1) then gives :

$$\sum_{p,q} f^{pq} \left[\omega^2 \sum_{m,n}'' \frac{2 k_p}{k_p^2 - k_m^2} \frac{2 k_q}{k_q^2 - k_n^2} \frac{\text{ch}(k_{mn}H)}{k_{mn} \text{sh}(k_{mn}H)} \cos(k_m x) \cos(k_n y) - (g + \gamma k_{pq}^2) \sin(k_p x) \sin(k_q y) \right] = 0$$

If we project along each product of sines, we now found an infinite set of equations which couple each f^{pq} to the others :

$$\sum_{p,q} \left[f^{pq} \omega^2 \gamma(p,q,p_0,q_0) \right] - \left[g + \gamma k_{p_0 q_0}^2 \right] f^{p_0 q_0} = 0$$

$$\text{where } \gamma(p,q,p_0,q_0) = \sum_{m,n}'' \frac{2 k_p}{k_p^2 - k_m^2} \frac{2 k_q}{k_q^2 - k_n^2} \frac{2 k_{p_0}}{k_{p_0}^2 - k_m^2} \frac{2 k_{q_0}}{k_{q_0}^2 - k_n^2} \frac{\text{ch}(k_{mn}z)}{k_{mn} \text{sh}(k_{mn}H)}$$

where the "'' denotes also the double selection rule, i.e. a mode with a given reflection symmetry along x and y (odd or even for each direction), interacts only with a mode of the same symmetry. We also note $\gamma(p,q) = \gamma(p,q,p,q)$.

This proves that the surface cannot be simply the product of two sines. But experimentally, it seems to be very close, especially for large p_0 and q_0 , so we assume that a Galerkin approximation is valid.

At the first order of this approximation, the surface is the product of two sines, which gives for the dispersion relation :

$$\omega^2 \gamma(p_0, q_0) = \left[g + \gamma k_{p_0 q_0}^2 \right]$$

$$\text{or } \omega^2 \sum_{m,n}'' \left(\frac{2 k_x}{k_x^2 - k_m^2} \right)^2 \left(\frac{2 k_y}{k_y^2 - k_n^2} \right)^2 \frac{\text{ch}(k_{mn}H)}{k_{mn} \text{sh}(k_{mn}H)} = \left[g + \gamma K^2 \right]$$

with $K^2 = k_x^2 + k_y^2$

One can notice that the term corresponding to the potential energy, i.e. to the free surface, is not changed from the usual dispersion relation, as in this first approximation the free surface is still sinusoidal. But, because of this new boundary condition, the flow is changed, and so is the kinetic energy term. One also notes its non trivial dependence on k_x and k_y .

The second order consists to approximate the surface with the sum of two products of sines. This gives :

$$f^{pq} \left[\omega^2 \gamma(p,q) - (g + \gamma k_{pq}^2) \right] + f^{p'q'} \gamma(p,q,p',q') = 0$$

$$f^{pq} \gamma(p,q,p',q') + f^{p'q'} \left[\omega^2 \gamma(p',q') - (g + \gamma k_{p'q'}^2) \right] = 0$$

By writing that the determinant is zero, one obtains the two corrections to the eigen frequencies of the two modes, and the eigen vectors give the corrections to the surface.

This can be generalized for all orders to obtain more and more accurate solutions. The validity of this approximation is checked by looking at the order of magnitude of the coupling terms $\gamma(p,q,p',q')$ compared to $\gamma(p,q)$.

For a first conclusion, we could say that the surface is now much more complicated, and that even in the approximation of a simple surface, the eigen frequency is changed. But all this preceding treatment is rather formal, and we now want to look at the validity, existence and shape of these solutions.

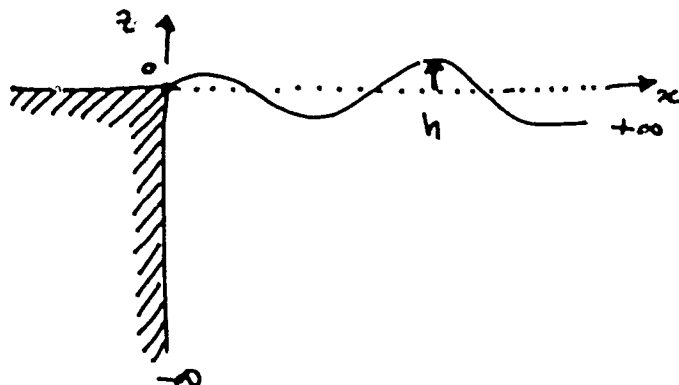
2 Examples on how to use the formal solution to obtain valid solutions

We use only the simple sinusoidal approximation for the free surface, but, as the problem is linear, this treatment can be extended to all orders.

We will first look at cells with one or more lateral wall at the infinite, and thus have integrals instead of discrete sums.

At this point, we notice that, in the transformation of $\Delta\phi = 0$, we used the condition that $\theta_x(+\infty) = 0$. When this is not true, it introduces a divergence in the formal solution. But this problem can be solved by subtracting an intuitive solution θ_0 : $\theta = \theta_0 + \theta'$ such that $\theta'_x(+\infty) = 0$.

2.1 Bidimensionnal case, infinite depth



If we take $h = h \sin(kx) e^{i\omega t}$

$$\phi = i\omega h \theta(x, z) e^{i\omega t}$$

the formal solution reads

$$\theta = \frac{2}{\pi} \int_0^{+\infty} \frac{k}{k^2 - r^2} \frac{e^{rz}}{r} \cos(rx) dr,$$

The integrant has a non-integrable divergence for $r=k$. This means that θ_x has an oscillating component of wave number k , at $+\infty$. This is trivial as, at $+\infty$, the fluid does not feel the wall and we must obtain the unbounded solution $\theta_0 = \sin(kx) \frac{e^{kz}}{k}$, as the oscillation of the free surface goes to infinity.

Thus we write $\theta = \theta_0 + \theta'$, and by using the formal identity

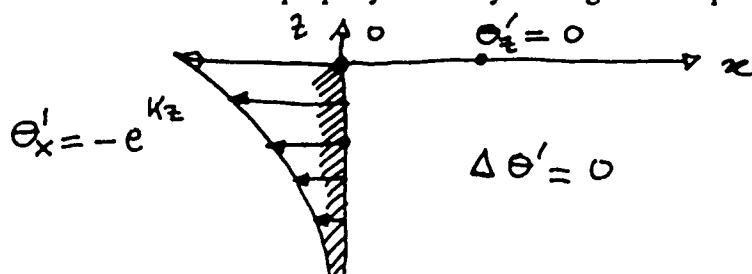
$$\sin(kx) = \frac{2}{\pi} \int_0^{+\infty} \frac{k}{k^2 - r^2} \cos(rx) dr$$

$$\text{we obtain } \theta' = \frac{2}{\pi} \int_0^{+\infty} \frac{k}{k^2 - r^2} \left[\frac{e^{rz}}{r} - \frac{e^{kz}}{k} \right] \cos(rx) dr, \text{ i.e.}$$

$$\theta = \sin(kx) \frac{e^{kz}}{k} + \frac{2}{\pi} \int_0^{+\infty} \frac{k}{k^2 - r^2} \left[\frac{e^{rz}}{r} - \frac{e^{kz}}{k} \right] \cos(rx) dr.$$

This solution is still not defined for $r=0$, but this problem disappears for the physical quantities θ_x and θ_y .

This solution can be more properly obtained by writing the new problem for θ' :



We see that for this correction flow induced by this new boundary condition, it must compensate the flow through the wall due to the simple solution θ_0 . Thus its boundary condition is no longer $\theta'_x = 0$. This is why the cosine transformation is still interesting in this case as

$$\int_0^{+\infty} \theta'_{xx} \cos(k_m x) dx = -\theta'_x(0) + [\theta'_x \cos(r x)](+\infty) - k_m^2 \int_0^{+\infty} \theta' \cos(k_m x) dx$$

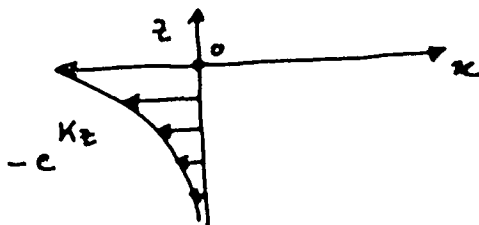
if one assume that $\theta'_x(+\infty) = 0$, one obtains :

$$\theta'_{rzz} + e^{kz} - r^2 \theta'_r = 0 ,$$

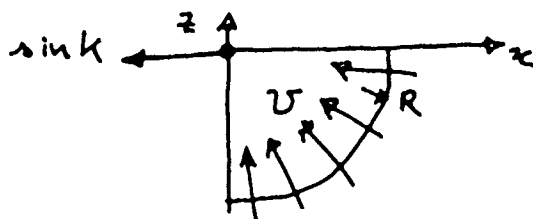
the solution of which is exactly the preceding one.

The interpretation of this correction flow θ' as the compensation of the flow through the wall due to

θ_0 :



allows to found directly a good approximation of this flow far from the corner, as this boundary condition is like a sink located at the corner :



.So the flow is radially symmetric for $kR > 1$, and, in order to preserve mass, i.e. the flux, one must

$$\text{have } U \frac{\pi R}{4} = \int_{-\infty}^0 e^{kz} dz = \frac{1}{k} ; \text{ so } U = \frac{4}{\pi k R} .$$

One checks that $U(+\infty) = 0$.

We can also check that $\theta'_x(0) = 0$, what is not directly apparent, by looking at the

$$\text{limit of } I = \frac{2}{\pi} \int_0^{+\infty} \frac{k}{k^2 - r^2} \left[e^{rz} - \frac{r e^{kz}}{k} \right] \sin(rx) dr , \text{ when } x \text{ goes to zero. For}$$

$$\text{this, we use the changement of variable } u = rx , \text{ so } I = \frac{2}{\pi} \int_0^{+\infty} \frac{k}{k^2 x^2 - u^2} \left[e^{uz/x} - \frac{u e^{uz/x}}{x k} \right] \sin(u) du .$$

$$\text{Now } \frac{k}{k^2 x^2 - u^2} \left[e^{uz/x} - \frac{u e^{uz/x}}{x k} \right] \sin(u) \sim e^{kz} \frac{\sin(u)}{u} \text{ when } x \rightarrow 0 , \text{ and } \frac{2}{\pi} \int_0^{+\infty} \frac{\sin(u)}{u} du = 1$$

so $I \sim e^{kz}$ when $x \rightarrow 0$, and we have exactly $\theta'_x \rightarrow 0$ when $x \rightarrow 0$.

Figures 2, 3 and 4 show the flow θ_0 , the correction θ' , and the final flow, with a zero normal velocity at the wall. Figure 5 presents the horizontal velocity U for different depth z , and one check that U goes to zero at the wall.

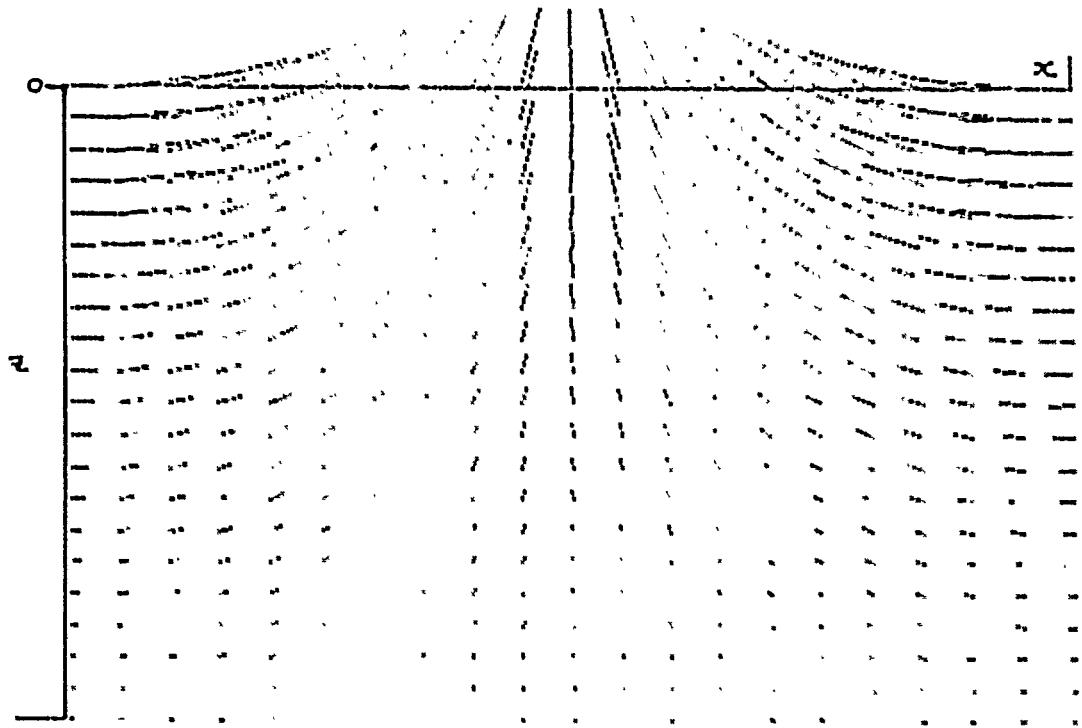


Fig. 2

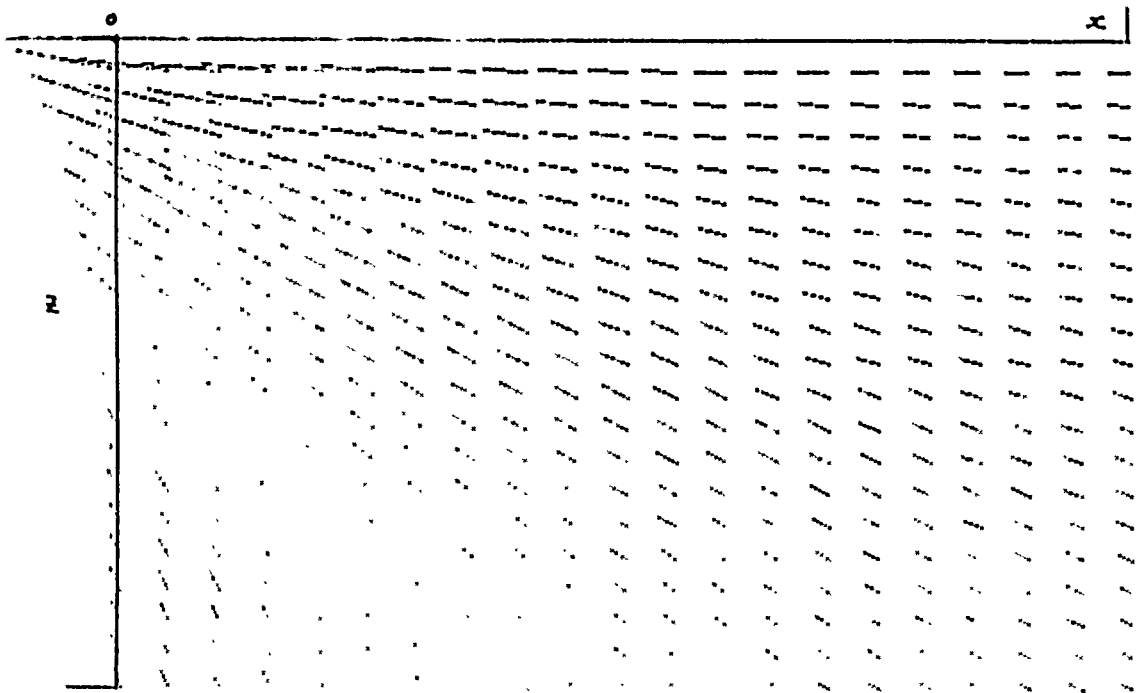


Fig. 3

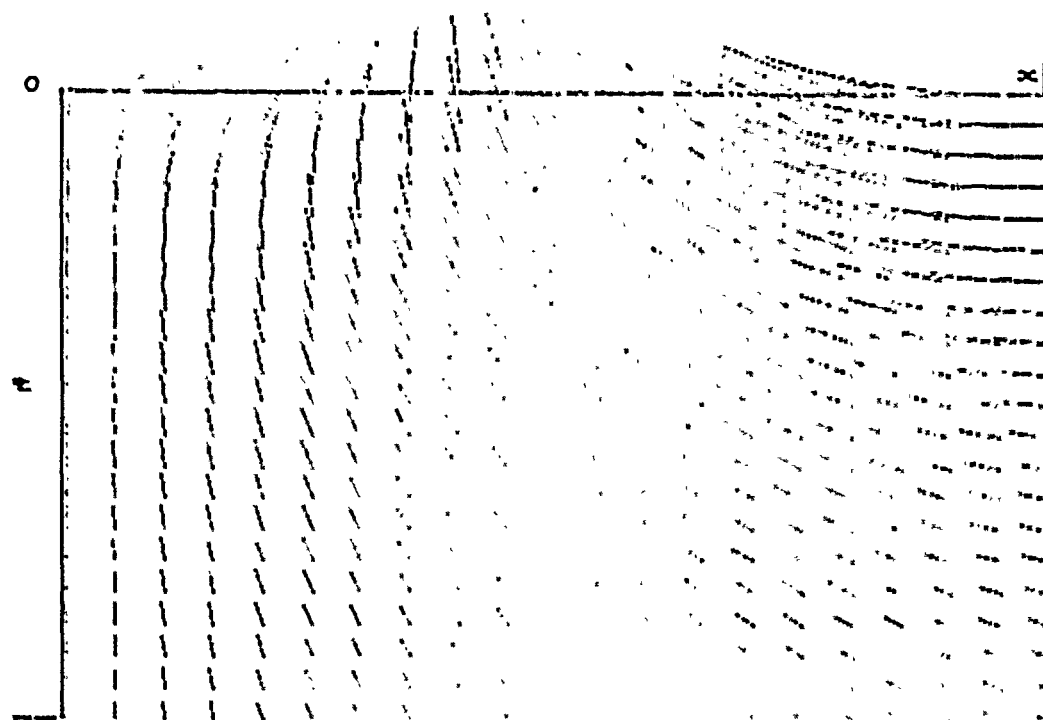


Fig. 4

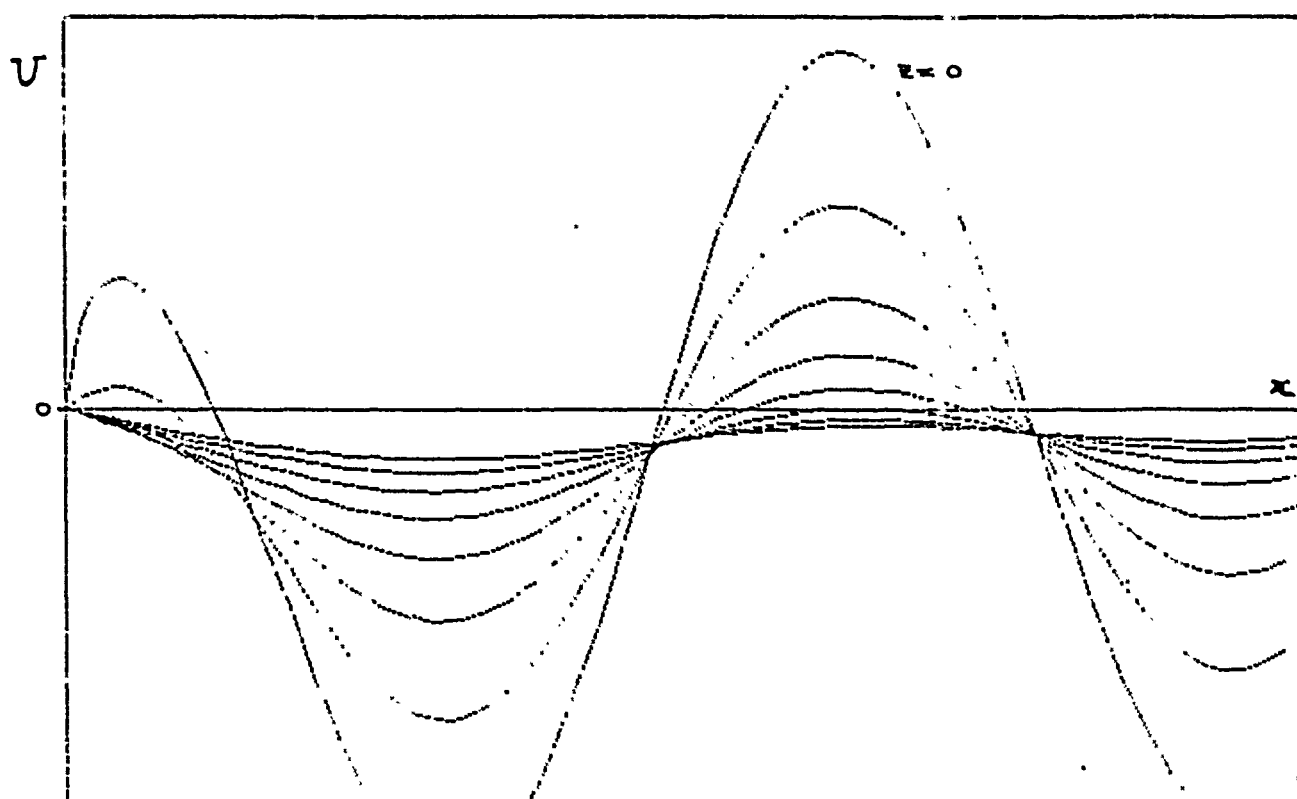
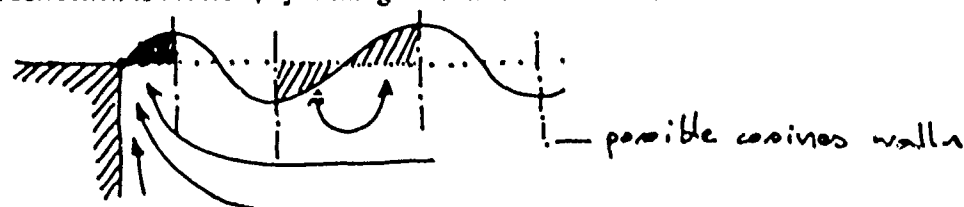


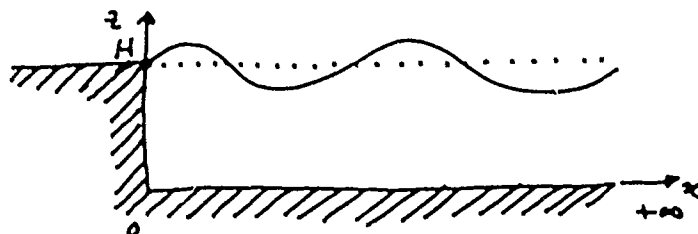
Fig. 5

At this point, one can also simply understand why this new boundary condition, i.e. with a surface of a sine, we must add a correction to the flow, by looking at the mass conservation :



the cosines always preserve mass, but the sine surface needs the addition of a small volume near the wall. The corresponding flow is the correction flow.

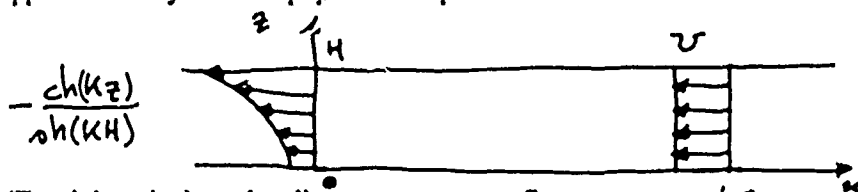
2.2 Bidimensionnal case with bottom



The changement from the preceeding solution is $\frac{e^{kz}}{k} \rightarrow \frac{\text{ch}(kz)}{k \text{ sh}(kH)}$

$$\text{thus } \theta = \sin(kx) \frac{\text{ch}(kz)}{k \text{ sh}(kH)} + \frac{2}{\pi} \int_0^{+\infty} \frac{k}{k^2 - r^2} \left[\frac{\text{ch}(rz)}{r \text{ sh}(rH)} - \frac{\text{ch}(kz)}{k \text{ sh}(kH)} \right] \cos(rx) dr$$

But now, θ_x is not defined from $r=0$, which means that there is a constant horizontal flow at $+\infty$. This appear naturally with the physical interpretation of the correction flow :



The sink at the lateral wall creates a constant flow at $+\infty$:

$$U H = \int_0^H \frac{\text{ch}(kz)}{\text{sh}(kH)} dz = \frac{1}{k} ; \text{ so } U = \frac{1}{kH} \quad \text{for } kx > 1. \text{ By subtracting this flow, and using the}$$

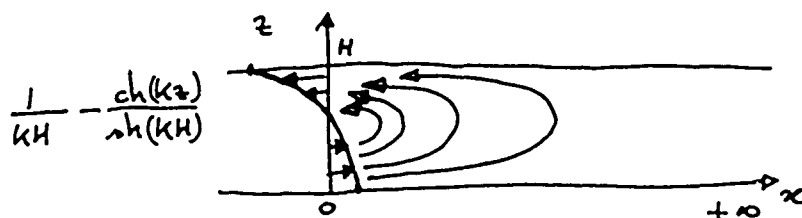
formal identity :

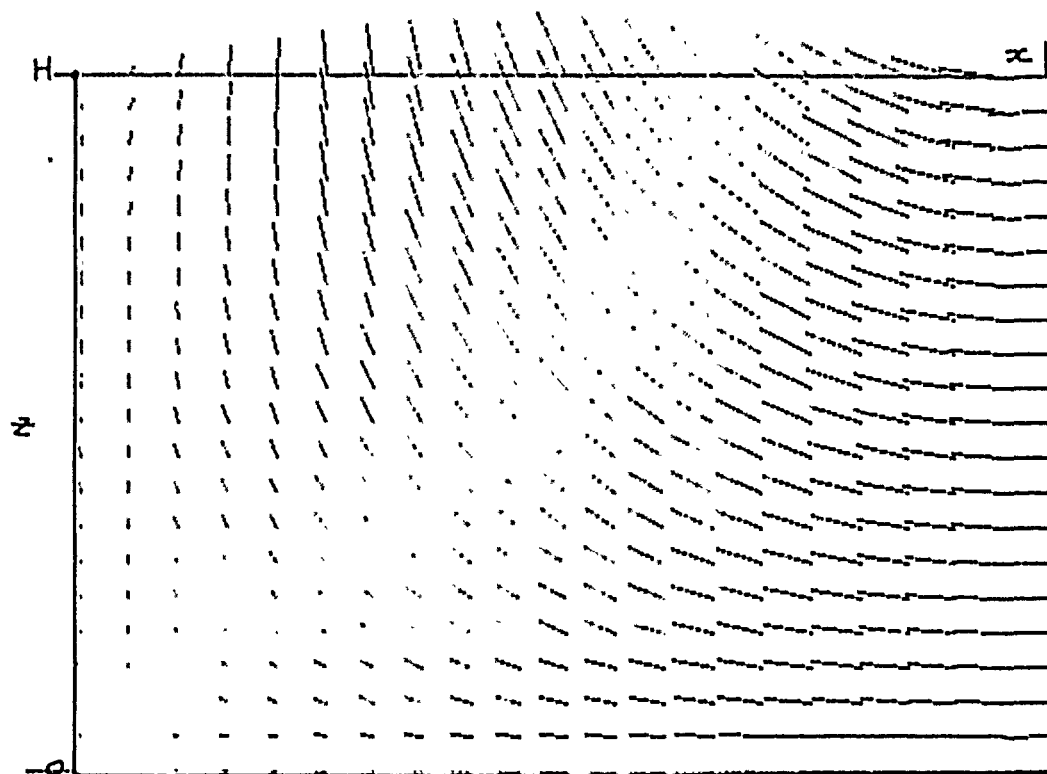
$$x = \frac{2}{\pi} \int_0^{+\infty} \frac{\cos(rx)}{r^2} dr, \text{ one finally obtains :}$$

$$\theta = \sin(kx) \frac{\text{ch}(kz)}{k \text{ sh}(kH)} - \frac{x}{kH} + \frac{2}{\pi} \int_0^{+\infty} \left[-\frac{1}{kH r^2} + \frac{k}{k^2 - r^2} \left[\frac{\text{ch}(rz)}{r \text{ sh}(rH)} - \frac{\text{ch}(kz)}{k \text{ sh}(kH)} \right] \right] \cos(rx) dr$$

which is well defined, and can also be correctly found if writing the problem for

$$\theta'' = \theta - \sin(kx) \frac{\text{ch}(kz)}{k \text{ sh}(kH)} + \frac{x}{kH}. \text{ One checks that } \theta''(+\infty) = 0 \text{ by the physical interpretation :}$$





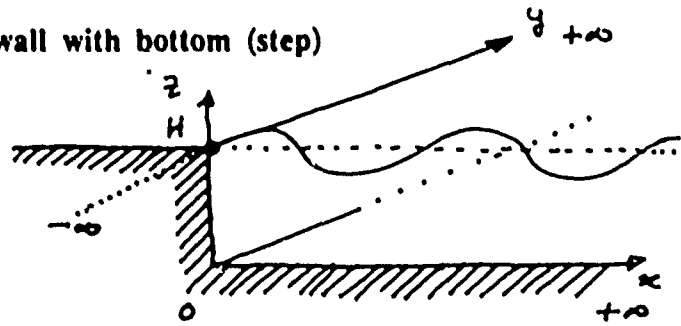
-Fig. 6

Figure 6 present the total flow.

One can also demonstrate by the same changement of variables that $\theta_x \rightarrow 0$ when $x \rightarrow 0$.

The simple interpretation of mass conservation is also valid.

2.3 Lateral wall with bottom (step)



$$h = h \sin(k_x x) \sin(k_y y) e^{i\omega t}$$

$$\phi = i\omega h \theta(x, z) \sin(k_y y) e^{i\omega t}$$

The formal solution for θ reads :

$$\theta = \frac{2}{\pi} \int_0^{+\infty} \frac{k}{k_x^2 - r^2} \frac{\text{ch}(qz)}{q \text{sh}(qH)} \cos(rx) dr$$

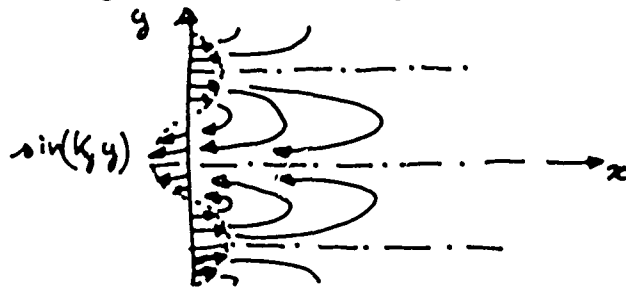
where $q^2 = k_y^2 + r^2$.

As always, it diverges for $r = k_x$, so we substract the usual solution :

$$\theta = \sin(k_x x) \frac{\text{ch}(Kz)}{K \text{sh}(KH)} + \frac{2}{\pi} \int_0^{+\infty} \frac{k_x}{k_x^2 - r^2} \left[\frac{\text{ch}(qz)}{q \text{sh}(qH)} - \frac{\text{ch}(Kz)}{K \text{sh}(KH)} \right] \cos(rx) dr$$

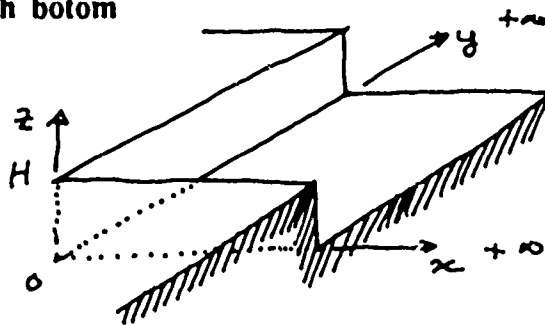
where $K^2 = k_x^2 + k_y^2$.

Contrary to the preceeding case, there is no divergence for $r = 0$. This can also be explain by a top vue of the flow :



One can also use the same tricks to check that $\theta_x \rightarrow 0$ when $x \rightarrow 0$.

2.4 Corner with botom



$$h = h \sin(k_x x) \sin(k_y y) e^{i\omega t}$$

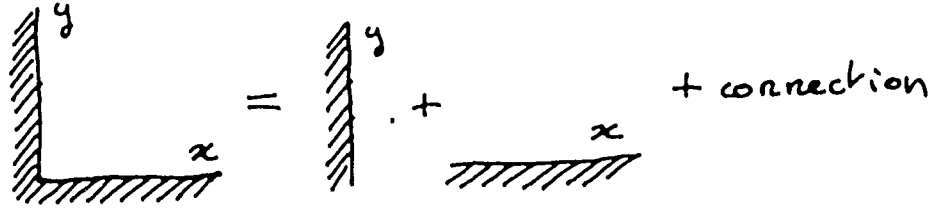
$$\phi = i\omega h \theta(x, y, z) e^{i\omega t}$$

The formal solution reads :

$$\theta = \int_0^{+\infty} \int_0^{+\infty} \frac{k_x}{k_x^2 - r^2} \frac{k_y}{k_y^2 - q^2} \frac{\text{ch}(Qz)}{Q \text{sh}(QH)} \cos(rx) \cos(qy) dr dq$$

where $Q^2 = r^2 + q^2$, is not defined from $r = k_x$ and $q = k_y$ separately. This means that we have again to subtract two solutions of the form $\sin(k_x x) \theta(y)$ and $\sin(k_y y) \theta(x)$, which correspond to the preceding solutions for two steps :

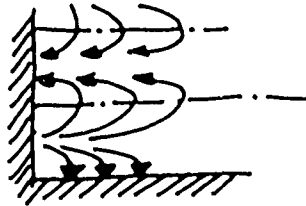
so



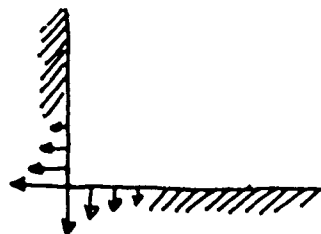
$$\begin{aligned} \theta = & \sin(k_x x) \sin(k_y y) \frac{\text{ch}(Kz)}{K \text{sh}(KH)} \\ & + \frac{2}{\pi} \sin(k_x x) \int_0^{+\infty} \frac{k_x}{k_x^2 - q^2} \left[\frac{\text{ch}(q'z)}{q' \text{sh}(q'H)} - \frac{\text{ch}(Kz)}{K \text{sh}(KH)} \right] \cos(q y) dq \\ & + \frac{2}{\pi} \sin(k_y y) \int_0^{+\infty} \frac{k_y}{k_y^2 - r^2} \left[\frac{\text{ch}(r'z)}{r' \text{sh}(r'H)} - \frac{\text{ch}(Kz)}{K \text{sh}(KH)} \right] \cos(r x) dr \\ & + \frac{4}{\pi^2} \int_0^{+\infty} \int_0^{+\infty} \frac{k_x}{k_x^2 - r^2} \frac{k_y}{k_y^2 - q^2} \left[\frac{\text{ch}(Qz)}{Q \text{sh}(QH)} - \frac{\text{ch}(q'z)}{q' \text{sh}(q'H)} - \frac{\text{ch}(r'z)}{r' \text{sh}(r'H)} + \frac{\text{ch}(Kz)}{K \text{sh}(KH)} \right] \cos(r x) \cos(q y) dr dq \end{aligned}$$

where $Q^2 = r^2 + q^2$,
 $r'^2 = r^2 + k_y^2$,
 and $q'^2 = k_x^2 + q^2$.

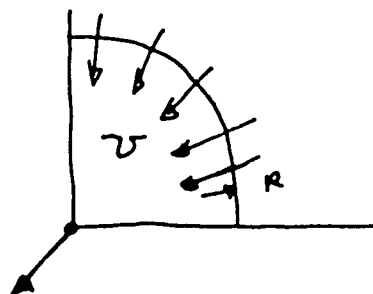
This solution is now perfectly defined, and there is no divergence from $Q=0$. This can be also understood by the same physical reasons : the solution for a step satisfies the boundary for its wall but not for the other one :



But the flow through the wall is located at the corner. Thus the flux condition for the last correction is located at the corner

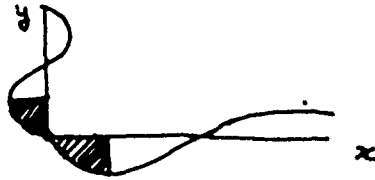


and far from it, it appears like a local sink :



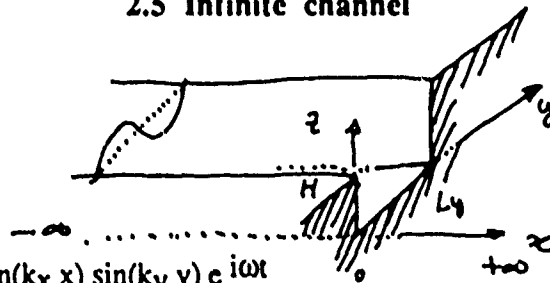
so also $U \sim 1/R$ for $KR > 1$.

Another way to obtain the shape of this flow is to notice that the mass is not conserved only at the corner on a surface corresponding to the quarter of the two wave-length :



One can also check that $\theta_x \rightarrow 0$ when $x \rightarrow 0$ and $\theta_y \rightarrow 0$ when $y \rightarrow 0$.

2.5 Infinite channel



$$h = h \sin(k_x x) \sin(k_y y) e^{i\omega t}$$

$$\phi = i\omega h \theta(y, z) \sin(k_x x) e^{i\omega t}$$

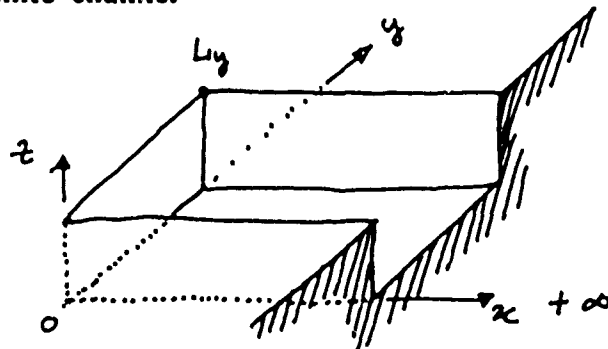
The formal solution reads :

$$\theta = \sum_p \frac{2 k_x}{k_x^2 - r^2} \frac{\text{ch}(qz)}{q \text{sh}(qH)} \cos(rx)$$

where $r = \frac{p\pi}{L_y}$ and $q^2 = k_x^2 + r^2$.

This solution is already well defined. But contrary to the preceding ones, it is not trivial to check that $\theta_y \rightarrow 0$ when $y \rightarrow 0$ and $y \rightarrow L_y$.

2.6 Half infinite channel



$$h = h \sin(k_x x) \sin(k_y y) e^{i\omega t}$$

$$\phi = i\omega h \theta(x, y, z) e^{i\omega t}$$

The formal solution reads :

$$\theta = \sum_p \frac{2}{\pi} \int_0^{+\infty} \frac{k_x}{k_x^2 - r^2} \frac{2 k_y}{k_y^2 - q^2} \frac{\text{ch}(Qz)}{Q \text{sh}(QH)} \cos(rx) \cos(qy) dr$$

where $q = \frac{p\pi}{L_y}$ and $Q^2 = r^2 + q^2$. This solution is not defined from $r = k_x$, so we have to subtract the preceding solution :

$$\theta = \sin(k_x x) \sum_p \frac{2 k_x}{k_x^2 - r^2} \frac{\text{ch}(q'z)}{q' \text{sh}(q'H)} \cos(qx) \\ + \sum_p \frac{2}{\pi} \int_0^{+\infty} \frac{k_x}{k_x^2 - r^2} \frac{2 k_y}{k_y^2 - q^2} \left[\frac{\text{ch}(Qz)}{Q \text{sh}(QH)} - \frac{\text{ch}(q'z)}{q' \text{sh}(q'H)} \right] \cos(rx) \cos(qy) dr$$

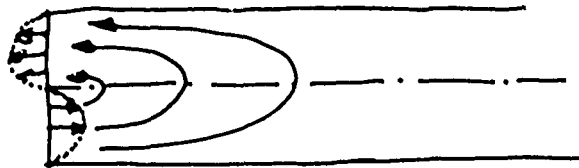
where $q = \frac{p\pi}{L_y}$, $q'^2 = k_x^2 + q^2$ and $Q^2 = r^2 + q^2$.

This solution is defined only for $m = k_y \frac{L_y}{\pi}$ even (so that q is never 0). Otherwise the first term of the discrete sum allows $q=0$ which makes the integral nondefined for $r=0$.

This also naturally appears when looking at the boundary condition near the wall :

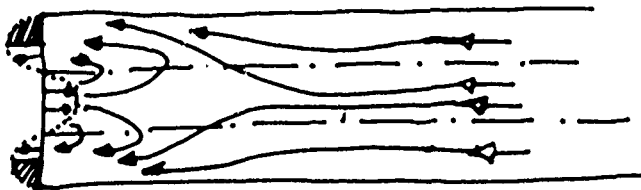
for m even :

no flow at $+\infty$



for m odd :

flow needed at $+\infty$



This problem of divergence due to the discrete sum is thus also due to the mass conservation, and is discussed in the following section.

2.7 Closed cell

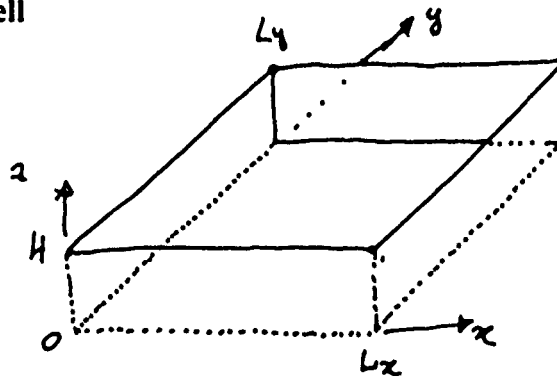
$$h = h \sin(k_x x) \sin(k_y y) e^{i\omega t}$$

$$\phi = i\omega h \theta(x, y, z) e^{i\omega t}$$

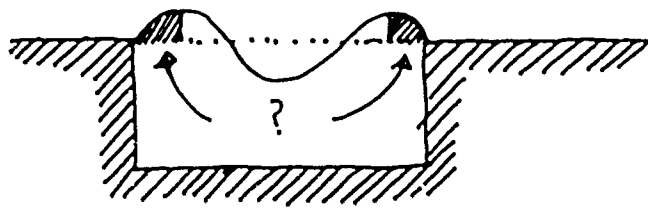
$$k_x = \frac{m_0 \pi}{L_x} \text{ and } k_y = \frac{n_0 \pi}{L_y}$$

The formal solution reads :

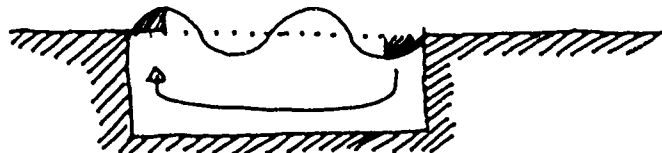
$$\theta = \sum_{m,n} \frac{2 k_x}{k_x^2 - k_m^2} \frac{2 k_y}{k_y^2 - k_n^2} \frac{\text{ch}(k_{mn} z)}{k_{mn} \text{sh}(k_{mn} H)} \cos(k_m x) \cos(k_n y)$$



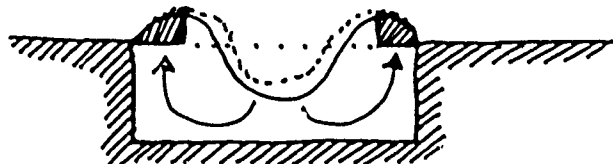
This solution is well defined except for m_0 and n_0 odd, as then $m=n=0$ is allowed and the first term of the sum is infinite. This divergence is also explained from the mass conservation :



for m_0 and n_0 odd the mode does not preserve the mass of the fluid. If one number is even there is then no problem :



The effect of an odd-odd mode is to suck down the center of the surface :



so that the mass is preserved. This can exactly be interpreted as the need of another mode, i.e. to say that the surface is not only a product of two sines, but the sum of several modes. We already know that from the study of the dispersion relation (see § II 1.2).

We can check this interpretation that the divergence just comes from the mass conservation by noticing that if we add two modes (of the same parities) such that the sum preserves the mass, then the divergence disappears :

$$\theta = \sum_{m,n} \left[\alpha \frac{2k_x}{k_x^2 - k_m^2} \frac{2k_y}{k_y^2 - k_n^2} + \beta \frac{2k'_x}{k'^2_x - k_m^2} \frac{2k'_y}{k'^2_y - k_n^2} \right] \frac{\text{ch}(k_{mn} z)}{k_{mn} \text{sh}(k_{mn} H)} \cos(k_m x) \cos(k_n y)$$

$$\text{with } \int_0^{L_x} \int_0^{L_y} [\alpha \sin(k_x x) \sin(k_y y) + \beta \sin(k'_x x) \sin(k'_y y)] dx dy = 0$$

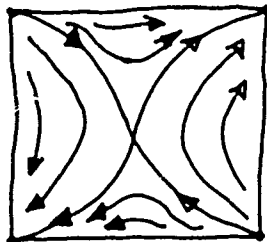
$$\text{i.e. } \frac{\alpha}{k_x k_y} + \frac{\beta}{k'_x k'_y} = 0, \text{ and this is exactly the first term (} m=n=0 \text{)}.$$

This remark is valid for whatever sum of modes one chooses such that the mass is preserved.

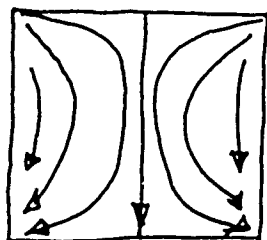
An interesting problem is now to look at the comparison between this condition of mass conservation and the different orders in the Galerkin approximation.

One can also, from the correction due to a corner, draw the correction to the flow in a rectangular cell, depending on the parities :

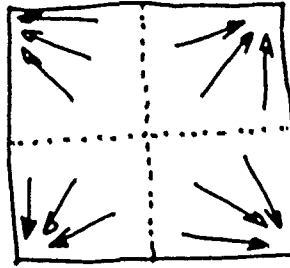
even-even :



even-odd :



odd-odd :

sucks down
the surface

3 Short study of the dispersion relation

From all the above exemples one can write the corresponding dispersion relations by reporting θ in the physical boundary condition.

Here we will focused only on case of an infinite channel, which was done with the tool of a variational principle by Benjamin & Scott.

We did not have time to study the dispersion relation in a closed wessel, and to look at the dependence on the aspect ratio $\frac{k_x}{k_y}$.

Figure 7 presents the dispersion relation at the first order of the galerkine aproximaton :

$$\omega^2 \sum_p \left(\frac{2 k_x}{k_x^2 - r^2} \right)^2 \frac{\text{ch}(qH)}{\text{qsh}(qH)} = [g + \gamma K^2]$$

where $k_x = \frac{m \pi}{L_x}$, $r = \frac{p \pi}{L_x}$, $q^2 = r^2 + k_y^2$ and $K^2 = k_x^2 + k_y^2$; for m odd and an infinite depth

($\text{ch}/\text{sh}=1$), and we have plotted $A = \frac{\omega^2}{[g + \gamma K^2]}$ as a function of K and k_y . For the usual dispersion relation, $A = K$, the diagonal line. The most surprising result is that, for the mode $m=1$, the dispersion relation is nearly $A = k_y$. This probably comes from the fact that the mode can not have less than one transverse modulation, and thus it does not appear in the dispersion relation.

Thus cuts of the curves $A(K)$ are natural as K can start only from k_y .

The fact that A goes to zero when k_y goes to zero for the modes $m>1$ is unphysical and just comes from the fact that an odd mode can not preserve mass in the cross direction, when the wave length becomes infinite in the long direction (a zero frequency mode is an unexisting mode). So other modes are needed, i.e. one needs to go at a higher order in the galerkine approximation, and this kill this effect.

4 Conclusion

As a conclusion for this part, we can point out the symplicity of the formal solution. The usual boundary condition gives quickly the usual simple result. But with the new boundary condition, the surface is no longer simple. However, we think that it can be simply aproximate by one or the sum of few products of two sines. Then one can found corresponding aproximate dispersion relations, presenting already the special dependences on $\frac{k_x}{k_y}$.

We also shown that the formal solution allow to write directly well defined solutions. The divergences can be understood in several way, the more physiscal corresponding to the mass conservation imposing a flow at $+\infty$. The nondefinitions coming from k_x , k_y , K , or 0 just tell us to substract the simple solutions in $\sin(k_x x)$, $\sin(k_y y)$, $\sin(k_x x) \cdot \sin(k_y y)$, or constant flow. After this, the solution is well defined, and, in the infinite case, one can check that $\theta_x \rightarrow 0$ when aproaching the wall. Simple reasonements with the mass conservation gives also by two different ways the shape of the flow.

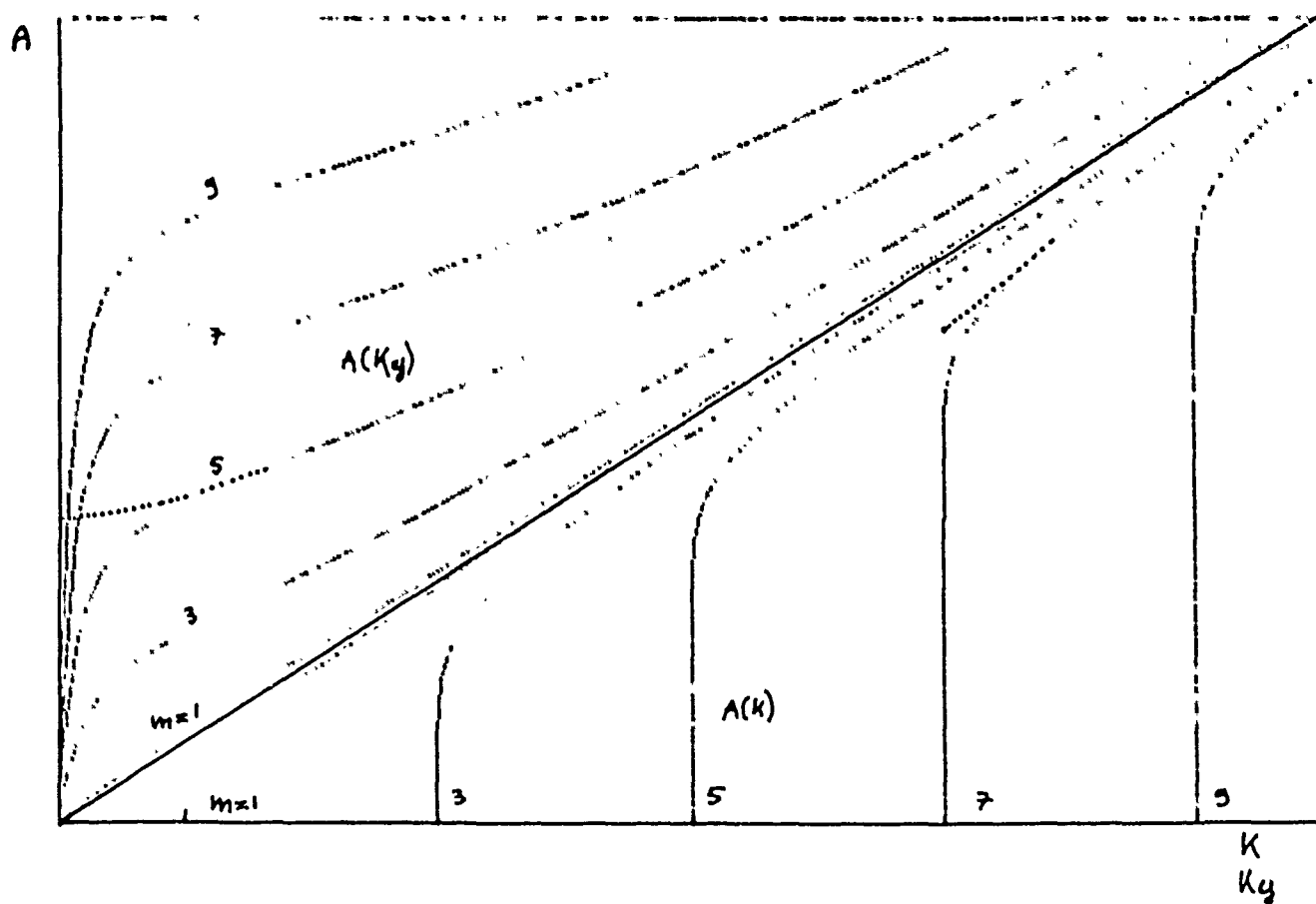


Fig. 7.

III DISSIPATION

With the approximation of a surface which is simply the product of two sines or cosines, we have seen in § I 3.2 that

$$\lambda = \sqrt{\nu \omega} \frac{\omega^2}{[g + \gamma K^2]} \frac{2}{L_x L_y} \frac{1}{\omega} \int_S (\nabla \theta)^2 ds.$$

We just have to compute the integral for the different solutions above. For this, we just have to know the same integrals :

$$\int_0^L \sin(kx)^2 dx = \int_0^L \cos(kx)^2 dx = \frac{L}{2}$$

$$\int_0^H \left(\frac{\text{ch}(Kz)}{\text{sh}(KH)} \right)^2 dz = \frac{1}{2} \left[\frac{\text{ch}(KH)}{K \text{sh}(KH)} - \frac{H}{\text{sh}(KH)^2} \right]$$

$$\int_0^H \left(\frac{\text{sh}(Kz)}{\text{sh}(KH)} \right)^2 dz = \frac{1}{2} \left[\frac{\text{ch}(KH)}{K \text{sh}(KH)} + \frac{H}{\text{sh}(KH)^2} \right]$$

We will present only few exemples, as the computation for each case is always the same.

1 First boundary condition

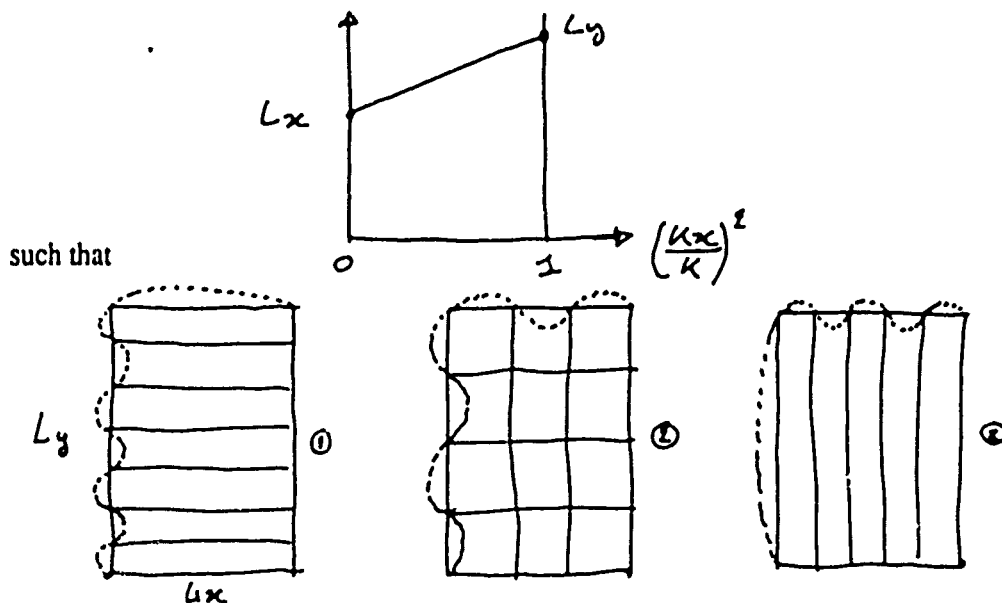
From § II 1.2 we know that the surface $f = \cos(k_x x) \cos(k_y y)$

and that $\theta = \frac{\text{ch}(Kz)}{K \text{sh}(KH)} \cos(k_x x) \cos(k_y y)$.

One obtains, after a few algebra, and adding the contributions of the bottom and the four side walls :

$$\begin{aligned} \int_S (\nabla \theta)^2 ds &= \frac{1}{2} \left[L_x \left(\frac{k_x}{K} \right)^2 + L_y \left(\frac{k_y}{K} \right)^2 \right] \left[\frac{\text{ch}(KH)}{K \text{sh}(KH)} + \frac{H}{\text{sh}(KH)^2} \right] \\ &+ \frac{1}{2} (L_x + L_y) \left[\frac{\text{ch}(KH)}{K \text{sh}(KH)} - \frac{H}{\text{sh}(KH)^2} \right] \\ &+ \frac{L_x L_y}{2} \frac{2}{\text{sh}(KH)^2} \end{aligned}$$

There is only one term depending on k_x and k_y , but this just comes from a different weight on the different size of the lateral walls. This is a linear dependance :



① dissipates more than ② which dissipates more than ③
 But this effect disappears in a square cell, as one then obtains :

$$\int_S (\nabla \theta)^2 ds = \frac{L}{2} \left[\frac{3 \operatorname{ch}(KH)}{K \operatorname{sh}(KH)} + \frac{H}{\operatorname{sh}(KH)^2} \right] + \frac{L^2}{2} \frac{1}{\operatorname{sh}(KH)^2}$$

So

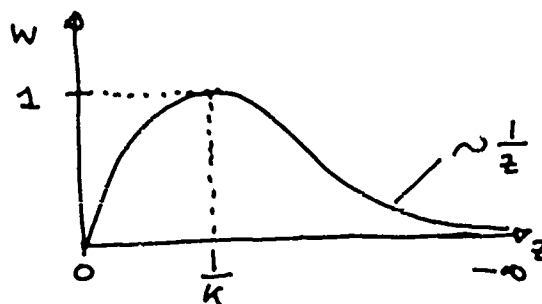
$$\begin{aligned} \lambda &= \sqrt{\nu \omega} \frac{1}{L^2} \left[\frac{L}{2} \left[3 - \frac{K \operatorname{ch}(KH)}{\operatorname{ch}(KH) \operatorname{sh}(KH)} \right] + \frac{L^2}{2} \frac{K}{\operatorname{ch}(KH) \operatorname{sh}(KH)} \right] \\ &\sim \sqrt{\nu \omega} \frac{1}{L} \quad \text{when } KH \gg 1 \quad \text{i.e. } \omega \gg 1 \\ &\sim \sqrt{\nu \omega} \frac{1}{L} \left(\frac{2}{L} + \frac{1}{2H} \right) \quad \text{when } KH \ll 1 \quad \text{i.e. } \omega \ll 1 \end{aligned}$$

In fact, one sees that the dissipation is principally due to the friction at the lateral wall, which is always important (term in $1/L$), except at small frequencies, where the friction at the bottom becomes comparable. One also sees the general expression of the dissipation in $\sqrt{\nu \omega}$, i.e. its increase with frequency.

2 Second boundary condition

2.1 Bidimensionnal case without bottom

As the simple solution has no tangential velocity at the lateral wall, all the dissipation comes from the correction flow, the form of which is :

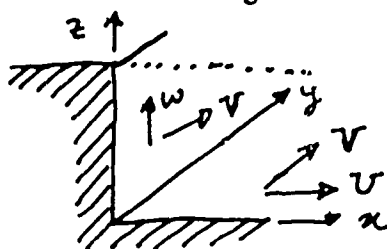


$$\text{So } \int_{-\infty}^0 w^2 dz \sim \frac{1}{K} + \int_{\frac{1}{K}}^{\infty} \frac{1}{z^2} dz \sim \frac{1}{K}$$

which is surprisingly exactly the same contribution than the preceding case !

2.2 Step (wall with bottom)

This case is more physical as it allows a tangential flow in both directions :



At the lateral wall, from the preceding solution, we found

$$w = \sin(k_y y) \frac{2}{\pi} \int_0^{+\infty} \frac{k_x}{k_x^2 + r^2} \left[\frac{\text{sh}(qz)}{\text{sh}(qH)} - \frac{\text{sh}(Kz)}{\text{sh}(KH)} \right] dr$$

As we are interested in its dependence on k_x , k_y and K , we adimensionalize this integral by expressing it as a function of $u = \frac{q}{K} = \frac{\sqrt{k_x^2 + r^2}}{K}$. Thus

$$w = \frac{k_x}{K} \sin(k_y y) f\left(Kz; \frac{k_y}{K}\right)$$

$$\text{with } f\left(Kz; \frac{k_y}{K}\right) = \frac{1}{\pi} \int_{\frac{k_y}{K}}^{+\infty} \frac{1}{1-u^2} \left[\frac{\text{sh}(Kzu)}{\text{sh}(KHu)} - \frac{\text{sh}(Kz)}{\text{sh}(KH)} \right] \frac{u}{\sqrt{u^2 - \left(\frac{k_y}{K}\right)^2}} du$$

We think that f does not depend to much in $\frac{k_y}{K}$ as it varies only in $]0, 1[$.

In the same way, one obtains :

$$v = \frac{k_y}{K} \cos(k_y y) g\left(Kz; \frac{k_y}{K}\right)$$

$$\text{with } g\left(Kz; \frac{k_y}{K}\right) = \frac{1}{\pi} \int_{\frac{k_y}{K}}^{+\infty} \frac{1}{1-u^2} \left[\frac{\text{ch}(Kzu)}{u \text{sh}(KHu)} - \frac{\text{ch}(Kz)}{\text{sh}(KH)} \right] \frac{u}{\sqrt{u^2 - \left(\frac{k_y}{K}\right)^2}} du$$

So one can write directly the geometrical factor corresponding to the lateral wall :

$$\int_{\text{Lat W}} (\nabla \theta)^2 ds = \frac{L_y}{2K} \left[\left(\frac{k_x}{K}\right)^2 F\left(KH; \frac{k_y}{K}\right) + \left(\frac{k_x}{K}\right)^2 \left(\frac{k_y}{K}\right)^2 G\left(KH; \frac{k_y}{K}\right) \right]$$

$$\text{with } F\left(KH; \frac{k_y}{K}\right) = \int_0^H f^2 dKz$$

$$\text{and } G\left(KH; \frac{k_y}{K}\right) = \int_0^H g^2 dKz$$

For the bottom, one found a similar structure for this geometrical factor :

$$\int_{\text{Bottom}} (\nabla \theta)^2 ds = \frac{L_x L_y}{K^2} \left[\left(\frac{k_x}{K}\right)^2 f'\left(KH; \frac{k_y}{K}\right) + \left(\frac{k_x}{K}\right)^2 \left(\frac{k_y}{K}\right)^2 g'\left(KH; \frac{k_y}{K}\right) + \left(\frac{k_y}{K}\right)^2 g''\left(KH; \frac{k_y}{K}\right) \right]$$

with

$$f'\left(KH; \frac{k_y}{K}\right) = \left[\frac{1}{\text{sh}(KH)^2} + \frac{1}{\pi} \int_{\frac{k_y}{K}}^{+\infty} \frac{1}{(1-u^2)^2} \left[\frac{1}{u \text{sh}(KHu)} - \frac{1}{\text{sh}(KH)} \right]^2 u \sqrt{u^2 - \left(\frac{k_y}{K}\right)^2} du \right]$$

$$g'\left(KH; \frac{k_y}{K}\right) = \frac{1}{\pi} \int_{\frac{k_y}{K}}^{+\infty} \frac{1}{(1-u^2)^2} \left[\frac{1}{u \text{sh}(KHu)} - \frac{1}{\text{sh}(KH)} \right]^2 \frac{u}{\sqrt{u^2 - \left(\frac{k_y}{K}\right)^2}} du$$

$$g''\left(KH; \frac{k_y}{K}\right) = \frac{1}{\text{sh}(KH)^2}$$

One can notice that the terms in $1/sh^2$ comes from the simple solution.

This structure of the dissipation can be found with the remark that the correction flow is created only to compensate the flow of the simple solution through the wall :



With $h = h \sin(k_x x) \sin(k_y y) e^{i\omega t}$

it gives $\phi^0 \sim \frac{\omega h}{K}$; so $U^0 \sim \omega h \frac{k_x}{K}$. Thus for the correction flow we have :

$\phi' \sim \omega h \frac{k_x}{K^2}$; so $U' \sim \omega h \left(\frac{k_x}{K}\right)^2$, $V' \sim \omega h \frac{k_x k_y}{K^2}$, and $W' \sim \omega h \frac{k_x}{K}$.

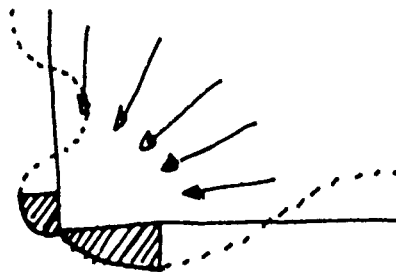
And thus one found the structure.

But in fact, the passage from U^0 to ϕ' is not so simple, and this is where the factors f, g, F, G, f', g' come from.

In this tridimensionnal case, the dissipation at the bottom also disappears at high frequency, as the correction flow does not go to infinity.

2.3 Square cell and corner

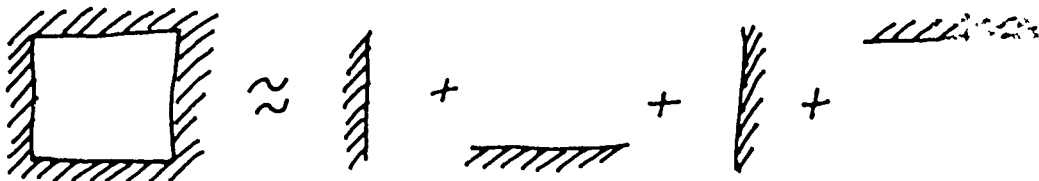
A first approximation for the corner would consist in adding at the dissipation due to two steps the dissipation due to a first approximation of the correction flow :



with the mass conservation, we found that $U \sim \frac{1}{k_x k_y} \frac{1}{RH}$.

One must note its strange divergence for k_x or k_y going to zero.

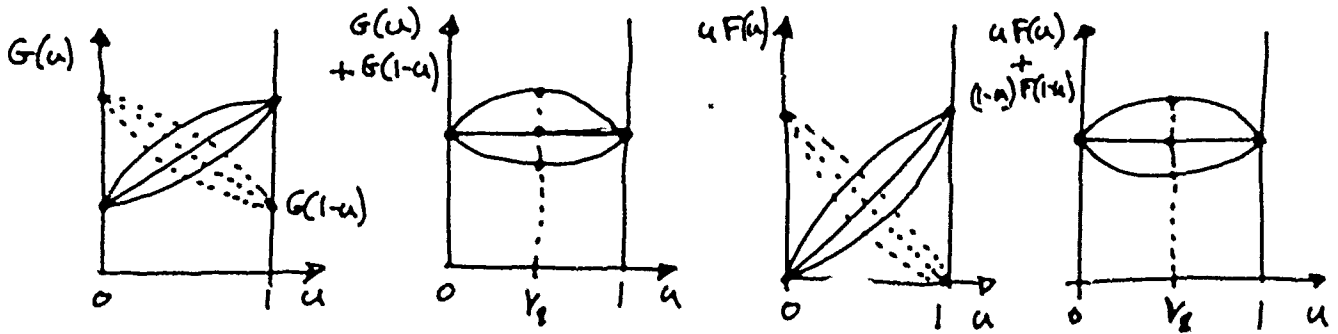
For a square cell, which is in reality our principal interest, a first approximation consist to take the dissipation given by the sum of four steps :



This gives :

$$\int_{W_S} (\nabla \theta)^2 ds = \frac{L}{K} \left[\left(\frac{k_x}{K}\right)^2 F'\left(KH; \frac{k_y}{K}\right) + \left(\frac{k_y}{K}\right)^2 F'\left(KH; \frac{k_x}{K}\right) + \left(\frac{k_x}{K}\right)^2 \left(\frac{k_y}{K}\right)^2 \left[G'\left(KH; \frac{k_y}{K}\right) + G'\left(KH; \frac{k_x}{K}\right) \right] \right]$$

This expression has two terms, the first one is nearly symmetric in k_x and k_y , and the second is in $k_x k_y$. The sum also diminish the small dependence of F' and G' in k_x and k_y ($u = \left(\frac{k_x}{K}\right)^2$):

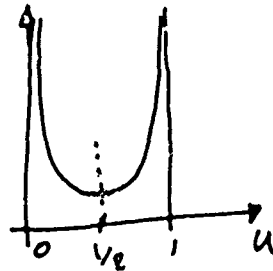


Thus the shape of the final solution is :

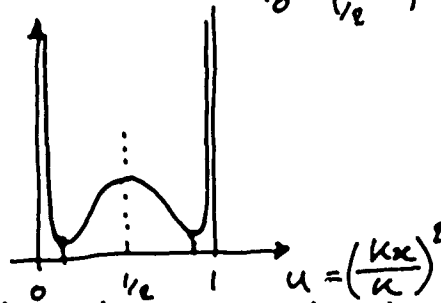


This is exactly the kind of dependence observed experimentally in a square cell.

A better approximation of a square cell would be to consider it as the sum of four corners. Now the correction of one corner to two step gives a term in $\frac{1}{k_x^2 k_y^2}$:



So the final solution would be like :



This shape explain that there would be a optimum aspect ratio, and perhaps explain the fact that at high frequency, one preferentially observes modes with a given small aspect ratio near 1/6.

4 conclusion

As a conclusion for this last part, it appears to be quite simple to compute directly the dissipation term of the amplitude equation. With the usual boundary condition, it does not give any dependance, except the trivial rectangular one, on k_x and k_y .

On the contrary, the new boundary condition gives the observed dependences, and this can be explain simply by the fact that the dissipation is due to the corection flow needed to compensate the flow through the wall of the usual solution.

The last result is very interesting as it could explain the shape of the modes in a very large cell, only by the selection from the dissipation.

CONCLUSION

Some experiments were performed with a simple boundary condition which consist to pin the free surface at the edge of the lateral walls. But it appears to give strange dependence of the eigen frequencies and dissipations of the eigen modes on the aspect ratio $\frac{k_x}{k_y}$.

By first looking at the structure of the problem, we shown that we need, and only need, to solve the inviscid problem with this new boundary condition ; and we shown how to found the real coefficients of the amplitude equation from the energy equation derived from Navier-Stokes. Especially we expressed simply the dissipation λ only as a function of the geometry of the inviscid flow at the cell walls.

In a second part we found a formal solution for the inviscid problem, and how to found more and more accurate approximations for the free surface and eigen frequencies. Benjamin & Scott used a similar approach, but by using a variationnal method they found more accurate eigen frequencies but lose all information on the free surface and on the flow. We shown also how from the formal solution to write well defined solutions for the flow with physical arguments derived from the mass conservation. These interpretations allow us to found the shape of the flow.

Finally we used these results to found the dissipation in a closed cell, and shown how the structure of the flow near the wall explain the experimental dependences. It can also predicts the shape of the modes in the limit of a very large cell, just before chaotic behaviors.

Extensions of this work

We will study in more details the surface and the dispersion relation. We would like also to compute the dissipation in a square cell.

It would be also interesting to look at the derivation of the nonlinear real terms of the amplitude equation, still from the energy equation.

Aknowledgments

I especially thanks Bill Young to have initiated this work, and helped me with his ideas, interest and remarks. I also want to thank the staff and fellows for interesting discussions, and everyone involved in this enjoyable and profitable summer.

References

- Benjamin & Scott "Gravity-capillary waves with edge constraints", J. Fluid Mech. , vol. 92, n° 2, 241 (1979)
- Douady & Fauve "Pattern selection in Faraday instability", Europhys. Letters, vol. 6, n°3, 221 (1988)
- Douady "experimental study of the Faraday instability" submitted to J. Fluid Mech.

Rotating Rayleigh-Bénard Convection with Fixed Flux Boundaries

Timothy E. Dowling

California Institute of Technology

I. Introduction

Convection between two horizontal plane boundaries, known as Rayleigh-Bénard convection, has been extensively studied for the case of fixed temperature (perfectly conducting) boundaries. The opposite extreme is the case of fixed heat flux (perfectly insulating) boundaries, and this problem has been taken up in recent years (cf., Sparrow, Goldstein, and Jonsson, 1964; Hurle, Jakeman, and Pike, 1967; Chapman and Proctor, 1980; Depassier and Spiegel, 1982). One significant distinction between the two extremes is the value of the horizontal wavenumber for the onset of convection, k_c . In the case of fixed temperature boundaries k_c is larger than zero, but in the case of fixed flux boundaries k_c is zero (ie., convection with infinite horizontal wavelength). We have extended the study of convection with fixed flux boundaries to the geophysically important case of a rotating system.

After describing the physical system and governing equations, we briefly review below the effects of varying the thermal boundary condition on the nonrotating case, and the effects of rotation on the case of fixed temperature boundaries. It will be seen that rotation introduces several new effects, including a tendency to increase k_c and the introduction of a second mode of convection arising from inertial oscillations, known as overstability. Two important questions then are these: What strength of rotation is required to make k_c bigger than zero for the fixed flux problem, and what strength of rotation is required for overstability? We study the linear problem, beginning with a small k analysis, which in particular will answer the former question. Next, we use a variational technique to study the system for all k . We will make a brief remark on the nonlinear problem, and then summarize our conclusions and point to future work.

II. Physical System and Governing Equations

The configuration to be examined is sketched in Fig. 1. We consider a Boussinesq fluid with kinematic viscosity ν , thermal diffusivity κ , and coefficient of thermal expansion α , confined between two horizontal plane boundaries separated by a vertical distance d . The Boussinesq approximation is not ideal for $k_c = 0$ systems because fluid which travels a great

horizontal distance may eventually see a significant change in density. More specifically, the Boussinesq and shallow-layer approximations do not commute (cf., Depassier and Spiegel, 1982). For this first pass we will nevertheless assume that density variations are only important when multiplied by g . (An extreme example of a non-Boussinesq, fixed flux (zero flux) system is bioconvection (cf., Childress, Levandowski, and Spiegel, 1975).)

The heat equation for the fluid is

$$\left(\frac{\partial}{\partial t} + \mathbf{v} \cdot \nabla\right) T = \kappa \nabla^2 T \quad (1)$$

where T is the temperature and $\mathbf{v} = (u, v, w)$ is the velocity. An adverse temperature gradient $\partial T / \partial z = -\beta$ is held fixed on the boundaries. It is customary to define a new variable θ by $T = T_0 - \beta z + \theta$, which yields

$$\left(\frac{\partial}{\partial t} + \mathbf{v} \cdot \nabla\right) \theta - \beta w = \kappa \nabla^2 \theta \quad (2)$$

The thermal boundary condition becomes

$$\frac{\partial \theta}{\partial z} = 0, \quad z = \pm \frac{1}{2}d. \quad (3)$$

The continuity equation is

$$\nabla \cdot \mathbf{v} = 0, \quad (4)$$

and the momentum equation for this rotating system is

$$\left(\frac{\partial}{\partial t} + \mathbf{v} \cdot \nabla\right) \mathbf{v} + f \hat{\mathbf{z}} \times \mathbf{v} = -\frac{1}{\rho_0} \nabla p + g \alpha \theta \hat{\mathbf{z}} + \nu \nabla^2 \mathbf{v}. \quad (5)$$

We nondimensionalize by redefining variables as follows: $\mathbf{v} \rightarrow \kappa/d \mathbf{v}$, $p \rightarrow \rho_0 \kappa^2/d^2 p$, $t \rightarrow d^2/\kappa t$, $\mathbf{x} \rightarrow d \mathbf{x}$, $\theta \rightarrow d\beta \theta$, $f \rightarrow \kappa/d^2 f$. The equations become

$$\left(\frac{\partial}{\partial t} + \mathbf{v} \cdot \nabla\right) \theta - w = \nabla^2 \theta, \quad (6)$$

$$\nabla \cdot \mathbf{v} = 0, \quad (7)$$

$$\left(\frac{\partial}{\partial t} + \mathbf{v} \cdot \nabla\right) \mathbf{v} + f \hat{\mathbf{z}} \times \mathbf{v} = -\nabla p + \sigma R \theta \hat{\mathbf{z}} + \sigma \nabla^2 \mathbf{v}, \quad (8)$$

where the Rayleigh and Prandtl numbers are defined as

$$R \equiv \frac{g \alpha \beta d^4}{\kappa \nu}, \quad \sigma \equiv \nu / \kappa. \quad (9)$$

We will focus on free slip boundaries, for which

$$w, \frac{\partial u}{\partial z}, \frac{\partial v}{\partial z}, \frac{\partial^2 w}{\partial z^2} = 0, \quad \text{on } z = \pm \frac{1}{2}. \quad (10)$$

We examine the onset of convection by determining the marginal curve $R(k)$ for which $\partial/\partial t = 0$ (stationary convection) and $\partial/\partial t = i\omega$ (overstability, defined in Sec. IV below). For values of R above the marginal curve the system convects. The minimum value of R on the marginal curve is denoted R_c , and the corresponding wavenumber is denoted k_c . Hence initially convection occurs with wavenumber k_c . We are after how R_c and k_c vary with rotation.

III. Nonrotating: Effect of Thermal Boundaries

Before proceeding to rotating systems, we will examine the effect of varying the thermal boundary condition from the fixed temperature case to the fixed flux case. A useful reference is the treatment by Hurle, Jakeman, and Pike (1967). They denote the diffusivities of the solid boundary and interior fluid by κ_S and κ_F , respectively. We will in addition define the corresponding thermal conductivities to be $K = \rho C_p \kappa$, where C_p is the heat capacity. The ratio of conductivities K_S/K_F , sometimes called the 'Biot number' (Sparrow, Goldstein, and Jonsson, 1964; Proctor, 1981), ranges from infinity to zero as we pass from the fixed temperature case to the fixed flux case. To see this, note that at the interface between the boundary and fluid, we must have continuity of heat flux:

$$K_S \frac{\partial}{\partial z} \theta_S = K_F \frac{\partial}{\partial z} \theta_F. \quad (11)$$

Thus in the limit $K_S/K_F = 0$ (or $\kappa_S/\kappa_F = 0$) we get the boundary condition $\partial\theta/\partial z = 0$. [Note: Both Hurle, Jakeman, and Pike (1967) and Proctor (1981) have apparently confused thermal diffusivity κ with thermal conductivity K in their equations for continuity of heat flux. This means their expressions involving finite Biot number are numerically correct only when $(\rho C_p)_S = (\rho C_p)_F$, which is not generally the case.]

The dependence of marginal stability on κ_S/κ_F , as calculated by Hurle, Jakeman, and Pike, is shown in Fig. 2. These curves are for rigid (no-slip) boundaries, but there is no qualitative difference with the free-slip case we are studying. In Fig. 2(a) the marginal $R(k)$ curves are shown for various κ_S/κ_F , and it may be seen that R_c and k_c both decrease with decreasing κ_S/κ_F . As mentioned above, $k_c = 0$ for the case $\kappa_S/\kappa_F = 0$. Fig 2(b) shows R_c and k_c as explicit functions of κ_S/κ_F , with their values for the fixed flux limit

denoted by dotted lines. The value of R_c ranges from 1707.8 to $6! = 720$ for the rigid-boundary case, and from $27\pi^4/4 = 657.5$ to $5! = 120$ for the free-boundary case. We will be required to recover the value $R_c = 120$ from our results of Sec. V below in the limit of no rotation.

IV. Rotating: The Case of Fixed Temperature Boundaries

Rotation adds three important new effects to the convecting system. Firstly, for very strong rotation, the Taylor-Proudman theorem applies and $\partial/\partial z = 0$ away from the boundaries; that is, vertical motions are inhibited in the interior. Thus, we expect R_c to increase with f . Secondly, a rotating fluid allows inertial oscillations. Thermal dissipation causes a parcel to return after one half-oscillation with a temperature different than its starting temperature. This can lead to growing oscillations, called overstability (or vibrational instability), and is a new, competing mode of convection. Thirdly, the Coriolis force deflects horizontal motions, and we therefore expect k_c to increase with f .

An excellent source for our purposes is Chandrasekhar (1961), from which most of what follows in this section will be drawn. An asymptotic treatment for large rotation is given in Heard and Veronis (1971), who deal with the question of viscous and thermal boundary layers. We will generally be examining rotation small enough so that the entire layer of fluid is an Ekman layer (i.e., friction and Coriolis forces are equally important).

The case of free-slip boundaries is easy (Chandrasekhar, 1961), and leads to the following expression for marginal stability:

$$R = \frac{1}{k^2} \left[(\pi^2 + k^2)^3 + \pi^2 T \right], \quad (12)$$

where the Taylor number T is $(f/\sigma)^2$ in nondimensional variables or $(fd^2/\nu)^2$ in dimensional variables.

The marginal curve ($\partial/\partial t = 0$) for $T = 10,000$ is shown in Fig. 3, and is labeled 'convection.' The remaining curves are for the marginal state leading to overstability ($\partial/\partial t = i\omega$), and are labeled by Prandtl number σ . Note that all curves go to infinity for small k . Figure 4 shows that R_c and k_c increase with increasing rotation, as expected. The overstability curves are for $\sigma = 0.025$, which is the Prandtl number for mercury.

We have briefly reviewed linear Rayleigh-Bénard convection theory, and now move on to the new problem of fixed flux boundaries in a rotating system.

V. Rotating: The Case of Fixed Flux Boundaries

i) Small k Analysis

We linearize the system about $v, \theta = 0$. The heat equation, eq. (6), becomes

$$\frac{\partial \theta}{\partial t} - w = \nabla^2 \theta. \quad (13)$$

We perform the standard operation of applying $\hat{z} \cdot \nabla \times$ and $\hat{z} \cdot \nabla \times \nabla \times$ to the momentum equation, eq. (8), which yields

$$\frac{\partial \zeta}{\partial t} - f \frac{\partial w}{\partial z} = \sigma \nabla^2 \zeta, \quad (14)$$

$$\frac{\partial}{\partial t} \nabla^2 w = \sigma R \nabla_\perp^2 \theta + \sigma \nabla^4 w - f \frac{\partial \zeta}{\partial z}, \quad (15)$$

where $\zeta \equiv \hat{z} \cdot \nabla \times v$. Next, we make a normal mode expansion with $\partial/\partial t \rightarrow s$, $\partial/\partial z \equiv D$, and $\nabla^2 \rightarrow D^2 - k^2$. The z dependences of the three dependent variables θ , ζ , and w will be denoted $\Theta(z)$, $Z(z)$, and $W(z)$. The equations become:

$$(D^2 - k^2 - s) \Theta = -W, \quad (16)$$

$$\left(D^2 - k^2 - \frac{1}{\sigma} s\right) Z = -T^{1/2} DW, \quad (17)$$

$$(D^2 - k^2) \left(D^2 - k^2 - \frac{1}{\sigma} s\right) W = T^{1/2} DZ + Rk^2 \Theta. \quad (18)$$

We will do an asymptotic expansion with k^2 as the small parameter, for the $s = 0$ (stationary convection) case. Expand in k^2 :

$$\Theta = \Theta_0 + k^2 \Theta_2 + k^4 \Theta_4 + \dots, \quad (19a)$$

$$Z = k^2 Z_2 + k^4 Z_4 + \dots, \quad (19b)$$

$$W = k^2 W_2 + k^4 W_4 + \dots, \quad (19c)$$

$$R = R_0 + k^2 R_2 + \dots \quad (19d)$$

We leave out W_0 , which may be seen to be zero for $\Theta = O(1)$ by integrating eq. (16) from $z = -1/2$ to $+1/2$, and applying the boundary conditions. That Z_0 is zero follows from a similar argument.

We are seeking $R_0(T)$ and $R_2(T)$. The critical $T = T_c$ where R_2 goes negative will mark the strength of rotation necessary to move k_c off of zero. The boundary conditions have become: $D\Theta$, DZ , W , and $D^2W = 0$, on $z = \pm 1/2$. The $O(1)$ problem is simply

$$D^2 \Theta_0 = 0. \quad (20)$$

Thus $D\Theta_0$ is a constant, which must be zero by the boundary conditions. This implies that Θ_0 is constant, which may be taken to be one without loss of generality:

$$\Theta_0 = 1. \quad (21)$$

In a nonlinear analysis we would find at this point $\Theta_0 = \Theta_0(x, y, t)$, and proceed to determine the 'planform' equation for Θ_0 . The $O(k^2)$ equations are:

$$D^2\Theta_2 - \Theta_0 + W_2 = 0, \quad (22)$$

$$D^2Z_2 + T^{1/2}DW_2 = 0, \quad (23)$$

$$D^4W_2 - T^{1/2}DZ_2 - R_0\Theta_0 = 0. \quad (24)$$

Equation (23) may be immediately integrated and used to eliminate Z_2 in eq. (24). This leads to an equation for W_2 :

$$D^4W_2 + TW_2 = R_0. \quad (25)$$

This is solved by

$$W_2 = \frac{R_0}{T} (1 + E(z)), \quad (26)$$

where E solves the homogeneous problem, and satisfies $E = -1$, and $D^2E = 0$ on $z = \pm 1/2$. Define $\alpha^4 = -T$, and note that $Re(\alpha^2) = 0$. Solving for E yields

$$E = -Re \left(\frac{\cosh(\alpha z)}{\cosh(\alpha/2)} \right). \quad (27)$$

The $O(k^2)$ solvability condition on eq. (22) is obtained by integrating over z :

$$\int_{-1/2}^{1/2} W_2 dz = 1,$$

which implies

$$\frac{R_0}{T} \left(1 + \int_{-1/2}^{1/2} E(z) dz \right) = 1,$$

thus yielding

$$R_0 = \frac{T}{1 - Re \left(\frac{2}{\alpha} \tanh\left(\frac{\alpha}{2}\right) \right)}. \quad (28)$$

For $T = 0$, this expression gives $R_0 = 5! = 120$, which is the correct value for zero rotation. Figure 5 shows R_0 vs. $x \equiv (T^{1/2}/2)^{1/2}$ ($2x$ is the inverse Ekman layer thickness). Included in the figure is eq. (28) expressed in terms of the real variable x .

The $O(k^2)$ solutions are as follows:

$$W_2 = \frac{R_0}{T} \left(1 - \operatorname{Re} \left(\frac{\cosh(\alpha z)}{\cosh(\alpha/2)} \right) \right), \quad (29)$$

$$\Theta_2 = \Theta_2(0) + \frac{1}{2} \left(1 - \frac{R_0}{T} \right) \left(z^2 - \frac{1}{4} \right) + \frac{R_0}{T} \operatorname{Re} \left(\frac{1}{\alpha^2} \frac{\cosh(\alpha z)}{\cosh(\alpha/2)} \right), \quad (30)$$

$$Z_2 = T^{-1/2} R_0 \operatorname{Re} \left(\frac{1}{\alpha} \frac{\sinh(\alpha z)}{\cosh(\alpha/2)} - z \right). \quad (31)$$

For small T ,

$$W_2 \sim 5(z^4 - 3/2 z^2 + 5/16), \quad (32)$$

$$Z_2 \sim -T^{1/2}(z^3 - 5/2 z^2 + 25/16 z), \quad \text{etc.} \quad (33)$$

To get R_2 , we must go to the $O(k^4)$ equations:

$$D^2 \Theta_4 - \Theta_2 + W_4 = 0, \quad (34)$$

$$D^2 Z_4 - Z_2 + T^{1/2} D W_4 = 0, \quad (35)$$

$$D^4 W_4 - 2D^2 W_2 - T^{1/2} D Z_4 - R_0 \Theta_2 - R_2 \Theta_0 = 0. \quad (36)$$

We use the $O(k^2)$ solutions above and eqs. (35) and (36) to get an equation for W_4 :

$$D^4 W_4 + T W_4 = 2D^2 W_2 + T^{1/2} \int_{-1/2}^z Z_2 dx + R_0 \Theta_2 + R_2 \Theta_0. \quad (37)$$

The solution for W_4 is

$$W_4 = \frac{R_0}{T} \left\{ -\frac{1}{2} \frac{R_0}{T} \left(z^2 - \frac{1}{4} \right) + \Theta_0(0) + \frac{R_2}{R_0} - \frac{1}{4} \left(3 + \frac{R_0}{T} \right) \operatorname{Re} \left(\frac{1}{\alpha} \frac{\sinh(\alpha z)}{\cosh(\alpha/2)} \right) + \xi \right\}, \quad (38)$$

where ξ satisfies the homogeneous problem and the boundary conditions on W_4 . Solving for ξ yields

$$\xi = \xi \left(\pm \frac{1}{2} \right) \operatorname{Re} \left(\frac{\cosh(\alpha z)}{\cosh(\alpha/2)} \right) + D^2 \xi \left(\pm \frac{1}{2} \right) \frac{1}{T^{1/2}} \operatorname{Im} \left(\frac{\cosh(\alpha z)}{\cosh(\alpha/2)} \right), \quad (39a)$$

$$\xi \left(\pm \frac{1}{2} \right) = -\Theta_2(0) - \frac{R_2}{R_0} + \frac{1}{16} \left(2 - 3 \frac{T}{R_0} + \frac{R_0}{T} \right), \quad (39b)$$

$$D^2 \xi \left(\pm \frac{1}{2} \right) = \frac{R_0}{T} + \frac{1}{4} \left(3 + \frac{R_0}{T} \right) \operatorname{Re} \left(2 + \frac{1}{2} \alpha \tanh(\alpha/2) \right). \quad (39c)$$

The $O(k^4)$ solvability condition on eq. (34) is obtained by integrating over z :

$$\int_{-\frac{1}{2}}^{\frac{1}{2}} W_4 dz = \int_{-\frac{1}{2}}^{\frac{1}{2}} \Theta_2 dz. \quad (40)$$

Evaluation of eq. (40) leads to our expression for R_2 :

$$R_2 = R_0 \left\{ Re(\alpha \tanh(\alpha/2)) \left(-\frac{1}{2} \frac{R_0}{T^2} + \frac{1}{2} \frac{R_0^2}{T^3} - \frac{1}{8} \frac{R_0}{T} \left(3 + \frac{R_0}{T} \right) \frac{1}{T^{1/2}} Im \left(\frac{2}{\alpha} \tanh(\alpha/2) \right) \right) \right. \\ \left. + \frac{1}{48} \left(11 + \frac{R_0}{T} - 7 \frac{R_0^2}{T^2} - 9 \frac{T}{R_0} \right) - \frac{3}{2} \frac{R_0}{T} \left(\frac{R_0}{T} + 1 \right) \frac{1}{T^{1/2}} Im \left(\frac{2}{\alpha} \tanh(\alpha/2) \right) \right\} \quad (41)$$

The limiting value for $T = 0$ is $\frac{3.1891}{3.7.11} = 23.61$ (cf., Chapman and Proctor, 1980). (The 11 in the denominator comes from the 11-th power term in the series expansion for the tanh functions of eq. (37)!) We plot $R_0(T)$ and $R_2(T)$ vs. T in Fig.(6). The critical value of T for which R_2 goes negative, and hence k_c moves off zero, is $T_c = 180.15$. This value corresponds to an Ekman layer thickness of about 0.2. The fact that the complicated expressions for R_0 and R_2 yield nearly perfectly straight lines is intriguing, and suggests a simple and accurate approximate analysis exists for the problem.

ii) Variational Estimate

We tried a small k analysis for the $s = i\omega$ case, without much success. Instead, we move on now to a variational estimate of the marginal stability curve $R(k)$. The functional expression for R derived below can be shown to be stationary for the case $s = 0$, but has not been shown to be so for $s = i\omega$. For this case we treat our expression as a useful first (and only) estimate of R , whose accuracy is to be validated later, perhaps numerically.

We multiply eq. (18) by $(D^2 - k^2 - \frac{1}{\sigma}s)W$, and integrate. After some integrations by parts, we obtain the expression:

$$R = \frac{\int [(D^2 - k^2 - \frac{1}{\sigma}s) DW]^2 + k^2 \int [(D^2 - k^2 - \frac{1}{\sigma}s) W]^2 + T \int [DW]^2}{k^2 \left(\int [W]^2 - s \left(1 - \frac{1}{\sigma} \right) \int W \Theta - \Theta DW \Big|_{-1/2}^{1/2} \right)}. \quad (42)$$

Our trial function for W will be the exact solution for the fixed temperature case:

$$W = \cos(\pi z). \quad (43)$$

Next, we find trial functions for Z and Θ which satisfy eqs. (16) and (17), and the boundary conditions:

$$Z = -\frac{\pi T^{1/2}}{\pi^2 + k^2 + \frac{1}{\sigma}s} \sin(\pi z), \quad (44)$$

$$\Theta = \frac{1}{\pi^2 + k^2 + s} \cos(\pi z) + \frac{b\pi}{\pi^2 + k^2 + s} \frac{\cosh(kz)}{k \sinh(k/2)}. \quad (45)$$

The variable b is one for our fixed flux case and zero for the fixed temperature case, and conveniently illustrates the effect of the thermal boundary condition.

Evaluating eq. (38) with the above trial functions yields our estimate for R :

$$R \simeq \frac{(\pi^2 + k^2)(\pi^2 + k^2 + \frac{1}{\sigma}s)^2 + \pi^2 T}{k^2 + \frac{4\pi^2 k}{\pi^2 + k^2 + s} \left(b \left(1 - \frac{s(1-\frac{1}{\sigma})}{\pi^2 + k^2} \right) \coth(k/2) - \frac{k}{4\pi^2} s \left(1 - \frac{1}{\sigma} \right) \right)}. \quad (46)$$

This expression is exact for $b = 0$ and any s , since the trial functions are exact solutions to that problem. Compare eq. (46) with $b, s = 0$ to eq. (12). For the case $s = 0$, eq. (46) estimates $R_0(T = 0) = 120.17$ and $T_c = 179.3$, to be compared with the correct values of 120 and 180.15, respectively.

If we now let $s = i\omega$ and separate eq. (42) into real and imaginary parts, we may find an expression for ω^2 ($q^2 \equiv (\pi^2 + k^2)$):

$$\omega^2 \simeq \frac{4\pi^2 b \coth(k/2) \left\{ q^4(2\sigma + 1) + \frac{\pi^2 T}{q^2}(2\sigma - 1) \right\} + k \{ q^6(\sigma + 1) + \pi^2 T(\sigma - 1) \}}{4\pi^2 b \coth(k/2) \left(2 - \frac{1}{\sigma} \right) - q^2 k \frac{1}{\sigma}(\sigma + 1)}. \quad (47)$$

For $b = 0$, we recover the exact solution for the fixed temperature case (cf., Chandrasekhar, 1961). For $\sigma \rightarrow 0$, $k = 0$,

$$\omega^2 \sim \sigma^2(T - \pi^4), \quad (48)$$

implying $T > \pi^4 = 97.4$ for overstability. Thus overstability can come in while k_c is still zero. Figure 7 shows marginal R vs. k curves from this analysis. The solid curves are for stationary convection, and the dotted curves are for overstability. It is interesting to note that the limiting overstability curve for $\sigma = 0$, which is independent of T , is just twice the stationary curve for $T = 0$. For instance, the minimum possible R_c for the onset of overstability is $R_c = 240$.

iii) Remark on Nonlinear Problem

Chapman and Proctor (1980) have examined the 2-D nonlinear problem for the case of fixed flux boundaries without rotation. The approach is to exploit the small k nature of

the system in a manner similar to our analysis in Sec. V i). As in the linear problem, the temperature perturbation does not depend on z to first order, i.e., $\Theta_0 = \Theta_0(x, t)$. Chapman and Proctor derive the following planform equation for Θ_0 (primes denote $\partial/\partial x$):

$$\frac{\partial \Theta_0}{\partial t} = A_1 \Theta_0'' + A_2 \Theta_0'''' + A_3 (\Theta_0')^2 + A_4 (\Theta_0' \Theta_0''). \quad (49)$$

We have begun to look at this problem with rotation. We find no new terms:

$$\frac{\partial \Theta_0}{\partial t} = B_1(T) \Theta_0'' + B_2(T) \Theta_0'''' + B_3(T) (\Theta_0')^2 + B_4(T) (\Theta_0' \Theta_0''). \quad (50)$$

However, the expressions for the $B_i(T)$ rival the expression for $R_2(T)$, eq. (41). A numerical attack on this problem will prove useful.

VI. Conclusions

We have studied the linear problem of Rayleigh-Bénard convection in a rotating system with fixed flux boundaries. We find two critical rotation strengths, at Taylor number $T \simeq 100$ and $T \simeq 180$. The first corresponds to the advent of overstability and the second to the point where k_c moves off of zero for stationary convection. In other words, for $0 \leq T < 100$, the system allows stationary convection with $k_c = 0$. For $100 < T < 180$, we get stationary convection with $k_c = 0$, or overstability, depending on the Prandtl number σ . For $T > 180$, we get stationary convection with $k_c > 0$ or overstability. Given T , overstability comes in with $k_c = 0$ for small σ and $k_c > 0$ for large σ .

The small k_c nature of fixed flux convection may help explain why convection in the Earth's troposphere tends to occur with a horizontal scale much greater than the vertical scale. If the thermal boundary conditions of a real physical system can be expressed using the parameter b , then eqs. (46) and (47) should yield important information about the onset of convection.

As mentioned in the beginning, $k_c = 0$ systems should get a non-Boussinesq treatment, which will be the next phase of this project. In the nonlinear problem, the new effect of overstability due to rotation should prove to be very interesting. Also, the effects of shear in fixed flux convection remain to be explored.

Acknowledgements

I thank the Woods Hole Oceanographic Institute for a summer fellowship, Prof. Ed Spiegel for stimulating advice and encouragement, and the other fellows and staff for their help on this project. In addition, I thank Prof. Kerry Emanuel for preparing and presenting

an excellent lecture series on the physics of moist convection and its effect on large-scale flows.

References

Chandrasekhar, S. 1961. *Hydrodynamic and hydromagnetic stability*. Oxford (Clarendon Press).

Chapman, C.J. and M.R.E. Proctor 1980. Nonlinear Rayleigh-Bénard convection between poorly conducting boundaries. *J. Fluid Mech.* 101, 759-782.

Childress, S., M. Levandowsky, and E.A. Spiegel 1975. Pattern formation in a suspension of swimming micro-organisms: equations and stability theory. *J. Fluid Mech.* 63, 591-613.

Depassier, M.C. and E.A. Spiegel 1982. Convection with heat flux prescribed on the boundaries of the system. 1. The effect of temperature dependence of material properties. *Geophys. Astrophys. Fluid Dynamics* 21, 167-188.

Heard, W.B. and G. Veronis 1971. Asymptotic treatment of the stability of a rotating layer of fluid with rigid boundaries. *Geophys. Fluid Dynamics* 2, 299-316.

Hurle, D.T.J., E. Jakeman, and E.R. Pike 1967. On the solution of the Bénard problem with boundaries of finite conductivity. *Proc. R. Soc. Lond. A* 296, 469-475.

Proctor, M.R.E. 1981. Planform selection by finite-amplitude thermal convection between poorly conducting slabs. *J. Fluid Mech.* 113, 469-485.

Sparrow, E.M., R.J. Goldstein, and V.H. Jonsson 1964. Thermal instability in a horizontal fluid layer: effect of boundary conditions and nonlinear temperature profile. *J. Fluid Mech.* 18, 513-528.

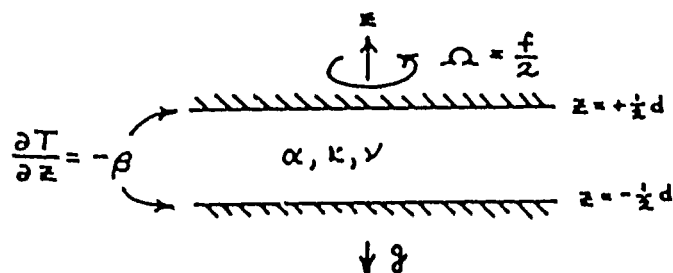


Fig. 1. The rotating Rayleigh-Bénard convection problem with fixed heat flux boundaries. Consider a Boussinesq fluid with kinematic viscosity ν , thermal diffusivity κ , and coefficient of thermal expansion α , confined between two horizontal plane boundaries separated by a vertical distance d . The vertical coordinate is z , and gravity g acts in the $-z$ direction. The system is rotating about the z axis with angular frequency $\Omega = f/2$. An adverse temperature gradient $dT/dz = -\beta$ is held fixed on the boundaries, e.g. the thermal boundary condition specifies fixed flux (insulating) boundaries as opposed to fixed temperature (conducting) boundaries.

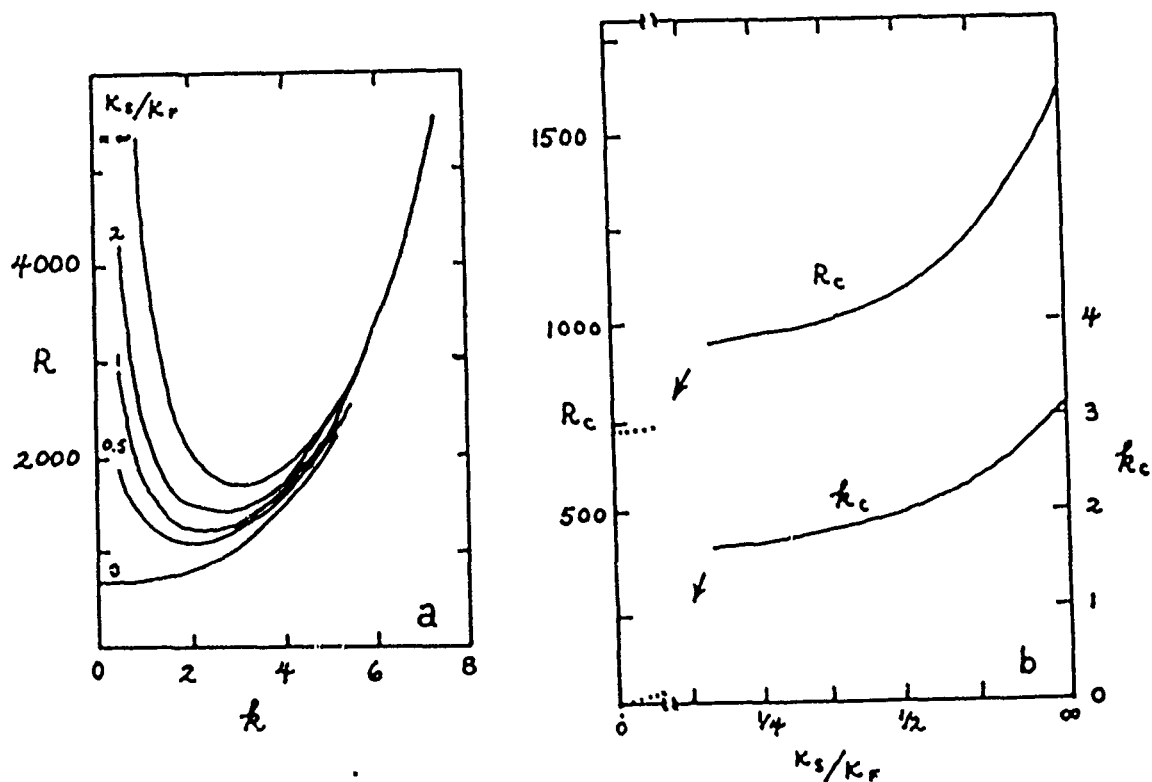


Fig. 2. Dependence of the condition of marginal stability on the thermal boundary condition (for the case of rigid boundaries). The thermal diffusivities of the solid boundary and interior fluid are denoted by κ_s and κ_F , respectively. [See note on thermal diffusivity κ versus thermal conductivity K in text.] Fixed temperature and fixed flux boundaries (our case) correspond to infinite and zero κ_s/κ_F , respectively. (a) Marginal Rayleigh number R vs. horizontal wavenumber k , for various values of κ_s/κ_F . For the case $\kappa_s/\kappa_F = 0$, the onset of convection occurs at $k_c = 0$ (eg., infinite horizontal wavelength). (b) The critical Rayleigh number for the onset of convection R_c , and the corresponding wavenumber k_c , vs. κ_s/κ_F . The limiting values for κ_s/κ_F tending to zero are indicated by the dotted lines (note the break in the abscissa). This figure is adapted from Hurle, Jakeman and Pike (1967).

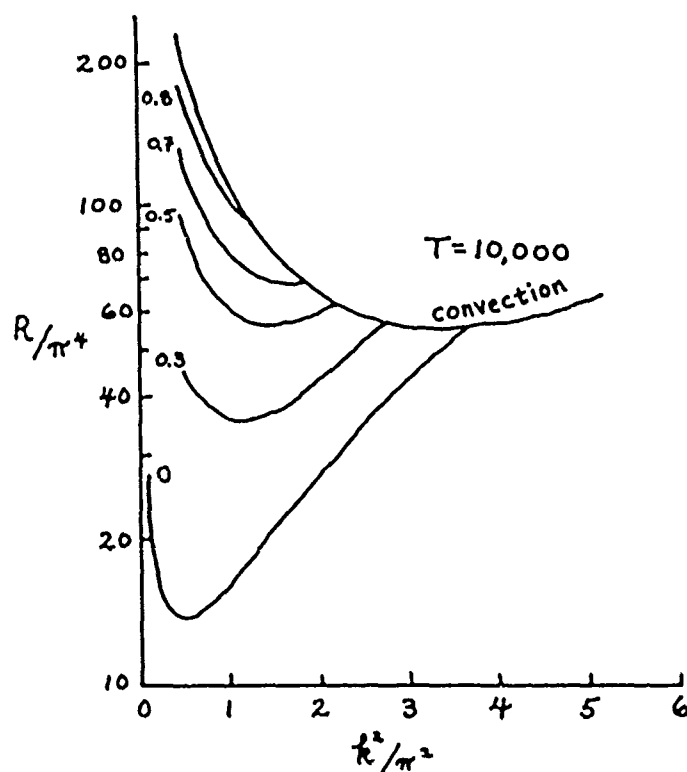


Fig. 3. Marginal R vs. k^2 , for the case of fixed temperature, free slip boundaries in a rotating system. The strength of the rotation is denoted by the Taylor number $T = (fd^2/\nu)^2$, and is equal to 10,000 in this figure. The single curve marked 'convection' is the marginal curve for the onset of stationary convection. Rotation introduces inertial oscillations and the possibility of a second mode of convection, called overstability (or vibrational instability). The marginal curves for overstability are included and labeled by the Prandtl number σ . This figure is adapted from Chandrasekhar (1961).

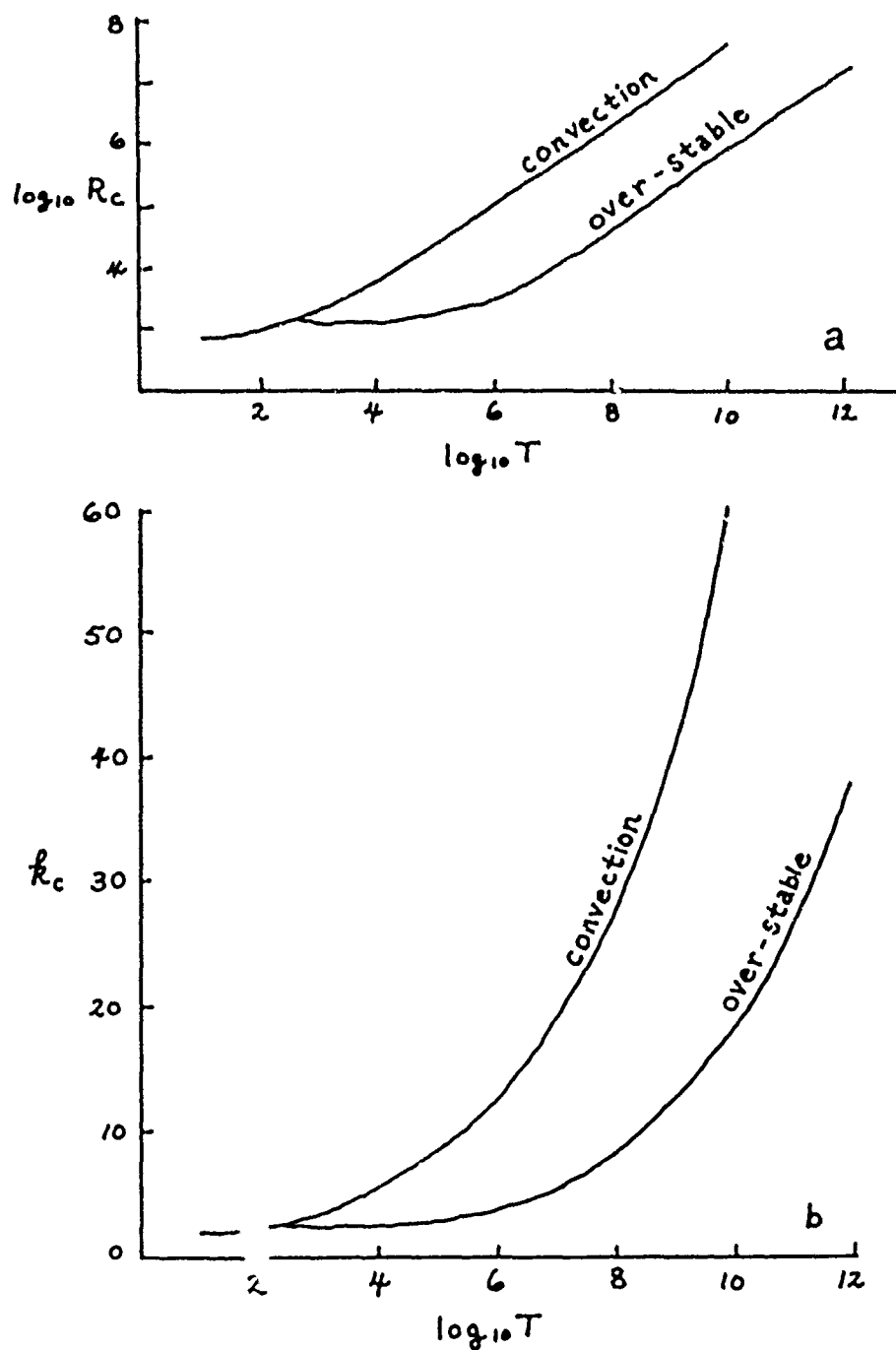


Fig. 4. Dependence of the condition of marginal stability on the strength of rotation, for the case of fixed temperature, free slip boundaries. (a) R_c vs. T for stationary convection and overstability. (b) k_c vs. T as above. This figure is adapted from Chandrasekhar (1961).

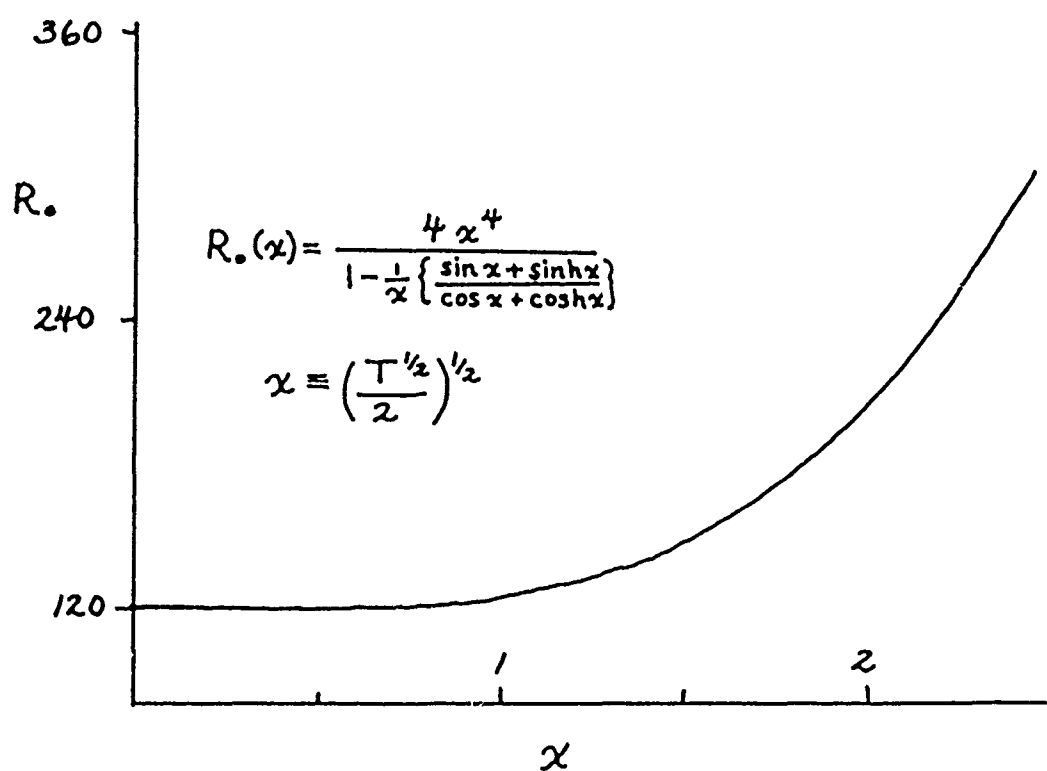


Fig. 5. Marginal Rayleigh number at $k = 0$, R_0 , vs. $x = (T^{1/2}/2)^{1/2}$ for fixed flux, free slip boundaries. The expression for R_0 written in terms of the real variable x is included.

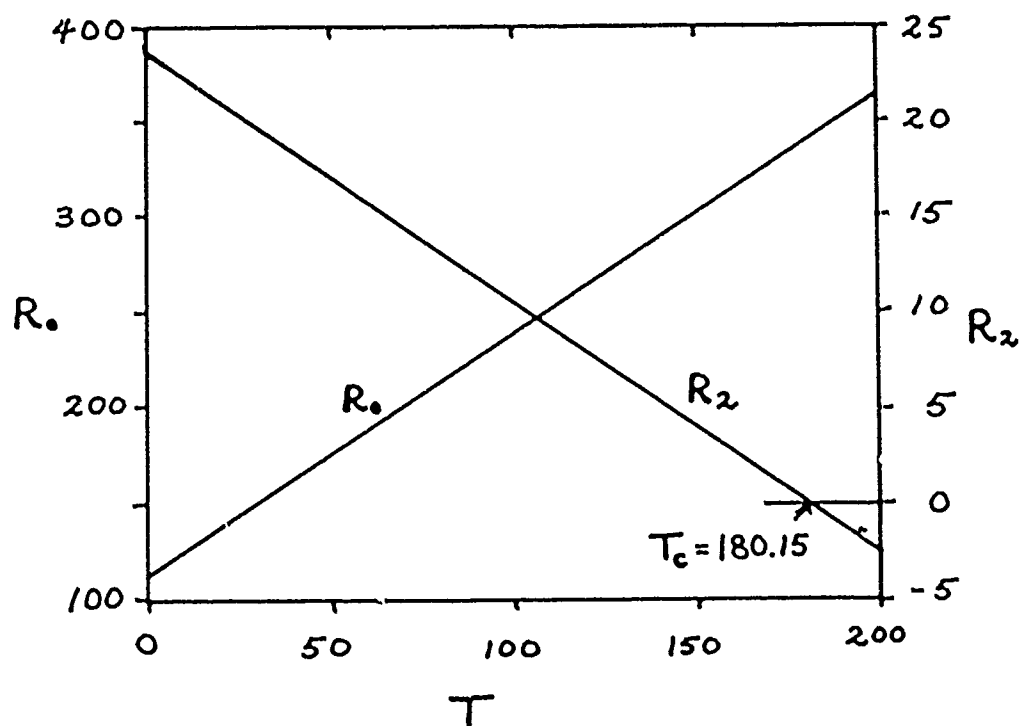


Fig. 6. R_0 and R_2 vs. T for the case of fixed flux, free slip boundaries. Note $R(k, T) = R_0(T) + k^2 R_2(T) + O(k^4)$. For rotation stronger than $T_c = 180.15$, R_c occurs at k greater than zero. Although the solutions for R_0 and R_2 are complicated expressions, they produce curves which are virtually indistinguishable from straight lines (the curves here are drawn straight, but differ from the actual solutions by about the line width).

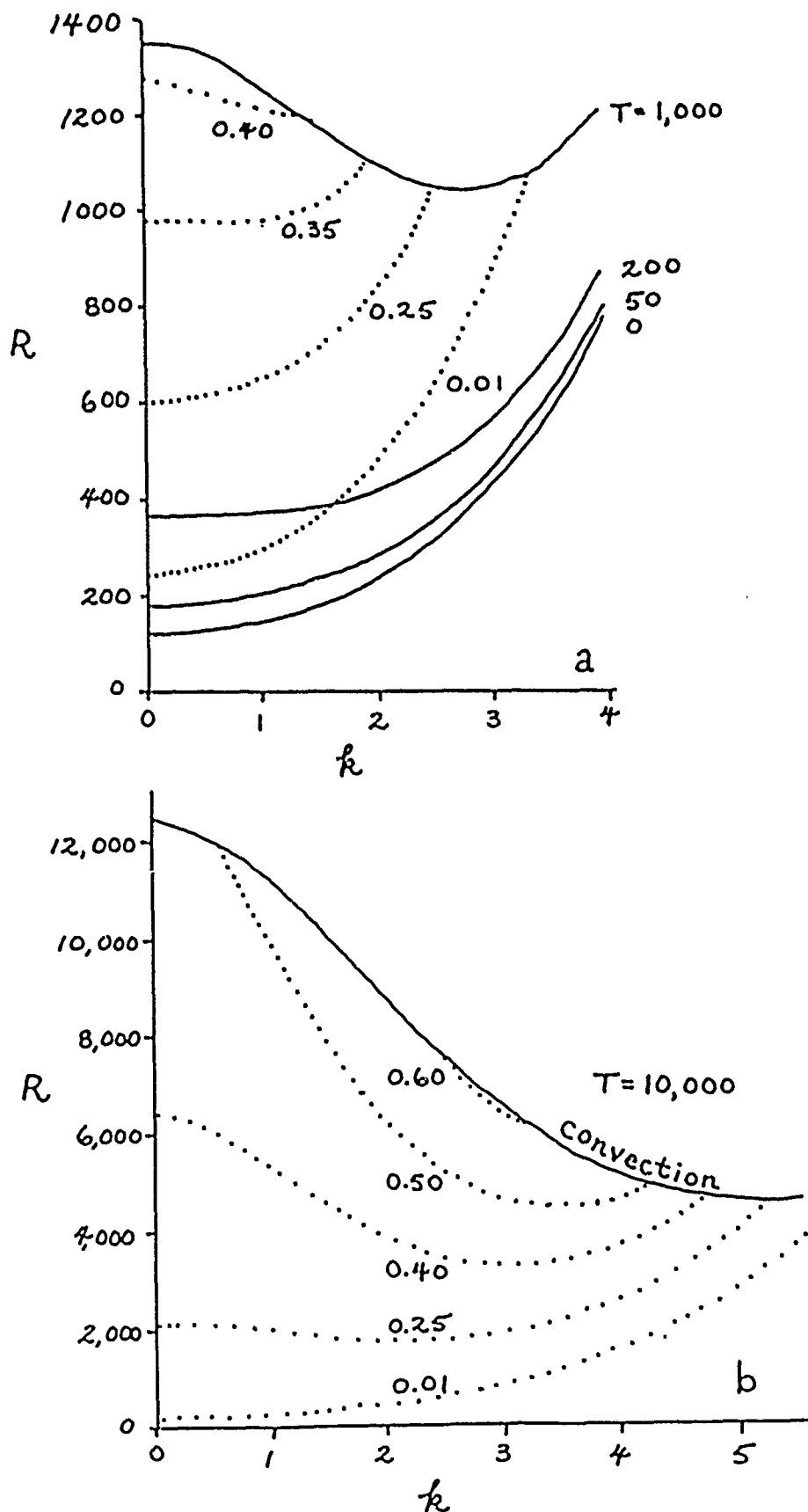


Fig. 7. Marginal R vs. k for the case of fixed flux, free slip boundaries in a rotating system. (a) The solid curves are the marginal $R(k)$ for the onset of stationary convection, and are labeled by T . The dotted curves are the marginal $R(k)$ for overstability estimated by eq. (46), for the case $T = 1,000$, and are labeled by the Prandtl number σ . (b) Same as above for the additional case $T = 10,000$. Note the rescaled ordinate.

Low Frequency Oscillations in a Coupled Atmosphere- Ocean Model

by
Mathew Maltrud
Scripps Institution of Oceanography

INTRODUCTION

This study is an attempt to look at low frequency oscillations (of the order of 1 cycle per year) in a coupled tropical ocean-atmosphere model. Previous studies of this sort have been motivated mostly by a desire to produce oscillations that resemble the El Nino-Southern Oscillation (ENSO) phenomenon. Models of all ranges of complexity have been explored, ranging from interactions restricted to only oceanic and atmospheric Kelvin waves (Lau, 1981), to numerical simulations of the shallow water equations (Anderson and McCreary, 1985), to simulations of the primitive equations (Cane and Zebiak, 1983). All of these studies found eastward propagating waves at low frequencies. This work is different from the others due to the use of a new atmospheric model proposed by Emanuel (1987). In addition, we will confine this work to a linear analysis.

THE MODEL

The model chosen to represent the atmosphere in this study is that introduced by Emanuel (1987). This model was developed in an attempt to explain the 30-60 day oscillation in the tropical atmosphere, invoking a wind-evaporation feedback mechanism that can support (linear) waves whose amplitudes grow exponentially with time. The momentum equations for this model, linearized about a mean zonal wind (U_a) on an equatorial β -plane, are:

$$\frac{\partial u_a}{\partial t} + U_a \frac{\partial u_a}{\partial x} = -\frac{\partial \phi}{\partial x} + \beta y v_a - \frac{2C_D}{h} |U_a| u_a$$

$$\frac{\partial v_a}{\partial t} + U_a \frac{\partial v_a}{\partial x} = -\frac{\partial \phi}{\partial y} - \beta y u_a - \frac{C_D}{h} |U_a| v_a$$

In these equations, u_a and v_a are the perturbation zonal and meridional velocities, respectively; ϕ is the perturbation geopotential; β is the gradient of the coriolis parameter; h is a boundary layer

scale height, and C_D is the drag coefficient since a bulk aerodynamic stress relation is assumed.

The relevant thermodynamic equation for this system, linearized about a mean state of radiative-convective equilibrium, is:

$$\frac{\partial s}{\partial t} + U_s \frac{\partial s}{\partial x} = -\frac{C_{\#}}{H} U_s (s_b - s_s) + \frac{C_p}{H} (S_s - S_b) \text{sgn}(U_s) u_{1s}$$

In this equation, S and s are the mean and fluctuating components of the moist entropy ($s = c_p \ln \theta_e$, where c_p is the specific heat at constant pressure, and θ_e is the equivalent potential temperature), with the subscripts b and s denoting the top of the boundary layer and the ocean surface, respectively; H is a tropospheric scale height, and C_p is the bulk aerodynamic transfer coefficient for the entropy flux. Perturbation radiative effects have been ignored. To close the system, it is assumed that moist entropy fluctuations in the boundary layer control the temperature structure in the troposphere (this is essentially a convection parameterization) so that the geopotential can be related to the entropy via the hydrostatic relation. For details, the reader is referred to Emanuel (1987).

The model ocean is chosen to be a reduced gravity, shallow water system representing the dynamically active thermocline on top of a semi-infinite deep layer that is static (Anderson and McCreary, 1985). The momentum and continuity equations, linearized about a mean zonal current (U_0), are:

$$\frac{\partial u_0}{\partial t} + U_0 \frac{\partial u_0}{\partial x} = -g \frac{\partial h_0}{\partial x} + \beta y v_0 + \tau^x$$

$$\frac{\partial v_0}{\partial t} + U_0 \frac{\partial v_0}{\partial x} = -g \frac{\partial h_0}{\partial y} - \beta y u_0 + \tau^y$$

$$\frac{\partial h_0}{\partial t} + U_0 \frac{\partial h_0}{\partial x} = -d \left(\frac{\partial u_0}{\partial x} + \frac{\partial v_0}{\partial y} \right)$$

In these equations, u_0 and v_0 are the perturbation velocities, d and h_0 are the mean and fluctuating layer depths, respectively; g is the reduced gravity, and τ^x and τ^y are mechanical stresses.

To close the full set of equations, and to introduce coupling between the ocean and the atmosphere, some more relations are needed. The positive stresses on the ocean are balanced by the drag on the atmosphere,

$$\tau^x = 2C_D |U_a| u_a \left(\frac{\rho_a}{\rho_w d} \right)$$

$$\tau^y = C_D |U_a| v_a \left(\frac{\rho_a}{\rho_w d} \right)$$

where ρ_a and ρ_w are the densities of air and water. At the sea surface, it can be shown that

$$ds_s = c_p \left(\frac{\Gamma_d}{\Gamma_m} \right) d(\ln T_o)$$

where Γ_d and Γ_m are the dry and moist adiabatic lapse rates, c_p is the specific heat of air, and T_o is the sea surface temperature (SST). This relation introduces a thermodynamic coupling in addition to the mechanical stress coupling. Two possible expressions for the SST are:

$$T_o = \alpha h_o$$

$$\frac{\partial T_o}{\partial t} + U_o \frac{\partial T_o}{\partial x} + u_o \frac{\partial T_m}{\partial x} = 0$$

The first of the above expressions is an attempt to model SST fluctuations as due to upwelling, i.e., a shallowing of the thermocline results in colder water being forced to the surface. The second expression models the temperature as a passive tracer with a mean zonal gradient, $\partial T_m / \partial x$. Thus our complete set of equations is:

$$\frac{\partial u_a}{\partial t} + U_a \frac{\partial u_a}{\partial x} = T_b \epsilon v \frac{\partial s}{\partial x} + \beta y v_a - \frac{2C_D}{h} |U_a| u_a$$

$$\frac{\partial v_a}{\partial t} + U_a \frac{\partial v_a}{\partial x} = T_b \epsilon v \frac{\partial s}{\partial y} - \beta y u_a - \frac{C_D}{h} |U_a| v_a$$

$$\frac{\partial s}{\partial t} + U_a \frac{\partial s}{\partial x} = -\frac{C_s}{H} |U_a| v (s - s_s) + \frac{C_s}{H} (S_s - S_b) \text{sgn}(U_a) u_a$$

$$\frac{\partial u_o}{\partial t} + U_o \frac{\partial u_o}{\partial x} = -g \frac{\partial h_o}{\partial x} + \beta y v_o + 2C_D |U_a| u_a \left(\frac{\rho_a}{\rho_w d} \right)$$

$$\frac{\partial v_o}{\partial t} + U_o \frac{\partial v_o}{\partial x} = -g \frac{\partial h_o}{\partial y} - \beta y u_o + C_D |U_a| v_a \left(\frac{\rho_a}{\rho_w d} \right)$$

$$\frac{\partial h_o}{\partial t} + U_o \frac{\partial h_o}{\partial x} = -d \left(\frac{\partial u_o}{\partial x} + \frac{\partial v_o}{\partial y} \right)$$

and either

$$T_o = \alpha h_o \quad \text{or} \quad \frac{\partial T_o}{\partial t} + U_o \frac{\partial T_o}{\partial x} + u_o \frac{\partial T_m}{\partial x} = 0$$

The system is nondimensionalized using the following scaling for dimensional variables denoted with an asterisk:

$$x^* = a_o x$$

$$y^* = A^{1/2} B^{-1/2} a_o^{1/2} y$$

$$t^* = a_o^{1/2} A^{-1/2} t$$

$$u^* = A^{1/2} a_o^{1/2} u$$

$$v^* = A^{3/4} B^{-1/2} a_o^{1/4} v$$

$$s^* = a_o H^{-1} C_p (S_s - S_b) T$$

$$h_o^* = a_o A g^{-1} h_o$$

$$T_o^* = a_o A g^{-1} T_o \quad \text{for} \quad T_o = \alpha h_o$$

or

$$T_o^* = a_o \left(\frac{\partial T_m}{\partial x} \right) T_o \quad \text{for} \quad \frac{\partial T_o}{\partial t} + U_o \frac{\partial T_o}{\partial x} + u_o \frac{\partial T_m}{\partial x} = 0$$

where a_o is the radius of the earth, and $A \equiv \epsilon v T_b H^{-1} C_p (S_s - S_b)$. Also, v is an order unity constant and ϵ , the atmospheric thermodynamic efficiency, is of order 0.1.

Since this a linear system, we will assume solutions of the form:

$$u_a(x, y, t) = u_a(y) e^{(\sigma t + i k x)}$$

where σ is complex and there are similar expressions for all six of the variables. After substitution into the (nondimensionalized) equations, the system takes the following form:

$$(D+2F)u_a = ikT + yv_a$$

$$(D+F)v_a = y \left[\frac{dT}{dy} - yu_a \right]$$

$$(D+F')T = F'\Gamma T_o + u_a \operatorname{sgn}(U_a)$$

$$D'u_o = -ikh_o + yv_o + 2Qu_a$$

$$D'v_o = -P \left[\frac{dh_o}{dy} + yu_o \right] + Qv_a$$

$$D'h_o = -G \left[iku_o + \frac{dv_o}{dy} \right]$$

$$T_o = \alpha h_o \quad \text{or} \quad D'T_o + u_o = 0$$

where $F \equiv C_D |U_a| a_o h^{-1}$; $P \equiv \beta A^{-1/2} a_o^{3/2}$; $F' \equiv F v C_p h / C_D H$; $Q \equiv F \rho_a h / \rho_w d$; $G \equiv g d / a_o \Lambda$; $D \equiv \sigma + ikU_a$; $D' \equiv \sigma + ikU_o$, and

$$\Gamma \equiv c_p \varepsilon g^{-1} \left(\frac{T_b}{T_o} \right) \left(\frac{\Gamma_d}{\Gamma_m} \right) \quad \text{for} \quad T_o = \alpha h_o$$

$$\Gamma \equiv c_p \varepsilon \left(\frac{T_b}{T_o \Lambda} \right) \left(\frac{\Gamma_d}{\Gamma_m} \right) \left(\frac{\partial T_m}{\partial x} \right) \quad \text{for} \quad D'T_o + u_o = 0$$

The overbar on T_o denotes a constant mean SST. If P is large, we can make the geostrophic approximation,

$$\frac{dT}{dy} = yu_a; \quad \frac{dT_o}{dy} = -yu_o$$

All of the equations, except for the u_a momentum equation, can then be combined to yield an ordinary differential equation for the meridional structure of the fields:

$$D' \frac{d^3 T}{dy^3} + \left\{ \frac{-4D'}{y} - y^* \operatorname{sgn}(U_a) [D'(D+F') - 2QF'\Gamma] \right\} \frac{d^2 T}{dy^2} \\ + \left\{ \frac{-y^2 D'}{G} + \frac{4D'}{y^2} + ik + 2^* \operatorname{sgn}(U_a) [D'(D+F') + 2QF'\Gamma] \right\} \frac{dT}{dy}$$

$$+ \left\{ \frac{y^3 D'}{G} (D+F') - iky(D+F') \right\} \text{sgn}(U_a) T = 0$$

To further simplify the system, one more assumption is made. The ocean and atmosphere each have solutions for which $v=0$ everywhere. For the ocean, these are simply Kelvin waves that have a (squared) phase speed $c_k^2 = G$ and a zero growth rate. Only the eastward propagating wave has an amplitude that decays away with latitude, and is thus the only physically realizable solution. For the atmosphere, the solutions can be linearly unstable, as discussed by Emanuel (1987). Well behaved solutions also propagate eastward and the mean zonal flow is required to be easterly. It is therefore assumed that the coupled system also has $v=0$ solutions, which reduces the system to:

$$(D+2F)u_a = ikT$$

$$\frac{dT}{dy} = yu_a$$

$$(D+F')T = F'\Gamma T_o - u_a$$

$$D'u_o = -ikh_o + 2Qu_a$$

$$\frac{dh_o}{dy} = -yu_o$$

$$D'h_o = -Giku_o$$

$$T_o = \alpha h_o \quad \text{or} \quad D'T_o = -u_o$$

where it has been assumed that $\text{sgn}(U_a) < 0$, i.e., the mean zonal wind is easterly. The five algebraic equations can be combined to yield the dispersion relation:

$$(D'^2 + Gk^2)[(D+2F)(D+F') + ik] = 2QF'\Gamma'Gk^2$$

where

$$\Gamma' \equiv \alpha \epsilon c_p g^{-1} \left(\frac{T_b}{T_o} \right) \left(\frac{\Gamma_d}{\Gamma_m} \right) \quad \text{for} \quad T_o = \alpha h_o$$

$$\Gamma' \equiv \epsilon c_p \left(\frac{T_b}{T_o} \right) \left(\frac{\Gamma_d}{\Gamma_m} \right) \left(\frac{\partial T_m}{\partial x} \right) \left(\frac{-i}{GkA} \right) \quad \text{for} \quad D'T_o = -u_o$$

Note that if the coupling is turned off, e.g., $\Gamma=0$, then the dispersion relations for the ocean and the atmosphere separately are recovered:

$$D'^2 + Gk^2 = 0 \quad \text{for the ocean}$$

$$(D+2F)(D+F') = -ik \quad \text{for the atmosphere}$$

The quartic dispersion relation is solved numerically using Newton's method.

SOME SOLUTIONS

Consider the case where $T_0 = \alpha h_0$. From Philander, et. al. (1984), α is chosen to be $1^\circ\text{C}/50\text{m}$. In addition, we choose $d=200\text{m}$, $U_0=0$, and $c_k^2 = 2 \text{ m}^2/\text{s}^2$ where c_k is the free Kelvin wave speed in the ocean. The atmospheric parameters are the same as those used by Emanuel (1987).

The system is first solved in the absence of the wind-evaporation feedback mechanism in the atmosphere, i.e., the u_a term is removed from the T equation. Of primary interest is the behaviour of the largest scale waves since we want to investigate a global scale ENSO phenomenon. It is found that all growing oceanic solutions (where an oceanic mode is identified by having a phase speed close to c_k) propagate toward the west, as seen in Fig. 1 and Fig. 2. Note that the assumption that the solutions have the form $e^{(\sigma + ikx)}$ leads to westward waves having positive phase speeds, contrary to the usual convention. The structure of one of these modes is seen in Fig.3. The ocean wave is seen to have a westward Kelvin wave structure, with the depth and velocity fields being 180° out of phase. The atmosphere is characterized by a balance between friction and pressure gradient acceleration. We will find this to be true in all cases due to the low frequency of the motions of interest.

When the wind-evaporation feedback mechanism is enabled, growing modes are found to propagate both eastward and westward, depending on the strength of the mean zonal wind (Fig.4 and Fig 5.). This is perhaps not too suprising since we know that this feedback drives eastward waves in the atmosphere. Figure 6 shows that an unstable mode that travels to the east in the ocean has the structure of an eastward Kelvin wave, with the depth and velocity fields in phase.

The structure of an unstable westward mode is almost identical to that of the corresponding mode without wind-evaporation feedback, although its phase speed is somewhat slower.

The solutions tend to be sensitive to the chosen value of α assumed to relate fluctuations in thermocline depth to surface temperature fluctuations. While the shape of the dispersion relation remains essentially unchanged over an order of magnitude change in α , the phase speed can change up to 50% and the growth rate can vary by an order of magnitude. It is also interesting to note that the largest growth rates occur at wavenumbers significantly greater than unity. If El Nino is assumed to be a lowest wavenumber disturbance, these results may have limited applicability.

Next, consider the case of ocean temperature as a passive tracer, $D'T_0 = -u_0$. The magnitude of the mean zonal temperature gradient, $\partial T_m / \partial x$, is chosen to be $10^\circ\text{C}/100^\circ\text{longitude}$, with all other parameters remaining the same as in the previous case. It is found that the model gives only westward propagating unstable modes for the case where $\partial T_m / \partial x < 0$, with or without the wind-evaporation feedback mechanism. If the sign of the mean zonal temperature gradient is reversed, then eastward traveling unstable modes are found, again, with or without wind-evaporation feedback (Fig. 7 and Fig. 8). The structure of one of these modes is shown in Fig. 9. Note that the ocean wave is not exactly a Kelvin wave, implying significant forcing.

Again, the solutions are sensitive to the choice of the value of $\partial T_m / \partial x$, and are sensitive in a way that is similar to the previous case, with growth rates responding almost in direct proportion to changes in the forcing constant. It is interesting to note, however, that the unstable modes have the largest growth rate for the smallest wavenumber in most cases, suggesting some possible relationship to an ENSO type of event. But it should also be noted that $\partial T_m / \partial x > 0$ is probably not a realistic assumption ($\partial T_m / \partial x < 0$ in the tropical Pacific) but is necessary to get eastward propagating waves that grow with time.

It is possible that the temperature fluctuations in the ocean behave more like some combination of the effects described above. The effect of combining them in the model has yet to be investigated, though the linear nature of the model would seem to suggest that a superposition of

each effect would describe the total response. It should also be noted that the time dependent ocean in this model had an extremely small effect on the free modes of the atmosphere.

COMMENTS

The solutions to the dispersion relation have some interesting characteristics, but it isn't yet clear when this dispersion relation is valid. The uncertainty rests on the assumption that $v=0$ everywhere, essentially resulting in an overdetermined system of six equations and four unknowns. The requirement that the T and h_0 fields have the same meridional structure as given by the geostrophic relations leads to an extra constraint on the system in addition to the dispersion relation, namely that

$$\frac{D'}{Gk} = \frac{k}{D + 2F}$$

Although this extra constraint has yet to be extensively investigated, it seems that the best that can be hoped for is a $v=0$ solution for very special values of some of the external parameters, such as poorly known drag coefficients, while the worst case would be no possible solution.

Another possible range of validity of the solved dispersion relation is in the vicinity of the equator. It is easy to see that the equations for $y=0$ are identical to those for $v=0$ except for the dv_0/dy term in the h_0 equation. Thus if $dv_0/dy \approx 0$ near the equator, we could expect our solutions to be approximately valid there. If v_0 is symmetric about $y=0$, then $dv_0/dy = 0$ there by definition. However, the momentum equations imply that v_0 is actually antisymmetric about the equator if u_0 and h_0 are symmetric, which must be true for non-trivial equations at the equator. Thus, the validity of our dispersion relation seems to rely on the size of dv_0/dy compared to the rest of the terms in the h_0 equation. It may be possible that an approximate expression for dv_0/dy near the equator can be obtained from a small y analysis of the full meridional structure equation, and hence the validity of the dispersion relation at the equator can be quantitatively dealt with. This analysis is planned for the near future.

Not knowing the meridional structure of the modes described above (e.g., Fig. 9) leads to another troubling question. Are these growing waves well behaved as $y \rightarrow \infty$? It is known that westward propagating free Kelvin wave solutions have an amplitude that diverges for large y , so the possibility that the westward modes found by this model do decay away as $y \rightarrow \infty$ must be treated with some skepticism. Again, it seems possible that an asymptotic analysis of the meridional structure equation in the large y limit could shed some light on which modes decay as $y \rightarrow \infty$. Initial investigation indicates that some westward modes are, in fact, well behaved, but more work needs to be done in this case as well.

CONCLUSION

The main conclusion of this study is that the given model system is capable of supporting growing disturbances of low frequency, though the relevance of these motions to ENSO remains to be seen. The presence of the wind-evaporation feedback mechanism can be quite important in amplifying eastward propagating modes and suppressing westward ones. However, the range of validity of the solutions of our dispersion relation remains in doubt until the question of the meridional mode structure is solved. This problem is slated for the near future.

ACKNOWLEDGMENTS

I would like to thank Dr. Kerry Emanuel for suggesting this project and for redirecting me after I had taken numerous wrong turns. Thanks also to Steve Siems for many illuminating discussions. And here's to the whole GFD gang, who gave me a glimpse of what happens in science.

REFERENCES

- Anderson, D.L.T, and J.P. McCreary, 1985: Slowly Propagating Disturbances in a Coupled Ocean-Atmosphere Model. *J. Atmos. Sci.*, **42**, 615-629.
- Cane, M., and S. Zebiak, 1985: A Theory for El Nino and the Southern Oscillation. *Science*, **228**, 1085-1087.

Emanuel, K.E., 1987: An Air-Sea Interaction Model of Intraseasonal Oscillations in the Tropics. *J. Atmos. Sci.*, **44**, 2324-2340.

Lau, K., 1981: Oscillations in a Simple Equatorial Climate System. *J. Atmos. Sci.*, **38**, 248-261.

Philander, S.G.H., T. Yamagata, R.C. Pacanowski: Unstable Air-Sea Interactions in the Tropics. *J. Atmos. Sci.*, **41**, 604-613.

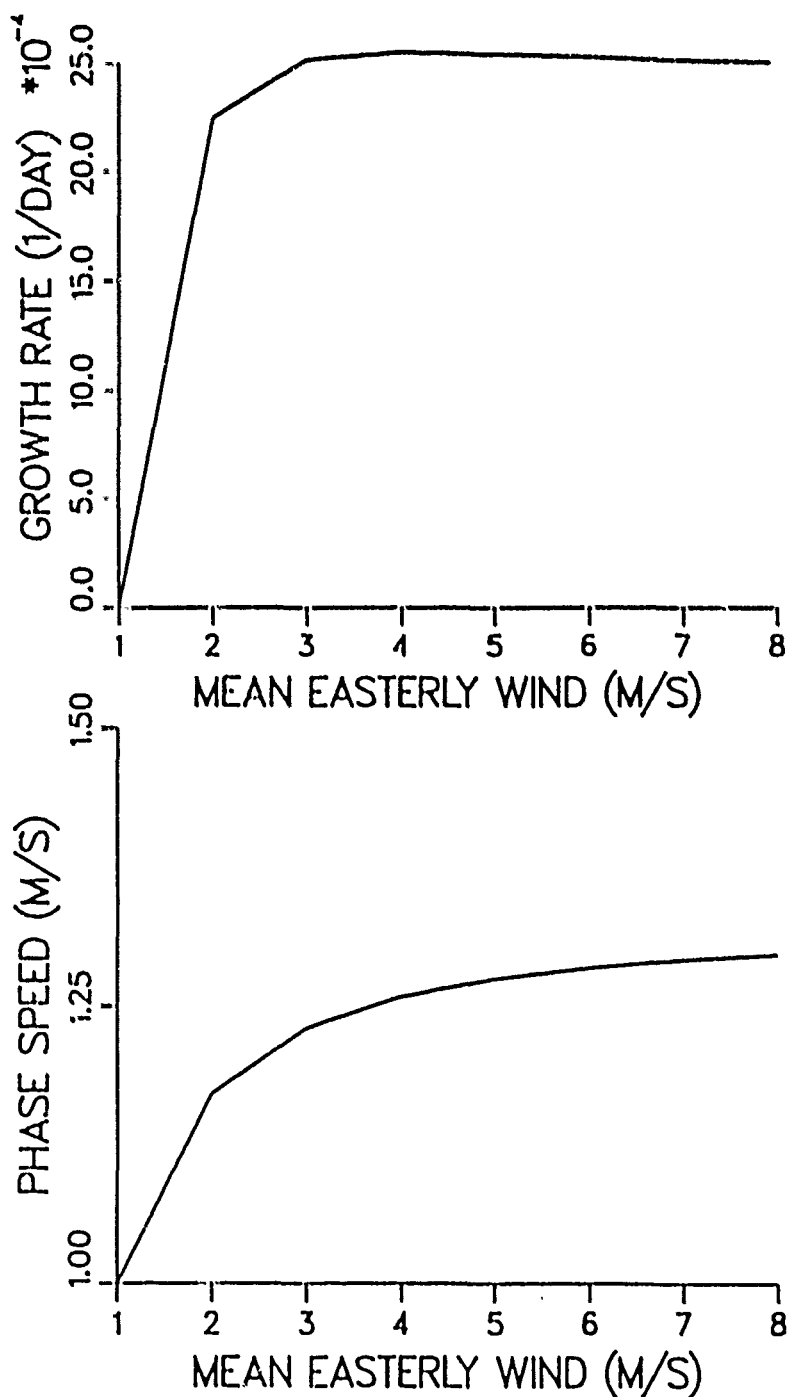


Figure 1. Growth rate and phase speed of the wavenumber $k=1$ unstable oceanic mode for various values of the atmospheric mean zonal wind in the absence of wind-evaporation feedback. Ocean temperature fluctuations are proportional to depth fluctuations.

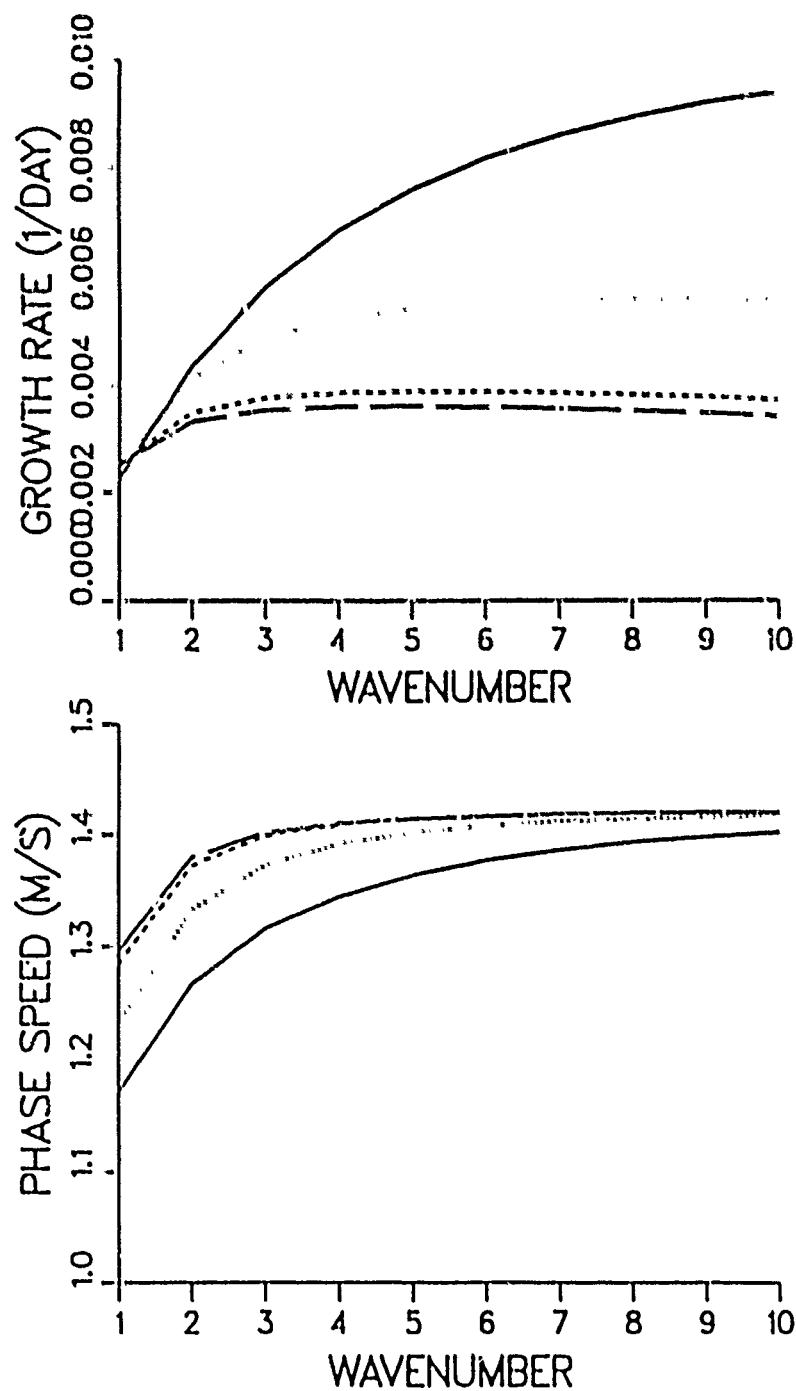


Figure 2. Growth rate and phase speed of the unstable oceanic modes for an atmospheric mean easterly wind $U_a = 2$ m/s (solid line), $U_a = 3$ m/s (dotted line), $U_a = 6$ m/s (dashed line), and $U_a = 8$ m/s (dot-dash line). Ocean temperature fluctuations are proportional to depth fluctuations and wind-evaporation feedback is absent.

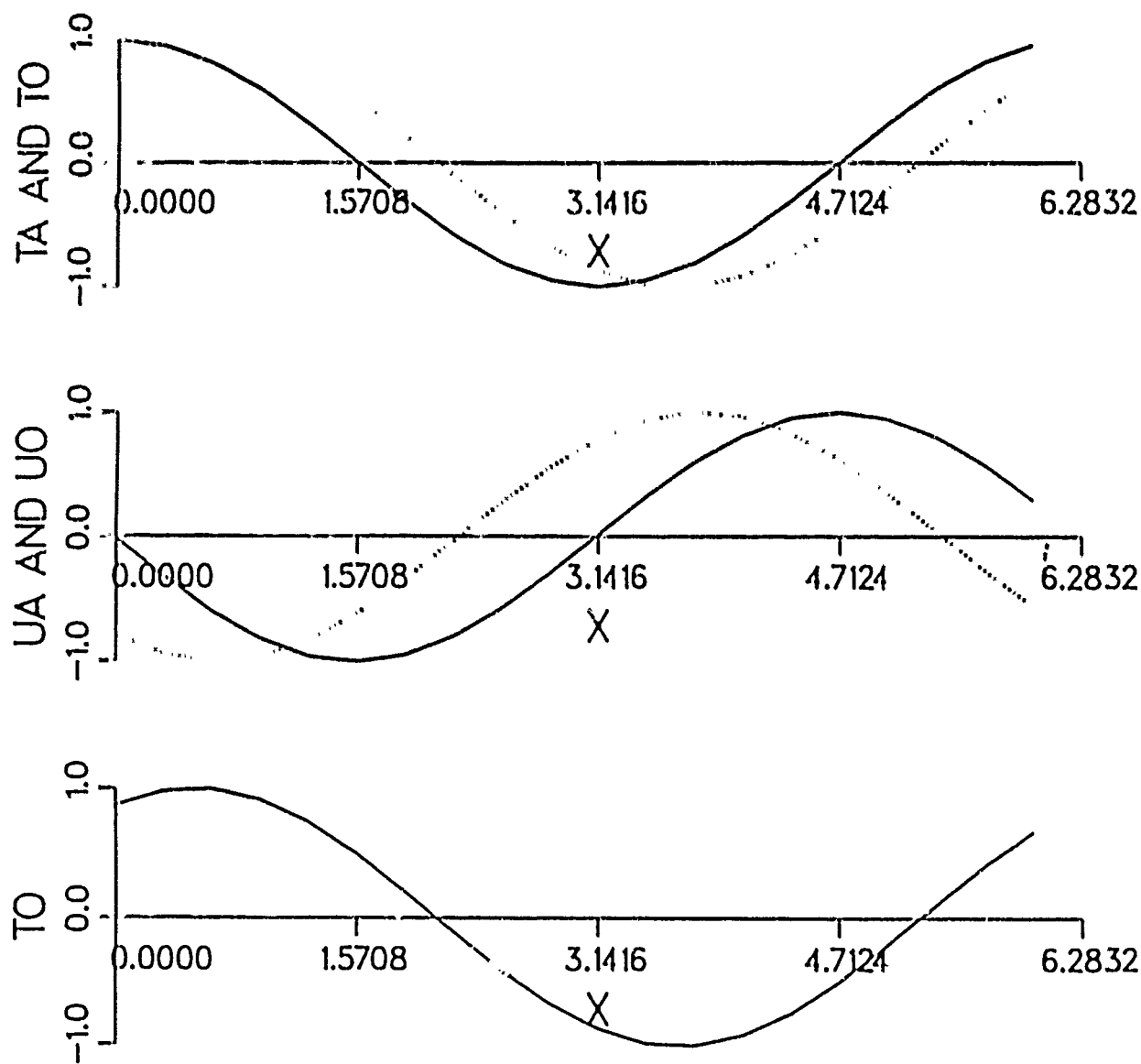


Figure 3. Zonal structure at the equator of an unstable oceanic mode with an atmospheric mean easterly wind $U_a=2$ m/s and wavenumber $k=1$. The growth rate and phase speed are 0.0023 1/day and 1.17 m/s, as seen in Figure 1 and Figure 2. The atmospheric temperature (TA) and zonal velocity (UA) perturbations are drawn with solid lines, while ocean temperature (TO) and zonal velocity (UO) perturbations are drawn as dotted lines. H is the thermocline depth perturbation (h_0), which in this case is proportional to TO. Amplitudes have all been normalized to unity for visual convenience. Actual dimensional amplitudes are such that an atmospheric zonal wind anomaly of 1 m/s will result in anomalies of 0.6°C , 12 cm/s, 0.6°C , and 33m in the atmospheric temperature, oceanic speed, oceanic temperature, and thermocline depth, respectively.

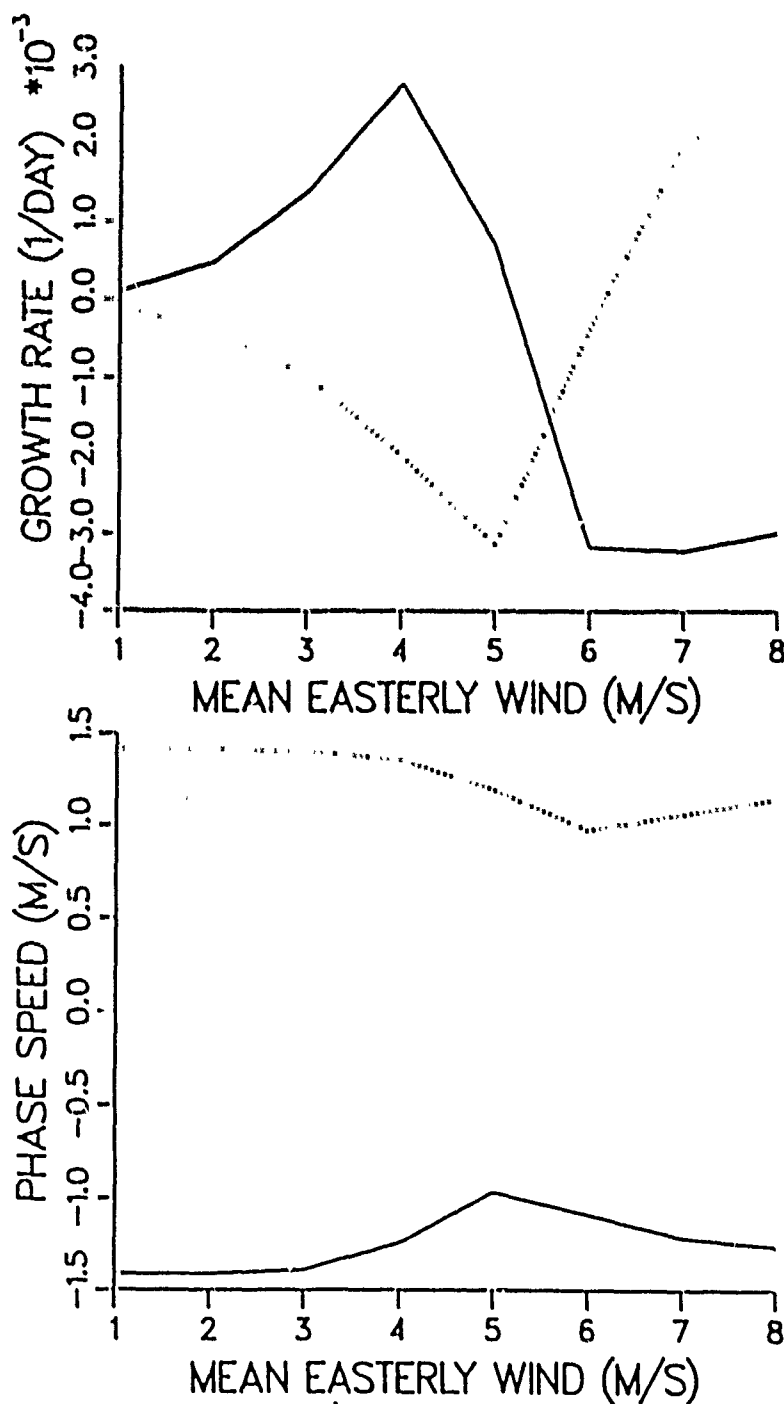
GROWTH RATE AND PHASE SPEED FOR $k=1$ 

Figure 4. Growth rate and phase speed of the two wavenumber $k=1$ oceanic modes for various values of the atmospheric mean zonal wind with the inclusion of wind-evaporation feedback. Note that the unstable modes propagate to the east for small values of U_a , and go west for large values of U_a . Ocean temperature fluctuations are proportional to depth fluctuations.

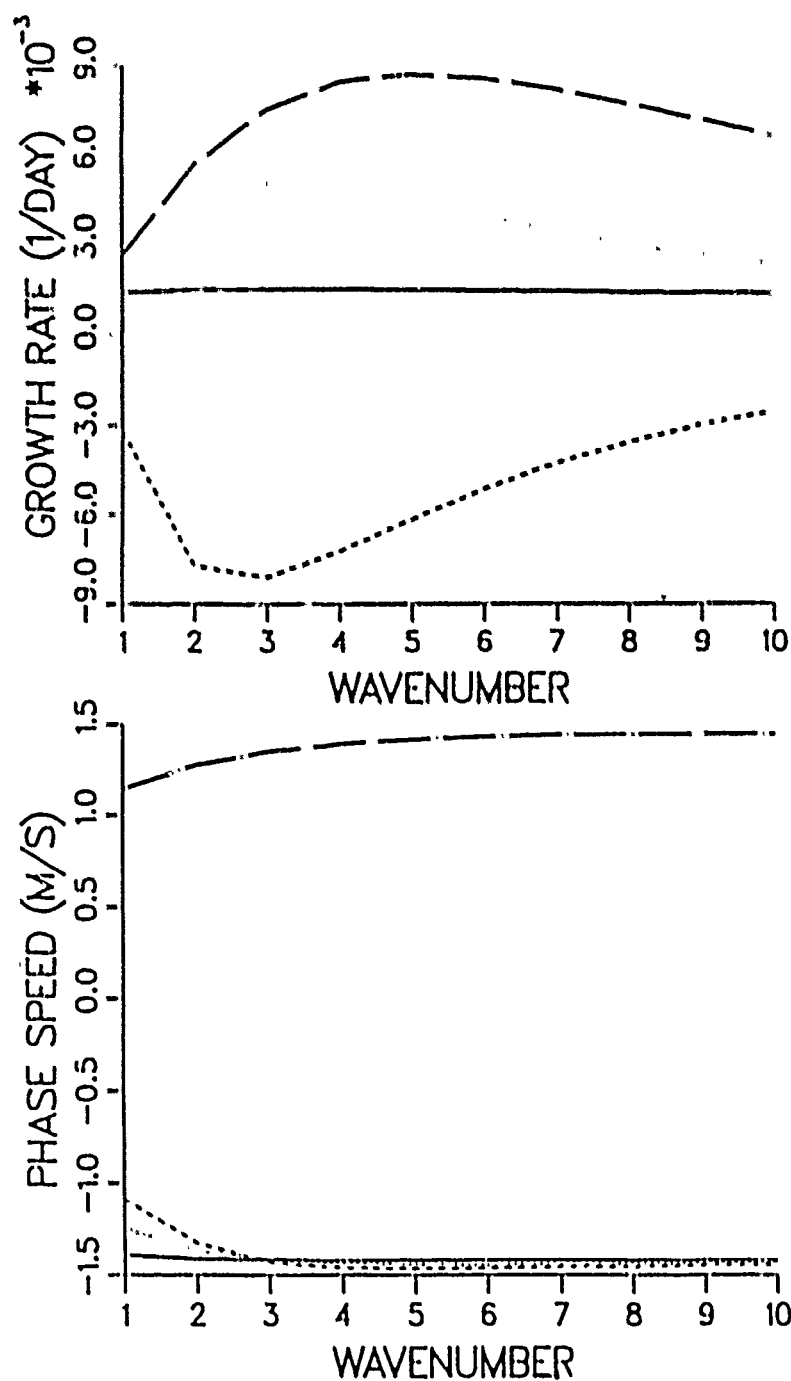


Figure 5. Growth rate and phase speed of the unstable oceanic modes for an atmospheric mean easterly wind $U_a = 3$ m/s (solid line), $U_a = 4$ m/s (dotted line), $U_a = 6$ m/s (dashed line, but not an unstable mode), and $U_a = 8$ m/s (dot-dash line). Ocean temperature fluctuations are proportional to depth fluctuations and wind-evaporation feedback is included.

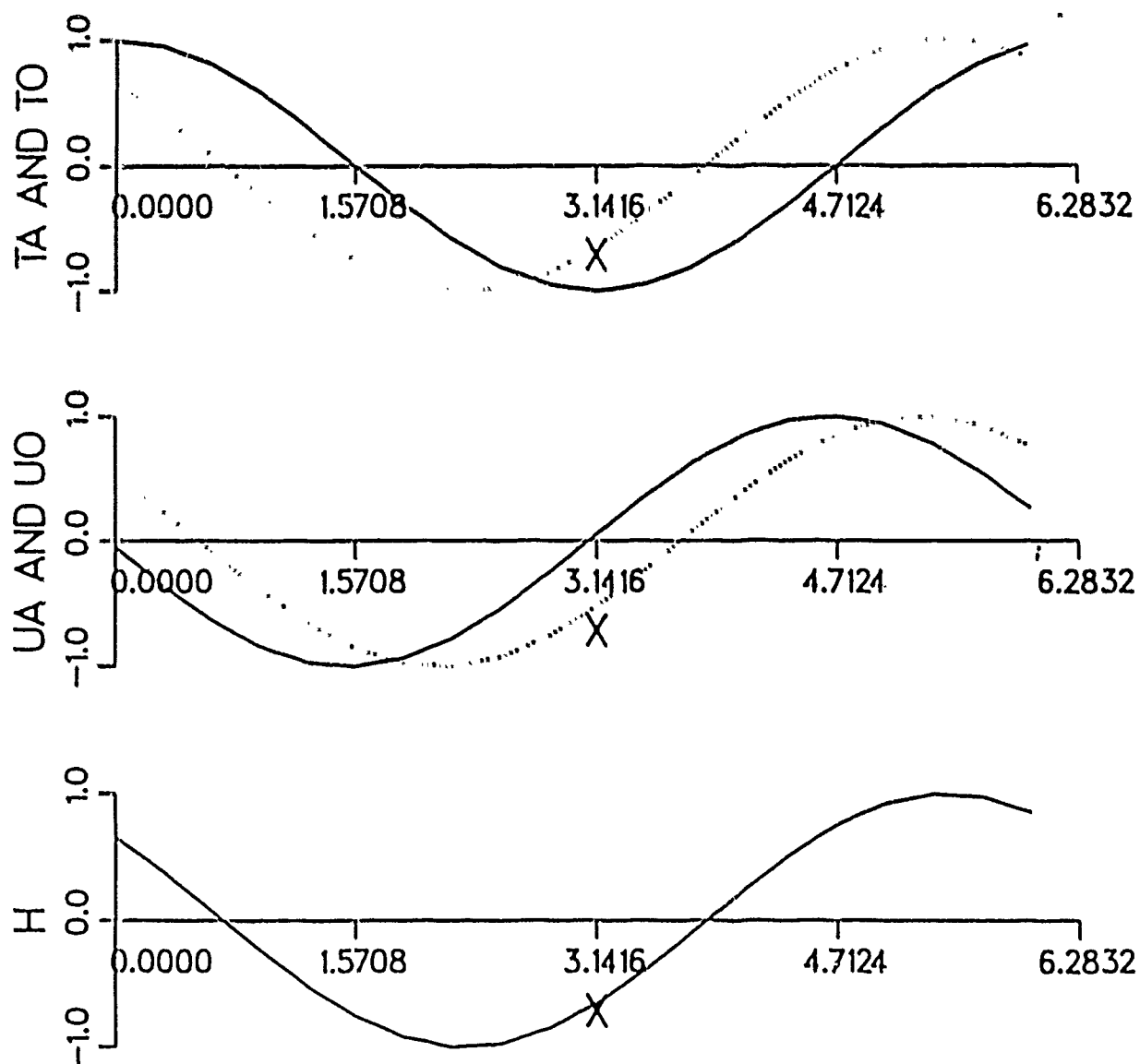
PERTURBATION FIELDS FOR $K=1$ AT $Y=0$ 

Figure 6. Zonal structure at the equator of an unstable oceanic mode with an atmospheric mean easterly wind $U_a=4$ m/s and wavenumber $k=1$. The growth rate and phase speed are 0.0028 1/day and -1.25 m/s, as seen in Figure 4 and Figure 5. Plotted quantities are the same as those plotted in figure 3. In this case, actual dimensional amplitudes are such that an atmospheric zonal wind anomaly of 1 m/s will result in anomalies of 1.2°C, 24 cm/s, 1.3°C, and 65m in the atmospheric temperature, oceanic speed, oceanic temperature, and thermocline depth, respectively.

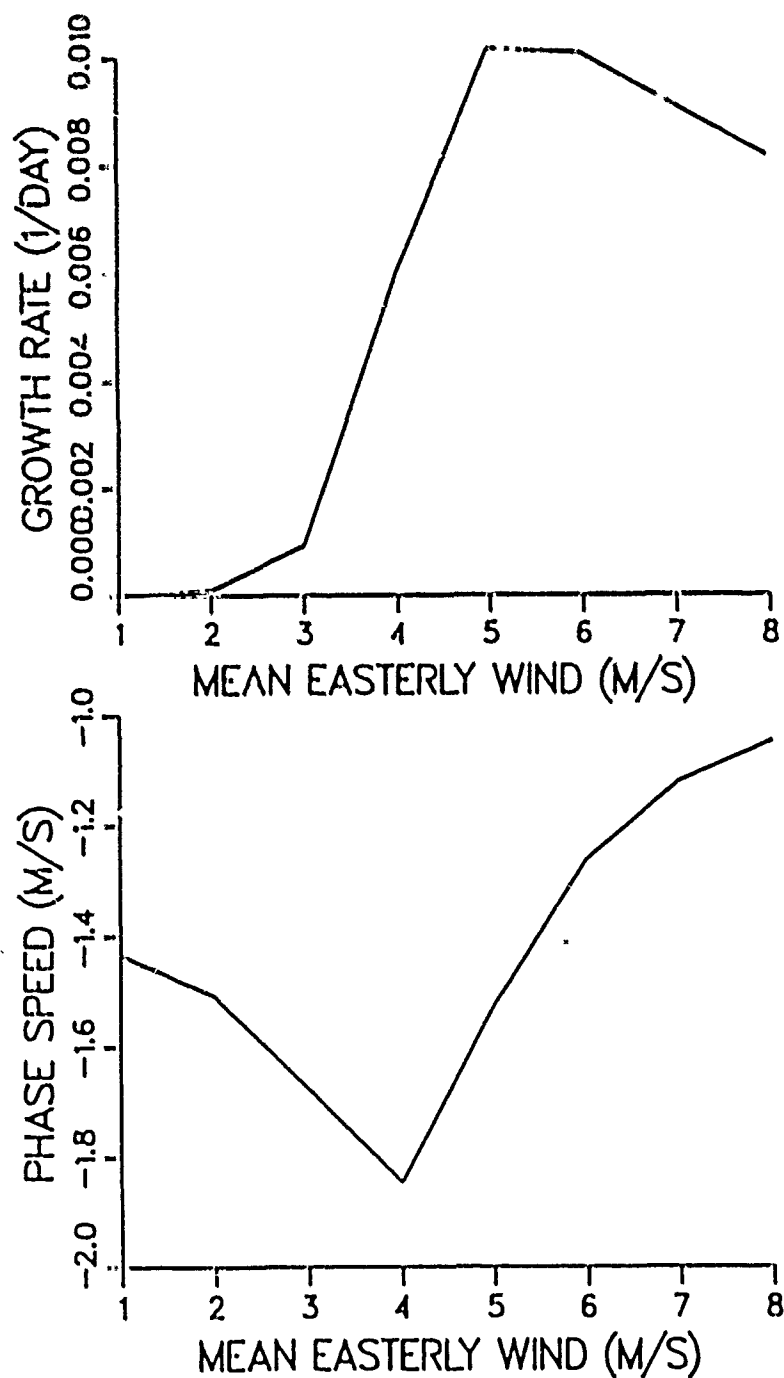


Figure 7. Growth rate and phase speed of the wavenumber $k=1$ unstable oceanic mode for various values of the atmospheric mean zonal wind with the inclusion of wind-evaporation feedback. Ocean temperature fluctuations are treated as a passive tracer, with the mean oceanic temperature increasing toward the east.

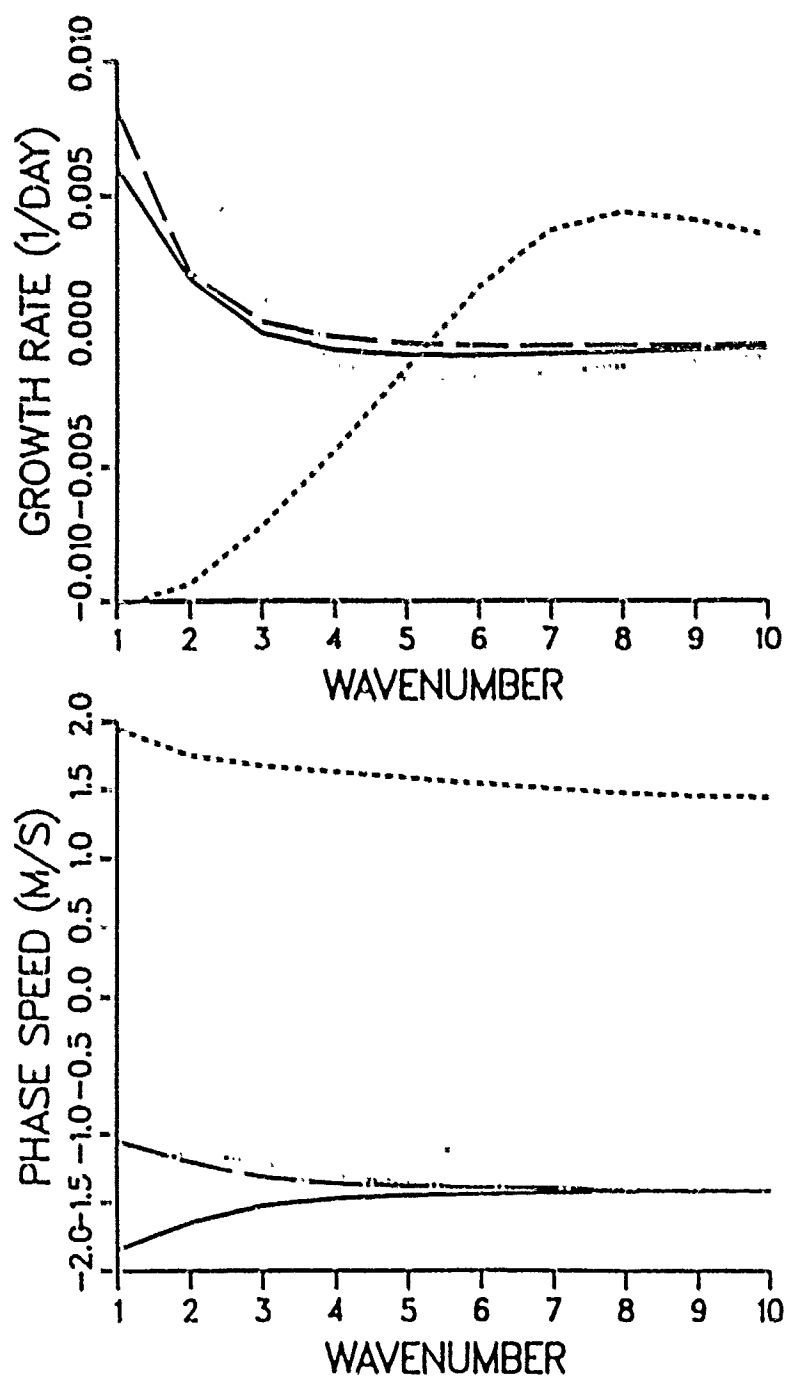
GROWTH RATE AND PHASE SPEED FOR $U = 4, 6, 6, 8$ 

Figure 8. Growth rate and phase speed of the unstable oceanic modes for an atmospheric mean easterly wind $U_a = 4$ m/s (solid line), $U_a = 6$ m/s (dotted line: this eastward mode is unstable for small wavenumbers), $U_a = 6$ m/s (dashed line: this westward mode is unstable for large wavenumbers), and $U_a = 8$ m/s (dot-dash line). Ocean temperature fluctuations are treated as a passive tracer, with the mean oceanic temperature increasing toward the east and wind-evaporation feedback is included.

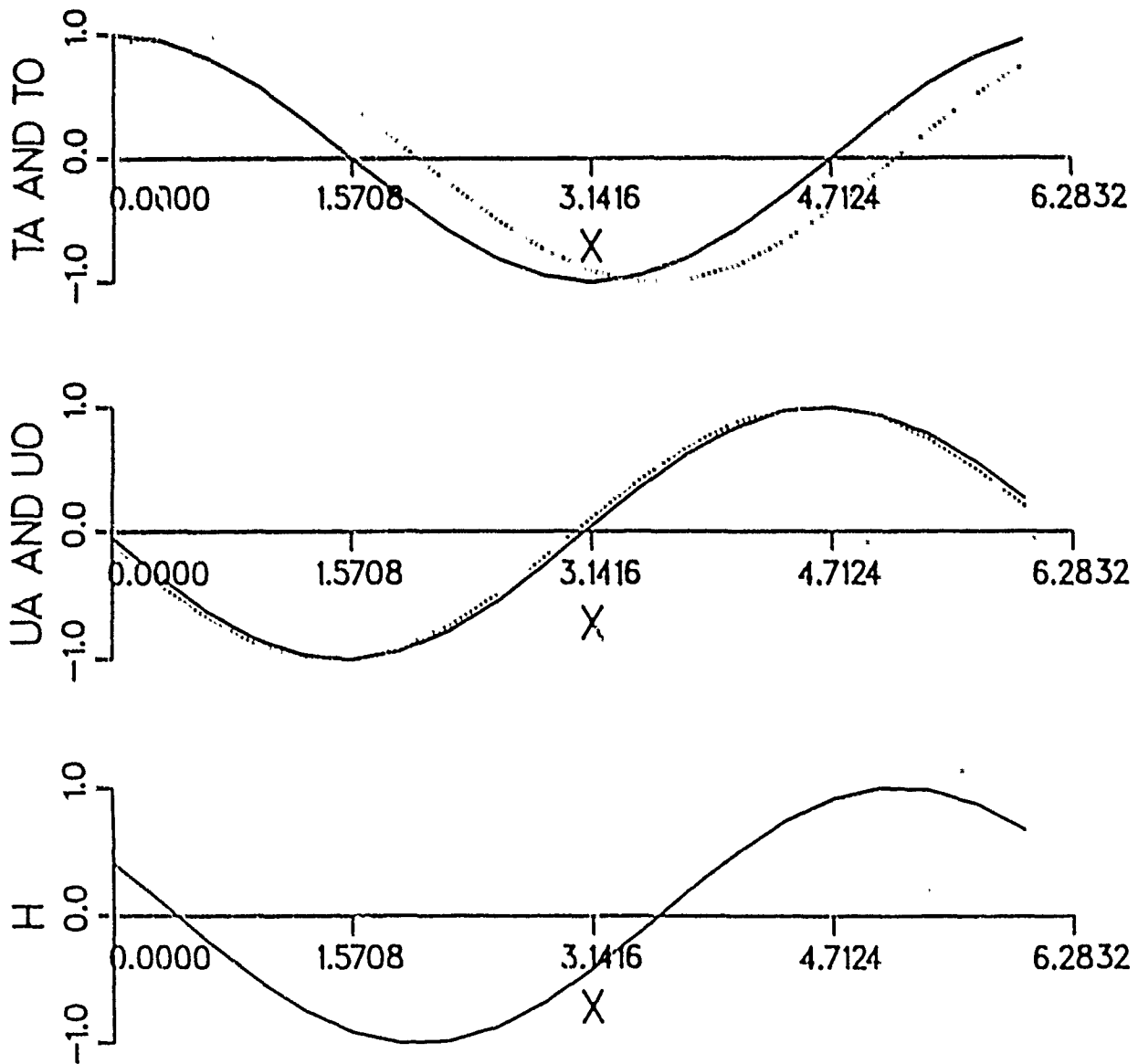
PERTURBATION FIELDS FOR $K=1$ AT $Y=0$ 

Figure 9. Zonal structure at the equator of an unstable oceanic mode with an atmospheric mean easterly wind $U_a=6$ m/s and wavenumber $k=1$. The growth rate and phase speed are 0.01 1/day and -1.26 m/s, as seen in Figure 7 and Figure 8. Plotted quantities are the same as those plotted in figure 3. In this case, actual dimensional amplitudes are such that an atmospheric zonal wind anomaly of 1 m/s will result in anomalies of 1.9°C, 26 cm/s, 1.1°C, and 36m in the atmospheric temperature, oceanic speed, oceanic temperature, and thermocline depth, respectively.

A ONE-DIMENSIONAL MODEL FOR MICROBURSTS

Steven T. Siems
University of Washington

I. Introduction

In 1976 Fujita studied intense, short-lived downdrafts with respect to the downing of an aircraft. Subsequently he defined a special class of these downdrafts known as microbursts. General characteristics of these downdrafts are a strong vertical velocity in the range of 10-20 m/s; a radius on the order of 500-1000 meters; and a peak lifetime of 5-10 minutes. Microbursts have been observed in a wide variety of locations. They commonly occur over the western plains states. Hjelmfelt [1987] also notes that Doppler Radar picks up a boundary layer convergence just below cloud base in connection with the occurrence of microbursts. One can also detect a general conical shape to the upper portion of these downdrafts as depicted by Hjelmfelt (figure 1.1). It is not hard to see the danger that these downdrafts can present to aircraft especially in the extreme cases of velocities of 30+ m/s on a radius of over 2 kilometers. Also their lifetime has been found to extend up to 20 minutes in rare events.

As a consequence of the recent classification and interest in microbursts, scientific projects have arisen to help understand the physical relations of the phenomena. Such programs include the Joint Airport Weathers Studies (JAWS, Colorado 1982) and Northern Illinois Meteorological Research on Downbursts (NIMROD, Illinois 1981). Further classifications have been made based on the newfound knowledge. Microbursts studied over the plains states have shown that the 'falling of rain into a dry planetary layer is fundamental in driving the microbursts by both evaporative cooling and liquid water loading. Typically, large regions of overlying cumulus clouds sink at velocities of 1.0 - 2.0 m/s into the dry lower layer while simultaneously raining into the layer. The drag induced by the rain together with the cooling of the air by evaporation creates the downdraft.

The recent classification of microbursts has also led to first-attempt models of the phenomena. The aim is primarily for understanding the complex interactions of the atmosphere, not a predictive model. One of the earlier models of downdrafts driven by evaporative cooling and liquid water loading [Kamboruva & Ludlam 1966] shows that stronger downdrafts are allowed as the underlying atmosphere approaches a dry adiabat. This is commonly observed to hold also. Many one-dimensional models have been studied providing an insight into the relation between the velocity and the buoyancy generation. One reported feature is

that the stronger downdrafts are thought to occur with smaller raindrop composition because of the enhanced evaporation.

Srivastava [1985] produced a more complex one-dimensional model for microbursts providing information on the vertical velocity, water vapor mixing ratio, temperature, raindrop size distribution and cloud water mixing temperature differences which have been found to be in good general agreement. However, the model is limited in that it forces a fixed entrainment rate based on a constant radius for the microburst column. It has been noted that this is possibly a source of inconsistency [Mahoney & Rodi, 1987].

II. The Model

The problem will be approached as an ideal plume of the type described by Morton, Taylor, & Turner [1954] with the additional complications of buoyancy sources from liquid water loading and evaporative cooling. Thus, we visualize the fully developed microburst as a steady-state, one dimensional plume descending through the neutrally stratified lower layer of the atmosphere. The deformation caused upon reaching the ground is not considered. This is an idealized local convective process. The evaporative cooling is handled by imagining a shower of monodispersed drops. These uniformly sized drops evaporate identically and fall at the same rate relative to the plume. This shower, or liquid water flux, is considered separate from the plume and does not directly interfere with the structure of the plume (figure 2.1). This is a crude method for the handling drops. A more appropriate method might be to discretize the raindrops distribution of Marshall and Palmer as in Srivastava. However, time prevented this. Srivastava notes that choosing an appropriate drop size in the mono-dispersed method was quite satisfactory when compared to the discrete Marshall-Palmer distribution results.

The conservation equations are developed in a similar manner to Emanuel [1981]. Conservation equation are developed over the radially averaged conserved quantities. It is assumed that plume remains radially symmetric at any depth. Emanuel notes the following assumptions for the plume:

1. Radial profiles of vertical velocity, buoyancy, vapor fluxes are geometrically similar at all heights.
2. The mean entrainment rate is proportional to the radially averaged vertical velocity. (This implicitly prevents the occurrence of detrainment from the plume.)

$$\bar{u} = \alpha \bar{w}$$

3. A Boussinesq fluid is idealized.

4. The Froude number is small. (This insures that aerodynamic effects are negligible.)
5. The plume is fully turbulent, ie. viscosity is negligible.
6. The environment moves at most with a uniform vertical velocity. In addition to this, the following assumptions are needed for the shower.
7. A mono-dispersed distribution of drops.
8. The fall velocity, V , of the drop relative to the plume is proportional to the root of the drop radius (Betts, 1981, based on Manton & Cotton).

$$V = 2.13 \left(\frac{\rho_l}{\rho} g r \right)^{1/2}$$

9. The drop mass evaporates as a function of the radius and the vapor difference up to the wetbulb vapor content.

$$\frac{dM}{dt} = \beta_1 r (q_{vp} - q_w)$$

This last equation is again an extreme oversimplification. As shown by Pruppacher & Beard [1971], the actual coefficient is not a constant but varies with the Reynolds and Schmidt number. Also this general form only holds for a limited range of drop sizes. The vapor difference uses the wetbulb temperature as this is a fair approximation to the temperature of the falling drop. Assumption 3. is perhaps a great weakness of the model as the density of the atmosphere will vary considerably over 4 kilometers.

The conservation equations are now developed in the manner of Morton, Taylor, & Turner. A cross-sectional disc of the plume is considered (figure 2.2). The fluxes of mass, momentum and heat must be conserved over this disc at all depths, z . In addition to the plume quantities, the fluxes of liquid water and vapor must be considered. The limit is then taken as the thickness of the disc approaches 0.

Conservation of Mass Flux

$$\frac{d}{dz} (\pi R_p^2 w_p) = 2\pi R_p \alpha w_p - \frac{d}{dz} (\pi R_g^2 (w+v) \ell_s \rho)$$

ρ - density of the air
 ℓ_s - liquid water content of the air

The right hand side of the equation contains the entrainment term as well as the evaporation term. All evaporated water is assumed to join the mass of the plume. Upon simplification one gets:

$$\frac{d}{dz} (R_p^2 w) = 2 R_p \alpha w - \frac{d}{dz} f$$

$$f = R_s^2 (w + v) l_s$$

Conservation of Momentum Flux

$$\frac{d}{dz} (\pi R_p^2 w^2 \rho) + \frac{d}{dz} (\pi R_s^2 (w + v_r)^2 l_s \rho) = \eta (\Delta \rho) \pi R_p^2 + g \pi R_s^2 l_s \rho$$

$g(\Delta \rho)$ - gravitational buoyancy effect of Boussinesq fluid

The right hand side contains the gravitational force on the plume and the rain drops. The left hand side is the net momentum flux of the plume and shower. The second term on the left was kept in the equations for all calculations even though it may be scaled out. The effect of neglecting this term has been seen to be negligible in the results of the computation. Upon simplification one gets:

$$\frac{d}{dz} (R_p^2 w^2) = R_p^2 B + g \frac{f}{w + v} + \frac{d}{dz} [f(w + v)]$$

Conservation of Heat Flux $B \equiv g \Delta \rho / \rho$

$$\frac{d}{dz} (\pi R_p^2 w^2 c_p \theta_p) = 2 \pi R_p \alpha w c_p \theta_e \rho - L_v \frac{d}{dz} [\pi R_s^2 (w + v_r) l_s \rho]$$

- θ_p - potential temperature of plume
- θ_e - potential temperature of environment
- L_v - latent heat of vaporization
- c_p - heat capacity of an ideal gas

The right side is the entrained heat and the cooling effect of evaporation, respectively. One substitutes (3.1) back into this equation and reduces it to the buoyancy flux equation:

$$\frac{d}{dz} (R_p^2 w B) = - R_p^2 w N^2 - M \frac{d}{dz} f$$

$$B = g \frac{\theta_p - \theta_e}{\theta} - \text{buoyancy}$$

$$M = g \left(\frac{L_v}{c_p \theta} - 1 \right) - \text{buoyant effect of shower}$$

$$N^2 = \frac{g}{\theta_p} \frac{d\theta_e}{dz} - \text{stratification of the environment}$$

If it is assumed that the liquid water flux, f , is zero, the equations reduce to the closed ideal system of Morton, Taylor, & Turner. One should then expect the earlier similarity behavior when the flux is completely evaporated. To close the system, an equation is needed for the evaporation. Upon noting that the flux is proportional to the drop size, one gets:

$$\frac{d}{dz} f = \beta_1 f^{1/3} (q_{vp} - q_w)$$

where β_1 depends on the number of drops in the shower.

In order to close the system now, one needs to find expressions for the vapor content of the plume, q_{vp} , and the wetbulb vapor, q_w . The vapor of the plume may be found by a conservation law similar to the mass flux:

$$\frac{d}{dz} (\pi R_p^2 w_p q_{vp}) = 2\pi R_p \alpha w q_{ve} - \frac{d}{dz} [\pi R_p^2 (w + v) \rho_s]$$

$$\text{or } \frac{d}{dz} (R_p^2 w q_{vp}) = 2 \alpha w q_{ve} R_p w - \frac{d}{dz} f$$

q_{ve} - vapor content of environment

The wetbulb temperature and vapor pressure may not be found in such a straight forward manner. The point is found by iteratively solving the relation

$$L_v (q_{vp} - q_w) = c_p (T - T_w)$$

where the wetbulb temperature is assumed to be saturated. Again, this is the temperature that a particle would have if it descended from its lifting condensation level along a moist adiabat. (fig. 2.3)

Finally, the fall velocity equation is brought in:

$$V = \beta_2 f^{1/6}$$

Again we have assumed that the flux is directly depended on the radius of the drops. β_1 is found from initial conditions on the flux and fall speed which are assumed to be specified.

One next nondimensionalizes in terms of the initial fall speed, V and the initial rain flux, Γ_0 . With the substitution of variables and nondimensionalization, the final system is:

$$\Omega = R_p^2 w \quad K = R_p^2 w B \quad \Psi = R_p^2 w q_{vr} \quad \phi = R_p w \quad r = \frac{d}{V} \quad \tau \equiv \frac{d}{V^2}$$

$$\dot{\Omega} = 2\alpha\phi - \dot{\Gamma}$$

$$\dot{\phi} = 2\Omega K + \frac{2\phi^2 \Gamma}{\phi^2/\Omega + V} - 2\phi^2 \left[\Gamma \left(\frac{\phi^2}{\Omega} + V \right) \right]$$

$$\dot{K} = -\eta^2 \Omega - \mu \dot{\Gamma}$$

$$\dot{\Gamma} = \beta_1 \Gamma^{1/2} (q_{vr} - q_w) \left(\frac{\phi^2}{\Omega} + V \right)^{-1}$$

$$\dot{\Psi} = 2\alpha q_{ve} \phi - \dot{\Gamma}$$

$\theta, \mu, \eta, \beta_1$ are
the nondimensionalized
 g, N^2, M , & β_1

(β_1 is reduced to one identically by the nondimensionalization.)

III. Initial Conditions & Solutions

In an effort to compare results with previous work, a sounding was selected from the literature [Hjelmfelt fig. 3.1]. The cloud base is at 550 mb, with a temperature of roughly 5 K. The underlying atmosphere is assumed to be well mixed lying along a dry adiabat with a constant vapor mixing ratio of 6 g/kg.

Initially, a sinking region of air, is assumed of a specified radius, temperature, rain water content, velocity and rain drop size (fall velocity). Base values were selected from the literature. The first solution below (fig 3.2) is shown with $R_0 = 500$ m, $w_0 = 2.0$ m/s, $V_0 = 10$ m/s, $\Delta T_0 = 0.0$ K, and $\Gamma_0 = 4$ g/kg.

In addition to this, initial values for the parameters of the equations are entered with the dimensional values of :

$$N^2 = 0 \quad (\text{atmosphere dry adiabatic})$$

$$M = 777 \quad \text{m}^2/\text{s}$$

Due to the gross simplification, values for β_1 , are rather arbitrary. A value was used in order to produce a reasonable gross rain flux profile over its depth. The effect of the variable has been considered in the future analysis.

This system of equations has only approached numerically to date. A simple leapfrog method is used in space. The method is started with a forward difference method. Forward differencing is also used at the step when the flux completely evaporates as

well as when the step size is changed for computational efficiency. The results for the base run are shown figure (3.2 a-c). These are the profiles versus the depth of the lower layer. The graphs are inverted with the bottom being at the cloud base of 550 mb. and "rising" as the microburst would descend. The 850 mb level mark corresponds roughly to the ground level over the western plains. Profiles were run out further to allow for a better interpretation. The depth at 850 mb is roughly 4 kilometer below cloud base. The graphs plot variables versus depth not pressure. The outer line in (fig a) corresponds to the radius of the plume. This is not constant as suggested by Srivastava. Initially, the radius contracts greatly to accomodate the increasing velocity. It then begins to increase as entrainment becomes more prominent. The constriction of the radius is similar to that of a stream of water falling from a faucet. The high level entrainment should create a convergence as reported by Hjelmfelt. The next graph is of the fall velocity, plume velocity, and buoyancy versus depth. The vertical velocity increases to nearly its maximum value in a relatively short depth. The range of velocity values easily falls within the category of micro-bursts. The final graph is of the rain flux and plume vapor mixing ratio versus depth. The rise in the vapor content has a great effect on the amount of evaporation as $\frac{1}{2}$ approaches 0 as $\frac{1}{2}$ approaches $\frac{1}{2}$. Once heavy entrainment begins to occur, the plume vapor content begins to approach the environment's allowing evaporation to increase again.

The direct effect of the evaporation may be seen through the graph of the flux. Figure 3.3(a-c) shows a similar run with the evaporation parameter increased by a factor of four. At such a high evaporation rate the rain flux does not last half the distance to the ground. When the flux runs out, the plume returns to the type idealized by Morton, Taylor, & Turner. Similar growth in the variables are seen. The peak velocity occurs when the flux reaches zero if this is above ground level. By varying $\frac{1}{2}$, a wide range of evaporation conditions are considered. While the crudeness of the model prevents subtle changes in the profile of the flux, the general behavior is well handled. Graph 3.1 shows how the plume velocity and radius at 850 mb vary with evaporation constant. As the evaporation is shut off it is seen that the downdrafts become too weak to be classified as microbursts. Increasing the evaporation appears to be limited, as the vapor content in the plume will quickly approach saturation, cutting off further evaporation. The radius of the plume is found to be surprisingly constant throughout.

To better understand the effect of the governing parameters, graphs are presented of their effect on the ground plume velocity and radius of the microbursts. Again, the ground radius is seen to be rather constant throughout. Graph 3.2 shows the variations of the initial radius. A limiting case again appears to be present. Graph 3.3 is of the vapor content of the environment. Clearly this is a weak relation, however, as expected, drier

well as when the step size is changed for computational efficiency. The results for the base run are shown figure (3.2 a-c). These are the profiles versus the depth of the lower layer. The graphs are inverted with the bottom being at the cloud base of 550 mb. and "rising" as the microburst would descend. The 850 mb level mark corresponds roughly to the ground level over the western plains. Profiles were run out further to allow for a better interpretation. The depth at 850 mb is roughly 4 kilometer below cloud base. The graphs plot variables versus depth not pressure. The outer line in (fig a) corresponds to the radius of the plume. This is not constant as suggested by Srivastava. Initially, the radius contracts greatly to accomodate the increasing velocity. It then begins to increase as entrainment becomes more prominent. The constriction of the radius is similar to that of a stream of water falling from a faucet. The high level entrainment should create a convergence as reported by Hjelmfelt. The next graph is of the fall velocity, plume velocity, and buoyancy versus depth. The vertical velocity increases to nearly its maximum value in a relatively short depth. The range of velocity values easily falls within the category of micro-bursts. The final graph is of the rain flux and plume vapor mixing ratio versus depth. The rise in the vapor content has a great effect on the amount of evaporation as $\frac{r}{r_s}$ approaches 0 as $\frac{r}{r_s}$ approaches 1. Once heavy entrainment begins to occur, the plume vapor content begins to approach the environment's allowing evaporation to increase again.

The direct effect of the evaporation may be seen through the graph of the flux. Figure 3.3(a-c) shows a similar run with the evaporation parameter increased by a factor of four. At such a high evaporation rate the rain flux does not last half the distance to the ground. When the flux runs out, the plume returns to the type idealized by Morton, Taylor, & Turner. Similar growth in the variables are seen. The peak velocity occurs when the flux reaches zero if this is above ground level. By varying $\frac{r}{r_s}$, a wide range of evaporation conditions are considered. While the crudeness of the model prevents subtle changes in the profile of the flux, the general behavior is well handled. Graph 3.1 shows how the plume velocity and radius at 850 mb vary with evaporation constant. As the evaporation is shut off it is seen that the downdrafts become too weak to be classified as microbursts. Increasing the evaporation appears to be limited, as the vapor content in the plume will quickly approach saturation, cutting off further evaporation. The radius of the plume is found to be surprisingly constant throughout.

To better understand the effect of the governing parameters, graphs are presented of their effect on the ground plume velocity and radius of the microbursts. Again, the ground radius is seen to be rather constant throughout. Graph 3.2 shows the variations of the initial radius. A limiting case again appears to be present. Graph 3.3 is of the vapor content of the environment. Clearly this is a weak relation, however, as expected, drier

Bibliography

- Beard, K.V. and H.R. Pruppacher, 1971: A wind tunnel investigation of the rate of evaporation of small water drops falling at terminal velocity, *J. Atmos. Sci.*, 28, 1455-1464.
- Betts, A.K. and M.F. Silva Dias, 1979: Unsaturated downdraft thermodynamics in cumulonimbus., *J. Atmos. Scie.*, 36, 1061-1071.
- Emanuel, K.A., 1981: A similarity theory for unsaturated downdrafts within clouds., *J. Atmos. Sci.*, 38, 1541-1557.
- Hjelmfelt, M.R., 1987: The microbursts of 22 June 1982 JAWS, *J. Atmos. Sci.*, 44, 1646-1665.
- Kamburova, P.L. and F.H. Ludlam, 1966: Rainfall evaporation in thunderstorm downdrafts, *Quart. J. Roy. Meteor. Soc.*, 92, 1890-1910.
- Mahoney, W.P. III and A.R. Kadi, 1987: Aircraft measurement on microburst development from hydrometeor evaporation, *J. Atmos. Sci.*, 44, 3037-3051.
- Morton, B.R., G. Taylor and J.S. Turner, 1956: Turbulent gravitational convection from maintained and instantaneous sources, *Proc. Roy. Soc. London*, A234, 1-23.
- Srivastava, R.C., 1985: A simple model of evaporatively driven downdraft: Application to microbursts downdraft, *J. Atmos. Sci.*, 42, 1004-1023.

Hjelmfelt [1987]

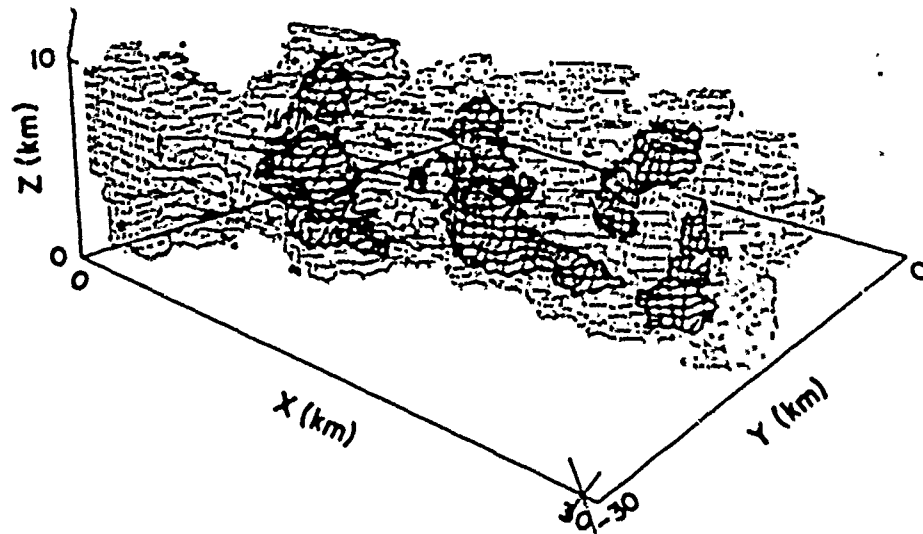
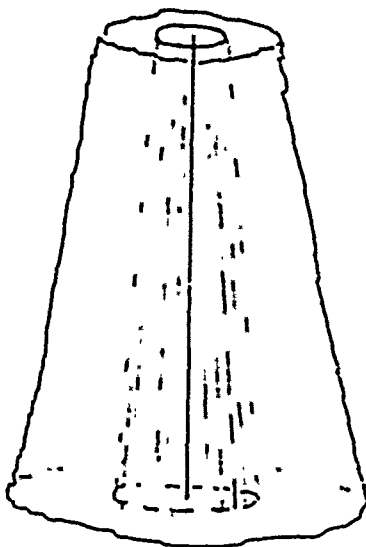
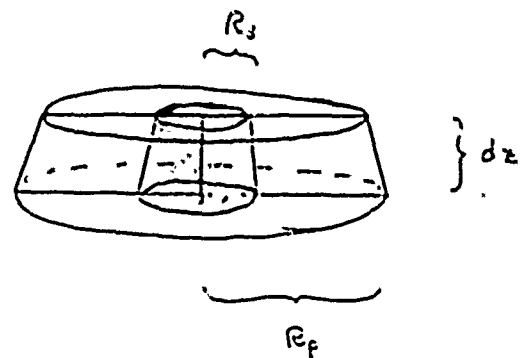


FIG. 8. Three-dimensional reflectivity structure of storm at 1612. Dark reflectivity cores are >45 dBZ. Half-tone shows reflectivity > 20 dBZ. The 0° km AGL level not shown. Two cores at left correspond to those shown in Fig. 5.

Fig. 2



steady-state plume



plume velocity w
rain velocity $(w + v)$

Fig. 2.2
cross section

Mahoney & Rodi [1987]

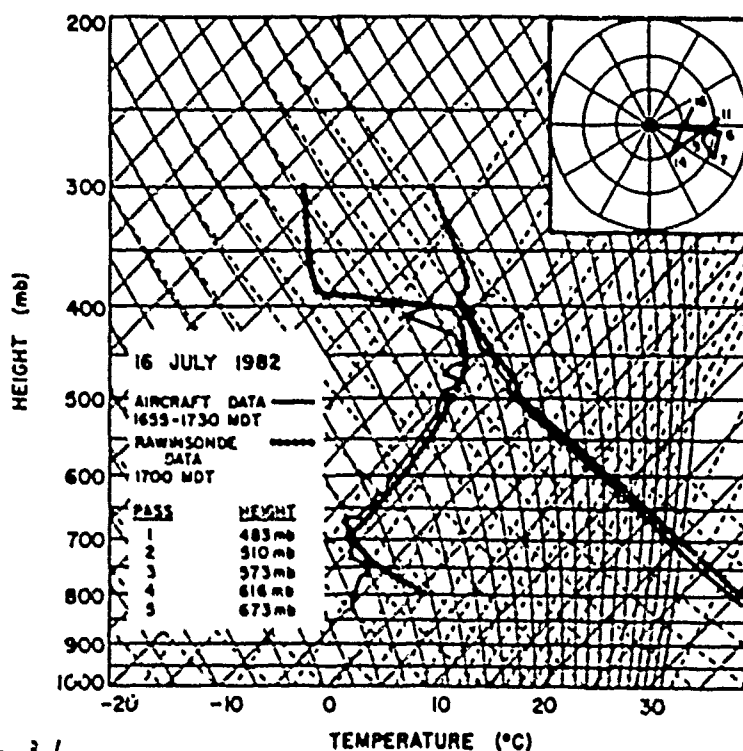
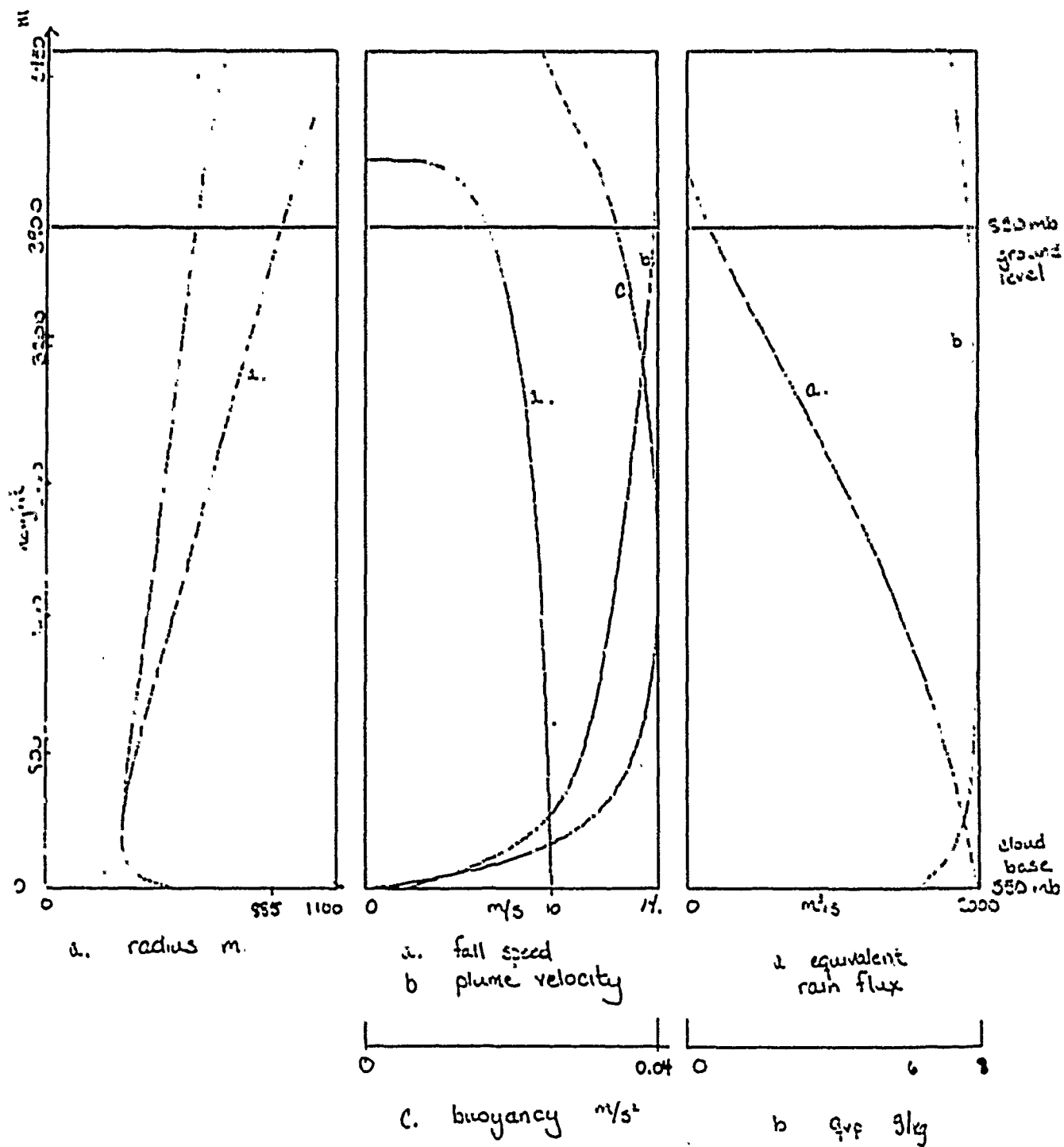


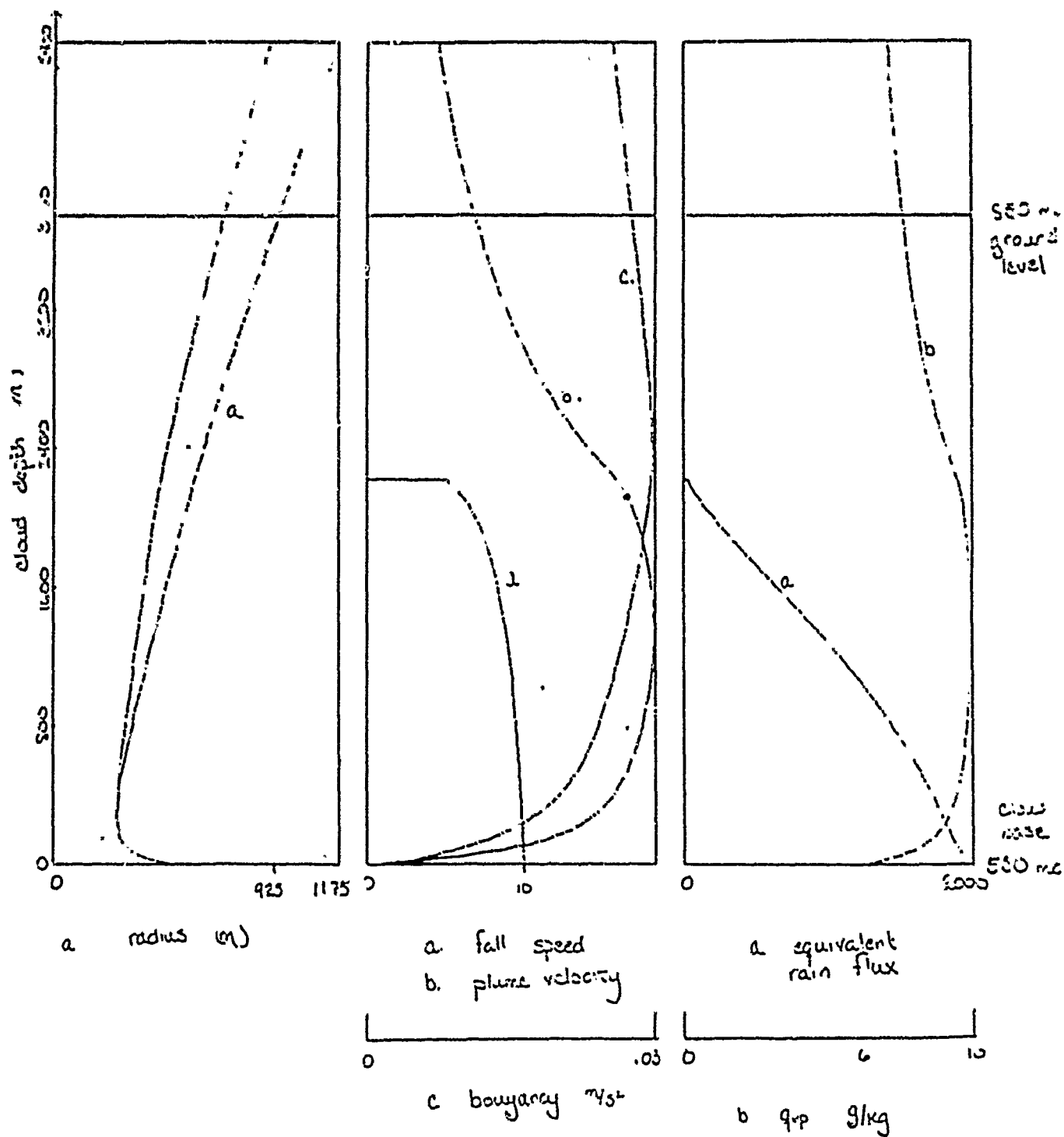
Fig 3.1

FIG. 1. Vertical profile of temperature and dewpoint measured by the aircraft and the 1700 MDT Denver rawinsonde on 16 July 1982. Hodograph rings are at 3 m s^{-1} intervals and levels are in thousands of feet. Cloud bases were measured at 460 mb (4.4 km AGL).

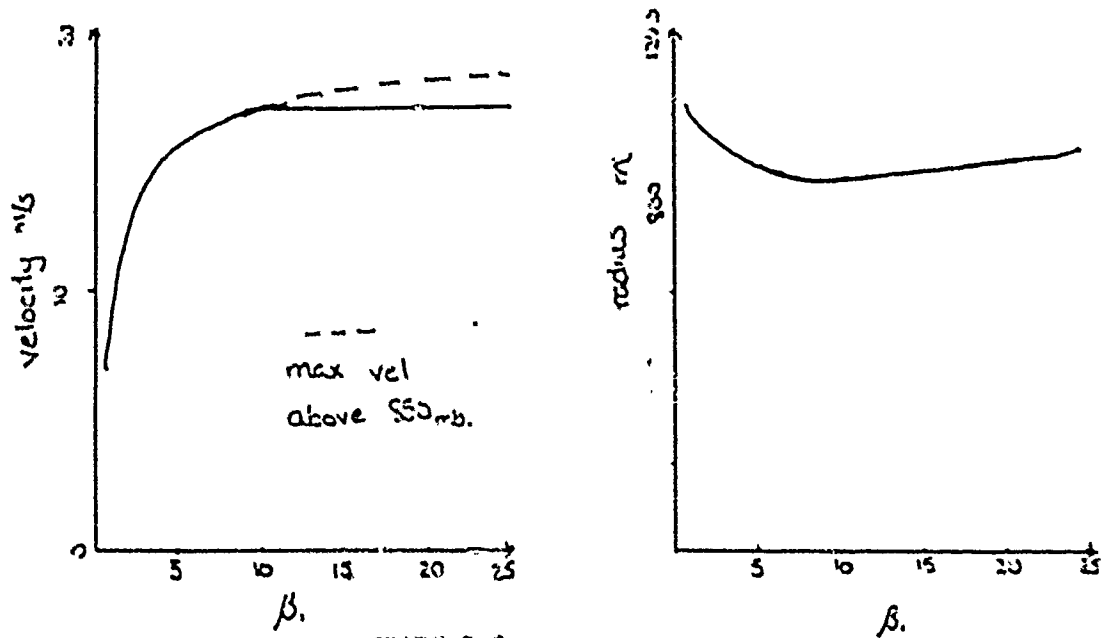
Vertical Profiles case run



Vertical Profiles high evaporation

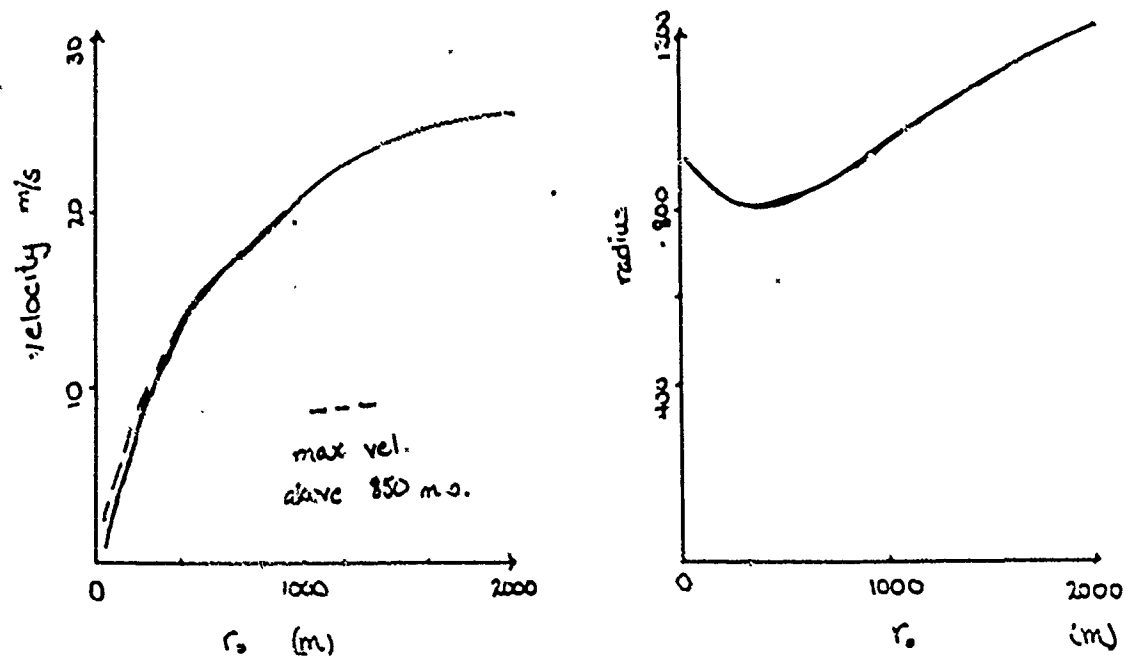


Effect of β_1

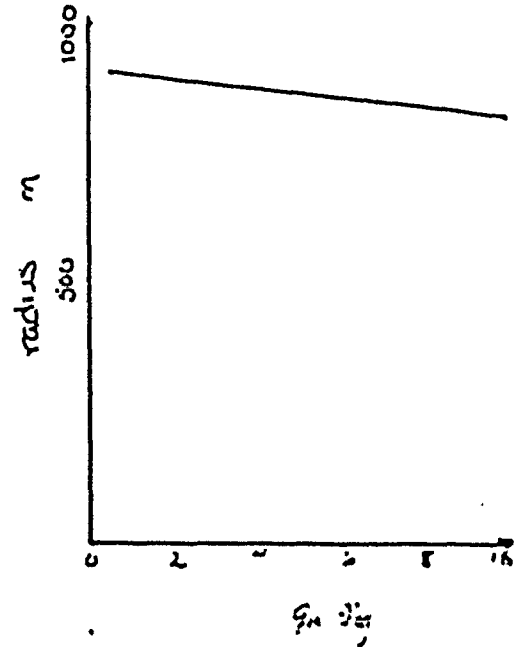
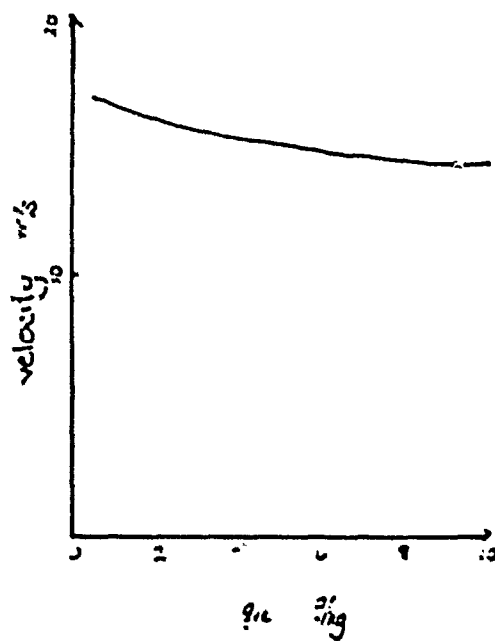


GRAPH 3.2

Effect of Initial Radius

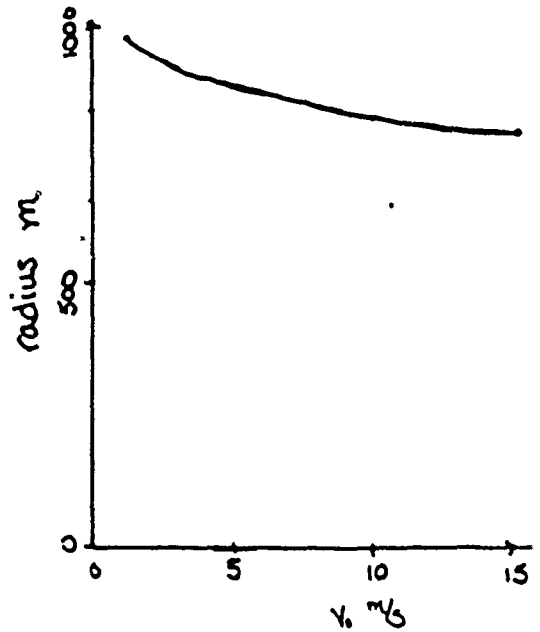
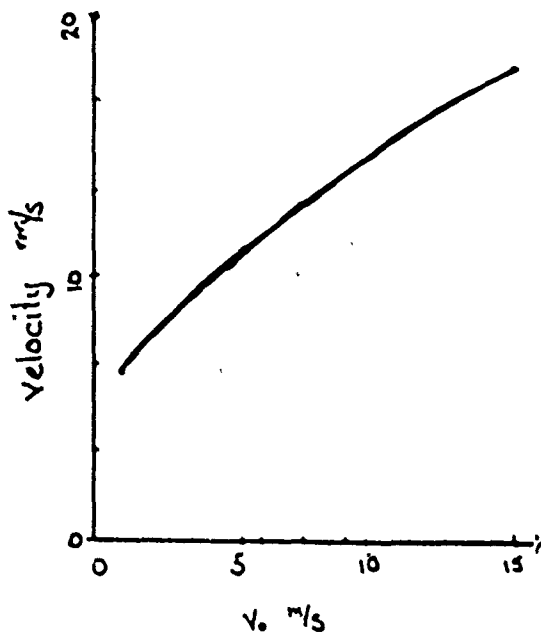


Effect of q_{re}

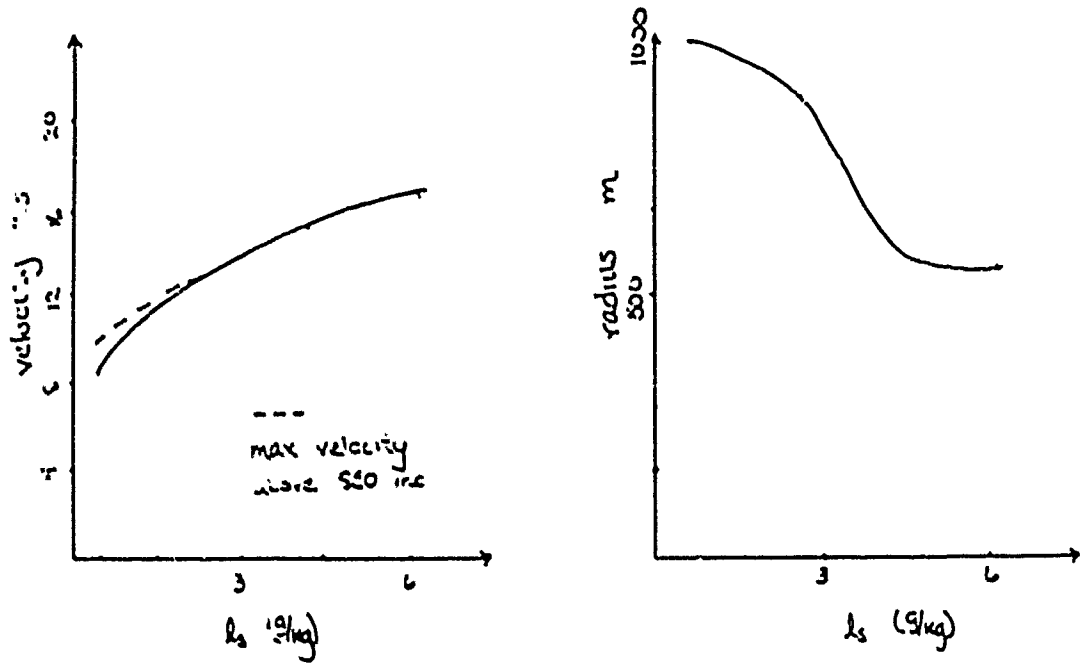


GRAPH 3.4

Effect of V_0
(initial drop fall speed)

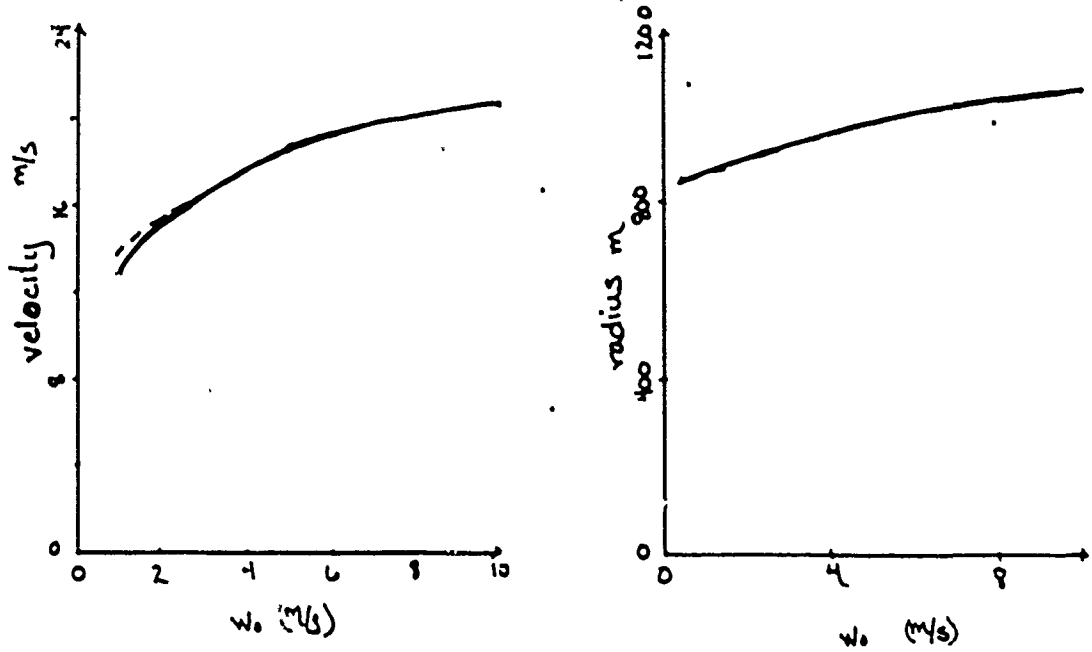


Effect of l_s



GRAPH 3.6

Effect of w_0
(initial prime speed)



**The 30–60 Day Oscillation in the Tropics —
Wind-Evaporation Feedback and Up-Down Asymmetry**

John Thuburn Aug/27/1988

Dept. Atmospheric, Oceanic and Planetary Physics,
Oxford, UK.

1 Introduction

Observations in the tropics of zonal wind, surface pressure and outgoing longwave radiation anomalies among other things have revealed signals which are baroclinic, (the wind in the upper troposphere is opposite in direction to that in the lower troposphere), global wavenumber predominantly 1, and eastward propagating with period in the range 30–60 days. There is some evidence that they are poleward phase propagating.

We will review a model of the phenomenon which relies on wind-evaporation feedback and show that it selects the shortest zonal scales. Here we extend this model by incorporating an asymmetry between upwelling and downwelling regions and show that this can select a global wavenumber 1.

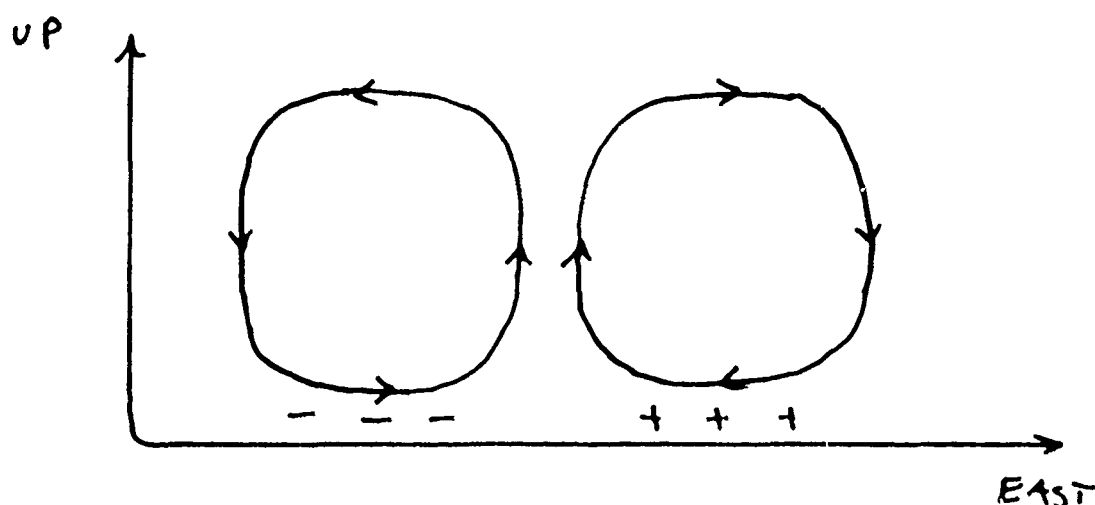


Figure 1. Schematic illustration of the wind-evaporation feedback mechanism (based on figure 1 of Emanuel [1987]). A positive surface heat flux anomaly (+++) in the region of easterly wind anomaly produces a net warming to the east of the updraft while a negative surface heat flux anomaly (- - -) in the region of westerly wind anomaly produces a net cooling there. The resulting pattern of geopotential perturbations causes the pattern to propagate eastwards.

2 A Wind-Evaporation Feedback Model

Emanuel [1987] and independently Neelin et al. [1987] proposed wind-evaporation feedback as a mechanism for producing growing eastward propagating disturbances. Because the mean flow in the tropics is easterly and because the surface heat flux increases as $|u|$ does at the top of the planetary boundary layer an easterly perturbation to the mean lower tropospheric wind will increase $|u|$ and hence increase the surface heat flux while a westerly perturbation will reduce $|u|$ and the surface heat flux. There is net heating to the east of the low level convergence tending to propagate the pattern eastwards. See figure 1.

Both Emanuel and Neelin et al. develop analytical models based on this mechanism. We will briefly review the model of Neelin et al. — the equations are the same as those of Emanuel but the interpretation of some of the terms differs. For more details see those papers and also lecture 10 in this volume.

The model is a two-layer equatorial beta-plane model linearised about a zonal flow \bar{u} , in which all perturbations are assumed to be purely baroclinic. The thermodynamic equation is

$$(\partial_t + \bar{u}\partial_x + K_T)c_p T + \Delta s \frac{w}{D} = \frac{LP}{D} \quad , \quad (1)$$

where T is a mid-tropospheric temperature, Δs is the dry static energy difference between the two layers — a measure of the stratification, K_T is a Newtonian cooling coefficient, L is the latent heat of evaporation, P is the rate of precipitation, D is proportional to the depth of a model layer and the vertical velocity, w , is given by the horizontal convergence in the lower level:

$$\frac{w}{D} = -(u_x + v_y) \quad (2)$$

The precipitation, P , is obtained from the equation for the lower layer specific humidity, q . We assume that to a first approximation the tropical atmosphere is saturated so that $q = q_{sat}$ and that $u \cdot \nabla q$ is negligible compared with $q \nabla \cdot u$.

$$-q_{sat} w = E - P \quad (3)$$

The perturbation evaporation rate, E , is given by

$$E = -Au \quad (4)$$

where A is a positive constant when \bar{u} is negative. Combining (1), (3) and (4) gives

$$(\partial_t + \bar{u} \partial_x + K_T) c_p T + w \Delta m = -\frac{Au}{D} \quad (5)$$

where $\Delta m = \Delta s - Lq_{sat}$ is the moist static energy difference between the two layers. It is a small difference of two large quantities and we believe it is not important for the phenomenon we are trying to model, so we neglect this term.

The temperature perturbation is proportional to -1 times the lower layer geopotential perturbation so, after non-dimensionalizing, we obtain

$$(\partial_t + \bar{u} \partial_x + r) \phi - au = 0 \quad (6)$$

while the horizontal momentum equations are

$$(\partial_t + \bar{u} \partial_x + 1)u - yv + \phi_x = 0 \quad (7)$$

$$(\partial_t + \bar{u} \partial_x + 1)v + B(yu + \phi_y) = 0 \quad (8)$$

We have used a Rayleigh friction coefficient, K_M , to define a time scale and the circumference of the earth, $2\pi R$, to define a zonal length scale. The non-dimensional coefficients are

$$a = \frac{A}{LK_M^2}, \quad B = \frac{2\pi R\beta}{K_M}, \quad r = \frac{K_T}{K_M} \quad (9)$$

and the meridional length scale is $2\pi RB^{-1/2}$. r and a are of order unity but B is very large, about 400.

If \bar{u} is independent of y , apart from its implicit effect on A , it simply doppler shifts any possible solutions so we will drop the $\bar{u}\partial_x$ terms.

These equations support growing normal modes with $v = 0$ everywhere and

$$u \propto \text{Re} \left\{ \exp \left(ik(x - ct) + \sigma t - (\sigma - ikc) \frac{y^2}{2} \right) \right\} \quad (10)$$

which are eastward propagating and have phase increasing polewards. However waves with the largest zonal wavenumber grow the fastest; $\sigma \propto k^{1/2}$ for large k . This is the major shortcoming of this model.

(The model equations also support fast growing, fast propagating modes with $v \neq 0$, which Emanuel calls 'non-geostrophic' modes, of the form

$$u \propto \text{Re} \left\{ y^n \exp \left(ik(x - ct) + \sigma t - (\sigma - ikc) \frac{y^2}{2} \right) \right\} \quad (11)$$

for positive integer n . The dispersion relation is approximately

$$\sigma - ikc \simeq (nB)^{1/3} (1/2 \pm i\sqrt{3}/2) \quad (12)$$

Note that the amplitude maximum is off the equator.)

3 Up-Down Asymmetry – A Possible Scale Selection Mechanism

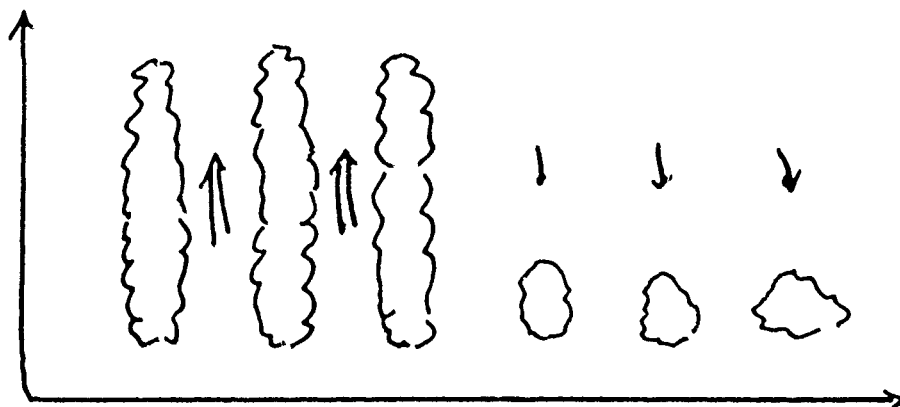


Figure 2. Schematic showing deep precipitating convection in a region of upwelling and shallow non-precipitating convection in a region of downwelling.

3.1 The Model

One of the features which distinguishes moist convection from dry convection is the breaking of symmetry between upward motions and downward motions; an unsaturated air parcel moving upwards may cool adiabatically and become saturated causing water to condense and releasing latent heat which makes the air parcel more buoyant. In downward motion an unsaturated air parcel generally remains unsaturated.

The works of Lilly [1960] and Bretherton [1987] suggest that this up-down asymmetry may select a large horizontal length scale for the region of downward motion and a short length scale for the updraft region.

Here we extend the model of Neelin et al. by allowing precipitation only where $w > 0$. See figure 2. In these regions we have deep convection which distributes heat from the planetary boundary layer throughout the depth of the troposphere. In the terminology of Emanuel's model, the saturation moist entropy, s^* , of the troposphere, (a measure of the temperature), is controlled by the moist entropy, s_b , of the boundary layer:

$$s^* = s_b \quad . \quad (13)$$

In regions of downwelling we have only shallow convection. This serves to dry out the boundary layer and maintain its moist entropy at the saturation moist entropy of the tropospheric air above:

$$s_b = s^* \quad . \quad (14)$$

In these downwelling regions we simply set $P = 0$ in the thermodynamic equation (1). The stratification defines a dry Kelvin wave speed c_0^2 .

Non-dimensionalizing gives the governing equations:

$$(\partial_t + 1)u - yv + \phi_x = 0 \quad , \quad (15)$$

$$(\partial_t + 1)v + B(yu + \phi_y) = 0 \quad , \quad (16)$$

$$(\partial_t + r)\phi - au = 0 \quad \text{where } w > 0 \quad , \quad (17a)$$

$$(\partial_t + r)\phi + c_0^2(u_x + v_y) = 0 \quad \text{where } w < 0 \quad . \quad (17b)$$

$c_0^2 = c_0^{*2}/(2\pi RK_M)^2$ is the non-dimensional dry Kelvin wave speed. It is typically of order unity.

In any solutions we derive we must ensure that at the interface between the up and down regions the normal velocity is continuous and the geopotential is continuous to ensure conservation of mass and momentum.

Note that these equations are no longer strictly linear. For example we can no longer superpose solutions unless the regions of upflow in each coincide.

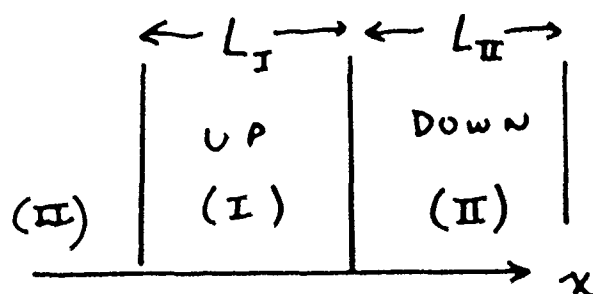


Figure 3. The periodic domain in which we seek 1-D solutions. (I) indicates the upwelling region and (II) the downwelling region. $L_I + L_{II} = 1$.

3.2 1-D Modes

Although, as mentioned above, equations (15)–(17) are no longer strictly linear, it is tempting to look for growing, propagating solutions of the form

$$u(x, t) = f(x - ct)e^{\sigma t} . \quad (18)$$

First we will look for solutions just on the equator with $v = 0$. see figure 3.

(15) and (17) become

$$(\sigma - c\partial_x + 1)u + \phi_x = 0 , \quad (19)$$

$$(\sigma - c\partial_x + r)\phi - au = 0 \quad \text{in (I)} , \quad (20a)$$

$$(\sigma - c\partial_x + r)\phi + c_0^2 u_x = 0 \quad \text{in (II)} . \quad (20b)$$

The general solution can be written

$$f(x) = u_1^I e^{\lambda_1^I x} + u_2^I e^{\lambda_2^I x} \quad \text{in (I)} , \quad (21a)$$

$$f(x) = u_1^{II} e^{\lambda_1^{II} x} + u_2^{II} e^{\lambda_2^{II} x} \quad \text{in (II)} , \quad (21b)$$

where the λ 's are related to σ and c through the dispersion relation in each region. (An exception occurs when in one region we have equal roots for λ . Then

$$f(x) = u_1^I e^{\lambda^I x} + u_2^I x e^{\lambda^I x} \quad \text{etc.}) \quad (22)$$

We have four unknown coefficients, the u 's, and the boundary conditions, continuity of u and ϕ give four homogeneous equations so there is a solvability condition of the form

$$\text{Det}(4 \times 4 \text{ matrix}) = 0 . \quad (23)$$

This can be solved numerically. This one constraint gives us surfaces of solutions in (σ, c, L_1) space. Having found a solution satisfying the boundary conditions we must check that it is consistent, i.e. that $w > 0$ in (I) and $w < 0$ in (II). This eliminates some of the solutions of (23).

However, there are still surfaces of consistent solutions. But note that for each pair (σ, c) there exists only a discrete set of L_1 's with a solution, not a continuum. This is relevant to §3.3.

3.3 2-D Modes

We now consider variations in the y -direction but keep $v = 0$ and again look for modes growing at rate σ and propagating at speed c . The y -momentum equation,

$$yu + \phi_y = 0 \quad , \quad (24)$$

now determines the meridional structure and this imposes stronger constraints than in the 1-D problem.

Equations (19) and (20) now apply at every latitude and, since σ and c are independent of y , L_1 must also be independent of y . This follows from the last point made in §3.2. The longitude of the boundaries between regions (I) and (II) may depend on y , lying at $x = X(y) + ct$ and $x = X(y) + L_1 + ct$ say. See figure 4.

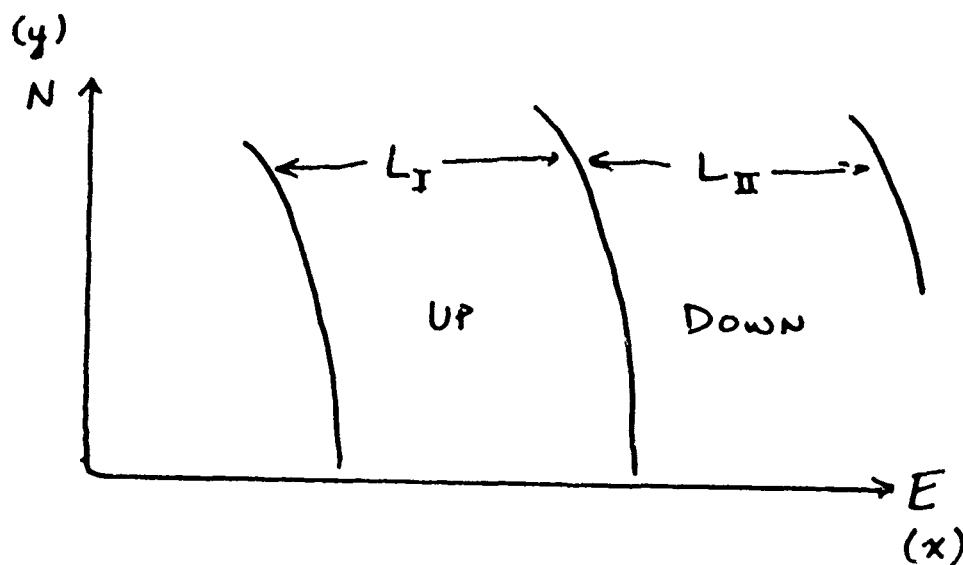


Figure 4. Schematic showing the boundaries between upwelling and downwelling regions in the 2-D problem.

So we must have the same 1-D solution at each latitude except for a possible shift of longitude and a possible scaling factor:

$$u(x, y, t) = f(x - ct - X(y))e^{\sigma t}g(y) \quad (25)$$

Integrating (24) gives

$$g = \exp(My^2) \quad (26)$$

where

$$M = \lambda_1^I X_0 - \frac{1}{D_1^I} = \lambda_2^I X_0 - \frac{1}{D_2^I} = \lambda_1^{II} X_0 - \frac{1}{D_1^{II}} = \lambda_2^{II} X_0 - \frac{1}{D_2^{II}} \quad (27)$$

and

$$X(y) = X_0 y^2, \quad (28)$$

i.e. the boundaries between regions of deep and shallow convection can only be parabolas, with X_0 to be determined, and

$$D_1^I = c - \frac{(\sigma + 1)}{\lambda_1^I} \quad \text{etc.} \quad (29)$$

The D 's are constants relating the zonal u structure to the zonal ϕ structure:

$$\phi_1^I = D_1^I u_1^I \quad \text{etc.} \quad (30)$$

Now, for a given M , (27) combined with (29) gives the same quadratic equation for each λ ; the four λ 's can take on two possible values. We've already assumed $\lambda_1^I \neq \lambda_2^I$ and $\lambda_1^{II} \neq \lambda_2^{II}$ so either $\lambda_1^I = \lambda_1^{II} \neq \lambda_2^I = \lambda_2^{II}$ or $\lambda_1^I = \lambda_2^{II} \neq \lambda_2^I = \lambda_1^{II}$. In either case $\lambda_1^I + \lambda_2^I = \lambda_1^{II} + \lambda_2^{II}$ and $\lambda_1^I \lambda_2^I = \lambda_1^{II} \lambda_2^{II}$. These give us some constraints on the coefficients in the two dispersion relations which are functions of σ and c . It turns out that the only solution is

$$\begin{aligned} \sigma &= -r, \\ u &\equiv 0, \end{aligned} \quad (31)$$

$$\phi = \text{const}(x, y)e^{-\sigma t},$$

i.e. simply a constant temperature perturbation decaying at the Newtonian cooling rate.

There are many other special cases to check. We have already mentioned that if, for example $\lambda_1^I = \lambda_2^I$ the general solution to the 1-D problem is different. Also if one or more of the coefficients e.g. u_1^I vanishes we can drop the corresponding constraints in (27) but

then the need to satisfy the boundary conditions gives us more constraints. It turns out that there are no non-trivial solutions of the form (25).

It is conceivable that there exist mode-like solutions with fixed propagation speed, c , and growth rate, σ , with non-zero v . I think that it is more likely that an analysis similar to the above will show no solutions in this case too. If this is true it leads us to ask ourselves what will happen in the initial value problem, since the flow cannot evolve into a mode.

3.4 Numerical Solutions

In order to answer the initial value problem a numerical model was developed to integrate the equations (15), (16) and (17). The values of u , v and ϕ are stored on a rectangular grid of points. For most of the integrations described here the resolution is 50 points in the zonal direction by 20 or 30 points in the meridional direction between the equator and some y_{\max} . Centered differences are used to approximate spatial derivatives. Time stepping is done using centered differences ('leapfrog') with implicit treatment of the Rayleigh friction and Newtonian cooling terms and lagged scale selective dissipation. A forward Euler step is used to start the integration and once every subsequent 100 steps to suppress the leapfrog computational mode.

The boundary conditions are that the solution is periodic in x , u and ϕ are symmetric and v antisymmetric about the equator and $v = 0$, $u_y = 0$ and $\phi_y = 0$ at $y = y_{\max}$. In the experiments described below $y_{\max} = 1.0$ or 1.5 corresponding to 20° or 30° respectively.

In choosing the initial conditions it is useful to have u and ϕ in geostrophic balance to avoid a large initial adjustment. For most of the experiments described here the initial conditions are

$$\begin{aligned} u &= \sin(2\pi x)e^{-4y^2} \quad , \\ \phi &= \frac{1}{8}u \quad , \\ v &= 0 \quad . \end{aligned} \tag{32}$$

For most of the runs the dimensionless parameters take the values

$$a = 0.38, \quad B = 395, \quad c_0^2 = 0.29, \quad r = 0. \tag{33}$$

The domain integral of the kinetic energy, $\propto \frac{1}{2}(u^2 + v^2/B)$, is used as a diagnostic of the disturbance amplitude.

3.4.1 Experiment 1

It was desirable to test the model first using equation (17a) everywhere: Emanuel's and Neelin et al.'s problem.

a) First the model was run with parameters and initial conditions as described above except that no scale selective was used. Very soon waves of the shortest resolved zonal scale grow rapidly with an e-folding time of around 1 day. This agrees with the normal mode theory which predicts that the shortest waves grow the fastest (§2). This suggests that in order to obtain some useful results from the model we should introduce some scale selective dissipation, $\mu \nabla^2$, to damp the shortest scale waves. If ∇^2 is intended to represent the divergence of a physical Fickian flux we should recall that x and y have been rescaled differently so

$$\nabla^2 \rightarrow \partial_x^2 + B \partial_y^2 \quad . \quad (34a)$$

If, on the other hand, it is intended merely as a numerical artifice we may prefer to use simply

$$\nabla^2 \rightarrow \partial_x^2 + \partial_y^2 \quad . \quad (34b)$$

b) Experiment 1a) was repeated with some scale selective dissipation, $\mu = 2.5 \times 10^{-4}$, which was estimated to be about that required to neutralize the shortest zonal waves, and the form (34a) was used for ∇^2 . This time a mode of zonal wavenumber 1 grows with an e-folding time of over 10 days. This is slower than the theoretical growth rate in the absence of scale selective dissipation and we can estimate that there is significant dissipation of the kinetic energy by the $\mu B(u_y)^2$ term.

c) The experiment was repeated with the same value of μ but using the form (34b) for ∇^2 . We see a growing disturbance which has zonal wavenumber 1 but has progressively wavier structure in the meridional direction as time goes on. See figure 5.

The amplitude peak lies off the equator and the meridional wavelength appears to become shorter as we begin to move away from the equator. Also the growth rate is faster than the theoretical value for the geostrophic mode and it increases as time goes on. Almost certainly we are seeing a succession of non-geostrophic modes of successively higher n and higher growth rate (but all of zonal wavenumber 1).

The scale selective dissipation used here is that used in all the experiments described below.

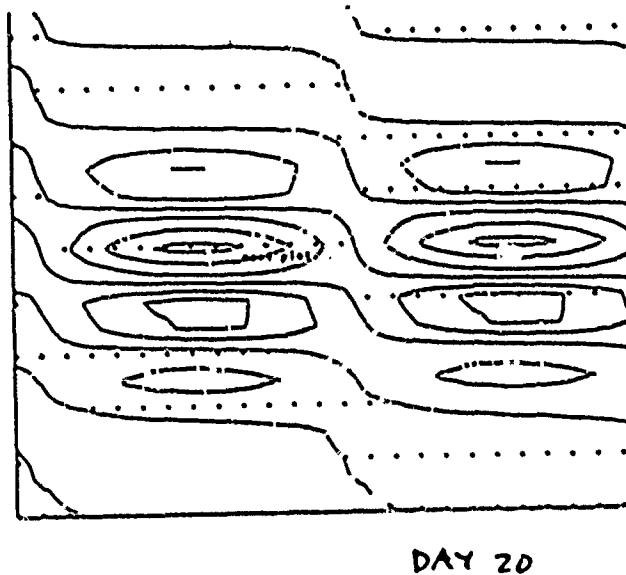


Figure 5. Plot showing contours of vertical velocity for day 20 of experiment 1c). The stippled region indicates $w > 0$. The horizontal axis corresponds to the equator and the vertical axis to an arbitrary meridian.

3.4.2 Experiment 2

The model was run for 20 days with the full physics: equation (17a) where $w > 0$ and (17b) where $w < 0$ using the wavenumber 1 initial conditions (32). A single dominant rainy region evolves with a very intense updraft on the equator. See figure 6. It moves eastwards about 180° in 20 days. Taking \bar{u} into account this suggests a period around 45–55 days. It also leans westwards as we move off the equator by about 60° of longitude in 30° of latitude. There are some small scale features ahead of the main wave which may be gravity wave-like or, more likely, smaller versions of the main wave. They may be resolution dependent.

There is little growth of the kinetic energy during the run.

This experiment will be used as a control for comparison with those described below.

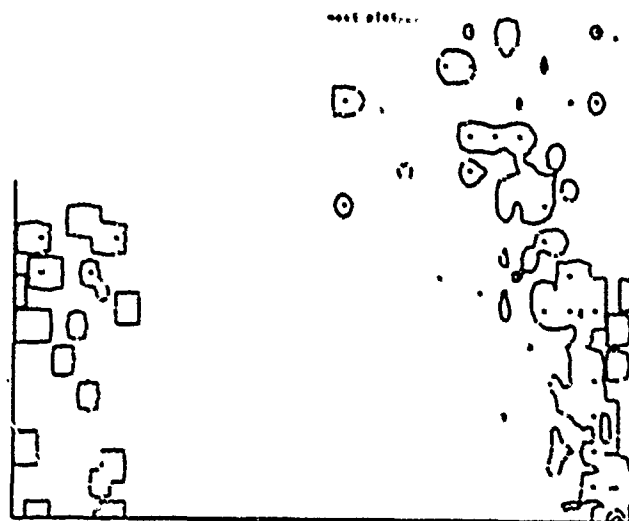


Figure 6. As in figure 5 for day 20 of experiment 2.

3.4.3 Experiment 3

Experiment 2 was repeated with different initial conditions; a zonal wavenumber 2 disturbance with a small amount of wavenumber 1 to break the symmetry;

$$u = (\sin(4\pi x) + \frac{1}{20} \sin(2\pi x))e^{-4y^2} ,$$

$$\phi = \frac{1}{8}u , \quad (35)$$

$$v = 0 .$$

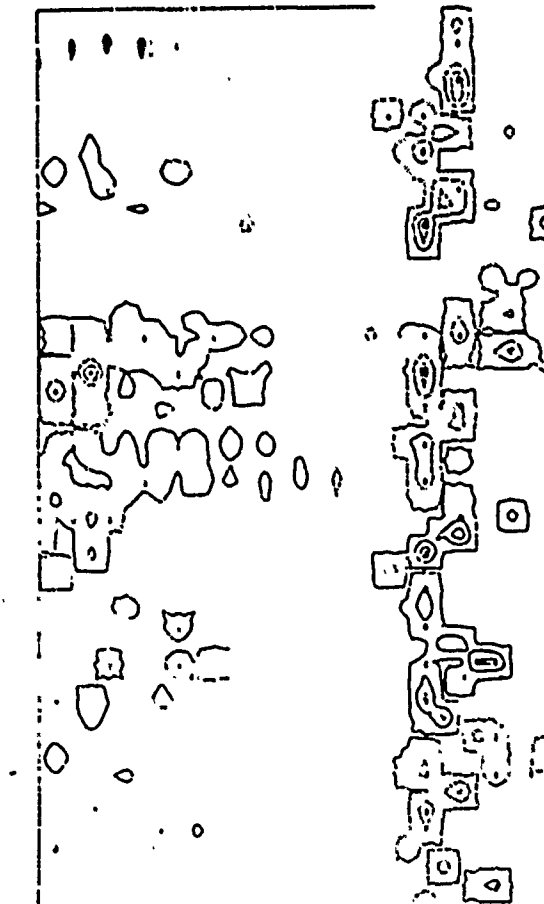
Again the deep convection organises itself into a single main region on the equator which propagates at a similar speed to that in experiment 1. In addition, at higher latitudes a band of upward motion appears which encircles the globe. See figure 7. It gradually moves polewards from about 20° at day 20 until it reaches the boundary at about 30° around day 50 and peters out.

The mechanism by which this rainy band propagates is basically the same as that of the eastward propagating wave on the equator. There is downwelling between the updraft and the boundary at y_{\max} and a low level equatorward flow between the two with a return poleward flow in the upper level. The coriolis force deflects the low level flow westwards and so in this region we have enhanced evaporation tending to move the updraft polewards.

The inter-tropical convergence zone (ITCZ) sometimes appears as a pair of convergence zones, one each side of the equator, rather than a single zone on the equator. The

Figure 7. As in figure 5 for day 30 of experiment 3.

feature described above may partly explain this, especially if some low level equatorward mean flow balances the tendency to propagate polewards.



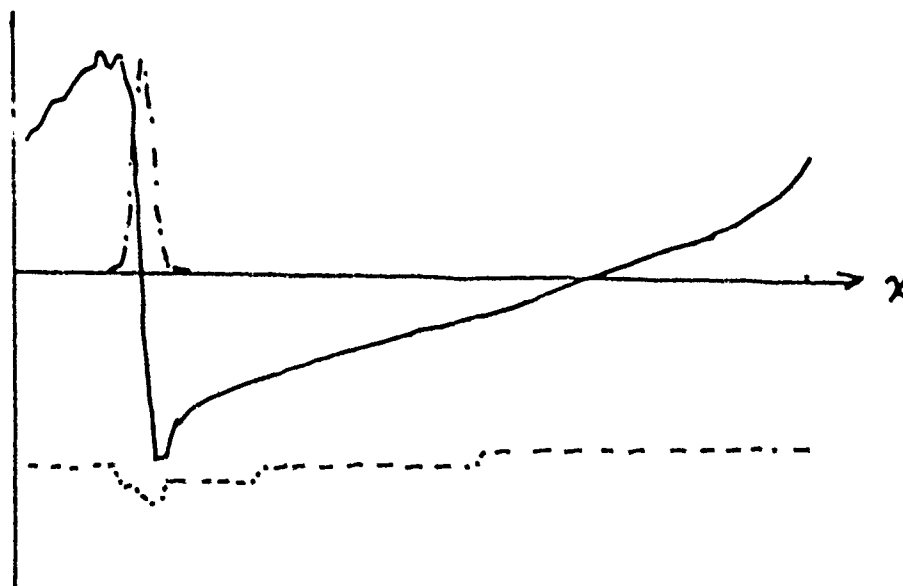


Figure 8. Normalized profiles along the equator of u (solid line), ϕ (short dashes) and w (longer dashes) for day 40 of experiment 4. The u and w profiles seem to be characteristic of the later stages of the waves evolution.

3.4.4 Experiment 4

Because there are discontinuities in the governing equations and because the first experiments have produced some small scale features it is prudent to test the sensitivity of the results to model resolution. Experiment 2 was repeated with the number of gridpoints in the zonal direction increased to 80. Up to day 20, (the limit of validity of experiment 2), the results were very similar to those of experiment 2 in the size and shape and speed of propagation of the region of deep convection, including the presence of small scale features ahead of the wave. However, beyond this time the updraft region continues to sharpen and the speed of propagation decreases; the deep convection region only moves about 70° eastward between days 20 and 40.

The zonal velocity profile (figure 8) seems to take on a characteristic 'mature' shape at this stage and the small scale features ahead of the wave have disappeared. This leads us to speculate that the propagation speed of the wave is a function of the updraft width which may depend on i) scale selective dissipation; ii) model resolution (ultimately); iii) other physics not included in the model, which may tend to disrupt the wave and smear out the updraft region, such as atmosphere-ocean coupling, land-sea contrast and other zonal asymmetries; iv) a mean non-zero vertical velocity; v) a better criterion for deep convection based on the moist static stability.

Resolution does not appear to be the model's biggest defect.

3.4.5 Experiment 5

As a first step towards exploring the sensitivity of the results to variations in the dimensionless parameters experiment 2 was repeated with the evaporation feedback parameter doubled: $\alpha=0.77$. The results are again very similar to those of experiment 2 up to day 20 except that now the kinetic energy grows significantly implying an e-folding time of around 14-days. Later, in the 'mature' stage, the kinetic energy grows even faster suggesting that the wave is now in the most efficient form for extracting energy from the wind-evaporation feedback mechanism.

4 Conclusions

We have shown that by including asymmetry between upward and downward motions in a wind-evaporation feedback model we can reproduce baroclinic, eastward propagating, growing disturbances with phase increasing polewards, period about 40 days or more depending on the width of the updraft region and global zonal wavenumber predominantly 1.

We have also accidentally discovered a possible explanation for the ITCZ appearing as a pair of deep convecting bands, one each side of the equator.

5 Future Work

We have only made a brief gesture towards testing the sensitivity of the model to the 'numerical' parameters; resolution (and scale selective dissipation), and the 'physical' parameters; α , B , r and c_0^2 (and scale selective dissipation). In particular we could allow \bar{u} and the evaporation feedback parameter, A , to be functions of latitude, and we could follow Bretherton [1987] and justify using a larger value of μ in the deep convecting region than in the downwelling regions because convection is a source of turbulence.

The criterion for deep convection in this model is that $w > 0$. This could be improved upon by integrating equations both for saturation moist entropy, s^* , and depth-mean moist entropy, \bar{s} , and making a convective adjustment when the atmosphere is statically unstable; $s^* < \bar{s}$.

One important task is to understand the relation between the size and shape of the updraft region on the equator and its propagation speed.

One possibility is to make the model fully nonlinear. If we make A largest on the equator we might hope to reproduce a Hadley cell type of mean circulation including mean low level easterlies on the equator because of the coriolis force. The mean low level equatorward flow may interact with the poleward propagation of the ITCZ-like bands of deep convection described in §3.4.3. Also a mean upward velocity on the equator may mean that the region with $w > 0$ is broader than in the quasi-linear model.

Having discovered the circumglobal convective bands in numerical simulations, (§3.4.3), it may be possible to go back and model these features analytically.

Acknowledgements

I am grateful to all the staff and fellows of the GFD Summer Program for a most enjoyable and instructive summer and especially to Professor Kerry Emanuel for all his help and encouragement with this project.

References

Bretherton, C. S., 1987: A theory for moist precipitating convection between two parallel plates. Part I: thermodynamics and linear solutions. *J. Atmos. Sci.*, **44**, 1809-1827.

Emanuel, K. A., 1987: An air-sea interaction model of intraseasonal oscillations in the tropics. *J. Atmos. Sci.*, **44**, 2324-2340.

Lilly, D. K., 1960: On the theory of deep convection in a stably stratified, additionally unstable atmosphere. *Mon. Wea. Rev.*, **88**, 1-17.

Neelin, J. D., I. M. Held and K. H. Cook, 1987: Evaporation-wind feedback and low frequency variability in the tropical atmosphere. *J. Atmos. Sci.*, **44**, 2241-2248.

3D INSTABILITY OF BOUNDED ELLIPTICAL FLOW

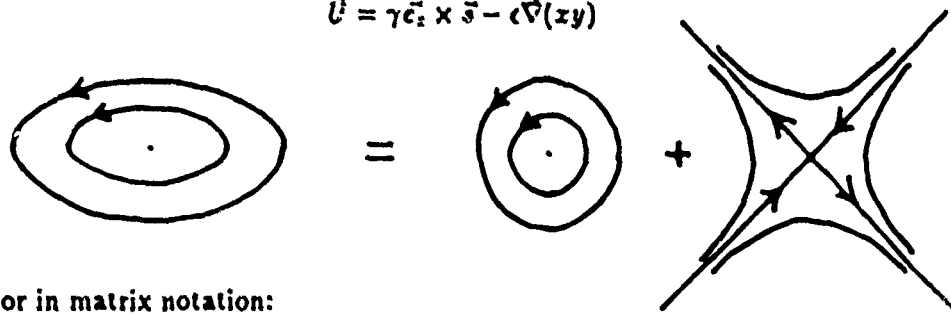
Fabian Waleffe

Massachusetts Institute of Technology

INTRODUCTION

The basic flow under consideration has elliptical streamlines and is the superposition of a rigid body rotation and a potential flow:

$$\vec{U} = \gamma \vec{e}_z \times \vec{s} - \epsilon \vec{\nabla}(xy)$$



or in matrix notation:

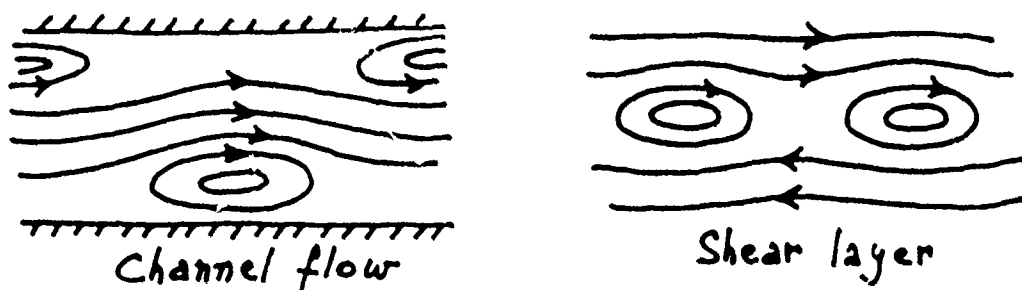
$$\vec{U} = \begin{pmatrix} 0 & -\gamma - \epsilon & 0 \\ \gamma - \epsilon & 0 & 0 \\ 0 & 0 & 0 \end{pmatrix} \begin{pmatrix} x \\ y \\ z \end{pmatrix}$$

where 2γ is the vorticity, ϵ the strain, and $|\epsilon| < |\gamma|$ for an elliptical flow.

This flow appears in many different situations. It comes up in the precession of an oblate spheroid (a model for the earth) as was first discovered by Poincaré. In that context, violent instabilities were observed experimentally by Malkus. He noted that for sufficiently large precession angles, shear layers would appear at 30 degree latitude from the equator of the fluid. Shortly after these shear layers would seem to break down. Busse extended the mathematical analysis of this problem and studied the singularity in the boundary layer leading to shear layers. In a different paper, he studied the stability of a shear layer in a rotating fluid. Since then it was believed that the instabilities in precession came from that two step evolution: first an eruption of the Ekman boundary layer leading to shear layers, followed by an instability of those shear layers.

Elliptical vortices are also present in several shear flows. One can see them in Stuart's non-linear, inviscid solutions for a shear layer, or in Orszag

& Patera's 2D developed Poiseuille flow for instance.



It has been shown recently that these 2D flows were violently (i.e. on a convective time scale) unstable to 3D disturbances.

The similarity between the 3D breakdown of these various solutions led Pierrehumbert to speculate that these instabilities were manifestations of the same phenomenon, namely, the instability of a single elliptical vortex. He showed numerically that a localized elliptical flow was indeed 3D unstable. Bayly, Landman & Saffman then considered an unbounded elliptical flow and confirmed Pierrehumbert's results by solving numerically a Floquet problem.

Their analysis can be done analytically, as shown by Waleffe, and this allows some interesting extensions.

All these investigations left aside some critical points. In particular it was not clear that this was relevant to more realistic bounded flows. If it did then the questions of where the energy came from, of the interaction of the growing disturbance with the mean flow and of its saturation were yet to be answered. It is well known that the rigid body rotation of a fluid is absolutely stable. That means stable to any disturbance, including finite amplitude ones. Many scientists then naturally thought that the elliptical instability would just slightly modify the elliptical flow to bring it back to solid rotation. This is the usual "Lenz's law". If the instability is due to the ellipticity, then it must act against it. That is how most physical systems usually react, they directly oppose to the cause which created them.

The following analysis provides an answer to these questions and, in particular, shows that for small ellipticity the mean flow is not just slightly modified. In fact a lot of energy can be extracted from it.

A simple exact non-linear solution:

Before getting into the study of a bounded domain, I will present a new exact non linear solution. Let $\vec{\omega}_*$, \vec{v} be the vorticity and velocity of the full flow. As usual it is decomposed into the basic elliptical flow and a perturbation.

One has: $\vec{\omega}_* = \vec{\Omega} + \vec{\omega}$, $\vec{v} = \vec{U} + \vec{u}$, $\vec{\Omega} = 2\gamma\vec{e}_z$.

The vorticity equation is:

$$D_t \vec{\omega}_* = \vec{\omega}_* \cdot \nabla \vec{v} + \nu \nabla^2 \vec{\omega}_*$$

and thus for the perturbation one has:

$$\partial_t \vec{\omega} + \vec{U} \cdot \nabla \vec{\omega} = \vec{\gamma} \times \vec{\omega} + D \cdot \vec{\omega} + 2\gamma \partial_z \vec{u} - \nabla \times (\vec{\omega} \times \vec{u}) + \nu \nabla^2 \vec{\omega}$$

where D is the strain matrix of the basic flow. Let us choose a perturbation which simply consists in a solid rotation around a horizontal axis:

$$\vec{u} = \frac{1}{2} \vec{\omega} \times \vec{s}, \quad \vec{\omega} \text{ uniform, } \vec{s} \text{ position vector.}$$

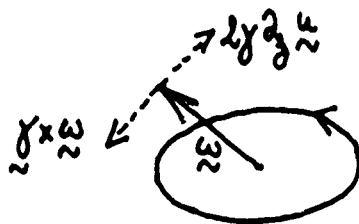
one checks easily that: $\partial_t \vec{\omega} = D \cdot \vec{\omega}$

or

$$\begin{aligned} \dot{\omega}_1 &= -\omega_2 \\ \dot{\omega}_2 &= \omega_1 \end{aligned}$$

And we have exponential growth if $\omega_1 = -\omega_2$ initially.

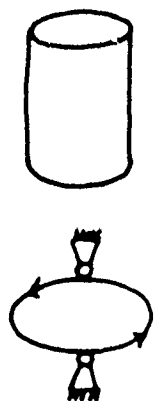
Thus we see that a rigid body rotation with vorticity in the plane of the ellipse and in the stretching direction, is an exponentially growing exact non-linear viscous solution of the problem. This is a 3D solution the vorticity of the perturbation being orthogonal to the original vorticity. This solution represents an ideal case were the tilting of the perturbation vorticity by the elliptical flow is exactly compensated by the tilting of the basic vorticity by the perturbation. The growth is due to vortex stretching.



This solution illustrates two points nicely. First it shows very simply the mechanism of the instability. Second it is a non-linear solution (as Bayly's, Landman & Saffman's) and for that reason, does not interact with the mean

flow. Its energy comes from the infinite reservoir permitted by the unbounded domain. One can legitimately ask whether this has any bearing on reality!

Analysis in a bounded domain:



The volume delimited by a solid elliptical cylinder is a natural domain to choose. The elliptical flow is possible in such a domain if the walls move adequately (as in Malkus' experiment where a rotating flexible cylinder is deformed in the inertial frame by fixed rollers), or if the fluid were inviscid. The effect of viscosity on the perturbation won't be considered in the following analysis. This is because the instability appears to be an inertial phenomenon taking place in the body of the fluid, on a time scale shorter than the spin-up time.

Previous studies (Bayly, Waleffe) suggest the use of elliptical polar coordinates.

These are defined by:
$$\begin{cases} x = \rho E \cos \theta \\ y = \rho \sin \theta \end{cases}$$

$\rightarrow \frac{x^2}{E^2} + y^2 = \rho^2$, and ρ is constant along an ellipse.

One advantage of these coordinates is that the material derivative takes the simple form:

$$\partial_t + \vec{U} \cdot \vec{\nabla} = \partial_t + \Omega \partial_\theta$$

where $\Omega = \sqrt{\gamma^2 - \epsilon^2}$ is the rotation period of a parcel of fluid. E is the aspect ratio of the ellipse ($E > 1$). We will also use $\beta = \frac{\epsilon}{\gamma} = \frac{E^2 - 1}{E^2 + 1}$, $0 < \beta < 1$.

The gradient is given by:
$$\begin{pmatrix} \partial_x \\ \partial_y \end{pmatrix} = \begin{pmatrix} \frac{\cos \theta}{E} & -\frac{\sin \theta}{E} \\ \sin \theta & \cos \theta \end{pmatrix} \begin{pmatrix} \partial_\rho \\ \frac{1}{\rho} \partial_\theta \end{pmatrix}$$

We still have to choose a system of dependent variables well suited to these coordinates. One of them should represent the velocity perpendicular to an ellipse, and then vanish along the elliptical wall.

Let then

$$\begin{cases} u = \frac{y}{E} \cos \theta + u_y \sin \theta \\ v = -u_x \frac{\sin \theta}{E} + u_y \cos \theta \end{cases} \quad (1)$$

where u_x, u_y are the cartesian velocities.

It can easily be checked that these choices lead to:

$$\vec{v} \cdot \vec{\nabla} = u \partial_r + \frac{v}{\rho} \partial_\theta + w \partial_z$$

$$\vec{\nabla} \cdot \vec{v} = \partial_r u + \frac{u}{\rho} + \frac{1}{\rho} \partial_\theta v + \partial_z w$$

These are exactly the same expressions as for circular cylindrical coordinates!

The (inviscid) Navier-Stokes equations read:

$$\begin{cases} D_t u - \frac{v^2}{\rho} + \partial_r p = \beta (\cos 2\theta \partial_r p - \sin 2\theta \frac{1}{\rho} \partial_\theta p) \\ D_t v + \frac{uv}{\rho} + \frac{1}{\rho} \partial_\theta p = \beta (-\sin 2\theta \partial_r p - \cos 2\theta \frac{1}{\rho} \partial_\theta p) \\ D_t w + \partial_z p = 0 \\ \vec{\nabla} \cdot \vec{v} = 0 \end{cases} \quad (2)$$

where $D_t = \partial_t + \vec{v} \cdot \vec{\nabla}$, and $\vec{v} \cdot \vec{\nabla}$ and $\vec{\nabla} \cdot \vec{v}$ are as given above.

The boundary conditions are $w = 0$ at $z = 0, L$ and $u = 0$ at $\rho = \rho_0$.

The pressure and vertical variables have been rescaled according to:

$p' = \frac{E^2+1}{2E^2} p$, $z' = \sqrt{\frac{E^2+1}{2E^2}} z$, $w' = \sqrt{\frac{E^2+1}{2E^2}} w$. These new variables are those appearing in the above equations with the primes dropped.

One will notice that the left hand side of these equations is identical to the Euler equations written in circular cylindrical coordinates. The boundary conditions are identical too, especially, they do not depend on the ellipticity.

In these variables the basic elliptical flow is $U = W' = 0$, $V = \Omega \rho$ (and $P = \frac{(E^2+1)^2}{4E^2} \frac{\Omega^2 \rho^2}{2} (1 + \beta \cos 2\theta)$).

Linearizing around t : state one gets:

$$\partial_t u + Lu + \nabla p = \frac{\beta}{2} [e^{i2\theta} N + e^{-i2\theta} N^*] \nabla p \quad (3)$$

$$\text{where } L = \begin{pmatrix} \partial_\theta & -2 & 0 \\ 2 & \partial_\theta & 0 \\ 0 & 0 & \partial_\theta \end{pmatrix} \quad N = \begin{pmatrix} 1 & i & 0 \\ i & i^2 & 0 \\ 0 & 0 & 0 \end{pmatrix}$$

A $(.)^*$ denotes a complex conjugate.

t has been non-dimensionalized using Ω .

Let us look for a solution around $\beta = 0$. For $\beta = 0$ the modes correspond to the inertial waves on a solid rotation seen from the inertial frame. This

problem was solved by Leonard Johnsson who looked at the precession of a circular cylinder. After some manipulations of his solutions, the inertial modes are given by $u = Qe^{i\sigma t}$, where:

$$Q = \frac{e^{im\theta}}{2(1-(\sigma+m)^2)} \left[\begin{array}{l} ik[(\sigma+m+2)J_{m-1}(k\rho) - (\sigma+m-2)J_{m+1}(k\rho)] \cos lz \\ -k[(\sigma+m+2)J_{m-1}(k\rho) + (\sigma+m-2)J_{m+1}(k\rho)] \cos lz \\ \frac{2i(\sigma+m)k^2}{l} J_m(k\rho) \sin lz \end{array} \right]$$

with $p = -J_m(k\rho)e^{im\theta} \cos lz e^{i\sigma t}$,

$$(\sigma+m+2)J_{m-1}(k\rho_0) = (\sigma+m-2)J_{m+1}(k\rho_0)$$

$$(\sigma+m)^2 = \frac{4l^2}{k^2+l^2}, \quad l = \frac{n\pi}{L}, \quad n = 0, \pm 1, \pm 2, \dots$$

Now let

$$\begin{aligned} u &= A(Q_0 + \beta Q_1 + \dots) + A^*(Q_0^* + \beta Q_1^* + \dots) \\ p &= A(p_0 + \beta p_1 + \dots) + A^*(p_0^* + \beta p_1^* + \dots) \end{aligned}$$

where $i\sigma Q_0 + LQ_0 + \nabla p_0 = 0$, i.e. Q_0, p_0 represent any of the inertial modes given above, $A = A(t)$.

Using this expansion in (3) above one gets:

$$\begin{aligned} (\dot{A} - i\sigma A)Q_0 + \beta [i\sigma Q_1 + LQ_1 + \nabla p_1]A + \\ (\dot{A}^* + i\sigma A^*)Q_0^* + \beta [-i\sigma Q_1^* + LQ_1^* + \nabla p_1^*]A^* = \\ \frac{\beta}{2} [e^{i2\theta} N + e^{-i2\theta} N^*] \nabla (Ap_0 + A^*p_0^*) + O(\beta^2) \end{aligned}$$

Proceeding as in Greenspan, one gets the solvability condition:

$$(\dot{A} - i\sigma A) \int_V Q_0^* Q_0 dV = \frac{\beta}{2} A^* \int_V Q_0^* N \cdot \nabla p_0^* e^{i2\theta} dV$$

Where all the terms which would disappear by integration over θ for any m have been discarded from the right hand side. The θ -dependency of this right hand side is in $e^{i2(1-m)\theta}$ and thus at first order in β , only $m = 1$ contributes.

We have:

$$N \cdot \nabla p_0^* = \begin{bmatrix} 1 & i \\ i & i^2 \end{bmatrix} \begin{bmatrix} \partial_\rho p_0^* \\ \frac{1}{\rho} \partial_\theta p_0^* \end{bmatrix} = (\partial_\rho p_0^* + \frac{i}{\rho} \partial_\theta p_0^*) \begin{bmatrix} 1 \\ i \end{bmatrix}$$

for $m = 1$, $p_0^* = -J_1(k\rho)e^{-i\theta} \cos lz$, which yields:

$$N \cdot \nabla p_0^* = -k e^{-i\theta} J_0(k\rho) \cos lz \begin{bmatrix} 1 \\ i \end{bmatrix}$$

Q_0^* is given by the conjugate of the expression for the inertial modes given above, with $m = 1$.

Putting it all together leads to:

$$e^{i2\theta} Q_0^* \cdot N \cdot \nabla p_0^* = \frac{ik^2}{4 - (\sigma + 1)^2} (\sigma + 3) J_0^2(k\rho) \cos^2 lz$$

$$Q_0^* \cdot Q_0 = \frac{k^2}{2(4 - (\sigma + 1)^2)^2} \{ \cos^2 lz [(\sigma + 3)^2 J_0^2(k\rho) + (\sigma - 1)^2 J_2^2(k\rho)] \\ + \frac{2(\sigma + 1)^2 k^2}{l^2} J_1^2(k\rho) \sin^2 lz \}$$

$$\text{also: } (\sigma + 1)^2 \frac{k^2}{l^2} = 4 - (\sigma + 1)^2$$

The solvability condition then reads:

$$\dot{A} = i\sigma A + i\beta\alpha A^*$$

where α is given by:

$$\alpha = \frac{(1 - \sigma)(3 + \sigma)^2 \int_0^{k\rho_0} x J_0^2(x) dx}{\int_0^{k\rho_0} x [(3 + \sigma)^2 J_0^2(x) + 2(3 + \sigma)(1 - \sigma) J_1^2(x) + (1 - \sigma)^2 J_2^2(x)] dx}$$

Let $A = a + ib$ then: $\ddot{a} = (\beta^2 \alpha^2 - \sigma^2) a$, $\Rightarrow a = a_0 \exp(\pm \sqrt{\beta^2 \alpha^2 - \sigma^2} t)$,
 $b = b_0 \exp(\pm \sqrt{\beta^2 \alpha^2 - \sigma^2} t)$, for the growing mode one needs: $\frac{a_0}{b_0} = \sqrt{\frac{\beta\alpha - \sigma}{\beta\alpha + \sigma}}$.
 (remark: from $|\sigma + m| < 2$ we get $-3 < \sigma < 1$ and thus $\alpha > 0$)

The maximum growth corresponds to $\sigma = 0$ which implies $A = R e^{i\frac{\pi}{4}}$, where R is real. The optimal mode is given by:

$$Q^{opt} = R [e^{i\frac{\pi}{4}} Q_0 + e^{-i\frac{\pi}{4}} Q_0^*], \sigma = 0, m = 1$$

That is :

$$Q^{opt} = R \begin{bmatrix} k(3J_0(k\rho) + J_2(k\rho)) \cos lz \sin(\theta + \frac{\pi}{4}) \\ k(3J_0(k\rho) - J_2(k\rho)) \cos lz \cos(\theta + \frac{\pi}{4}) \\ \frac{2k^2}{l} J_1(k\rho) \sin lz \sin(\theta + \frac{\pi}{4}) \end{bmatrix}$$

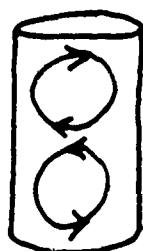
with $p^{opt} = \frac{1}{2} R J_1(k\rho) \cos lz \cos(\theta + \frac{\pi}{4})$.

These optimal modes are only possible in some special containers; we need $\sigma = 0$ and thus $3J_0(k\rho_0) + J_2(k\rho_0) = 0$ or $aJ_0(a) + J_1(a) = 0$ (using the recurrence relations between Bessel functions) where $a = k\rho_0$. Also for $\sigma = 0$ we need $k^2 = 3l^2 = 3\frac{\pi^2}{L^2}$, and thus a "resonant" cylinder must obey:

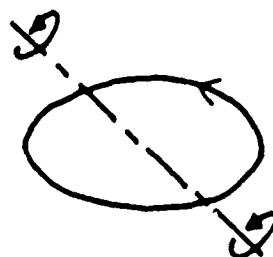
$$\frac{L}{2\rho_0} = \frac{\sqrt{3}\pi}{2a_i} n$$

where L is the length of the cylinder, ρ_0 its radius, n is an integer and a_i is a root of $aJ_0(a) + J_1(a) = 0$. ($a_1 \approx 2.735, a_2 \approx 5.695, \dots$)

Near the vertical axis this optimal mode appears as a rotation around a horizontal axis oriented in the stretching direction, exactly as the exact non-linear solution in an unbounded domain presented earlier. For a_1 this corresponds to $\frac{L}{2\rho_0} \approx n$, i.e. the aspect ratio is an integer.



side view



top view

The nice simple picture is only valid near the axis. There is some significant distortion as one gets closer to the wall.

Interaction with the mean flow

(I will look only at the optimal case of a resonant cylinder ($\sigma = 0$).)

The important next step is to look at the interaction of the growing mode with the mean flow. Let us decompose the full flow into a mean plus a perturbation: $\vec{v} = \vec{V}(\rho, t) + \vec{u}$. From the boundary conditions and the

co. inuity equation we get: $\bar{U} = \bar{V} = 0$, $\bar{V} = \bar{V}(\rho, t)$. An overbar denotes an average over z and θ (i.e. over elliptical cylinders).

In the case where the perturbation is assumed to be the optimal mode presented above, one gets from averaging the Euler equations (2) over θ and z :

$$\partial_t \bar{V} + \frac{1}{\rho^2} \partial_\rho (\rho^2 \bar{u} \bar{v}) = -\beta \left(\sin 2\theta \partial_\rho p + \frac{\cos 2\theta}{\rho} \partial_\theta p \right)$$

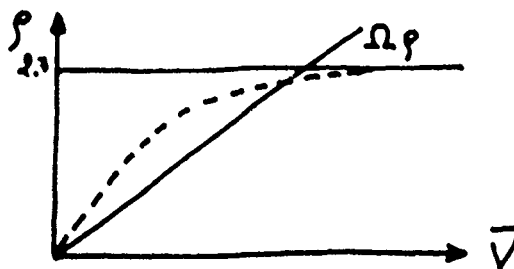
Doing things cleanly (that is eliminating the pressure from (2) by multiplying the equations by the inverse of the matrix acting on the pressure gradient, then integrating over θ and z) one gets:

$$\partial_t \bar{V} = \beta \left(\sin 2\theta \left(\partial_\rho u^2 + \frac{u^2 + v^2}{\rho} \right) + \cos 2\theta \partial_\rho uv \right)$$

or

$$\partial_t \bar{V} = \frac{3}{4} R^2 \beta k^2 \partial_\rho (3J_0^2(k\rho) + J_1^2(k\rho)) e^{2\beta \alpha t}$$

where R is the amplitude of the mode. And then the mean flow is modified according to the following picture:



The center is despun, while a small layer near the wall is actually spun-up. If one looks at the total angular momentum of the fluid, one gets:

$$\frac{d}{dt} \langle \rho \bar{V} \rangle = -\frac{9}{2} R^2 \beta \left(\int_0^{k\rho_0} x J_0^2(x) dx \right) e^{2\beta \alpha t}$$

where $\langle \rho \bar{V} \rangle$ is the total angular momentum of the fluid. The right-hand side is negative and angular momentum is exponentially taken away from the fluid.

Energy Transfer:

For completeness, let us look at the total kinetic energy of the disturbance. The kinetic energy, computed from (1), is given by the following expression in elliptico-polar coordinates where u, v, w are the variables appearing in (2):

$$K.E. = \frac{1+E^2}{4} [u^2(1 + \beta \cos 2\theta) - 2\beta uv \sin 2\theta + v^2(1 - \beta \cos 2\theta)] + \frac{E^2}{E^2+1} w^2$$

The average total kinetic energy of the perturbation varies as:

$$\frac{d}{dt} \langle K.E. \rangle = \frac{1+E^2}{2} \beta \int_0^{\rho_0} \left[\cos 2\theta uv \left(\frac{d\bar{V}}{d\rho} + \frac{\bar{V}}{\rho} \right) + \sin 2\theta \left(u^2 \frac{d\bar{V}}{d\rho} - v^2 \frac{\bar{V}}{\rho} \right) \right] \rho d\rho$$

That is for the basic flow, $\bar{V} = \Omega \rho$:

$$\frac{d}{dt} \langle K.E. \rangle = \frac{E^2-1}{2} \Omega \int_0^{\rho_0} (2 \cos 2\theta uv + \sin 2\theta (u^2 - v^2)) \rho d\rho$$

(This expression is valid for any perturbation)

For the optimal growing mode this is:

$$\frac{d}{dt} \langle K.E. \rangle = \frac{E^2-1}{16} \Omega \int_0^{k\rho_0} [18J_0^2(x) + 12J_0J_2 - 2J_2^2] x dx \exp(2\beta\alpha t)$$

and after some acrobatic juggling with the Bessel functions, this can be rewritten as:

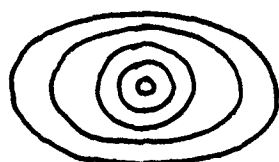
$$\frac{d}{dt} \langle K.E. \rangle = \frac{E^2-1}{2} \Omega [1 + (k^2 \rho^2 - 1) J_0^2(k\rho_0) + \frac{1}{2} \int_0^{k\rho_0} (x J_0^2 + \frac{2J_1^2}{x}) dx] e^{2\beta\alpha\Omega t}$$

and this expression is positive definite.

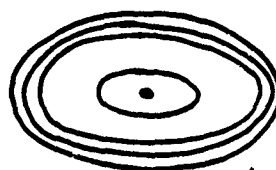
Conclusions & Speculations:

It has been demonstrated that there are indeed growing modes in a bounded geometry. Only modes with an $e^{i\theta}$ spatial structure can grow, and the growth is dependent on the aspect ratio of the container. Resonant cylinders correspond closely to an integer aspect ratio (length/diameter). Near the axis the unstable solutions appear as a rigid body rotation around horizontal preferred directions and of alternating sign as one moves a diameter

along the axis. The interaction with the mean flow shows that the Reynolds stresses correlate with the ellipticity to de-spin the center. This is an interesting result. It suggests that a weak departure from solid rotation is unstable to a disturbance which non linearly destroys the primary rotation and not the "weak departure". The disturbance could indeed "circularize" the flow, at least in the center, whereas it actually stops the rotation there. streamlines:



possible effect

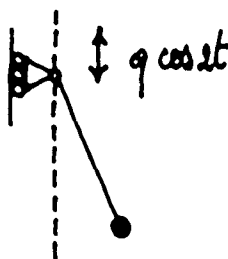


actual effect

In other words the ellipticity acts as a catalyst for the extraction of the energy from the rotation. One wonders if all the vertical angular momentum will disappear or if this process will saturate in some way. The amplitude equation should look like:

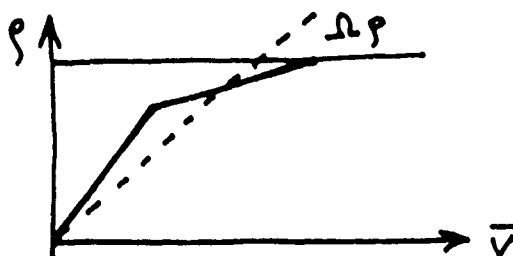
$$\dot{A} = i\sigma A + i\beta\alpha A^* + iK|A|^2 A$$

The question is then what is K ? and what is the nature of that cubic term? It is valuable at this point to note that this amplitude equation is identical to the one derived for the Faraday instability (Douady) or the physically similar Mathieu pendulum. The Mathieu pendulum is a pendulum whose support oscillates vertically.



For infinitesimal oscillation this system is described by the Mathieu equation: $\ddot{x} + (p + q \cos 2t)x = 0$. For $p=1$ there are growing (unstable) solutions. If q is finite this is true for some interval of values of p around 1. The difference between p and 1 corresponds to a "linear de-tuning" and limits the growth rate in the way σ modified the growth rate in the previous discussion. The primary growing disturbance has a frequency equal to half that of the

excitation, exactly as the 2θ modulation due to the ellipticity gave rise to a growing $e^{i\theta}$ disturbance. This is a well-known fact in parametric instability. Note that we have a spatial forcing instead of a temporal forcing though. The saturation is easy to understand for the Mathieu pendulum. The natural frequency of the pendulum is a function of the amplitude of oscillation (This is a fairly general statement about waves). As the disturbance increases, its oscillation frequency drifts until the oscillator is sufficiently detuned that the instability is suppressed. This picture is appealing however its application to the elliptical instability is not necessarily straightforward. Looking back at the interaction with the mean flow, one distinguishes two distinct regions where the fluid is roughly in solid rotation, slower in the center, faster near the wall.



This is a centrifugally stable configuration. The outer layer is very stable in particular. Its dynamics is also much faster than that of the inner core. I would speculate that the effect of this radial distribution is to "bring in the walls". The outer layer acts as a wall for the inner core. This would be the way the system can "detune" itself, by effectively modifying the aspect-ratio. The concept of "non-linear detuning" is in keeping with Greenspan's (1969) study. He looked at the non-linear interaction between an inertial wave and a geostrophic flow. He found that there were no resonant interactions and that the only effect could only consist in a change of the frequency of the inertial wave. Finally it seems fairly easy to include the effect of viscosity in the analysis, at least at lowest order. Most of the dissipation occurs in boundary layers near the wall. This is well-documented in the context of the theory of rotating fluids. In connection with this discussion, let me mention that while one can see evidence of the inviscid instability described above during the initial developments in Malkus' experiment, the latter behavior is quite interesting and raises many questions. So far it has not been possible to reach an equilibrated, steady solution. The initial growing mode eventually breaks down into small scale motions, leaving an inner core almost totally despun. The walls then proceed to spin up the fluid and a

similar evolutions takes place. The flow never seems to quite go back to the initial state and the initial growing disturbance .

Appendix: To avoid confusion I would like to stress the similitudes and differences between this problem and the one of precession of a cylinder (Johnsson 1967). In both cases the same inertial wave is excited. For the elliptical cylinder this is an instability (of parametric type) while it is a forced response for the precessing cylinder. In precession an extra body force appears due to the variation of the rotation vector (in addition to the Coriolis and centrifugal forces there is a $\ddot{\Omega} \times \vec{r}$ inertial force). In short precession corresponds to an equation of the type $\ddot{x} + x = \epsilon \cos t$, while the elliptical instability corresponds to $\ddot{x} + (1 + \epsilon \cos 2t)x = 0$.

Acknowledgements:

I would like to thank Prof. W.V.R. Malkus for sharing with me his interest, enthusiasm and intuition about this problem, and for designing the experiment. His constant insistence on the physically relevant questions and the perpetual confrontation with the experiment were very demanding, but provided much guidance and in the end were very rewarding.

I enjoyed and benefited greatly from discussions with Stéphane Douady on the Faraday instability.

The GFD program indeed is a unique experience, and I wish to thank all its participants and especially this year's director, Glenn Flierl, for giving so much of himself.

Finally, I'm glad I was part of the softball team which beat P.O.! ...

References:

Bayly, B. *Phys. Rev. Lett.* 57, 2160 (1986)

Busse, F. *J. Fluid Mech.* 33,p.739 (1968)

Douady, S. " Experimental study of the Faraday instability", *submitted to J.Fluid Mech.*

Greenspan, H. "The Theory of Rotating Fluids", *Cambridge Univ. Press*, 1968

Greenspan, H. "On the Non-linear Interaction of Inertial Waves", *J.Fluid*

Mech., 36, p257 (1969)

Johnsson, L. *WHOI GFD 1967, fellow report*

Malkus, W.V.R. "Precession of The Earth as the Cause of Geomagnetism", *Science*, 160, p259 (1968)

Orszag, S.A. & Patera, A. J. *Fluid Mech.*, 128, p347 (1983)

Pierrehumbert, R.T. *Phys. Rev. Lett.* 57, p 2157 (1986)

Stuart, T. J. *Fluid Mech.* 29, p.417 (1967)

Waleffe, F. "3D instabilities of unbounded elliptical flows", in preparation

A Model of Squall Line Propagation.

Andrew W. Woods

D.A.M.T.P., Silver Street, Cambridge, England.

September, 1988.

Abstract

A simple model of the precipitating convection which generates squall lines is developed and analysed. This includes separate treatments of the region of rising, condensing, saturated air ahead of the squall line and the region of downwardly-displaced, unsaturated air behind the squall line, into which the rain water falls and evaporates. Solutions, which grow from a quiescent state, are found in an unbounded domain. It is demonstrated that the squall line propagates into the condensing region. It is also shown that such squall lines can only exist under certain atmospheric conditions, when the ratio of the ambient stable stratification is neither too small nor too large. These limits on the atmospheric stratification both become larger as the water loading increases. We discuss how these results may be extended to bounded domains.

1. Introduction.

A squall line is operationally defined as any line or narrow band of thunderstorms. In a squall line, the flow varies only slowly along the line, in contrast to its variation across the line and this suggests that the process is essentially two-dimensional (Thorpe, Miller & Moncrieff, 1982, Seitter & Kuo, 1983). However, the mechanism by which squall lines develop and propagate has not been explained by a simple, consistent theory. In moist, precipitating convection there are sinks of buoyancy caused by the gravitational force exerted on the air by the rain distribution and the evaporation which are uncoupled from the displacement of air parcels; this allows for the propagation which is impossible in the equivalent non-precipitating convective problem.

A number of two-dimensional numerical models of squall lines have been developed over the years, and these have indicated the qualitative nature of the flow across the squall line (e.g. Seitter & Kuo, 1983). From numerical results, a simple explanation of the basic mechanism of squall line propagation was proposed by Seitter & Kuo, (1983). This may be readily understood from figure 1 which shows a sloping squall line propagating towards the region of upward-rising, saturated air. In the region of upward-rising air, water vapour condenses to produce liquid water. As the vapour condenses, it releases latent heat, providing the source of thermal buoyancy for the upward motion. The liquid water then generates a gravitational force on the air, which we refer to as the condensate or rain loading. As the squall line moves, some of the rain crosses the line into the region of downward-moving, unsaturated air. In this region, the downward motion is caused by both the evaporation of the rain, which cools the air, and the condensate loading. Thus the squall line is a region of strong shear and may be regarded as a sheet of negative vorticity, maintained by the temperature gradient across the interface.

Seitter & Kuo (1983) proposed that it is the effect of the condensate loading which

causes the squall line to propagate; in the condensing region of upward motion the fraction of liquid water increases as we approach the squall line, since the rain falls across the propagating squall line (figure 1). The liquid rain will therefore generate more negative vorticity just ahead of the line. In the region beyond the squall line, the liquid rain content decreases with distance behind the squall line, as it evaporates, generating positive vorticity in this region of the air. The effect of this additional vorticity field, produced by the rain, is to move the point of minimum vorticity into the region of upward rising air away from the interface. In turn this causes the interface to move toward the region of upward motion, and so the squall line propagates.

In their numerical solutions, Seitter & Kuo (1983) also identified a mechanism by which an applied shear maintains the slope of the line in a bounded domain. Since the rain falls downwards, the horizontal rain gradient increases with depth in the cloud and so the squall line tends to propagate faster at its base. The application of a wind shear blowing into the unsaturated region can oppose this effect and generate a fixed slope. If the slope becomes too large, the rain accumulates even more ahead of the line in the region of upward rising air, causing the line to propagate faster and its slope to decrease. If the slope becomes too small the wind shear dominates and increases the slope of the line.

In an attempt to understand the process more fully, Emanuel (1986) developed a simple linear model of precipitating convection in which the above mechanism of propagation obtains. In his model the upward and downward motions were treated identically. In the region of upward motion, the saturated air generates positive buoyancy by condensing out rain water, while in the region of downward motion the air is forced to remain saturated by condensing out 'negative rain'; thus generating negative buoyancy. Figure 2(i,ii) shows qualitatively the vorticity and rate of vorticity generation by rain water loading through a horizontal section as derived from the figures for the streamlines and rain contours given in Emanuel's paper, reproduced here in figures 2 (iii),(iv). From these figures, it is seen

that there is a phase lag between the vorticity field and the rate of generation of vorticity, and it is this that causes the propagation.

However, this is not a realistic model of rainfall lines in which there is an asymmetry between the upward and downward motions. In a squall line, in the region of downward motion, instead of the unphysical production of negative rain to keep the air saturated, the negative buoyancy is generated by the rain water evaporation and loading. This produces both a spatial and a temporal asymmetry in the solution unlike Emanuel's model. However, we note that Emanuel's model is an appropriate model of the perturbation rain field in a different situation in which the basic state is one of uniform water distribution and so the air may be kept saturated even in the region of downward motion; this may be regarded as a 'shower head' model.

The main purpose of this work is to develop and investigate a consistent analytical model of a squall line by modelling separately the different physical processes particular to both the region ahead of the squall line which for clarity we call the 'condensation region', and the region behind the squall line, which we call the 'evaporating region'. This model is able to demonstrate the importance of several new processes associated with squall-line dynamics. In section 2, we introduce the model of the cloud microphysics, the equations of motion, and conservation of buoyancy and rain for the two regions. We also discuss the matching conditions across the squall line which forms the interface between these two regions. We then develop a hierarchy of solutions of the system. In section 3, we consider stationary squall line solutions in an unbounded domain, which we generalise to solutions in which the squall line propagates in section 4. These solutions grow exponentially from a state of rest. We also present a simple argument which shows that the condensate loading is crucial for the existence of propagating squall line solutions. In section 5, we discuss the more difficult problem of finding solutions in a bounded domain and introduce an initial attempt at tackling this problem. We also briefly consider how the physics of the problem

may be changed in order to introduce a natural vertical bound on the problem. We draw some conclusions about the present study in section 6.

2. The Physical Model

Throughout this paper, we consider motions of the system whose time scale is much longer than the condensation time scale so that the system remains in thermodynamic equilibrium.

(i) Cloud Microphysics.

A detailed study of the microphysics of clouds was carried out by Kessler (1969). In summary, the liquid water in a cloud may be divided into two categories which we call cloud water and rain water. The cloud water is advected with the flow in the cloud, while the rain water (consisting of the larger drops of water) falls out under gravity, at approximately its terminal velocity.

For the present model, we assume that all the liquid water that forms in the condensation region is rain water and that it falls out at its terminal velocity as soon as it forms. This is an idealisation, but retains the essential physical ingredients of the problem (Scitter & Kuo, 1983). We also assume that all the rain falls at a fixed terminal velocity, V_T , relative to the air.

This simple model of the micro physics gives rise to the linearised equation for the conservation of the liquid water

$$l_t - V_T l_z = L, \quad (2.1)$$

where l is the liquid water content and L represents a source or sink of liquid water corresponding to condensation or evaporation, with z the upward vertical coordinate and t the time.

In the condensation region, the water vapour condenses out according to the vertical gradient of the water vapour saturation mixing ratio, q_s , which represents the maximum

water vapour content of the air at a given pressure and temperature, giving

$$L = -w \frac{dq_s}{dz}, \quad (2.2)$$

where w is the upward, vertical velocity. We assume that $\frac{dq_s}{dz}$ is constant, except in section 5 where we consider vertically bounded domains. Note that everywhere in the condensation region, $w > 0$, in order that the air remains saturated.

In the evaporation region, we must assume some law for the evaporation of the rain. We follow Sietter & Kuo (1983) and assume a simple linear evaporation law $L = -El$, where E is the evaporation rate, here assumed to be constant. In order that the air remains unsaturated in the evaporation region we require the vertical displacement of the air from the time of entering this region, t_0 , to be negative, i.e. $\int_{t_0}^t w dt < 0$. The problem of defining each of these regions and their boundaries is addressed in the approach to finding a solution.

(ii) The Momentum Equations.

For simplicity, we assume that the flow is inviscid and we seek disturbances growing from the stationary state. This gives rise to the linearised, two-dimensional momentum equations (Takeda, 1971, Emanuel, 1986)

$$w_t = B - gl - p_z \quad (2.2.1)$$

and

$$u_t = -p_x \quad (2.2.2).$$

In equation (2.2.1) the term B represents the force due to the buoyancy which is generated by condensation or evaporation combined with the background temperature gradient. The term gl represents the condensate loading, with g the acceleration due to gravity, and p is the pressure field.

By continuity we can introduce a streamfunction ψ for the velocity field $(u, w) = (-\psi_x, \psi_z)$ and then combine (2.2.1) and (2.2.2) to give the vorticity equation

$$\nabla^2 \psi_t = B_x - g l_x \quad (2.2.4)$$

(iii) The Buoyancy Equations.

To complete our description of the physical system, we need to consider how the temperature field varies in the two regions.

In the condensation region the release of latent heat on condensation produces an unstable stratification which we may denote by

$$N_c^2 = -g \frac{\Gamma_m}{\Gamma_d} (\ln(\bar{\theta}_e))_x \quad (2.3.1)$$

where Γ_m and Γ_d are the moist and dry adiabatic lapse rates and $\bar{\theta}_e$ is the mean state equivalent potential temperature. This represents the temperature the parcel would have if it were allowed to rise along a moist adiabat until all its water has condensed out and then returned to its initial pressure along a dry adiabat (Durrant & Klemp, 1982). This gives the buoyancy equation

$$B_t = N_c^2 \psi_x. \quad (2.3.2)$$

In this paper we assume that N_c^2 is a constant except in section 5, where we consider vertically bounded domains. Note that in the upward moving air, the amount of condensation produced is such as to keep the air just saturated.

In the evaporation region, there is a basic stable background temperature field (the dry adiabat) with buoyancy frequency N_e^2 , which we also assume to be constant, but in addition the evaporation of the liquid water cools the air generating negative buoyancy. Thus the buoyancy equation in this region is

$$B_t = -N_e^2 \psi_x - MEl, \quad (2.3.3)$$

where M is the Stefan number of evaporation, $M = \frac{L_v}{C_p T_c}$.

(iv) Non-Dimensionalisation.

We non-dimensionalise these equations using the natural length scale of the system $\frac{V_T}{N_c}$, and the time scale $\frac{1}{N_c}$. In addition we non-dimensionalise the water content by the change in the saturation water vapour mixing ratio over the natural length scale of the problem, $-\frac{dq_s}{dz} \frac{V_T}{N_c}$. This gives rise to a set of equations for each of the two regions:

I. Condensation Region:

$$\nabla^2 \psi_t = B_z - A l_z \quad (2.4.1a)$$

$$B_t = \psi_z \quad (2.4.1b)$$

$$l_t - l_z = \psi_x \quad (2.4.1c)$$

$$\psi_x \geq 0, \quad (2.4.1d)$$

II. Evaporation Region:

$$\nabla^2 \psi_t = B_z - A l_z \quad (2.4.2a)$$

$$B_t = -N^2 \psi_x - A M E l \quad (2.4.2b)$$

$$l_t - l_z = -E l \quad (2.4.2c)$$

$$\int \psi_x dt \leq 0, \quad (2.4.2d)$$

where N^2 is the ratio N_c^2/N_c^2 .

Before proceeding further, we pause to note the fundamental difference between the structure of these two sets of equations.

In the condensation region we can solve for the liquid rain along lines $z + t = \text{const}$ to obtain

$$l = l_0 + \int_0^s \psi_x ds ; \quad t = t_0 + s ; \quad z = -s + z_0. \quad (2.4.3)$$

We deduce that the rain is a function of the vertical velocity in this region. Equation (2.4.1a) also demonstrates that the velocity field is a function of the rain field everywhere in the condensation region.

In contrast, in the evaporation region, we may solve for the rain field l to obtain

$$l = l_0 e^{Es} ; \quad t = t_0 + s ; \quad z = z_0 - s. \quad (2.4.4)$$

Thus the rain evolves independently of the velocity field and is not influenced by the velocity field. However, (2.4.2a) again indicates that the velocity field is dependent upon the rain field, which is an inhomogeneous forcing term in the equation.

We deduce that the motion in the condensation region drives the motion in the evaporation region; this acts as an important constraint on the nature of the squall line.

(v) Boundary Conditions.

We now consider the matching conditions across the squall line. As a parcel of air passes through the propagating squall line, its velocity remains continuous as there cannot be any impulses generated by the squall line. In order to be dynamically consistent, the pressure is also continuous. By similar arguments the rain and buoyancy fields are continuous. This yields five boundary conditions across the interface. Note that in the case of a non-propagating squall line, the velocity condition reduces to a condition on the normal velocity. Additionally we seek solutions which decay to zero away from the squall line.

3. Non-propagating growing modes in an unbounded domain.

Some of the simplest solutions admitted by the system are the non-propagating, growing modes in an unbounded domain. As an initial investigation we seek solutions of the form

$$f(x, z, t) = e^{\sigma t} g(x - \gamma z) \quad (3.1)$$

in which the velocity is everywhere parallel to the direction $z = x/\gamma$, and we choose the squall line to have this same slope, $\frac{1}{\gamma}$. Without loss of generality we choose the squall line to be coincident with the line $x = \gamma z$ and the condensation region to be $x \leq \gamma z$.

If $\psi = e^{\sigma t + k(x - \gamma z)}$ in the condensation region, then at the interface $l = \frac{k}{\sigma + \gamma k}$. Therefore in the evaporation region, the liquid water and streamfunction are given by

$$l = \left(\frac{k}{\sigma + \gamma k} \right) e^{\sigma t - \frac{\sigma + k}{\gamma} (x - \gamma z)} \quad (3.2)$$

$$\psi = l \quad (3.3).$$

We call this the 'rain wave solution'. In this solution $k > 0$ in order that $\psi \rightarrow 0$ as $x - \gamma z \rightarrow -\infty$. For consistency this solution must satisfy the two dispersion relations

$$\sigma^2 = \beta \left(1 - \frac{A\sigma}{\sigma + \gamma k} \right) \quad (3.4)$$

for the condensation region and

$$\sigma^2 + N^2 \beta = \left(\frac{\gamma}{E + \gamma} \right) A(ME + \sigma) \left(\frac{k}{\sigma + \gamma k} \right) \beta \quad (3.5)$$

for the evaporation region, where

$$\beta = \frac{1}{1 + \gamma^2}. \quad (3.6)$$

Note $\beta = 0$ ($\gamma = \infty$) corresponds to a horizontal interface and $\beta = 1$ ($\gamma = 0$) to a vertical interface.

We deduce that $\sigma \leq 1$ and $\gamma k \leq \sigma(A - 1)$ and note that this solution satisfies the boundary conditions automatically. Figure 3 shows how the solutions $\sigma(\beta)$ evolve as the parameter N^2 , which represents the ratio of the stratification in the stable layer to that in the unstable layer, is varied. As expected, the growth rate increases as the slope of the squall line increases and as N^2 decreases.

In the limit of a horizontal interface, $\beta \rightarrow 0$, $\sigma = \sigma_0\beta^{1/2}$ and $\gamma k = r_0\beta^{1/2}$ where

$$\sigma_0^2 = 1 - \frac{A\sigma_0}{\sigma_0 + r_0} \quad (3.7)$$

and

$$\sigma_0^2 + N^2 = \frac{AMr_0}{\sigma_0 + r_0}. \quad (3.8)$$

Thus we have

$$\sigma_0^2 = 1 - \frac{1}{M}(AM - \sigma_0^2 - N^2) \quad (3.9)$$

and so for $\sigma_0^2 > 0$ we require

$$N^2 > M(A - 1) \quad (3.10)$$

and so

$$r_0 = \frac{N^2 - (A - 1)}{(M - 1)((M - 1)A + (A - 1) - N^2)}. \quad (3.11)$$

We deduce that $N^2 > A - 1$ and $N^2 < MA - 1$ for a solution to exist. It was shown numerically that the upper bound of N^2 occurs as $\beta \rightarrow 0$ and that the lower bound for N^2 occurs as $\beta \rightarrow 1$. The results are shown in figure 4, giving the range of atmospheric conditions which admit stationary squall line solutions. The region between the upper solid and lower dotted lines is the maximum range of solutions; in the region between the lower solid line and the dotted line no solutions with $\beta = 0$ exist. This may be seen most readily by considering the bounds on N^2 as $\beta \rightarrow 0$ where $\sigma \rightarrow \sigma_0\beta^{1/2}$ and $\gamma k \rightarrow r_0\beta^{1/2}$.

As N^2 decreases, solutions exist for sloping squall lines ($\gamma \leq \infty$) which do not exist for horizontal squall lines ($\gamma \rightarrow \infty$). This is because the steeper the squall line, the less rain that falls out. Therefore, for the same water loading (A), as γ decreases the stabilising stratification required for the atmosphere to adjust to the rain forcing decreases. There is a maximum stabilising stratification above which no solutions exist since above this value the atmosphere is too stable and over-compensates for the rain disturbance. The ratio of the buoyancy frequencies of the stable stratification to the unstable stratification, N^2 , attains its largest value when $\beta \rightarrow 0$, i.e. the interface is horizontal ($\beta = 0$); in this limiting case no rain forms and all the flow is horizontal.

4. Propagating, Growing Modes in an unbounded domain.

We now generalise the results of section 3 and seek the simplest form of propagating modes in an unbounded domain. We follow the approach of section 3 and look for solutions with parallel flow and a linear squall line ($x + ut = \gamma z$)

$$\psi = \exp(\sigma t) \exp(k(x + ut - \gamma z)). \quad (4.1)$$

Before proceeding with any detailed analysis we make several remarks about the above class of squall line solution.

First we note that $\partial_z = \gamma \partial_x$ and so the boundary conditions in a moving frame in which $\partial_t \rightarrow \partial_t + u \partial_x$ become

$$[\psi] = [\psi_x] = [\psi_{xx}] = 0. \quad (4.2)$$

In the condensation region, $\psi_x \geq 0$, but at the squall line in the evaporation region, $\psi_x \leq 0$. Thus $\psi_x = 0$ at the squall line and so there is no vertical flow there.

Secondly, we require both that the solution decay as $x + ut - \gamma z \rightarrow -\infty$ and that $\psi_x \geq 0$ everywhere in the condensation region. The simplest solution satisfying both of

these conditions is the sum of two exponential decaying modes. We will use this result shortly to find the solution in the condensation region.

In the evaporation region, the forced rain wave solution is a single exponentially decaying mode forced from the rain distribution on the squall line (as in section 3). Therefore, we need some other mode in this region in order to satisfy the boundary condition $\psi_x = 0$ at the interface. The only other modes which can occur in the evaporative region are gravity wave modes, which represent the adjustment of the environment to the flow at the squall line in order to conserve the flow properties B, l, u, p across the interface. Therefore, the solution in the evaporative region is a combination of the rain wave and a gravity wave.

It follows from (2.4.2) that the gravity wave mode satisfies

$$(\sigma + ku)^2 = -\beta N^2 \quad (4.3)$$

giving

$$k = -\frac{\sigma}{u} \pm i\beta^{1/2} \frac{N}{u}. \quad (4.4)$$

In order that this mode decays as $x + ut - \gamma z \rightarrow \infty$, we require $u > 0$. This constraint implies that the squall line can only propagate into the condensation region. We investigate the mechanism of this propagation later in this section.

We also note that the modes in the condensation region, $x + ut < \gamma z$, satisfy

$$(\sigma + uk)^2 = \beta \left(1 - A \frac{\sigma + ku}{\sigma + ku + k\gamma}\right) \quad (4.5)$$

and so in order that $\psi_x \geq 0$ and that the solution decays as $x + ut - \gamma z \rightarrow -\infty$, we require two positive roots for k . Therefore $k\gamma > (A - 1)(\sigma + ku)$ and hence $\gamma > (A - 1)u$. We deduce that if $A > 1$ then the squall line must slope into the evaporation region and cannot be vertical. This is because the rain leaves the condensing region more rapidly when the squall line slopes. If the water loading exceeds the unstable stratification ($A > 1$) in the

condensing region then in order to maintain upward flow the density of the rain must be reduced; this is achieved by having a sloping squall line.

There exist two positive solutions for k in both the cases $A > 1$ and $A < 1$. This is readily seen graphically by plotting the dispersion relation (4.5) as shown in figure 5. We deduce that for $A < 1$ there can only be two solutions of (4.5) if the value of $y(k)$, where

$$y(k) = \sqrt{\beta} \left(1 - A \frac{(\sigma + ku)}{\sigma + k(u + \gamma)} \right) \quad (4.6)$$

exceeds the value $uk + \sigma$ at the point at which $\frac{dy}{dk} = u$. After some algebra, this condition may be shown to reduce to the condition $\gamma > 2u \frac{1-A}{A}$. Hence when $A < 1$ the squall line must also slope away from the vertical, and as $A \rightarrow 0$, the squall line becomes horizontal. We will show that such a solution is not possible when N^2 is too large because as $A \rightarrow 0$, the downward condensate loading is insufficient to balance the upward unstable motion produced by the latent heat release.

To simplify the solutions we will now work in the frame of reference moving with the squall line, $x' = x + ut$. We choose the line $x' = \gamma z$ to correspond to the position of the squall line. From now on we drop the prime.

(i) Solution in the Condensation Region. Analysis of the Mechanism of Propagation.

Following the above discussion, we can immediately write down the streamfunction in the condensation region, ($x < \gamma z$), as

$$\psi = \exp(\sigma t + k_1(x - \gamma z)) - \frac{k_1}{k_2} \exp(\sigma t + k_2(x - \gamma z))$$

where $k_2 > k_1 > 0$ are the two solutions for k . This solution clearly satisfies the conditions $\psi_x = 0$ at $x = \gamma z$ and $\psi_x > 0$ for $x < \gamma z$. The rain field is found from (2.4.2) to be

$$l = \frac{k_1}{\sigma + k_1(u + \gamma)} \exp(k_1(x - \gamma z)) - \frac{k_1}{\sigma + k_2(u + \gamma)} \exp(k_2(x - \gamma z)) \quad (4.7)$$

and the thermal field is

$$B = \frac{k_1}{\sigma + k_1 u} \exp(k_1(x - \gamma z)) - \frac{k_1}{\sigma + k_2 u} \exp(k_2(x - \gamma z)). \quad (4.8)$$

From these solutions we can understand the mechanism of propagation of the squall line. The simplest means of understanding the propagation mechanism is to follow the approach of Seitter & Kuo and examine the vorticity field and its generation. Returning to the stationary frame, we have

$$\nabla^2 \psi_t = B_x - Al_x \quad (4.9).$$

Figure 6 shows the variation with distance from the squall line of the vorticity field, $\nabla^2 \psi$, and the terms representing the rate of generation of vorticity due to the buoyancy field (B_x), the rain loading ($-Al_x$) and their sum.

Near the squall line the buoyancy generation term dominates which causes the vorticity field to decrease. Therefore the point of minimum vorticity and hence the squall line propagate to the left. In this region, the rain field weakly opposes this buoyancy generation of negative vorticity. However, as we move some distance ahead of the squall line, the condensate loading also begins to generate negative vorticity and a little further ahead the vorticity generated by the rain-loading dominates the generation of vorticity caused by the buoyancy field. The rain loading controls the propagation to the left in this region ahead of the squall line, up to the point even further ahead of the interface where the sum of the vorticity generation terms becomes positive. Beyond this point the buoyancy generation of vorticity dominates the rain loading generation of vorticity again. In this very simple analytical solution there is a more complex mechanism of propagation than that suggested by Seitter & Kuo (1983). We have determined that the phase difference between the rain field, buoyancy field and streamfunction cause the propagation of the squall line; however, this more complex mechanism also depends crucially on the presence of the water loading.

(ii) Non-existence of Propagating Modes when $A = 0$.

In order to emphasize the importance of the presence of the water loading, parameterised by A , we now show that no propagating modes exist when $A = 0$. In this case the dispersion relation in the condensation region becomes

$$(\sigma + k_c u)^2 = \beta \quad (4.10)$$

and for the gravity mode in the evaporation region it becomes

$$(\sigma + k_e u)^2 = -N^2 \beta, \quad (4.11)$$

where k_c and k_e are the wavenumbers in each of the regions. Thus $k_c = -\frac{\sigma}{u} \pm \frac{\beta^{1/2}}{u}$ and $k_e = -\frac{\sigma}{u} \pm i \frac{\beta^{1/2}}{u}$. However we require two decaying modes in $x < \gamma z$ and so $u > 0$. This implies that in $x > \gamma z$ the gravity mode grows as $x - \gamma z \rightarrow \infty$.

Hence no such propagating solutions exist. Essentially, this is because when $A = 0$ we have adjacent regions of unstable and stable fluid (Bretherton, 1987).

(iii) Solution in the evaporation region.

This solution consists of the rain wave produced by the rain moving across the squall line from the condensation region (section 3) and the gravity wave which is the response of the stable stratification to the forcing at the interface.

From the solution in the condensation region, (4.7), we have the value of the rain at the squall line

$$l = \frac{k_1}{\sigma + k_1(u + \gamma)} - \frac{k_1}{\sigma + k_2(u + \gamma)} \quad (4.12)$$

and so the rain wave has the solution

$$\psi_r = a_r \exp \left[\sigma t - \left(\frac{\sigma + E}{u + \gamma} \right) (x - \gamma z) \right] \quad (4.13),$$

where

$$a_r = \frac{\beta A k_1 (k_2 - k_1) \left[\frac{(u+\gamma)M}{(\sigma+E)} + \frac{(\sigma\gamma-Eu)}{E(u+\gamma)} \right]}{(N^2 + k_r^2)(\sigma + k_1(u + \gamma))(\sigma + k_2(u + \gamma))} \quad (4.14).$$

We may associate the term in M with the flow produced by the evaporative cooling while we associate the term in $\frac{1}{E}$ with the condensate loading. Therefore, in this region, either of these mechanisms will suffice to produce the downward motion and the associated positive vorticity generation.

The gravity wave mode has the form

$$\psi_g = \exp(\sigma t - \frac{(x - \gamma z)\sigma}{u}) \left(a_1 \cos \left[\frac{\beta^{1/2} N}{u} (x - \gamma z) \right] + a_2 \sin \left[\frac{\beta^{1/2} N}{u} (x - \gamma z) \right] \right).$$

and we may determine a_1 and a_2 most readily from the boundary conditions $\psi_{g,z} + \psi_{r,z} = 0$, $\psi_g + \psi_r = \psi_c$ at $x = \gamma z$ where the subscripts c, r and g denote the condensation region solution, the gravity wave and the rain wave.

The interfacial condition

$$\psi_{g,zz} + \psi_{r,zz} = \psi_{c,zz}$$

at $x = \gamma z$ then is used to determine the value of σ for the given value of k and γ .

(iv) Description of Full Solution.

Before considering how the solutions evolve as the atmospheric conditions change, it is instructive to examine how the vertical velocity, ψ_z , the buoyancy, B and the liquid water, l vary from some distance ahead of the squall line, through the squall line, to some distance behind the squall line. In figure 7, it may be seen that in the condensation region the vertical velocity (ψ_z) has a maximum well ahead of the interface, while the buoyancy maximum occurs nearer to the squall line, and the liquid water maximum is even closer. It was shown earlier that this phase shift between the upward motion and the buoyancy and liquid water fields maintains the propagation of the squall line.

In the evaporation region the rain distribution decays exponentially with distance from the squall line as it evaporates. The temperature drops rapidly with distance behind the squall line. Near the squall line this is due primarily to the continuity of temperature across the interface coupled with the exponential growth with time of the mode in the condensation region. However, further behind the line it is primarily due to the production of negative buoyancy by rainwater evaporation.

Just behind the squall line, the velocity field is controlled dominantly by this production of negative buoyancy. However, further behind the line the gravity wave becomes more important in controlling the buoyancy distribution and the velocity field. However, the generation of negative buoyancy by evaporation dominates the velocity field, maintaining the vertical position of all air parcels below their height on passing through the squall line so that the air remains unsaturated.

(v) Consistency condition.

We now develop the consistency condition that once a parcel of air moves behind the squall line it should remain undersaturated and therefore below the height it had when passing through the squall line. We may formally express this condition as $\int_0^t \psi_x dt < 0$, where $x = \gamma z$ at $t = 0$.

Substituting the full solution for the evaporating region into this expression and after some algebra, the condition reduces to

$$W \cos \left[\frac{\sqrt{(\beta)N}x}{u} + \chi \right] < Y \exp \left[\left(\frac{\sigma}{u} - k_r \right) x \right] + Z, \quad (4.15)$$

where W, X, Y, Z may be determined in terms of a_r, a_3, a_4 as

$$X = \tan^{-1} \left(\frac{a_4 \sqrt{(\beta)N} - a_3 \sigma}{a_3 \sqrt{(\beta)N} + \sigma a_4} \right)$$

$$W = \left(k_r^2 a_r^2 + \frac{1}{u^2} (a_3 \sqrt{(\beta)N} + \sigma a_4)^2 \right)^{\frac{1}{2}}$$

$$Y = \frac{\sqrt{(\beta)Na_r(\sigma + E)}{(\sigma - uk_r)(u + \gamma)}$$

and

$$Z = \frac{a_3\sqrt{(\beta)N}}{u} + \frac{\sigma a_4}{u}$$

where

$$k_r = \frac{\sigma + E}{u + \gamma}.$$

We can readily demonstrate that in principle some solutions can satisfy this condition. We consider two separate cases.

(a) if $\chi > 0$ there are consistent solutions if

$$Y \exp\left(\left(\frac{\sigma}{u} - k_r\right)(2\pi - \xi)\right) + Z < W.$$

This inequality expresses the condition that the exponential term can only equal the cosine term at $x = 0$, as shown in figure 8(i), since the exponential term is constrained to increase faster than the cosine at $x = 0$

(b) if $\chi < 0$ then figure 8(ii) shows that in this case there can be no further roots, since the exponential term is constrained to increase faster than the cosine at $x = 0$ (i.e. $\psi_x < 0$).

(vi) Constraints on Atmospheric Conditions and Squall Line Velocity.

Solutions for the class of squall lines satisfying the conditions outlined above were found as follows. The two roots, k_1 and k_2 , > 0 , for the dispersion relation in the condensation region were found for given σ and β and then the value for N^2 which allowed the dispersion relation in the stable region to be satisfied was determined. The consistency of the solution was then checked using the method described in section (v) above.

This procedure generates the family of solutions in (σ, β, N^2) space for each value of u and A . A typical set of such solutions is shown in figure 9 where the growth rate, σ

is shown as a function of N^2 for given u and A . We note that this predicts a maximum and minimum for N^2 and a maximum value for $\sigma(N^2)$. In each of the solution curves, β increases along the line and N^2 decreases along the line. σ increases from one line to the next for given β in the direction of increasing N^2 . Therefore the solution of minimum N^2 corresponds to the solution with a relatively large value of β , i.e. a near vertical interface, but as the upper bound for N^2 decreases, this value is less than the maximum value of β .

It is of interest to plot the locus of maximum growth rates as a function of u , the squall line speed and water loading. Figure 10(i) shows how the locus of the maximum growth rate, σ , varies as a function of N^2 and u for given A . Figure 10(ii) shows how the locus of maximum σ varies as a function of β and u for given A ; in these solutions N^2 is allowed to vary and these solutions correspond to those shown in figure 10(i).

As u increases, the growth rate decreases but the value of N^2 for which the growth rate is a maximum increases with u . Also the range of solutions for N^2 decreases with u , implying that the faster the squall line the smaller the possible range of atmospheric conditions which can support such an event. The value of β at which σ has its maximum is less than the maximum value of β for the given values of u and A .

Figure 11 shows how the locus of maximum growth rate, σ , varies for given u as a function of N^2 and A . When $A < 1$, $N^2 > 0$. However, for $A \geq 1$, the minimum stratification is greater than zero since the rain loading exceeds the unstable stratification causing the squall line to slope so that more rain falls into the evaporation region. In order that the environment can adjust to match the flow properties at the boundary we now require finite stratification.

Figure 12 summarises the range of atmospheric conditions in which these squall lines can exist for different values of the squall line propagation speed. As u increases the solution space collapses to a very small range of environmental conditions.

5. Solutions in a vertically bounded domain

In this section, we address the problem of finding squall line solutions in a vertically bounded domain. Figure 13 shows the qualitative nature of a propagating squall line, in the frame of reference moving with the squall line, in such a bounded domain. A finite region of rain of the shape shown follows the squall line. Behind this there is unsaturated air with no liquid water. The upper boundary is a streamline and a line of zero rain so that rain is not supplied from above. The lower boundary is also a streamline. The shape of the squall line becomes an unknown to be determined as part of the solution. This may readily be seen by considering the equations governing the flow.

In the condensation region the coupling between the rain content and the motion gives rise to a fifth order equation for ψ in x in the moving frame

$$(\partial_t + u\partial_x)^2(\partial_t + u\partial_x - \partial_z)\nabla^2\psi = (\partial_t + u\partial_x - \partial_z)\psi_{xx} - A(\partial_t + u\partial_x)\psi_{xx} \quad (5.1)$$

which requires five matching conditions across the interface. In the evaporation region the independence of the rain from the motion gives rise to a fourth order equation for the motion, with the rain field a forcing term in the equation

$$(\partial_t + u\partial_x)^2\nabla^2\psi = -N^2\psi_{xx} - A(ME + (\partial_t + u\partial_x))l_x \quad (5.2)$$

and the equation for the liquid water is

$$(\partial_t + u\partial_x - \partial_z)l = -El. \quad (5.3)$$

This only requires four matching conditions for ψ at the squall line, hence the squall line shape provides the extra degree of freedom to solve the problem. In the unbounded domain case, this degree of freedom was manifested as the slope of the squall line.

(i) Imposed horizontal boundaries.

As a first attempt to solve the problem we address the simplest problem which contains some of the new physics. We consider non-propagating squall lines, with no water loading in the cloud and seek solutions of the form $f(x, z, t) = e^{\sigma t} g(x, z)$. We obtain

$$\sigma^2 \nabla^2 \psi = \psi_{xx} \quad (5.4)$$

in the condensation region and

$$\sigma^2 \nabla^2 \psi = -N^2 \psi_{xx} + f(l) \quad (5.5)$$

in the evaporation region, where $f(l)$ represents the generation of vorticity due to the evaporation of the liquid rain, together with the rain conservation equations. Since in the unbounded domain the growth rate is bounded by unity, we investigate modes with

$$\sigma^2 < 1.$$

In the condensation zone, we have a simple hyperbolic equation

$$\sigma^2 \psi_{xx} = (1 - \sigma^2) \psi_{xx} \quad (5.6)$$

with solution

$$\psi = \cos \left[z + \sigma x (1 - \sigma^2)^{-1/2} \right] - \cos \left[z - \sigma x (1 - \sigma^2)^{-1/2} \right]. \quad (5.7)$$

Given an interface shape, we can then solve for the flow in the evaporation zone numerically, using just one of the matching conditions across the interface, since it simply involves inverting an inhomogeneous elliptic equation. Note, however, that this is not a solution of the full system, since by assuming an interface shape we lose a degree of freedom and so cannot impose one of the boundary conditions. In the present study, the interface shape was assumed to be linear and the solution in the evaporation region was found using

the continuity of streamfunction boundary condition. The slope was then varied to find the slope for which the pressure was best matched across the interface. A typical numerical solution is shown in figure 14 showing (i) the streamfunction and (ii) the rain distribution.

It was found that as the slope of the squall line is reduced, the pressure across the interface matches more closely. In the limit, there is a pure horizontal flow and no rain forms. We conclude that a more complex interface shape is required. A closed form expression for this shape may be derived in a formal manner, however, it is a highly non-linear and complicated equation.

(ii) Natural vertical bounds of the system.

An alternative approach to generate bounded solutions is to allow the physical properties of the system to vary with height. In practice, the gradient of the water vapour saturation mixing ratio may vary with height. This can impose a natural vertical scale on the system, and remove the need for an upper boundary to be imposed on the system. By imposing a variation of the saturation vapour mixing ratio on a scale much greater than the exponential decay scale of the present set of solutions, the present solutions can be continuously changed with height and thus bounded.

To this end we seek solutions of the form

$$l(x, z, t) = l(z) \exp(fx + \int g(z) dz + \sigma t) \quad (5.8)$$

and

$$\psi(x, z, t) = \exp(fx + \int g(z) dz + \sigma t) \quad (5.9)$$

for the flow in the condensation region, for $z > 0$. In order that such solutions be vertically bounded we impose that

$$\frac{dz}{dx} \rightarrow 0 \text{ as } z \rightarrow H$$

along the lines $fx + \int g(z)dz = \text{const.}$ Thus $g(z) \rightarrow \infty$ as $z \rightarrow H$.

With the solutions (5.8), (5.9), the equation for conservation of the liquid water becomes

$$l(z)(fu + \sigma - g(z)) = fs(z)$$

where $s(z)$ is the vertical gradient of the water vapour saturation mixing ratio. $s(z)$ remains finite as $z \rightarrow H$ and so

$$g(z) \sim \lambda \frac{1}{l(z)} \text{ as } z \rightarrow H$$

where $\lambda = -fs(H)$.

Again using the solutions (5.8) and (5.9), the equation of motion in the condensation region becomes

$$(uf + \sigma)^2(f^2 + g' + g^2) = \frac{N_c^2(z)}{N_c^2(0)}f^2 - l(z)Af(uf + \sigma).$$

where the unstable stratification, N_c^2 , has now become a function of z . As $z \rightarrow H$,

$$g' + g^2 \sim 0$$

and so $g(z) \sim -\frac{1}{(H-z)}$. Therefore

$$\frac{1}{l(z)} \sim \frac{fs(H)}{H-z} \text{ as } z \rightarrow H.$$

Using these asymptotic results, if we assume that $l(z) = \frac{H-z}{fs(H)}$ and $g(z) = \frac{1}{z-H}$ then we can readily deduce that

$$s(z) = \left(\frac{(H-z)}{f^2s(H)} \right) \left(fu + \sigma - \frac{1}{z-H} \right)$$

and

$$N_c^2(z) = (uf + \sigma) \left(uf + \sigma + \frac{A(H-z)}{s(H)} \right).$$

In this solution, the streamlines in the condensation region are parallel to the line $z = H(1 - \exp(-fx))$ and along such characteristics $l(z) = \frac{H \exp(-fx)}{f s(H)}$. Note that in these solutions, the streamlines are bounded above by the line $z = H$. Alternatively, from the asymptotic arguments we could have chosen $l(z) = \frac{H-z}{f s(z)}$ and $\frac{g(z)-1}{H-z}$, which gives rise to a different functional dependence $s = s(z)$.

Only those solutions for which the water vapour saturation mixing ratio is zero at the point $z = H$ are physically admissible, since if $q_s(H) > 0$, then any further upward motion would generate more positive buoyancy, and thus more upward motion. This condition may be formally expressed as $\int_0^H s(z) dz - q_s(0) = 0$. The rain distribution in the evaporation region is readily determined by integrating from the squall line along the lines $z = -x/u + \text{const}$ as outlined in section 2(iv). The flow solution in the evaporation region may then be found numerically by solving the equation of motion, given the rain distribution everywhere in the region. Figure 15 is a schematic of the qualitative nature of this solution.

This approach suggests a method of extending the results of section 4 to a more realistic class of vertically bounded squall line solutions and many of the features of those solutions are present in these bounded solutions. However, the problem of imposing a lower horizontal boundary on the squall line remains unsolved. Possibly, the present solutions may be matched at $z = 0$ to a distinct region below the squall line, in which the strong upflows may perhaps originate by mixing at the sea surface.

6. Conclusions

We have developed a realistic but simple model of the dynamics governing the propagation of a squall line in which we consider separately the motion in the region of upward-moving, saturated condensing air and the region of downward-displaced, unsaturated air. Simple growing and propagating squall line solutions of this system were found and they predict some very strong constraints on the motion of squall lines, as well as specifying the range of atmospheric conditions in which such solutions may exist. These solutions exist in the absence of wind shear.

They predict that

1. Squall lines only propagate into the region of upward-moving, condensing air.
2. Squall lines slope away from their direction of propagation. A significant amount of condensate thus falls into the region of unsaturated air behind the squall line.
3. Squall lines can only propagate when the atmospheric stratification lies between an upper and lower bound, both of which increase as the water loading increases. These bounds are shown in figure 12.
4. As the speed of the squall line increases, the range of atmospheric conditions in which such solutions exist decreases.
5. The propagation of the squall line is caused by an interaction of the rain (liquid water) field and the buoyancy field, with the buoyancy field causing the propagation near to the squall line and far ahead of the squall line, while the rain (liquid water) loading causes the propagation in the region between these two extremes.

It has also been shown that a natural bound on the vertical extent of the squall line may be imposed by decreasing the gradient of the saturated vapour mixing ratio with height, so that the amount of condensate formed decreases as the parcel rises.

Acknowledgements.

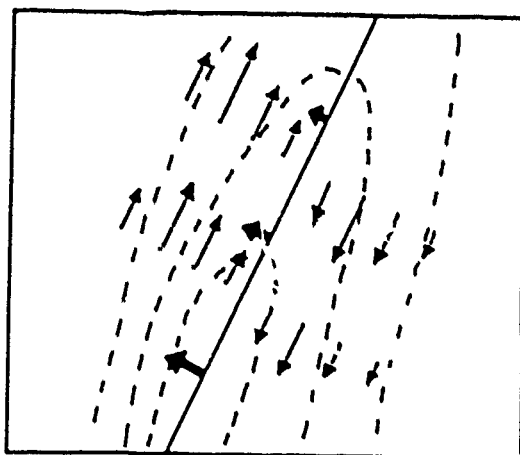
I should like to thank Professor Kerry Emanuel for introducing me to this subject and for his many useful comments and advice about the work. I would like to thank the Fellowship committee for giving me the opportunity of participating in this 1988 GFD summer study program and Professor Glen Flierl for having coordinated the summer. I had a most stimulating summer at Walsh Cottage, and enjoyed interacting with the wide range of people who passed through during the summer, and who gave useful comments about my project. I am also grateful to St. John's College, Cambridge for a travel grant for the trans-Atlantic crossing.

References.

- Bretherton, C.S., 1987, Linear propagating and non-precipitating moist convection, J.A.S., 44, 14, 1869-1874.
- Durran, D.R. & Klemp, J.B., 1982, On the effects of moisture on the Brunt- Väisälä frequency, J.A.S., 39, 2152-2158.
- Emanuel, K.A., 1986, Some dynamical aspects of precipitating convection, J.A.S., 43, 20, 2183-2198.
- Kessler, E., 1969, On the distribution and continuity of water substance in atmospheric circulation, Meteor. Monogr., no. 32, Amer. Meteor. Soc., 84 pp.
- Scitter & Kuo, 1983, The dynamical structure of squall-line type thunderstorms J.A.S., 40, 293 2-2954.
- Takeda, 1971, Numerical simulation of a precipitating cloud: The formation of a long lasting cloud, J.A.S., 28, 350-376.
- Thorpe, Miller & Moncrieff, 1982, Two-dimensional convection in non-constant shear; a model of mid-latitude squall lines, Q. J. Roy. Meteor. Soc., 102, 458, 739.

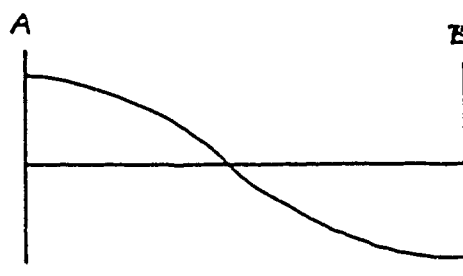
Figure Captions

1. Schematic diagram of a squall line, showing wind velocity, rain contours and motion of the squall line.
2. (i) Vorticity and (ii) rate of vorticity generation by rainwater along a horizontal section of Emanuel's precipitating convection solutions. (iii) streamlines and (iv) rain contours as given in Emanuel (1986) figure 9(a,b), from which the present figures 2(i,ii) were derived (approximately).
3. Growth rate of non-propagating disturbances, σ as a function of β , the slope parameter for various values of N^2 .
4. Upper and lower bounds for N^2 for non-propagating squall lines.
5. Plots of the dispersion relation (4.5) for (i) $A > 1$ and (ii) $A < 1$ showing the existence of two solutions for k , the wavenumber.
6. Plot of (i) the vorticity field, (ii) the total rate of generation of vorticity, (iii) the rate of generation of vorticity by buoyancy and (vi) the rate of generation of vorticity by rain loading. This shows the phase difference between the vorticity field and the rate of generation of vorticity which causes the propagation of the squall line.
7. Typical solution of the rain, buoyancy and vertical velocity distributions.
8. Demonstration of the consistency condition (section 4(v)) for the cases (i) $\chi > 0$ and (ii) $\chi < 0$.
9. Growth rate, σ , for a propagating disturbance as a function of N^2 for u and A fixed and variable β .
10. (i) Variation of the maximum value of σ as a function of N^2 and u for A fixed and (ii) variation of the maximum value of σ as a function of β and u for A fixed.
11. Variation of the maximum value of σ as a function of N^2 and A for u fixed.
12. Upper and lower bounds for N^2 as a function of A for various values of u . This gives the range of atmospheric conditions for which such a growing, propagating squall line can exist. Note that these bounds were found for values of β in the range (0.01,0.99), and so do not include disturbances in which the squall line is either vertical or horizontal.
13. Qualitative nature of the squall line, and the rain field, in a vertically bounded, propagating squall line.
14. (i) Streamfunction and (ii) rain distribution for a typical solution of the vertically bounded flow in which there is no propagation, the pressure is not matched across the interface and there is no rain loading. As the interface becomes horizontal the pressure is better matched for this interface shape.
15. Schematic of the squall line solution in which a vertical bound is incorporated into the problem by decreasing the saturation mixing ratio with height.

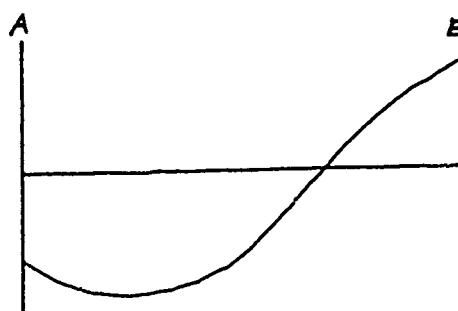


→ winds
 / rain contours
 ➔ motion of interface

Figure 1



Vorticity



Role of
 Vorticity generation
 by rain loading

Figure 2 (i), (ii)

Figure 2 (iii)

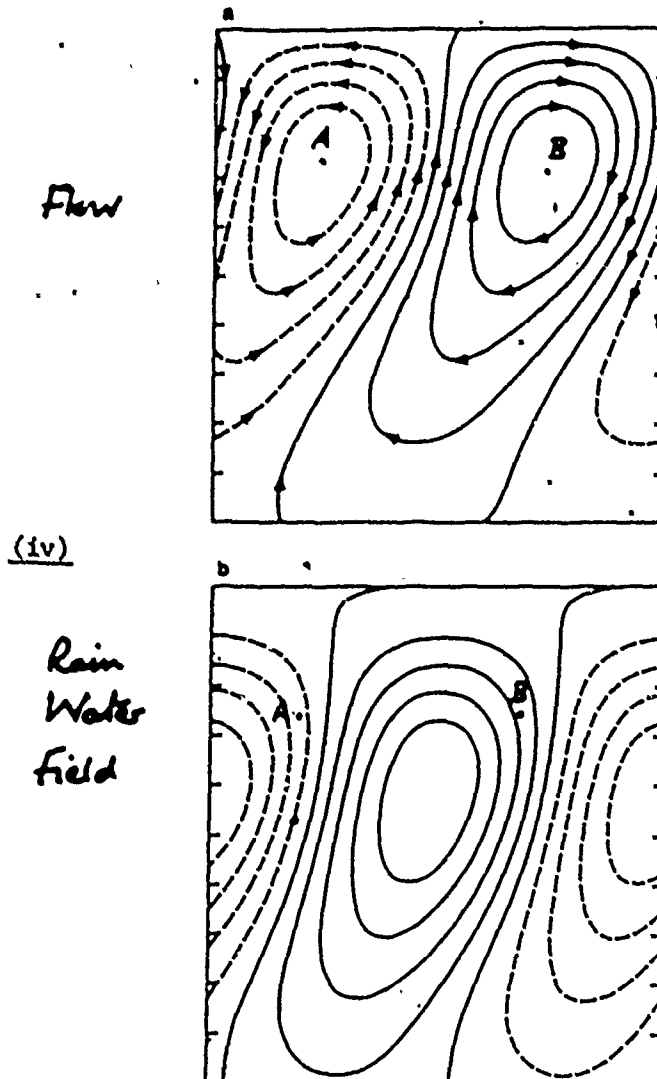


FIG. 9. (a) Example of streamfunction (with normalized amplitude of 1.0) where $a = 0.5$, $V_T = 0.1$ and $k = 6.0$; mode shown moves from right to left at a speed of 0.008 and has a growth rate of 0.625. (b) Liquid water perturbation associated with mode shown in (a); amplitude = 7.72.

Figure 3

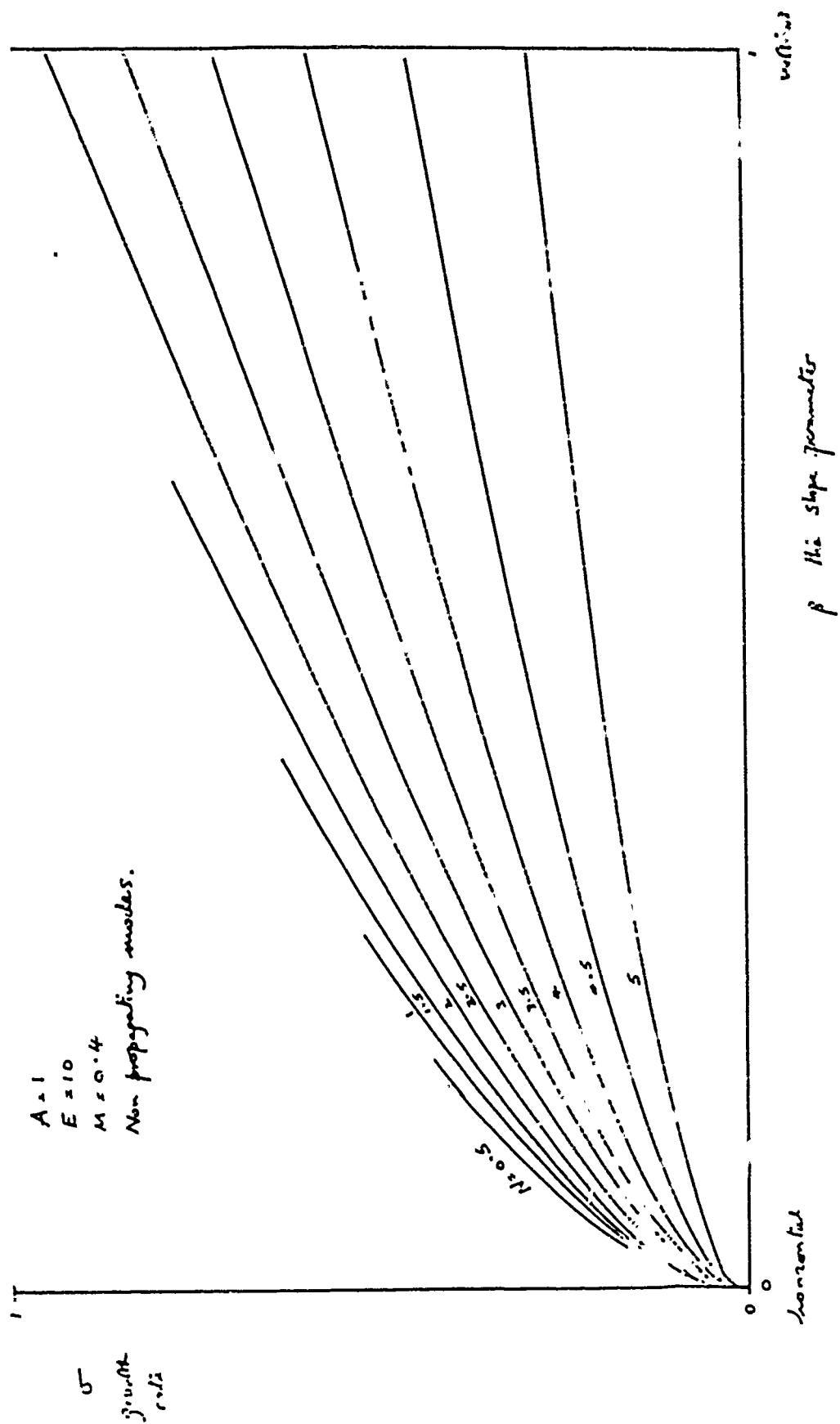


Figure 4

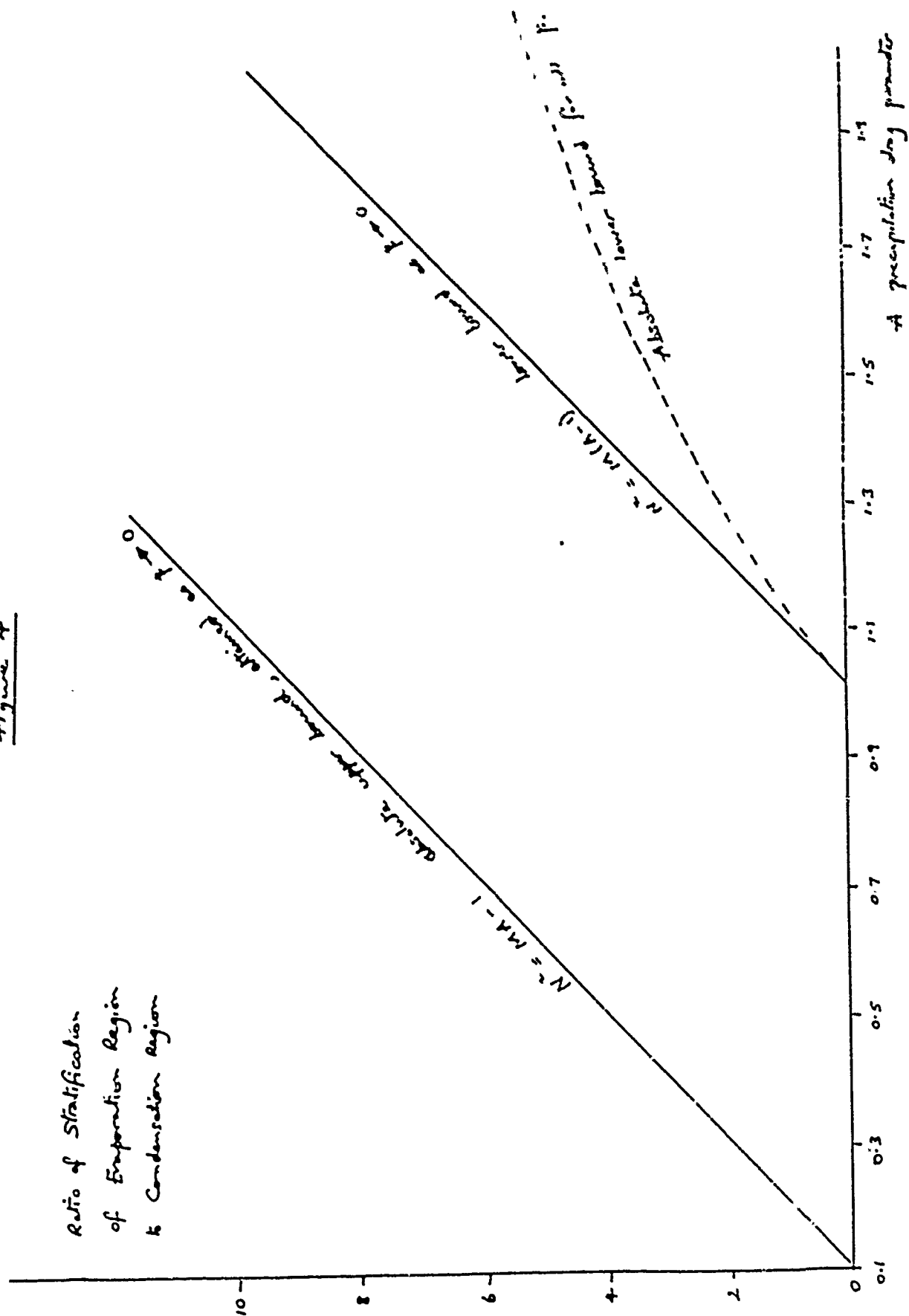
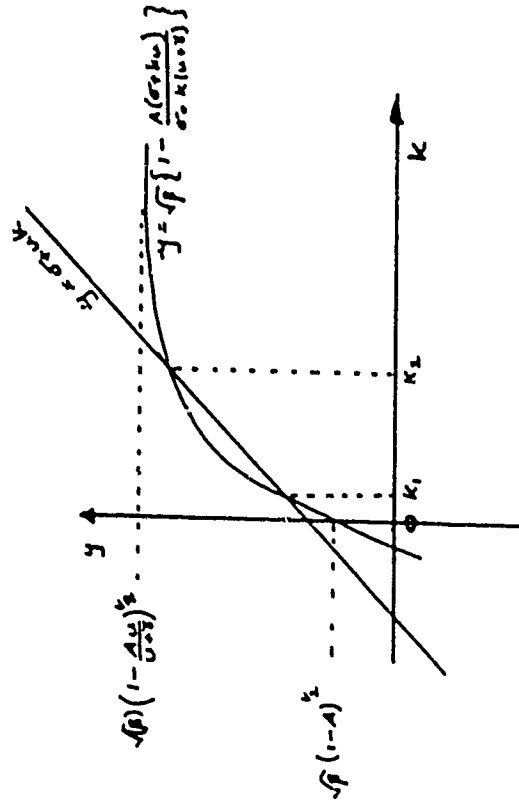
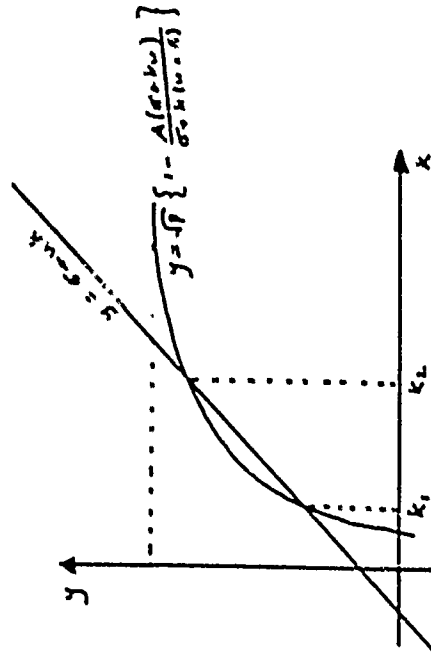


Figure 5

(i) $A < 1$



(ii) $A > 1$



k_1 and k_2 are the roots of the dispersion relation.

Figure 6 Mechanism of Propagation in Vorticity Fall

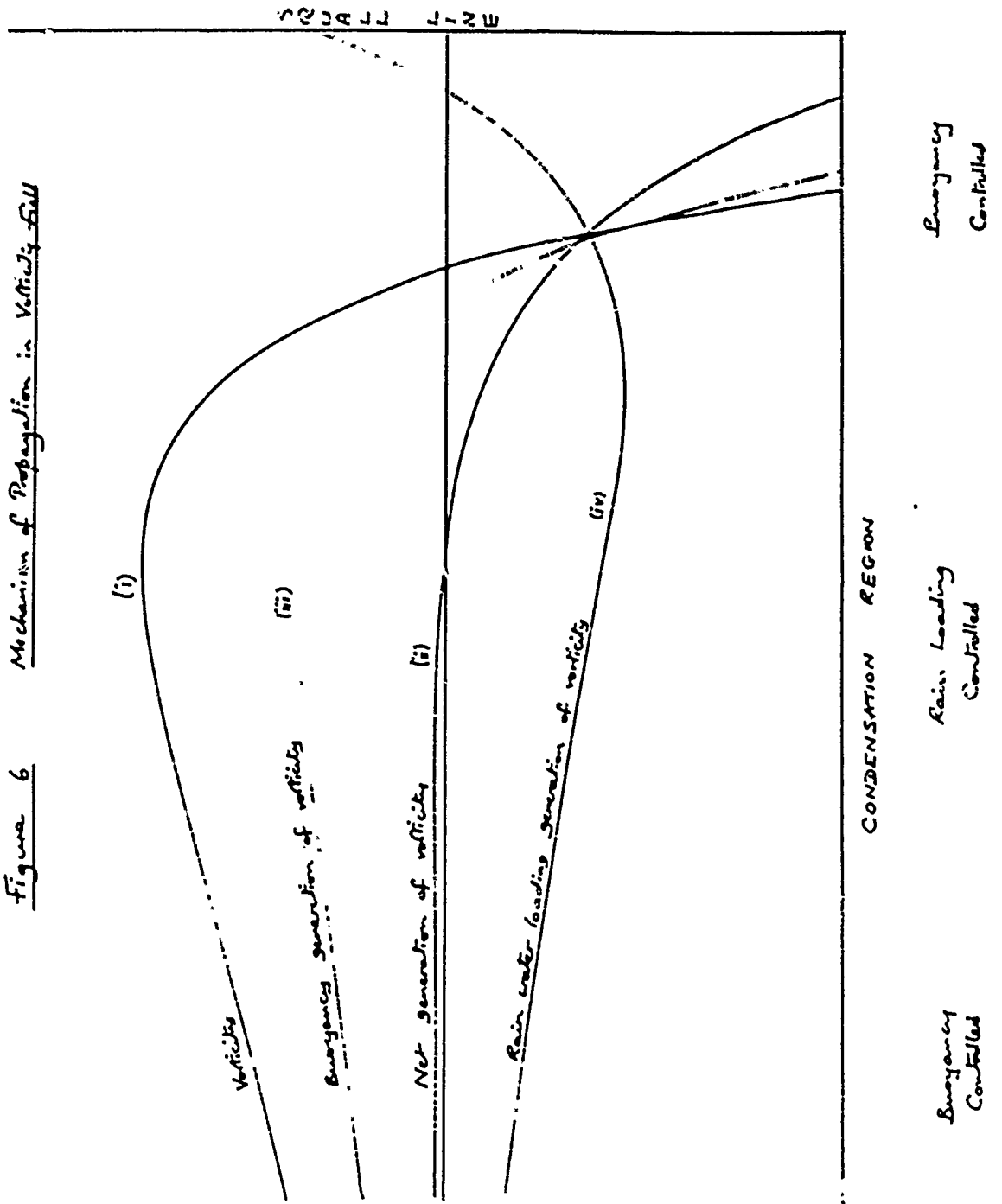


Figure 7
Decomposition of Flow Variables

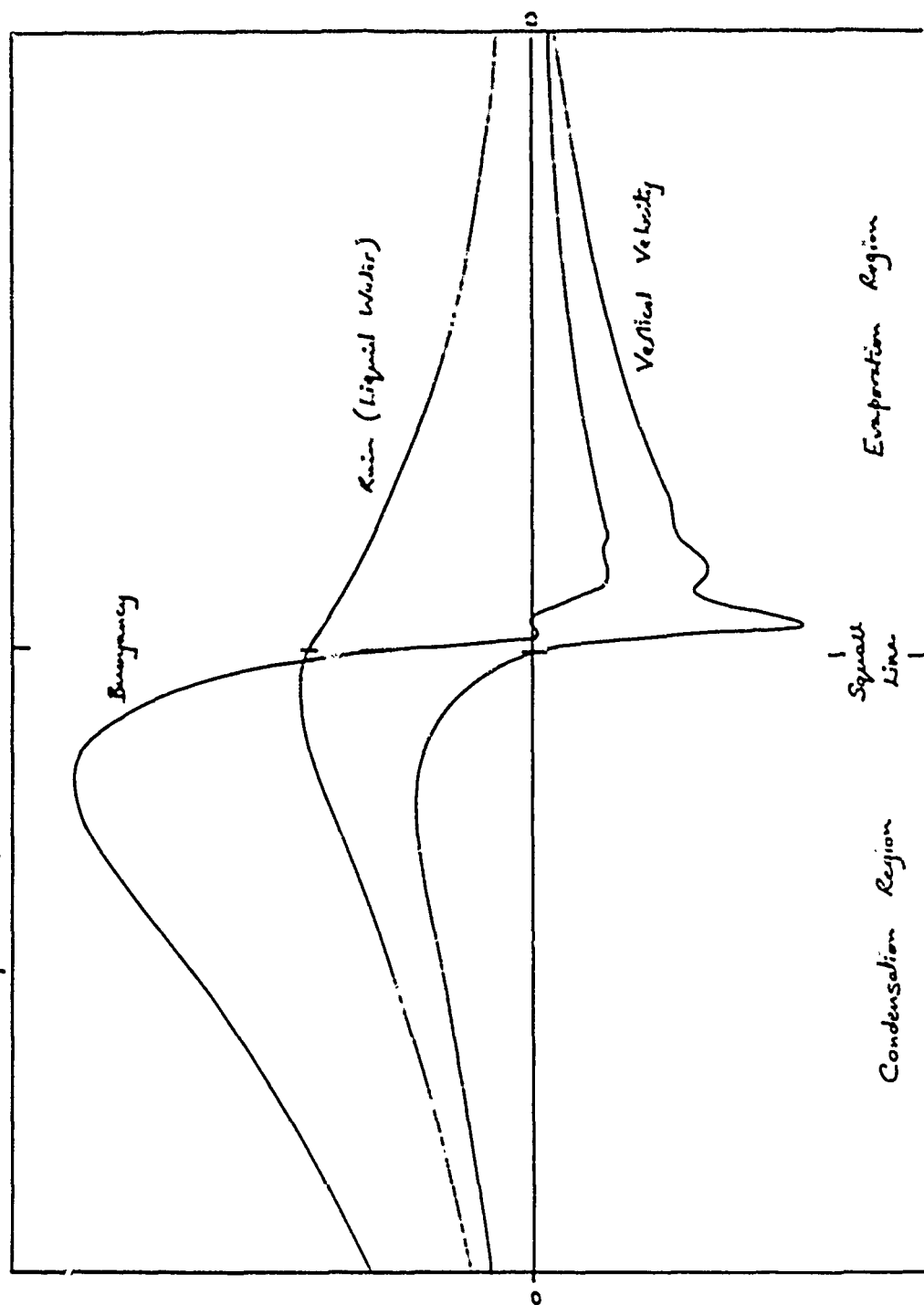
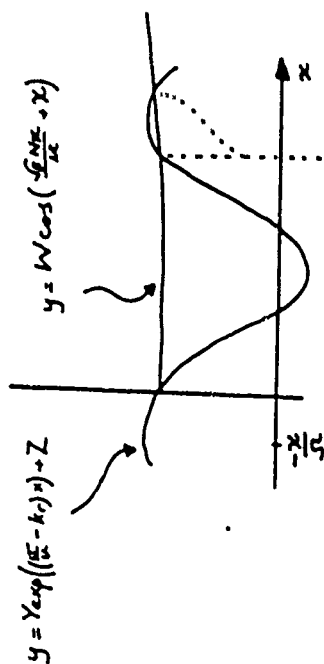
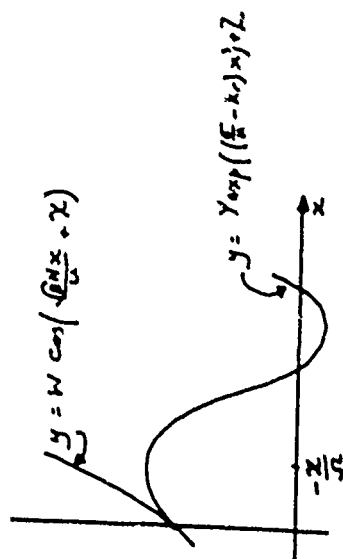


Figure 8

(i) $x > 0$ 

possible additional roots
if exponential does not
grow sufficiently rapidly

(ii) $x < 0$ 

no possible roots
other than $x = 0$.

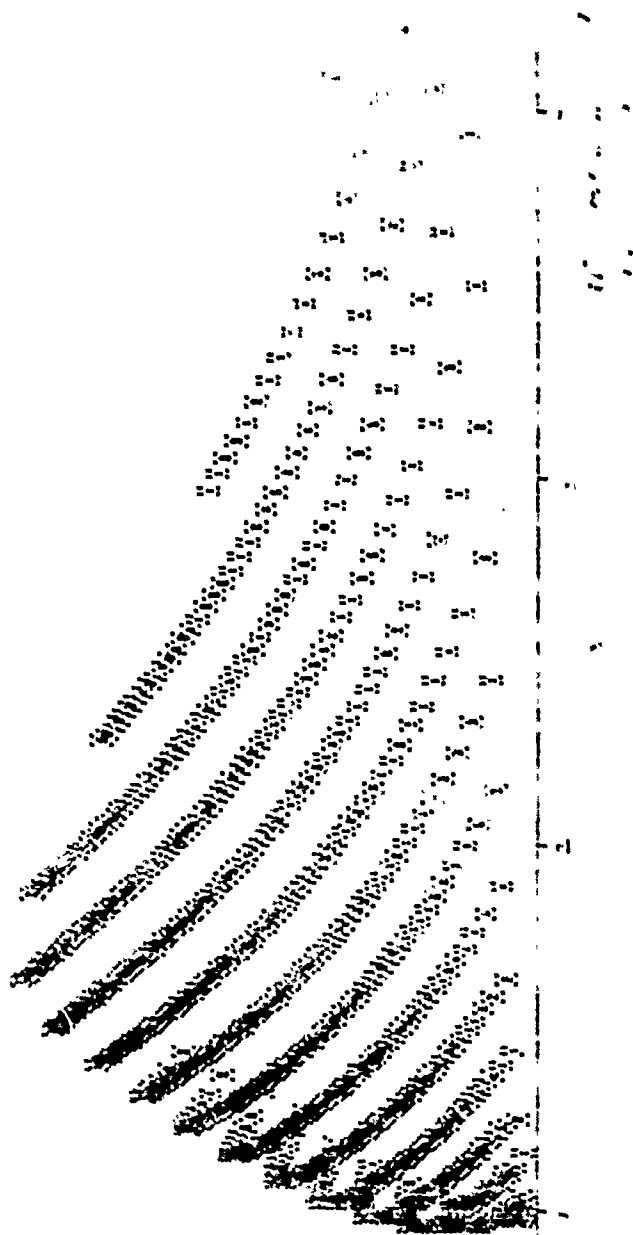
Growth
Rate

Figure 3

$A = 1.1 \times 10^{-1}$

Solution for σ as N and β are varied

$\sigma = \sigma(N, \beta)$

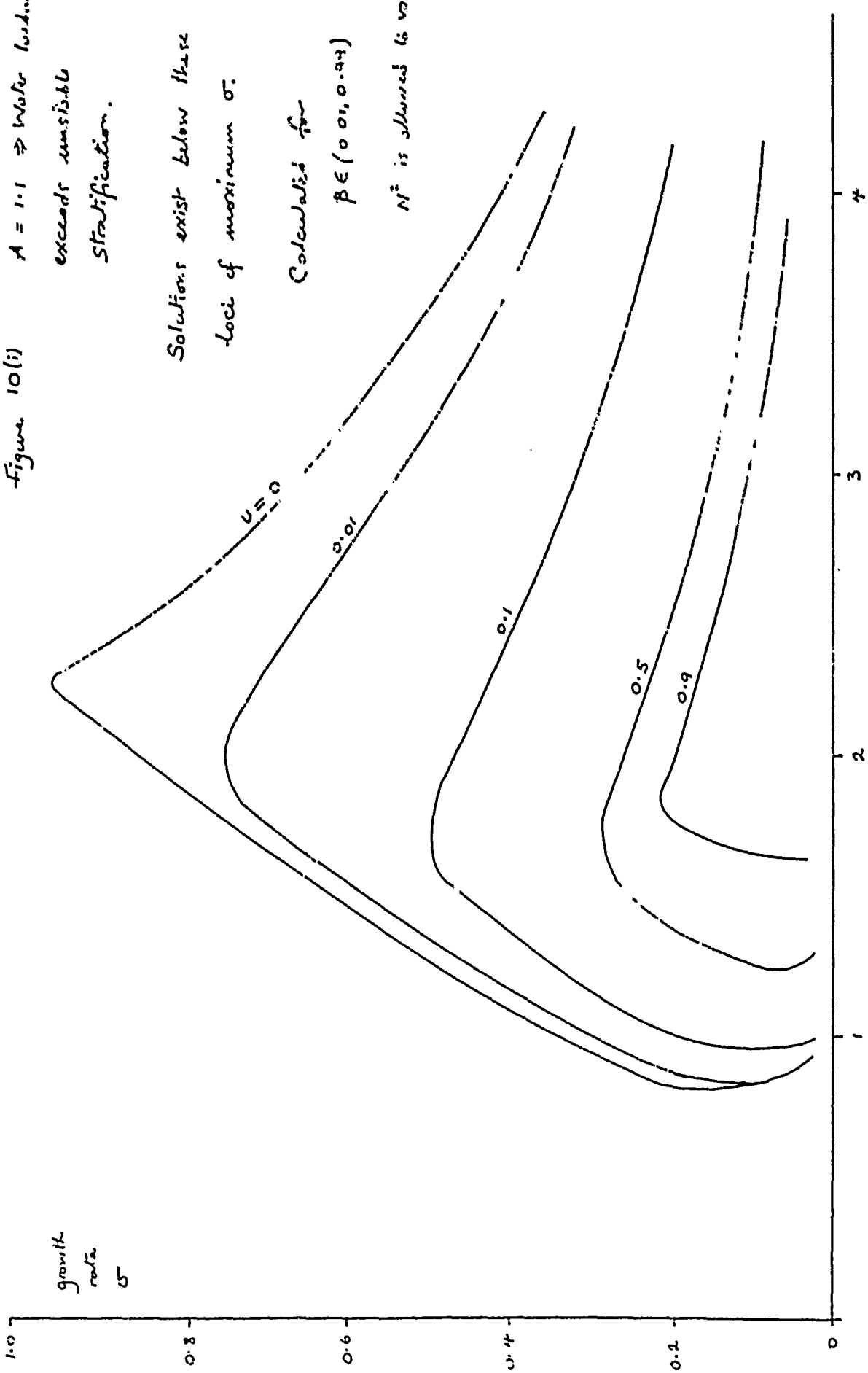


exceeds unstable
stratification.

Solutions exist below these
loci of maximum σ .

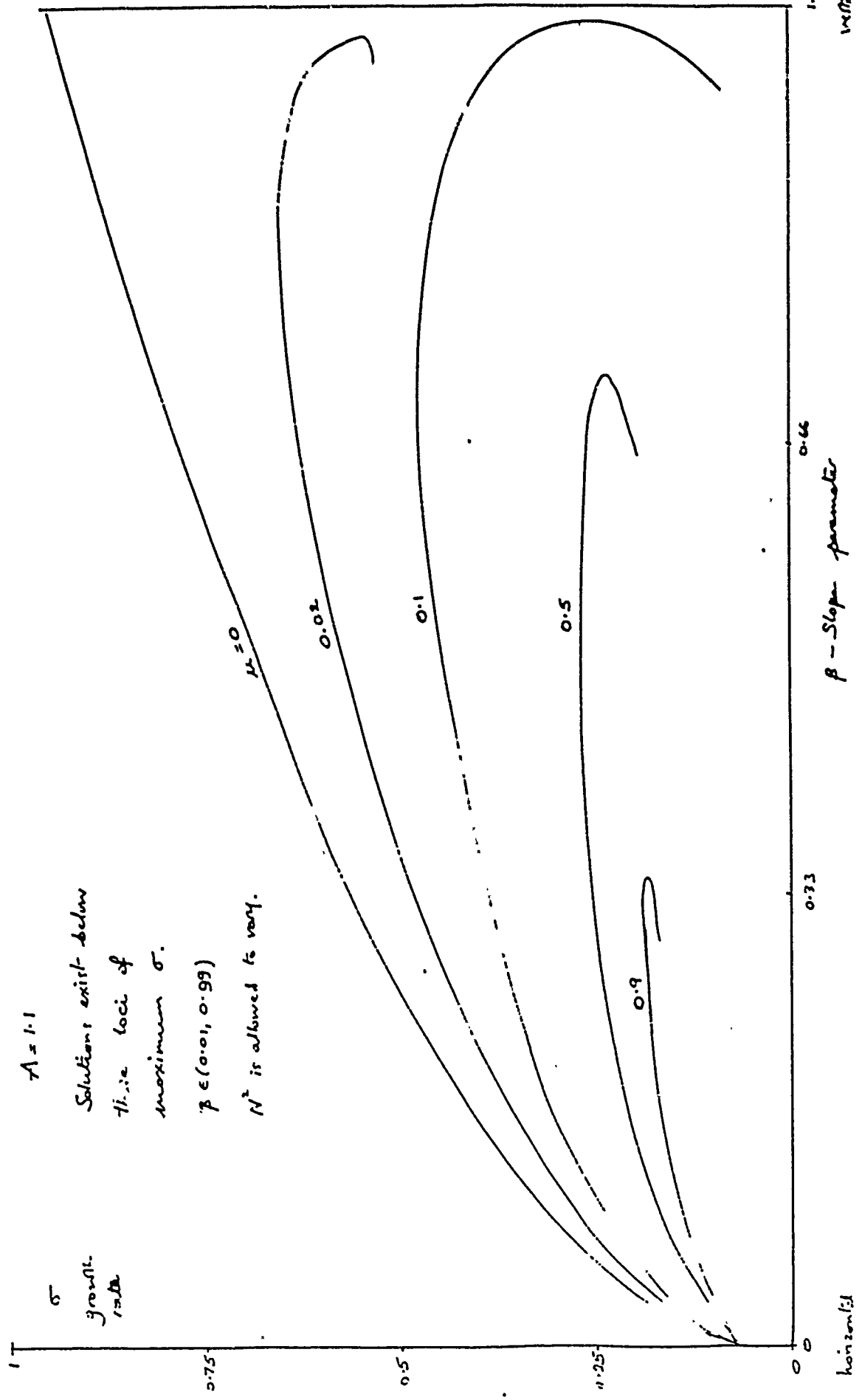
Calculated for
 $\beta E(0.01, 0.94)$

N^2 is allowed to vary.



N^2 ratio of stratification of stellar composition
region to unstable convection region

Figure 10(ii)



$A = 1.1$

Solutions exist below
the loci of
maximum σ^* .

$p \in (0.01, 0.99)$

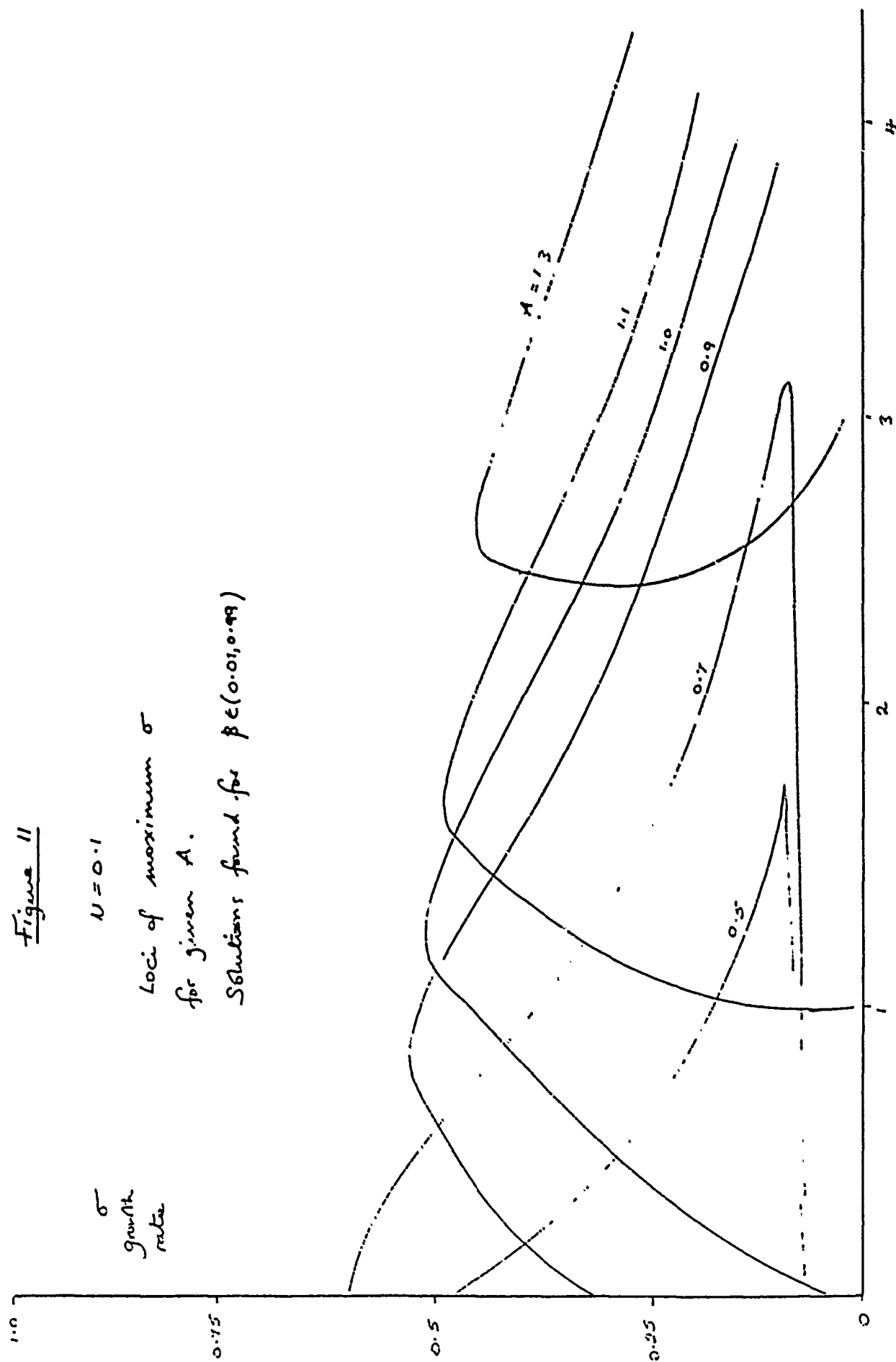
N^2 is allowed to vary.

Figure 11

$$U = 0.1$$

Loci of maximum σ
for given A .

Solutions found for $\beta \in (0.01, 0.99)$

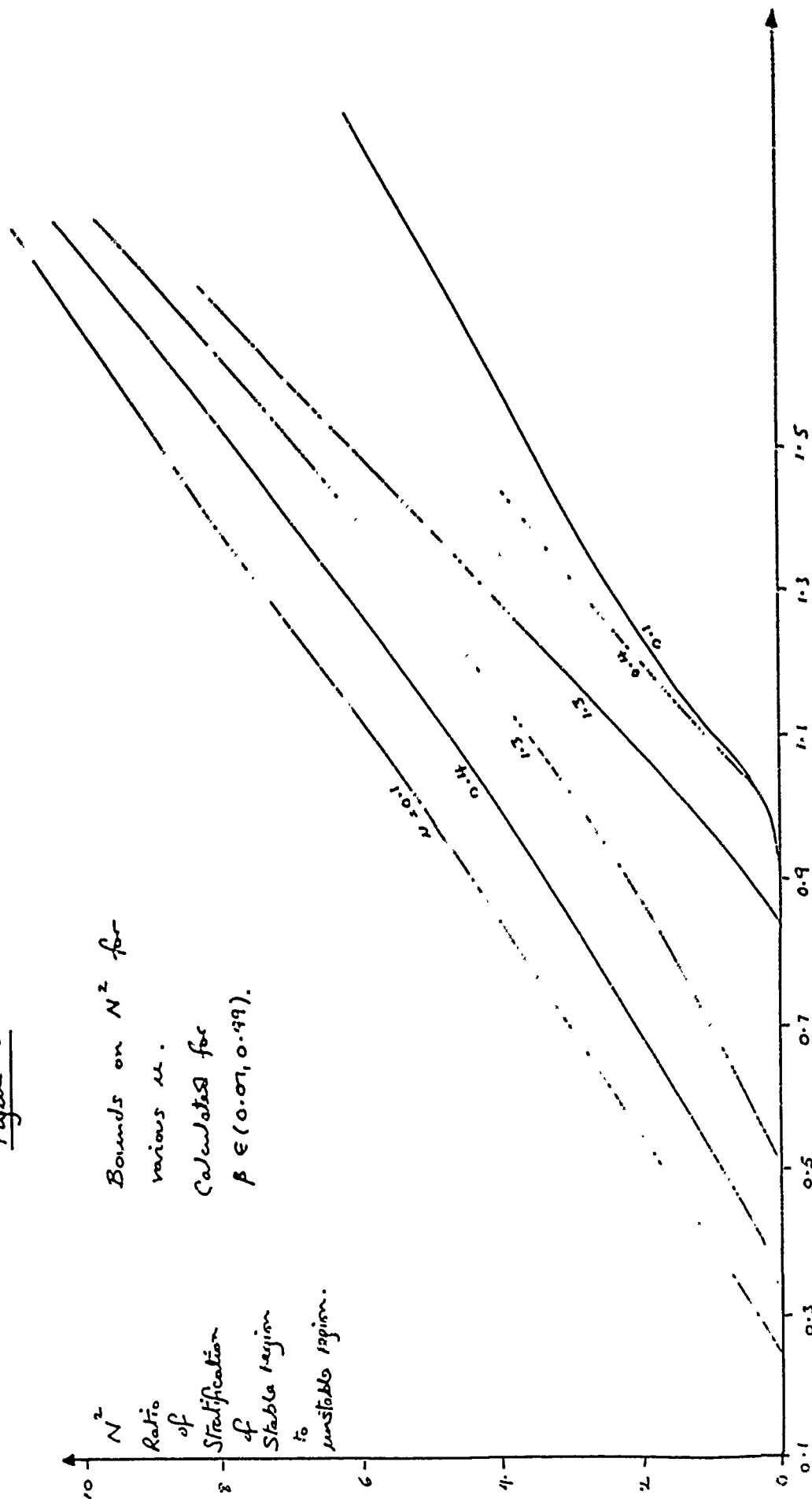


N^2 ratio of stratification of convection
region to condensation region

Figure 12

Bounds on N^2 for
various μ .
Calculated for
 $\beta \in (0.07, 0.49)$.

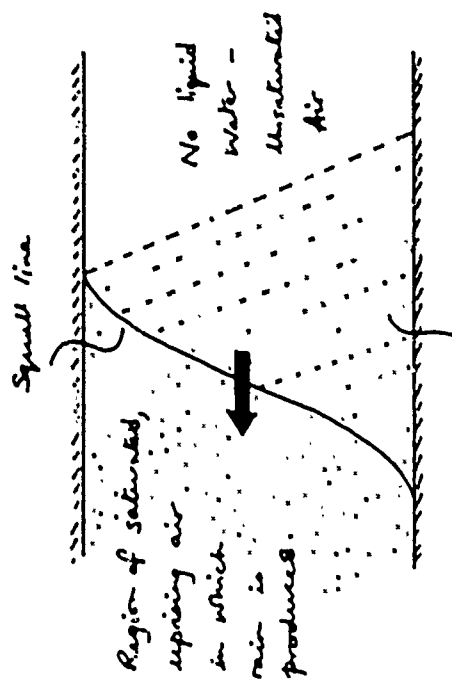
N^2
Ratio
of
Stratification
of
Stable region
to
unstable region.



A - precipitation day

Figure 13

Schematic of squall line
in a vertically bounded domain, in
frame moving with Squall line.



Region of rain falling
out behind squall
line. Unsaturated air
with evaporation.

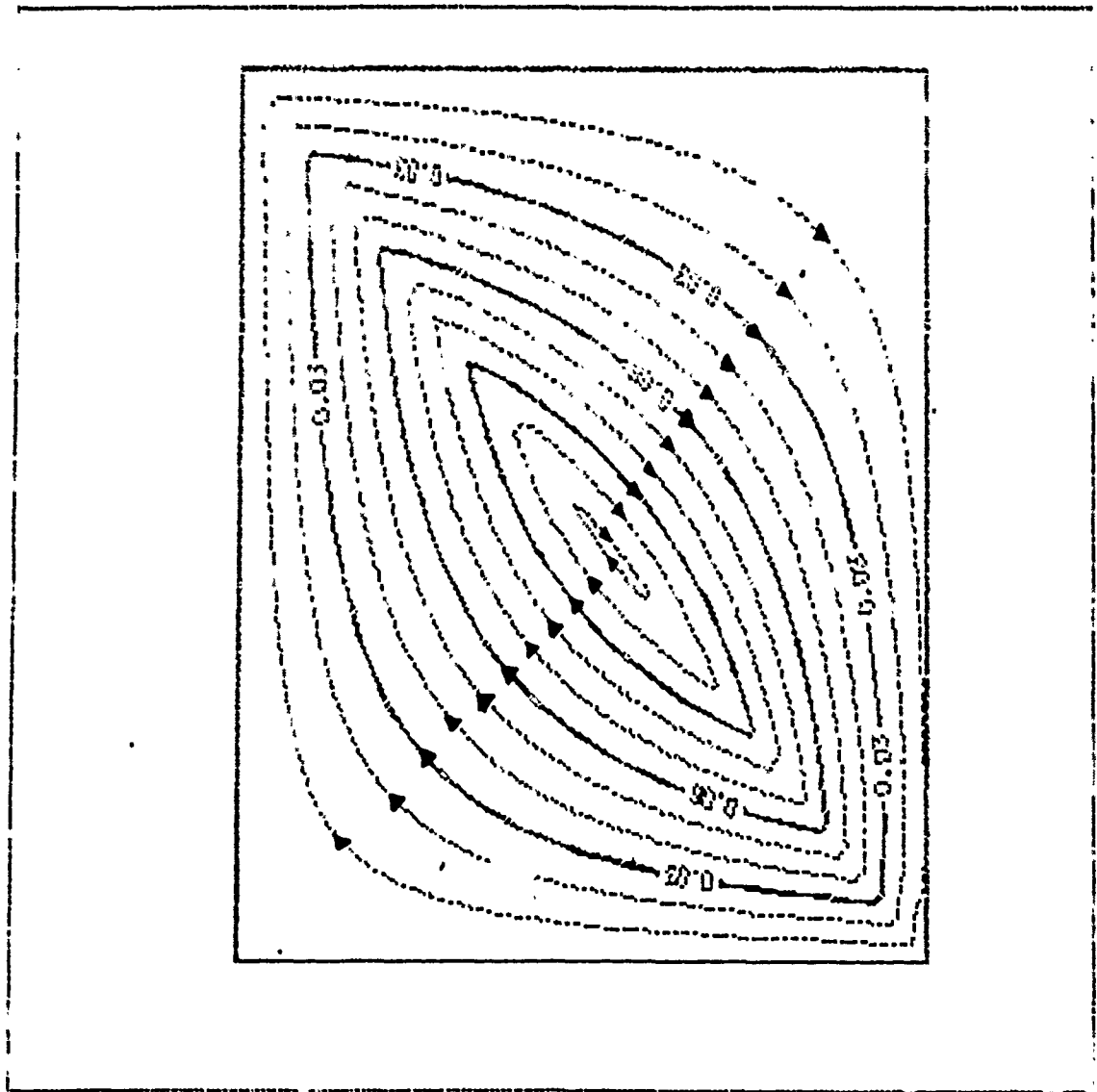


Figure 14

(i)

Streamfunction

solution

(no pressure
matching across
synclinal line.)

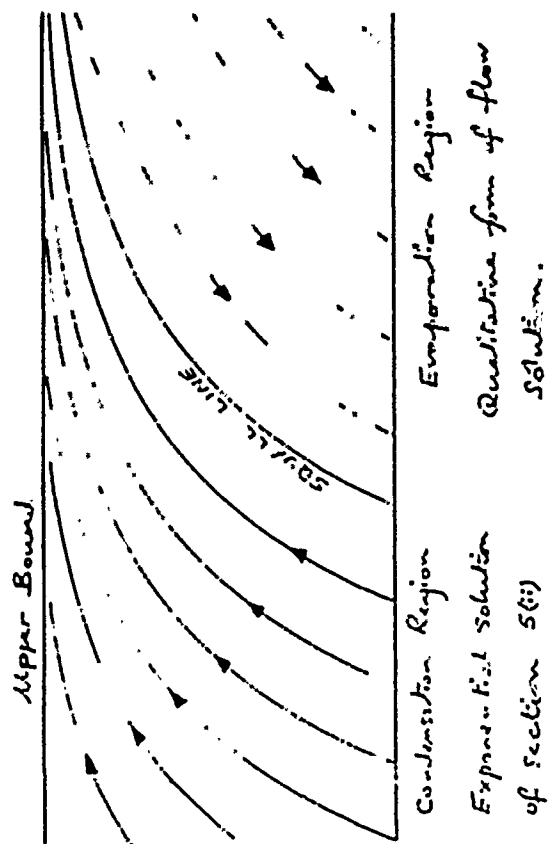
$$\sigma = 0.5$$

$$N^2 = 1$$

$$h = 4$$

(aspect ratio H/L)

Figure 15



DOCUMENT LIBRARY

July 5, 1989

Distribution List for Technical Report Exchange

Attn: Stella Sanchez-Wade
Documents Section
Scripps Institution of Oceanography
Library, Mail Code C-075C
La Jolla, CA 92093

Hancock Library of Biology &
Oceanography
Alan Hancock Laboratory
University of Southern California
University Park
Los Angeles, CA 90089-0371

Gifts & Exchanges
Library
Bedford Institute of Oceanography
P.O. Box 1006
Dartmouth, NS, B2Y 4A2, CANADA

Office of the International
Ice Patrol
c/o Coast Guard R & D Center
Avery Point
Groton, CT 06340

Library
Physical Oceanographic Laboratory
Nova University
8000 N. Ocean Drive
Danla, FL 33304

NOAA/NESDIS Miami Library Center
4301 Rickenbacker Causeway
Miami, FL 33149

Library
Skidaway Institute of Oceanography
P.O. Box 13687
Savannah, GA 31416

Institute of Geophysics
University of Hawaii
Library Room 252
2525 Correa Road
Honolulu, HI 96822

Library
Chesapeake Bay Institute
4800 Atwell Road
Shady Side, MD 20876

MIT Libraries
Serial Journal Room 14E-210
Cambridge, MA 02139

Director, Ralph M. Parsons Laboratory
Room 48-311
MIT
Cambridge, MA 02139

Marine Resources Information Center
Building E38-320
MIT
Cambridge, MA 02139

Library
Lamont-Doherty Geological
Observatory
Columbia University
Palisades, NY 10964

Library
Serials Department
Oregon State University
Corvallis, OR 97331

Pell Marine Science Library
University of Rhode Island
Narragansett Bay Campus
Narragansett, RI 02882

Working Collection
Texas A&M University
Dept. of Oceanography
College Station, TX 77843

Library
Virginia Institute of Marine Science
Gloucester Point, VA 23062

Fisheries-Oceanography Library
151 Oceanography Teaching Bldg.
University of Washington
Seattle, WA 98195

Library
R.S.M.A.S.
University of Miami
4600 Rickenbacker Causeway
Miami, FL 33149

Maury Oceanographic Library
Naval Oceanographic Office
Stennis Space Center
NSTL, MS 39522-5001

Marine Sciences Collection
Mayaguez Campus Library
University of Puerto Rico
Mayaguez, Puerto Rico 00708

REPORT DOCUMENTATION PAGE	1. REPORT NO. WHOI-89-26	2.	3. Recipient's Accession No.
4. Title and Subtitle 1988 Summer Study Program in Geophysical Fluid Dynamics The Influence of Convection on Large-Scale Circulations		5. Report Date July 1989	
7. Author(s) Glenn R. Flierl, Edited by Pamela J. Goulart		8. Performing Organization Rept. No. WHOI-89-26	
9. Performing Organization Name and Address The Woods Hole Oceanographic Institution Woods Hole, Massachusetts 02543		10. Project/Task/Work Unit No.	
12. Sponsoring Organization Name and Address The Office of Naval Research; and The National Science Foundation		11. Contract(C) or Grant(G) No. (C) N00014-82-G-0079 (G) DMS-85-04166	
		13. Type of Report & Period Covered Technical Report	
15. Supplementary Notes This report should be cited as: Woods Hole Oceanog. Inst. Tech. Rept., WHOI-89-26.		14.	
16. Abstract (Limit: 200 words) <p>This summer, the principal lecturer, Kerry Emanuel, presented the fundamentals of atmospheric convection in both dry and moist air, including the dynamical effects of precipitation. He described plumes and the incorporation of moist processes into models of larger scale circulations—tropical cyclones, intraseasonal oscillations, and coupled movements of the air and the sea. The theory of convection has been discussed at Walsh Cottage for many years; the new insights into the role of moisture in the dynamics excited much interest. Other meteorological lectures described results from observations and numerical models. A number of lectures on oceanic convection and results from laboratory experiments presented different perspectives on the way thermal processes generate large scale circulations.</p> <p>As always, staff members and visitors lectured on new developments in a wide range of areas. Abstracts of these lectures are contained in this volume. We were pleased to welcome three speakers, Chris Garrett, Ruby Krishnamurti, and Frank Richter, for a 30th anniversary celebration.</p> <p>At the summer's end, the fellows presented their research in brief lectures with fuller reports contained in this volume. All found interesting topics, in many cases in areas new to themselves, and made progress towards solving the problem.</p> <p>This document should be treated as an unpublished manuscript. The fellows' reports may become part of Ph.D. work or publications. Permission of the author should be obtained if you wish to reference work in this document.</p>			
17. Document Analysis a. Descriptors 1. Geophysical Fluid Dynamics 2. Convection 3. Atmospheric Convection b. Identifiers/Open-Ended Terms c. COSATI Field/Group			
18. Availability Statement Approved for publication; distribution unlimited.		19. Security Class (This report) UNCLASSIFIED	21. No. of Pages 367
		20. Security Class (This report) UNCLASSIFIED	22. Price